# Advances in Mechanical Engineering Research

David E. Malach
Editor

Volume 2

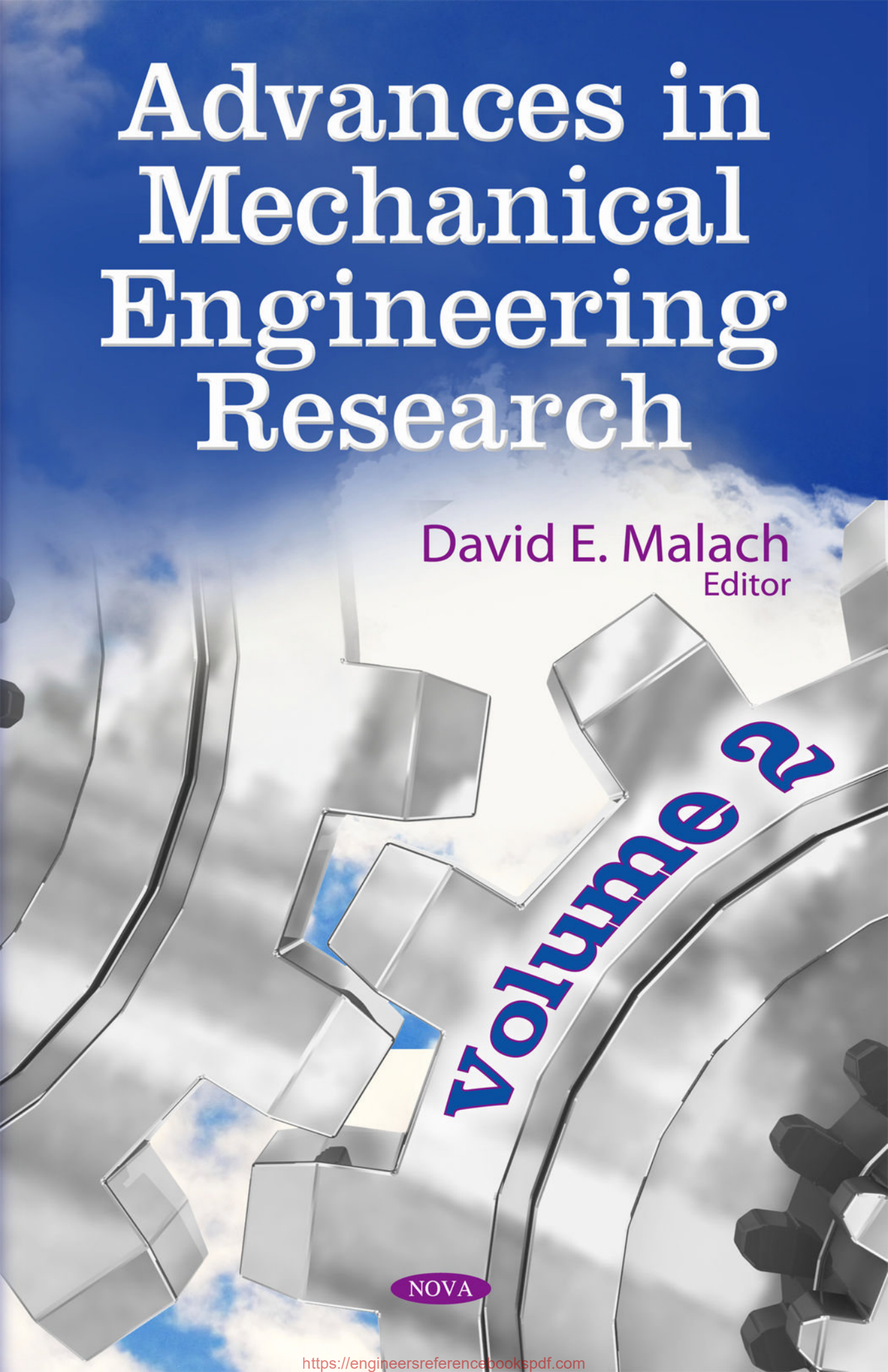

NOVA

# ADVANCES IN MECHANICAL ENGINEERING RESEARCH VOLUME 2

# ADVANCES IN MECHANICAL ENGINEERING RESEARCH

Additional books in this series can be found on Nova's website under the Series tab.

Additional E-books in this series can be found on Nova's website under the E-books tab.

# ADVANCES IN MECHANICAL ENGINEERING RESEARCH
# VOLUME 2

**DAVID E. MALACH**
**EDITOR**


**Nova Science Publishers, Inc.**
*New York*

For permission to use material from this book please contact us:
Telephone 631-231-7269; Fax 631-231-8175
Web Site: http://www.novapublishers.com



Library of Congress Cataloging-in-Publication Data

ISBN: 978-1-61122-393-4 (eBook)

ISSN: 2159-1989

*Published by Nova Science Publishers, Inc.* † *New York*

# CONTENTS

# PREFACE

Mechanical engineering is an engineering discipline that applies the principles of physics and materials science for analysis, design, manufacturing, and maintenance of mechanical systems. This book covers leading-edge research in a cross-section of fields centering on mechanical engineering including current research data on the fracture mechanics of wood and wood-like reinforced polymers; thulium-doped fiber amplifiers; the role of microalloying elements on the microstructure of hot rolled steels; and high-strength titanium base alloys.

Chapter 1 - This chapter discusses the theory of fracture mechanics based on the flat elliptical crack; the derivation of the mixed "mode I - II" - interaction equation, with the relations between the mode I and mode II stress intensities and energy release rates, based on an orthotropic-isotropic transformation of the Airy stress function; the derivation of the softening curve with the explanation of the measurements; the derivation of the power law; the energy method of notched beams and of joints loaded perpendicular to the grain; and the necessary rejection of the applied crack growth models and fictitious crack models.

Chapter 2 - Magnetic resonance imaging (MRI) has developed into one of the most versatile techniques in clinical imaging and biomedical research by providing non-invasively high resolution, three-dimensional anatomical and contrast-enhanced images of living tissue. The two most common groups of contrast-enhancing agents are gadolinium-based complexes and magnetic nanoparticles. Both types of contrast agents shorten locally the relaxation time of bulk water protons via rapid exchange of water molecules employing inner- or outer-sphere magnetic interactions to provide $T_1$-, $T_2$-, or $T_2$*-based contrast enhancement. The quest for disease-specific and individualized approaches to imaging requires contrast agents with a relatively high sensitivity and has propelled the development of novel functional or target-specific agents. With this aim, the shift properties of paramagnetic complexes other than gadolinium have been exploited for designing new types of contrast agents with highly specific reporter functionalities. The particularly beneficial chemical shift properties of thulium(III) and their thermal sensitivity, therefore, have stimulated the development of novel thulium(III)-based contrast agents for MR imaging. An important group of such agents is formed by those that generate contrast based on the transfer of saturated magnetization from the contrast agent or from water molecules interacting with a lanthanide shift reagent to the bulk water (chemical exchange saturation transfer (CEST) agents). Magnetization saturation is created using either exchangeable protons of the paramagnetic thulium(III) chelate complex (paraCEST agents), or using water molecules that interact with a thulium shift reagent encapsulated in a liposomal carrier (lipoCEST agents). Various strategies have already been devised to modulate the CEST effect in response to a physiologically meaningful parameter,

such as pH, metabolite concentration, or enzyme activity. MR thermometry is another important target in the development of novel thulium(III)-based contrast agents. Such temperature mapping is based on the strong temperature dependence of the hyperfine chemical shifts of thulium(III) complexes, which can be measured in-vivo with different MR techniques. Upcoming applications of thulium-based contrast agents include disease-specific targeted contrast agents and theranostic agents suitable for image-guided drug delivery.

Chapter 3 - Due to the tremendous increase in communication traffic in recent years, more and more efforts in research have been directed towards developing highly efficient broad-band fiber amplifiers that will fully exploit the low-loss band of silica fibers in order to increase the transmission capacity of wavelength-division multiplexing (WDM) networks. These broad-band amplifiers must be able to amplify the new short wavelength band (S-band) in addition to the existing C- and L-bands. Thulium-doped fiber amplifiers (TDFAs) are a promising candidate for the S-band amplification because the amplification bandwidth of the TDFA is centered at 1470 nm, which falls within the S-band. This chapter reviews the structure and amplification mechanism of various TDFAs. The mathematical model of single pass and double pass TDFAs is also described in detail. A development of hybrid S-band optical amplifier using a TDFA and a fiber Raman amplifier is also presented at the end of this chapter. The wide-band hybrid amplifier is suitable for application in S-band optical telecommunication systems.

Chapter 4 - Some micro elements are very sensitive to long time creep rupture properties. It is well known that harmful impurities such as S, O, Bi, Sb and Pb diffuse to local areas such as grain boundaries, interface between inclusion and matrix and surface of grain boundary cavity during creep exposure, and accelerate nucleation and growth of grain boundary cavity and crack, which lead to premature and low ductility grain boundary fracture. On the contrary, beneficial trace and microalloying elements such as B, Zr, Ca, Ti, V, Nb and Ta counteract the injurious elements by the grain boundary, the interface and the surface refinements, which improve properties of local areas, and prevent premature and low ductility fracture. In this paper actual effects of these microalloying and trace elements on long time creep rupture properties of heat resistant steels are reported. In addition new microalloying methods preventing grain boundary fracture are introduced.

At National Institute for Materials Science Japan long time creep rupture data including longer than 100,000h have been obtained on several heats of principal heat resistant materials. The long time creep rupture life and ductility show a considerable amount of scattering among several heats of a same kind of steels, and it was thought that the scattering might include new effects of microelements on long time creep rupture properties, since the scattering is difficult to explain by using well-known effects. Experimental results showed that main cause of the scattering is difference in microelements. It was indicated that very small amount of Mo and N in solid solution causes the scattering for carbon steels, and also trace of Al content in austenitic stainless steels causes long time creep rupture strength drop. Mo and soluble N atoms in the steels diffuse to dislocations, and the segregated pairs of the elements immobilizes dislocations. The Al in 12Cr and austenitic stainless steels precipitates as AlN at grain boundaries and accelerates nucleation and growth of creep cavities.

It is found that very small amount of B and N in austenitic stainless steels diffuse to creep cavity surface and cover creep cavity surface by segregation of B or precipitation of BN when S is removed almost completely. The segregated B and precipitated BN decrease surface diffusion rate of creep cavity and also creep cavity growth rateremarkably. The B segregates

and also BN precipitates to creep cavity surface autonomously during creep exposure and provide the steels with self-healing function for the creep damage. The self-healing of creep cavity by B segregation and BN precipitation is a new and promising research area for improving creep rupture properties.

Chapter 5 - The mitigation of seismic damage to masonry housing structures is considered in this study. Traditional high-damping rubber bearings (HDRBs), two hybrid systems involving the use of HDRBs and shape memory alloy (SMA) wire, and fiber-reinforced bearings (FRBs) are numerically modeled as base isolators for a typical confined masonry, two-family house. The house is elastically modeled using multiple degrees-of-freedom (MDOF) that are based on experimental data collected through ambient vibration testing. Fuzzy logic is utilized to numerically model dynamic behavior of the HDRBs, SMA wire, and FRBs based on experimental and analytical data. The earthquake used for optimization of each isolation system is generated to match the design spectrum based on Chilean code through means of RSPMatch2005, an algorithm thatmodifies historic ground motions in the time domain through incorporation of wavelets. A suite of ground motions is used to evaluate seismic performance of the structure that is augmented with each of the isolation systems mentioned; results are compared to the performance of the traditionally-constructed structure. Simulations indicate that each of the isolation systems can be effective in reducing the structural shear, interstory drift, and floor acceleration of the structure compared to the fixed-base case, although the HDRB-only system exhibits superior performance overall.

Chapter 6 - In this work, a comparative study of some of the most important effects of the diverse microalloying elements on austenite and ferrite microstructure of hot rolled microalloyed steels is carried out. Microalloying elements dissolved in austenite have a considerable effect on microstructure, but the main reason for the presence of these elements in microalloyed steels lies in their precipitation. Titanium is the most effective element to control grain growth at high reheating temperatures and a hypostoichiometric Ti/N ratio close to 2 is recommended. Aluminum can be useful to control grain growth at moderate temperatures, but it is found that its addition to Ti steels can be detrimental and promote abnormal grain growth below 1100 ºC. The fine initial austenite grain size of Ti steels ensures a fast recrystallization kinetics and a minor reduction of austenite grain size during hot rolling. Besides, the pinning forces exerted by TiN particles precipitated at high temperatures are about two orders of magnitude lower than the driving forces for recrystallization. This explains why the austenite in Ti-steels hardly experiences hardening during rolling. On this regard, niobium, even at very low contents, is the most effective microalloying element to inhibit static recrystallization of austenite during hot rolling, due to the adequate precipitation temperature range at deformation temperatures and the strong pinning effect of niobium carbonitrides. The incomplete recrystallization of austenite at temperatures below the no-recrystallization temperature ($T_{nr}$) causes the progressive strengthening of austenite, which can be characterized by the magnitude defined as “accumulated stress” ($\Delta\sigma$). It has been found that the accumulated stress measured at the end of hot rolling and prior to the austenite→ferrite transformation informs about the density of potential nucleation sites for ferrite and consequently the chances to refine the final ferritic grain microstructure. Finally, it has also been found that the preferential nucleation of intragranular ferrite on particles such as vanadium carbonitrides (precipitated at lower temperatures than NbCN) makes an important contribution to enhance the ferrite grain refinement. In this paper the effect of the different

types of microalloying elements and kinds of precipitates is discussed in terms of the values of different aspects such as pinning and driving forces, size of precipitates, activation energies or diffusion coefficients.

Chapter 7 - Vacuum casting is widely used as an investment casting method for small parts of complex geometry. Selection of casting conditions for acquiring sound castings is not a trivial process. In modern casting machines, the application of pressure directly after completion of melt pouring is used to ensure proper filling of the very fine details of the casting tree.The present work concerns examination of casting conditions of brass on a modern vacuum-pressure casting machine, in order to reveal their influence on part quality. A parametric investigation was carried out with respect to pressure in the upper chamber and vacuum in the lower chamber of the machine. The obtained cast samples were examined with optical microscopy in order to identify possible defects, while image analysis was used in order to quantify porosity in each sample.In addition, casting simulation software was exploited to enhance process knowledge. The major issue in obtaining realistic results from simulation was the determination of the interfacial heat transfer coefficient (HTC). This was achieved using experimental cooling curves, obtained with K-type thermocouples during casting under pre-defined conditions. The heat transfer coefficient, once estimated in eachcase from the corresponding simulations, was, then, used in further typical casting scenarios. These scenarios were analyzed with commercially available casting simulation software. The purpose was to determine the influence of casting parameters on mould filling time, porosity and solidification time.

Chapter 8 - The improvement of the strength and plasticity in titanium alloys has attracted considerable research interest. Strategies have been developed to improve their mechanical properties (strength, ductility or toughness) by introducing heterogeneities of multiple length scales into the microstructure, or called bimodal microstructure. In this chapter, it will show that the recently developed titanium alloys with multiple length-scale microstructure can be easily obtained in bulky form through simple and inexpensive casting techniques. These advanced titanium alloys exhibit superior mechanical properties, including high strength of 2000 − 2700 MPa and large plasticity up to 15%. The microstructure as well as the deformation and fracture behavior will be described in nanostructured/ultrafine-grained titanium alloys with different microstructure features. Of special interest is the interdependence between solidification conditions, alloy and microstructure design by composition variation *via* micro-alloying and the resulting mechanical properties and deformation mechanisms of the titanium alloys with multiple length-scale microstructure.

Chapter 9 - Microalloying elements are generally Nb, V and Ti which are added to the steel either separately or in combination up to 0.1 wt. % primarily because of their tendency to form fine dispersions of alloy carbides and carbonitrides in either austenite or ferrite. It has also been found that the microalloying elements such as Nb and V increase the hardenability of austenite if they are in solid solution. In the recent work of Nb microalloyed weather resistant steel (C: 0.1%), Mn: 0.9%), increase in soaking temperature from 1000 to $1100^0$C has increased the YS, UTS and hardness of the rolled steel at a given rolling temperature and deformation due to dissolution of Nb (C, N) in the austenite which results in replacement of a part of pearlite into granular bainite. Increasing the rolling deformation from 25 to 50% has increased the YS but not UTS markedly. For $1100^0$C soaking, rolling 25% at 800, 900 or $1000^0$C results in much lower YS than that of simply air cooled samples. The YS is also lowered due to 50% reduction at $1000^0$ and $900^0$C. The inferior YS due to controlled rolling,

though surprising, is attributed to lower amount of granular bainite. The optical microstructure after $1000^0$C soaking is ferrite-pearlite at 900 and 800C rolling temperatures whereas in addition to ferrite-pearlite, acicular ferrite/granular bainite are also observed after rolling at $740^0$C. After soaking at $1100^0$C, considerable amount of granular bainite has formed for all the rolling temperatures due to increase in hardenability. The TEM micrographs show ferrite and pearlite at 800 and $900^0$C rolling temperatures and acicular ferrite also at $740^0$C rolling after $1000^0$C soaking. On the other hand, presence of considerable amount of acicular ferrite and M/A (martensite – austenite) constituent is taken as an indication of granular bainite in addition to ferrite and pearlite after soaking at $1100^0$C and rolling at 1000-$800^0$C.

The properties of Nb + V microalloyed weather resistant steel (C: 0.2%, Mn: 1.0%) have also been studied after the steel was deformed by rolling 50% at 900, 800 and $700^0$C. This study gave some very interesting results. The properties at $1100^0$C especially the UTS and % EL, were vastly superior in comparison to the $1000^0$C soaking for a given rolling temperature and 50% deformation. The variation in all the properties, YS, UTS, Hv or %EL with respect to rolling temperature was insignificant in comparison to those observed after soaking at $1000^0$C. While the enhancement in properties is attributed to the presence of martensite (though termed M/A constituent) along with ferrite that contains fine precipitates of Nb, V (C, N),the virtual consistency of these properties is also due to lack of any difference in the microstructure of the as rolled products.

In view of the above, controlled rolling to be effective, higher soaking temperature (≥ 1100C) lower rolling temperature (≥ $800^0$C) and higher rolling reduction (≥ 50%) are recommended to take maximum advantage of the microalloying additions.

Chapter 10 - Consequences of minor earthquakes on masonry stone stoves in Scandinavia (Northern Europe) are reviewed. Emphasis is laid on the earthquakes of June 23, 1882 and November 4, 1898 in the vicinity of the Bay of Bothnia. Cracked stoves posed an indirect earthquake hazard through increasing the proneness to fires. Fire prevention measures were therefore necessary also after minor earthquakes.

Chapter 11 - The recent development of non-contact digitizing systems dedicated to dental applications has introduced innovative procedures, based on Reverse Engineering techniques, for the production of artificial teeth. Starting from the reconstructed 3D model of each tooth, first the mold CAD model is created and then the milling path is computed for machining. At the moment there is no indication of the quality of such innovative procedure, so it is investigated in this chapter by evaluating the deviation introduced by each manufacturing step. For this purpose, a new methodology for quality control, based on the use of Reverse Engineering contactless devices in inspection activities, is proposedand applied to a machined mold for the production of molars and premolars. The error of mold machining is computed by comparing the original mold CAD model with the scan data. Then some teeth, produced by the same mold, are selected as manufactured samples. The samples are digitized by means of two different non-contact scanners before and after finishing. Each sample is compared with its original CAD model to compute molding error. Scan data of such samples allow us to evaluate the deviations introduced by each operation. A comparison of two optical digitizers is based on the results of this study and economic considerations related to costs and times are also included.

In: Advances in Mechanical Engineering Research. Volume 2 ISBN: 978-1-61761-984-7
Editor: David E. Malach 

*Chapter 1*

# FRACTURE MECHANICS OF WOOD AND WOOD-LIKE REINFORCED POLYMERS

***T.A.C.M. van der Put****
TU-Delft, Civil Engineering and Geosciences, Timber Structures and wood technology,
PO Box 5048, NL-2600 GA Delft, Netherlands

## ABSTRACT

This chapter discusses the theory of fracture mechanics based on the flat elliptical crack; the derivation of the mixed "mode I - II" - interaction equation, with the relations between the mode I and mode II stress intensities and energy release rates, based on an orthotropic-isotropic transformation of the Airy stress function; the derivation of the softening curve with the explanation of the measurements; the derivation of the power law; the energy method of notched beams and of joints loaded perpendicular to the grain; and the necessary rejection of the applied crack growth models and fictitious crack models.

## 1. INTRODUCTION

The development of the inexact singularity approach of fracture mechanics is at its dead end because it is not possible to describe real failure at the crack boundary and to replace the real failure criterion by general energy conditions as is applied now, and the method remains empirical. Therefore, the theoretical approach based on the elliptical flat crack has to be followed, leading to the possibility to derive and explain the empirical mixed "mode I - II" - interaction equation.

As a result of this derivation, the right fracture energy and theoretical relation between mode I and II stress intensities, and energy release rates are obtained. Based hereupon, the derivation of the orthotropic mode I strain softening curve is possible. It appears that real softening does not exist. It is a matter of unloading of the specimen outside the fracture zone

* Tel: +31 152851980, E-mail: vanderp@xs4all.nl

where the ultimate stress remains. This ultimate stress on the intact area of the fracture plane determines any moment the strength of every point of the softening curve. The area under the load-displacement softening curve gives the total external work on the test specimen and not the fracture energy. The fracture energy follows from half this area which is equal to the critical strain energy release rate at the initial crack extension. For wood, this correctly is applied for mode II. For mode I however, as for other materials, wrongly the total area is regarded as fracture energy, a factor 2 too high. However, this is compensated at softening by the apparent too low specific fracture energy due to a small crack joining mechanism when the ultimate state of the ligament of the test-specimen is reached. Post fracture behaviour thus is shown to be different from initial macro crack extension. The derivations lead to an adaption of the energy approach for fracture of square notched beams and joints loaded perpendicular to the grain,providing a simple design method. It further is shown that nearly all fracture mechanics models applied to wood, as the Dugdale model, the fictitious crack model and the crack growth models (which should follow from exact molecular deformation kinetics), are questionable and have to be replaced by the developed theory.

## 2. THE BOUNDARY VALUE PROBLEM OF FRACTURE MECHANICS

### 2.1. Basic Airy Stress Function

For the solution of the boundary value problem of notches in wood, the orthotropic Airy stress function is based on the spreading out of the reinforcement to act as a continuum, satisfying the equilibrium, compatibility and strength conditions. This behaviour only is possible by interaction of reinforcements through the matrix. Thus also the equilibrium conditions and strength criterion of the matrix, as determining element, have to be satisfied. This only is possible to solve the Airy stress function for the stresses in the isotropic matrix and then to derive the total (orthotropic) stresses from this solution. None of the applied solutions (given, e.g., in chapter 2.1 of [6]) satisfies this requirement. This analysis in total stresses is as follows:

The stress-strain relations for the two-dimensional flat crack problem are:

$$\varepsilon_x = c_{11}\sigma_x + c_{12}\sigma_y\,; \quad \varepsilon_y = c_{12}\sigma_x + c_{22}\sigma_y\,; \quad \gamma_{xy} = c_{66}\tau_{xy}\,. \tag{2.1}$$

This can be written:

$$\varepsilon_x = \sigma_x / E_x - \upsilon_{21}\sigma_y / E_y\,; \quad \varepsilon_y = -\nu_{21}\sigma_x / E_y + \sigma_y / E_y\,; \quad \gamma_{xy} = \tau_{xy} / G_{xy} \tag{2.2}$$

The Airy function follows from:

$$\sigma_x = \frac{\partial^2 U}{\partial y^2}\,; \quad \sigma_y = \frac{\partial^2 U}{\partial x^2}\,; \quad \tau_{xy} = -\frac{\partial^2 U}{\partial x \partial y}\,, \tag{2.3}$$

satisfying the equilibrium equations:

$$\frac{\partial \sigma_x}{\partial x}+\frac{\partial \tau}{\partial y}=0 \text{ and } \frac{\partial \tau}{\partial x}+\frac{\partial \sigma_y}{\partial y}=0 \tag{2.4}$$

Substitutions of eq.(2.1): $\varepsilon_x = c_{11}\frac{\partial^2 U}{\partial y^2}+c_{12}\frac{\partial^2 U}{\partial x^2}$, etc. in the compatibility condition:

$$\frac{\partial^2 \varepsilon_x}{\partial y^2}+\frac{\partial^2 \varepsilon_y}{\partial x^2}=\frac{\partial^2 \gamma_{xy}}{\partial x \partial y}, \tag{2.5}$$

gives:

$$c_{22}\frac{\partial^4 U}{\partial x^4}+\left(c_{66}+2c_{12}\right)\frac{\partial^4 U}{\partial x^2 \partial y^2}+c_{11}\frac{\partial^4 U}{\partial y^4}=0 \tag{2.6}$$

This equation also can given as:

$$\left(\frac{\partial^2}{\partial x^2}+\alpha_1\frac{\partial^2}{\partial y^2}\right)\left(\frac{\partial^2}{\partial x^2}+\alpha_2\frac{\partial^2}{\partial y^2}\right)U=0 \tag{2.7}$$

where $\alpha_1\alpha_2 = c_{11}/c_{22}$ and $\alpha_1+\alpha_2=\left(c_{66}+2c_{12}\right)/c_{22}$. Introducing 3 sets of polar coordinates for this case, $x+iy=re^{i\theta}$, $x+iy/\sqrt{\alpha_1}=re^{i\theta_1}$, $x+iy/\sqrt{\alpha_2}=re^{i\theta_2}$, eq.(2.7) has e.g. elementary solutions as: $r_1^{\pm m}\cos(m\theta_1)$, $r_1^{\pm m}\sin(m\theta_1)$, $r_2^{\pm m}\cos(m\theta_2)$, $r_2^{\pm m}\sin(m\theta_2)$, leading to:

$$\left\{\sigma_r,\sigma_\theta,\sigma_{r\theta}\right\}=\frac{K_A}{\left(2\pi r\right)^m}\left\{f_1(\theta),f_2(\theta),f_3(\theta)\right\} \tag{2.8}$$

in the vicinity of a notch root as stress singularity at $r = 0$,

As solution, always only smaller powers than $m = 0.5$ are found, showing the (isotropic) singularity approach with the power $m = 0.5$ to be not a real solution for an orthotropic material. Thus the singularity approach only may apply for the stresses of the isotropic wood-matrix. Wood acts as a reinforced material. Lignin is isotropic and hemicellulose and cellulose are transversely isotropic, which means that only one stiffness factor in the main direction has an n-fold higher stiffness in proportion to the higher stiffness of the reinforcement with respect to the matrix. Thus wood material can be treated to contain a shear-reinforcement and a tensile reinforcement in the main direction and eq.(2.9) applies for equilibrium of the matrix stresses:

$$\frac{\sigma_x}{n_1}=\frac{\partial^2 U}{\partial y^2};\quad \sigma_y=\frac{\partial^2 U}{\partial x^2};\quad \frac{\tau_{xy}}{n_6}=-\frac{\partial^2 U}{\partial x\partial y}, \tag{2.9}$$

Instead of using the matrix stresses and the matrix stiffness, the n-fold higher total stresses and n-fold higher stiffness can be used to give the same compatibility condition (thus the same condition for the matrix and reinforcement). Inserting the total stresses in the compatibility equation, eq.(2.5), gives:

$$c_{22}\frac{\partial^4 U}{\partial x^4}+\left(n_6 c_{66}+(1+n_1)c_{12}\right)\frac{\partial^4 U}{\partial x^2\partial y^2}+n_1 c_{11}\frac{\partial^4 U}{\partial y^4}=0 \tag{2.10}$$

For the isotropic matrix is: $n_1 c_{11}/c_{22}=1$ and $(n_6 c_{66}+(1+n_1)c_{12})/c_{22}=2$ giving:

$$\frac{\partial^4 U}{\partial x^4}+2\frac{\partial^4 U}{\partial x^2\partial y^2}+\frac{\partial^4 U}{\partial y^4}=\nabla^2(\nabla^2 U)=0 \tag{2.11}$$

and

$$n_1=\frac{c_{22}}{c_{11}}=\frac{E_x}{E_y};\quad n_6=\left(2-\frac{c_{12}}{c_{22}}-\frac{c_{12}}{c_{11}}\right)\cdot\frac{c_{22}}{c_{66}}=\left(2+\nu_{21}+\nu_{12}\right)\cdot\frac{G_{xy}}{E_y} \tag{2.12}$$

This orthotropic-isotropic transformation of the Airy stress function and the calculation method based on the matrix stresses is used in the following.

## 2.2. The Elliptical Flat Crack Solution

As shown above, the singularity approach does not apply for the orthotropic case andalso prevents the derivation of areal failure criterion. Instead of such a criterion, critical values are assumed of, e.g., the strain energy density, or the maximal principal stress, or a non local stress function, all at a distance away from the crack tip, thus away from the fracture site. A realfailure criterion only can be based on the real ultimate stress in the material which occurs near the crack-tip boundary. A real physical possible crack form is the flat elliptical crack. When “flow” occurs around the crack tip, the ultimate strain condition at the crack-boundary determines the extension of this flow area. The elastic-plastic boundary then acts as an enlarged crack boundary with the “flow”-stress as ultimate elastic stress for the linear elastic fracture mechanics calculation.

### *2.2.1. The Elliptic Hole in an Infinite Region*

The classical way of analyzing the elliptic crack problem is to use complex variables and elliptic coordinates. The Airy stress function can be expressed in terms of two analytic

functions [1], of the complex variable z (= x + iy) and the transformation to elliptic coordinates in Figure 2.1, gives:

$z = x + iy = c \cdot \cosh(\xi + i\eta)$ or: $x = c \cdot \cosh(\xi) \cdot \cos(\eta)$; $y = c \cdot \sinh(\xi) \cdot \sin(\eta)$.

For an elliptic hole, $\xi = \xi_0$, in an infinite region with uniaxial stress $p$ at infinity in a direction inclined at $\beta$ to the major axis Ox of the ellipse, the Airy stress function $U$, satisfying $\nabla^2(\nabla^2 U) = 0$, and satisfying the conditions at infinity and at the surface $\xi = \xi_0$, showing no discontinuity of displacement, thus being the solution, is given in [2] and applied in [1]. Determining for the strengthis the tangential stress $\sigma_t$ at the crack surface $\xi = \xi_0$ due to a stress $p$ at an angle $\beta$(of Figure 2.3) to the crack

$$\sigma_t = \frac{p(\sinh(2\xi_0) + \cos(2\beta) - \exp(2\xi_0) \cdot \cos(2(\beta - \eta))}{\cosh(2\xi_0) - \cos(2\eta)} \tag{2.13}$$

eq.(2.13) can be extended for two mutual perpendicular principal stresses $p_1$ and $p_2$ (see Figure2.3) by a simple addition leading to eq.(2.23) below.

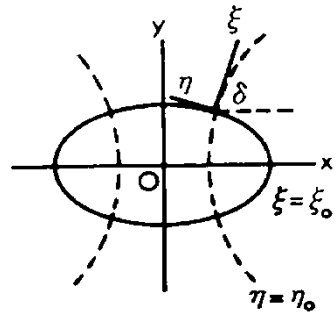


Figure 2.1 - Elliptic hole and coordinates.

### *2.2.2. The Mathematical Flat Crack Solution*

For stresses in the wood-matrix, the results of the limit case of the elliptical notch with $\xi_0$ approaching zero should be comparable with the results of the mathematical flat crack of the singularity method. To obtain the singularity equations, new coordinates $X$, $Y$ with the origin in the focus of the ellipse are necessary (see Figure 2.2). Thus:

$$X = x - c = c(\xi^2 - \eta^2)/2, \quad Y = y = c\xi\eta \tag{2.14}$$

or in polar coordinates:

$$r = \left(X^2 + Y^2\right)^{0.5}, \; X = r \cdot \cos(\theta), \; Y = r \cdot \sin(\theta) \tag{2.15}$$

and from eq.(2.14):

$$\xi^2+\eta^2=2\left(X^2+Y^2\right)^{0.5}/c=2r/c \tag{2.16}$$

$$\xi=\sqrt{2r/c}\cdot\cos\left(\theta/2\right),\quad \eta=\sqrt{2r/c}\cdot\sin\left(\theta/2\right),\quad \eta/\xi=\tan\left(\theta/2\right)=\tan\left(\delta\right) \tag{2.17}$$

To obtain the singularity, $\xi_0=0$ is inserted in the general solution of the elliptic Airy stress function, [1]. Then the tangential stress $\sigma_\theta$ along a crack boundary $r_0$, due to a stress p at infinity at an angle $\beta$ with the notch is:

$$\left(8r_0/cp^2\right)^{0.5}\sigma_\theta=-3\sin\left(\theta/2\right)\cos^2\left(\theta/2\right)\sin\left(2\beta\right)+2\cos^3\left(\theta/2\right)\sin^2\left(\beta\right) \tag{2.18}$$

for a small value of $r_0$, so that all terms containing not the factor $r_0^{-0.5}$ are negligible. For the, for wood always applied, singularity method, the flat crack in the grain direction is supposed to propagate in that direction. Thus $\theta$ = 0 and eq.(2.18) becomes:

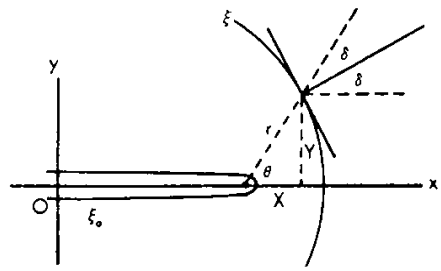


Figure 2.2. Confocal coordinates.

$$\left(8r/cp^2\right)^{0.5}\sigma_\theta=2\sin^2\left(\beta\right) \tag{2.19}$$

with $\sigma_r=\sigma_\theta$ and $\tau_{r\theta}=\sigma_\theta$ cotg($\beta$). Mode I failure $\sigma_\theta=\sigma_t$ occurs when $\beta=\pi/2$. Thus when:

$$p=\sigma_t\sqrt{(2r_0/c)} \tag{2.20}$$

For pure shear loading, thus for superposition of $p_1=S$ at $\beta$ = $\pi$/4 and $p_2=-S$ at $\beta$ = 3$\pi$/4 in eq.(18) and in the other equations of the solution is for crack extension$\theta$ = 0:

$$\left(2r/cS^2\right)^{0.5}\tau_{r\theta}=\left(\cos(\theta/2)\cdot\left(3\cos^2(\theta/2)-2\right)\right)_{\theta=0}=1$$

or :

$$S=\tau_{r\theta}\sqrt{(2r_0/c)} \tag{2.21}$$

with now $\sigma_r=\sigma_\theta=0$, leading to an ultimate shear failure criterion.

Eq.(2.20) and (2.21) are maximum stress conditions for the strengths in the main planes. Thus fracture is predicted to occur when the tensile strength is reached perpendicular to the grain and/or when the shear strength in this plane is reached. Thus: $K_I\le K_{Ic}$ and $K_{II}\le K_{IIc}$ for all stress states (without the interaction). This also is predicted for the n-fold higher orthotropic stresses and is shown by eq.(2.30) to be not right.Thus also for the isotropic matrix, the applied singularity approach gives no right results. The right failure condition for combined stresses is derived below. The singularity failure equations are applicable as lower bound solution for matrix stresses by a chosen equilibrium system for co-axial macro-crack propagation as applied below for fracture of joints and beams with square end-notches, wherefore the mode I energy release rate is chosen as specific fracture energy.

## 2.3. Derivation of the Mixed I- II- Mode Equation

A general failure criterion [3] follows from the limited ultimate tensile stress which occurs at the crack boundary. By an extension of eq.(2.13) (by superposition) to $p_1=\sigma_1$ inclined at an angle π/2 + $\beta$ to the Ox-axis and $p_2=\sigma_2$ inclined at an angle $\beta$, (see Figure2.3), eq.(2.13) turns to:

$$\sigma_t=\frac{2\sigma_y\sinh(2\xi_0)+2\tau_{xy}[(1+\sinh(2\xi_0))\cdot\cot(2\beta)-\exp(2\xi_0)\cdot\cos(2(\beta-\eta))\,\mathrm{cosec}(2\beta)]}{\cosh(2\xi_0)-\cos(2\eta)}, \tag{2.22}$$

where the stresses are given in notch coordinates with the x-axis along the notch. For small values of $\xi_0$ and $\eta$ (flat notches), this equation becomes:

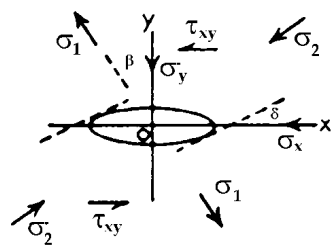


Figure 2.3. Stresses in the notch plane Ox.

$$\sigma_t = \frac{2\left(\xi_0\sigma_y - \eta\tau_{xy}\right)}{\xi_0^2 + \eta^2} \tag{2.23}$$

The maximum (critical) value of the tangential tensile stress $\sigma_t$, depending on location $\eta$, is found by: $d\sigma_t / d\eta = 0$, giving the critical value of $\eta$:

$$-2\tau_{xy} / \left(\xi_0^2 + \eta^2\right) - \left(2\left(\xi_0\sigma_y - \eta\tau_{xy}\right)\cdot 2\eta\right) / \left(\xi_0^2 + \eta^2\right)^2 = 0,$$

or:

$$-\tau_{xy}\left(\xi_0^2 + \eta^2\right) = 2\eta\left(\xi_0\sigma_y - \eta\tau_{xy}\right) = \eta\sigma_t\left(\xi_0^2 + \eta^2\right) \tag{2.24}$$

where the second equality sign is due to the substitution of eq.(2.23).
From the first and last term follows that:

$$\eta\sigma_t = -\tau_{xy} \tag{2.25}$$

and from the first 2 terms:

$$\eta / \xi_0 = \left(\sigma_y \pm \sqrt{\sigma_y^2 + \tau_{xy}^2}\right) / \tau_{xy} \tag{2.26}$$

or with eq.(2.23):

$$\xi_0\sigma_t = \sigma_y \pm \sqrt{\sigma_y^2 + \tau_{xy}^2} \tag{2.27}$$

and eq.(2.27) can be written:

$$1 = \frac{\sigma_y}{\xi_0\sigma_t / 2} + \frac{\tau_{xy}^2}{\xi_0^2\sigma_t^2} \tag{2.28}$$

According to eq.(2.17) is, for small values of θ at the crack tip: $\xi_0 = \sqrt{2r_0 / c}$, giving in eq.(2.28):

$$1 = \frac{\sigma_y\sqrt{\pi c}}{\sigma_t\sqrt{2\pi r_0} / 2} + \frac{\left(\tau_{xy}\sqrt{\pi c}\right)^2}{\left(\sigma_t\sqrt{2\pi r_0}\right)^2} \tag{2.29}$$

which is identical to the empirical parabolic interaction equation of Wu [4], measured on Balsa and on fiber reinforced plastic plates:

$$\frac{K_I}{K_{Ic}} + \frac{\left(K_{II}\right)^2}{\left(K_{IIc}\right)^2} = 1 \tag{2.30}$$

The fact that $K_{IC} = \sigma_y \sqrt{\pi c_c} = \sigma_t \sqrt{\pi r_0 / 2}$ is constant and therefore is regarded as material property, shows that failure is always by the same initial small cracks with tip-radius $r_0$ by the uniaxial cohesion strength $\sigma_t$. This applies for every level down to the molecular level. In [7] the estimation method of the relation between engineering macro stresses and molecular stresses at the bond breaking sites is given. For Balsa wood with a low density of reinforcement, nearly isotropic strength behaviour is found for crack extension. Thus $K_{IIc} = 2K_{Ic}$ according to eq.(2.28) and (2.30) as verified by the data of Wu of Balsa by: $K_{IIc} \approx 140\,\mathrm{psi}\cdot\mathrm{in}^{0.5}$ and $K_{Ic} \approx 60\,\mathrm{psi}\cdot\mathrm{in}^{0.5}$.

Eq.(2.30) is generally applicable also when $\sigma_y$ is a compression stress as follows from the measurements of Figure 2.4. When the compression is high enough to close the small notches ($\sigma_{y,cl} \approx 2G_{xy}\xi_0$), $\tau_{xy}$ has to be replaced by the effective shear stress: $\tau^*_{xy} = \tau_{xy} + \mu\left(\sigma_y - \sigma_{y,cl}\right)$ in eq.(2.28) or:

$$1 = \frac{\sigma_{y,cl}}{\xi_0 \sigma_t / 2} + \frac{\left(\tau^*_{xy}\right)^2}{\xi_0^2 \sigma_t^2}, \tag{2.31}$$

what is fully able to explain fracture by compression perpendicular to the notch plane (see Figure 2.4). In this equation is $\mu$ the friction coefficient.

For species, with denser layers than those of Balsa, a much higher value of $K_{IIc}$ than twice the value of $K_{Ic}$ is measured because due to the reinforcement, $\eta$ is smaller than the isotropic critical value of eq.(2.26). To read the equation in applied total orthotropic stress values, the matrix stress $\tau_{iso}$ has to be replaced by $\tau_{ort} / n_6$ and the maximum slope of the tangent, slope $\delta$ in Figure 2.2 of the location of the failure stress, is:

$$\left|\tan\delta\right| = \left|\eta_m\right| / \xi_0 = K_{Ic} / K_{IIc} = 1 / 2n_6 \tag{2.32}$$

For small values of $\eta = -|\eta|$, eq.(2.23) can be written, neglecting $(\eta/\xi_0)^2$ :

$$\frac{\sigma_y}{\xi_0\sigma_t/2}=1+\frac{\eta^2}{\xi^2}-\frac{\tau_{xy}}{\xi_0^2\sigma_t/\left(2|\eta|\right)}\approx 1-\frac{\tau_{xy}}{\xi_0^2\sigma_t/\left(2|\eta|\right)} \tag{2.33}$$

where $|\eta|$ is the absolute value of negative $\eta$. Thus:

$$\frac{K_I}{K_{Ic}}+\frac{K_{II}}{K_{IIc}}\approx 1 \tag{2.34}$$

This is a lower bound, with:

$$K_{IIc}=\left(\xi_0/|\eta_m|\right)\cdot K_{Ic} \tag{2.35}$$

and the maximal value of $\eta=\eta_m$ is found by measuring $K_{Ic}$ and $K_{IIc}$, giving e.g. a value of about $\xi_0/\eta_m\approx 7.7$, showing that the disregard of $\left(\eta/\xi_0\right)^2$ = 0.017 with respect to 1 is right. Measurements between the lines eq.(2.30) and (2.34) thus indicate a strong difference between $K_{IIc}$ and $K_{Ic}$ of the local structure that is crossed by the propagating crack.

Thus far, the equations are given in matrix stresses. To change this in the real applied orthotropic stresses, $\tau_{iso}=\tau_{ort}/n_6$ has to be inserted in eq.(2.28) giving:

$$1=\frac{\sigma_y}{\xi_0\sigma_t/2}+\frac{\tau_{iso}^2}{\xi_0^2\sigma_t^2}=\frac{\sigma_y}{\xi_0\sigma_t/2}+\frac{\tau_{ort}^2}{\xi_0^2\sigma_t^2n_6^2}=\frac{K_I}{K_{Ic}}+\frac{\left(K_{II}\right)^2}{\left(K_{IIc}\right)^2} \tag{2.36}$$

and it follows that:

$$\frac{K_{IIc}}{K_{Ic}}=\frac{\xi_0\sigma_t n_6}{\xi_0\sigma_t/2}=2n_6 \tag{2.37}$$

according to eq.(2.12) is e.g. for small clear specimens:

$2n_6=2\cdot\left(2+\nu_{21}+\nu_{12}\right)\cdot\left(G_{xy}/E_y\right)$ = 2(2 + 0.57)/0.67 = 7.7 for Spruce

and: 2(2 + 0.48)/0.64 = 7.7 for Douglas Fir in TL-direction.

This is in this case independent of the densities of respectively 0.37 and 0.50 at a moisture content of 12 %. Thus, for $K_{Ic}\approx 265\,\mathrm{kN/m^{1.5}}$ is

$K_{IIc} = 7.7 \cdot 265 = 2041\ kN/m^{1.5}$ in the TL-direction. This agrees with measurements [6]. In RL-direction this factor is 3.3 to 4.4. Thus, when $K_{IIc}$ is the same as in the TL-direction, the strength in RL-direction is predicted to be a factor 1.7 to 2.3 higher with respect to the TL-direction. This however applies at high crack velocities ("elastic" failure) and is also dependent on the site of the notch. At common loading rates a factor lower than 410/260 = 1.6 is measured [6] and at lower cracking speeds, this strength factor is expected to be about 1 when fracture is in the "isotropic" middle lamella. It then thus is independent of the TL and RL-direction according to the local stiffness and rigidity values. To know the mean influence, it is necessary to analyze fracture strength data dependent on the density and the elastic constants of $n_6$. From the rate dependency of the strength follows an influence of viscous and viscoelastic processes. This has to be analyzed by Deformation Kinetics [7].

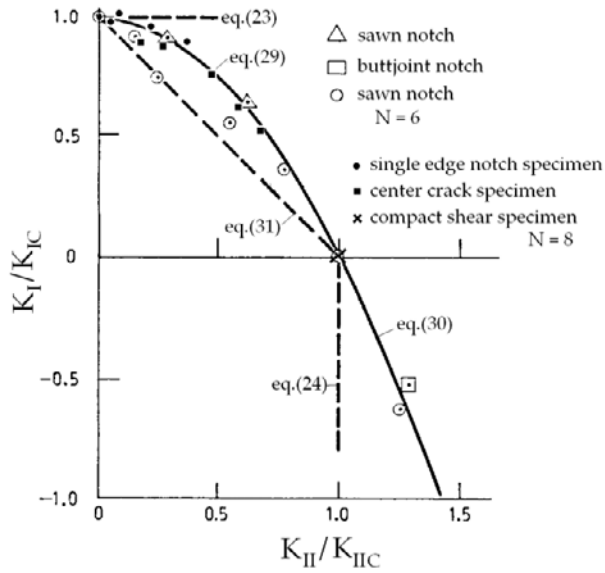


Figure 2.4. Fracture strength under combined stresses [5], [6].

A general problem is further the possible early instability of the mode I-tests. This means thatsmall-cracks failure outside the notch-tip region may be determining as e.g. in the tests of [6]. In thiscase constants should be compared with the related to mode II data.

## 2.4. Remarks Regarding Crack Propagation

Because the mixed mode failure criterion shows that crackstends to propagates in the direction perpendicular to greatest principal tensile stress, the, in literature mentioned, empirical principle, that the crack follows the direction that maximises G, the energy release, is now explained to be the result of the failure criterion. This maximizing G principle does not hold and is opposite principle a compression stress. Then the crack direction tends to become parallel to the stress where the crack is not any more affected by this stress. For wood these maximizing and minimizing principles don't apply, because fracture follows the weak planes

along the grain and jumps periodically to the next growth layer in a zigzag way around the critical direction, determined by the Wu failure criterion

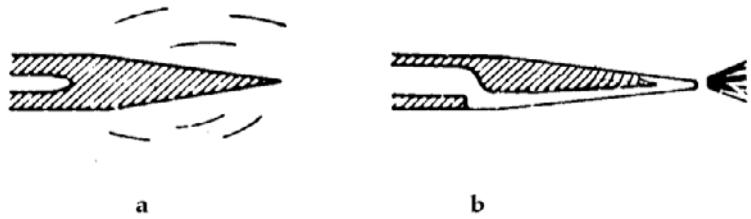


Figure2.5. a) Crazing at the crack tip and b) Possible crack extension along the fractured zone in glassy polymers.

In Figure2.5-b, it can be seen that mixed mode crack propagation starts at an angle with its plane but may bend back along the fractured zone to its original direction where crazing and fractured zone formation starts again. Stage b of this crack propagation is due to small-cracks merging from the fractured zone which extend to the macro-crack tip. For wood stage b occurs in a parallel crack plane. Co-axial crack propagation in this case is due to the small-crack joining mechanism discussed below. If, by the high stress near the macro-crack tip, each two adjacent small cracks in the weak main plane propagate towards each other, their out of plane directions for crack extension are opposed causing tensile stress interference in this weak plane which is sufficient for crack propagation in this plane because of the sufficiently close mutual distances in the critical state.

## 2.5. Additional Remarks Regarding the Empirical Confirmation

Measurements are given in Figure2.4. The points are mean values of a series of 6 or 8 specimens. The theoretical line eq.(2.30) is also the mean value of the extended measurements of Wu on balsa plates. Only the Australian sawn notch data deviate from this parabolic line and lie between eq.(2.30) and the theoretical lower bound eq.(2.34). This is explained by the theory of a too high $K_{IIc}/K_{Ic}$-ratio, indicating a mistake in manufacture. The theoretical prediction that $K_{IIc} = 2K_{Ic}$, for dominant isotropic behaviour of the matrix, is verified for Balsa with its very low fiber density. The prediction that $K_{IIc}/K_{Ic} = 2\cdot(2+\nu_{21}+\nu_{12})\cdot(G_{xy}/E_y)$ agrees with the measurements, using general mean values of the constants. However, precise, local values of the constants at the notches are not measurable and there is an influence of the loading rate and cracking speed. Thus safe lower bound values have to be used in practice.

The theory also fully explains the influence of compression perpendicular to the notch plane on the shear strength, eq.(2.31) in Figure 2.4.

The conclusion thus is that all measurements are explained by the theory.

## 2.6. References

[1] van der Put T.A.C.M., A new fracture mechanics theory for orthotropic materials like wood, *Engin. Fract. Mech*. 74, (2007) 771-781.
[2] Timoshenko S. and Goodier J.N., *Theory of elasticity*, McGraw-Hill bookcomp., N.Y. 1951, 179-204.
[3] van der Put, T.A.C.M., Explanation of the mixed mode interaction equation, COST 508 workshop 2, Bordeaux, April 1992
[4] Wu E.M., Application of fracture mechanics to anisotropic plates, *ASME J. Appl. Mech. Series E*, 34 4, Dec. 1967, pp. 967-974..
[5] Leicester R.H., Fracture strength of wood, First Australian Conf. on Engin. Materials, Univ. of New South Wales, 1974.
[6] RILEM state of the art report on fracture mechanics, Espoo, 1991.
[7] van der Put, T.A.C.M., *Deformation and damage processes in wood*, Delft University press, 1989.

# 3. Mode I Softening Behaviour and Fracture Energy

## 3.1. Introduction

The derivation of the softening behaviour is discussed and it is shown that the area under the load-displacement softening curve of, e.g.,Figure3.3, 3.4, 3.6 or 3.7, divided by the crack area,is not the fracture energy, but the total external work of the fracture process. The fracture energy ishalf this valueand is equal to the critical strain energy release rate at the top of the curve. For wood this correctlyis applied for mode II. For mode I a two times too high value is applied as done for other materials. The fracture energy is a function of the Griffith strength and, as the strain energy release rate, related to the effective width of the test specimen and not to the length of the fracture plane. The strain energy release rate is determined at the top of the top of the softening curve as start of macro-crack extension. This top is determined by the critical small-crack density. Proceeded small-crack extension also determines the softening curve and post fracture behaviour.

The analysis is based on matrix stresses for mode I failure in the weak planes because of the necessary correction of the fracture energy. The analysis, according to the equilibrium method, then is the same as for an isotropic material.

Authors of fracture mechanics of wood call the plane of co-axial crack propagation, in the test specimen, the ligament, probably because a crack may extend over a part of the width of the specimen, causing the formation of a ligament which has to collapse, for a total crack extension. Because of possible misunderstanding this plane is further called “fracture plain”.

## 3.2. Compliance and Energy Release Rate

As most materials, wood shows near failure an apparent plastic behaviour and the loading curve can be approximated by equivalent elastic-plastic behaviour. Therefore linear elastic

fracture mechanics can be applied based on the ultimate stress at the elastic-plastic boundary around the crack tip. The dissipation by microcracking, plastic deformation and friction within this boundary, called fracture process zone, then is regarded as part of the fracture energy of the macro crack extension. Also the equilibrium method is applicable. When a specimen is loaded until just before the start of softening and then unloaded and reloaded, the behaviour is elastic until failure making the linear elastic derivation of the softening curve possible based on the derivation of the compliance of the fractured specimen as follows:

In Figure 3.1, a mode I, center notched test specimen is given with a length "*l*", a width "*b*" and thickness "*t*", loaded by a stress $\sigma$ showing a displacement $\delta$ of the loaded boundary due to a small crack extension. The work done by the constant external stress $\sigma$ on this specimen, during this crack extension is equal to

$$\sigma \cdot b \cdot t \cdot \delta = 2W \tag{3.1}$$

This is twice the increase of the strain energy *W* of the specimen. Thus the other half of the external work, equal to the amount *W*, is the fracture energy, used for crack extension. Thus the fracture energy is equal to half the applied external energy which is equal to the strain energy increase *W* and follows, for the total crack length, from the difference of the strain energy of a body containing the crack and of the same body without a crack:

$$\frac{\sigma^2}{2E_{eff}} blt - \frac{\sigma^2}{2E} blt = W \tag{3.2}$$

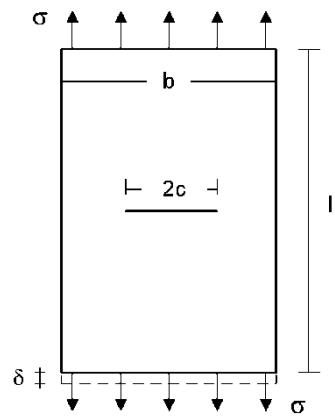


Figure 3.1. Specimen *b* x *l* and thickness *t*, containing a flat crack of 2*c*.

The fracture energy is also equal to the strain energy decrease at fixed grips conditions when $\delta = 0$:

$$W = t\sigma \int_{-c}^{+c} v da = \pi \sigma^2 c^2 t / E \tag{3.3}$$

where the last two terms give the strain energy to open (or to close) the flat elliptical crack of length 2*c* and where "*v*" is the displacement of the crack surface in the direction of $\sigma$. From eq.(3.2) and eq.(3.3) follows that:

$$\frac{\sigma^2}{2E_{eff}} blt - \frac{\sigma^2}{2E} blt = \pi\sigma^2 c^2 t / E \tag{3.4}$$

Thus the effective Young's modulus of the specimen of Figure 3.1, containing a crack of 2*c*, is:

$$E_{eff} = \frac{E}{1 + 2\pi c^2 / bl} \tag{3.5}$$

The equilibrium condition of the critical crack length is:

$$\frac{\partial}{\partial c}\left(W - G_c 2ct\right) = 0 \tag{3.6}$$

where $G_c$ is the fracture energy for the formation of the crack surface per unit crack area. Eq.(3.6) also can be regarded as the law of energy conservation of Thermodynamics. Because $G_c = \partial W/\partial(2ct)$, it clearly also is a strain energy release rate when applied to eq.(3.3).

With *W* of eq.(3.2) or of eq.(3.3), eq.(3.6) becomes:

$$\frac{\partial}{\partial c}\left[\frac{\pi\sigma^2 c^2 t}{E} - G_c 2ct\right] = 0,$$

or:

$$\frac{\partial}{\partial c}\left[\frac{\sigma^2 blt}{2E}\left(1 + \frac{2\pi c^2}{bl}\right) - \frac{\sigma^2 blt}{2E} - G_c 2ct\right] = 0 \tag{3.7}$$

giving both the Griffith strength:

$$\sigma_g = \sqrt{\frac{G_c E}{\pi c}} \tag{3.8}$$

This stress is related to the width *b* of the specimen of Figure 3.1. The real mean stress in the determining weakest cross section with width $b - 2c$, where fracture occurs, is:

$$\sigma_r = \sqrt{\frac{G_c E}{\pi c}} \cdot \frac{b}{b-2c} = \sqrt{\frac{G_c E}{\pi b}} \cdot \frac{1}{(\sqrt{c/b}) \cdot (1-2c/b)} \tag{3.9}$$

and:

$$\frac{\partial \sigma_r}{\partial(\sqrt{c/b})} = \sqrt{\frac{G_c E}{\pi b}} \cdot \frac{6c/b - 1}{(c/b) \cdot (1-2c/b)^2} > 0\,, \tag{3.10}$$

when *c/b*> 1/6, what always is the case for critical crack lengths. Thus the real stress $\sigma_r$ increases monotonically with the increase of the crack length *c* and no softening behaviour exists at the critical site. Softening thus only exists outside the critical cross section and is identical to elastic unloading of the specimen outside the fracture zone in order to maintain equilibrium. Softening thus is not a material property as is assumed in the existing models for wood and other materials.

### 3.3. The Softening Curve

Softening should be described by the damage theory of Deformation Kinetics [1] but a simple description of the softening behaviour as a result of former crack propagation alone is possible by the Griffith theory. Straining the specimen of Figure 3.1 to the ultimate load at which the initial crack will grow, gives, according to eq.(3.5):

$$\varepsilon_g = \sigma_g / E_{eff} = \sigma_g \cdot (1 + 2\pi c^2 / bl) / E \tag{3.11}$$

Substitution of $c = G_c E / \pi \sigma_g^2$, according to eq.(3.8), gives:

$$\varepsilon_g = \sigma_g / E + 2G_c^2 E / \pi \sigma_g^3 bl \tag{3.12}$$

This is the equation of critical equilibrium states applying along the softening curve (for a not limiting, sufficient long length of the fracture plane of the test specimen). This curve, called Griffith locus, has a vertical tangent $d\varepsilon_g / d\sigma_g = 0$, occurring at a crack length of:

$$c_c = \sqrt{bl/6\pi}\,. \tag{3.13}$$

Smaller cracks than $2c_c$ are unstable because of the positive slope of the locus (according to eq.(3.16)). These small cracks, (near the macro-crack tip) extend during the loading stage, by the high peak stresses at the notch of the test specimen, to a stable length and only higher crack lengths than $2c_c$ are to be expected at the highest stress before softening, giving the stress-strain curve of Figure3.2 with $\sigma_c$ as top value.

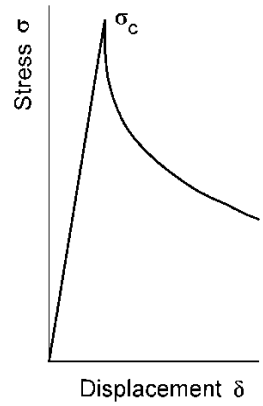


Figure3.2. Softening curve according to eq.(3.12) for the specimen of Figure3.1 or 3.5.

For a distribution of small cracks, *b* and *l* in eq.(3.13) are the crack distances and the critical crack distance for extension is about 2.2 times the crack length.Because, when $b \approx 2.2\cdot(2c_c)$ and $l \approx 2.2\cdot(2c_c)$, then$bl \approx 19\cdot c_c^2 \approx 6\pi c_c^2$ according to eq.(3.13). This critical distance also is predicted by Deformation Kinetics [1] and is used in Section3.6 to explain softening by small-crack propagation in the fracture plane.

According to eq.(3.13), the softening line eq.(3.12) now can be given as:

$$\varepsilon_g = \frac{\sigma_g}{E}\left(1+\frac{\sigma_c^4}{3\sigma_g^4}\right), \tag{3.14}$$

where

$$\sigma_c = \sqrt{EG_c/\pi c_c} \tag{3.15}$$

is the ultimate load with $c_c$ according to eq.(3.13). The negative slope of the stable part of the Griffith locus, being the softening line, is:

$$\frac{\partial\sigma_g}{\partial\varepsilon_g} = -\frac{E}{\frac{\sigma_c^4}{\sigma_g^4}-1} = -\frac{E}{\frac{c^2}{c_c^2}-1} \tag{3.16}$$

Vertical yield drop occurs at the top at $\sigma_g = \sigma_c$, and the strain then is: $\varepsilon_{gc} = (\sigma_c/E)\cdot(1+1/3)$ and eq.(3.14) becomes:

$$\frac{\varepsilon_g}{\varepsilon_{gc}} = 0.75 \cdot \left( \frac{\sigma_g}{\sigma_c} + \frac{\sigma_c^3}{3\sigma_g^3} \right), \tag{3.17}$$

More in general eq.(3.14) can be written, when related to a chosen stress level $\sigma_{g1}$:

$$\frac{\varepsilon_g}{\varepsilon_{g1}} = \frac{\sigma_g}{\sigma_{g1}} \cdot \frac{1+\sigma_c^4/3\sigma_g^4}{1+\sigma_c^4/3\sigma_{g1}^4} \tag{3.18}$$

To control whether $\sigma_c$ changes, eq.(3.18) can be written like:

$$\frac{\sigma_c}{\sigma_{g1}} = \left( \frac{3\cdot(\sigma_g/\sigma_{g1})^3 \cdot \left((\varepsilon_g/\varepsilon_{g1}) - (\sigma_g/\sigma_{g1})\right)}{1-(\varepsilon_g/\varepsilon_{g1})\cdot(\sigma_g/\sigma_{g1})^3} \right)^{0.25} \tag{3.19}$$

with the measured values at the right hand side of the equation. When the occurring softening curve starts to differ from the Griffith locus, $\sigma_c$ decreases, causing a steeper decline of the curve, due to additional clear wood failure of the fracture plane. This small-crack joining mechanism is discussed in Section 3.6.

## 3.4. Fracture Energy as Area Under the Softening Curve

The basic theory of the energy method, leading to eq.(3.1) and (3.2), should be confirmed by the loading curve (Figure3.3 and 3.4). This will be discussed in the now following.

When a test specimen is mechanical conditioned, the effective stiffness is obtained given e.g. by the lines OA and OC in Figure 3.3 and 3.4. In Figure3.3, the area OAB, written as $A_{OAB}$, is the strain energy of the specimen of Figure3.1 with a central crack (or with two side cracksaccording to Figure3.5) with a width "*b*", length "*l*" and thickness "*t*", loaded to the stress $\sigma$.

During the quasi static crack extension from B to D in Figure3.3, the constant external load $\sigma$ does the work on the specimen of: $\sigma \cdot b \cdot t \cdot \Delta\varepsilon_{BD} \cdot l = \sigma \cdot b \cdot t \cdot \delta_{BD} = A_{ABDC}$, where $\Delta\varepsilon_{BD}$ is the strain increase due to the cracking and $\delta_{BD}$ the corresponding displacement. The strain energy after the crack extension is $A_{OCD}$ and the strain energy increase by the crack extension thus is in Figure3.3: $A_{OCD}$ - $A_{OAB}$ = $A_{OCD}$ - $A_{OCB}$ = $A_{CBD}$ = $A_{ABDC}/2$,

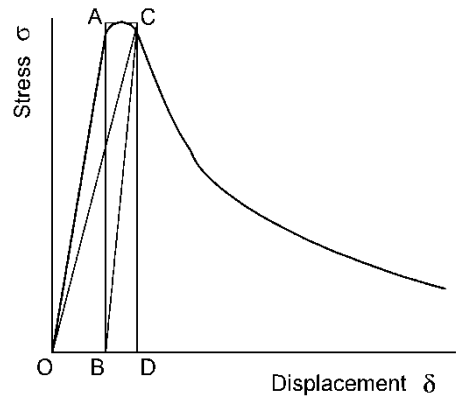


Figure3.3. Stress - displacement curve for tension, of the specimen of Figure3.1 or 3.5.

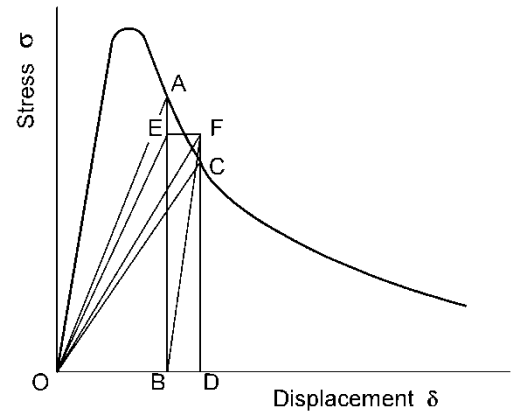


Figure3.4. Descending branch of the stress - displacement curve of Figure3.3.

Thus half of the external energy: $A_{ABDC} = \sigma \cdot b \cdot t \cdot \delta_{BD} / 2$ is the amount of increase of the strain energy due to the elongation by $\delta$, and the other half thus is the fracture energy which is equal to this increase of strain energy.The same follows at unloading at yield drop. Because every point of the softening curve gives the Griffith strength, which decreases with increasing crack length, unloading is necessary to maintain equilibrium. The fracture with unloading step AC in Figure 3.4 is energetic equivalent to the unloading steps AE and FC and the fracturing step EF at constant stress EB = FD = (AB +DC)/2. Thus $A_{ABDC} = A_{EBDF}$. Identical to the first case of Figure3.3, the increase in strain energy due to crack extension is:

$$A_{ODF} - A_{OBE} = A_{ODF} - A_{OBF} = A_{BFD} = 0.5 \cdot A_{EBDF} = 0.5 \cdot A_{ABDC},$$

equal to half the work done by the external stresses during crack propagation and thus also equal to the other half, the work of crack extension. It thus is shown that half the area under the load-displacement curve represents the fracture energy. For mode II, only line OACO in

Figure3.3 is measured and $A_{OAC}$ is regarded to be the fracture energy. Because $A_{OAC} = A_{BAC} = 0.5 \cdot A_{ABDC}$, thus equal to half the area under the load displacement curve, the right value is measured and mode II needs no correction.

Because eq.(3.2) is based on the total crack length and the strength is a Griffith stress, the initial value 2*c* of the crack length should be accounted and $\sigma$ and $G_c$ should be related to the whole crack length, including the initial value, and thus should be related to the whole specimen width *b* and not to the reduced width of the fracture plane: *b* – 2*c* as is done now. After the correction by a factor 2, this is the second necessary correction of the mode I fracture energy $G_c$. A third correction occurs when $\sigma_c$ of eq.(3.14) changes. The apparent decrease of $G_c$ at the end stage of the fracture process is due to an additional reduction of the intact area of the fracture plane of the specimen due to an additional clear-wood failure mechanism discussed in Section 3.6.

In [2], not $A_{ABDC}/2$ is regarded for the fracture energy the totally different amount $A_{OACO}$ of Fig 3.3. This is the irreversible energy of a loading cycle by a crack increment when the specimen is regarded as one giant molecule. The elastic unloading-energies outside the fracture plane of: $A_{OEA}$ and $A_{OCF}$ are now additional measures of the bond reduction for the total specimen, representing a decrease of the apparent enthalpy and entropy terms of the activation energy. The triangle $A_{OACO}$ thus represents the activation energy of the process [1] which is equal to the reversible work done on the system also represented by $A_{OACO}$. This is the case because this elastic energy is given by the elastic unloading parts, outside the fracture plane $A_{OEA}$ and $A_{OCF}$ together with $A_{OEF}$, the strain energy increase. As discussed in [3], the measurements of [2] indicate the presence of a mechanosorptive process, acting in the whole specimen. Thus $A_{OACO}$ gives no separate information on the fracture process at the fracture plane and should not be applied as measure of the fracture energy.

## 3.5. Empirical Confirmation

The measurements of [4] are complete by measuring the whole loading and softening curve and using the compact tension tests as control, being a control by the different loading case.

The graphs of [4], Figure3.6 and 3.7, are the result of tension tests on the specimen of Figure 3.5.

The length of the specimen was *l* = 3 mm, the width and thickness: *b* = *t* = 20 mm and the notch length 2*c* = 2x5 = 10 mm with a notch width of 0.5 mm.

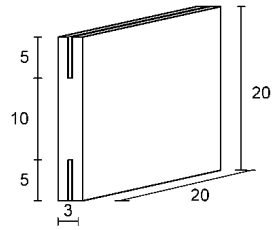


Figure3.5. Geometry of the specimens [4].

In figures 3.6 and 3.7, the measured stress-displacement is given together with the lines 1 and 2 according to eq.(3.17). The strain $\varepsilon_g$ follows from the displacements at the *x*-axis of the figures divided through 3 mm, the measuring length and length of the specimen. Because of the small length of 3 mm, not the whole width *b* of the specimen is active. Assuming a possible spreading of 1.2:1, through the thickness of 1.25 mm above and below the side notches, the working width $b_{eff}$ is equal to the length of the fracture plane plus 2 times 1.2 x 1.25 or $b_{eff}$ = 10 + 3 = 13 mm. Thus the notch lengths in Figure 3.5 should be regarded to be 1.5 mm instead of 5 mm. The stresses in the figures 3.6 and 3.7 of [4], are related to the length of the fracture plane and not to $b_{eff}$, according to the Griffith stress. Thus the given stresses have to be reduced by a factor 10/13 = 0.77.

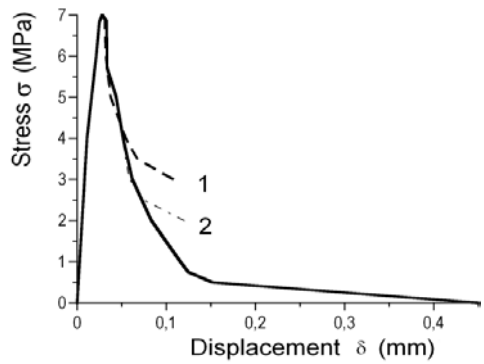


Figure3.6. Stress - displacement of specimen T 1409 of [4].

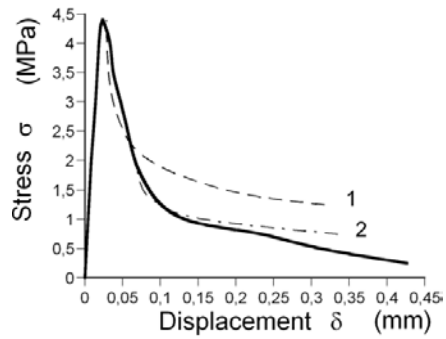


Figure3.7. Stress - displacement of specimen T 1509 of [4].

The standard compact tension tests of [4] did show a stress intensity $K_{Ic}$ of 330 $\mathrm{kNm}^{-3/2}$. This result is independent on the chosen stiffness as follows from the calculation according to the series solution or according to the energy method. This is verified in [4] by comparing the series solution with a finite element compliance calculation using the isotropic and theorthotropic stiffness and the quite different orthotropic stiffness of [5]. The value of $K_{Ic}$ = 330 $\mathrm{kNm}^{-3/2}$, found in all cases, thus also should follow from the area under the softening curve of that compact tension test. When half the area of that diagram is taken to be the fracture energy, instead of the total area, then $K_{Ic}$, mentioned in [4], indeed is corrected to the right value of: 467/√2 = 330 $\mathrm{kNm}^{-3/2}$, giving the first empirical verification of the theory.

Regarding the short double edge notched specimens of Figure3.5, the measured E-modulus should be related to the effective width of 13 mm instead of the width of 10 mm of the fracture plane and therefore is *E* = 700x10/13 = 700x0.77 = 539 MPa. The critical energy release rate then is:

$$G_c = K_{Ic}^2 / E = 330^2 / 539 = 200 \text{ N/m} \tag{3.20}$$

The measured value of $G_c$ from the area under the stress-displacement curve is given in [4] to be 515 N/m. But, because half this area should have been taken and this value is wrongly related to the length of the fracture plane instead of on $b_{eff}$, the corrected value is:

$$G_c = 1/2\text{x}515\text{x}0.77 = 200 \text{ N/m}, \tag{3.21}$$

as found above, eq.(3.20), giving again an empirical verification of the theory, now by the tests on the short double edge notched specimens.

As shown before, the softening curve of Figure3.6 has a vertical tangent at the top $d\sigma_g / d\varepsilon_g = \infty$. The critical crack length for softening is: $c_c = \sqrt{bl/6\pi}$ according to eq.(3.13). Thus:

$$c_c = \sqrt{\frac{b_{eff} l}{6 \cdot \pi}} = \sqrt{\frac{13 \cdot 3}{6 \cdot \pi}} \cdot 10^{-3} = 1.4 \cdot 10^{-3} = 1.4 \text{ mm} \tag{3.22}$$

This confirms the mentioned initial St. Venant crack length of the specimen to be as small as about 1.5 mm.

In Figure3.6, at the Griffith maximal stress of (0.77)·7 = 5.39 MPa, is: $K_{Ic} = \sigma\sqrt{\pi c}$ or:

$$\mathrm{K_{Ic}} = 5.39 \cdot \sqrt{\pi \cdot 1.4 \cdot 10^{-3}} = 0.36 \,\mathrm{MNm}^{-3/2}. \tag{3.23}$$

Thus above the mean value of 0.33 $\mathrm{MNm}^{-3/2}$ for this strong specimen.

Line 1 of Figure3.6 gives the primary crack extension, eq.(3.17), with $\sigma_c$ = (0.77)·7 = 5.39 MPa and a displacement of about 0.03 mm, (or a strain of 0.03/3 = 0.01). The strength of the fracture plane of 7 to 8 MPa is rather high and only measured 6 times of the 117 tests. The crack does not propagate in a free space, but in the limited length of the fracture plane and this area will be overloaded. Curve 1 therefore levels off from the measurements at $\sigma$ = 0.77·4 MPa. Thus:

$$\sigma_g = \sqrt{\frac{EG_c}{\pi 3c_c}} = 0.57\cdot(0.77\cdot 7) = 0.77\cdot 4 \text{ MPa} \tag{3.24}$$

Thus this happens when the crack length has become about 3 times the initial critical value $c_{c,0}$. The remaining intact length of the fracture plane then is: 4.4 mm or 4.4/13 = 0.34, while the remaining intact length is 5 mm for small-crack pattern A (of Section 3.6), or 5/13 = 0.38. Thus less fracture energy is required for small-crack failure and it thus is probable that macro-crack extension is always due to small-crack propagation toward the macro-crack tip. The level above 4 (to 4.6) MPa is measured in 3 of the 10 specimens of the discussed series T1309/2309 of [4] and an example is given in Figure3.7. The other specimens of this series did show lower strength values than 4 MPa, indicating that this strength of the fracture plane according to crack-pattern A was determining for softening. The same applies for further softening. The transition to crack pattern B and to pattern C is according to eq.(3.18), verified by eq.(3.19), showing that in Figure3.6, $\sigma_c$ is constant and equal to $\sigma_c$/0.77 = 7 MPa for $\sigma_g$/0.77 = 7 down to $\sigma_g$/0.77 = 4 MPa and then reduces gradually to $\sigma_c$/0.77 = 4.5 at $\sigma_g$/0.77 = 2 and further to $\sigma_c$/0.77 = 3 at $\sigma_g$/0.77 = 1 MPa. The same applies for Figure3.7, $\sigma_c$/0.77 = 7 MPa above $\sigma_g$/0.77 = 4 MPa and then reduces in the same way. These results are given in Table 1. The departure from the Griffith theory by the gradual decrease of $\sigma_c$, below $\sigma_g$/0.77 = 4 MPa, is due to the failure of the high loaded fracture plane what is explained in the next section.

## 3.6. Crack Joining Mechanism

The discussed apparent decrease of the fracture energy $G_c$ of the Griffith theory, due to reduction of intact area of the fracture plane of the specimen by small crack extensions at the fracture plane, can be explained, using the equilibrium method, by the joining of the small cracks as follows:.

In [3] it is shown that the critical intermediate small crack distance of a fracture process in “clear” wood, and thus in the fracture plane, is about equal to the crack length, as given in scheme A below. In Section 3.3, a crack distance of 2.2 times the crack length is found, what for simplicity of the model is rounded down here to 2, giving slightly too high stresses (see Table 1). For these small cracks, the critical crack length according to eq.(3.13) then is:

2c 2c 2c 2c 2c 2c 2c 2c 2c 2c 2c 2c 2c 2c . A

6c 2c 6c 2c 6c 2c 6c . B

14c 2c 14c . C

$c_c = \sqrt{lb/6\pi} = \sqrt{2\cdot(2c_0)\cdot 2\cdot(2c_0)/(6\pi)} = 0.92\cdot c_0 \approx c_0$, for the specimen with row A.

The distance $l$ between the rows, above each other, is always two times the crack length, being the Saint-Venant distance for building up the stress again behind a crack to be able to form a new crack. Thus $l = 2\cdot 2c$ for row A, and $l = 2\cdot 6c = 12c$ in row B, and $2\cdot 14c = 28c$ in row C. The crack distance b in row A is $b = 4c$, and b = $8c$ in row B, and $16c$ in row C. Thus when crack pairs of row A join together, a crack length of $6c$ occurs, at a distance $8c$, and so on. The critical crack length thus is for row B:

$c_c = \sqrt{lb/6\pi} = \sqrt{12\cdot 8\cdot c_0^2/(6\pi)} = 2.26\cdot c_0$ and is

$c_c = \sqrt{lb/6\pi} = \sqrt{28\cdot 16\cdot c_0^2/(6\pi)} = 4.88\cdot c_0$ for row C.

The critical stress $\sigma_c$ is for row A:

$$\sigma_c = \sqrt{\frac{EG_c}{\pi 0.92 c_0}} = 1.04\cdot\sqrt{\frac{EG_c}{\pi c_0}} = 1.04\cdot\sigma_{cm} \approx 1.0\cdot 0.77\cdot 7 = 0.77\cdot 7.0 \text{ MPa},$$

and for row B:

$$\sigma_c = \sigma_{cm}\cdot\left(1/\sqrt{2.26}\right) = \sigma_{cm}\cdot 0.67 = 0.67\cdot 0.77\cdot 7 = 0.77\cdot 4.6 \text{ MPa},$$

and for row C:

$$\sigma_c = \sigma_{cm}\cdot\left(1/\sqrt{4.88}\right) = \sigma_{cm}\cdot 0.45 = 0.45\cdot 0.77\cdot 7 = 0.77\cdot 3.1 \text{ MPa}$$

The determining strength of the intact part of the fracture plane is:

$\sigma_m = \sigma_u\cdot 2c/b = \sigma_u\cdot 2c/4c = \sigma_u/2 = 4\cdot 0.77$ MPa for case A;

$\sigma_m = \sigma_u\cdot 2c/8c = \sigma_u/4 = 2\cdot 0.77$ MPa for case B, and

$\sigma_m = \sigma_u\cdot 2c/16c = \sigma_u/8 = 1\cdot 0.77$ MPa for case C.

Thus the decrease of the Griffith values $\sigma_c$ and $G_c$ is fully explained by the strength of the intact part of the fracture plane $\sigma_g = \sigma_m$ as is verified by the measurements. As mentioned before, eq.(3.19) of $\sigma_c$, of the softening curve gives the measurement of Figure3.6 and 3.7 in the first two columns of Table 1, together with the prediction of the crack joining mechanism in column 5 and 6. This mechanism thus precisely explains the decrease of $\sigma_c$ of the softening curve, which also can be approximated by three equations (3.18) for the 3 critical crack densities A, B and C. The strength decrease by a factor 0.5 between these crack densities in column 6 causes a decrease of the top-value $\sigma_c$ of eq.(3.17) of a factor 0.657 in column 1 and 5. Thus: 0.657·7 = 4.6 and 0.657·4.6 = 3. Thus a simple practical approximation of the mean softening curve of all specimens of the series, is possible by applying eq.(3.17) twice (or three times for the highest values), according to line 1 and 2 in Figure 3.6 and 3.7.

**Table 1. Softening by macro crack propagation followed by fracture plane failure**

| eq.(3.19), data Figure 3.6 | | | | crack joining | |
|---|---|---|---|---|---|
| $\sigma_c / 0.77$ eq.(3.19) | $\sigma_g / 0.77$ Chosen points | $\sigma_g / \sigma_{g1}$ data | $\varepsilon_g / \varepsilon_{g1}$ data | $\sigma_c / 0.77$ 3 crack densities | $\sigma_m / 0.77$ strength fract.plane |
| 7 | 7 | | | | |
| 7 | 4 | 4/7 | 7.5/4 | 7 | A: 4 |
| 4.6 | 2 | 2/7 | 11.5/4 | 4.6 | B: 2 |
| 3.0 | 1 | 1/7 | 16/4 | 3.1 | C: 1 |

The analysis above shows that in general:

$2c_{n+1} = 2 \cdot 2c_n + 2c_0$, giving $2c_1 = 6c_0$ and $2c_2 = 2 \cdot 2c_1 + 2c_0 = 14c_0$.

The increase of the crack length is: $\Delta(2c)' = 2c_{n+1} - 2c_n = 2c_n + 2c_0$. Including the initial crack length of $2c_0$, the increase of the total crack length is:

$$\Delta(2c) = 2c_{n+1} - 2c_n - 2c_0 = 2c_n . \tag{3.25}$$

More general for any crack distance this is: $\Delta(2c) = \beta_1 \cdot 2c$ and because the strength decrease is proportional to the area decrease of the fracture plane area of the test specimen, due to the small cracks extension there, the equation becomes:

$$\Delta(2c)/(2c) = -\beta_2 \cdot \Delta(G_c) \tag{3.26}$$

giving the explanation of the decrease of $\sigma_c$.

Eq.(3.26) also can be expressed in the mean crack velocities by replacing c by $\dot{c}t$, the mean crack velocity $\dot{c}$ times time t. Thus: $\Delta(2c)/(2c) = \Delta(ct)/\dot{c}t = \Delta\dot{c}/\dot{c}$. Then integration of eq.(3.26) leads to:

$$G_{c,a} = G_{c,a,1} - \gamma \cdot \ln(\dot{c}), \tag{3.27}$$

This is measured in [2] and mentioned in [6] for the irreversible work of loading cycles.

It is shown in [3] that G is proportional to the activation energy and thus proportional to the driving force $K_I$ with reversed sign and Eq.(3.27) can be written relative to a reference $\dot{c}_m$:

$$\frac{\sigma_t}{\sigma_{t,m}} = 1 + \frac{1}{n}\ln\left(\frac{\dot{c}}{\dot{c}_m}\right) = \frac{K_I}{K_{I,m}} \tag{3.28}$$

This semi log-plot, eq.(3.28), is given, as empirical line, in many publications from experiments on, e.g., ceramics, polymers, metals and glasses, and is, e.g., given in [6] for wood. Because the slope is small, also the empirical double log-plot is possible.

The kinetics shows the same behaviour as for clear wood indicating that small-crack propagation is always determining. As shown in [1], two coupled processes act, showing the same time-temperature and time-stress equivalence. One process, with a very high density of sites, provides the sites of the second low site density process, as follows from a very long delay time of the second process. The notched specimen discussed here also shows the low concentration reaction by the strong softening behaviour. Probably the coupled processes are the numerous small-cracks growing towards the macro notch, providing the site for the macro crack to grow as second low (crack-) concentration process. This failure mechanism thus applies for every bond breaking process at any level.

## 3.7. References

[1] T.A.C.M van der Put, *Deformation and damage processes in wood*, Delft University Press, The Netherlands, (1989).

[2] Y.W. May, On the velocity-dependent fracture toughness of wood, *Wood Science*, July 1975

[3] T.A.C.M van der Put, A new fracture mechanics theory of orthotropic materials like wood, *Engin. Fract. Mech.* 74/5 (2007) pp 771-781.

[4] L. Bostrom, Method for determination of the softening behaviour of wood etc. Thesis, Report TVBM-1012, Lund, Sweden, (1992).

[5] G.C. Sih, P.C. Paris and G.R. Irwin, On cracks in rectilinearly anisotropic bodies, *Int. J. of Fract. Mech.* 1 (1965) 189-203.

[6] G.H. Valentin, L. Bostrom, P.J. Gustafsson, A. Ranta-Maunus, S. Gowda, RILEM state-of-the-art report on fracture mechanics, VTT Report 1262, Espoo, Finland July 1991

# 4. DISCUSSION OF THE FRACTURE MECHANICS MODELS APPLIED TO WOOD

## 4.1. Introduction

The always applied singularity approach of fracture mechanics contains no physical failure criterion for the ultimate state because stresses go to infinity at the singularity and therefore energy methods are necessary and additional models to constitute such failure criteria as for instance the J-integral to determine the strain energy release rate and the fictitious crack models to obtain finite ultimate stresses etc. The general applicability of these models will be discussed in this section while criteria based on a critical energy are discussed in the next section.

## 4.2. The Fictitious Crack Models

The high stresses near the crack tip, are replaced by a plastic zone in the Dugdale model following from elastic superposition of closing stresses, equal to the yield stress, on the crack tip zone of a fictitious enlarged crack of such a length that the stress in the elastic singularity point becomes zero. The length of that plastic zone is $r_p$ according to:

$$r_p = \frac{\pi}{8} \cdot \left( \frac{K_{Ic}}{\sigma_f} \right)^2 = \frac{\pi^2 \sigma^2 c}{8 \sigma_f^2} \tag{4.1}$$

where $\sigma_f$ is the yield stress or is regarded to be a cohesive stress.

This leads to a maximal crack opening displacement $\delta_c$ at the crack tip of:

$$\delta_c = \frac{8}{\pi E} \cdot \sigma_f \cdot r_p = \frac{K_{Ic}^2}{E \sigma_f} = \frac{\pi \sigma^2 c}{E \sigma_f} \tag{4.2}$$

when $r_p$ from eq.(4.1) is substituted.

According to the theory of Section 2 applies, for Mode I, at the crack tip boundary $r_0$, at the start of flow, the condition: $r_0 = 2c\left(\sigma / \sigma_f\right)^2$ according to eq.(2.29) for the elliptic crack tip and approximately $r_0 = c\sigma^2 / 2\sigma_f^2$ according to eq.(2.20) for the circular crack tip,

showing a difference by a factor 4, depending on the form of the crack tip and thus depending on the value of the tangential tensile stress along the crack-tip boundary. The Dugdale numerical factor $\pi^2/8 = 1.23$ is between the values of 0.5 and 2 but is too far away from the elliptic value 2 which applies generally. Also the theoretical elastic elliptic crack opening displacement of $\delta_c = (2\sigma c)/E$ is far above the Dugdale value. The Dugdale model thus is a model according to the equilibrium method, based on a chosen, allowable equilibrium system, providing however a too low and thus rejectable lower bound with respect to the theoretical description of Section 2. The same applies for the Hillerborg model which is not based on a constant closing stress $\sigma_f$, but on closing stresses proportional to the softening curve. This of course is not right because there is no softening at the fracture plane. The real stress in the intact area is the ultimate yield stress and yield drop thus is a system property indicating how much broken area with zero stress there is in the fracture plane (see Section 3).

For wood it is sufficient to account for apparent plasticity zones around the crack-tip by regarding effective crack dimensions and to regard the critical state at these elastic-"plastic" boundaries.

## 4.3. Crack Growth Models

The acknowledged, in principle identical crack growth models for wood of Williams, Nielsen and Schapery, mentioned in [1], are based on linear viscoelasticity and on the Dugdale-Barenblatt model in order to try to derive the empirical crack rate equation:

$$\frac{da}{dt} = A \cdot K_I^n \tag{4.3}$$

This procedure is contrary to normal and can not lead to a real solution because the rate equations are constitutive and follow from Deformation kinetics theory [2], [3], as applies for all materials. Constitutive equations only can follow from the theory and not from general thermodynamic considerations.

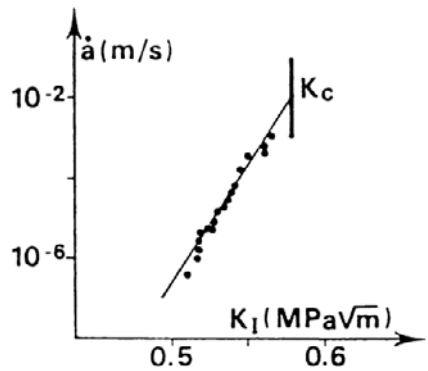


Figure 4.1. Crack growth tests of Mindess (Figure 10 of [1]).

In [1] is stated that Fig 4.1 represents eq.(4.3). However, eq.(4.3) is a straight line on a double log-plot, while Figure 4.1 gives the semi-log-plot which confirms the applicability of the damage equation of Deformation Kinetics [2] in the form: $\dot{a} \approx C \cdot \exp(\phi\sigma_v)$, or:

$$\ln(\dot{a}) = \ln(C) + \phi\sigma_v \tag{4.4}$$

This equation is equal to eq.(3.28), discussed in Section 3. More appropriate forms of theexact damage equations and power law forms, with the solutions as e.g. the yield drop in the constant strain rate test, are discussed in [2] and the meaning of the power law equation, eq.(4.3), is discussed below.

The impossibility of the derivation of the fracture rate equation from the Dugdale-Barenblatt equations follows e.g. from the derivation in [6, Section 2.2] of eq.(4.5):

$$K_{Ic} = E_0 \cdot \dot{a}^n \cdot \sqrt{\delta_c \varepsilon_y} \cdot r_p^{-n} \tag{4.5}$$

based on the relations: $\varepsilon_y = \sigma_c / E$ and $K_{Ic} = \sqrt{E\sigma_c\delta_c}$, with $E = E_0 \cdot t^{-n}$ and $r_p = \dot{a} \cdot t$. These four relations thus also can be used now to eliminate 4 parameters, e.g. $K_{Ic}$, $\varepsilon_y$, $r_p$ and $E_0$ to obtain an equation in *E*, *t*, $\dot{a}$ $\sigma_c$ and $\delta_c$. When this is done, eq.(4.5) turns to an identity: *E* = *E*, and eq.(4.5) thus is not a new derived crack rate equation but an alternative writing of the four relations. The same follows for the other models of Section 2.2 of [1] showing comparable parameter manipulations of many critical parameter values which can not be applied independently because they are part of the same failure condition. The models further are based on linear viscoelasticitywhich does not exist for polymers. It is shown in e.g. [2], page 97, and by the zero creep and relaxation tests at page 119, that a spectrum of retardation or relaxation times does not exist. The superposition integral eq.(28) or eq.(51) of [1]:

$$\varepsilon(t) = \int_{-\infty}^{t} C(t-\tau)\frac{d\sigma(\tau)}{d\tau}\,d\tau \tag{4.6}$$

thus has no physical meaning. This also applies for the power law models of time and power law equation, eq.(4.3) making predictions and extrapolations outer the fitted range of the data impossible.

## 4.4. Derivation of the Power Law

The power law may represent any function f(x) as follows from the following derivation. It thus also may represent, in a limited time range, a real damage equation giving then a meaning of the power *n* of the power law eq.(4.3).

Any function *f(x)* always can be written in a reduced variable $x/x_0$

$$f(x) = f_1(x / x_0) \tag{4.7}$$

and can be given in the power of a function:

$f(x) = f_1(x / x_0) = \left( \left( f_1(x / x_0) \right)^{1/n} \right)^n$ and expanded into the row:

$$f(x) = f(x_0) + \frac{x - x_0}{1!} \cdot f'(x_0) + \frac{(x - x_0)^2}{2!} \cdot f''(x_0) + .....$$

giving:

$$f(x) = \left[ \left\{ f_1(1) \right\}^{1/n} + \frac{x - x_0}{x_0} \frac{1}{n} \left\{ f_1(1) \right\}^{1/n-1} \cdot f'(1) + ..... \right]^n = f_1(1) \cdot \left( \frac{x}{x_0} \right)^n \tag{4.8}$$

when:

$$\left( f_1(1) \right)^{1/n} = \frac{1}{n} \left( f_1(1) \right)^{1/n-1} \cdot f'(1) \quad \text{or: } n = f_1'(1) / f_1(1),$$

where:

$$f_1'(1) = \left( \partial f_1(x / x_0) / \partial (x / x_0) \right)_{(x/x_0)=1}$$

and

$$f_1(1) = f(x_0)$$

Thus:

$$f(x) = f(x_0) \cdot \left( \frac{x}{x_0} \right)^n$$

with

$$n = \frac{f_1'(1)}{f_1(1)} = \frac{f'(x_0)}{f(x_0)} \tag{4.9}$$

It is seen from this derivation of the power law, using only the first 2 expandedterms, that the equation only applies in a limited range of *x* around $x_0$.

Using this approach on the damage equation: $\dot{a} = 2C \cdot \sinh(\phi\sigma) \approx C \exp(\phi\sigma)$ gives:

$$\dot{a} = C \cdot \exp(\phi\sigma) \approx \dot{a}_0 \cdot \left(\frac{\sigma}{\sigma_0}\right)^{\phi\sigma_0} \tag{4.10}$$

The power $n = \phi\sigma_0$ of the power law equation follows from the slope of the double log-plot:

$$\ln(\dot{a}) = \ln(\dot{a}_0) + n \cdot \ln(\sigma / \sigma_0) \tag{4.11}$$

Thus: $n = d\ln(\dot{a}) / d\ln(\sigma / \sigma_0)$ and $n = \phi\sigma_0$ gives a meaning of $n$ as the activation volume parameter $\phi\sigma_0$ of the exact equation. The values of "$n$" and the matching activation energies of the different creep and damage processes in wood, with the dependency on stress moisture content and temperature, are given in [2]. The constancy of the initial value of the parameter $\phi\sigma_0$, independent of $\sigma_0$ explains the time-temperature and time- stress equivalence and explains, by the physical processes, why and when at high stresses, the in [1] mentioned value of $n + 1 \approx 60$ is measured and at lower stresses, half this value (see [2]).

### 4.5. References

[1] RILEM state of the art report on fracture mechanics, Espoo, 1991.
[2] van der Put, T.A.C.M., *Deformation and damage processes in wood*, Delft University press, 1989.
[3] van der Put, T.A.C.M., Transformations in wood, Delft University, *Stevin-laboratory Research Report*, 2003-3/ME-2.

## 5. Energy Theory of Fracture

### 5.1. Introduction

The failure criterion of clear wood, i.e. wood with small defects, is the same as the failure criterion of notched wood, showing again that the small-crack extension towards the macro-crack tip is the cause of macro-crack propagation. This small-crack failure criterion thus delivers essential information on macro-crack behaviour.

### 5.2. Critical Distortional Energy as Fracture Criterion

The failure criterion of wood consist of an orthotropic third degree tensor polynomial [1], which, for the same loading case, is identical to the Wu-mixed mode I-II-equation [2], eq.(5.3). The second degree polynomial part of the failure criterion is shown to be the orthotropic critical distortional energy principle for initial yield [3] showing the start of

dissipation of elastic distortional energy as also confirmed by the orthotropic finite element calculation of [4]. By this dissipation according to the incompressibility condition, the minimum energy principle is followed providing therefore the exact initial yield criterion as:

$$\frac{\sigma_x^2}{XX'}+\frac{\sigma_x}{X}-\frac{\sigma_x}{X'}-2F_{12}\sigma_x\sigma_y+\frac{\sigma_y^2}{YY'}+\frac{\sigma_y}{Y}-\frac{\sigma_y}{Y'}+\frac{\tau^2}{S^2}=1 \qquad (5.1)$$

where $X$, $Y$ are the tension strengths and $X', Y'$ the compression strength in the main directions and $S$ is the shear strength and: $2F_{12}=1/\sqrt{XX'YY'}$

This value of $F_{12}$ is necessary for the elastic state which also applies at the starting point of initial stress redistribution and micro-cracking of the matrix. After further straining, $F_{12}$ becomes zero, $F_{12}\approx 0$, at final failure initiation. The absence of this coupling term $F_{12}$ between the normal stresses indicates symmetry, thus (possible random oriented) initial small-cracks are extended during loading to their critical length in the weak planes, the planes of symmetry, only. Then, when these small-cracks arrive at their critical crack-density (discussed in Section 3.6) and start to extend further, a type of hardening occurs because the reinforcement prevents crack extension in the matrix in the most critical direction. Then, due to hardening, $F_{12}$ and all third degree coupling terms of the tensor polynomial become proportional to the hardening state constants [3] and therefore also dependent on the stability of the test and equipment. For the mixed I-II-loading of the crack plane by tension $\sigma_2$ and shear $\sigma_6$, the polynomial failure criterion reduces to:

$$F_2\sigma_2+F_{22}\sigma_2^2+F_{66}\sigma_6^2+3F_{266}\sigma_2\sigma_6^2=1 \quad \text{or:} \quad \frac{\sigma_6}{S}=\sqrt{\frac{(1-\sigma_2/Y)\cdot(1+\sigma_2/Y')}{1+c\sigma_2/Y'}} \qquad (5.2)$$

with: $c=3F_{266}Y'S^2\approx$ 0.9 to 0.99, depending on the stability of the test. When c approaches $c\approx$ 1, Eq.(5.2) becomes Eq.(5.3), the in Section 2.3 theoretically explained Wu-equation, with a cut off by the line: $\sigma_2=Y$.

$$\left(\frac{\sigma_6}{S}\right)^2+\frac{\sigma_2}{Y}\approx 1 \quad \text{or:} \quad \frac{K_{II}^2}{K_{IIc}^2}+\frac{K_I}{K_{Ic}}=1 \qquad (5.3)$$

This equation contains no hardening constants and thus is the critical distortional energy equation for this case. Wrongly for wood and other orthotropic materials, Eq.(5.2) is generally replaced in literature by:

$$\frac{\sigma_2^2}{Y^2}+\frac{\tau^2}{S^2}=1, \text{ written as: } \frac{K_I^2}{K_{Ic}^2}+\frac{K_{II}^2}{K_{IIc}^2}=1, \qquad (5.4)$$

which surely is not a summation of energies, as is stated, but is identical to eq.(5.1) when it wrongly is assumed that the compression and tension strength are equal for wood and orthotropic materials.

## 5.3. Revision of the Critical Energy Release Rate Equation

Based on the failure criterion of Section 5.2, adaption of the energy release equation is necessary.

The Griffith strength equation, eq.(3.8) of Section 3: $\sigma_y^2 = G_c E_y / \pi c$ can be extended by superposition to:

$$\sigma_y^2 + \tau_{xy}^2 = G_c E_y / \pi c \tag{5.5}$$

This only is right, when $G_c$ is not constant but depends on $\sigma_y / \tau_{xy}$, because else, for $\sigma_y$ = 0, Eq.(5.5) predicts a too low shear strength. This already was noticed by Griffith. The fracture toughness calculation of Section 2.3 shows a two times higher shear strength of the isotropic matrix than according to the energy method. This was explained by supposing that there is enough energy for failure, but that the shear stresses are too low for failure. Only the energy of high stresses is involved in failure. This however means that $G_f$ also has to satisfy the failure condition eq.(5.3).

In orthotropic stresses, Eq.( 5.5) is: $\sigma_y^2 + \tau_{xy}^2 / n_6^2 = G_f E_y / \pi c$ and when $\tau_{xy} = 0$, is

$G_f = G_{Ic}$

and $K_{Ic} = \sqrt{E_y G_{Ic}}$

When $\sigma_y = 0$ is: $\tau_{xy}^2 \pi c = n_6^2 G_{IIc} E_y = 4 n_6^2 G_{Ic} E_y$, because

$K_{IIc} = 2 n_6 K_{Ic}$ (eq.(2.37)). Thus: $K_{IIc} = n_6 \sqrt{E_y G_{IIc}} = 2 n_6 \sqrt{E_y G_{Ic}}$ or:

$$G_{IIc} = 4 G_{Ic} \tag{5.6}$$

The failure condition Eq.(5.3) can be written in fracture energies:

$$\frac{K_I}{K_{Ic}} + \frac{\left(K_{II}\right)^2}{\left(K_{IIc}\right)^2} = 1 = \frac{\sqrt{G_I}}{\sqrt{G_{Ic}}} + \frac{G_{II}}{G_{IIc}} = \frac{\sqrt{\gamma \cdot G_f}}{\sqrt{G_{Ic}}} + \frac{\left(1-\gamma\right) \cdot G_f}{G_{IIc}} \tag{5.7}$$

where:

$$G_f = G_I + G_{II} = \gamma \cdot G_f + (1-\gamma) \cdot G_f \tag{5.8}$$

Thus: $\dfrac{\gamma G_f}{(1-\gamma) G_f} = \dfrac{K_I^2}{K_{II}^2}$ or: $\gamma = \dfrac{1}{1+\dfrac{K_{II}^2}{K_I^2}} = \dfrac{1}{1+\dfrac{\tau_{xy}^2}{\sigma_y^2}}$ (5.9)

and $\gamma$ depends on the stress combination $\tau_{xy} / \sigma_y$ in the region of the macro notch-tipand not on the stresses of the fracture energy. This stress combination may follow from a chosen stress field according to the equilibrium method as applied in Section 6 and 7.

With eq.(5.6): $G_{IIc} / G_{Ic} = 4$, eq.(5.7) becomes:

$$G_f = 4G_{Ic} / (1+\sqrt{\gamma})^2 = G_{IIc} / (1+\sqrt{\gamma})^2 \tag{5.10}$$

The use of $G_f$ according Eq.(5.10) explains the differences in fracture energies depending on the notch depth and structure and shear slenderness of the beam by the different occurring $\tau_{xy} / \sigma_y$ -values according to Eq.(5.9).

Applications of the theory with the total critical fracture energy $G_f$ are given in Section 6 and 7.

### 5.4. References

[1] van der Put, T.A.C.M. (1982) A general failure criterion for wood, CIB-W18/IUFRO meeting Boras, Sweden

[2] Wu, E.M. (1967) Application of fracture mechanics to anisotropic plates, *ASME J. Appl. Mech*. Series E, 34 4, pp. 967-974.

[3] van der Put T.A.C.M. (2009) A continuum failure criterion applicable to wood. *J. of Wood Sci*, Vol. 55 No.5. (DOI: 10.1007/s10086-009-1036-2)

[4] Gopu, Vijaya K. A. (1987) Validity of Distortion-Energy-Based Strength Criterion for Timber Members, *J. Struc. Eng*. 113, No. 12 pp. 2475-2487.

## 6. Energy Approach for Fracture of Notched Beams

### 6.1. Introduction

The theory of total fracture energy, discussed in Section 5, was initially developed to obtain simple general design rules for beams with square end-notches and edge joints, loaded

perpendicular to the grain design rules of square notches and joints for the Dutch Building Code and later, as modification of the method of [1], published in [2] with the extensions for high beams. Horizontal splitting in short, high beams, loaded close to the support, causes no failure because the remaining beam isstrong enough to carry the load and vertical transverse crack propagation is necessary for total failure. This is not discussed here because it is shown that also the standard strength calculation is sufficient. In [3] and [4] the theory is applied to explain behaviour, leading to the final proposal for design rules for the Eurocode, given at Section 7.5, and to an always reliable simple design method.

In the following, the theoretical basis and implementation of the new developments of the theory of the energy approach for fracture of notched beams are given and it is shown that the predictions of the theory are verified by the measurements. The presentation of more data can be found in [2].

## 6.2. Energy Balance

When crack-extension occurs over the length $\Delta x$, along the grain, then the work done by the constant load $V$ is $V{\cdot}\Delta\delta$, where $\Delta\delta$ is the increase of the deformation at $V$. This work is twice the increase of strain energy of the cantilever part: $V{\cdot}\ \Delta\delta/2$. Thus half of the external work done at cracking is used for crack formation being thus equal to the other half, the strain energy increase.

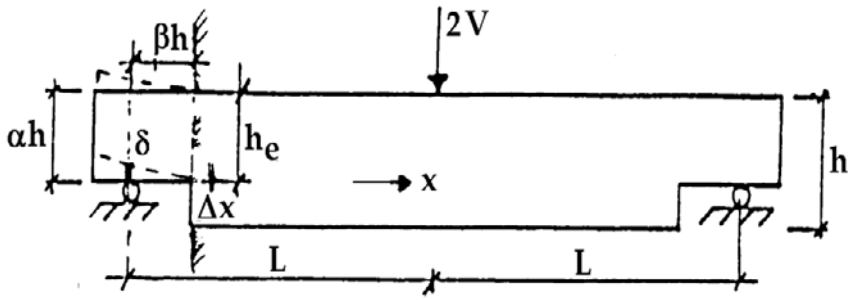


Figure 6.1. Notched beam.

Thus in general, when the change of the potential energy $\Delta W = V{\cdot}\Delta\delta/2$ becomes equal to the energy of crack formation, crack propagation occurs. The energy of crack formation is: $G_c b\Delta x = G_c bh\Delta\beta$, where $G_c$ is the crack formation energy per unit crack area. Thus crack propagation occurs at $V = V_f$ when:

$$\Delta W = V\Delta\delta / 2 = V^2\Delta(\delta / V) / 2 = G_c bh\Delta\beta,$$

thus when:

$$V_f = \sqrt{\frac{2G_c bh}{\frac{\partial(\delta / V)}{\partial \beta}}} \tag{6.1}$$

and only the increase of the compliance δ/V has to be known.

The deflection $\delta$ can be calculated from elementary beam theory as chosen allowable equilibrium system as a lower bound of the strength. This is close to real behaviour because, according to the theory of elasticity, the deflection can be calculated from elementary beam theory while the difference from this stress distribution is an internal equilibrium system causing no deflection of the beam and also the shear distribution can be taken to be parabolic according to this elementary theory, as only component of this polynomial expansion, contributing to the deflection.

According to the Figure 6.2, the notch can be seen as a horizontal split, case: a = a', and case a can be split in the superposition of case b and c, where b = b'.

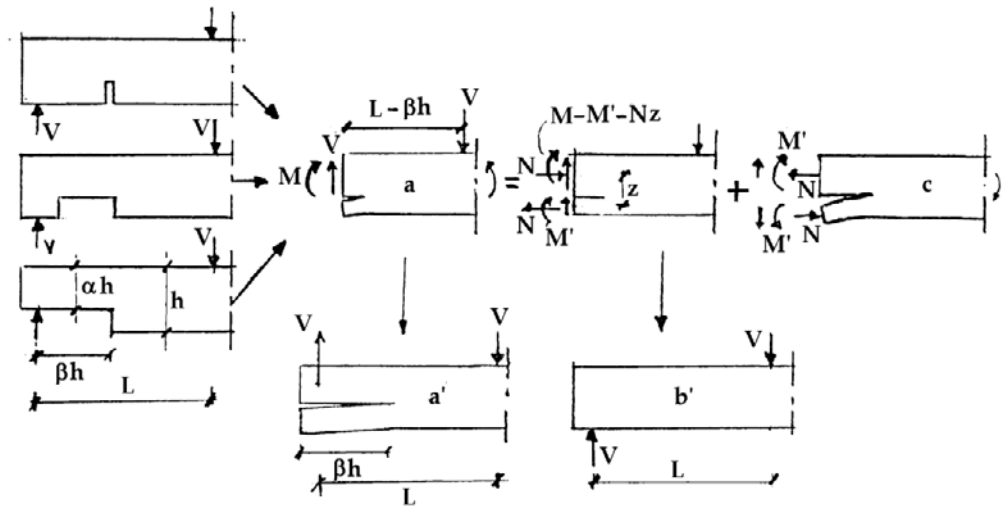


Figure 6.2. Equivalent crack problem according to superposition.

Case c now is the real crack problem by the reversed equal forces that can be analyzed for instance by a finite element method, etc. From the principle of energy balance it is also possible to find the critical value of case c by calculating the differences in strain energies or the differences in deflections $\delta$ by $V$ between case: b' and case a', thus differences in deformation of the cracked and un-cracked part to find $\Delta(\delta/V)$ for eq.(6.1).

Deformations due to the normal stresses $N$ of case c, are of lower order in a virtual work equation and should not be accounted. It then follows that case c of Figure 6.2 is equal to a mode I test and $G_c = G_{Ic}$. When the beam is turned upside down, or when V is reversed in direction, then $M'$ and $V'$ are reversed closing the crack and fracture only is possible by shear, identical to the mode II test and then $G_c = G_{IIc}$

The change of $\delta$ by the increase of shear deformation is, with $h_e = \alpha \cdot h$:

$$\delta_v = \frac{1.2}{G}\left(\frac{\beta h}{b\alpha h} - \frac{\beta h}{bh}\right)\cdot V \tag{6.2}$$

The change of $\delta$ by the increase of the deflection is:

$$\delta_m = \frac{V(\beta h)^3}{3Eb(\alpha h)^3/12} - \frac{V(\beta h)^3}{3Ebh^3/12} = \frac{4V\beta^3}{Eb}\cdot\left(\frac{1}{\alpha^3} - 1\right) \tag{6.3}$$

Thus:

$$\frac{\partial(\delta/V)}{\partial\beta} = \frac{1.2}{Gb}\cdot\left(\frac{1}{\alpha} - 1\right) + \frac{12\beta^2}{Eb}\cdot\left(\frac{1}{\alpha^3} - 1\right) \tag{6.4}$$

The critical value of $V$ thus is according to eq.(6.1):

$$V_f = \sqrt{\frac{1.67G_c hb^2}{\frac{1}{G}\left(\frac{1}{\alpha} - 1\right) + \left(\frac{1}{\alpha^3} - 1\right)\cdot\frac{10\beta^2}{E}}} \tag{6.5}$$

or:

$$\frac{V_f}{b\alpha h} = \frac{\alpha\sqrt{GG_c/h}}{\sqrt{0.6(\alpha^3 - \alpha^4) + 6\beta^2\left(\alpha - \alpha^4\right)G/E}} \tag{6.6}$$

For small values of β eq.(6.6) becomes:

$$\frac{V_f}{b\alpha h} = \frac{\sqrt{GG_c/h}}{\sqrt{0.6\cdot(\alpha - \alpha^2)}} \tag{6.7}$$

For high values of $\beta$, eq.(6.6) becomes:

$$\frac{V_f}{b\alpha h} = \frac{\alpha\sqrt{EG_c/h}}{\beta\sqrt{6(\alpha - \alpha^4)}} \tag{6.8}$$

## 6.3. Experimental Verification

A verification of the prediction of the theory for high values $\beta$, eq.(6.8), when the work by shear is negligible, is given by Table 6.1 of an investigation of Murphy, mentioned in [1], regarding a notch starting at $\beta = 2.5$ and proceeding to $\beta = 5.5$. Further also beams were tested with a slit at a distance: $\beta = 2.5$. Because the exact eq.(6.6) gives a less than 1 % higher value, eq.(6.8) applies. ($\sqrt{GG_c}$ = 11.1 resp. 10.9 $\mathrm{N/mm^{1.5}}$) and: $\sqrt{EG_c}$ = 48.8 $\mathrm{N/mm^{1.5}}$. This value is used in table 6.1 for comparison of eq.(6.8) with the measurements, showing an excellent agreement between theory and measurement. For all specimens was: $\alpha = 0.7$; $\eta = L/h = 10$ ($L$ is distance field loading to support) and b = 79 mm. The other values are given in table 6.1. The fracture energy is: $G_c = \left(48.8\right)^2 / 14000 = 0.17\mathrm{N/mm} = 170\,\mathrm{N/m}$, which agrees with values of the critical strain energy release rate. The value of $K_{Ic}$ is about: $K_{Ic} \approx \sqrt{0.17 \cdot 700} = 10.9\ \mathrm{N/mm^{1.5}}$ = 345 $\mathrm{kN/m^{1.5}}$, as to be expected by the high density of Douglas fir.

**Table 6.1. Strength of clear laminated Douglas firwith notches in the tensile zone in MPa**

| ***h* mm** | $\beta$ | **number** | ***V/αbh* tests eq.(6.8)** | |
|---|---|---|---|---|
| 305 | 2.5 | 2 | 0.46 | 0.47 |
| 305 | 5.5 | 2 | 0.24 | 0.22 |
| 457 | 2.5 | 2 | 0.38 | 0.38 |
| 457 | 5.5 | 1 | 0.16 | 0.17 |

In table 6.2, data are given of Spruce for low values of $\beta$, to verify the then predicted theoretical behaviour according toeq.(6.7) with energy dissipation by shear stresses only. It appears for these data that the difference between the mean values according to eq.(6.7) and eq.(6.6) are 10 % and thus not negligible small and also the values of eq.(6.6) are given to obtain a possible correction factor.

It follows from table 6.2 for Spruce that: $\sqrt{GG_c} = 6.8\,\mathrm{N/mm^{1.5}}$ or: $G_c = 6.8^2 / 500 = 0.092\mathrm{N/mm} = 92\mathrm{N/m}$.

For Spruce is $K_{Ic}$ ≈ 6.3 to 7.6 according to [5], depending on the grain orientation and then also applies: $E_2 \approx G$ and: $K_{Ic} = \sqrt{E_2 G_c} = 6.8\ \mathrm{N/mm^{1.5}}$.

Although the fracture energy is shear-stress energy, failure still is by mode I (of Figure 6.2) and not by the shear mode II, as is supposed by other models. Thus the total work contributes to failure, whether it is bending stress energy (Table 6.1) or shear stress energy (Table 6.2)and $\gamma = 1$ (eq.(5.9) for failure of this type of notch by the high tensile stress perpendicular to the grain at the notch root.

In [2] more data are given regarding the strength of square notches. The size influence, or the influence of the height of the notched beam on the strength, is tested on beams with notch

parameters $\alpha$ = 0.5 and 0.75; $\beta$ is 0.5 and heights $h$ = 50, 100 and 200 mm with $b$ = 45 mm at moisture contents of 12, 15 and 18%. The strength $\sqrt{GG_f}$ appeared to be independent ofthe beam depth as to be expected for macro crack extension along an always sufficient long fracture plane. The value of $\sqrt{GG_f}$ at moisture contents of resp. 12, 15 and 18% was resp.: 6.7; 7.7 and 8.0 $\mathrm{Nmm}^{1.5}$.

**Table 6.2. Strength of notched beams, Spruce, Mohler and Mistler**

| h mm | $\alpha$ | $\beta$ | η/α | b mm | n | V/bαh N/mm$^2$ | var. coef. % | $\sqrt{GG_f}$ | |
|---|---|---|---|---|---|---|---|---|---|
| | | | | | | | | eq.(6.6) | eq.(6.7) |
| | | | | | | | | N/mm$^{1.5}$ | |
| 120 | .917 | .25 | 3.4 | 32 | 6 | 2.36 | 11 | (5.8) | (5.5) |
| | .833 | | 3.8 | | 27 | 1.93 | 15 | 6,4 | 6.1 |
| | .75 | | 4.2 | | 43 | 1.68 | 19 | 6.6 | 6.2 |
| | .667 | | 4.7 | | 14 | 1.52 | 18 | 6.5 | 6.1 |
| | .583 | | 5.4 | | 10 | 1.5 | 18 | 6.8 | 6.3 |
| | .5 | | 6.3 | | 49 | 1.59 | 18 | 7.4 | 6.7 |
| | .333 | | 9.5 | | 10 | 1.48 | 16 | 7.0 | 5.9 |
| **mean** | | | | | | | | **6.8** | **6.2** |
| Testing time more than 1 min., m.c. 11%, ρ = 510 kg/m$^3$ | | | | | | | | | |

Higher values of $\sqrt{GG_f}$ of Spruce, given in [2], are possible for loads close to the support. Then horizontal splitting does not cause failure because the remaining beam is strong enough to carry the total load and the derivation is given by regarding vertical crack propagation necessary for total failure (bending failure of the remaining beam). For this mode I,

$\sqrt{GG_m}$ = 57.5 N/ $\mathrm{mm}^{1.5}$ = 1818 kN/ $\mathrm{m}^{1.5}$ (comparable with 1890 kN/ $\mathrm{m}^{1.5}$ of[5])

For still higher values of $\alpha$, above α = 0.875, compression with shear failure is determining by direct force transmission to the support. In [3] is shown that Foschi's finite element prediction and graphs, given in [5] can be explained and are identical to eq.(6.8).

## 6.4. References


[1] P.J. Gustafsson, A Study of Strength of Notched Beams, CIB-W18A-21-10-1, meeting 21,Parksville, Vancouver Island, Canada, Sept. 1988.

[2] T.A.C.M. van der Put, Tension perpendicular to the grain at notches and joints. CIB-W18A-23-10-1, meeting 23, Lisbon, Portugal, Sept. 1990

[3] T.A.C.M. van der Put, Modified energy approach for fracture of notched beams. Proceed. COST 508 conf. on fracture mechanics. Bordeaux, April 1992.

[4] T.A.C.M. van der Put, A.J.M. Leijten, Evaluation of perpendicular to the grain failure of beams, caused by concentrated loads of joints. CIB-W18A/33-7-7, meeting 33, Delft, The Netherlands, August 2000.
[5] RILEM state of the art report on fracture mechanics, Espoo, 1991.

# 7. Energy Approach for Fracture of Joints Loaded Perpendicular to the Grain

## 7.1. Introduction

As for square end-notches, the analysis can be based on the compliance change by an infinitesimal crack increase. Because measurements show no difference in strength and fracture energy between joints at the end of a beam (Series G6.1 and G6.2 of [1]) and joints in the middle of the beam (the other G-series), and also the calculated clamping effect difference by crack extension is of lower order, this clamping effect of the fractured beam at the joint in the middle of a beam, has to be disregarded as necessity of the virtual energy equation of fracture. This is according to the limit state analysis which is based on the virtual work equations. For end-joints, the split off part is unloaded and there is no normal force and no vierendeel-girder action at all and the situation and fracture equations are the same as for the notched beams of Section 6. For joints in the middle of the beam, splitting goes in the direction of lower moments and is stable until the total splitting of the beam. The analysis in [1] and [2] shows this stable crack propagation because the terms in the denominator become smaller at crack length increase, until the shear term remains, giving the maximal value of V according to eq.(7.6), the same value as for end-joints.

It thus is not true, as is stated in the CIB/W18-discussion of [1], that the analysis and theory are incorrect when virtual lower order terms are omitted in the analysis and that splitting of joints analysis is not comparable to splitting of notched beam analysis. The proof that this neglecting of the vierendeel-action is right is (outer the empirical proof by the measurements) given by the complete analysis for this case in [3], where also the influence on the strain of normal stresses is accounted, leading to eq.(7.5) containing the negligible clamping effect term in the denominator, (based on the assumption that not total splitting of the beam is the end state).

## 7.2. Energy Balance

For a simplecalculation of the compliance difference of the cracked and un-cracked state, (maintaining the clamping action in the end state) half a beam is regarded, as given in Figure 7.1, loaded by a constant load $V$. At the start of cracking, the deflection at $V$ increases with $\delta$ (see Figure 7.2) and the work done by the force V is: $2\Delta W = V \cdot \delta$, which is twice the increase of the strain energy ($\Delta W = V \cdot \delta/2$) of the beam and therefore the amount $\Delta W$ is used to increase the strain energy and the other equal amount of $\Delta W$ is used as fracture energy. Because $\delta$ is the difference of the cracked and "un-cracked" state, only the deformation of the cracked part $\beta h$ minus the deformation of that same part $\beta h$ in the un-cracked state, need to be

calculated, because the deformation of all other parts of the beam by load V are the same in cracked and un-cracked state. As discussed at 6.2, the deflection δ can be calculated from elementary beam theory of elasticity. It thus is not right to regard an additional deformation $\delta_r$, as is done, due to the non-linearity and clamping effect of the cantilevers *βh*, formed by the crack. The clamping effect change is of lower order at aninfinitesimal crack extension. If this effect would have an influence, there should be a difference in notched beams in the splitting force for a real square notch of length *βh* and a vertical saw cut at a distance *βh* from the support, because that slit has at least twice that clamping effect (see Figure 6.2).

For a connection at the middle of a beam the following applies after splitting (see Figure 7.1). The part above the crack (stiffness $I_2 = b(1-\alpha)^3 h^3/12$) carries a moment $M_3$ and normal force N and the part below the crack (stiffness $I_1 = b\alpha^3 h^3/12$) carries a moment $M_1$, normal force N and a shear force V. and at the end of the crack a negative moment of about: $M_2 \approx -M_1$. Further is $M_2 = M_1 - V\lambda$, thus $M_1 = V\lambda/2$.

The deformation of beam 2 of the cracked part *βh* is equal to the un-cracked deformation $\delta_{un}$ of that part and the deformation of beam 1 is $\delta_{un}$ plus the crack opening $\delta$ (see Figure 7.1 and 7.2) and $\delta$ is:

$$\delta = \frac{1}{2}\cdot\frac{V\lambda^2}{EI_1}\cdot\frac{2}{3}\cdot\lambda - \frac{1}{2}\frac{M_1\lambda^2}{EI_1} = \frac{1}{3}\cdot\frac{V\lambda^3}{EI_1} - \frac{1}{4}\cdot\frac{V\lambda^3}{EI_1} = \frac{1}{12}\cdot\frac{V\lambda^3}{EI_1} = \frac{V\beta^3}{bE\alpha^3} \tag{7.1}$$

The deflection difference of the cracked and un-cracked state is total:

$$\delta = \frac{1.2}{G}\left(\frac{\beta h}{b\alpha h} - \frac{\beta h}{bh}\right)\cdot V + \frac{V\beta^3}{bE\alpha^3} \tag{7.2}$$

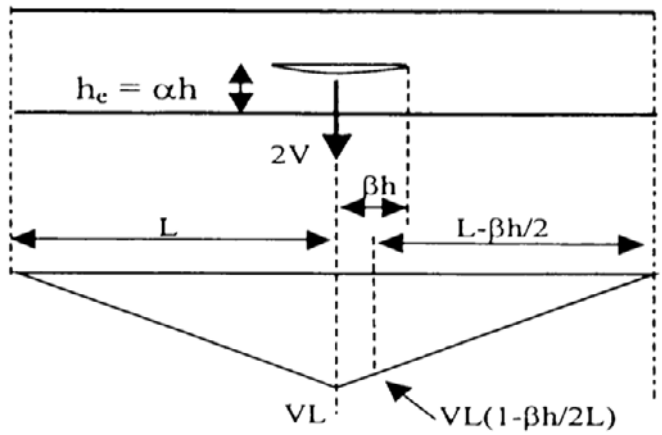


Figure 7.1. Beam with crack by the dowel force of a joint and bending moment.

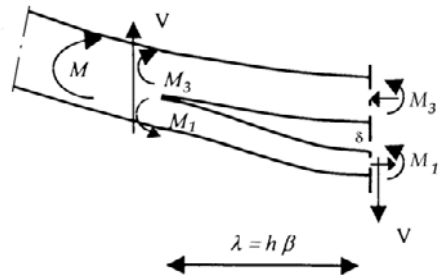


Figure 7.2. Statics of half the crack.

The condition of equilibrium at crack length β is:

$$\partial\left(V\cdot\delta/2-G_c b\beta h\right)/\partial\beta=0 \quad \text{or:} \quad \left\{\partial\left(\delta/V\right)/\partial\beta\right\}\cdot V^2/2=G_c bh$$

or:

$$V_f=\sqrt{\frac{2G_c bh}{\partial(\delta/V)/\partial\beta}} \tag{7.3}$$

where $G_c$ is the fracture energy. It follows from eq.(7.2) that:

$$\frac{\partial\left(\delta/V\right)}{\partial\beta}=\frac{1.2}{bG}\left(\frac{1}{\alpha}-1\right)+\frac{3\beta^2}{Eb\alpha^3} \tag{7.4}$$

and eq.(7.3) becomes:

$$V_f=b\alpha h\sqrt{\frac{GG_c/h}{0.6\left(1-\alpha\right)\alpha+1.5\beta^2G/(\alpha E)}} \tag{7.5}$$

giving, for the always relatively small values of $\beta$, the previous found eq.(6.7):

$$\frac{V_f}{b\alpha h}=\frac{\sqrt{GG_c/h}}{\sqrt{0.6\cdot(1-\alpha)\cdot\alpha}} \tag{7.6}$$

which thus also applies for notched beams and for end-joints and verifies the lower bound of the strength, predicted by the theory of [1]. This also indicates that only work by shear stresses contributes to fracture. The fit of the equation with vierendeel action, eq.(7.5), to the data is not better than the fit by eq.(7.6) what shows that the term $1.5\beta^2G/\alpha E$ is small with respect to $0.6(1-\alpha)\alpha$ and also that $\beta$ is about proportional to $\alpha$ and is of the same order. Comparison of eq.(7.5) and eq.(6.6) shows that the higher value of the end joint is

determining for this definition of the strength and the same design rules as for notches are possible for joints when not the joint but splitting is determining. However design should be based on "flow " of the joint before splitting of the beam and the interaction of joint failure and beam splitting has to be regarded as follows.

When crack extension starts of a cantilever beam loaded by a constant load $V$, giving a deflection increase of $\delta$ at $V$, then the applied energy to the beam is $V{\cdot}\delta$. The energy balance equation then is:

$$V\delta = V\delta/2 + E_c \tag{7.7}$$

where $V\delta/2$ is the increase of the elastic energy and $E_c$ the energy of crack extension.

Thus: $E_c = V\delta/2$ (7.8)

Thus the energy of crack extension is equal to the increase of elastic energy.
Eq.(7.8) also can be written with de incremental deflection $\delta = \mathrm{d}u$:

$$E_c = V^2\,\mathrm{d}(u/V)/2 = = G_f bh\,\mathrm{d}(\beta)$$

or:

$$V = \sqrt{\frac{2G_f bh}{\partial(u/V)/\partial\beta}} \tag{7.9}$$

where $G_f$ is the fracture energy per unit crack surface and "$bh\mathrm{d}(\beta)$" the crack surface increase with "$b$" as width and "$h$" the height of the beam with a crack length $l = \beta h$. When the load on the cantilever beam, mentioned above, is prevented to move, the energy balance, eq.(7.7) becomes:

$$0 = E_e + E_c, \text{ or: } E_c = -E_e = -V\delta/2 \tag{7.10}$$

for the same crack length and now the energy of crack extension is equal to the decrease of elastic energy in the beam.

When the joint at load $V$ becomes determining and just start to flow at $\delta_1$ when splitting of the beam occurs, then eq.(7.7) becomes:

$$V\delta = (V\delta_1)/2 + V(\delta - \delta_1) + E_c \tag{7.11}$$

where again $V\delta_1/2$ is the increase of the elastic energy and $V(\delta - \delta_1)$ the plastic energy of the flow of the joint. From eq.(7.11) then follows:

$$E_c = V\delta_1 / 2 \tag{7.12}$$

the same as eq.(7.8), despite of the plastic deformation.

For connections, plastic deformation in the last case will not yet occur because it is coupled with crack extension. When the dowels of the joint are pressed into the wood, the crack opening increases and thus also crack extension. It can be seen in eq.(7.11), that when flow occurs, the total applied energy $V\delta$ is used for plastic deformation. This is a comparable situation as given by eq.(7.10), and the at the plastic flow coupled crack extension will cause a decrease of the elastic energy. eq.(7.11) thus for joints is:

$$V\delta = (V\delta_1 - \delta_2)/2 + V(\delta - \delta_1) + E_s \tag{7.13}$$

where $V\delta_2 / 2$ is the decrease of the elastic energy by the part of crack extension due to the plastic deformation. From eq.(7.13) now follows:

$$E_s = V(\delta_1 + \delta_2)/2 \tag{7.14}$$

and eq.(7.9) becomes:

$$V = \sqrt{\frac{2G_f bh}{\partial((u_1 + u_2)/V)/\partial\beta}} \tag{7.15}$$

From eq.(7.12) and (7.14) follows that $V_c\delta_{1c} = V(\delta_1 + \delta_2)$, where $V_c\delta_{1c}$ is the amount when the connection is as strong as the beam. Thus:

$$\frac{\delta_1 + \delta_2}{\delta_{1c}} = \frac{V_c}{V} = \frac{n_c V_n}{n V_n} = \frac{n_c}{n} \tag{7.16}$$

where $V_n$ is the ultimate load of the dowel at flow and *n* the number of dowels.

Substitution of eq.(7.16) into eq.(7.15) gives:

$$V = \sqrt{\frac{2G_f bh}{\partial(u_{1c}/V)/\partial\beta} \cdot \frac{n}{n_c}} \tag{7.17}$$

what is equal to $\sqrt{n/n_c}$ times the strength according to eq.(7.9) for $u = u_{1c}$, thus $\sqrt{n/n_c}$ times the splitting strength of the beam as is applied in [1].

According to eq.(7.13), the theoretical lower bound of *V* according to eq.(7.17) occurs at $\delta_1 = \delta_2$, Thus when $n/n_c$ = 1/2. In [1], the empirical value of 0.5 to 0.4 is mentioned according to the data giving:

$$V = \sqrt{\frac{2G_f bh}{\partial(u_{1c}/V)/\partial\beta}} \cdot \sqrt{0,45} = \sqrt{\frac{2G_f bh}{\partial(u_{1c}/V)/\partial\beta}} \cdot 0.67 \tag{7.18}$$

This requirement for "flow" of the joint at failure: $\sqrt{GG_f}$ = 0,67·18 = 12 $\mathrm{Nmm}^{-1.5}$ is included in the Eurocode (see Section 7.5).

The condition $\delta_1 = \delta_2$ means that there is sufficient elastic energy for total unloading and thus full crack extension with sufficient external work for plastic dissipation by the joints. According to eq.(7.13) is for that case:

$$E_c = V\delta_1 \tag{7.19}$$

## 7.3. Experimental Verification

The value of $E_c$ of eq.(7.19) is 12 $\mathrm{Nmm}^{-1.5}$ as follows from the test data given in [1]. In [1], first test-results of 50 beams of [4] with one or two dowel connections are given of beams of 40x100 and 40x200 mm with $\alpha-$values between 0.1 and 0.7 and dowel diameters of 10 and 24 mm. In all cases $n \le 0.5 \cdot n_c$ and not splitting but flow of the connection is determining for failure reaching the in [1] theoretical explained high embedding strength by hardening as to be expected for the always sufficient high spreading possibility of one- (or two-) dowel joints. The same applies for the 1 and 2 dowel joints of the Karlsruhe investigation. Splitting then is not the cause of failure but the result of post-failure behaviour due to continued extension by the testing device.

Table 7.1 of [1] shows that for series B, splitting of the beam is determining. Whether there are 10, 15, 20 or 25 nails per shear plane, the strength is the same: $\sqrt{GG_c} = 16.7$ $\mathrm{Nmm}^{-1.5}$. This is confirmed by the too low value of the embedding strength of the nails $f_c$ of series B. A more precise value of $\sqrt{GG_c}$ follows from the mean value of 17.1 $\mathrm{Nmm}^{-1.5}$ of series B2 to B4. Then the value for 10 nails of series B1 is a factor 15.5/17.1 = 0.9 lower.

Thus $\sqrt{n/n_c} = \sqrt{10/n_c} = 0.9$. Thus $n_c = 12$ for series B. This means that the number of 5 nails of series A is below $n_c/2 = 6$ and the measured apparent value of $\sqrt{GG_c}$ is the minimal value of $\sqrt{GG_c} \cdot \sqrt{0.5 n_c/n_c} = 17.1 \cdot \sqrt{0.5} = 12.1$ $\mathrm{Nmm}^{-1.5}$. The same value should have been measured for series C because the number of 3 nails also is below $n_c/2 = 6$. Measured is 11.7 $\mathrm{Nmm}^{-1.5}$. For the 53 beams of all the series G of [1] this is 12.0 $\mathrm{Nmm}^{-1.5}$. As mentioned a mean value of 12 is now the Eurocode requirement.

The value of $0.5 \cdot n_c$, depends on dimensioning of the joint and thus on amount of hardening by the spreading effect of embedding strength. Thin, long nails at larger distances

in thick wood members are less dangerous for splitting and show a high value of $n_c$. For series G, with $b$ = 100 mm, $n_c / 2$ is at least below 8 nails. For series V of [1] with dowels of 16 mm, $n_c = 8.6$. For design, $n_c$ need not to be known. But dimensioning of the joint to meet also the requirement of $\sqrt{GG_c}$ = 12 $\text{Nmm}^{-1.5}$, will lead to the number of nails of $n_c / 2$. This dimensioning also determines the value of $f_c$. The value of $f_c$ = 4.4 MPa of series A is lower than $f_c$ = 6.2 MPa of series C, in proportion to the square root of the spreading lengths per nail as expected from theory [1].

**Table 7.1. TU-Karlsruhe test data No.1: Joint with nails**

| Type | No | $d$ | rows | Col | $a=\alpha h$ | $a_r$ | $f_c$ | $\sqrt{GG_c}$ | $\eta=L/h$ | $F/b\alpha h$ |
|---|---|---|---|---|---|---|---|---|---|---|
| Test | tests | | m | N | | | [1] | eq.(7) | | |
| | | mm | | | mm | mm | MPa | $\text{N/mm}^{1.5}$ | | MPa |
| | beam: b.h=40.180 mm | | | | | | | | | |
| A1 | 8 | 3.8 | 5 | 1 | 28 | 76 | 3.7 | 13.9 | 2.37 | 7.37 |
| A2 | 4 | 3.8 | 5 | 1 | 47 | 76 | 4.3 | 13.3 | 2.37 | 5.82 |
| A3 | 3 | 3.8 | 5 | 1 | 66 | 76 | 4.2 | 11.3 | 2.37 | 4.52 |
| A4 | 3 | 3.8 | 5 | 1 | 85 | 76 | 4.2 | 10.2 | 2.37 | 3.94 |
| A5 | 3 | 3.8 | 5 | 1 | 104 | 76 | 5.5 | 11.7 | 2.37 | 4.54 |
| | beam: b.h =40.180mm | | | | | **mean** | **4.4** | **12.1** | | |
| B1 | 4 | 3.8 | 5 | 2 | 47 | 76 | 3.5 | 15.5 | 2.37 | 6.77 |
| B2 | 3 | 3.8 | 5 | 3 | 66 | 76 | 3.8 | 17.9 | 2.37 | 7.15 |
| B3 | 3 | 3.8 | 5 | 4 | 85 | 76 | 3.3 | 16.1 | 2.37 | 6.21 |
| B4 | 3 | 3.8 | 5 | 5 | 104 | 76 | 3.6 | 17.2 | 2.37 | 6.69 |
| | beam: b.h = 40.120 m | | | | | **mean** | **3.6** | **16.7** | | |
| C1 | 3 | 3.8 | 2 | 1 | 28 | 76 | 6.8 | 15.3 | 2.18 | 8.51 |
| C2 | 3 | 3.8 | 2 | 1 | 28 | 57 | 6.2 | 13.0 | 2.26 | 7.21 |
| C3 | 3 | 3.8 | 2 | 1 | 28 | 38 | 5.6 | 10.9 | 2.34 | 6.07 |
| C4 | 3 | 3.8 | 2 | 1 | 28 | 19 | 5.7 | 10.3 | 2.42 | 5.73 |
| C5 | 3 | 3.8 | 1 | 1 | 28 | 0 | 6.9 | 11.2 | 2.50 | 6.21 |
| C6 | 3 | 8 | 1 | 1 | 28 | 0 | 5.8 | 9.7 | 2.50 | 5.40 |
| | beam: b.h=40.180 mm | | | | | **mean** | **6.2** | **11.7** | | |
| L8 | 1 | 8 | 1 | 1 | 28 | 0 | 5.0 | 8.8 | 2.50 | 4.64 |

## 7.4. Design Equation of the Eurocode 5

As discussed in [1], the shear capacity is (for $h_e \leq 0.7\ h$)

$$\frac{V_u}{b\sqrt{h}} = 10.3\sqrt{\frac{\alpha}{(1-\alpha)}} = 10.3\sqrt{\frac{h_e}{(h-h_e)}}$$

where

$10.3 = (2/3)\sqrt{(GG_c / 0.6)}$ is the characteristic value.

This can be replaced by the tangent line through this curve at point$\alpha$ = 0.5 giving:

$$\frac{V_u}{b\alpha\sqrt{h}} = 1.7\sqrt{GG_c} = 1.7 \cdot (2/3) \cdot 12 = 13.6 \ \text{Nmm}^{-1.5}.$$

## 7.5. References


[1] T.A.C.M. van der Put, A.J.M. Leijten, Evaluation of perpendicular to the grain failure of beams, caused by concentrated loads of joints. CIB-W18A/33-7-7, meeting 33, Delft, The Netherlands, August 2000.

[2] T.A.C.M. van der Put, Tension perpendicular to the grain at notches and joints. CIB-W18A-23-10-1, meeting 23, Lisbon, Portugal, Sept. 1990

[3] DWSF Technical note

[4] M. Ballerini: A set of tests on beams loaded perpendicular to the grain by dowel type of joints. CIB-W18/32-7-2. Graz. Austria.


# CONCLUSION

- Because the failure criterion for "clear" wood and for macro-crack extension is the same, fracture mechanics of wood and comparable materials is determined by small-crack propagation towards the macro-crack tip. The influence of small-crack propagation is noticeable by the Weibull volume effect of the strength. There is no influence on macro-crack propagation of the geometry of notches and sharpness of the macro crack-tip in wood (against orthotropic theory). Thus orthotropic fracture mechanics is not determining. This also follows from the nearly same fracture toughness and energy release rate for wide and slit notches and the minor influence of rounding the notch (again against orthotropic theory). Determining thus is the influence of small cracks in the isotropic matrix for the total behaviour, having the same influence at the tip of wide as well as slit notches.
- The always applied singularity approach of fracture mechanics does not satisfy the limit analysis requirements for orthotropic materials and prevents the use of the right failure criterion at the crack boundary. Instead therefore, the complete solution of the Airy stress function, based on the flat elliptical crack, has to be applied.
- The empirical mixed I-II-mode fracture criterion is explained by the elliptical small-crack approach, providing the exact theoretical basis of this criterion. This criterion is the consequence of the ultimate uniaxial cohesive strength along the micro-crack boundary. The theory therefore also explains the relations between $K_{Ic}$ and $K_{IIc}$ in TL- and in RL-direction and the relations between the related fracture energies. This

leads to one overall apparent critical energy release rate which may be different for different structures but is independent of the stress combinations of the dissipated strain energy of fracture. Whether, for a square end-notch, work is done by only bending or by only shear deformation, failure is in mode I and not in mode II in the last case as predicted by the other models.

- The orthotropic approach, based on equilibrium of the homogenized reinforcement in wood gives incorrect results, because the matrix is not in equilibrium and does not satisfy the strength criterion. It therefore is necessary to start with equilibrium, compatibility and strength requirements of the isotropic matrix stresses providing a simple orthotropic-isotropic transformation of the Airy-stress function. for the total solution.
- Based on this approach is: $K_{Ic} = \sqrt{E_y G_{Ic}}$ , $K_{IIc} = n_6 \sqrt{E_y G_{IIc}}$ and $G_{IIc} = 4G_{Ic}$ $G_f = 4G_{Ic}/(1+\sqrt{\gamma})^2 = G_{IIc}/(1+\sqrt{\gamma})^2$ with : $\gamma = 1/\left(1+\tau_{xy}^2/\sigma_y^2\right)$ and: $n_6 = \left(2+\nu_{21}+\nu_{12}\right)\cdot\left(G_{xy}/E_y\right)$
- The theoretical value of $G_{IIc} = 4G_{Ic}$ is verified by reported measurements where ratio 3.5 is found ($R^2$ = 0.64) instead of 4. This lower measured ratio is due to the applied too high value of $G_{Ic}$ which should be corrected to be equal to the energy release rate.
- It is shown, that the models applied to wood, (as necessary replacement of the infinite fracture stresses of the singularity approach), as e.g. the Dugdale model, fictitious crack model and crack growth models are incorrect and have to be replaced by the general theory.
- A derivation of the softening curve is given based on small-crack extensions. The softening curve follows at the start the stable part of the Griffith locus. This means that every point of the softening curve gives the Griffith strength. This curve depends on only one parameter, the maximal critical Griffith stress $\sigma_c$ and therefore depends on the critical crack density. This applies until half way of unloading. The fracture energy is down to this point equal to the critical energy release rate. After that, the strength of the fracture plane of the test specimen becomes determining due to a crack joining mechanism, changing the crack density and intact area of the fracture plane and therefore causing a decrease of $\sigma_c$ and an apparent decrease of the fracture energy. The strength at every point of the softening curve is fully determined by the strength of the intact area of the fracture plane. Softening thus is a matter of elastic unloading of the specimen outside the fracture zone and softening thus is not a material property.
- The fracture energy for mode I is stated in literature to be equal to the area under the softening curve divided through the crack length. This is not right. It is half this area when the fracture plane is not limiting. This is applied and accepted for mode II in wood.
- It also is stated that the area of a loading cycle at softening, divided by the area of the crack increment, is equal to the fracture energy. This also is not right. It is shown that

this energy is proportional to the apparent activation energy of all processes in the whole test specimen.

- A revision is necessary of all published mode I data of the fracture energy, based on the area of the softening curve, because of the dissimilar behaviour of post fracture behaviour giving no right prediction of the fracture energy. Therefore this area method should not be used anymore. A right simple description follows from the derived apparent energy release rate adapted to the measured strength data.
- The theory shows that the Eurocode design rules for beams with rectangular end notches or joints should be corrected to the right real compliance difference and the right measured uniaxial stiffness.
- The verification of the derived theory by measurements shows the excellent agreement. The method provides an exact solution and is shown to be generally applicable also for joints and provides as simple design equations as wanted.

# 9. Appendix: Weibull Size Effect in Fracture Mechanics of Wide Angle Notched Timber Beams

Because the Weibull size effect is normally not a fracture mechanics subject, this influence is discussed in a separate appendix to the main theory of this chapter.

## 9.1. Summary

A new explanation is given of the strength of wide angled notched timber beams by accounting for a Weibull type size effect in fracture mechanics. The strength of wood is described by the probability of critical initial small crack lengths. This effect is opposed by toughening by the probability of having a less critical crack tip curvature. The toughening effect dominates at the different wide angle notched beams showing different high stressed areas by the different angles and thus different influences of the volume effect. This is shown to explain the other power of the depth in Eq.(9.18) and (9.19) than the sharp notch value of 0.5 of Eq.(9.17). It further is shown to explain why for very small dimensions, also for sharp notches, the volume effect applies. The explanation by the Weibull effect implicates that the strength depends on small crack extension, in the neighbourhood of the macro crack tip. This initial crack population can be different for full scale members indicating that correction of the applied data is necessary and that additional toughness tests have to be done on full scale (or semi full scale) test specimens.

## 9.2. Introduction

Fracture mechanics of wood is normally restricted to fracture along the grain. It is e.g. not possible to have shear crack propagation across the grain. Also the mixed mode crack follows the weak material axes and only may periodically jump to the next growth layer at a weak spot. Thus the direction of the collinear crack propagation is known and is not e.g. dependent

on a local critical value of a strain energy density. As shown in [1], the singularity approach gives no right results in this case and the analysis has to be based on linear elastic flat elliptic crack extension by the maximal stress at the elastic-plastic boundary around the small crack. This response at randomized stress raisers near weak spots is indicated by the volume effect of the strength. There also is no clear influence on macro-crack propagation of the crack geometry and notch form and sharpness of the macro crack tip, showing orthotropic fracture mechanics to be not decisive. This also is indicated by the not orthotropic, but isotropic relation between mode I stress intensity and strain energy release rate of wood. The determining small crack behaviour also follows from the failure criterion of common un-notched wood being of the same form as the theoretical explained fracture mechanics criterion for notched wood.

Wood should be regarded as a reinforced material. The commonly applied orthotropic Airy stress function is based on spread out of the reinforcement to act as a continuum, satisfying the equilibrium, compatibility and strength conditions. This only is possible by interaction through the matrix and the solution by the orthotropic plane equilibrium methodappears to be not right because thedetermining equilibrium conditions and strength criterion of the matrix then are not satisfied. It thus is necessary to solve the Airy stress function for the stresses in the isotropic matrix and this appears to give the right solution providing the theoretical derivation [1] of the Wu-mixed mode I - II fracture criterion. As a result, the right fracture energies and theoretical relations between mode I and II stress intensities and energy release rates then are obtained. This also applies for the relations between the mode I critical stress intensities of the different main material planes. For wood the matrix thus is determining for initial failure and not the reinforcement.Also the failure criterion of unnotched wood shows no coupling term between the reinforcements in the main directions confirming the orthotropic strength schematization to be not determining. The determining small crack dimension follows from the Weibull size effect. The here treated strength of wide angle notched beams is an example of a determining size effect in fracture mechanics.

The strength analysis of [2] of wide angle notched beams, given in Figure9.1, was based on the orthotropic Airy stress function. However, despite of the dominant mode I loading, none of the solutions of this function are close enough to the measurements to be a real solution. The reason of this is the absence of the Weibull size effect in the equations as will be shown in this article. The in [2] chosen solutions of the biharmonic Airy stress function are:

$r_1^{\pm n}\cos(n\theta_1)$, $r_1^{\pm n}\sin(n\theta_1)$, $r_2^{\pm n}\cos(n\theta_2)$, $r_2^{\pm n}\cos(n\theta_2)$ resulting in:

$$\{\sigma_r,\sigma_\theta,\sigma_{r\theta}\}=\frac{K_A}{(2\pi r)^n}\{f_1(n\theta),f_2(n\theta),f_3(n\theta)\} \tag{9.1}$$

where $K_A$ is the stress intensity factor and "$r$" the distance from the notch root. In the direction of crack extension, along the grain ($\theta=0$), the tensile strength perpendicular to the grain $\sigma_\theta$ is determining for fracture. The boundary conditions for the different notch angles

*a/g* provide different values of the power "*n*"and thus different slopes of the lines in Figure 9.2. However, it is theoretically not possible that these lines intersect trough one point, as is measured, because the different boundary conditions by the different notch angles cannot be satisfied at the same time and the chosen mathematical solution of [2] thus have to be rejected. The fact that these lines cross one point, at the elementary volume, indicates the existence of a volume effect of the strength. This has to be introduced in the fracture mechanics calculation what simply can be based on the energy method as discussed in section 9.4.

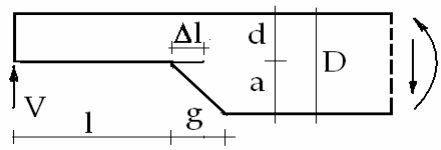


Figure9.1. Wide angle notched beam element.

In section 9.3, the derivation of the size effect is given to show the analogous derivation of the toughening size effect in section 9.4.

## 9.3. Size Effect

Due to the initial small crack distribution, clear wood shows a brittle like failure for tension and shear.According to the Weibull model, the probability of rupture, due to propagation of the biggest crack in an elementary volume $V_0$ is equal to $1-P_0(\sigma)$, when $P_0$ is the probability of survival. For a volume *V* containing $N = V/V_0$ elementary volumes the failure probability is $1-P_s = (1-P_0)(1-P_0)(1-P_0)\cdots = (1-P_0)^N$. Thus $\ln(1-P_s) = N\ln(1-P_0) \approx -NP_0$ because $P_0 << 1$. Thus the probability of survival of a specimen with volume *V*, loaded by a constant tensile stress $\sigma$, as in the standard tensile test, is given by:

$$P_s(V) = \exp(-NP_0) = \exp\left(-\frac{V}{V_0}\left(\frac{\sigma}{\sigma_0}\right)^k\right) \tag{9.2}$$

where $P_0(\sigma) = (\sigma/\sigma_0)^k$ is chosen, because the power law of $\sigma$ may represent any function of $\sigma$ around a chosen stress value as e.g. the mean failure stress (see Section 9.5 for the proof). For a stress distribution, Eq.(9.2) becomes:

$$P_s(V) = \exp\left( -\int_V \left( \frac{\sigma(x,y,z)}{\sigma_0} \right)^k dx \cdot dy \cdot dz / V_0 \right) \tag{9.3}$$

This specimen has an equal probability of survival as the standard test specimen Eq.(9.2) when the exponents are equal thus when:

$$\int_V \left( \frac{\sigma(x,y,z)}{\sigma_0} \right)^k dV = \left( \frac{\sigma_s}{\sigma_0} \right)^k V_s \tag{9.4}$$

For a constant stress $\sigma(x,y,z) = \sigma$, the specimen strength thus will decrease with its volume *V* according to:

$$\sigma = \sigma_s \cdot \left( \frac{V_s}{V} \right)^{1/k} \tag{9.5}$$

where $\sigma_s$ is the mean strength of the specimen with volume $V_s$. The power *k* depends on the coefficient of variation $s/\sigma$ according to:

$$\left( \frac{s}{\sigma} \right)^2 = \frac{\Gamma(1+2/k)}{\Gamma^2(1+1/k)} - 1 \tag{9.6}$$

From the row-expansion of the Gamma-functions it can be seen that:

$$k \cdot \frac{s}{\sigma} = f\left( \frac{s}{\sigma} \right) \approx 1.2 \tag{9.7}$$

where f( $s/\sigma$ ) is normally a little varying function. Thus: $1/k = s/(1.2 \cdot \sigma)$

For a stress distribution, Eq.(9.4) becomes:

$$\int \left( \frac{\sigma_m}{\sigma_0} \right)^k \left( \frac{\sigma(x,y,z)}{\sigma_m} \right)^k dxdydz = \left( \frac{\sigma_m}{\sigma_0} \right)^k V_{ch} = \left( \frac{\sigma_s}{\sigma_0} \right)^k V_s \tag{9.8}$$

where $\sigma_m$ is the determining maximal stress in volume *V* and $V_{ch} = \int (\sigma/\sigma_m)^k \, dV$, a characteristic volume. Eq.(9.8) thus becomes:

$$\sigma_m = \sigma_s \left( \frac{V_s}{V_{ch}} \right)^{1/k} = \sigma_s \left( \frac{V_s}{V_{ch}} \right)^{s/1.2\sigma} \tag{9.9}$$

This applies for the strength of common unnotched specimens.
This strength also is determined by fracture mechanics. The tensile strength is e.g.:

$$f_t = \frac{K_{Ic}}{\sqrt{\pi c}} \quad \text{or} \quad f_t = f_{t,s} \sqrt{\frac{c_s}{c}} \,. \tag{9.10}$$

where $K_{Ic}$ is the stress intensity factor.
Substitution of the strength according to Eq.(9.5) (or Eq.(9.9)) leads to:

$$f_t = f_{t,s} \sqrt{\frac{c_s}{c}} = f_{t,s,V} \left( \frac{c_s}{c} \right)^{0.5} \left( \frac{V_s}{V} \right)^{1/k} \tag{9.11}$$

This equation gives the probability of a critical Griffith crack length *c* leading to fracture. Also in this case, a crack toughening mechanism is thinkable,discussed in section 9.4, leading to the opposite volume effect with a negative value of the exponent 1/*k*. This can not be distinguished and the resultant value of 1/*k* then is given by Eq.(9.11). Because for every type of wood material the value of *c* is specific, determining the specimen strength, Eq.(9.9), as shortcut of Eq.(9.11), is applied in practice.

The fracture mechanics derivation for wood can be based on the elastic full "plastic" approximation of flow and microcracking at the crack tip. Thus the crack dimensions are replaced by the elastic-plastic boundary around the crack and linear elastic fracture mechanics is applicable outside this boundary. According to [3], the stress intensity factor of Eq.(9.10) is: $K_{Ic} = \sigma_t \sqrt{\pi r / 2}$ where $\sigma_t$ is the equivalent cohesion strength at the crack tip boundary and $r$ is the radius of the elastic-plastic boundary of the crack tip zone. A constant stress intensity factor $K_{Ic}$ means that $\sigma_t \sqrt{r}$ is constant and only the crack length *c* is a variable as for brittle fracture. Toughening means an increase of the plastic zone, thus of *r* of the small cracks, within the characteristic volume. This influence is visible at the different wide angle notches as discussed in section 9.4.

Because fracture across the grain is tough and the lengths of applied beams don't vary much, the size effect of the length dimension is small and the volume effect for bending is replaced by a height effect of the beam only. It is postulated that this absence of a width effect is explained by the constant widths of $2b'$ of2 planes of weakness adjacent to the sides of the beam due to cutting at manufacturing. Then: $\left(V_s / V_{ch}\right)^{1/k} = \left(2b' h_s l / 2b' hl\right)^{1/k} = \left(h_s / h\right)^{1/k}$, becomes the height factor of the Codes. This width effect is applied in section 9.4.

## 9.4. Size Effect of Wide Notched Beams

The analysis of the strength of the notched beams can be based on the energy method where the critical fracture energy is found from the difference of the work done by the constant force due to its displacement by a small crack extension minus the increase of the strain energy due to this displacement. According to this approach of [3], the bending stress $\sigma_m$ at the end of the notched beam at $l = \beta D$ in Figure 9.1 is:

$$\sigma_m = \frac{6V_f \beta D}{b(\alpha D)^2} \approx \frac{\sqrt{6EG_c / D}}{\sqrt{\left(\alpha - \alpha^4\right)}} \tag{9.12}$$

when the notch is not close to the support. In [2] is chosen: $\alpha$ = *d/D* = 0.5, what means that *d* = *a*.Further the length is *l* = 2*D* when *g/a* = 0 and 2, while *l* = 4D for *g/a* = 4in Figure 9.1.*E* is the modulus of elasticity and $G_c$ the critical energy release rate, given in [3]. Eq.(9.12) applies for the rectangular notch (*g* = 0). For wide notch angles a more complicated expression applies because of the changing stiffness over length $\Delta l$ of the crack extension. However, for given dimensions and loading, the basic form of the equation is the same as Eq.(9.12), thus:

$$\sigma_m = B\sqrt{EG_c / D} \tag{9.13}$$

where *B* is a constant depending on dimensions and notch angle. According to [3] is, as mentioned, $\sqrt{EG_c} \triangleq K_c \triangleq \sigma_t \sqrt{r}$ , where $\sigma_t$ is the equivalent cohesion strength and the crack tip radius $r$ is the only parameter of the notch strength. The volume effect depending on the stress follows from section 9.3 and the analysis thus can be based on the flow stress and the characteristic volume around the notch tip, For the probability of a critical value of *r*, of the small initial cracks within the high stressed characteristic volume around the notch tip, the probabilistic reasoning of section 9.3 can be repeated as follows. The probability of having a critical flaw curvature $1/r$ in an elementary volume $V_0$ is equal to $1 - P_0(1/r)$, when $P_0$ is the survival probability. For a volume *V* containing $N = V/V_0$ elementary volumes the survival probability is in the same way:

$$P_s(V) = \exp\left(-NP_0\right) = \exp\left(-\frac{V}{V_0}\left(\frac{r}{r_0}\right)^{-k}\right) \tag{9.14}$$

where $P_0\left(1/r\right) = \left(r_0 / r\right)^k$, because the power law may represent any function in 1/*r*. At "flow", this probability is not a function of $\sigma$, but of the flow strain, given by critical *r*

Equal exponents for the same probability of failure in two cases now lead to:

$$r = r_s \left(V / V_s\right)^{1/k} \tag{9.15}$$

and Eq.(9.13) becomes:

$$\sigma_m \approx \frac{B'\sigma_t\sqrt{r_s}}{\sqrt{D}} \cdot \left(\frac{V}{V_s}\right)^{1/2k} \quad \text{or:} \quad \sigma_m = \sigma_{m0}\left(\frac{D}{D_0}\right)^{-0.5}\left(\frac{V}{V_0}\right)^{1/2k} \tag{9.16}$$

For the notch angle of 90°, ($g$ = 0 in Figure 9.1), or smaller angles, the high stressed elastic region around the crack tip is, as the fracture process zone itself, independent of the beam dimensions. Thus in characteristic dimensions $V = b'l'h' = V_0$ and Eq.(9.16) becomes:

$$\sigma_m = \sigma_{m0}\left(\frac{D}{D_0}\right)^{-0.5} . \tag{9.17}$$

independent of a volume effect. For the widest notch angle of 166° ($g/a$ = 4), there is a small stress gradient over a large area and $V$ is proportional to the beam dimensions. Thus: $V$ (:) $b{\cdot}d{\cdot}l = \gamma D{\cdot}\delta D{\cdot}\beta D = \gamma{\cdot}\beta{\cdot}\delta\, D^3$ and: $V/V_0 = (\gamma\delta\beta\, D^3/\gamma\delta\beta\, D_0^3) = \left(D / D_0\right)^3$. Thus is, with $1/k$ = 0.18:

$$\sigma_m = \sigma_{m0}\left(\frac{D}{D_0}\right)^{-0.5+3/(2k)} = \sigma_{m0}\left(\frac{D}{D_0}\right)^{-0.23} \tag{9.18}$$

For the angle of 153.40°, ($g/a$ = 2), the high stressed region dimensions becomes proportional to the dimensions $b$ and $D$ and:

$V/V_0 = (bdl)/(b_0 d_0 l) = (\gamma\delta D^2/\gamma\delta D_0^2) = (D^2/D_0^2)$ and with$1/k$ = 0.18 is:

$$\sigma_m = \sigma_{m0}\left(\frac{D}{D_0}\right)^{-0.5+2/(2k)} = \sigma_{m0}\left(\frac{D}{D_0}\right)^{-0.32} \tag{9.19}$$

It follows from Figure9.2, that the values of exponents of – 0.5, - 0.32, and -0.23 are the same as measured. The coefficient of variation of the tests must have been: 1.2·0.18 = 0.22, as common for wood. According to the incomplete solution of [2], discussed in the Introduction, these values of the exponents were respectively - 0.437, - 0.363 and - 0.327, thus too far away from the measured values.

The explanation of no volume effect of sharp notches due to the invariant characteristic volume, independent of the beam dimensions, explains also why for very small beams, also for sharp notches, there is a volume effect because then the beam dimensions are restrictive for the characteristic volume. As shown above, the exponent may change from – 0.5 to -0.23

with decrease of the beam dimensions. This is measured and e.g. discussed at pg. 85 of [4] and it now is shown that toughening (and not nonlinear behaviour) is the explanation of this volume effect.

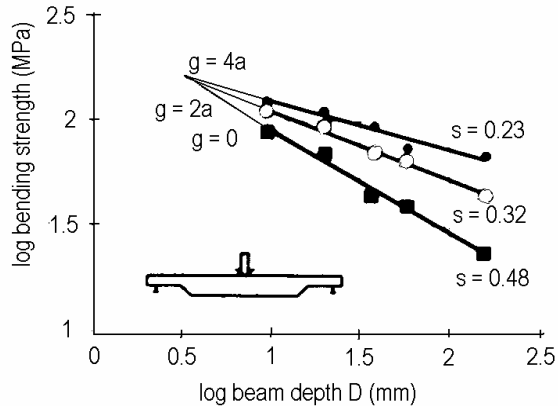


Figure 9.2. Measured bending strengths for different sizes and notch angles.

The lines in Figure 9.2 intersect at the elementary Weibull volume wherefore the depth dimension is $10^{0.6} = 4$ mm with a material bending strength of 147 MPa.

## 9.5. Derivation of the Power Law Applied in Section 9.3

Any function f($x$) always can be written in a reduced variable $x / x_0$.

$$f(x) = f_1(x / x_0)$$

and can be given in the power of a function:

$$f(x) = f_1(x / x_0) = \left[ \left\{ f_1\left(x / x_0\right) \right\}^{1/n} \right]^n \quad \text{and expanded into the row:}$$

$$f(x) = f(x_0) + \frac{x - x_0}{1!} \cdot f'(x_0) + \frac{(x - x_0)^2}{2!} \cdot f''(x_0) + \ldots\ldots \text{ giving:}$$

$$f(x) = \left[ \left\{ f_1(1) \right\}^{1/n} + \frac{x - x_0}{x_0} \frac{1}{n} \left\{ f_1(1) \right\}^{1/n-1} \cdot f_1'(1) + \ldots\ldots \right]^n = f_1(1) \cdot \left( \frac{x}{x_0} \right)^n$$

when: $\left( f_1(1) \right)^{1/n} = \left( f_1(1) \right)^{1/n-1} \cdot f_1'(1) / n$ or: $n = f_1'(1) / f_1(1)$

where: $f_1'(1) = \partial f_1(x/x_0) / \partial(x/x_0)$ for $x = x_0$ and $f_1(1) = f(x_0)$

Thus: $f(x) = f(x_0) \cdot \left(\frac{x}{x_0}\right)^n$ with $n = \frac{f_1'(1)}{f_1(1)} = \frac{f'(x_0)}{f(x_0)}$

This derivation of the power law, using only the first 2 expanded terms applies in a limited range of *x* around $x_0$. This is not restrictive for strength problems. and one reference value $x_0$ is sufficient.

## 9.6. Conclusions Regarding the Size Effect

- A explanation is given of the strength of wide angled notched beams of [2] by introducing the Weibull type size effectin fracture mechanics based on the critical curvature of the initial small cracks near the high stressed notch tip zone.
- For sharp notch angles, up to 90°, there is no volume effect due to the constant volume of the characteristic volume, containing the fracture process zone. For wider notch angles, the peak stresses and stress gradients become lower and are divided over a larger region and influenced by the dimensions and thus a volume effect correction applies.
- The intersect of the three lines in Figure9.2, with different values of "*n*" of Eq.(9.1), due to different boundary conditions by the different notch angles, can not be explainedby the boundary value analysis. This intersect only can be explained to be due to the volume effect of the strength indicating failure by small crack extension within the high stressed region at the notch tip.
- Using the Energy approach and the volume effect correction according to Eq.(9.16), the measured values of the powers of the depths (or the slopes of the lines of Figure9.2) are precisely explained.

## 9.7. References

[1] T.A.C.M. van der Put, A new fracture mechanics theory of orthotropic materials like wood, *Eng. Fract. Mech*. 74, (2007), 771-781.

[2] R.H. Leicester, Design specifications for notched beams in AS 1720, CIB-W18/38-6-1, meeting 38, Karlsruhe, Germany, August 2005.

[3] T.A.C.M. van der Put, Modified energy approach for fracture of notched beams, COST 505 workshop on fract. mech. Bordeaux, April 1992.

[4] Smith, E. Landis, M. Gong, *Fracture and Fatigue in Wood*, J. Wiley & Sns.

In: Advances in Mechanical Engineering Research. Volume 2 ISBN: 978-1-61761-984-7
Editor: David E. Malach 

*Chapter 2*

# THULIUM-BASED CONTRAST AGENTS FOR MAGNETIC RESONANCE IMAGING (MRI)

***Dirk Burdinski,[1,2*] Jeroen A. Pikkemaat[3] and Sander Langereis[1]***
Philips Research Europe, High Tech Campus 11, 5656 AE Eindhoven, The Netherlands, and Cologne University of Applied Sciences, Chempark Leverkusen E39, Kaiser-Wilhelm-Allee, 51368 Leverkusen, Germany

## ABSTRACT

Magnetic resonance imaging (MRI) has developed into one of the most versatile techniques in clinical imaging and biomedical research by providing non-invasively high resolution, three-dimensional anatomical and contrast-enhanced images of living tissue. The two most common groups of contrast-enhancing agents are gadolinium-based complexes and magnetic nanoparticles. Both types of contrast agents shorten locally the relaxation time of bulk water protons via rapid exchange of water molecules employing inner- or outer-sphere magnetic interactions to provide $T_1$-, $T_2$-, or $T_2$*-based contrast enhancement. The quest for disease-specific and individualized approaches to imaging requires contrast agents with a relatively high sensitivity and has propelled the development of novel functional or target-specific agents. With this aim, the shift properties of paramagnetic complexes other than gadolinium have been exploited for designing new types of contrast agents with highly specific reporter functionalities. The particularly beneficial chemical shift properties of thulium(III) and their thermal sensitivity, therefore, have stimulated the development of novel thulium(III)-based contrast agents for MR imaging. An important group of such agents is formed by those that generate contrast based on the transfer of saturated magnetization from the contrast agent or from water molecules interacting with a lanthanide shift reagent to the bulk water (chemical exchange saturation transfer (CEST) agents). Magnetization saturation is created using either exchangeable protons of the paramagnetic thulium(III) chelate complex (paraCEST agents), or using water molecules that interact with a thulium shift

[1] Department of Bio-Molecular Engineering, Philips Research
[2] Faculty of Applied Natural Sciences, Cologne University of Applied Sciences
[*] Author Email Address: dirk.burdinski@fh-koeln.de
[3] Department of Materials Analysis, MiPlaza, Philips Research

reagent encapsulated in a liposomal carrier (lipoCEST agents). Various strategies have already been devised to modulate the CEST effect in response to a physiologically meaningful parameter, such as pH, metabolite concentration, or enzyme activity. MR thermometry is another important target in the development of novel thulium(III)-based contrast agents. Such temperature mapping is based on the strong temperature dependence of the hyperfine chemical shifts of thulium(III) complexes, which can be measured in-vivo with different MR techniques. Upcoming applications of thulium-based contrast agents include disease-specific targeted contrast agents and theranostic agents suitable for image-guided drug delivery.

Keywords: thulium complexes, magnetic resonance imaging, contrast agents, chemical exchange saturation transfer (CEST), magnetic resonance thermometry, molecular imaging, chemical shift, paramagnetic complexes, supramolecular complexes.

## INTRODUCTION

Magnetic resonance imaging (MRI) is a non-invasive and safe clinical imaging technique that offers a unique combination of advantages including the recording of anatomical images with a high temporal and spatial resolution. The diagnostic value of MRI for many types of diseases can be increased dramatically through the application ofparamagnetic contrast agents during or prior to the actual image acquisition. To allow for a deeper understanding of the mechanism, by which MRI contrast agents increase the image information, and the rationale behind their molecular design, we will first summarize some basic principles of MRI contrast generation.

In MRI, the spatial distribution of the concentration and relaxation properties of a particular atomic nucleus is measured and displayed as a two- or three-dimensional image. The most abundant atomic nucleus in the human body is the hydrogen nucleus ("$^1$H" or "proton"). This nucleus is mainly present in water and fat molecules, which are ubiquitously found in large quantities in most types of tissues. Both sources of the $^1$H nuclei yield intense MR signals, which can be imaged either simultaneously or separately. The water signal, however, has clinically the most relevance. Therefore, current MRI contrast agents have been developed to exclusively affect the water signal and the discussion below will focus on this proton source. It should be noted, nevertheless, that protons in fatty tissues may cause artifacts in some MRI techniques, which will not be elaborated on in this review.

In the MRI image acquisition procedure, the human subject is placed in a uniform static $B_0$ field. Since the hydrogen nuclei possess a small magnetic moment, they have a tendency to orient along the direction of $B_0$ (defined as the z-axis), but they have no preferred orientation in the x,y-plane. In the equilibrium situation the sum of the proton magnetic moments, therefore, yields a net water magnetization in the z-direction (longitudinal magnetization). This magnetization vector can be (partly) tilted into the x,y-plane by applying radiofrequency (RF) waves to the subject, usually in the form of a short RF pulse. This process is called excitation. Immediately after excitation, the water magnetization - because of its "spin" - starts to rotate around $B_0$, very much like the slow rotating movement of a tilted spinning top around the earth's gravity field. This movement is called "precession". The time-varying component of the precessing magnetization (i.e. the component in the x,y-plane or the "transverse magnetization") causes an AC current in a nearby radiofrequency coil, which is

detected as the MRI signal. The frequency of this AC current, the so-called resonance frequency ($\omega$), is proportional to the magnetic field strength ($B$) (Equation 1).

$$\omega = \gamma \cdot B \tag{1}$$

Here, the gyromagnetic ratio ($\gamma$) is constant for a given atomic nucleus (42.58 MHz/T for the hydrogen nucleus). If, on top of the static $B_0$field, a known spatially dependent magnetic field, e.g. with a linear magnetic-field gradient in the x-direction ($g_x$) according to Equation 2 is applied during the detection of the MR signal, a continuum of superimposed signals with different frequencies is detected, from which the exact position in the subject can be calculated using Equations 1 and 2.

$$B = B_0 + g_x \cdot x \tag{2}$$

Except for the precession movement, two additional processes occur after excitation that both result in a slow return of the magnetization to the equilibrium situation. The faster one of those, called transverse relaxation, is an exponential decay of the magnitude of the transverse magnetization down to zero with a rate $R_2$ (or $R_2$*). The second one, called longitudinal relaxation, is an exponential 'decay' of the longitudinal magnetization back to the equilibrium magnetization at a rate $R_1$. Both types of relaxation are governed by interactions of the magnetic moments of the hydrogen nuclei with local non-uniform magnetic fields, e.g. resulting from the magnetic moments of nearby hydrogen nuclei or unpaired electrons. In the longitudinal relaxation process, transitions between different energy levels occur and, as a consequence, the interactions must be time-dependent with frequencies near the resonance frequency of the relaxing nucleus. These relaxation processes are extremely important for MRI since they appear as contrast in the MR image and are different for different types of tissue.

At a first level of approximation, the MR signal and, consequently, the contrast in the three-dimensional MR image is proportional to the amount of excitation, which is maximal if the magnetization is tilted completely in the x,y plane upon application of a so-called 90 degree RF pulse. It is also roughly proportional to the concentration of the hydrogen atomic nuclei, thus the water or fat concentration, generally referred to as the 'proton density'. The differences in MR contrast between various (diseased) tissues are often small in a "proton-density weighted" MR image, because the excitation is usually homogenous and the proton density does not vary much between different tissues except for bone tissue. Alternatively, MR images can be recorded "$T_2$-weighted" ($T_2 = 1/R_2$) by adding a specific delay period between excitation and detection of the MR signal. During this period, transverse relaxation causes the signal to decay. Thus, tissues with a fast $R_2$ will appear dark in the $T_2$-weighted image, whereas tissues with a slow $R_2$ will appear white. Likewise, the MR images can be made "$T_1$-weighted" ($T_1 = 1/R_1$) by decreasing the delay between two consecutive excitations to values below about $2/R_1$. Then, the magnetization does not return completely to the equilibrium value between consecutive excitations and the magnitude of the starting magnetization for the second excitation will be less than that of the first one. After several excitations, the signal intensity will reach a plateau value that is significantly lower than it would be if the time between the excitations would be infinitely long. Then, the signal is said

to be saturated. Signals from tissues with a fast $R_1$ are less easily saturated. These tissues will appear white in the $T_1$-weighted image, whereas tissues with a slow $R_1$ will appear dark.

Although new types of contrast mechanisms are constantly being explored in the academic and clinical research community, daily clinical practice still relies mostly on these two basic types of image contrast: $T_1$- and $T_2$-weighted MRI. Contrast differences between different types of tissues appear as a result of differences in the viscosity, in the concentrations of paramagnetic compounds, and in the local variations of the magnetic susceptibility, e.g., as a result of tissue heterogeneity, all of which influence $R_1$ and $R_2$.

In many situations, natural MRI contrast differences are insufficient for discrimination between healthy and diseased tissues. For this reason MRI contrast agents have been developed. Obvious key properties of effective MRI contrast agents are (i) good contrast enhancement in the MR image, (ii) a low toxicity, and (iii) a preferential accumulation in the tissue of interest, usually the diseased tissue.

Already soon after the introduction of the first prototype MRI scanners it was recognized that paramagnetic ions could be used to selectively enhance the MR image contrast for diagnostic purposes [1,2]. Paramagnetic ions, because of their large magnetic moment, strongly increase the longitudinal and transverse relaxation rates, a fact that was discovered in the early days of magnetic resonance [3]. Hence, areas within the studied subject containing high concentrations of paramagnetic ions appear hyperintense (white) in a $T_1$-weighted MR image and hypointense (dark) in a $T_2$-weighted MR image. The predominant contrast agents in commercial use today are comprised of gadolinium(III) ions bound to chelating multidentate ligands based on a polyaminoalkylcarboxylate motif (Figure 1) [4-6]. At present, such contrast agents are used in approximately 50% of the MRI examinations world-wide (> 1 million doses per year). The "free" $Gd^{3+}$ ion in aqueous solution, $[Gd(H_2O)_9]^{3+}$, is an excellent relaxation agent by itself, but is highly toxic to humans even in low concentrations (LD50 values are in the range of 0.1-0.5 $mmol \cdot kg^{-1}$) [7]. Chelation of the $Gd^{3+}$ ion with ligands like $H_4$dota or $H_5$dtpa causes an only about two-fold decrease of the relaxivity, even though eight out of nine coordinated water molecules are replaced by the octadentate ligand. Apparently, the water molecules that are directly bound to the gadolinium ion as part of the “first coordination sphere” contribute only partly to the total relaxation enhancement. About half of the relaxation enhancement is mediated by water molecules that are weakly associated with the chelate complex in, the “second coordination sphere” as well as by nearby water molecules that are not directly bound to the complex and form the so-called “outer coordination sphere”. The overall toxicity of the chelate as compared to the free ion, however, is reduced by a remarkable one to two orders of magnitude. This is mainly brought about by the exquisite biochemical inertness of the complex, combined with its large stability constant and its fast renal excretion [7].

The molecular weight of the contrast agent strongly determines its biodistribution. Low molecular-weight contrast agents, after intravenous injection, preferably accumulate in various types of diseased tissue, for example in tumors (Figure 2). This site-specific contrast enhancement results from the higher “leakiness” (permeability) of blood vessels in diseased tissue as compared to those in healthy tissue, allowing for an enhanced extravasation of small to medium sized molecular species. Large molecular-weight contrast agents mainly remain in the blood vessels. Such “blood-pool contrast agents” are widely used to improve contrast in MR angiography or perfusion imaging, for example to study special types of tumors that increase blood perfusion without altering the permeability of the blood vessels.

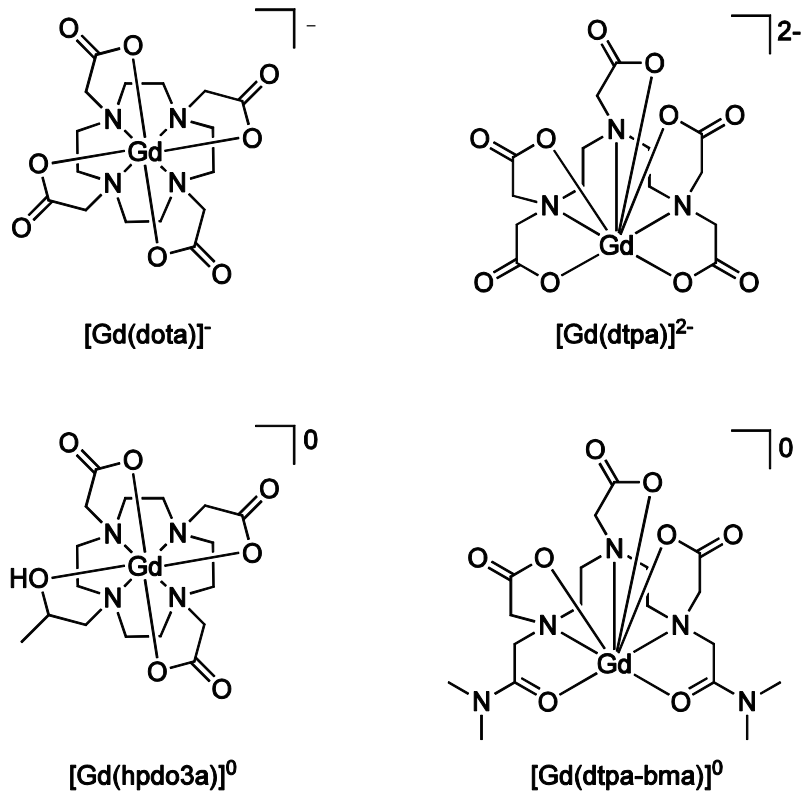


Figure 1. Typical examples of gadolinium(III)-based MRI contrast agents that are currently used in the clinical practice.

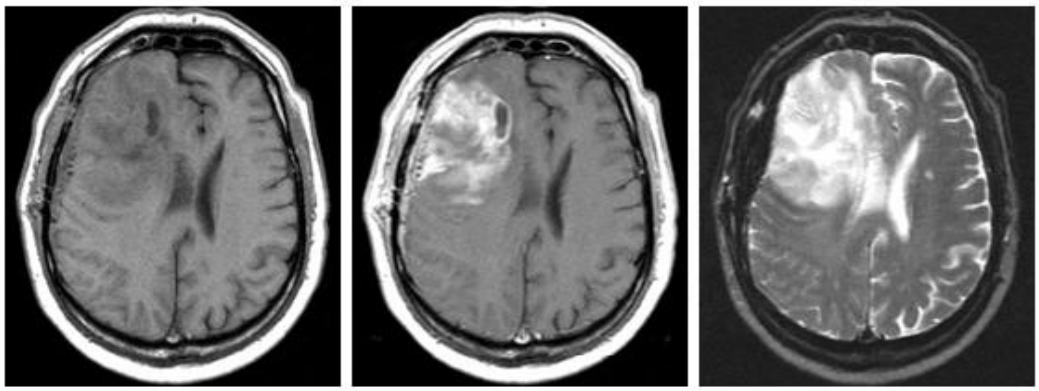

Personal communication of Marinette van de Graaf.

Figure 2. MR images of a patient with an anaplastic oligoastrocytoma. Left: $T_1$-weighted MR image without contrast enhancement; center: $T_1$-weighted MR image after intravenous administration of $[Gd(dtpa)]^{2-}$; right: $T_2$- weighted MR image without contrast enhancement.

Although compounds based on gadolinium(III) ions account for practically all clinically used MRI contrast agents, the use of alternative metal ions for this purpose has been under investigation extensively in-vitro and in preclinical studies. Particularly compounds based on manganese, iron, and dysprosium were used successfully in a number of cases [8-10]. In this

review, we focus particularly on the importance of thulium(III)-containing compounds for the next generation MRI contrast enhancement, such as improved $T_1/T_2$ relaxation enhancement in $^1$H MRI, temperature mapping in $^1$H MRI, $T_1/T_2$ relaxation enhancement in sodium MRI, separate mapping of intra and extracellular sodium and lithium, $T_1/T_2$ relaxation enhancement in fluorine MRI, and in particular chemical-exchange saturation transfer (CEST) $^1$H MRI.

## $T_1$ Contrast Enhancement

The longitudinal relaxation rate of the tissue is in a first approximation proportional to the concentration of the contrast agent [CA] (if [CA] is smalland $T$ and $B_0$are constant) [11]. Therefore, the efficiency of $T_1$ contrast agents is usually expressed as the longitudinal relaxivity, $r_1$, according to Equation 3.

$$r_1 = (R_1 - R_{1,0})/[\mathrm{CA}] \tag{3}$$

Here, $R_{1,0}$ is the relaxation rate in the absence of the $T_1$ contrast agent. The $R_1$ and the $R_{1,0}$ of a solution or a tissue can be accurately measured with the use of an inversion-recovery experiment [12]. First, the equilibrium magnetization is tilted from the z-direction to the (–z)-direction by applying a short 180° RF pulse. Then, the magnetization is allowed to partially recover through longitudinal relaxation during a recovery delay time. Finally, the partially recovered magnetization is tilted into the x,y-plane with a short 90° RF pulse and the resulting MR signal is acquired. This experiment is repeated several times with different values of the recovery delay time. Curve fitting of the experimental MR signal intensities as a function of the recovery time with an exponential model usually yields accurate values of $R_1$.

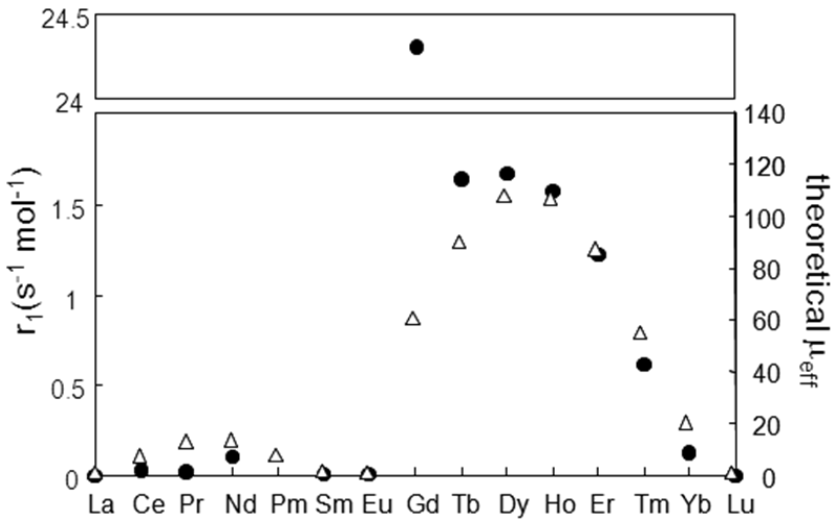


Adapted from Burdinski and coworkers [13].

Figure 3. Relaxivities at 7 Tesla of the $[Ln(ttham)]^{3+}$ complex (black dots) and the square of the theoretical electron magnetic moment ($\mu_{eff}^2$, white triangles) as a function of the lanthanide ion.

$T_1$relaxation is caused by the interaction between the magnetic field of the water $^1$H nucleus (water proton) and other –fluctuating– magnetic fields, e.g. the fluctuating magnetic field of a nearby paramagnetic molecule that is randomly tumbling as a result of Brownian motion. Theoretically, the $r_1$ relaxivity of a paramagnetic contrast agent is proportional to the square of its magnetic moment and inversely proportional to a distance parameter being the sum of the sixth power of the distances between the agent and its surrounding water molecules [7,14,15]. Indeed, this was nicely illustrated for the lanthanide complexes of the decadentate ttham ligand, which completely fills the first coordination sphere of the encapsulated lanthanide ions preventing the direct binding of water molecules to the metal ion [13]. Within the $[Ln(ttham)]^{3+}$ series the experimental relaxivities were therefore found to be roughly proportional to the square of the lanthanide magnetic moment (Figure 3). Apparently, for this series, the effect of the decreasing distance parameter as a result of the lanthanide contraction is partially compensated by the concomitant decrease of the number of water molecules surrounding the chelate.

**Table 1. $^1$H MR relaxivities of various $Tm^{3+}$ chelates and – if available – of the corresponding $Gd^{3+}$ chelates at various magnetic field strengths and at various temperatures**

| Ligand L | $r_1$ / $mM^{-1}s^{-1}$ | | $B_0$ / T | $T$ / °C | ref. |
|---|---|---|---|---|---|
| | [Tm(L)] | [Gd(L)] | | | |
| $cdta^{4-}$ | 3.1 | 5.8 | 0.25 | 23.5 | [19] |
| $ttha^{6-}$ | 5.2 | 12.5 | 0.25 | 23.5 | [19] |
| $dtpa^{5-}$ | 4.5 | 8.3 | 0.25 | 23.5 | [19] |
| ttham | 0.031 | 1.22 | 7.1 | 37 | [13] |
| 1bttpam | 0.026 | | 7.1 | 37 | [13] |
| 4bttpam | 0.040 | | 7.1 | 37 | [13] |
| $ttha\text{-}tm^{2-}$ | 0.034 | | 7.1 | 37 | [13] |
| dotami | 0.092 | | 7.1 | 37 | [16,17] |
| $dotam\text{-}gly^{4-}$ | 0.074 | | 9.4 | 37 | [20] |
| $(H_2O)_9$ | 0.375 | 24.37 | 0.06 | 30 | [21] |
| $dotam\text{-}gly\text{-}lys^{4-}$ | 0.027 | | 9.4 | 37 | [18] |
| $dotam\text{-}gly\text{-}lys^{4-}$ + BSA | 0.019 | | 9.4 | 37 | [18] |

If the lanthanide(III) magnetic moment and the distance parameter would have been the sole important properties, $Tm^{3+}$ chelates may well have evolved as common $T_1$ MRI contrast agents in clinical practice. If one would considerthe magnetic moments of the various lanthanide ions only, the relaxivity of $Tm^{3+}$ chelates should be similar to that of $Gd^{3+}$ chelate complexes. At the same time $Tb^{3+}$, $Dy^{3+}$, and $Ho^{3+}$ chelates should have even higher longitudinal relaxivities, but the concomitantly higher transverse relaxivities would probably make them less effective in practice. However, for a high $^1$H longitudinal relaxivity, the frequency of the fluctuations must critically be in the same range as the magnetic resonance frequency of either the $^1$H nucleus (40 – 130 MHz at the magnetic field strengths of 1 – 3 T typically used in clinical MRI scanners) or the electron (100 – 300 GHz for $Tm^{3+}$ and $Gd^{3+}$ ions at 1 – 3 T). Molecular tumbling of low-molecular-weight lanthanide chelates (Figure 1) typically occurs in the lower GHz range and should therefore be fairly effective for $^1$H

longitudinal relaxation at clinically used magnetic field strengths. Slowing down molecular tumbling to the high MHz range, e.g. by increasing the molecular weight or by binding to endogenous proteins like human serum albumine (HSA) should even further increase the effectiveness. Unfortunately, for most lanthanides, electronic transitions occur at a much faster time scale, typically in the THz range. These transitions cancel the effect of the molecular tumbling and reduce the longitudinal relaxivity by several orders of magnitude.

The fortunate exception is gadolinium. Because of the special electronic configuration of the $Gd^{3+}$ ion (all seven f-orbitals are occupied by a single electron) the electronic transitions occur at a much longer time scale, typically in the MHz range. For this reason the $r_1$ relaxivities of $Gd^{3+}$ chelates are significantly higher than those of all other lanthanides, which explains the dominance of gadolinium for this application. To our knowledge, $Tm^{3+}$ chelates have not yet been tested in-vivo for $T_1$ contrast enhancement. For some $Tm^{3+}$ chelates, nevertheless, longitudinal relaxivities have been determined in-vitro (see Table 1). Most of the reported low-molecular-weight $Tm^{3+}$ chelates show $r_1$ relaxivities between $2{\cdot}10^{-2}$ $mM^{-1}s^{-1}$ and $9{\cdot}10^{-2}$ $mM^{-1}s^{-1}$. These are significantly smaller than the relaxivities of the corresponding $Gd^{3+}$ chelates, which were not measured in most of the cases, but are expected to be well above 1 $mM^{-1}s^{-1}$. Interestingly, the $[Tm^{III}(dotami)]^{3+}$ chelate [16,17] showed a higher relaxivity than the other $Tm^{3+}$ chelates studied at 7 T and 37°C [13]. This can be explained considering the fact that this complex, unlike the other $Tm^{3+}$ chelates, has one coordination site available for binding of a water molecule. Another interesting observation is that the $r_1$ relaxivity of $[Tm^{III}(dotam\text{-}gly\text{-}lys)]^-$, unlike that of $[Gd^{III}(dotam\text{-}gly\text{-}lys)]^-$, did not increase upon addition of bovine serum albumine (BSA), which is known to decrease tumbling of the chelate molecule [18]. This corroborates the assumption that longitudinal relaxation by $Tm^{3+}$ is governed by electronic fluctuations instead of molecular tumbling. Sosnovski and coworkers reported significantly higher $r_1$ relaxivities for several low-molecular-weight $Tm^{3+}$ chelates at a very low magnetic field strength of 0.25 T [19]. Here, the $r_1$ relaxivities of the $Tm^{3+}$ chelates are fairly close to those of their $Gd^{3+}$ counterparts. These unexpectedly high values are currently unexplained.

## $T_2$ Contrast Enhancement

In analogy with the longitudinal relaxivity, the efficiency of $T_2$ contrast agents is expressed as the transverse relaxivity, $r_2 = (R_2 - R_{2,0})/[CA]$, where $R_{2,0}$ is the relaxation rate in the absence of the $T_2$ contrast agent. The $R_2$ is usually measured in an CPMG MR experiment [22,23]. First, the equilibrium magnetization is tilted from the z-direction to the x-direction. Then, the magnetization is allowed to partially dephase in the x,y-plane through $T_2$ relaxation during a relaxation delay time. Unwanted additional dephasing through other mechanisms (e.g. $T_2$* relaxation) is suppressed by applying a CPMG pulse sequence during the entire relaxation delay time. Finally, the remaining MR signal is acquired. This experiment is repeated several times with different values of the relaxation delay time. Curve fitting of the experimental MR signal intensities as a function of the relaxation delay time with an exponential model yields $R_2$. For this type of contrast enhancement a potential role has been suggested for lanthanides other than gadolinium, especially at high magnetic field strengths, where $T_1$ relaxation enhancement of $Gd^{3+}$ chelates becomes less effective due to the

increasing frequency mismatch between the electron magnetic resonance and the molecular tumbling. In addition, at high magnetic-field strengths a special $^1$H relaxation mechanism, "Curie relaxation", can be exploited,which is proportional to the fourth power of the electron magnetic moment [24,25]. Hence the lanthanides with a large magnetic moment, terbium(III), dysprosium(III), and holmium(III), seem most promising for this application. Thus far, only chelates of dysprosium(III) have been studied as alternatives to gadolinium(III) chelates for $T_2$ contrast enhancement [26-28]. Future use of $Tm^{3+}$ chelates for this purpose is unlikely since the electron magnetic moment of thulium is significantly smaller than that of dysprosium.

### $T_2$* or Susceptibility Contrast Enhancement

$T_2$* or susceptibility contrast is generated in the same way as $T_2$ contrast, except that no RF pulses are used to keep the magnetization in a single direction in the x,y-plane. Therefore, $R_2$* (or $1/T_2$*) is the sum of $R_2$ and an additional rate constant that is proportional to the locally existing magnetic-field gradients. Such local magnetic-field gradients can be induced by paramagnetic contrast agents, provided that the agent is compartmentalized, for example when it is restricted to the capillaries in a certain tissue [29]. If the contrast agent is homogeneously distributed in this tissue, which is the case for small molecules after extravasation into the interstitial space of well-perfused tumors, the $r_2$* of the agent becomes equal to its $r_2$.

Like $T_2$ contrast enhancement, $T_2$* contrast enhancement is mainly determined by the size of electron magnetic moment of the paramagnetic contrast agent [30,31]. Of the lanthanide chelates, to our knowledge, only $Gd^{3+}$ and $Dy^{3+}$ have been tested in-vivo for $T_2$* contrast enhancement thus far. Even $Dy^{3+}$ chelates, however, are outclassed by the superparamagnetic iron-oxide particles that are currently applied successfully as $T_2$* contrast agents because of their high magnetic moment and slow extravasation [32].

## CHEMICAL EXCHANGE SATURATION TRANSFER (CEST) CONTRAST AGENTS

It is the above discussed combination of their relatively low proton relaxivity and their efficiency as chemical shift agents that makes most prominently thulium but also some of the other late non-gadolinium lanthanide ions particularly useful as key components of contrast agents for a new MRI technique, dubbed chemical exchange saturation transfer (CEST) MRI [4,33-36]. CEST agents are conceptually different from classical gadolinium-based $T_1$- or $T_2$-contrast agents, which locally shorten the relaxation time of bulk water protons essentially without external control.

Contrast generation in CEST MRI exploits the exchange between labile protons of low-concentration solutes of interest and water protons, which allows for a very sensitive detection of the compound of interest at concentrations below the detection limits of common direct MRI methods. The solute of interest may be an endogeneous compound with suitable proton exchange sites, such as a polyamide or protein, in which case the method has been

dubbed Amide Proton Transfer (APT) MRI [37]. It may, nevertheless, as well be an external CEST contrast agent with optimized chemical shift and exchange properties, which in principle can be applied similar to classical $T_1$- or $T_2$-contrast agents to generate additional contrast in MRI images indicative of the spatial distribution of the CEST-active agent.

In contrast to classical MRI contrast agents, however, in the presence of a CEST agent the signal intensity of the bulk water protons and thus the contrast enhancement can be altered at will. Control over the local signal intensity is gained by selectively saturating, with a weak, multi-second RF pulse, the resonance frequency of mildly acidic protons of the CEST agent, which are in an exchange equilibrium with the protons of the bulk water. The magnitude of the magnetization transfer from the CEST agent to the bulk water, the CEST effect, and hence the extent of $^1$H MRI signal attenuation, is usually calculated according to Equation 4.

$$\%CEST = \frac{M_0 - M_S}{M_\infty} \cdot 100\% \tag{4}$$

$M_S$, $M_0$, and $M_\infty$ are MR intensities measured immediately after an RF saturation pulse has been applied at the resonance frequency of the contrast agent's exchangeable protons ($\omega_S$), at the respective frequency on the opposite side of the bulk water signal ($\omega_0$) to correct for non-selective saturation, most prominently direct water saturation, and at a second reference frequency, at which the MR signal is not affected by magnetization transfer effects ($\omega_\infty$). The use of $M_S$ instead of $M_\infty$ as the baseline reference frequency results in artificially enhanced CEST effects, if the chemical shift of the exchangeable protons is very small [38].

An important feature of this technique is that the CEST-based contrast enhancement can be controlled by the operator. The information obtained in the CEST-enhanced image can therefore be correlated easily with an unenhanced reference image, because the pre-contrast image can be recorded almost simultaneously to the post-contrast one as their acquisition simply differs in the on/off switch of the irradiation field. Even more importantly, this new approach offers the intriguing possibility of visualizing more than one agent in the same region, thus opening new exciting perspectives for the MRI applications in the biomedical field [39,40].

## ParaCEST Contrast Agents for MRI

The use of low-molecular-weight molecules with exchangeable protons as exogeneous contrast agents was first proposed by Balaban and coworkers [41,42]. They found that a number of such diamagnetic molecules showed the ability to alter the MR signal intensity of the bulk water at concentrations above 10 mM in a typical CEST experiment. The Z spectrum, in which the relative intensity of the bulk water signal ($M_S$) is plotted as a function of the presaturation frequency, of barbituric acid (Figure 4) showed a decrease of the main water signal at the origin (resonance of the bulk water peak set to 0 ppm) as well as an additional peak at about +5 ppm resulting from the pool of exchangeable amide protons of the CEST agents.

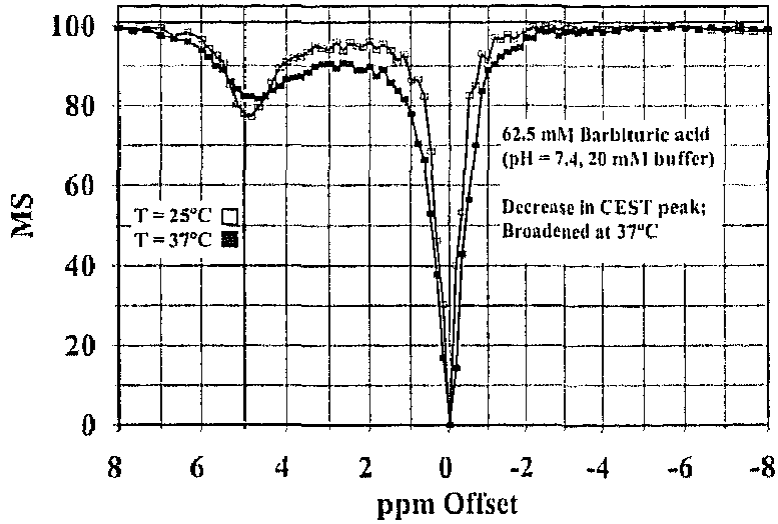


Rreprinted from ref [41], Copyright (2000), with permission from Elsevier.

Figure 4. The Z spectrum of barbituric acid (7 T, 332 K).

Based on these initial CEST studies it was soon realized that, in order to develop CEST contrast agents suitable for in-vivo imaging, the chemical shift difference between the exchangeable protons of the CEST agents and the signal of the bulk water had to be increased significantly, to allow for a sufficient selectivity in addressing only these CEST-active protons with the presaturation pulse without affecting significantly the protons of the bulk water. This selectivity could be achieved by making use of the chemical shift properties of the lanthanide ions (paraCEST agents), of which again mainly thulium will be discussed here.

The proximity of suitable, mildly acidic protons, typically those of organic amide groups, to a paramagnetic lanthanide ion in paraCEST agents causes the resonances of the exchangeable protons to be significantly shifted from the bulk water resonance signal. In realizing this approach to obtain more efficient CEST contrast agents, the generally high toxicity of the lanthanide ions must be taken into account [5,19,43,44]. Therefore it had to be ensured that these metals were not bioavailable by encapsulating them within stable and strongly binding chelate ligands that prevent them from being taken up by cells and entering metabolic processes. Aime and coworkers realized a first thulium-based paraCEST agent by using a derivative of the dotam ligand, which is a tetraamide of the well studied 1,4,7,10-tetraazacyclododecane-1,4,7,10-tetraacetate ligand ($dota^{4-}$, see Figure 1 for the respective $Gd^{3+}$ complex) [38]. The charge imposed on the CEST agent by the incorporation of the lanthanide ion was compensated for by further substituting the metal-coordinating dotam ligand with four non-coordinating glycine groups each bearing one negative charge in its deprotonated state yielding the tetraanionic dotam-gly ligand. The obtained monoanionic thulium complex $[Tm(dotam\text{-}gly)]^-$ (Figure 5) was expected to be better tolerated in-vivo compared to a respective tripositively charged compound missing the gly-substituents on the dotam ligand, because for compounds like the latter hydrolase activity on biological substrates had been documented. The compound could be detected in-vivo at bolus concentrations of 2 mM [45,46].

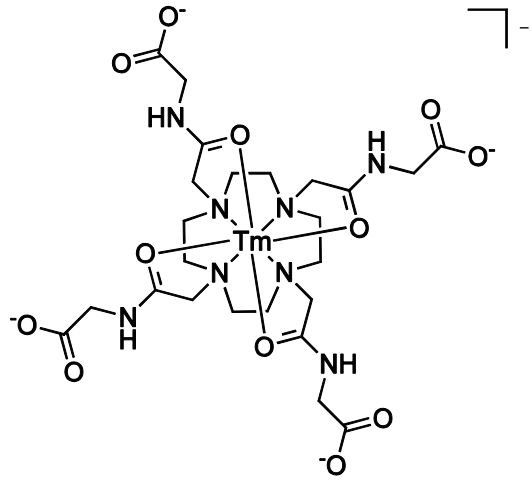


Figure 5. Structural formula of $[Tm(dotam\text{-}gly)]^{3+}$.

The CEST-active protons of the four symmetry-equivalent amide groups exhibited a chemical shift of -51 ppm increasing the absolute shift difference to the bulk water signal (at 0 ppm) by one order of magnitude compared to common diagmagnetic CEST agents like bartituric acid. A selective variation of the metal ion along the lanthanide series confirmed those amide protons to exhibit the largest negative chemical shift for the thulium compound and the largest positive chemical shift for the respective dysprosium complex (Figure 6, triangles).

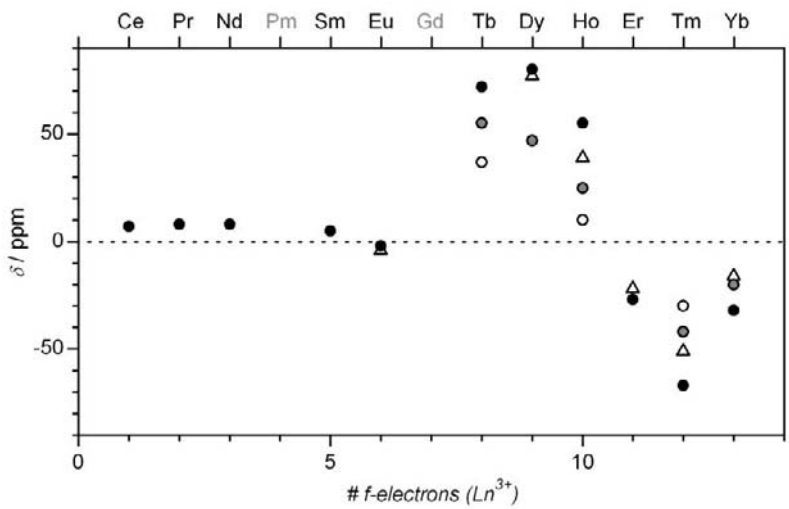




Figure 6. Chemical shift ($\delta$ in ppm) between the amide N-H protons and bulk water for $[Ln(dotam\text{-}gly)]^-$ complexes (7.05 T, 312 K) (triangles) [38] and for $[Ln(ttham)]^{3+}$ complexes (7.0 T, 310 K) (circles). Adapted with permission from ref [13].

An exhaustive study of the dependence of the chemical shift of lanthanide-coordinated amide protons and their CEST effect on the type of metal was presented by Burdinski and coworkers, which confirmed the general trend described by the Aime group also for a series of paraCEST agents comprising the potentially decadentate ligand triethylenetetramine-*N*,*N*,*N*′,*N*″,*N*‴,*N*‴-hexaacetamide (ttham) (Figure 6, circles) [13,47]. $[Tm(ttham)]^{3+}$ (Figure 7) was found to exhibit a lower relaxivity than the respective dysprosium complex $[Dy(ttham)]^{3+}$, and this lower relaxivity was expected to be beneficial for maintaining a high magnetic presaturation and thus to achieve high overall CEST efficiencies.

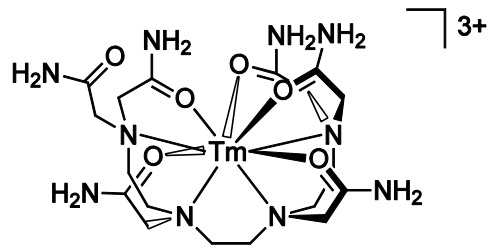


**[Tm(ttham)]$^{3+}$**

Figure 7. Structural formula of $[Tm(ttham)]^{3+}$.

Various strategies were investigated with the aim of obtaining more sensitive paraCEST agents, which would eventually be useful as reporters for molecular processes. The most promising of those strategies is based on increasing the number of CEST-active protons per agent molecule. In the first example of this approach Aime and coworkers studied the in-situ formation of supramolecular adducts between diamagnetic CEST-active peptide molecules and $[Tm(Hdotp)]^{4-}$, a paramagnetic shift agent, to impose an additional paramagentic shift contribution on the exchangeable protons of a poly-L-arginine polypeptide [48]. Even though in the absence of the shift agent, the exchange rate of the mobile guanidine protons at 312 K was too fast to observe a significant CEST effect, upon addition of $[Tm(Hdotp)]^{4-}$ a CEST effect of more than 50% could be observed with a chemical shift of 20-30 ppm. The supramolecular CEST agent could be detected down to concentrations of 50 µm and 2.8 µM of $[Tm(Hdotp)]^{4-}$ and poly-L-arginine, respectively. This approach may benefit from covalently linking the shift reagent to a polymer carrier –the same molecule or a second polymer chain– using, for instance, thulium complexes of alkenyl-substituted $H_3$do3a ($H_3$do3a = 1,4,7,10-tetraazacyclododecane-1,4,7-tracetic acid) derivatives [49].

The design of the above discussed $[Ln(ttham)]^{3+}$ complexes similarly aimed at providing a maximum number of CEST-active groups coordinated to a single lanthanide ion. At the same time water molecules were excluded from the first coordination sphere to minimize the relaxivity and maximize the saturation magnetization [47]. Even though in $[Er(ttham)]^{3+}$ all six amide groups of the decadentate ligand were indeed coordinated to the $Er^{3+}$ ion, the coordination mode changed from 10-coordinate to 9-coordinate moving from $[Er(ttham)]^{3+}$ to $[Tm(ttham)]^{3+}$ in the solid state, as well as in solution, because of the lanthanide contraction effect. The dangling sixth amide group of the 9-coordinate Tm complex caused this asymmetric molecule to exhibit dynamic conformational changes in solution resulting in an interesting temperature and pH-dependence of the CEST effect, with the potential for

simultaneous temperature and pH mapping using a ratiometric CEST approach. Upon replacing the dangling sixth amide with a benzyl group, the less flexible, 9-coordinate complex $[Tm(1bttpam)]^{3+}$ was obtained (Figure 8), which therefore exhibited significantly sharper CEST peaks [13].

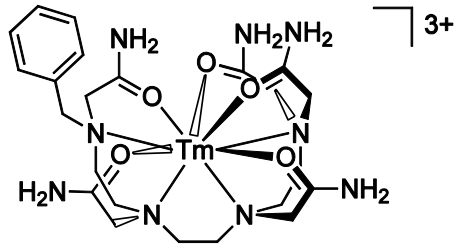


[Tm(1bttpam)]3+

Figure 8. Structural formula of $[Tm(1bttpam)]^{3+}$.

Another common approach to increase sensitivity and specificity of paraCEST agents focuses on the exchange properties of the individual CEST-active group. While most paraCEST agents comprise amide-functionalized chelate ligands directly coordinated to a paramagnetic lanthanide ion, such as ytterbium or preferably thulium, in which complexes the amide ligand binds to the lanthanide ion via the amide O-atom, and the CEST-active amide protons are directed away from the paramagnetic ion, alternative approaches have been explored more recently. Woods and coworkers studied europium complexes bearing H-atoms of alcohol donor groups, which could be coordinated directly to the metal ion via the alcoholic O-atom, and which were, therefore, expected to exhibit particularly large chemical shifts [50]. Further elaborating on this approach to induce large chemical shifts of exchangeable protons, Burdinski and coworkers brought mildly acidic imidazol protons in close proximity to a thulium ion, by employing directing hydrogen bonds between the heterocyclic N–H protons and coordinating amide carbonyl groups of the same pendent ligand arm [16]. The complex $[Tm(dotami)]^{3+}$ (Figure 9, dotami = 1,4,7,10-tetrakis{[N-(1H-imidazol-2-yl)carbamoyl]methyl}-1,4,7,10-tetraazacyclododecane) exhibited a CEST effect at +67 ppm, which was particularly strong at low pH values, caused by a fast exchange reaction.

New synthetic methods have been evaluated to provide dotam derivatives bearing more than a single amino acid side group on each pendent arm and the CEST properties of the resulting thulium complexes were studied [18,51,52]. The effect of the sequence of the oligopeptide side chains on the paraCEST effect was studied systematically suggesting an important impact of the steric demands of these second-sphere substituents on the overall CEST effect [53,54]. When derivatizing the amide derivative of the parent $dota^{4-}$ ligand, in addition to the constraints implied by the modified side chains, a general consideration is the impact on the basic chelating properties of the $dota^{4-}$ framework, which can adapt various coordination symmetries in the respective thulium complexes [55].

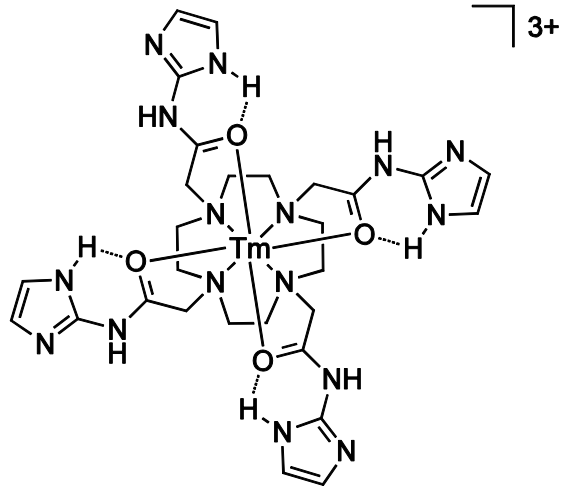


Figure 9. Structural formula of $[Tm(dotami)]^{3+}$.

MR contrast agents with a high sensitivity can generally be obtained by utilizing the ability of enzymes to catalyze the formation or cleavage of chemical bonds. If this bond transformation is associated with the activation or deactivation of the contrast agent´s mode of action, agents with a high potential for imaging specific diseases are obtained that are characterized by the activity or hyperactivity of the targeted enzyme. While this amplification strategy had been used successfully for more than a decade in combination with classical Gd-based contrast agents [56,57], the Pagel group was the first to demonstrate a highly sensitive Tm-based paraCEST agent for the detection of caspase-3, an important biomarker in apoptosis [58]. They linked the well-known caspase-3 substrate DEVD (Asp-Glu-Val-Asp) to the amino group on one sidearm the parent $dota^{4-}$ ligand, which was anchored on a polymer support (Figure 10) [59]. The amide of DEVD-(Tm-DOTA) showed a paraCEST effect with MR saturation at -51 ppm. After cleavage of the amide bond of the DEVD-(Tm-DOTA) agent by caspase-3, the free amine group was exposed, which showed paraCEST activity with saturation at +8 ppm, whereas the amide of DEVD-(Tm-DOTA) showed a paraCEST effect with MR saturation at -51 ppm (Figure 11).

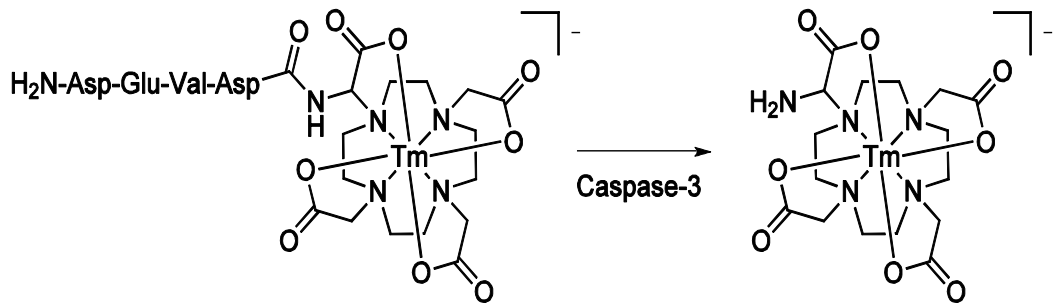


Figure 10. Caspase-3 catalyzed amide bond cleavage in the DEVD-(Tm-DOTA) amide [58].

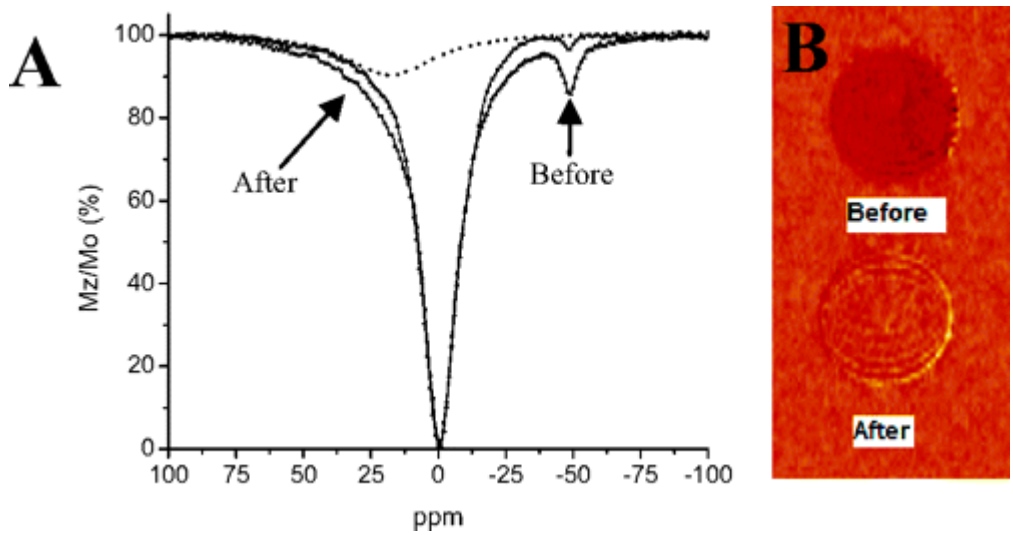


Reprinted with permission from ref [58]. Copyright 2006 American Chemical Society.

Figure 11. ParaCEST spectra (A) and MR parametric map (B) of DEVD-(Tm-DOTA) amide before and after addition of caspase-3 (see Figure 10). The deconvoluted paraCEST spectrum of the product after reaction, showing a paraCEST effect at +8 ppm, is also shown (dotted line). The parametric map was obtained by subtracting the MR image with a saturation offset at -51 ppm from the MR image with saturation offset at +51 ppm.

Using this "double-catalytic" approach of combining chemical exchange magnetization transfer (CEST) with catalytic contrast agent activation, caspase-3 concentrations as low as 3.5 nM could be detected and a selectivity for caspase-3 over caspase-8 was demonstrated [60].

## LipoCEST Contrast Agents for MRI

The need for even higher sensitivities in CEST MR imaging stimulated Aime and coworkers to develop a fundamentally new class of innovative CEST MRI contrast agents based on the encapsulation of paramagnetic lanthanide complexes, such as $[Tm(dotma)]^-$ or [Tm(hpdo3a)] (Figure 12), in the aqueous lumen of a liposome (*i.e.* lipoCEST) [9,61,62].

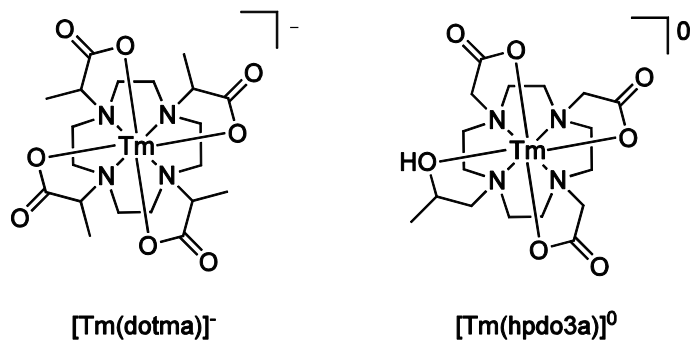


Figure 12. Structural formulas of $[Tm(dotma)]^-$ and $[Tm(hpdo3a)]^0$.

In this class of contrast agents, the CEST effect arises from the selective building up of a magnetization saturation of the intraliposomal pool of water molecules, which are in exchange with the extraliposomal pool of bulk water molecules (Figure 13).

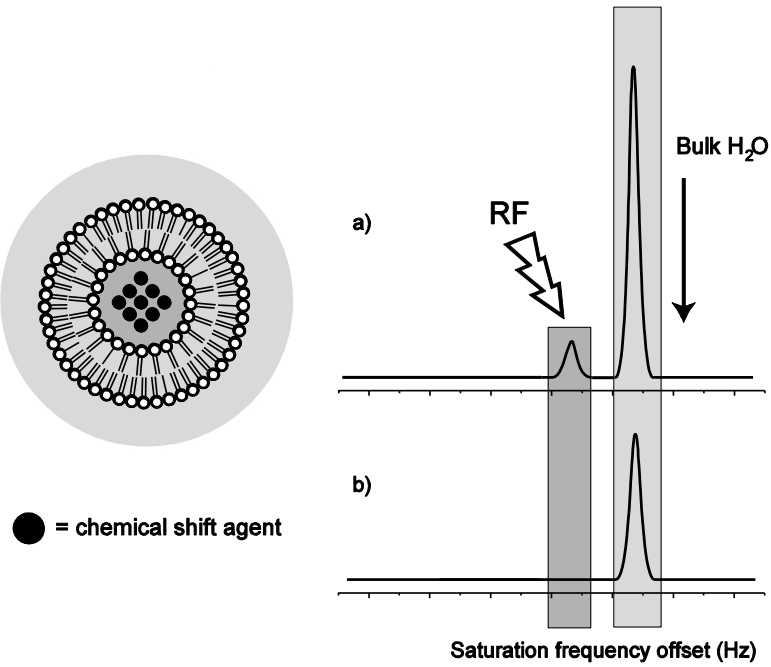


Figure 13. The basic principle of lipoCEST: selective saturation of the intraliposomal water signal with a radio frequency (RF) pulse (a); transmembrane water exchange across the lipid bilayer results in partial saturation of the bulk water signal and, as a consequence, negative contrast enhancement in the MR image (b).

To allow for the selective addressing of the intraliposomal water protons with the presaturation RF pulse, achieving a large, well-defined chemical shift of the intraliposomal water protons is essential. This chemical shift is induced by the encapsulated lanthanide complex and originates generally from the sum of two terms, namely a dipolar contribution and the bulk magnetic susceptibility effect[61,62].If these liposomes have a spherical shape and encapsulate only a hydrophilic lanthanide complex in the aqueous core (first generation lipoCEST contrast agents, Figure 14(a)), the chemical shift of the intraliposomal water protons depends exclusively on the dipolar contribution of the transiently metal-coordinated water molecules averaged with the contribution of the uncoordinated but compartimentalized water molecules, with which they are in an exchange equilibrium. In this case, the chemical shift of the intraliposomal water protons relative to that of the bulk water is proportional to the concentration of the encapsulated chemical shift agent. For this type of lipoCEST agents maximum relative chemical shift values of about ±4 ppm have been reported [63]. An increase of the chemical shift of the intraliposomal protons could be achieved by deformation of the liposomes in response to an osmotic pressure, thereby exploiting the bulk magnetic susceptibility effect. Interestingly, it was observed that the direction of the shift induced by the magnetic susceptibility effect in all reported so-called second generation lipoCEST agents is positive (Figure 14(b)) [61]. A further increase of the chemical shift could be achieved by

the incorporation of hydrophobic lanthanide complexes within the liposomal lipid bilayer (third generation lipoCEST contrast agents, Figure 14(c)) [61].

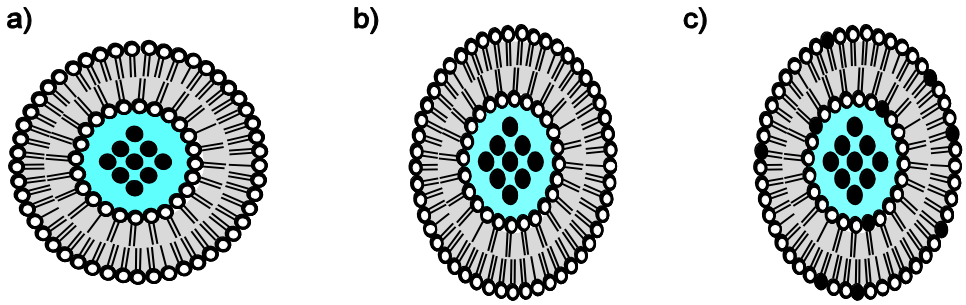


Figure 14. Schematic representation of different generations lipoCEST contrast agents. (a) Spherical liposomes encapsulating a hydrophilic lanthanide complex (first generation lipoCEST contrast agent); (b) non-spherical liposomes encapsulating a hydrophilic lanthanide complex (second generation lipoCEST contrast agent); (c) non-spherical liposomes encapsulating a hydrophilic lanthanide complex in the lumen and incorporating an amphiphilic lanthanide complex in the bilayer (third generation lipoCEST contrast agent).

For both compounds, the encapsulated hydrophilic as well as the incorporated amphiphilic lanthanide complex, thulium(III) and dysprosium(III) are the paramagnetic ions of choice, because of their large magnetic moment and the opposite sign of their magnetic anisotropy constant $\Delta\chi$ ($\Delta\chi < 0$ for $Dy^{3+}$and $\Delta\chi > 0$ for $Tm^{3+}$ ions). The magnetic anisotropy is particularly important for non-spherical lipoCEST agents, because these liposomes orient in a static magnetic field and this orientation depends on the sign of $\Delta\chi$ of the used lanthanide complexes, particularly on that of the amphiphilic complex incorporated in the lipid bilayer, which has a significantly larger impact on the shift direction than the encapsulated complex. Even though it is possible to predict the orientation of liposomes incorporating, for instance, a certain thulium complex in the bilayer, if the orientation is known of those liposomes with a similar composition incorporating the respective dysprosium complex instead (or *vice versa*), an *a priori* prediction of the orientation and thus the respective intraliposomal water shift of lipoCEST agents comprising yet unknown amphiphilic complexes is still a challenge [64]. Here other factors come into effect, including the overall structure of the amphiphilic complex (see Figure 15 for some recently studied amphiphilic thulium(III) and dysprosium(III) complexes), its orientation relative tothe liposomal membrane, and potentially the way, in which it is incorporated [62].

A method for the direct assessment of the orientation of third-generation lipoCEST agents in an external magnetic field was recently described by Burdinski and coworkers, who modified such non-spherical liposomes with adamantyl-based targeting groups that allowed for multivalent binding to a cyclodextrin-modified capillary surface [64]. In bulk solution, the used oblate (lens-shaped) liposomes incorporating a thulium(III) or a dysprosium(III)-containing amphiphile (Figure 15A) were, independent of the orientation of the capillary container, respectively oriented parallel or perpendicular relative to the external magnetic field. Upon binding to the capillary surface, however, both types of liposomes became aligned parallel with the capillary surface and they maintained this local surface alignment independent of the capillary orientation in the external magnetic field, which was deduced from the variation of the chemical shift of the intraliposomal water protons with the

orientation of the capillary in the magnetic field. In this multivalent binding situation, therefore, the enforced mechanical alignment of these lipoCEST contrast agents outweighed the preferred magnetic orientation in determining the MR properties of the liposomes.

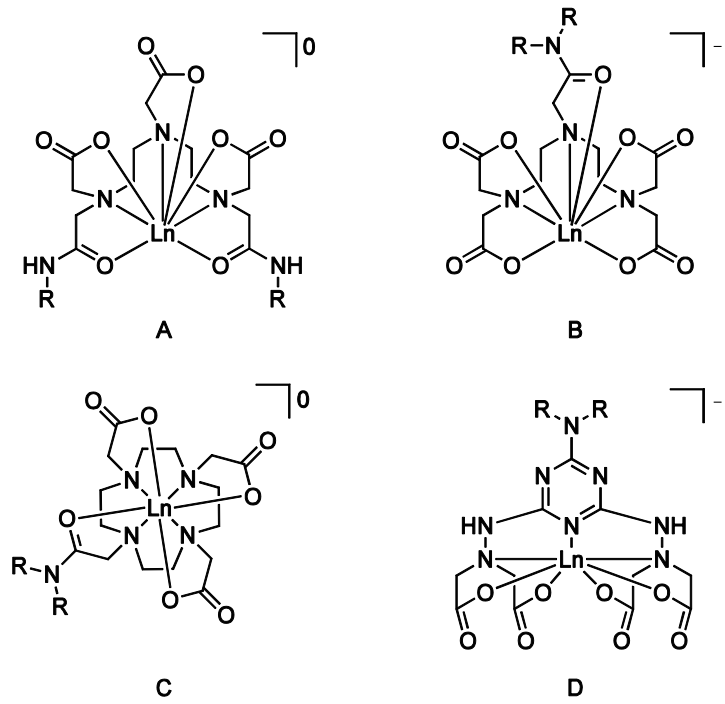


Figure 15. Amphiphilic lanthanide ($Dy^{3+}$ or $Tm^{3+}$) complexes suitable for incorporation in the lipid bilayer of third generation lipoCEST agents (R = $C_{16}H_{33}$, $C_{18}H_{37}$).

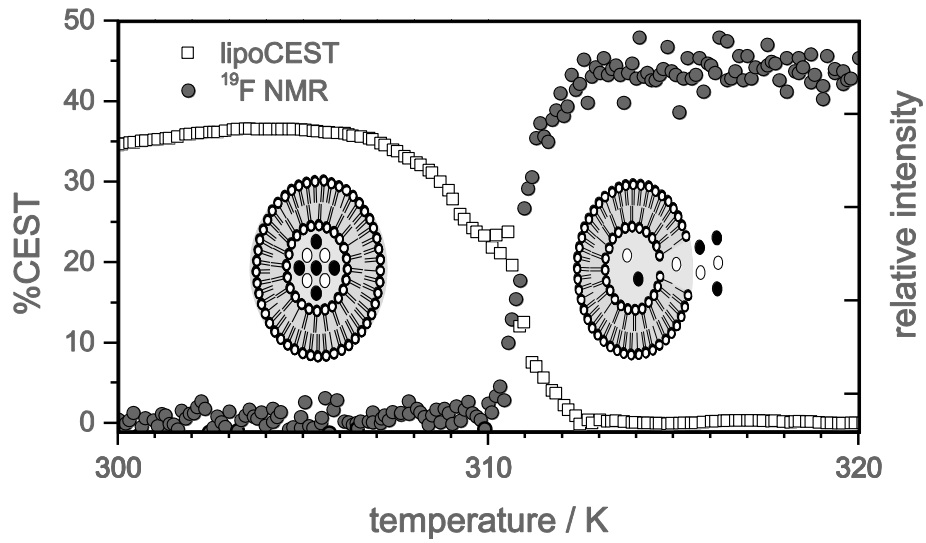




Figure 16. Temperature-sensitive liposomes as responsive MRI contrast agents. Adapted with permission from ref [65].

Taking advantage of the carrier properties such liposomes, which allows them to be loaded with solubilized or dispersed pharmacologically active compounds, lipoCEST MRI contrast agents have been explored for applications in image-guided drug delivery. Langereis and coworkers designed temperature-sensitive liposomal contrast agents for CEST and $^{19}$F MRI that release their payload at temperatures near the melting phase transition temperature ($T_m$) of the lipid bilayer (Figure 16) [65]. As long as the hydrophilic lanthanide complex remained encapsulated, a CEST effect was observed, whereas the $^{19}$F NMR signal of the co-encapsulated $^{19}$F probe ($PF_6^-$) was negligible as a result of severe line broadening caused by the paramagnetic shift reagent [Tm(hpdo3a)]. Upon further temperature increase the CEST signal vanished, because the chemical shift of the intra- and extraliposomal water protons became identical. Simultaneously the $^{19}$F signal became detectable, because the paramagnetic thulium complexes was diluted, which resulted in a sharpening of the $^{19}$F resonance lines [65].

## TEMPERATURE-RESPONSIVE MRI CONTRAST AGENTS

Paramagnetic thulium complexes have been proposed as responsive probes in MR thermometry for the diagnosis of metabolic abnormalities and hyperthermia related medical procedures [66,67]. The temperature-dependency of the hyperfine chemical shift of such complexes generally allows for an accurate temperature measurement with a high spatial and temporal resolution. The sensitivity of MR thermometry methods utilizing thulium chelate complexes is typically two orders of magnitude higher compared to MR methods based on the chemical shift of the bulk $^1$H water signal (0.01 ppm/°C). For instance, Zuo and coworkers demonstrated that the chemical shifts of $^1$H and $^{31}$P in $[Tm^{III}(dotp)]^{5-}$ (Figure 17, $dotp^{8-}$ = 1,4,7,10-tetraazacyclododecane-1,4,7,10-tetrakis(methylene phosphonate)) are strongly affected by the temperature at 7 T [68].

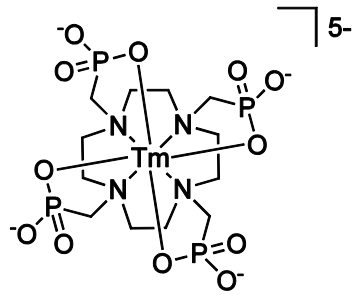


Figure 17. Structural formula of $[Tm(dotp)]^{5-}$.

The temperature sensitivity of the $^1$H chemical shift of the $[Tm^{III}(dotp)]^{5-}$ ethylene protons was found to be 0.89 ppm/°C between 25°C and 47°C, whereas the $^{31}$P chemical shift over the same temperature range was 2.18 pm/°C. Interestingly, the combination of $^1$H and $^{31}$P NMR chemical shifts of $[Tm^{III}(dotp)]^{5-}$ principally allows for simultaneous measurement

of pH and temperature [69]. More recently, simultaneous measurements of temperature and pH in rats undergoing hyperthermia were reported by Sun and coworkers [70]. In their work, both, temperature and pH were calculated using two magnetically non-equivalent groups of protons of $[Tm^{III}(dotp)]^{5-}$. Coman and coworkers exploited the use of $[Tm^{III}(dotp)]^{5-}$ to obtain temperature and pH maps of the rat brain [71]. Preclinical studies disclosed a temperature of 33 – 34°C in the cerebral cortex with pH values between 7.3 and 7.4. However, the competitive binding of $[Tm^{III}(dotp)]^{5-}$ to $Ca^{2+}$ ions could potentially limit its in-vivo applicability. Thulium-based chelates for MR thermometry that are not sensitive to the concentration of $Ca^{2+}$ and pH are $[Tm^{III}(dota)]^{-}$ (dota = 1,4,7,10-tetraazacyclododecane-1,4,7,10-tetraacetate) [72-74] and $[Tm^{III}(dotma)]^{-}$ ($dotma^{4-}$ = 1,4,7,10-tetraazacyclododecane-1,4,7,10-tetra(1-methylacetate)) [75,76]. $[Tm^{III}(dota)]^{-}$ consists of six magnetically non-equivalent sets of protons that display a linear temperature dependency between 20 and 55°C. Similarly to $[Tm^{III}(dotp)]^{5-}$, the chemical shifts of the ethylene protons of $[Tm^{III}(dota)]^{-}$ were found to be about two orders of magnitude more temperature-sensitive in comparison to the shift of the bulk water signal [73]. Recently, in-vivo studies in tumor bearing rats were performed under controlled radiofrequency hyperthermia using $[Tm^{III}(dotp)]^{5-}$ for MR thermometry [67]. Absolute temperature measurements with an accuracy of 0.3°C using $[Tm^{III}(dotma)]^{-}$ were performed in rats at 9.4 T [76]. The above examples illustrate that small-molecule probes based on thulium chelate complexes are promising candidate agents for in-vitro and in-vivo MR thermometry and a fast advancement to clinical practice is expected in the years to come.

## Sodium ($^{23}$Na) Imaging

Virtually all clinical MRI examinations employ the resonance of the hydrogen nucleus ($^{1}$H), which is the most sensitive nucleus (except for radioactive $^{3}$H), and also the most abundant nucleus in most tissues. Nevertheless, imaging of other MR-active nuclei has some clinical relevance as well. Especially the sodium nucleus ($^{23}$Na), which has a natural isotopic abundance of 100%, a relatively high MR sensitivity, a relatively high endogenous concentration, and very important biological functions, has been given serious attention in the academic MRI community. $^{23}$Na MRI is expected to have promising clinical applications in the diagnosis and treatment of stroke and acute cardiac arrest. In healthy brain and myocardial cells, the sodium/potassium-ATPase ion channel maintains a high sodium gradient across the cell membrane by pumping sodium ions out of the cell and potassium into the cell at the expense of ATP. This gradient is essential for many of the tissue's basic physiological functions. Mapping of the difference between intra- and extracellular $Na^{+}$ concentrations may therefore be used for treatment planning and follow up. For this purpose, it is essential to address the intra- and extracellular sodium ions separately.

This has been achieved by the administration of lanthanide complexes that selectively reduce the relaxation time or shift the resonance frequency of the extracellular $^{23}$Na nuclei with respect to those of the intracellular $^{23}$Na nuclei. Lanthanide complexes suitable for this purpose ideally have the following characteristics [77]: They should have a high negative charge, since this will favor electrostatic interactions between the agent and the positively charged metal ions, which in turn will increase the efficacy of the agent to induce a

paramagnetic shift of the resonance frequency or a relaxation enhancement of the MR signal of the $^{23}$Na ion. In addition, a high negative charge will prevent the agent to enter the cell and affect the intracellular sodium fraction. In the case of a relaxation-enhancing contrast agent, the lanthanide complex should, of course, have a high relaxivity for the $^{23}$Na nucleus. This requires somewhat different properties than those required for achieving a high $^{1}$H relaxivity, since the resonance frequency of the $^{23}$Na nucleus is four times smaller than that of the $^{1}$H nucleus.

Unlike water molecules, the positively charged sodium ions, can, because of Coulomb-repulsion effects, not directly coordinate to the positively charged lanthanide ion. Therefore, the toxicity of $^{23}$Na MRI contrast agents, when compared to $^{1}$H MRI contrast agents, can potentially be reduced even further by using ligands with 9 or 10 coordination sites, instead of the usual number of eight. This is expected to result in more stable lanthanide complexes, from which less of the toxic, free lanthanide ions are released under in-vivo conditions. For a sodium-specific chemical shift reagent, the paramagnetic species should have a high magnetic moment and a short value of the electronic relaxation time, for which reason dysprosium(III), terbium(III), and thullium(III) are the most promising lanthanide ions. It is generally known that those chemical shift reagents that are axially symmetric complexes with cation binding sites along the main symmetry axis are most effective. So far in preclinical settings the following complexes have been studied as contrast agents for $^{23}$Na magnetic resonance imaging: $[Dy(ppp)_2]^{7-}$, $[Dy(ttha)]^{3-}$, $[Dy(dotp)]^{5-}$, and $[Tm(dotp)]^{5-}$. Of these compounds $[Tm(dotp)]^{5-}$ has been studied by far most extensively.

For instance, Seshan and coworkers measured the in-vivo $^{23}$Na MR signal of the a kidney during intravenous infusion of $[Tm(dotp)]^{5-}$ using a cumulative dose of up to 0.67 mmol/kg and an infusion time of up to 35 minutes. The resonance frequency of the extracellular fraction of the $^{23}$Na MR signal decreased as a function of the cumulative dose, whereas the intracellular fraction remained invariant. A third fraction, appearing as a broad line at very low frequencies, originated from the sodium in the kidney filtrate [78]. Baseline resolution of the intracellular and extracellular $^{23}$Na fractions was achieved after administration of 0.5 mmol of $[Tm(dotp)]^{5-}$. Intravenous administration of this thulium chelate also yielded a baseline resolution of the intracellular and extracellular $^{23}$Na fractions in $^{23}$Na MRI of the rat heart [79], the rat liver [80], the rat skeletal muscle [81], and subcutaneously implanted tumors in the rat [82,83]. In-vivo application of negatively charged chemical-shift reagents in the intact brain is more difficult, because such compounds do not easily cross the blood-brain barrier [84]. Nevertheless, $[Tm(dotp)]^{5-}$ was also successfully used to resolve the intra- and extracellular $^{23}$Na signal of the in-vivo rat brain in conjunction with partial disruption of the blood-brain barrier with an intravenously administered aqueous solution of mannitol [85].

## Lithium ($^{7}$Li) Imaging

$^{7}$Li is another example of a nucleus with a fair MR sensitivity and a high clinical relevance. The mapping of $Li^{+}$ ions in the brain, for example, has potential applications in the therapy of common psychiatric disorders [86]. $[Tm(dotp)]^{5-}$ was used by Nikolakopoulos and coworkers as a $^{7}$Li chemical-shift reagent to separate the intra- and extracellular $^{7}$Li MR signals, similar to the application of $[Tm(dotp)]^{5-}$ in $^{23}$Na MR as described in the previous

paragraph [87]. In this way, first-order rates of influx and wash-out of the $Li^+$-ion for neuroblastoma SH-SY5Y cells in agarose threads could be determined.

## Fluorine ($^{19}$F) Imaging

MRI using the fluorine nucleus ($^{19}$F) is appealing for several reasons. The nucleus is nearly as sensitive as the $^1$H nucleus, and its natural abundance is approximately 100%. The virtual absence of $^{19}$F in the body offers a unique advantage, which are particularly important in the field of cell tracking, where the contrast agent is contained only in the sparsely distributed foreign cells, and in the field of molecular imaging, where the contrast agent preferentially binds to relatively rare, disease-specific markers. Here, the large background signal intensity inevitably present in $^1$H MR imaging poses a severe problem in detecting the relatively small signal enhancement generated by $^1$H MR-specific contrast agents.

Targeted perfluorocarbon emulsions in combination with $^{19}$F MR molecular imaging have successfully been used for the detection and quantification of angiogenesis in experimental valve disease and to track foreign cells in the living body [88,89]. An additional advantage of the $^{19}$F nucleus is that its resonance frequency is very sensitive to the chemical environment, such as the local oxygen concentration [90]. Thus, it may be used as a responsive contrast agent for the three dimensional quantitative detection (mapping) of dioxygen. The mapping of dioxygen is clinically very relevant, because the therapeutic effect of radiation therapy is strongly correlated with tumor oxygenation.

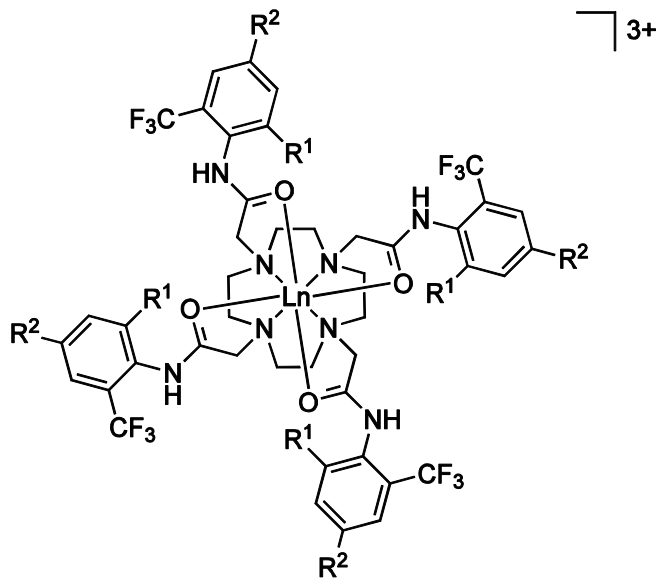


$[Ln(L^{CF3})]^{3+}$

Figure 18. Structural formula of $[Ln(L^{CF3})]^{3+}$.

For all these applications, insufficient sensitivity (signal-to-noise ratio) is expected to be the most significant problem. Chalmers and coworkers showed in an elegant study that the signal-to-noise ratio in $^{19}$F-MR spectroscopy and certain types of $^{19}$F-MR imaging could be increased by at least one order of magnitude by linking a lanthanide complex to the fluorinated contrast agent via a covalent bond in the series of complexes $[Ln^{III}(L^{CF3})]^{3+}$ (Figure 18) [91]. As a result of the lanthanide-induced increase of the $^{19}$F longitudinal relaxation rate, the acquisition repetition rate for the purpose of signal averaging could be increased by at least two orders of magnitude without significant saturation effects. This corresponded to a 10-fold increase in sensitivity. Gadolinium(III) is the most effective lanthanide ion to reduce the $^{19}$F-MR longitudinal relaxation time. Nevertheless, it is not the most suitable lanthanide for biomedical $^{19}$F-MR imaging and spectroscopy, because it significantly increases the transverse relaxation rate as well, which adversely affects the $^{19}$F-MR signal-to-noise ratio. Therefore those complexes of the $[Ln^{III}(L^{CF3})]^{3+}$series were tested that comprised alternative lanthanide ions with high magnetic moments: $Tb^{3+}$, $Dy^{3+}$, $Ho^{3+}$, $Er^{3+}$, and $Tm^{3+}$. Of these, as expected when considering the size of the magnetic moment, the thulium(III) showed the smallest $r_1$ and $r_2$ relaxivities. Nevertheless, for applications with relatively long echo times, the thulium complex may well have the optimum pair of relaxivities.

Chalmers and coworkers further found that the $^{19}$F MR resonance frequencies of several of the studied paramagnetic fluorine-containing compounds, including the thulium(III) complex, were very sensitive to the pH of the solution, especially in the clinically relevant area between pH 6 and pH 8 [91]. The authors therefore considered an application of such contrast agents for the extracellular pH mapping with $^{19}$F-MRI.

## CONCLUSION

The rapid development of magnetic resonance imaging (MRI) into one of the most versatile techniques in clinical imaging and biomedical research has stimulated and was nurtured by the advancement of growing research efforts to obtain more sensitive contrast-enhancing agents, which provide more diagnostically valuable information at the same time (smart contrast agents). Whereas classical gadolinium-based contrast agents and magnetic iron oxide nanoparticles shorten locally the relaxation time of bulk water protons via rapid exchange of water molecules employing inner- or outer-sphere magnetic interactions to provide contrast enhancement, smart contrast agents comprising other lanthanide ions can potentially offer more detailed and even disease-specific information. In particular the shift properties of thulium(III) complexes have been exploited for designing new types of contrast agents with highly specific reporter functionalities. Chemical exchange saturation transfer (CEST) agents generate contrast based on the transfer of saturated magnetization from the contrast agent or from water molecules interacting with a lanthanide shift reagent to the bulk water signal. Such magnetization saturation is created by either using exchangeable protons of suitable functional groups, such as amide groups, of a paramagnetic thulium(III) chelate complex (paraCEST agents), or by using water molecules that interact with a thulium-based shift agent encapsulated in a liposomal carrier (lipoCEST agents). The advantage of CEST agents for the operator is the external control of the contrast enhancement, which allows for a

straightforward correlation of the contrast-enhanced image with an unenhanced reference image, as well as for the intriguing possibility of visualizing more than one agent in the same region. The sensitivity of the proton and water exchange on the environmental conditions has allowed for the development of thulium-based contrast agents as local probes for disease-specific parameters and physiological processes employing the local thulium-induced changes of the chemical shift in either direct measurements or via the exchange-mediated CEST contrast enhancement mechanism. Upcoming applications of thulium-based contrast agents include their use as shift reagents for other nuclei, such as $^{7}$Li and $^{19}$F, and as theranostic agents suitable for image-guided drug delivery.

## REFERENCES


[1] Carr, D. H.; Brown, J.; Bydder, G. M.; Weinmann, H. J.; Speck, U.; Thomas, D. J.; Young, I. R. Intravenous chelated gadolinium as a contrast agent in NMR imaging of cerebral tumours. *Lancet* 1984, *323*, 484-486.

[2] Lauterbur, P. C.; Mendonca-Dias, M. H.; Rudin, A. M. Augmentation of tissue water proton spin-lattice relaxation rates by in-vivo addition of paramagnetic ions. In *Frontiers of Biological Energetics*, Dutton, P. L.; Leigh, J. S.; Scarpa, A., Eds. Elsevier Academic Press Inc: New York, 1978; pp 752-759.

[3] Bloch, F.; Hansen, W. W.; Packard, M. The Nuclear Induction Experiment. *Phys. Rev.* 1946, *70*, 474-485.

[4] Aime, S.; Geninatti Crich, S.; Gianolio, E.; Giovenzana, G. B.; Tei, L.; Terreno, E. High sensitivity lanthanide(III) based probes for MR-medical imaging. *Coord. Chem. Rev.* 2006, *250*, 1562-1579.

[5] Bottrill, M.; Kwok, L.; Long, N. J. Lanthanides in magnetic resonance imaging. *Chem. Soc. Rev.* 2006, *35*, 557-571.

[6] Caravan, P.; Ellison, J. J.; McMurry, T. J.; Lauffer, R. B. Gadolinium(III) Chelates as MRI Contrast Agents: Structure, Dynamics, and Applications. *Chem. Rev.* 1999, *99*, 2293-2352.

[7] Lauffer, R. B. Paramagnetic metal complexes as water proton relaxation agents for NMR imaging: theory and design. *Chem. Rev.* 1987, *87*, 901-927.

[8] Viswanathan, S.; Kovacs, Z.; Green, K. N.; Ratnakar, S. J.; Sherry, A. D. Alternatives to Gadolinium-Based Metal Chelates for Magnetic Resonance Imaging. *Chem. Rev.* 2010, *110*, 2960-3018.

[9] Terreno, E.; Delli Castelli, D.; Viale, A.; Aime, S. Challenges for Molecular Magnetic Resonance Imaging. *Chem. Rev.* 2010, *110*, 3019-3042.

[10] Villaraza, A. J. L.; Bumb, A.; Brechbiel, M. W. Macromolecules, Dendrimers, and Nanomaterials in Magnetic Resonance Imaging: The Interplay between Size, Function, and Pharmacokinetics. *Chem. Rev.* 2010, *110*, 2921-2959.

[11] Koenig, S. H.; Brown 3$^{rd,}$ R. D. Relaxation of solvent protons by paramagnetic ions and its dependence on magnetic field and chemical environment: implications for NMR imaging. *Magn. Reson. Med.* 1984, *1*, 478-495.

[12] Vold, R. L.; Waugh, J. S.; Klein, M. P.; Phelps, D. E. Measurement of spin relaxation in complex systems. *J. Chem. Phys.* 1968, *48*, 3831-3832.

[13] Burdinski, D.; Pikkemaat, J. A.; Lub, J.; de Peinder, P.; Nieto Garrido, L.; Weyhermüller, T. Lanthanide Complexes of Triethylenetetramine Tetra-, Penta-, and Hexaacetamide Ligands as Paramagnetic Chemical Exchange-Dependent Saturation Transfer Contrast Agents for Magnetic Resonance Imaging: Nona- versus Decadentate Coordination. *Inorg. Chem.* 2009, *48*, 6692-6712.

[14] Bloembergen, N.; Purcell, E. M.; Pound, R. V. Relaxation Effects in Nuclear Magnetic Resonance Absorption. *Phys. Rev.* 1948, *73*, 679-712.

[15] Peters, J. A.; Huskens, J.; Raber, D. J. Lanthanide induced shifts and relaxation rate enhancements. *Prog. Nucl. Magn. Reson. Spectros.* 1996, *28*, 283-350.

[16] Burdinski, D.; Lub, J.; Pikkemaat, J. A.; Langereis, S.; Grüll, H.; ten Hoeve, W. The Thulium Complex of 1,4,7,10-Tetrakis{[*N*-(1*H*-imidazol-2-yl)carbamoyl]methyl}-1,4,7,10-tetraazacyclododecane (dotami) as a ParaCEST Contrast Agent. *Chem. Biodivers.* 2008, *5*, 1505-1512.

[17] Burdinski, D., Pikkemaat, J. A., unpublished results.

[18] Li, A. X.; Suchy, M.; Jones, C. K.; Hudson, R. H. E.; Menon, R., S.; Bartha, R. Optimized MRI contrast for on-resonance proton exchange processes of PARACEST agents in biological systems. *Magn. Reson. Med.* 2009, *62*, 1282-1291.

[19] Sosnovsky, G.; Rao, N. U. M. Gadolinium, neodymium, praseodymium, thulium and ytterbium complexes as potential contrast enhancing agents for NMR imaging. *Eur. J. Med. Chem.* 1988, *23*, 517-522.

[20] Liu, G.; Ali, M. M.; Yoo, B.; Griswold, M. A.; Tkach, J. A.; Pagel, M. D. PARACEST MRI with improved temporal resolution. *Magn. Reson. Med.* 2009, *61*, 399-408.

[21] Roberts, N.; Rimmington, J. E.; Foster, M. A. A new role for tripositive lanthanide ions in test objects designed to quality control checks on magnetic resonance imaging systems. *Phys. Med. Biol.* 1992, *37*, 1977-1984.

[22] Carr, H. Y.; Purcell, E. M. Effects of Diffusion on Free Precession in Nuclear Magnetic Resonance Experiments. *Phys. Rev.* 1954, *94*, 630-638.

[23] Meiboom, S.; Gill, D. Modified spin-echo method for measuring nuclear relaxation times. *Rev. Sci. Instrum.* 1958, *29*, 688-691.

[24] Bertini, I.; Capozzi, F.; Luchinat, C.; Nicastro, G.; Xia, Z. Water proton relaxation for some lanthanide aqua ions in solution. *J. Phys. Chem.* 1993, *97*, 6351-6354.

[25] Gueron, M. Nuclear relaxation in macromolecules by paramagnetic ions: a novel mechanism. *J. Magn. Reson.* 1975, *19*, 58-66.

[26] Bulte, J. W. M.; Wu, C.; Brechbiel, M. W.; Brooks, R. A.; Vymazal, J.; Holla, M.; Frank, J. A. Dysprosium-DOTA-PAMAM Dendrimers as Macromolecular $T_2$ Contrast Agents: Preparation and Relaxometry. *Invest. Radiol.* 1998, *33*, 841-845.

[27] Kellar, K. E.; Fossheim, S. L.; Koenig, S. H. Magnetic field dependence of solvent proton relaxation by solute dysprosium(III) complexes. *Invest. Radiol.* 1998, *33*, 835-840.

[28] Vander Elst, L.; Roch, A.; Gillis, P.; Laurent, S.; Botteman, F.; Bulte, J. W. M.; Muller, R. N. Dy-DTPA derivatives as relaxation agents for very high field MRI: The beneficial effect of slow water exchange on the transverse relaxivities. *Magn. Reson. Med.* 2002, *47*, 1121-1130.

[29] Villringer, A.; Rosen, B. R.; Belliveau, J. W.; Ackerman, J. L.; Lauffer, R. B.; Buxton, R. B.; Chao, Y.-S.; Van Wedeenand, J.; Brady, T. J. Dynamic imaging with lanthanide

chelates in normal brain: Contrast due to magnetic susceptibility effects. *Magn. Reson. Med.* 1988, *6*, 164-174.

[30] Fossheim, S.; Johansson, C.; Fahlvik, A. K.; Grace, D.; Klaveness, J. Lanthanide-based susceptibility contrast agents: Assessment of the magnetic properties. *Magn. Reson. Med.* 1996, *35*, 201-206.

[31] Fossheim, S.; Sæbø, K. B.; Fahlvik, A. K.; Rongved, P.; Klaveness, J. Low molecular weight lanthanide contrast agents: In vitro studies of mechanisms of action. *J. Magn. Reson. Imaging* 1997, *7*, 251-257.

[32] Bonnemain, B. Superparamagnetic Agents in Magnetic Resonance Imaging: Physicochemical Characteristics and Clinical Applications A Review. *J. Drug Target.* 1998, *6*, 167-174.

[33] Zhou, J.; van Zijl, P. C. M. Chemical exchange saturation transfer imaging and spectroscopy. *Prog. Nucl. Magn. Reson. Spectros.* 2006, *48*, 109-136.

[34] Sherry, A. D.; Woods, M. Chemical Exchange Saturation Transfer Contrast Agents for Magnetic Resonance Imaging. *Annu. Rev. Biomed. Eng.* 2008, *10*, 391-411.

[35] Delli Castelli, D.; Gianolio, E.; Geninatti Crich, S.; Terreno, E.; Aime, S. Metal containing nanosized systems for MR-Molecular Imaging applications. *Coord. Chem. Rev.* 2008, *252*, 2424-2443.

[36] Terreno, E.; Delli Castelli, D.; Aime, S. Encoding the frequency dependence in MRI contrast media: the emerging class of CEST agents. *Contrast Media Mol. Imaging* 2010, *5*, 78-98.

[37] Zhou, J.; Payen, J.-F.; Wilson, D. A.; Traystman, R. J.; van Zijl, P. C. M. Using the amide proton signals of intracellular proteins and peptides to detect pH effects in MRI. *Nature Med.* 2003, *9*, 1085-1090.

[38] Aime, S.; Barge, A.; Delli Castelli, D.; Fedeli, F.; Mortillaro, A.; Nielsen, F. U.; Terreno, E. Paramagnetic Lanthanide(III) complexes as pH-sensitive chemical exchange saturation transfer (CEST) contrast agents for MRI applications. *Magn. Reson. Med.* 2002, *47*, 639-648.

[39] Aime, S.; Delli Castelli, D.; Geninatti Crich, S.; Gianolio, E.; Terreno, E. Pushing the Sensitivity Envelope of Lanthanide-Based Magnetic Resonance Imaging (MRI) Contrast Agents for Molecular Imaging Applications. *Acc. Chem. Res.* 2009, *42*, 822-831.

[40] Ali, M. M.; Liu, G.; Shah, T.; Flask, C. A.; Pagel, M. D. Using Two Chemical Exchange Saturation Transfer Magnetic Resonance Imaging Contrast Agents for Molecular Imaging Studies. *Acc. Chem. Res.* 2009, *42*, 915-924.

[41] Ward, K. M.; Aletras, A. H.; Balaban, R. S. A New Class of Contrast Agents for MRI Based on Proton Chemical Exchange Dependent Saturation Transfer (CEST). *J. Magn. Reson.* 2000, *143*, 79-87.

[42] Ward, K. M.; Balaban, R. S. Determination of pH using water protons and chemical exchange dependent saturation transfer (CEST). *Magn. Reson. Med.* 2000, *44*, 799-802.

[43] Misra, S. N.; Gagnani, M. A.; Devi, I.; Shukla, R. S. Biological and clinical aspects of lanthanide coordination compounds. *Bioinorg. Chem. Appl.* 2004, *2*, 155-192.

[44] Reichert, D. E.; Lewis, J. S.; Anderson, C. J. Metal complexes as diagnostic tools. *Coord. Chem. Rev.* 1999, *184*, 3-66.

[45] Vinogradov, E.; He, H.; Lubag, A.; Balschi, J. A.; Sherry, A. D.; Lenkinski, R. E. MRI detection of paramagnetic chemical exchange effects in mice kidneys in vivo. *Magn. Reson. Med.* 2007, *58*, 650-655.

[46] Vinogradov, E.; Zhang, S.; Lubag, A.; Balschi, J. A.; Sherry, A. D.; Lenkinski, R. E. On-resonance low *B*1 pulses for imaging of the effects of PARACEST agents. *J. Magn. Reson.* 2005, *176*, 54-63.

[47] Burdinski, D.; Lub, J.; Pikkemaat, J. A.; Moreno Jalón, D.; Martial, S.; Del Pozo Ochoa, C. Triethylenetetramine Penta- and Hexa-Acetamide Ligands and their Ytterbium Complexes as ParaCEST Contrast Agents for MRI. *Dalton Trans.* 2008, 4138-4151.

[48] Aime, S.; Delli Castelli, D.; Terreno, E. Supramolecular Adducts between Poly-L-arginine and [$Tm^{III}$dotp]: A Route to Sensitivity-Enhanced Magnetic Resonance Imaging-Chemical Exchange Saturation Transfer Agents. *Angew. Chem. Int. Ed.* 2003, *42*, 4527-4529.

[49] Schumann, H.; Kuse, K. Lanthanoidkomplexe von 1-(2-Propenyl)- und 1-(3-Butenyl)-1,4,7,10-tetraazacyclododecan-4,7,10-triessigsäure. *Z. anorg. allg. Chem.* 2008, *634*, 2954-2958.

[50] Woods, M.; Woessner, D. E.; Zhao, P.; Pasha, A.; Yang, M.-Y.; Huang, C.-H.; Vasalitiy, O.; Morrow, J. R.; Sherry, A. D. Europium(III) Macrocyclic Complexes with Alcohol Pendant Groups as Chemical Exchange Saturation Transfer Agents. *J. Am. Chem. Soc.* 2006, *128*, 10155-10162.

[51] Woods, M.; Woessner, D. E.; Sherry, A. D. Paramagnetic lanthanide complexes as PARACEST agents for medical imaging. *Chem. Soc. Rev.* 2006, *35*, 500-511.

[52] Zhang, S.; Merritt, M.; Woessner, D. E.; Lenkinski, R. E.; Sherry, A. D. PARACEST Agents: Modulating MRI Contrast via Water Proton Exchange. *Acc. Chem. Res.* 2003, *36*, 783-790.

[53] Wojciechowski, F.; Suchy, M.; Li, A. X.; Azab, H. A.; Bartha, R.; Hudson, R. H. E. A Robust and Convergent Synthesis of Dipeptide-DOTAM Conjugates as Chelators for Lanthanide Ions: New PARACEST MRI Agents. *Bioconjugate Chem.* 2007, *18*, 1625-1636.

[54] Suchý, M.; Li, A. X.; Bartha, R.; Hudson, R. H. E. Analogs of $Eu^{3+}$ DOTAM-Gly-Phe-OH and $Tm^{3+}$ DOTAM-Gly-Lys-OH: Synthesis and magnetic properties of potential PARACEST MRI contrast agents. *Bioorg. Med. Chem.* 2008, *16*, 6156-6166.

[55] Polášek, M.; Kotek, J.; Hermann, P.; Císařová, I.; Binnemans, K.; Lukeš, I. Lanthanide(III) Complexes of Pyridine-N-Oxide Analogues of DOTA in Solution and in the Solid State. A New Kind of Isomerism in Complexes of DOTA-like Ligands. *Inorg. Chem.* 2008, *48*, 466-475.

[56] Querol, M.; Bogdanov Jr., A. Amplification strategies in MR imaging: Activation and accumulation of sensing contrast agents (SCAs). *J. Magn. Reson. Imaging* 2006, *24*, 971-982.

[57] De Leon-Rodriguez, L. M.; Lubag, A. J. M.; Malloy, C. R.; Martinez, G. V.; Gillies, R. J.; Sherry, A. D. Responsive MRI Agents for Sensing Metabolism in Vivo. *Acc. Chem. Res.* 2009, *42*, 948-957.

[58] Yoo, B.; Pagel, M. D. A PARACEST MRI Contrast Agent To Detect Enzyme Activity. *J. Am. Chem. Soc.* 2006, *128*, 14032-14033.

[59] Yoo, B.; Pagel, M. D. Peptidyl Molecular Imaging Contrast Agents Using a New Solid-Phase Peptide Synthesis Approach. *Bioconjugate Chem.* 2007, *18*, 903-911.

[60] Yoo, B.; Raam, M. S.; Rosenblum, R. M.; Pagel, M. D. Enzyme-responsive PARACEST MRI contrast agents: a new biomedical imaging approach for studies of the proteasome. *Contrast Media Mol. Imaging* 2007, *2*, 189-198.

[61] Terreno, E.; Cabella, C.; Carrera, C.; Delli Castelli, D.; Mazzon, R.; Rollet, S.; Stancanello, J.; Visigalli, M.; Aime, S. From Spherical to Osmotically Shrunken Paramagnetic Liposomes: An Improved Generation of LIPOCEST MRI Agents with Highly Shifted Water Protons. *Angew. Chem. Int. Ed.* 2007, *46*, 966-968.

[62] Delli Castelli, D.; Terreno, E.; Carrera, C.; Giovenzana, G. B.; Mazzon, R.; Rollet, S.; Visigalli, M.; Aime, S. Lanthanide-loaded paramagnetic liposomes as switchable magnetically oriented nanovesicles. *Inorg. Chem.* 2008, *47*, 2928-2930.

[63] Aime, S.; Castelli, D. D.; Terreno, E. Highly sensitive MRI chemical exchange saturation transfer agents using liposomes. *Angew. Chem. Int. Ed.* 2005, *44*, 5513-5515.

[64] Burdinski, D.; Pikkemaat, J. A.; Emrullahoglu, M.; Costantini, F.; Verboom, W.; Langereis, S.; Grüll, H.; Huskens, J. Targeted LipoCEST Contrast Agents for MRI: Alignment of Aspherical Liposomes on a Capillary Surface. *Angew. Chem. Int. Ed.* 2010, *49*, 2227-2229.

[65] Langereis, S.; Keupp, J.; van Velthoven, J. L. J.; de Roos, I. H. C.; Burdinski, D.; Pikkemaat, J. A.; Grüll, H. A Temperature-Sensitive Liposomal $^{1}$H CEST and $^{19}$F Contrast Agent for MR Image-Guided Drug Delivery. *J. Am. Chem. Soc.* 2009, *131*, 1380-1381.

[66] Hekmatyar, S. K.; Kerkhoff, R. M.; Pakin, S. K.; Hopewell, P.; Bansal, N. Noninvasive thermometry using hyperfine-shifted MR signals from paramagnetic lanthanide complexes. *Int. J. Hyperthermia* 2005, *21*, 561-574.

[67] James, J. R.; Gao, Y.; Soon, V. C.; Topper, S. M.; Babsky, A.; Bansal, N. Controlled radio-frequency hyperthermia using an MR scanner and simultaneous monitoring of temperature and therapy response by $^{1}$H, $^{23}$Na, and $^{31}$P magnetic resonance spectroscopy in subcutaneously implanted 9L-gliosarcoma. *Int. J. Hyperthermia* 2010, *26*, 79-90.

[68] Zuo, C. S.; Bowers, J. L.; Metz, K. R.; Nosaka, T.; Sherry, A. D.; Clouse, M. E. TmDOTP$^{5-}$: A substance for NMR temperature measurements in vivo. *Magn. Reson. Med.* 1996, *36*, 955-959.

[69] Zuo, C. S.; Metz, K. R.; Sun, Y.; Sherry, A. D. NMR temperature measurements using a paramagnetic lanthanide complex. *J. Magn. Reson.* 1998, *133*, 53-60.

[70] Sun, Y.; Sugawara, M.; Mulkern, R. V.; Hynynen, K.; Mochizuki, S.; Albert, M.; Zuo, C. S. Simultaneous measurements of temperature and pH in vivo using NMR in conjunction with TmDOTP$^{5-}$. *NMR Biomed.* 2000, *13*, 460-466.

[71] Coman, D.; Trubel, H. K. T., Robert E.; Hyder, F. Brain temperature and pH measured by $^{1}$H chemical shift imaging of a thulium agent. *NMR Biomed.* 2009, *22*, 229-239.

[72] Zuo, C. S.; Mahmood, A.; Sherry, A. D. TmDOTA$^{-}$: A Sensitive Probe for MR Thermometry in Vivo. *J. Magn. Reson.* 2001, *151*, 101-106.

[73] Hekmatyar, S. K.; Poptani, H.; Babsky, A.; Leeper, D. B.; Bansal, N. Non-invasive magnetic resonance thermometry using thulium-1,4,7,10-tetraazacyclododecane-1,4,7,10-tetraacetate (TmDOTA$^{-}$). *Int. J. Hyperthermia* 2002, *18*, 165-179.

[74] Hekmatyar, S. K.; Hopewell, P.; Pakin, S. K.; Babsky, A.; Bansal, N. Noninvasive MR thermometry using paramagnetic lanthanide complexes of 1,4,7,10-tetraazacyclodoecane-α,α´,α´´,α´´-tetramethyl-1,4,7,10-tetraacetic acid ($DOTMA^{4-}$). *Magn. Reson. Med.* 2005, *53*, 294-303.

[75] Pakin, S. K.; Hekmatyar, S. K.; Hopewell, P.; Babsky, A.; Bansal, N. Non-invasive temperature imaging with thulium 1,4,7,10-tetraazacyclododecane-1,4,7,10-tetramethyl-1,4,7,10-tetraacetic acid ($TmDOTMA^{-}$). *NMR Biomed.* 2006, *19*, 116-124.

[76] James, J. R.; Gao, Y.; Miller, M. A.; Babsky, A.; Bansal, N. Absolute Temperature MR Imaging With Thulium 1,4,7,10-Tetraazacyclododecane-1,4,7,10-Tetramethyl-1,4,7,10-Tetraacetic Acid ($TmDOTMA^{-}$). *Magn. Reson. Med.* 2009, *62*, 550-556.

[77] Aime, S.; Fasano, M.; Terreno, E. Lanthanide(III) chelates for NMR biomedical applications. *Chem. Soc. Rev.* 1998, *27*, 19-29.

[78] Seshan, V.; Germann, M. J.; Preisig, P.; Malloy, C. R.; Sherry, A. D.; Bansal, N. $Tmdotp^{5-}$ as a $^{23}Na$ shift reagent for the in vivo rat kidney. *Magn. Reson. Med.* 1995, *34*, 25-31.

[79] Navon, G. Complete elimination of the extracellular $^{23}Na$ NMR signal in triple quantum filtered spectra of rat hearts in the presence of shift reagents. *Magn. Reson. Med.* 1993, *30*, 503-506.

[80] Winter, P. M.; Seshan, V.; Makos, J. D.; Sherry, A. D.; Malloy, C. R.; Bansal, N. Quantitation of intracellular [$Na^{+}$] in vivo by using $TmDOTP^{5-}$ as an NMR shift reagent and extracellular marker. *J. Appl. Physiol.* 1998, *85*, 1806-1812.

[81] Babsky, A. M.; Topper, S.; Zhang, H.; Gao, Y.; James, J. R.; Hekmatyar, S. K.; Bansal, N. Evaluation of extra- and intracellular apparent diffusion coefficient of sodium in rat skeletal muscle: Effects of prolonged ischemia. *Magn. Reson. Med.* 2008, *59*, 485-491.

[82] Winter, P. M.; Bansal, N. $TmDOTP^{5-}$ as a $^{23}Na$ shift reagent for the subcutaneously implanted 9L gliosarcoma in rats. *Magn. Reson. Med.* 2001, *45*, 436-442.

[83] Winter, P. M.; Bansal, N. Triple-Quantum-Filtered $^{23}Na$ NMR Spectroscopy of Subcutaneously Implanted 9L Gliosarcoma in the Rat in the Presence of $TmDOTP^{5-}$. *J. Magn. Reson.* 2001, *152*, 70-78.

[84] Bansal, N.; Germann, M. J.; Lazar, I.; Malloy, C. R.; Sherry, A. D. In vivo Na-23 MR imaging and spectroscopy of rat brain during $TmDOTP^{5-}$ infusion. *J. Magn. Reson. Imaging* 1992, *2*, 385-391.

[85] LaVerde, G. C. Sodium MRI for studying ischemic tissue in acute stroke. Ph.D. Thesis, University of Pittsburgh, Pittsburgh, 2006.

[86] Komoroski, R. A. Biomedical applications of $^{7}Li$ NMR. *NMR Biomed.* 2005, *18*, 67-73.

[87] Nikolakopoulos, J.; Zachariah, C.; Stubbs Jr., E. B.; Ramasamy, R.; Castro, M. M. C. A.; Geraldes, C., F. G. C. $^{7}Li$ Nuclear Magnetic Resonance Study for the Determination of $Li^{+}$ Properties in Neuroblastoma SH-SY5Y Cells. *J. Neurochem.* 1998, *71*, 1676-1684.

[88] Waters, E.; Chen, J.; Allen, J.; Zhang, H.; Lanza, G.; Wickline, S. Detection and quantification of angiogenesis in experimental valve disease with integrin-targeted nanoparticles and 19-fluorine MRI/MRS. *J. Cardiovascular Magn. Reson. Imaging* 2008, *10*, 43-51.

[89] Ruiz-Cabello, J.; Walczak, P.; Kedziorek, D. A.; Chacko, V. P.; Schmieder, A. H.; Wickline, S. A.; Lanza, G. M.; Bulte, J. W. M. In vivo ldquohot spotrdquo MR imaging

of neural stem cells using fluorinated nanoparticles. *Magn. Reson. Med.* 2008, *60*, 1506-1511.

[90] Yu, J.-X.; Kodibagkar, V. D.; Cui, W.; Mason, R. P. $^{19}$F: A Versatile Reporter for Non-Invasive Physiology and Pharmacology Using Magnetic Resonance. *Curr. Med. Chem.* 2005, *12*, 819-848.

[91] Chalmers, K. H.; De Luca, E.; Hogg, N. H. M.; Kenwright, Alan M.; Kuprov, I.; Parker, D.; Botta, M.; Wilson, J. I.; Blamire, Andrew M. Design Principles and Theory of Paramagnetic Fluorine-Labelled Lanthanide Complexes as Probes for $^{19}$F Magnetic Resonance: A Proof-of-Concept Study. *Chem. Eur. J.* 2010, *16*, 134-148.

In: Advances in Mechanical Engineering Research. Volume 2 ISBN: 978-1-61761-984-7
Editor: David E. Malach 

*Chapter 3*

# THULIUM-DOPED FIBER AMPLIFIERS

***S.D. Emami, P.Hajireza, H. A. A. Rashid and S. W. Harun***
Photonics Research Center, University Malaya,
Kuala Lumpur, Malaysia

## ABSTRACT

Due to the tremendous increase in communication traffic in recent years, more and more efforts in research have been directed towards developing highly efficient broad-band fiber amplifiers that will fully exploit the low-loss band of silica fibers in order to increase the transmission capacity of wavelength-division multiplexing (WDM) networks. These broad-band amplifiers must be able to amplify the new short wavelength band (S-band) in addition to the existing C- and L-bands. Thulium-doped fiber amplifiers (TDFAs) are a promising candidate for the S-band amplification because the amplification bandwidth of the TDFA is centered at 1470 nm, which falls within the S-band. This chapter reviews the structure and amplification mechanism of various TDFAs. The mathematical model of single pass and double pass TDFAs is also described in detail. A development of hybrid S-band optical amplifier using a TDFA and a fiber Raman amplifier is also presented at the end of this chapter. The wide-band hybrid amplifier is suitable for application in S-band optical telecommunication systems.

## INTRODUCTION

In fiber optic communication, data is transmitted from source to destination via optical fiber by using light as a tool. A fiber optic communication system wasfirst developed in 1970;it can provide a higher bandwidth with a longer transmission distance compared with the conventional system, which uses a copper wire as a transmission medium [1]. Recently, many research works have been focused on the fiber-optic devices for optical communication systems. One of the main interests is on the optical amplifiers to boost a weak signal in the communication systems. One of the effective ways to extend the gain bandwidth of the optical amplifiers is to use a hybrid amplifier that combines several amplifiers with different gain bandwidths. Due to the tremendous increase in communication traffic in recent years,

more and more efforts in research have been directed towards developing highly efficient fiber amplifiers that operate in the short wavelength band (S-band) region [2].

Thulium-doped fiber amplifier (TDFA) and fiber Raman amplifier (FRA) are two promising candidates for the S-band amplifiers. In this chapter, a review of the structure and amplification mechanism ofvarious TDFAs is presented. The mathematical model of single pass and double pass TDFAs is also described in detail. A development of hybrid S-band optical amplifier using a TDFA and a FRA is also presented.

## ATTENUATION IN A FIBER OPTIC COMMUNICATION LINK

Figure 1 shows the wavelength division Multiplexing (WDM) network which is one of the most popular optical communication networks. In this network, multiple optical carrier signals are transmitted into a single optical fiber by using a different wavelength of laser light. The multiple signals are multiplexed at the transmitter side and are de-multiplexed at the receiver side [3]. Because of the light attenuation in the glass fiber, an optical amplifier is used in the transmission link to amplify the optical signals. Inset of Figure1 shows a hierarchical of the optical path cross connect system for the large scale WDM network. In this system, grate bands are located on the top of the fiber physical layer. The grate band is a group of WDM channels [4].

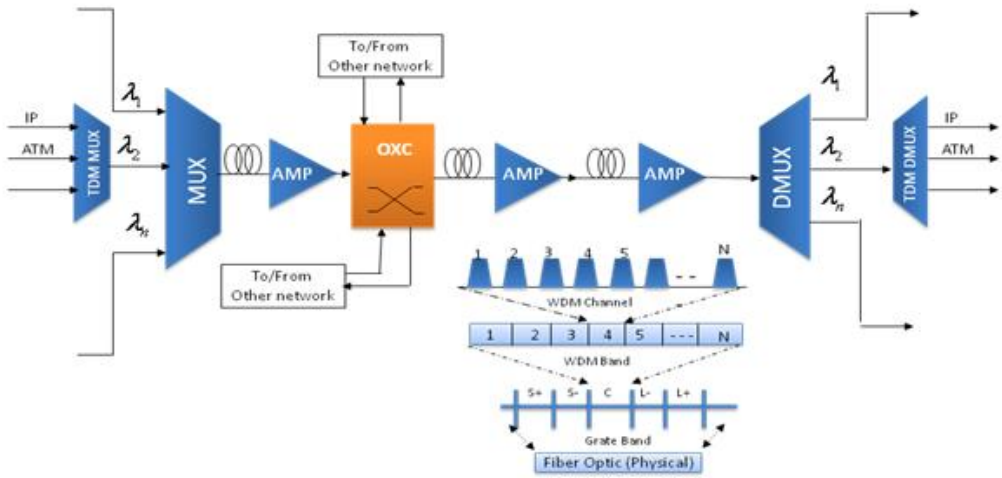


Figure 1. DWDM optical network. Inset shows a hierarchical of the optical path cross connect system.

One of the most important considerations in designing a fiber optic communication system is optical attenuation of the transmission signal. The transmission distance of any fiber optic communication system is limited by fiber attenuation. We have to make sure the signal power at the receiver is above the minimum level of photodiode sensitivity. Therefore, there is a limitation for total transmission length in a fiber-optic transmission system. Signal attenuation is defined as the ratio of optical input power ($P_i$) to the optical output power ($P_o$). Optical input power is the power injected into the fiber from an optical source. Optical output

power is the power received at the fiber end or optical detector [1]. The following equation defines signal attenuation per unit length in dB:

$$\text{Attenuation (dB)} = \left(10 \log_{10} \frac{P_{in}}{P_{out}}\right) / L \qquad \text{(Eq. 1)}$$

The loss also occurs in many points in the transmission link such as at the channel input coupler, splicing point and connectors.

Figure 2 shows the loss spectrum in a standard communication fiber, which is taken from 1200 nm to 1700 nm. The low loss region is approximately around 1550nm, which covers three communication windows: S-, C- and L-band [5]. The first telecommunication window is actually at 850nm which is most cost effective and has application for short distance communication systems. Higher attenuation in this window brings about theuse of second and third, which is 1310 nm and 1550 nm, windows respectively for fiber optic communication [6, 7]. Because of the availability of an optical amplifier in the 1550nm region, the third window is more preferred especially for long-haul applications. As shown in Figure 2, the third window consists of three operating bands: S-, C- and L-bands. S band is a short wavelength band and the wavelengths range from 1460 nm to 1530 nm. C band is a conventional band, which operates within the 1530 nm to 1560 nm wavelength region. L band or long wavelengths band operates at wavelengths ranging from 1565 nm to 1610nm [8]. The mechanisms that are responsible for attenuation of signal within the optical fiber are absorption loss, scattering loss, and bending loss due to geometrical effect. These mechanisms are influenced by the material compositions, preparation and purification technique during the fabrication process as well as the waveguide structure of the fiber [2].

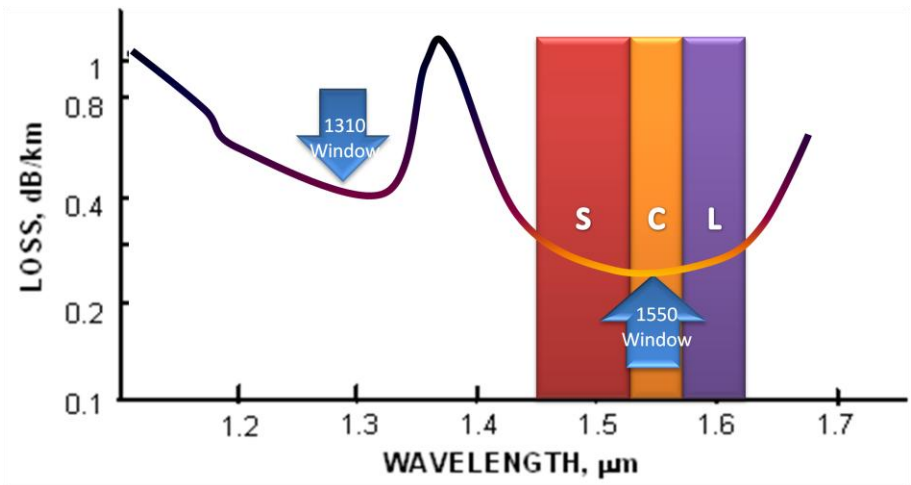


Figure 2. Loss spectrum of the standard SMF and communication windows.

## OPTICAL AMPLIFIERS TO COMPENSATE FOR THE ATTENUATION

In**a** long haul optical communication system, optical amplifiers are needed to compensate for the attenuation. They are designed to boost the weakened signal to a specific power level and ready it for the next transmission distance. Optical amplifiers are devices that amplify the

optical signal directly without any conversion to an electric domain. In a conventional repeater, optical signal is converted into the electrical signal so that it can be amplified electrically. The amplified signal is converted back into the optical signal for further transmission. This type of repeater is bulky, bit rate dependent and only can support a single transmission. Therefore it is not suitable for application in a modern DWDM system [4]. The structure of optical amplifier is similar to laser without an optical cavity, or one in which feedback from the cavity is suppressed. Stimulated emission process in the amplifier's gain medium is used for amplification of incoming light. Semiconductor optical amplifiers, active fiber or doped fiber amplifiers and Raman amplifiers are the three major types of optical amplifiers [7]. Figure 3 shows the types of optical amplifiers and its operating wavelength region. Different optical amplifiers have a different amplification wavelength ranges. Fiber Raman Amplifier (FRA) can use for almost all wavelength ranges. Thulium Doped Fiber Amplifier (TDFA) and depressed cladding Erbium Doped Fiber Amplifier (EDFA) is use for amplification in S-band region. EDFA and gain-shifted EDFA (GS-EDFA) is used for amplification in C- and L-band region respectively [1].

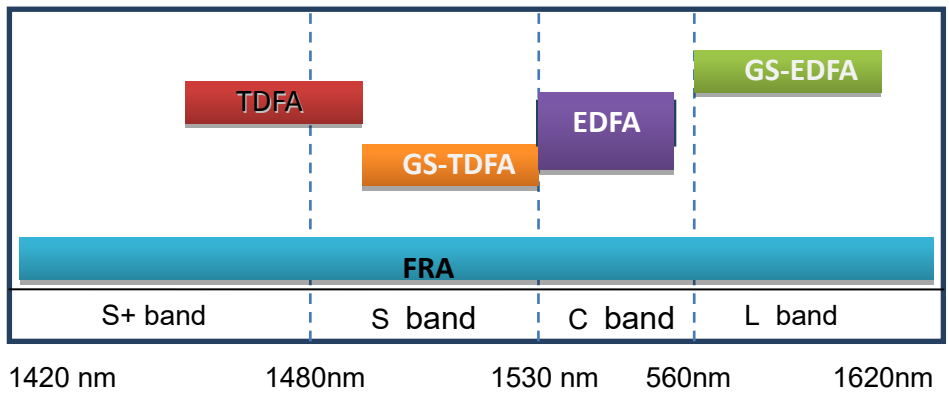


Figure 3. Types of optical amplifiers.

## THULIUM-DOPED FIBER AMPLIFIERS FOR OPTICAL AMPLIFICATION

When thulium doped into the glass a number of transitions in thulium become dominated by multi photon decay due to the closeness of the next lowest energy level and high relatively of phonon energy of glass. TDFAs can reach gain by stimulated emission from rare earth ions doped into the fiber core. Thulium produces stimulated emission from a transmission above the ground state. It causes thulium inherently less efficient, so the pump source and glass host optimization is very important. Some of the spectroscopic challenge encountering the amplification in TDFA that are listed below:

i) Nonradiative transitions dominate the decay from the upper and lower amplifying level [8].
ii) The lower amplifying level has a longer lifetime than upper amplifying level and it make the transition self terminate [9].

iii) Competing transitions reduce the gain from s band amplifying transition [10].
iv) At high thulium concentrations a cross relaxation process can reduce the population in the upper amplifying level and it redu8ce the gain [11, 12].
v) Amplified spontaneous emission from upper level reduces the gain [12].

Figure 4 showed the energy level diagram of thulium in silica glass. It also presents the possible ground and excited absorption of TDFA. According to the energy level diagram there is a wide choice of pump wavelengths are available including 1550 nm, 800 nm, 640 nm, 14XX nm, 1050 nm and etc [13]. Lasing and amplification at 800 nm, 1470 nm and 1900 nm region is one of important features of thulium [14]. For most of these cases a choice of pump wavelength are available. In some case pumping at two wavelengths is suitable for increasing the performance [15, 16]. Amplifying at 800nm region can be obtained by the $^3f_4$—$^3h_6$ transition. Amplifiers operation near 830 nm in the first telecommunications window has application for short distance distribution and local area networks [17, 18]. For amplification in 800 nm, we have to pump the TDF by 780 nm pump wavelength. $^3f_4$ to $^3h_6$ transitions can also demonstrate the amplification at 1900 nm region [19]. Currently, the main application of TDFA is amplification in 1470 nm or S band region. In TDFA, the stimulated emission at 1470 nm range can be obtained by the population inversion between two excited levels $^3H_4$ and $^3F_4$. For achieving this, many pumping wavelength were suggested such as 1050 nm, 1400 nm, 1560 nm 800nm and etc [20, 21]. In Figure 4 spontaneous emission from level i to level j was shown by $A_{ij}$, stimulated absorption and emission from level i to level j was represented by $W_{ij}$ and nonradiative decay rate from the level $j$ is $A^{nr}{}_j$.

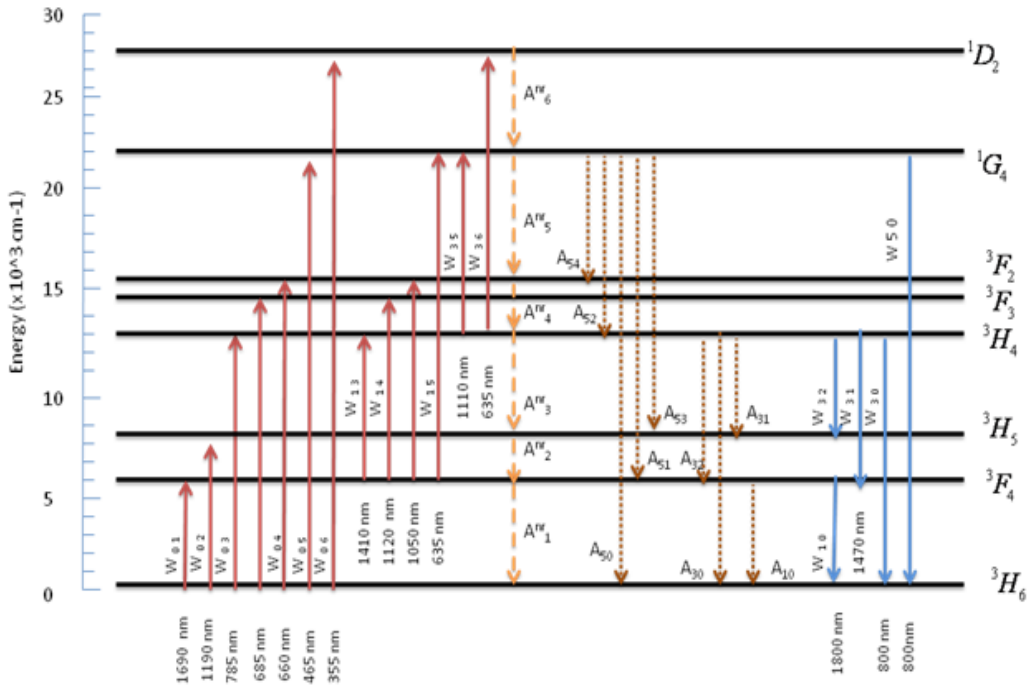


Figure 4. Energy level diagram of thulium ion.

The main research activity on TDFA is to shift the gain region to a longer wavelength from 1485 to 1530 nm where fiber attenuation is lower.[22, 23 ,24] One approach to have gain shift is to dope the TDF with thulium ion with concentration above 6000 part per million (ppm) [11, 25]. The high density of thulium atoms allows interactions between them, which changes transition probabilities and make it possible to produce the low population inversion needed to shift the gain band to longer wavelength [11]. Another way to shift gain to a longer S-band region and increase the efficiency is to employ a dual wavelength pumping scheme [26, 27]. This scheme decreases the population inversion in TDF by matching one pump wavelength to transition from ground state, and the second wavelength to transition from lower laser level.

## RECENT DEVELOPMENT ON THEORETICAL AND EXPERIMENTAL WORKS ON S-BAND TDFA

Since 1995 several pump configurations have been suggested in order to enhance the gain and noise figure performance of the TDFA in S-band region. Thulium behaves as four level laser systems and life time of upper level is shorter than lower level and thus the population inversion can be hardly achieved with direct pumping to the upper laser level. In year 1995, Komukai et. al proposed up-conversion pumping using 1064 nm laser to solve this problem [28]. He managed to obtain a TDFA's gain up to 22 dB by single pump 1064nm with 150 mW. In year 2000, Aozasa et al. reported gain shifted TDFA by using high concentration TDF [11, 12, 29]. The fluoride-based TDF was bidirectionally pumped with 1064 nm. By changing thulium ion concentration from 2000 to 8000 ppm the gain region was shifted to 1453-1483nm region. Aozasa et al. was also the first person that reporting the TDFA with the best conversion efficiency of 42% in year 2001[30]. They used two bidirectional 1410 nm pump power in fluoride host glass and managed to obtain gain up to 26 dB. In the same year Kasamatsu report gain shifted TDFA by using a dual pumping scheme at 1560 nm 1047 nm [22]. In their setup, 1560 nm pump is used as an auxiliary pump power to increase the population at lower level leading to a low fraction inversion and gain shifting [5].

In year 2003, Martins-Filho had improved the Kasamatsu design by using optical frequency domain reflectometry to obtain 28 dB gain which is 8 dB improved compared to the previous design [31]. In year 2005, Yam et al. presented a novel pumping scheme for a fluoride-based TDFA by using the combination of 690 nm and 1050 nm pump power [8]. Since year 2002, the majority of TDFA works were based on fluoride-host TDF. This was attributed to the transition from $^3H_4$ to $^3F_4$ level in silica glass causes the large probability of nonradiative decay via intermediate level $^3H_5$, Therefore probability of nonradiative decay is higher in the silica glass and reduces the efficiency of the TDFA [8]. However, fluoride-based TDF has difficulty in fabrication process as well as impossibility of splicing to telecommunication fiber. This necessitates the use of mechanical splices that and prone to damage under high power pumping [32]. In year 2001, Samson et al. has published the first paper on silica-based TDFA with more than 20dB gain [28]. However, the fiber used still cannot be spliced to a standard silica optical fiber. Recently, gain of 10 dB and 12 dB were reported using silica based TDF by Orara in year 2002 and Cole in year 2001 respectively [6]. Figure 5 shows the up-conversion pumping schemes for TDFA that have been reported so far.

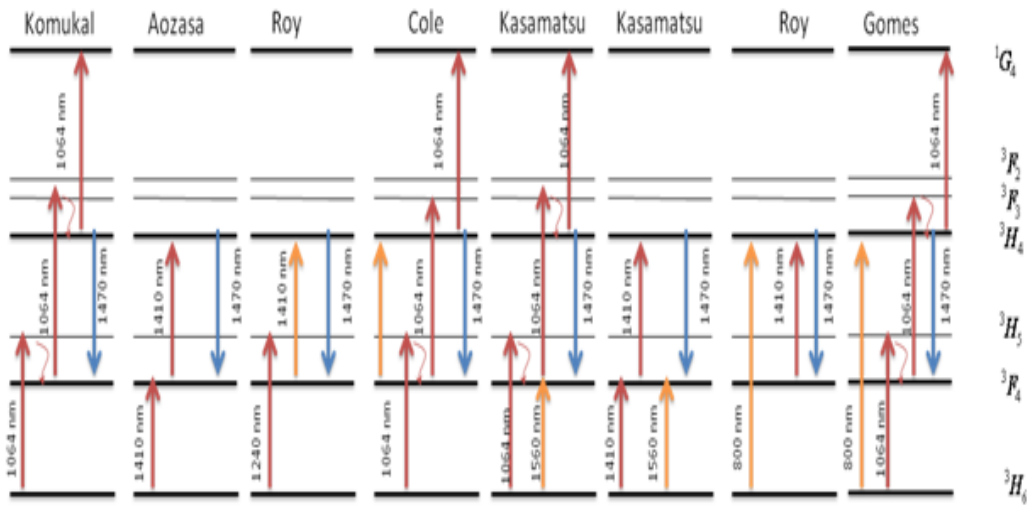


Figure 5. The reported up-conversion pumping schemes for TDFAs.

Besides experimental works, there are also many theoretical works in this area. During 1991 to 2001 several theoretical works have been published such as multimode fluoride-based TDFA operating at 800 nm by Lincoln and multimode silica-based TDF laser operating at 2000nm by Jackson. The first numerical model of S-band TDFA was demonstrated in 2002 by Lee [33]. Two other S-band TDFAs theoretical model have been proposed by Kasamatsu and Roy in year 2000 and both were dealing with fluoride-based fiber host [26]. The small signal model of TDFA first was demonstrated by Watekar in year 2006 [32]. Modeling of ground state absorption using 1050 nm and 14xx nm pump power was also reported by Yam [33]. In year 2007, Aozasa had proposed the employing of high thulium concentration doping to increase the efficiency [11]. The modeling and experimental results on silica-based TDFA is then reported by Watekar [32].

## TDFA Architectures with 1050nm Pumping

The basic architecture of the single pass and double pass TDFAs are depicted in Figure 6. Figure 6(a) shows the setup of the single pass TDFA, which consists of a TDF, a wavelength division multiplexing (WDM) coupler, a pump laser and two isolators. A WDM coupler is used to combine the pump light from 1050nm laser diode with the input signal. Optical isolators are used to ensure unidirectional operation of the optical amplifier. In the double pass configuration of Figure 6 (b), an optical circulator is placed at the input part of the amplifier to inject an input signal and to route an amplified signal into the output port. A fiber mirror is used as a reflector to reflect a selected wavelength[34].

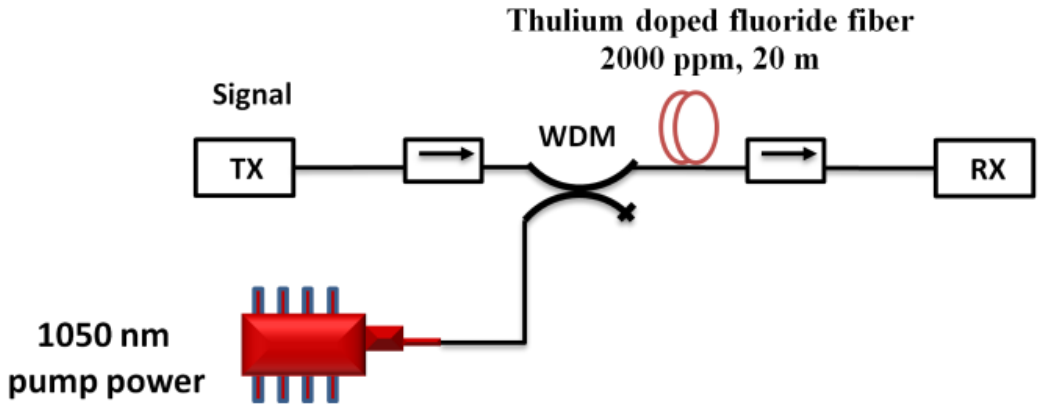


(a) single-pass

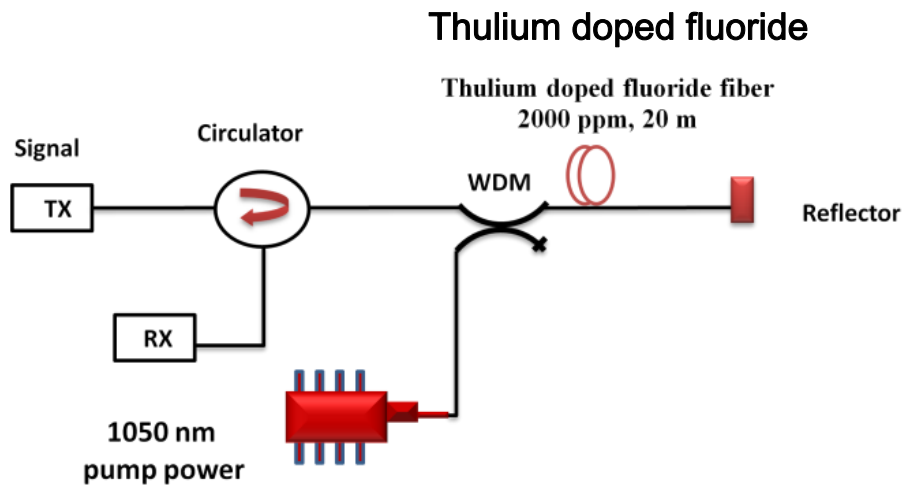


(b) double-pass

Figure 6. Configurations of the TDFA (a) single-pass (b) double-pass.

## THEORETICAL ANALYSIS FOR SINGLE-PASS AND DOUBLE-PASS TDFAS

Atomic rate equations are normally used to describe the TDFA in term of the interaction between pump, signal and ASE light in the TDFA. The equations are used to estimate populations in the energy levels under any pump and signal power conditions. From the rate equations, the gain coefficient for signal light and absorption coefficient for pump light are defined by considering the absorption and stimulated emission cross sections. To obtain the rate equations, an analysis of a six level energy system is discussed [19]. Figure 7 shows the

energy level diagram of trivalent thulium ion in fluoride glass. Figure 7 (a) and (b) show the absorption and emission transitions, respectively in the TDFA with 1050 nm pump.

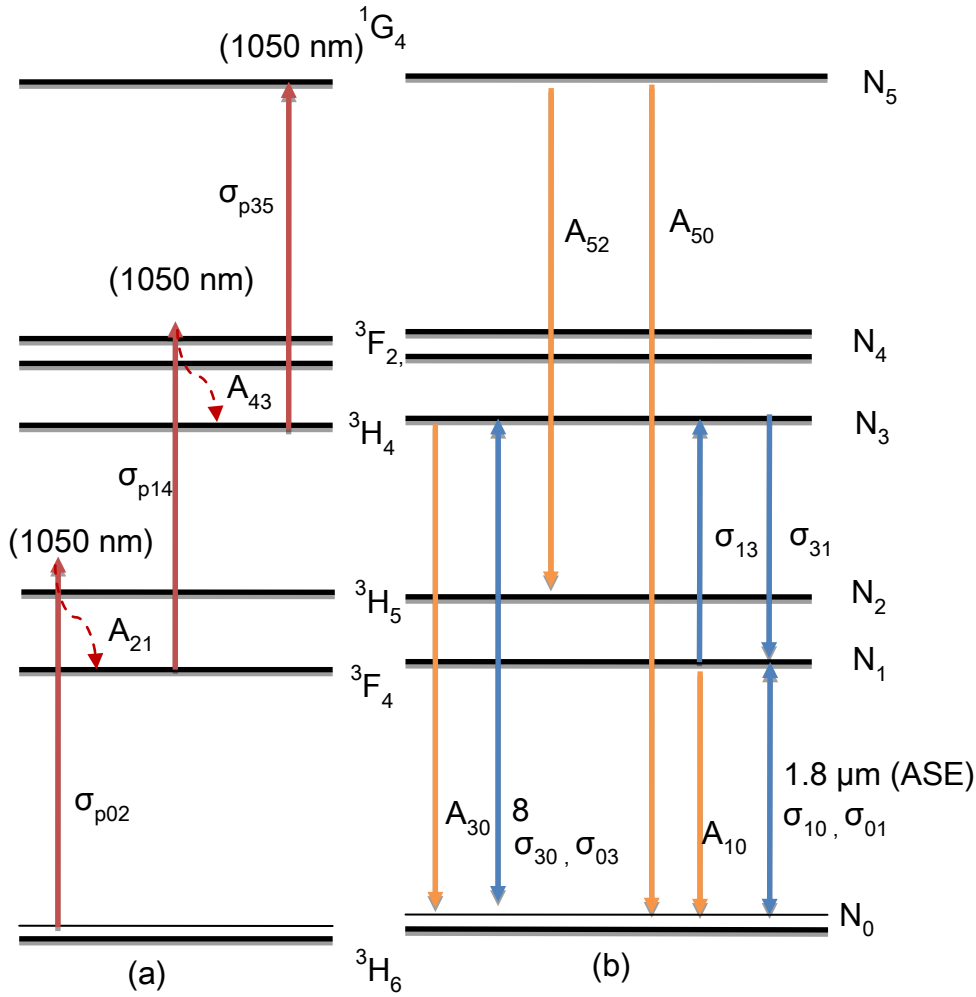


Figure 7. Pumping mechanism of a 1050nm pumped TDFA (a) absorption or pump transitions (b) signal and ASE emission transitions.

The main transition used for S-band amplification is from the $^3H_4$ to $^3F_4$ energy levels. This amplification is made possible by an up-conversion pumping method, which forms a population inversion between $^3H_4$ and $^3F_4$ levels [25]. When the TDF is pumped with 1050 nm laser, the ground state ions in the $^3H_6$ energy level can be excited to the $^3H_5$ energy level and then relaxed to the $^3F_4$ energy level by non-radiative decay. The $^3F_4$ energy level ions are then re-excited to the $^3F_2$ energy level and experience non-radiative decay to the $^3H_4$ energy level via excited state absorption. The 1050nm pump alone can provide both the ground-state and excited-state absorptions. Figure 8 shows the amplified spontaneous emission spectrum for transition between $^3H_4$ to $^3F_4$ level [20].

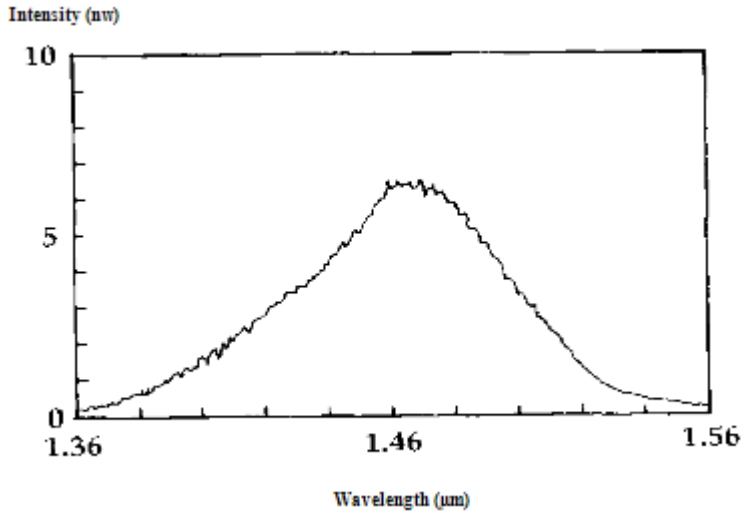


Figure 8. Emission spectrum from transition between $^3H_4$ to $^3F_4$ level.

In the rate equation models, the energy level of the $^3F_2$ and $^3F_3$ energy levels are nearly the same and can be treated as one level for simplicity. The variables $N_0$, $N_1$, $N_2$, $N_3$, $N_4$, and $N_5$ are used to represent population of ions in the $^3H_6$, $^3F_4$, $^3H_5$, $^3H_4$, $^3F_2$, and $^1G_2$ energy levels respectively. According to the Figure8 we can write the rate of population for each layer for single pass and double TDFA as follows [34, 35]:

$$\frac{dN_0}{dt} = -(W_{p02} + W_{18a} + W_{8a})N_0 + (A_{10} + W_{18e})N_1 + (A_{30} + W_{8e})N_3 + A_{50}N_5 \quad (1)$$

$$\frac{dN_1}{dt} = (W_{18a})N_0 - (A_{10} + W_{p14} + W_{sa} + W_{18e})N_1 + (A_{20})N_2 + (W_{se})N_3 \quad (2)$$

$$\frac{dN_2}{dt} = (W_{p02})N_0 - (A_{21}{}^{nr})N_2 + (W_{52})N_5 \quad (3)$$

$$\frac{dN_3}{dt} = (W_{8a})N_0 + (W_{sa})N_1 - (A_{30} + W_{p35} + W_{se} + W_{8a})N_3 + (A_{43})N_4 \quad (4)$$

$$\frac{dN_4}{dt} = (W_{p14})N_1 - (A_{43}{}^{nr})N_4 \quad (5)$$

$$\frac{dN_5}{dt} = (W_{p35})N_3 - (A_{50} + A_{52})N_5 \quad (6)$$

$$\sum_i N_i = \rho \tag{7}$$

where $W_{p02}$, $W_{p14}$, $W_{p35}$ are transition rates of the 1050 nm pump. Signal stimulated absorption and emission are described by $W_{sa}$ and $W_{se}$ respectively. The transition rates of amplified spontaneous emission (ASE) at 800 nm ($^3H_4 \rightarrow {}^3H_6$) and 1800 nm ($^3F_4 \rightarrow {}^3H_6$) are governed by $W_8$, $W_{18}$ respectively. The non-radiative transition rate from $^3F_2$ to $^3F_4$ and from $^3H_5$ to $^3F_4$ energy levels are defined as $A_{43}^{nr}$ and $A_{21}^{nr}$, respectively, and $A_{i\,j}$ is the radiative rate from level *i* to level *j*.

Equations (1) ~ (6) can be solved by considering the steady state regime where the populations are time independent, $dN_i/dt=0$ $(i=0,1,\ldots5)$. The average thulium ion concentration in the core is denoted as ρ and is quantified by [36]:

$$\rho = \frac{2}{b^2}\int_0^{\infty} n(r) r dr \tag{8}$$

where b is the doping radius and N(r) is thethulium ions concentration profile. The interaction of the electromagnetic field with the ions or thetransition rate ($W_{ij}$) for a single pass TDFA can be written as [35]:

$$W_{p02,p14,p35} = \lambda_{P1}\sigma_{p02,p14,p35}\left(\frac{P_{P1}^{+}}{hcA_{eff}}\right) \tag{9}$$

$$W_{8a,8e,18a,18e} = \lambda_{ASE}^{8,18}\sigma_{03,30,01,10}\left(\frac{P_{ASE}^{8,18+} + P_{ASE}^{8,18-}}{hcA_{eff}}\right) \tag{10}$$

$$W_{sa,se} = \lambda_{ASE}^{8,18}\sigma_{sa'se}\left(\frac{P_{ASE}^{8,18+} + P_{ASE}^{8,18-}}{hcA_{eff}}\right) + \lambda_s\sigma_{sa,se}\left(\frac{P_S}{hcA_{eff}}\right) \tag{11}$$

where $\sigma_{p02}$, $\sigma_{p14}$, $\sigma_{p35}$ are the $^3H_6 \rightarrow {}^3H_5$, $^3F_4 \rightarrow {}^3F_2$, $^3H_4 \rightarrow {}^1G_4$ absorption cross sections of the 1050nm forward pumping respectively. The stimulated absorption cross section at 800nm is denoted by $\sigma_{8a}$ and the stimulated emission cross section at 800nm and 1800 nm are denoted by $\sigma_{8e}$, and $\sigma_{18e}$ respectively. $P_p^{1+}$ and $P_s$ are the 1050 nm pump power and signal power respectively. $P_{ase}$, $P_{ase8}$, and $P_{ase18}$ are the amplified spontaneous emission (ASE) at S-band, 800nm and 1800nm, respectively in the forward (+) and backward (-) directions along the fiber. The light-wave propagation equations along the thulium fiber (in the z direction) can be established as follows [35];

$$\frac{dP_{ASE}^{\pm}}{dz} = \pm\Gamma(\lambda_{ASE})(\sigma_{se}N_3 - \sigma_{se}N_1 + \sigma_{p01}N_0)\times P_{ASE}^{\pm} \pm \Gamma(\lambda_{ASE})2h\nu\Delta\nu\sigma_{se}N_3 \mp \alpha P_{ASE}^{\pm} \tag{12}$$

$$\frac{dP_{ASE}^{8\pm}}{dz} = \pm\Gamma(\lambda_8)(\sigma_{30}N_3 - \sigma_{03}N_1)\times P_{ASE}^{8\pm} \pm \Gamma(\lambda_8)2h\nu\Delta\nu\sigma_{30}N_3 \mp \alpha P_{ASE}^{8\pm} \tag{13}$$

$$\frac{dP_{ASE}^{18\pm}}{dz} = \pm\Gamma(\lambda_{18})(\sigma_{10}N_1 - \sigma_{01}N_0)\times P_{ASE}^{18\pm} \pm \Gamma(\lambda_{18})2h\nu\Delta\nu\sigma_{10}N_1 \mp \alpha P_{ASE}^{18\pm} \tag{14}$$

$$\frac{dP_{P1}^{+}}{dz} = -\Gamma(\lambda_{P1})(\sigma_{p02}N_0 + \sigma_{p14}N_1 + \sigma_{p02}N_3)\times P_{P1}^{+} - \alpha P_{P1}^{-} \tag{15}$$

$$\frac{dP_s}{dz} = -\Gamma(\lambda_s)(\sigma_{se}N_3 - \sigma_{sa}N_1 - \sigma_{p01}N_0)\times P_s - \alpha P_s \tag{16}$$

where α is thebackground scattering loss, which is assumed to be constant for all wavelengths. $\lambda_{ASE}$, $\lambda_{ASE8}$ and $\lambda_{ASE18}$ are the signal wavelengths, 800 nm ASE and 1800 nm ASE respectively. The overlapping factors between each radiation and the fiber fundamental mode, Γ (λ) can be expressed as [36]:

$$\Gamma(\lambda) = 1 - e^{-\frac{2b^2}{w_0^2}} \tag{17}$$

$$w_0 = a\left(0.761 + \frac{1.237}{V^{1.5}} + \frac{1.429}{V^6}\right) \tag{18}$$

where $w_0$ is the mode field radius defined by equation (18), a is the core diameter, b is the thulium ion-dopant radius and V is the normalized frequency.

In the double pass configuration of Figure 6(b), two signals propagate in the opposite direction of each other in the active medium. After the first signal passes through the active material, the amplifier's forward propagating signal ($P_s^+$) is reflected back by the fiber mirror and passes through the active material as a backward propagating signal ($P_s^-$) for further amplification. Therefore, in order to calculate the stimulated absorption and emission rate of thedouble pass TDFA, both $P_s^+$ and $P_s^-$ are calculated in the equation (11) in the following way [35]:

$$W_{sa,se} = \lambda_{ASE}^{8,18}\sigma_{sa,se}\left(\frac{P_{ASE}^{8,18+} + P_{ASE}^{8,18-}}{hcA_{eff}}\right) + \lambda_s\sigma_{sa,se}\left(\frac{P_S^+ + P_S^-}{hcA_{eff}}\right) \tag{19}$$

The steady state populations from level 1 to level 6 are calculated based on the newly calculated $W$ rate. The equations describing the spatial development of $Ps^+$ and $P_s^-$ are written as:

$$\frac{dP_s^+}{dz} = -\Gamma(\lambda_s)(\sigma_{se}N_3 - \sigma_{sa}N_1 - \sigma_{p01}N_0) \times P_s^+ - \alpha P_s^+ \tag{20}$$

$$\frac{dP_s^{--}}{dz} = +\Gamma(\lambda_s)(\sigma_{se}N_3 - \sigma_{sa}N_1 - \sigma_{p01}N_0) \times P_s^- + \alpha P_s^- \tag{21}$$

The equations describing the spatial development of $P_p$ , $P_{ase}$, $P_{ase8}$, and $P_{ase18}$ in the double pass TDFA remain the same as that of the single pass TDFA. During the reflection of the signal by the fiber mirror, mirror losses need to be considered. The initial value of backward signal power at the end of double pass TDFA is calculated by [32]:

$$P^{--}_{Sinitial} = P^{+}_{Sinitial} * G_{firstpass} * \text{Mirror loss} \tag{22}$$

where $G_{firstpass}$ is the gain of the signal after the first pass through the double pass TDFA and $P^+_{Sintial}$is the initial signal power in forward direction which is input into the double pass TDFA .

Noise figure is generated by spontaneous emission and therefore is closely related to ASE. The number of spontaneous photon is given by [34]:

$$\eta = \frac{\frac{\sigma_{SE}}{\sigma_{SA}}N_3}{\frac{\sigma_{SE}}{\sigma_{SA}}N_3 - N_2} \tag{23}$$

The noise figure (NF) of the double pass TDFA at the signal wavelength is calculated as:

$$NF(\lambda_s) = \frac{1+2\eta[G-1]}{G} \tag{24}$$

where G is the total gain of the double pass TDFA. The noise figure can also be calculated using the following equation;

$$NF = 1/G + P_{ASE}/(G \times h \times \nu \times \Delta\nu) \tag{25}$$

where $P_{ASE}$ is the ASE power, h is Planck's constant, ν is the frequency of the signal and Δν is the resolution of the measuring device such as an optical spectrum analyzer [34].

The spectral emission cross-section at S-band of Thulium ion [36] and the spectral absorption cross-section at S-band can be estimated by the modified McCumber's relation [34]:

$$\sigma_a(\nu) = \frac{\sigma_e(\nu)}{\eta^{peak}} \exp(\left\{\frac{h(\nu - \nu^{peak})}{k_B T}\right\} \tag{30}$$

$$\eta^{peak} = \frac{\sigma_e^{peak}}{\sigma_a^{peak}} \tag{31}$$

where $k_B$ is Boltzmann constant and T is temperature. As observed experimentally, the absorption cross section peak is approximately 70% of the emission peak. Figure 9 shows the spectra of the emission and absorption cross section of the TDF in fluoride glass, which were obtained from equation (30).

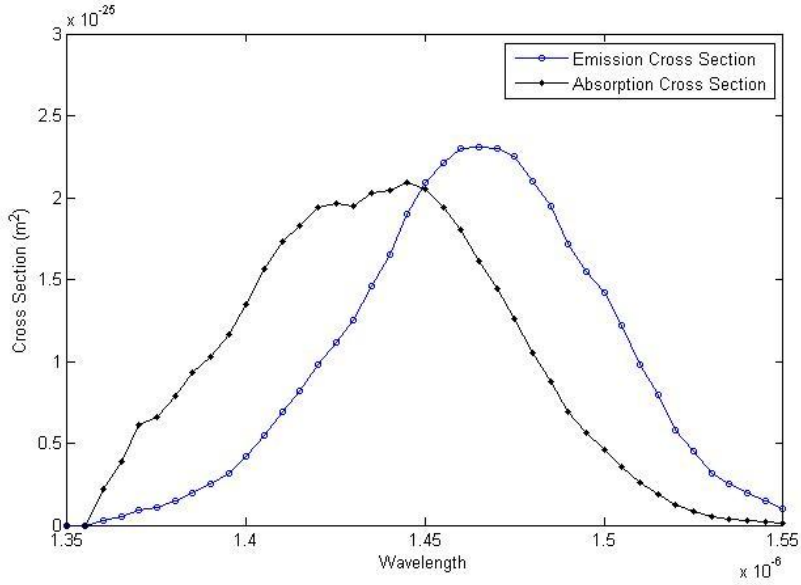


Figure 9. Emission and absorption cross-section spectra of the TDFA.

## OPTIMIZATION OF THE DESIGN PARAMETER FOR THE TDFAS

Optimization of the length of the TDF used is one of the most important issues that need to be considered for designing a TDFA in order to obtain the best gain with the lowest noise figure. In the case of remote pumping, the location of the amplifiers are far away from the source and an optimized pump power is essential. The gain and noise figure of the TDFA are strongly dependent on the TDF length and the operating pump power. The optimum TDF length is also dependent on the operating pump power and therefore a reference TDF length is firstly determined in a theoretical work. Then the operating pump power is optimized with respect to the reference TDF length. Careful considerations are necessary during the selection of the reference TDF length. If the reference TDF length is too short, the TDFA will be saturated at a very low pump power and this does not provide a high gain. Saturation takes place in TDFA due to the fixed thulium ion concentration and therefore after a certain amount

of pump power, the $N_3$ state population climbs to an almost constant level. In a simulation study, saturation is defined as the condition where the increment of gain is less than 0.4 dB with respect to an increment of 1 mW pump power. In the case of a short TDF, the total population is very low and hence the TDF is fully inverted by a very low amount of pump power. If this low amount of pump power is selected as the operating pump power then the optimized TDF length with respect to this low amount of pump power is very short [37,38] .

Figs. 10(a), (b) and (c) show the gain and noise figure of 1460nm signal as a function of pump power for both single-pass and double-pass TDFAs at different reference length of 12m, 20m and 34m, respectively. In this simulation work, the input signal power is fixed at -37 dBm. As shown in these figures, the gain for both single-pass and double-pass amplifiers increases with the increment of pump power and the gain for the double-pass amplifier is higher than that of the single-pass amplifier. On the other hand, the noise figure improves or reduces with the increment of pump power. The result clearly shows that the increment of gain and the decrement of NF are very low with respect to the increment of pump power after the pump power exceeds 100 mW for the single pass and 125 mW for the double pass TDFA [34]. At a pump power of 100 mW and 12m TDF length, the TDFA is able to provide a gain of 11 dB and 16dB for the single-pass and double-pass configuration respectively, as shown in Figure 10 (a). If a 12m long TDF is selected as a reference then based on the saturation characteristics of the TDFA as shown in Figure 10 (a), a 100 mW and 125 mW pump power should be selected as the operating pump power for single-pass and double pass TDFA configurations respectively. Since, the optimized TDF length with respect to 100 mW and 125 mW pump power is very short, the total cumulative gain of the TDFA is also very low [34].

On the other hand, if the length of TDF is longer then a greater pump power is required to invert the population of the entire TDF, especially toward the end of the TDF. The saturation pump power is also higher as shown in Figs. 10 (b) and (c) for the reference length of 20m and 34m, respectively. As seen in Figure 10 (b), a gain saturation of 15dB and 30dB are obtained at a pump power of 120mW and 150mW for single-pass and double-pass TDFA respectively. Figure 10 (b) shows that the increment of gain and decrement of noise figure with respect to the increment of pump power are very low after the pump power exceeds these saturation levels. Figure 10 (c) shows that the gain saturation of 24 and 55 dB are obtained at pump power of 130mW and 170mW respectively for single-pass and double-pass TDFA respectively. In the optical network, an amplifier is mainly designed to obtain a gain as high as possible with a low noise figure using a minimum pump power. Although the 34 m long TDFA architecture which has the optimum operating pump power of 170 mW is able to provide the highest gain but the use of a high pump power is in conflict with the main objective of the TDFA design which requires a smaller pump power especially for long haul applications. For this reason, a very long TDF is not recommended to be considered as a reference TDF length during the design of single and double pass TDFAs [35].

The length of the TDF can be also optimized by calculating the gain as a function of TDF length for various operating pump powers as shown in Figure 11. The input signal power and wavelength is fixed at -37dBm and 1470nm, respectively and the 1050nm pump power is varied from 100 to 200mW. The single-pass configuration of Figure 11(a) is used in this simulation work. As shown in Figure 11, the maximum gain is obtained at 25, 31 and 34dB with the pump powers of 100, 150 and 200mW respectively. The maximum gain is obtained at a TDF length of 54, 41 and 36m for pump power of 100, 150 and 200mW, respectively.

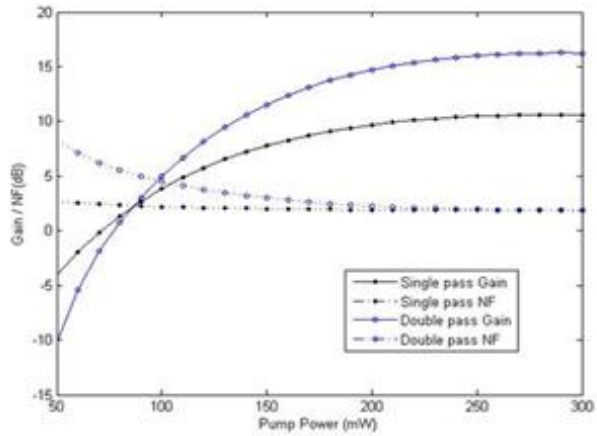


**(a) Reference length = 12m**

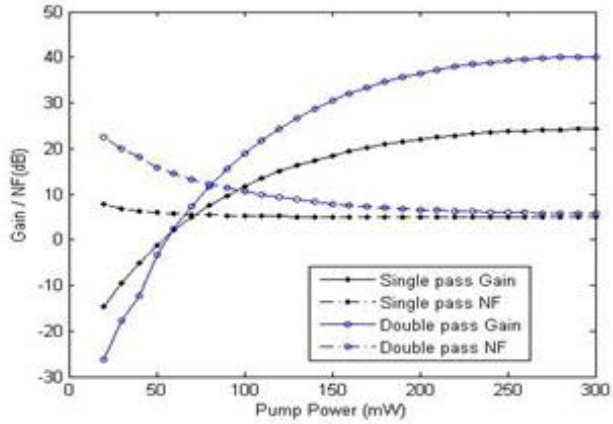


**(b) Reference length = 20m**

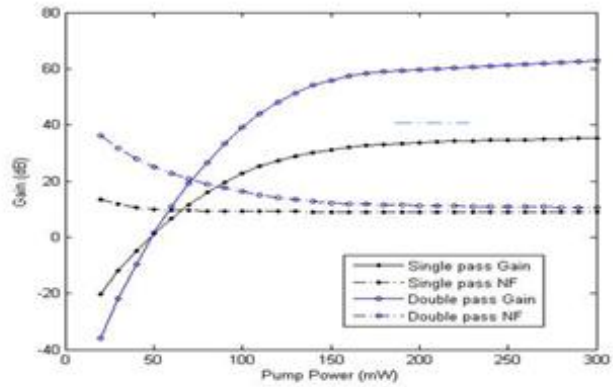


**(c) Reference length = 34m**

Figure 10. The gain and noise figure against pump power for both single-pass and double-pass TDFA at various reference TDF length (a) 12m (b) 20m and (3) 34m.

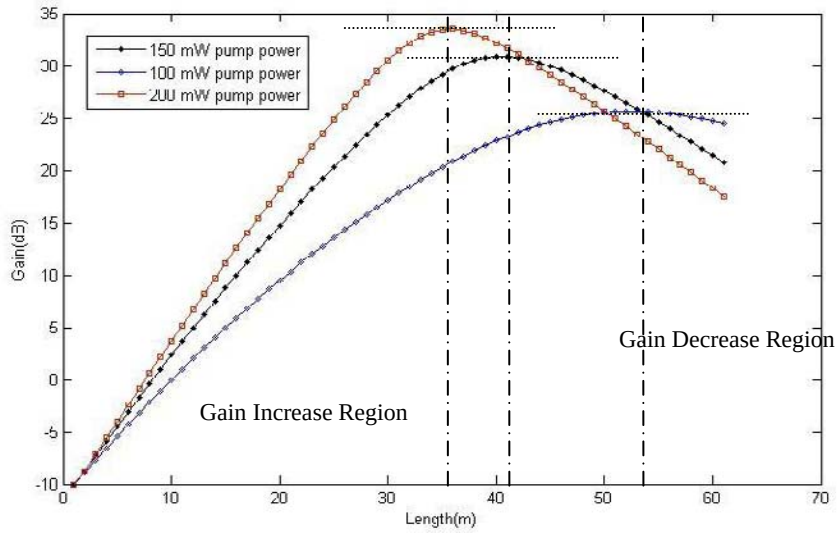


Figure 11. Gain against TDF length for different pump powers.

These results show that the TDFA is saturated at a shorter length with a higher gain value as the operating pump power increases. The gain gradually drops after the peak value as the TDF length increases. This is attributed to the pump power being fully absorbed in this region and saturates the gain. The upconversion and losses inside the TDF contribute to the gain drop at the saturation region [34].

The ASE has a noticeable effect on the total gain of both the single pass and double pass TDFAs. Figure 3.10 shows a forward and backward traveling ASE power of both single-pass and double-pass TDFAs as a function of position in the TDF for different TDF length settings. The 1050nm pump power is fixed at 200mW. As shown in the figure, the backward ASE is higher than the forward ASE for both single-pass and double-pass TDFAs. For instance, the forward and backward ASE power are obtained at 0.03mW and 0.05mW respectively for double-pass TDFA. This is due to the inversion at the beginning of the TDF length being much higher than the inversion at the end of TDF. The backward ASE is amplified along a well inverted piece of TDF before exiting the TDF, while the forward ASE travel along a piece of TDF that is progressively less inverted and thus has less gain per unit length than the backward ASE does. The results also show that the forward and backward ASE in the double pass configuration is higher than single pass TDFA. This is due to the higher inversion in the double-pass system, which has the backward signal [37].

Figure 12 also shows that the 40m long TDF provides the highest backward ASE compared to the shorter lengths. In this TDFA, the backward ASE travels over a longer distance and become much more higher at the beginning of the TDF. However, at a TDF length of more than the optimum length, the higher backward ASE depletes the inversion and robs the gain at the expense of the signal as well as forward ASE. Both signal and forward ASE powers will be reduced due to the less inverted portion of the TDF at the end [35].

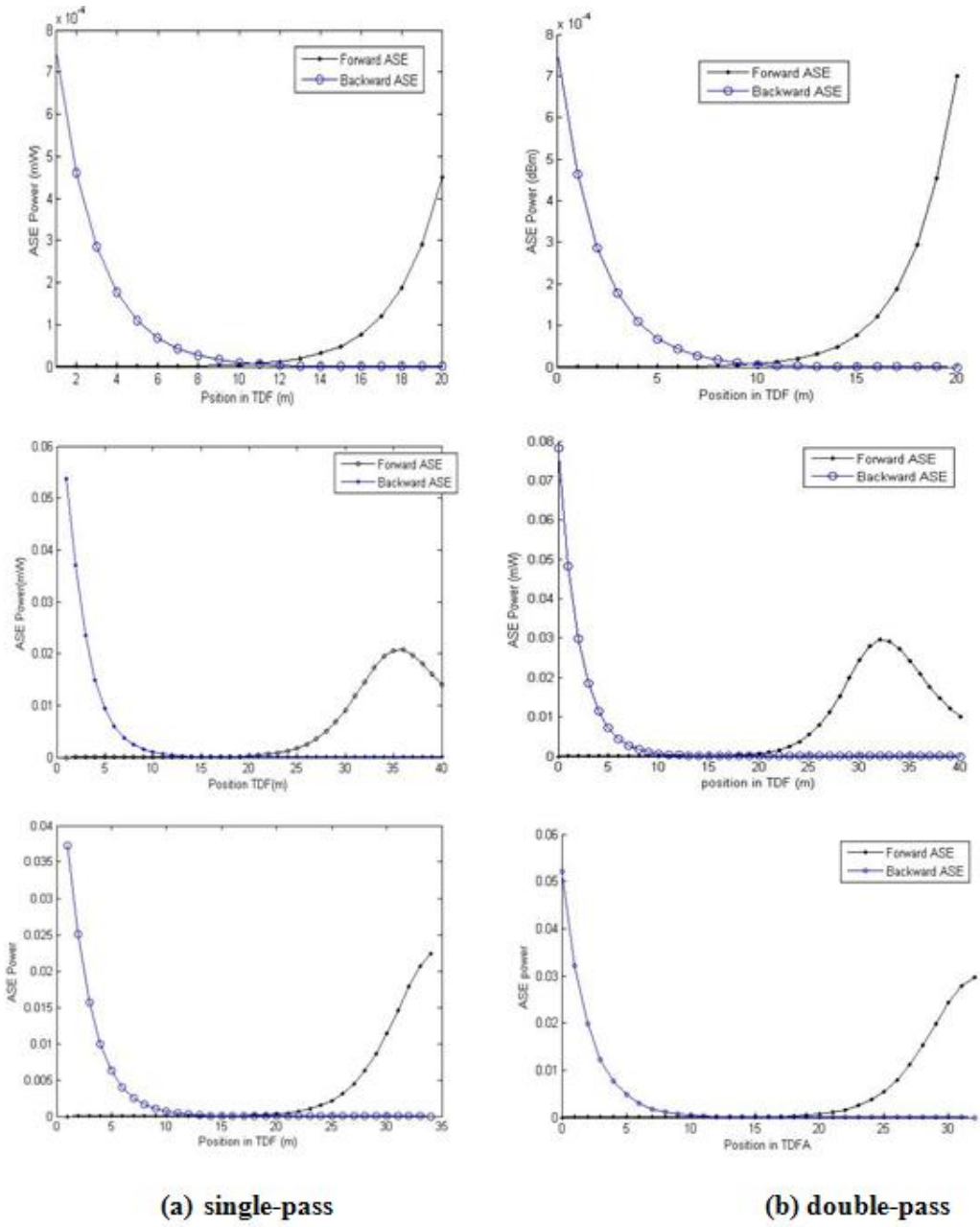


Figure 12.The forward and backward traveling ASE power against the position in TDF for both (a) single-pass and (b) double-pass TDFA.

Figure 13 shows the propagation of forward and backward amplified signals in the double-pass amplifier as a function of position along a 20, 35 and 40 m long TDF at 1470 nm signal wavelength using 200 mw pump power and an injected signal power of -40 dBm. As shown in the figure, the input forward signal is amplified to -10, 3 and -1dBm during the first pass for 20, 35 and 40m long TDFs of the double-pass amplifier. The signal is further amplified in the backward direction to 18, 41 and 38dBm for the cases of 20, 35 and 40m

respectively. According to these results a 35 m long double pass TDFA provides a gain that is 3dB higher than the 40m long double pass TDFA. If a TDFA of length less than the optimum length is used, the backward ASE is lower at the beginning of the TDF. Thus, the depletion of the pump power is lower at the beginning of the TDF compared to at the optimum length. As a result, a portion of the pump power remains unused which causes more population inversion and hence the increment of the gain. According to these results, a 20m long TDF provides less backward ASE than a 35 m long TDF and therefore the 35m long double pass TDFA provides a 20 dB higher gain than the 20m long double pass TDFA. From the above discussion the 35 m long double pass TDFA provide the maximum gain.

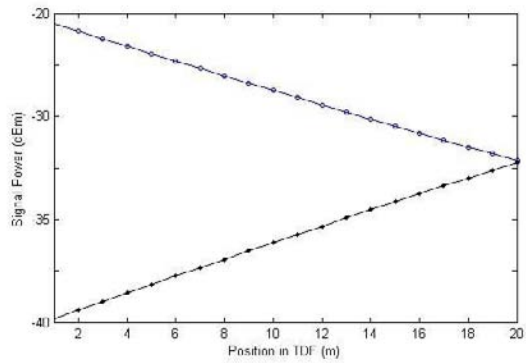


**(a)**

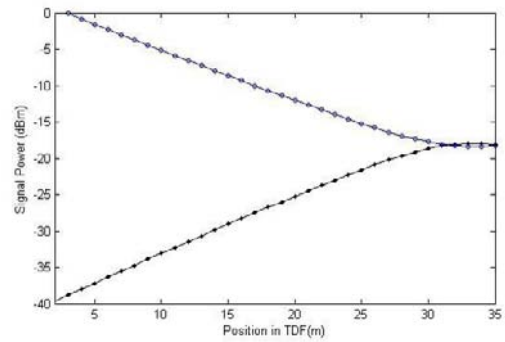


**(b)**

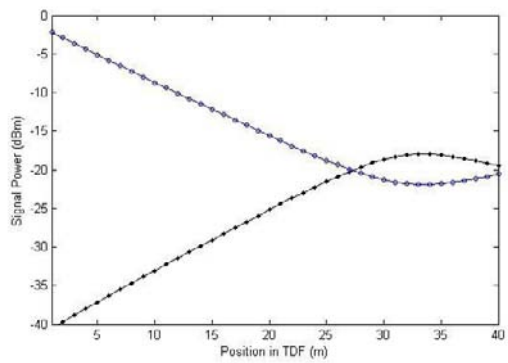


**(c)**

Figure 13. The propagation of the forward and backward amplified signal in the double-pass TDFA for different TDF length (a) 20m (b) 35m and (c) 40m.

The numerical simulation was also developed for a double pass TDFA to help the designers to carry out the design of an optimal double pass TDFA. Figs. 14(a) and (b) show the gain and noise figure spectra of the double-pass TDFA respectively with variations of 1050 nm pump power from 50 to 300 mW in conjunction with variations of input signal power from -40 to 0 dBm. The TDF length and input signal wavelength is set at 24 m and 1470 nm respectively. As shown in Figure 14(a), the gain gradually decreases with the increment of input signal power. This is due to the pump being unable to replenish the inversion as fast as the input signal is depleting it. The gain also increases with pump power and finally saturates at a certain pump power. The saturation pump power reduces with the increase of input signal power as shown in Figure 14(a). The maximum gain of 42 dB is obtained at an input signal power of -40 dBm with a pump power of 300mW. The noise figure can be reduced (improved) by either increasing the pump power or reducing the input signal power as shown in Figure 14(b). The mathematical equation obtained in the previous section shows that the noise figure reduces as the gain increases which is in agreement with our experimental results [38].

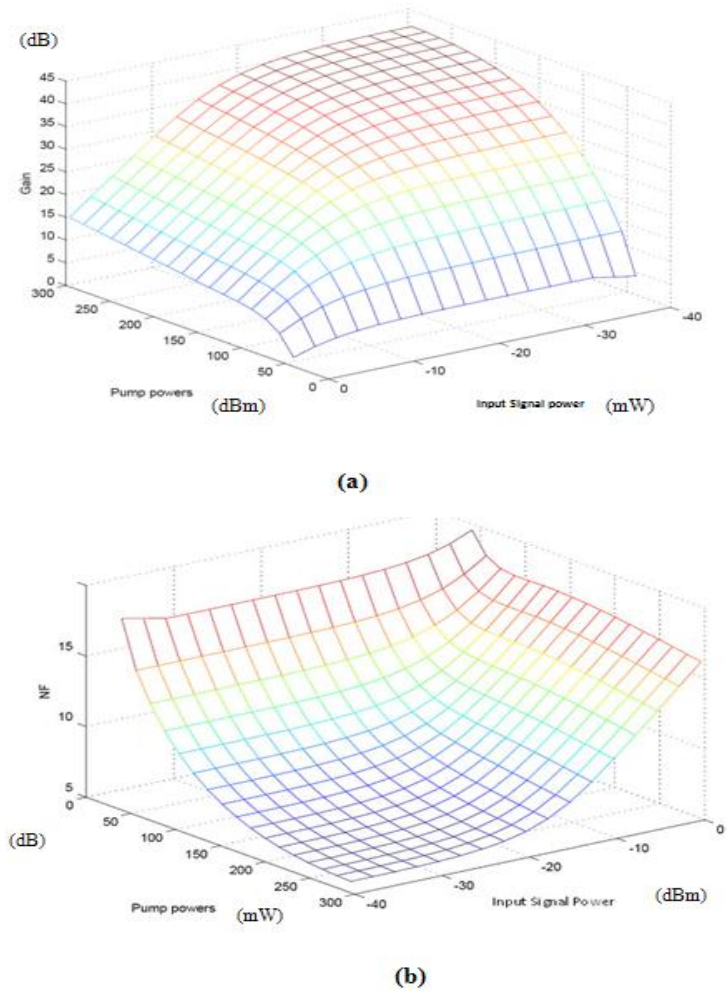


Figure 14. Gain and noise figure against pump power and input signal power (a) Gain (b) noise figure.

Figure 15 shows the comparison between the simulation results and the experimental work by Bastos-Filho et al. [39] that represents the double-pass TDFA pumped by a 1050 nm laser diode with the same setup. In the comparison, the 1050 nm pump and input signal powers are set at 250 mW and -30 dBm, respectively. The double-pass amplifier achieves a maximum gain of 32 dB at 1465 nm, which is 15 dB higher than the single-pass TDFA. The gain enhancement is attributed to the longer effective length in the double-pass TDFA. However, the noise figure is higher in the double-pass amplifier compared to the single-pass as shown in the Figure 15. . For instance, a 1 dB noise figure penalty is observed at 1470 nm in the double-pass amplifier compared with the single-pass amplifier. This increase in the noise figure is due to the counter-propagating ASE at the input part of the TDFA which reduces the population inversion at the input part of the fiber and subsequently increases the noise figure. The simulation result is in good agreement with the experimental result as shown in Figure 15.

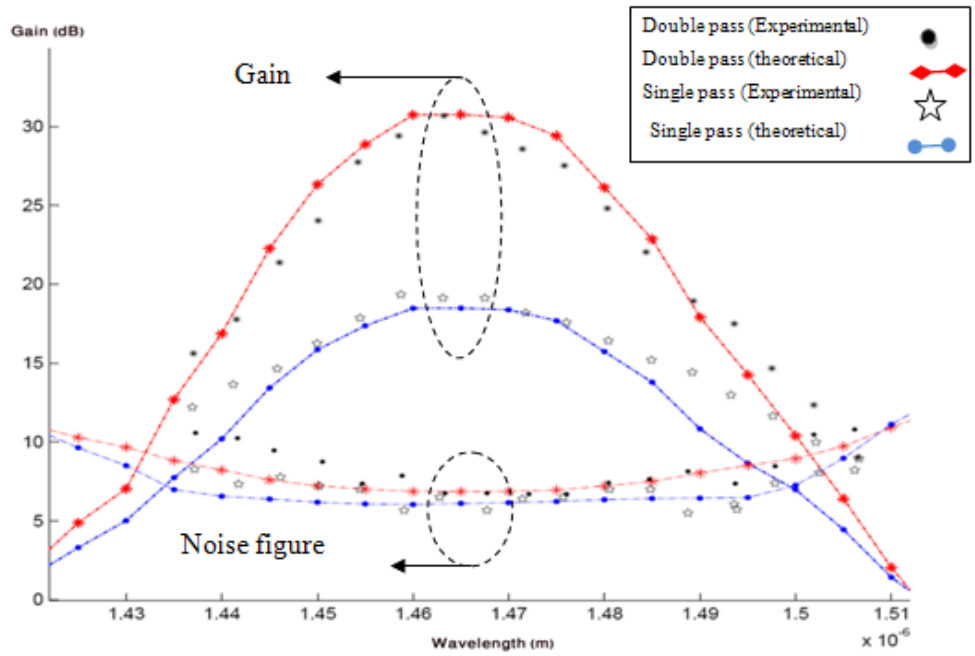


Figure 15. Gain and noise figure spectra for both single-pass and double-pass TDFAs.

## EFFECT OF AN AUXILIARY PUMP ON THE PERFORMANCE OF TDFA

A variety of pumping schemes such as 1047, 1050, or 1064 nm are proposed to obtain the population inversion in a thulium-doped fiber. The main transition of a thulium ion is from $^3H_4$ to $^3F_4$ in which stimulated emission emits photons in the 1470-nm wavelength region [40]. However, this transition is problematic due to the lifetime of $^3F_4$ being shorter than the lifetime of $^3H_4$, which makes it difficult to form a population inversion. One way to overcome this problem is by reducing the accumulated population at $^3H_4$ through an up-conversion pumping process. This is a two-step process, where the thulium ions are first excited from the

$^3H_6$ to $^3F_4$ energy level by ground-state absorption and, then, further excited to the upper energy level via excited-state absorption (second-stage pumping from the $^3H_4$ to $^3F_4$ energy level). In this section, an efficient TDFA is demonstrated theoretically using a dual pumping scheme at 1050 and 1560 nm. The 1050-nm pump provides the up-conversion and the 1560-nm pump enhances the ground-state absorption to achieve a high gain, a low noise figure, and a high-power conversion efficiency [40].

## TDFA with Dual Pumping Architecture

Figure 16 shows the setup of the TDFA, which consists of a fluoride-based TDF, two WDM couplers (WDM-1 and WDM-2), two pump lasers and two isolators. The TDF used is 20 m long and has a Tm ion concentration of 2000 ppm. WDM couplers are used to combine the pump light with the input signal. The 1050nm and 1560nm laser diodes are used as the main and secondary pumps respectively, with the main pump placed immediately before the TDF in the configuration. Optical isolators are used to ensure unidirectional operation of optical amplifier [40].

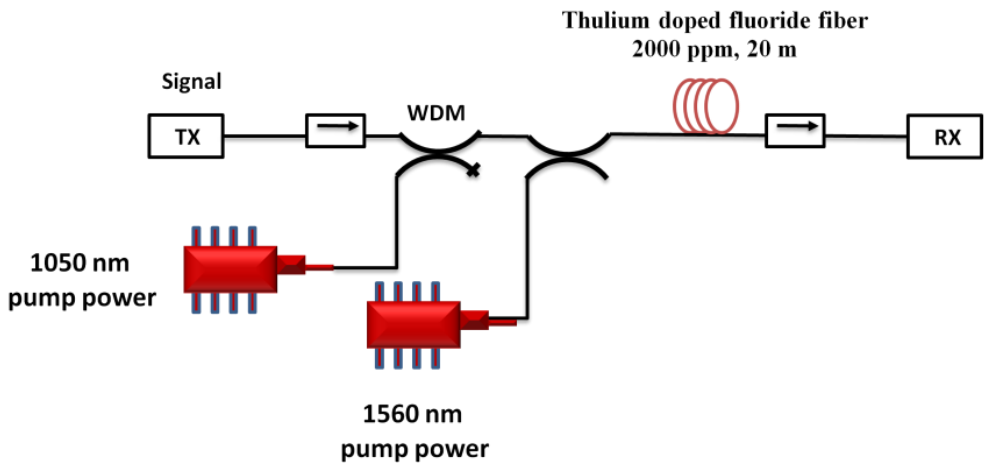


Figure 16. Configuration of the dual pumping TDFA.

While 1050 nm pump alone is possible to provide both ground state absorption and exited state absorption, using a secondary pump at 1550nm region can make the ground state absorption process more efficient due to low ground state absorption of 1050 nm pump. This can be seen through 1560 nm pumping which has strong ground state absorption that can help

in populating $^3F_4$ energylevel. The use of the 1050nm pump in conjunction with the 1560 nm pump can improve the performance of S-band TDFA by achieving higher gain, lower noise figure. 1560 nm pumping increases the population of the $^3H_4$ layer which in turn improves the gain and noise figure. Additionally, gain shifting can also be observed in S-band TDFAs if the 1050 nm pump transition from the $^3H_4$ to the $^3F_4$ energy levels is less active than ground state absorption.

Figure 17 shows the energy transitions in the TDFA with 1050- and 1560-nm pumps. Figs. 17 (a) and (b) show the absorption and emission transitions respectively. 1050nm pumping enables an up-conversion process, where ions at the $^3H_6$ energy level are excited to the $^3H_5$ energy level via ground state absorption, and then relax to the$^3F_4$ energylevel by non-radiative decay. The $^3F_4$ energy levelions are then re-excited to the $^3F_2$ energy level and experience non-radiative decay to the$^3H_4$ energylevel via excited state absorption. However, excited state absorption from the $^3H_4$ to $^1G_4$ energylevel reduces the population of the $^3H_4$ energy level. Therefore, an auxiliary pump source at 1560 nm is used to excite the $^3H_6$ energy level ions (lower layer) and increase the population of $^3F_4$ energy level [41].

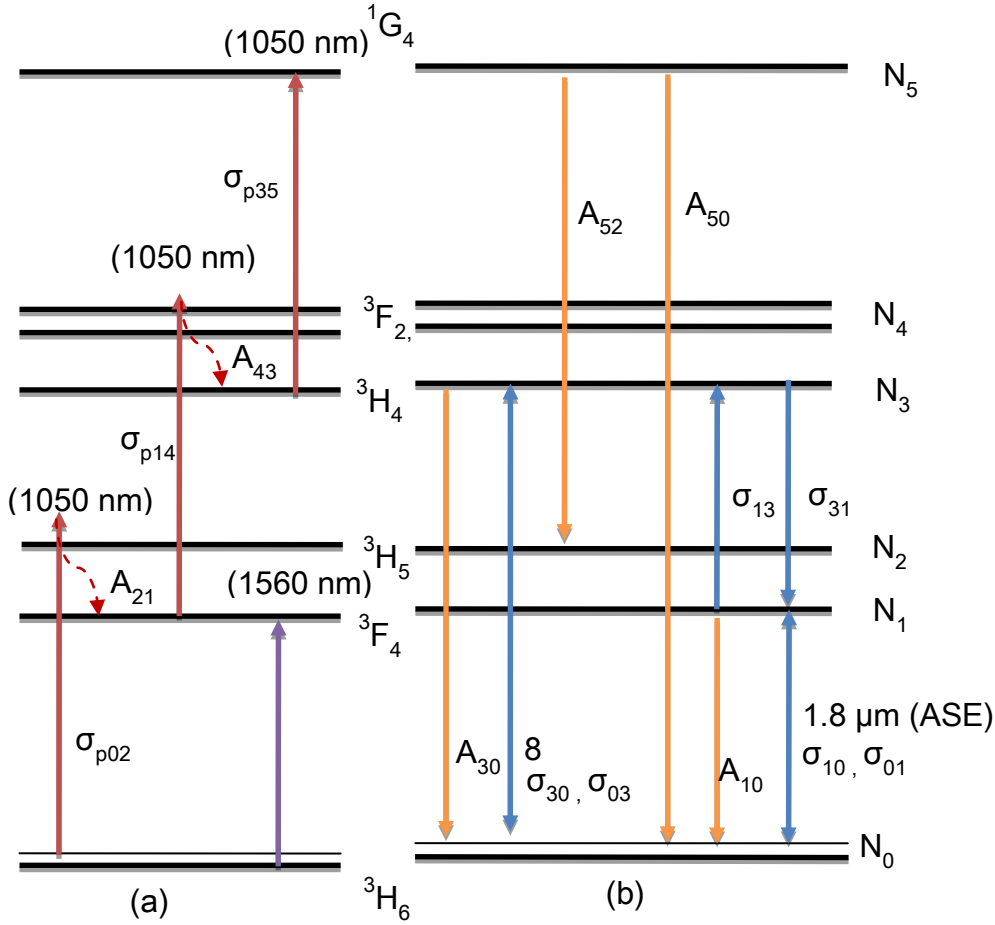


Figure 17. Pumping mechanism of a 1050 and 1560nm pumped TDFA (a) pump transitions (b) signal and ASE emission transitions.

## Gain Shifting Characteristic

Fractional inversion (typically 0.4) in the TDF is the main key to achieving gain shift in fiber amplifiers. Fractional inversion in TDF is defined as $\Delta N=N_3/ (N_1+N_3)$. The gain per unit length spectra as a function of different fractional inversion is shown in Figure 18. The equation of gain per unit length as a function of wavelength can be defined as GPL ($\lambda$) $=N_3\sigma_{se} - N_1\sigma_{sa}$, where $\sigma_{se}$ and $\sigma_{se}$ are the emission and absorption cross-sections between the $N_3$ and $N_1$ levels, respectively [41]. For achieving low fractional inversion two kinds of GS-TDFA have been developed so far . One of the efficient way is using a high Thulium concentration doped TDFA that proposed by [9]. Using dual pumping 050+1560 nm is also the other efficient method has been suggested. The 1560 nm secondary pumping efficiently increases the population at the lower level ($N_1$), and simultaneously reduces the fractional inversion. If the fractional inversion is lower than 0.4, the gain of TDFA will be shifted to a new peak at approximately 1490 nm [24].

By using high concentration thulium, cross relaxation occurs between the thulium ions. Energy of thulium ion which is excited at the $^3H_4$ level transfers to a neighboring thulium ion in the ground state level, and both ions enter the $^3F_4$ metastable state. Result of this level energy transfer cause that the amount of population ion at $N_1$ level becomes high, which means that the population inversion state between the $^3H_4$ and $^3F_4$ levels becomes lower than 40% [41].

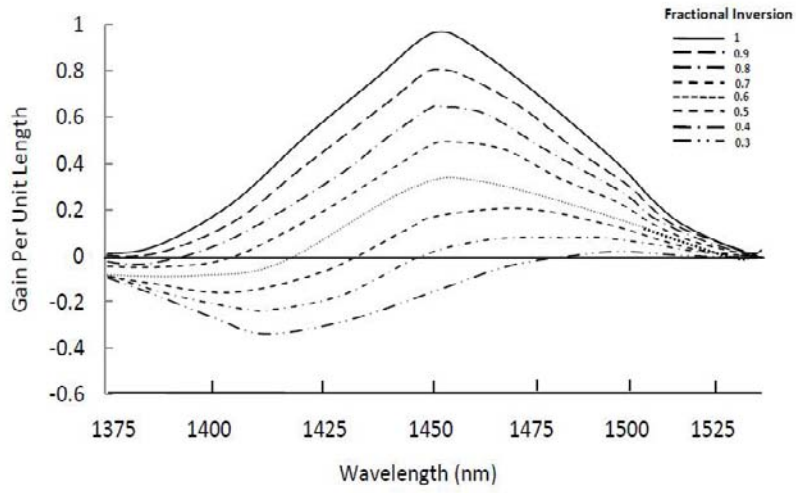


Figure18. Gain per unit length spectra.

Figure 19 shows the fractional inversion, which is calculated by $\Delta N=N3 /( N3+ N1)$ at different longitudinal positions of the fiber. As shown in the figure, thefractional inversion of 0.99 is maintained at all longitudinalpositions with only a 1050-nm pump power(200 mW) is injected into the 20-m TDF. However, thefractional inversion drops to 0.45 at a shorter longitudinalposition with the injection of a 1560-nm pumppower. The position depends on the amount of theinjected 1560-nm pump power, for which the higherpower reduces the fractional inversion at a shorter distanceand, therefore, increases the efficiency of theTDFA. The 1560-nm pumping will cause the ground stateabsorption to help in populating the $^3F_4$

energylevel, so that the 1050-nm light can excite the ion to thehigher $^3H_4$ layer efficiently. This increases the populationinversion between the $^3F_4$ and $^3H_4$ level, which, inturn, increase the stimulated emission in the S-bandregion. The reduction of the fractional inversion to alevel of less than 0.4 by the 1560-nm pumping will alsoshift the gain of the TDFA to a longer wavelength [41].

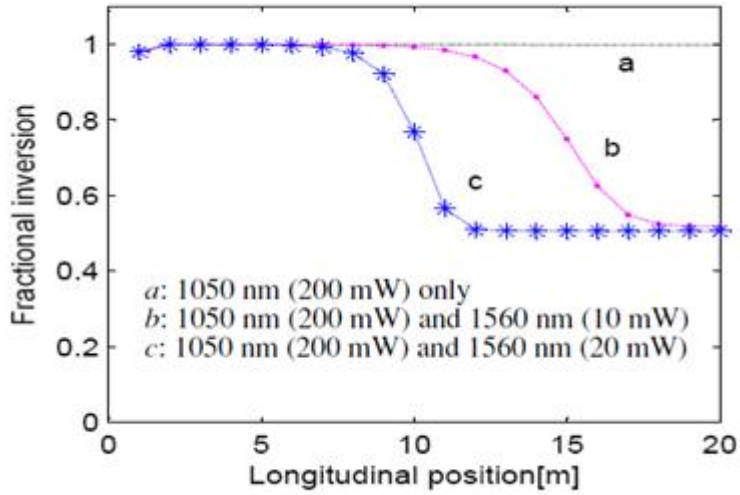


Figure 19. Fractional inversion as a function of TDF length for different pumping scheme (a) 1050nm (200 mW) pumping (b) 1050nm (200mW) and 1560 nm (10 mW) pumping and (c) 1050nm (200mW) and 1560 nm (20mW) pumping.

Figure 20 and 21 show gain and noise figure as function of TDF length. The input signal is fixed at 1460 nm and power is maintained at -30 dBm. In the analysis, the 1050 nm pump power is fixed at 100mW and 1560nm pump power is varied from 0mW to 20 mW. As the 1560 nm pump power increases, the gain along the length of TDF increases as shown in Figure 20. The noise figure also reduces as the 1560 nm pump power increases as shown in Figure 21 because the high gain contributes to a lower noise figure. The gain increases with the fiber length as clearly shown in the result until the length of 20 m. However, the gain starts to decrease for lengths above 20m since the pump powers are fully utilized. The extra length of TDF remains unpumped and this portion of TDF absorbs the signal through the up conversion process.

Figs. 22 and 23 show small signal gain and noise figure spectra with variations of 1560 nm pump power from 0 to 35 mW. The TDF length, the 1050-nm pump power, and the input signal power is fixed at 20 m, 100 mW, and –30 dBm, respectively. As is shown in the figures, the gain and noise figure at a signal wavelength of 1470 nm are obtained at approximately 15 and 5 dB, respectively, without the 1560-nm pump. However, the gain and noise figure are improved by increasing the 1560-nm pump power up to 17 mW due to the population inversion at a lower layer. At a 1560-nm pump power of 20 mW and above, the transition from the $^3H_4$ to $^3F_2$ energy levels due to the 1050-nm pumping is less active compared with the ground-state absorption due to the 1560-nm pumping. This causes the gain profile to flatten and the gain peak to shift to a longer wavelength.

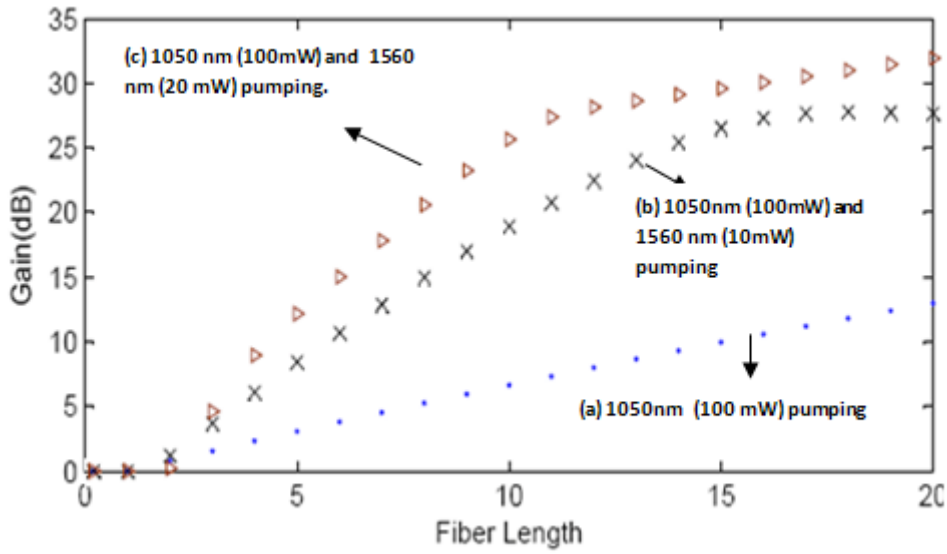


Figure 20.Gain in dB as a function of TDF length at different pumping scheme (a) 1050nm (100 mW) pumping (b) 1050nm (100mW) and 1560 nm (10mW) pumping and (c) 1050 nm (100mW) and 1560 nm (20 mW) pumping.

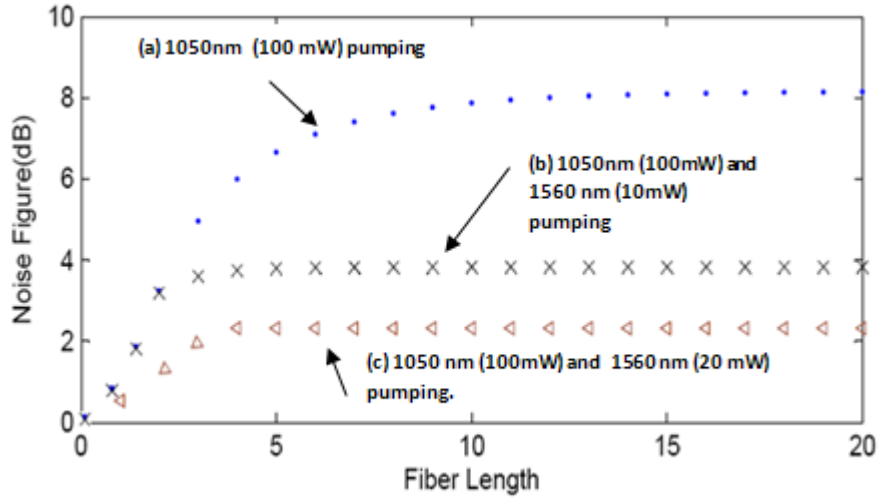


Figure 21. Gain in dB as a function of TDF length at different pumping scheme (a) 1050nm (100 mW) pumping (b) 1050nm (100mW) and 1560 nm (10mW) pumping and (c) 1050 nm (100mW) and 1560 nm (20 mW) pumping.

A maximum gain ofmore than 30 dB is observed at 1470 nm at 35 mW of a1560-nm pump power as shown in Figure 22. A gainimprovement of more than 10 dB is obtained at the 1470-nm region with the use of an auxiliary pump laser at 1560 nm of more than 20 mW as shown in the figure. This is attributed to the use of an auxiliary pump at 1560 nm, which is used for ground state absorption to control the population inversion factor between $^3F_2$ and $^3H_4$ level. The efficiency of the excited-state absorption, which is accomplished by the main

pump at 1050 nm increases with increasing the 1560-nm pump power. This is because of the increased population of the $^3F_4$, which, in turn, increases the gain of the TDFA.

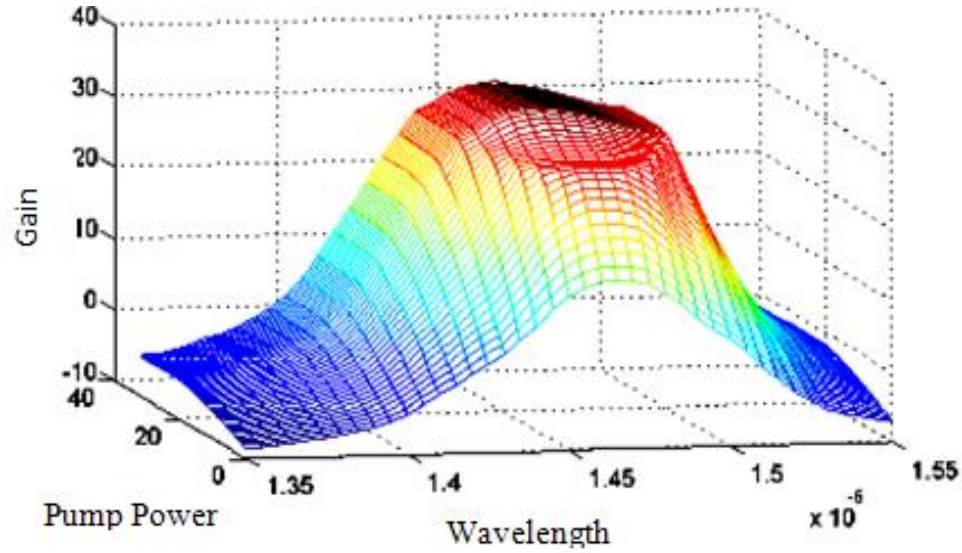


Fig 22. 3D gain characteristics for dual wavelengths 1050 nm and 1560 nm pumped TDFA with 20m TDF.

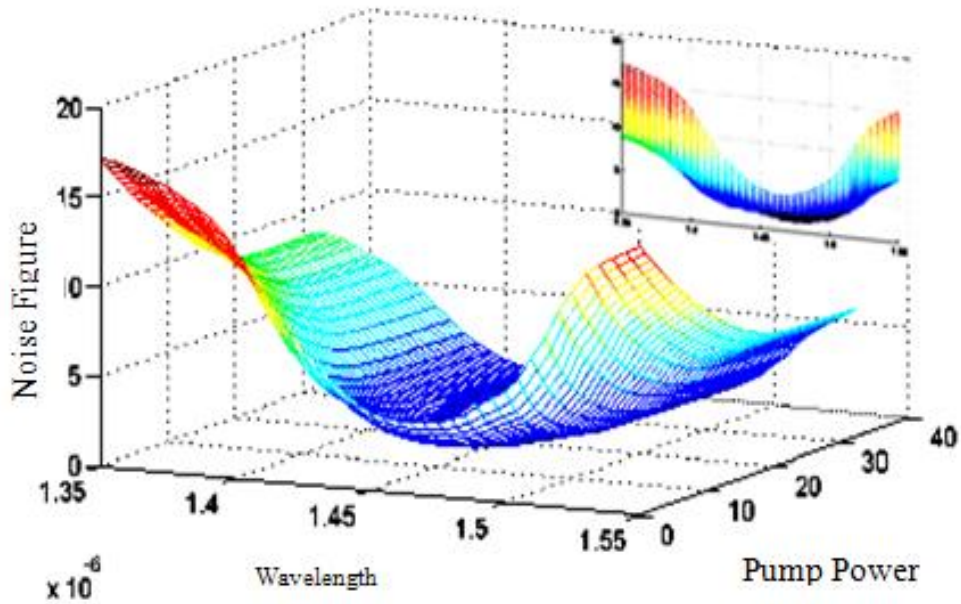


Figure 23. 3D noise figure characteristics for dual wavelengths 1050 nm and 1560 nm pumped TDFA with 20m fiber.

## 1420 NM SINGLE PUMPED TDFA ARCHITECTURE

Figure 24 shows the setup of the single pass TDFA, which consists of a fluoride-based TDF, one WDM pump laser and two isolators. The TDF used is 20 m long and has a Tm ion concentration of 2000 ppm. WDM couplers are used to combine the pump light with the input signal. The 1420nm laser diodes are used as the main pump power [42].

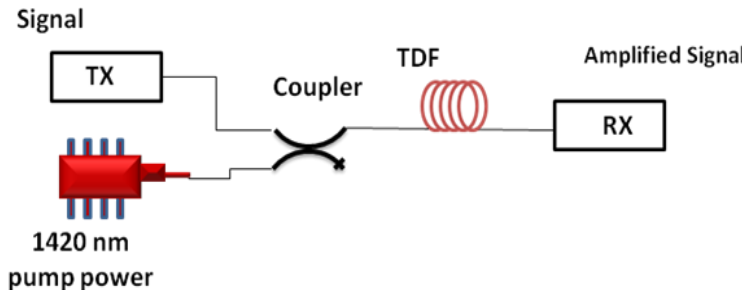


Figure 24. Configuration of the TDFA with 1420nm pumping scheme.

Figure 25 shows the energy level diagram of the TDFA with the up-conversion pumping scheme of 1420 nm. The variables $N_0$, $N_1$, $N_2$ and $N_3$ are used to represent population of ions in the $^3H_6$, $^3F_4$, $^3H_5$and $^3H_4$ energy levels respectively. The 1420 nm pump is used for ground state absorption (1st stage pumping from $^3H_6$ to $^3F_4$) and also excited state absorption (2nd stage pumping from $^3H_4$ to $^3F_4$). The 1420 nm pumped TDFA first excites the ground-state $^3H_6$ ions to above the lower level ($^3F_4$) and then excited state absorption (ESA) at the $^3F_4$ level excite electrons to the upper energy state ($^3F_4$) [42].

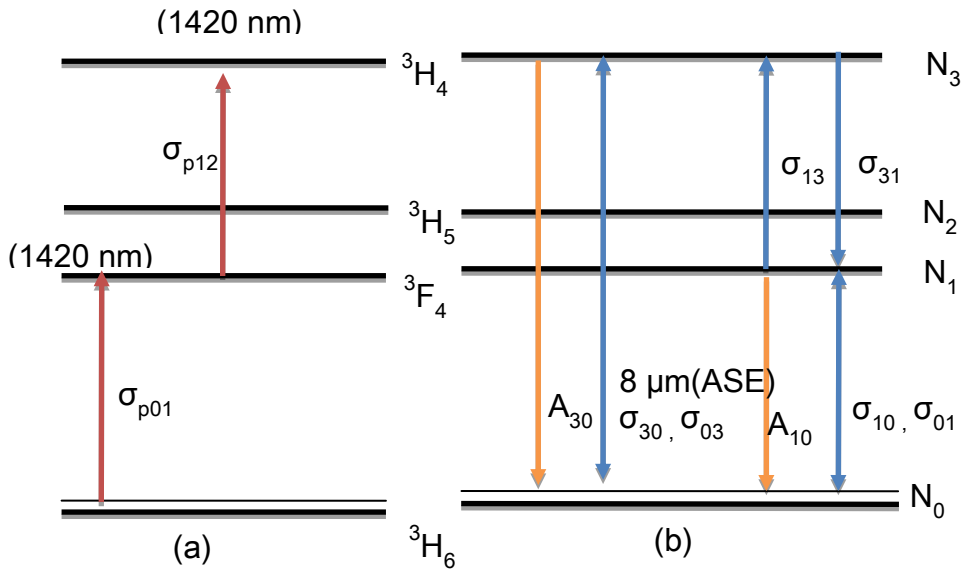


Figure 25. Pumping mechanism of a 1420nm pumped TDFA (a) absorption or pump transitions (b) signal and ASE emission transitions.

Figs. 26 and 27 show the gain and noise figure of 1420 nm pumped TDFA respectively with variations of 1420 nm pump power from 300 to 400 mW and variations of input signal power from -40 to 0 dBm. The TDF length and input signal wavelength are fixed at 20 m and 1470 nm, respectively. Pumping at 1420 nm takes advantage of the strong excited state absorption (ESA) rather than the ground state absorption, so 1420 nm is the primary source of excitation. Ground state absorption of 1420 nm and (or) WDM signals at the $^3H_6$ ground state must have enough ions in order to populate the $^3F_4$ level. Due to a high excited absorption (using this 1420 nm pumping), the increment of input WDM signals increases the population at the lower energy state ($^3H_4$), from which the excited ions are elevated to the upper energy state ($^3F_4$) due to excess pump power. Consequently, increase in signal input power increases the signal gain [43].

As shown in Figure 26, by varying the input signal from -40 dB to -10 dB, the gain gradually increases with the increment of input signal power. From -10dB to 0 dB input signal power pump is unable to replenish the inversion as fast as the input signal is depleting it, so gain gradually decreases with increasing of signal power. The gain also increases with pump power and finally saturates at a certain pump power. The maximum gain of 20 dB is obtained at an input signal power of -10 dBm with a pump power of 400mW. The noise figure can be reduced (improved) by either increasing the pump power or reducing the input signal power as shown in Figure 27.

Figs. 28 and 29 show the small signal gain and noise figure spectra with variations of 1420 nm pump power from 100 to 600 mW. The TDF length is fixed at 20 m. As shown in Figs. 28 and 29, gain and noise figure are obtained at 2 dB and 8.3 dB, respectively at 100 mw pump power. However, the gain and noise figure are improved up to 28 dB by increasing the pump power to 600 mW. The noise figure is calculated by the equation; $NF=1/G + P_{ASE}/(G\times h\times \nu\times \Delta\nu)$ where G and $P_{ASE}$ is gain and ASE power at the particular wavelength. This equation shows that the noise figure reduces as the gain increases which is in agreement with our results.

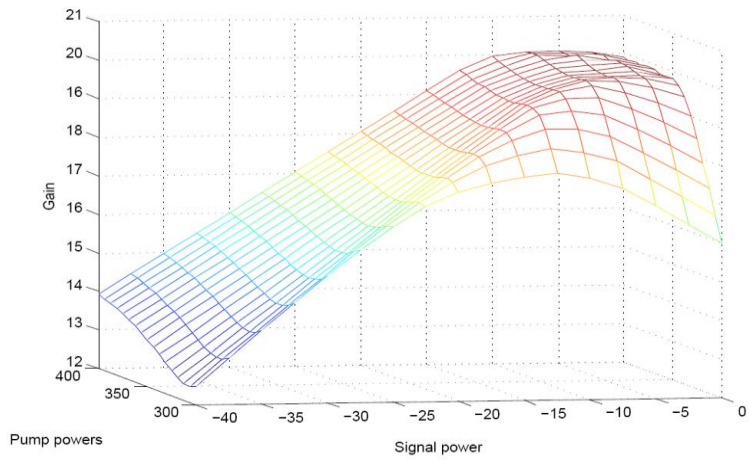


Figure 26. 3D gain characteristic as a function of pump power and signal power using a 20 m long TDF and a 1460 nm input signal wavelength.

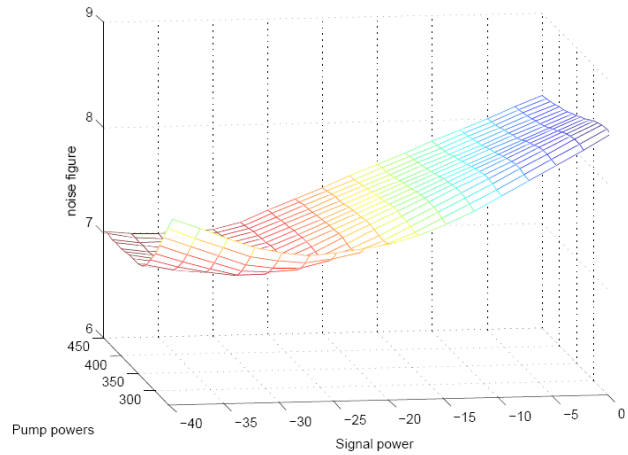


Figure 27. 3D noise figure characteristic as a function of pump power and signal power using a 20 m long TDF and a 1460 nm input signal wavelength.

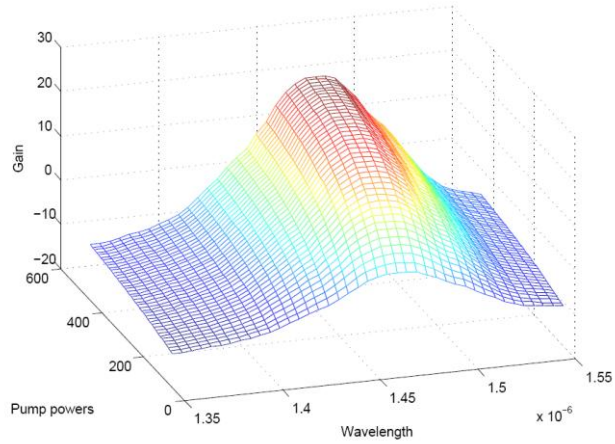


Figure 28. 3D gain characteristics for 1420 nm pumped TDFA with 20m TDF.

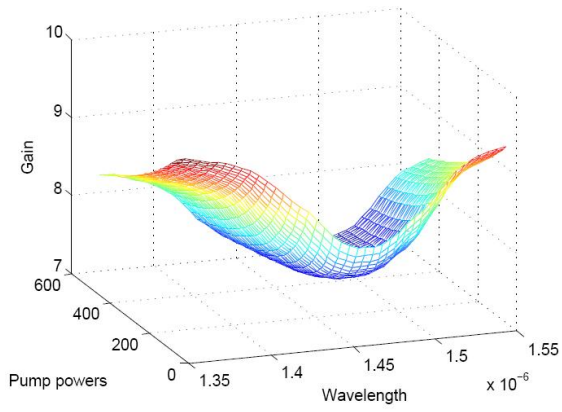


Figure 29. 3D noise figure characteristics for 1420 nm pumped TDFA with 20m TDF.

## Configuration of the Hybrid Amplifier

The configurations of the hybrid amplifier with single stage and double stage TDFA are shown in Figure 30 and Figure31 respectively, in which the TDFs and Raman amplifier are cascaded in series with same pump laser wavelength. 1420 nm pump lasers are used as the pump source for all amplifiers. For the first configuration the TDF used in this study is 20 m long with thulium ion concentration of 2000 ppm. A 10km long dispersion compensating fiber (DCF) is used as a Raman gain medium [44]. For the second configuration, another stage TDFA is added in the last configuration. 1420 nm pump powers are delivered into amplifiers as shown in the Figure 30. The low concentration TDF used in this study is 20 m long with thulium ion concentration of 2000 ppm and high concentration TDF used in this study is 4 m long with 4000 ppm concentration. A 10km long dispersion compensating fiber (DCF) is used as a Raman gain medium [42].

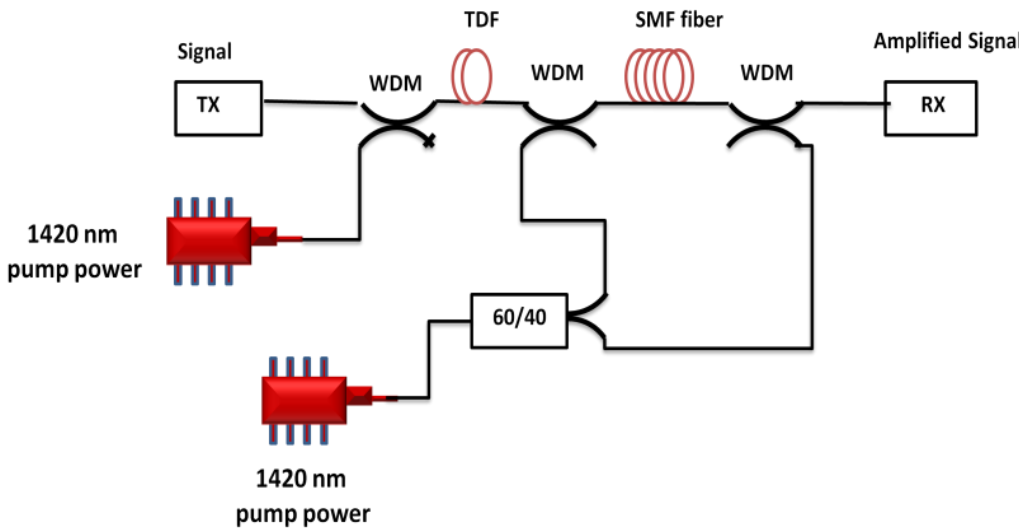


Figure 30. Basic configurations of the hybrid TDFA/FRA.

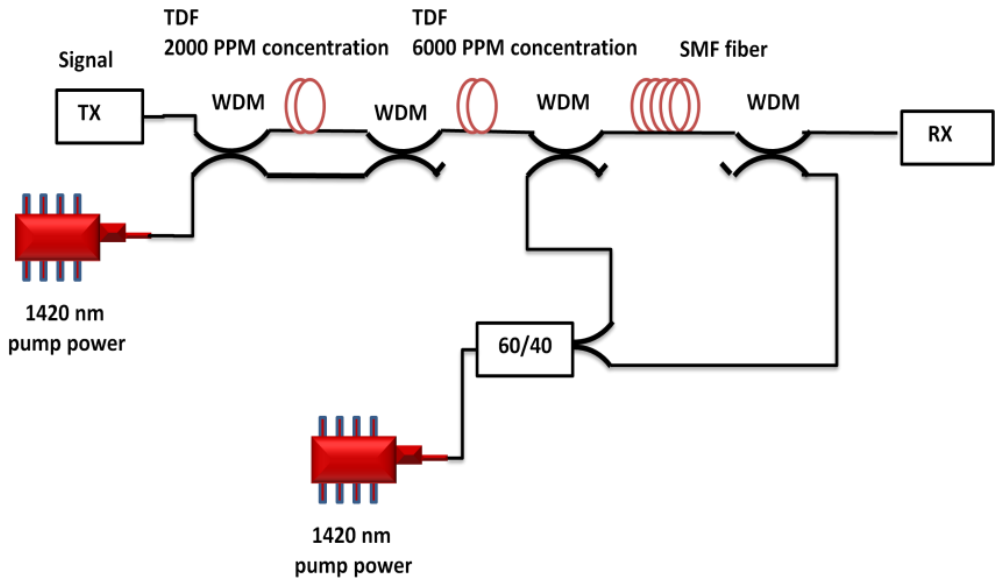


Figure 31. Improved configurations of the hybrid TDFA/FRA.

## MATHEMATICAL MODEL FOR FIBER RAMAN AMPLIFIER (FRA)

In order to obtain Raman amplification, a large pump wave power must be launched into the gain medium at a lower frequency to generate a stimulated Raman scattering (SRS) at a longer wavelength region. Raman gain depends on the amount of pump power and the frequency offset between pump source and signal. Amplification occurs when the lower frequency pumping photons transfers their energy to new high frequency photons at the signal wavelength. For a single signal, the pump power threshold that is required to achieve the SRS is given by:

$$P_{th} = \frac{16\, A_{eff}}{K_p L_{eff} g_r} \tag{32}$$

where $K_p$ is the polarization constant which is around 2. $A_{eff}$ and $L_{eff}$ are the effective area and length of SMF fiber respectively. The overall Raman gain can be expressed in terms of the pump power and pump intensity as

$$g(v) = g_r(v) I_p = g_r(v) \frac{P_p}{A_{eff}} \tag{33}$$

The above equation shows that gain is depending on the pump wavelength and pump power.

The interaction between the forward pump and signal pump as well as a backward pump power and signal power during the SRS process are governed by the following three coupled

equations. These equations describe the pump and signal power transfer along a length of fiber and are derived from the Maxwell's equations.

$$\frac{dP_s}{dz} = \frac{g_r}{A_{eff}} P_p^{\pm} P_s - \alpha_s P_s \tag{34}$$

$$\frac{dP_p^+}{dz} = -\frac{\omega_p}{\omega_s} P_p^+ P_s - \alpha_p P_p^+ \tag{35}$$

$$\frac{dP_p^-}{dz} = \frac{\omega_p}{\omega_s} P_p^- P_s + \alpha_p P_p^- \tag{36}$$

where z is signal propagation direction, $A_{eff}$ is effective area of the Raman fiber as well as $\alpha_s$ and $\alpha_p$ account for fiber losses at signal frequency and pump frequency respectively. One of the critical design issues is the Raman gain efficiency which is defined as $g_{R\_eff} = g_R / A_{eff.}$ The efficiency is depended on the effective areas, material and structure of the gain medium and therefore different fibers will have different gain efficiency. In SRS process, the pump power provides the energy for amplification and depletes as the pump signal propagates along the fiber. Therefore, the gain reduces as the pump signal transfer all of its energy to input signal power, which resulted in gain saturation. The power along the length of the fiber is also reduced by the fiber losses, which occur in the medium due to its intrinsic properties. The pump depletion must be included for complete description of SRS but it is neglected for purpose of estimating the Raman threshold pump power. If the first term on the right hand side of equations (35) and (36) ignores the pump depletion, then these equations can be summarized as[42]:

$$P_p^+(z) = P_{P\_in}^+ e^{-\alpha_p L(z)} \tag{37}$$

$$P_p^-(z) = P_{P\_in}^- e^{+\alpha_p L(z)} \tag{38}$$

Here, $P_{P\_in}^+$ and $P_{P\_in}^-$ is the forward and backward Raman pump powers at the beginning of the transmission fiber respectively. However, in case of bidirectional pumping, the coupled equation can be slightly more complicated because two pump lasers, which are located at both fiber ends, are used. The pump power evolution in the fiber for the bidirectional FRA is described by [42]:

$$P_p\ (z) = P_{P\_in}\{r_f e^{-\alpha_p L(z)} + (1 + r_f\ ) e^{-\alpha_p (L - L(z))} \tag{39}$$

where $r_f$ is the ratio of the amount pump power launched in forward direction compared to the total pump power and it varies from 0 to 1. Using this equation, the signal intensity evolution in the fiber can also be described as:

$$\frac{dP_s}{dz} = \frac{g_r}{A_{eff}} P_{P\_in}^{\pm} e^{-\alpha_{pz}} P_s - \alpha_s P_s \tag{40}$$

By solving this equation, we obtain

$$P_{s(z)} = P_{s\_in(z)} e^{\frac{g_R P_{in}^{\pm}}{A_{eff}(-\alpha_p)}(e^{-\alpha_p z-1})-\alpha_s z} \quad (41)$$

Hence, the signal intensity at fiber output of length L can be determined as:

$$P_{s(l)} = P_{s\_in(0)} e^{(\frac{g_R P_0^{\pm} L_{eff}}{A_{eff}}-\alpha_s z)} \quad (42)$$

where $L_{eff}$ is the effective length, which is defined as

$$L_{eff} = \frac{1-e^{-\alpha_p L}}{\alpha_P} \quad (43)$$

Thus, the net Raman gain is calculated as:

$$G(z) = \frac{P_s(z)}{P_s(0)} = \exp(\, g_R \int_0^z P_p(z)\, dz - \alpha_s z) \quad (44)$$

Raman gain is defined as the ratio of the power of the signal with and without Raman amplification and it is given by:

$$G_A = e^{Lg_0} \quad (45)$$

where $g_0$ is small signal gain and is defined as

$$g_0 = \frac{g_R P_0}{A_{eff}\alpha_p L} \quad (46)$$

Rayleigh scattering is one of the most important phenomena that limit the performance of Raman amplifier. Rayleigh scattering cause small parts of light back scattered. Normally, this Rayleigh back scattering is negligible. However in FRA this scattering may be amplified over a long length of transmission fiber by the Raman pump and affects the amplification performance in two ways. Firstly, double Rayleigh scattering of the signal in optical fiber creates a crosstalk component in the forward direction and secondly, backward propagating noise part appears in the forward direction and enhancing the noise figure. The noise figure is strongly dependent on the ASE power [42]. The ASE power in the transmission fiber is given by:

$$P_{ASE} = \eta_{sp}(G_r - 1)hV_s B_0 \quad (47)$$

where, h is Planks constant, $V_s$ is signal frequency, $B_0$ is the electrical bandwidth and $\eta_{sp}$ is the spontaneous emission and calculated as:

$$\eta_{sp} = \frac{\eta N_2}{\eta N_2 - N_1} \quad (48)$$

where $\eta = \frac{\sigma_{SE}}{\sigma_{SA}}$ (49)

## Numerical Simulation

The theoretical results of TDFA are obtained by solving the rate equations of the pump, signal power and ASE using a numerical method. *ode45* built in Matlab function was used to solve the numerical equations. The variable used in the numerical calculation and their corresponding values are shown in Table 2.

**Table 1. Numerical parameter used in the TDFA's simulation**

| Parameter | Unit | Symbol | Value |
|---|---|---|---|
| Thulium concentration | $1/m^3$ | $\rho$ | $1.68\times10^{25}$ |
| Numerical aperture | | NA | 0.3 |
| Fiber Length | m | L | 20 |
| Background lost | dB/m | $\alpha$ | $1.68\times10^{25}$ |
| Effective area | $m^2$ | $A_{eff}$ | $2.096\times10^{-12}$ |
| Division along fiber | | | 12 |
| 800nm ASE bandwidth | nm | $\Delta\nu_8$ | 10 |
| 1800nm ASE bandwidth | nm | $\Delta\nu_{18}$ | 100 |
| ASE bandwidth | nm | $\Delta\nu$ | 2 |
| Signal absorption cross section | $m^2$ | $\sigma_{sa}$ | Figure 9 |
| Signal stimulated emission cross section | $m^2$ | $\sigma_{se}$ | Figure 9 |
| 800nm transition cross section | $m^2$ | $\sigma_{03}, \sigma_{30}$ | $6.2\times10^{-25}$ |
| 1800nm transition cross section | $m^2$ | $\sigma_{01}, \sigma_{10}$ | $5.2\times10^{-25}$ |
| Radiative decay rate | 1/s | $A_{10}$ | 172.4 |
| Radiative decay rate | 1/s | $A_{30}$ | 702.8 |
| Radiative decay rate | 1/s | $A_{50}$ | 676.3 |
| Radiative decay rate | 1/s | $A_{52}$ | 492.9 |
| Nonadiative decay rate | 1/s | $A_{43}^{nr}$ | 52976 |
| Nonadiative decay rate | 1/s | $A_{21}^{nr}$ | 165626 |

**Table 2. Numerical parameter used in the FRA's simulation**

| Parameter | Unit | Symbol | Value |
|---|---|---|---|
| Numerical aperture | | NA | 0.3 |
| Fiber Length | Km | L | 12 |
| Background lost | dB/m | $\alpha$ | $1.68\times10^{25}$ |
| Effective area | $m^2$ | Aeff | 70e-12 |
| Signal wavelength | nm | $\lambda s$ | 1550 |
| Pump wavelength | nm | $\lambda p$ | 1420 |
| Input signal Power | nm | $P_{s\_in}$ | 0.1 |
| Raman Gain coefficient | m/W | $g_R$ | 1.0324886e-03 |

## PERFORMANCE OF A HYBRID TDFA AND FRA

Figure32 shows the calculated fractional inversion as a function of longitudinal position along the fiber. Curve (a) shows the result corresponds to a1420 nm pumped with 6000 ppm concentration. Fractional inversion is nearly unity (0.6) at the first miter of fiber and then decrease to 0.3 at 4 miter long fiber. Note that the 1420 nm-pumped TDFA with low concentration 2000 ppm has a very high fractional inversion of nearly unity (0.95) in the whole position as shown in curve b.

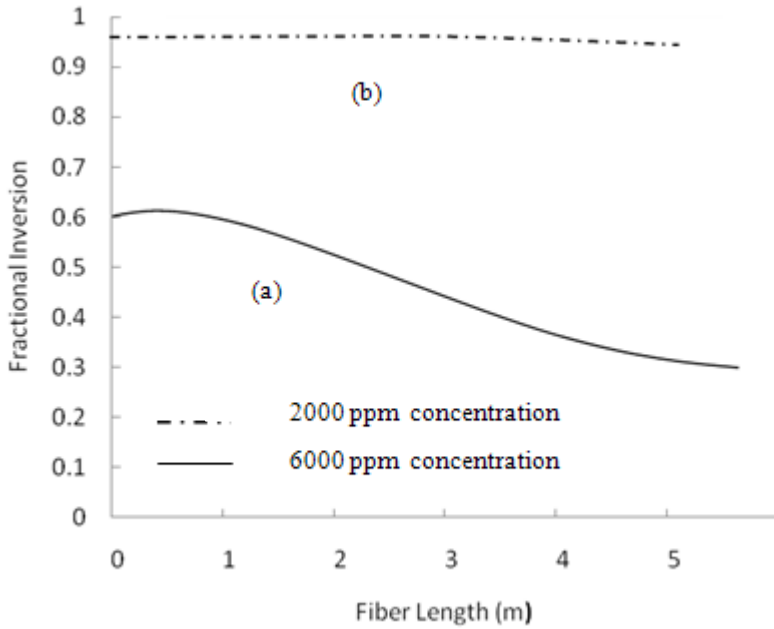


Figure 32. Fractional inversion as a function of length.

Figure 33 shows the gain spectra of a wideband hybrid low concentration TDFA and Raman amplifier and the individual TDFA and FRA. In this experiment 250 mW pump power for TDF, and 550 mW pump power for Raman fiber amplifier e at 1420nm was fixed. The TDFA and FRA gain peaks obtained at around 24dB as shown in the Figure 33. For achieving the gain flattened hybrid amplifier the second TDFA gain compensate the gap as shown in figure. The high concentration TDFA has peak at 1495 nm by using 190 mW pump power. In figs. 33 and 34 the experimental work which is done by S. R. Lüthi [45] also presented. The superposition of these gain spectra by the hybrid amplifier has significantly wider the gain bandwidth. As shown in Figure 34 a relatively flat gain spectrum is obtained without any gain equalizer by the single-wavelength pumping approach. .

The gain variation to gain ratio ΔG/G is generally used to characterize the gain variation, where ΔG and G are the gain excursion and the average gain value, respectively [46]. In order to define the gain flatness of amplifier, the ΔG/G for the TDFA and Raman fiber hybrid amplifier with and without high concentration is compared between 1460 and 1535 nm under the same condition. The gain variation ΔG/G for TDFA and Raman fiber hybrid amplifier with high concentration TDFAwas 0.05 (1.3 dB / 24.14 dB), which is a improvement 70 %

compared to TDFA and Raman fiber hybrid amplifier without high concentration TDFA which is 0173 (4.2 dB / 24.14 dB [46].

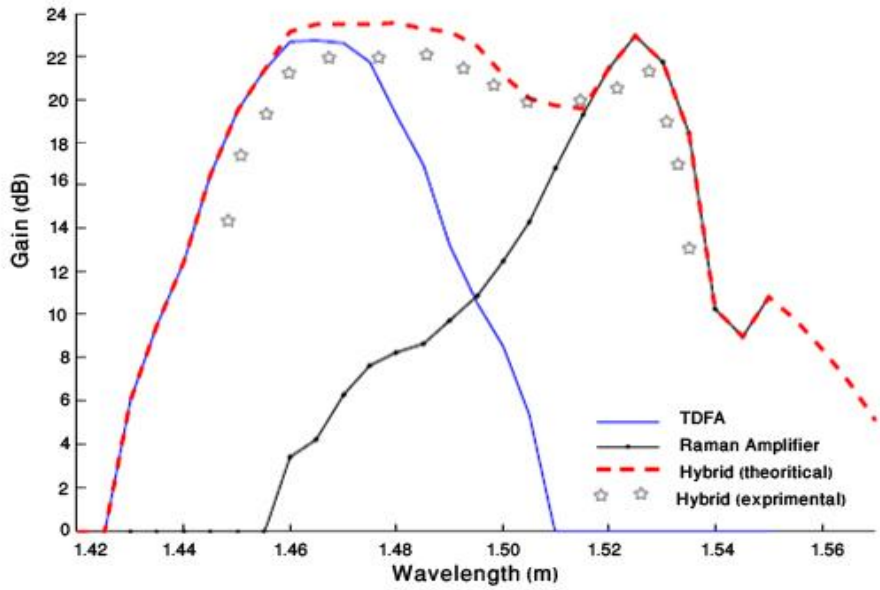


Figure 33. Gain spectra of a wideband hybrid TDFA and Raman amplifier.

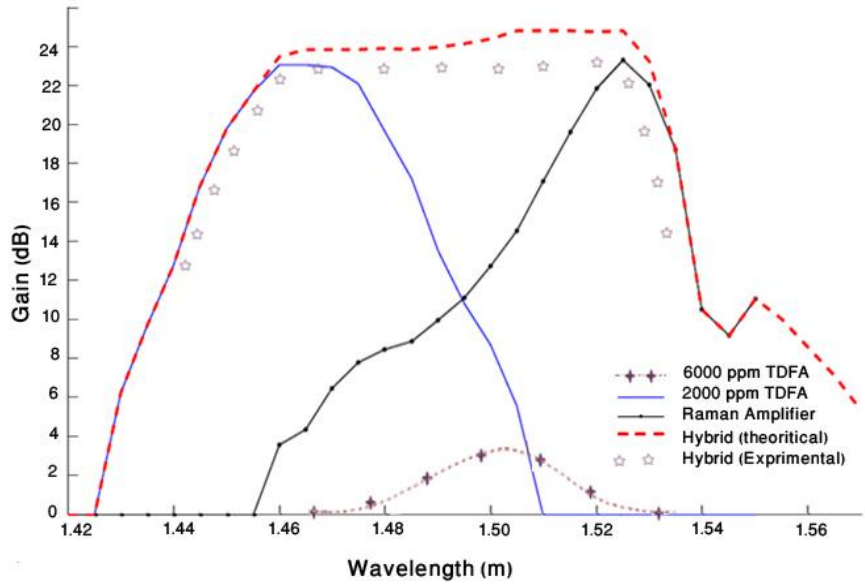


Figure 34. Gain spectra of a wideband hybrid TDFA and Raman amplifier with second stage TDFA.

Figure 35 shows the gain spectra obtained in the hybrid amplifier without second TDFA at different pump powers of 700, 750 and 800 mW. As expected, the gains of the hybrid amplifier increase with input pump power. The gain of the hybrid amplifier peaks at around

24, 25.5 and 27 dB with 700, 750 and 800 mW of pump power, respectively. As seen in the Figure 35, the effect of pump power on TDFA is higher than Raman amplifier and therefore the gain is flattening as the pump power increases. Figure 36 shows the gain spectra obtained in the hybrid amplifier with second TDFA. The second TDFA was pumped 190, 200, 210 mW respectively. By the help of this high concentration TDFA we reach to gain flattened TDFA at all pump power configurations.

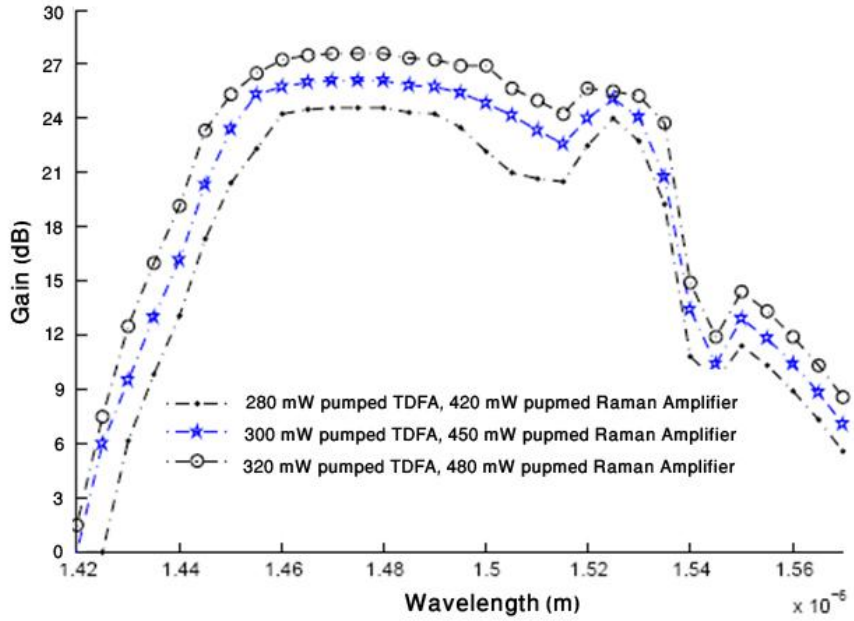


Figure 35. Gain spectra of the hybrid TDFA and Raman amplifier without secound stage TDFA at various pumping power.

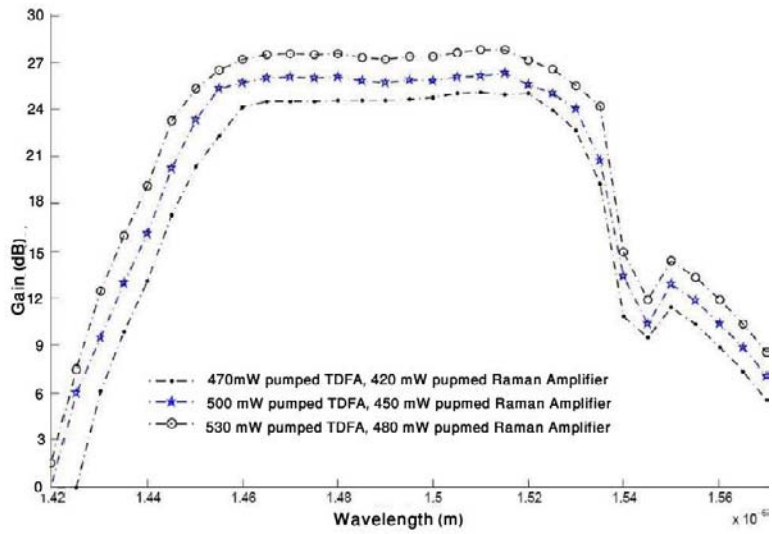


Figure 36. Gain spectra of the hybrid TDFA and Raman amplifier with secound stage TDFA at various pumping power.

## SUMMARY

Over the duration of this chapter, a systematic approach towards attaining a mathematical model of single pass and double pass Thulium-doped fiber amplifiers (TDFAs), fiber Raman amplifier (FRA) and a hybrid amplifier using the TDFA and FRA was conducted. The effects of design parameters on TDFA and Raman amplifier were shown and described. An efficient design procedure was introduced to optimize the single-pass and double-pass TDFAs. The performance parameters of these amplifiers were characterized and presented in this chapter. Signal propagation characteristics in the TDFA were illustrated using various pump configurations for fiber optic communication system. Robustness of the developed mathematical model was also discussed. Numerical results were used to describe the design procedure of an optimized single pass and double pass TDFA using 1050 nm pump power and 1050–1550 nm dual pumping. Efficiency of optimized and non-optimized single pass and double pass TDFA using 1050 nm pump power were compared. Gain as a function of signal wavelength by various pump powerswascalculated. The effect of 1550 nm pump power on performance of 1050 nm pump power was described. At the next step the mathematical model of 1420 nm pumped TDFA developed based on the design parameters and intrinsic fiber parameters. The models were able to measure any changes in the system performance with respect to the change in the design parameters and intrinsic fiber parameters. At the end TDFA and Raman amplifier hybrid was presented. The configuration with a forward pumped TDFA followed by bidirectional Raman amplifier gave the best optical performance development of reliable high-power diode lasers in the 1420 nm wavelength range and will make this type of wide-band hybrid amplifier an interesting candidate for S-band optical telecommunication systems.

## REFERENCES

[1] G.P. Agrawal, *Fiber-Optic Communication Systems*, 2nd ed. Wiley, New York, NY, 1997.

[2] T. Sakamoto, “S-band fiber optic amplifiers”, *Optical Fiber Communication Conference and Exhibit*, 2001.vol. 2, pp:TuQ1-1 - TuQ1-4, 2001

[3] Y. Miyamoto, H. Masuda, A. Hirano, S. Kuwahara, Y. Kisaka, H. Kawakami, M. Tomizawa, Y. Tada, S. Aozasa “S-band WDM coherent transmission of 40×43-Gbit/s CS-RZ DPSK signals over 400 km DSF using hybrid GS-TDFAs/Raman amplifiers.” *Electronics Letters*, vol. 38, no. 24, pp:1569 – 1570, 2002.

[4] Gred, Keiser.*Optical Fiber Communications*. Singapore: McGraw-Hill, 2000.

[5] T. Kasamatsu, Y. Yano, T. Ono” Laser-diode-pumped highly efficient gain-shifted thulium-doped fiber amplifier operating in the 1480-1510-nm band.” *IEEE Photonics Technology Letters*, vol. 13, no. 5, pp: 433 – 435, 2001.

[6] B. Cole, M. L. Dennis” S-band amplification in a thulium doped silicate fiber.” *Optical Fiber Communication Conference and Exhibit*, vol. 2, pp: TuQ3-1 - TuQ3-3, 2001.

[7] J. Michael, F. Digonnet, *Rare-earth-doped Fiber Lasers and Amplifiers*CRC Press, 2001

[8] S. S. H.Yam, Y. Akasaka, Y. Kubota, H. Inoue, K. Parameswaran ”Novel pumping schemes for fluoride-based thulium-doped fiber amplifier at 690 and 1050 nm (or 1400 nm).” *IEEE Photonics Technology Letters*, vol.17, no.5, pp.1001 – 1003, 2005.

[9] M. H. Aly, M. Nasr, H. E. Seleem.“Thulium doped fiber amplifier in the S/S+ band employing different concentration profiles” The Fifth Workshop on Photonics and Its Application, pp. 39 – 49, 2005.

[10] R. Caspary, M. M. Kozak, W. Kowalsky.“Avalanche Pumping of Thulium Doped S-Band Fiber Amplifiers”.*Transparent International Conference on Optical Networks*, vol. 1, pp. 166 - 169, 2006.

[11] S. Aozasa, H. Masuda, M. Shimizu, M. Yamada “Highly Efficient S-Band Thulium-Doped Fiber Amplifier Employing High-Thulium-Concentration Doping Technique.” *IEEE Journal of Lightwave Technology*, Vol. 25, no. 8, pp. 2108 – 2114, 2007.

[12] S. Aozasa, H. Masuda, M. Shimizu.“S-band thulium-doped fiber amplifier employing high thulium concentration doping technique” *IEEE Journal of Lightwave Technology*, vol. 24, no. 10, pp. 3842 – 3848 , 2006.

[13] M. M. Kozak, R. Caspary, W. Kowalsky” Thulium-doped fiber amplifier for the S-band” *Proceedings of 2004 6th International Conference on Transparent Optical Networks*, vol. 2, pp:51 –54 ,2004.

[14] T. Sakamot, S. Aozasa , M. Yamada, M. Shimizu. “Hybrid fiber amplifiers consisting of cascaded TDFA and EDFA for WDM signals” *IEEE Journal of Lightwave Technology*, vol. 24, no. 6, pp.2287 – 2295, June 2006.

[15] M. Nix, S. S. H. Yam “Highly Efficient Dual Wavelength Pumping Scheme for Thulium-Doped Fiber Amplifier” *IEEE Lasers & Electro-Optics Society*, pp. 390 – 391, 2006.

[16] C. Floridia, M.T. Carvalho , M. L. Sundheimer , A. S. L. Gomes “Modeling the distributed gain of single (1050 nm or 1400 nm) and dual-wavelength (800 nm + 1050 nm or 800 nm + 1410 nm) pumped TDFAs” *Optical Fiber Communication Conference*, vol. 1, pp.23-27, 2004.

[17] S.S.H.Yam, Y.Akasaka, Y.Kubota, H. Inoue, K. Parameswaran “Novel pumping scheme study for fluoride-based thulium-doped fiber amplifier at 690 nm” *Optical Fiber Communication Conference*, vol. 3, pp.3, 2005.

[18] T. Segi, T. Aizawa, T. Sakai, A. Wada “Silica-based composite fiber amplifier with 1480-1560 nm seamless gain-band” *European Conference on Optical Communication*, vol. 2, pp.228 – 229, 2001.

[19] J. Michael, F. Digonnet *Rare-earth-doped Fiber Lasers and Amplifiers*CRC Press, 2001.

[20] S. S. H. Yam, J. Kim, “Ground state absorption in thulium-doped fiber amplifier: experiment and modeling” *IEEE Journal of Quantum Electronics*, vol. 12, No. 4, pp. 797 – 803, 2006.

[21] T. Tamaoka, S. Tanabe “Comparison of gain characteristics of Tm-doped fiber amplifier by different pumping schemes.”*Optical Fiber Communications Conference*, pp.630 - 631 vol.2, 2003

[22] T. Kasamatsu, Y. Yano, T. Ono “Gain-shifted dual-wavelength-pumped thulium-doped fiber amplifier for WDM signals in the 1.48-1.51-μm wavelength region” *IEEE Photonics Technology Letters*, vol. 13, no. 1, pp: 31 – 33 ,2001.

[23] S. Aozasa, H. Masuda, H. Ono, T. Sakamoto, T. Kanamori, Y. Ohishi, M. Shimizu, "1480-1510 nm-band Tm doped fiber amplifier (TDFA) with a high power conversion efficiency of 42 %" *Optical Fiber Communication Conference and Exhibit*, vol. 4, pp. PD1-1 - PD1-3, 2001.

[24] F. Roy , F. Leplingard, L. Lorcy, A. Sauze, P. Baniel, D. Bayart "48 % power conversion efficiency in a single-pump gain-shifted thulium-doped fiber amplifier" *Optical Fiber Communication Conference and Exhibit*, vol. 4, pp. PD2-1 - PD2-3, 2001.

[25] H. Shalibeik,; A. Behrends, M. Kozak , W. Kowalsky, R. Caspary, "Characterization of 1050-nm Pumped S-Band TDFA With Different Dopant Concentrations by Coherent Optical Frequency-Domain Reflectometry", *IEEE Photonics Technology Letters*, vol. 19, no. 4, pp.188 – 190, 2007.

[26] T. Kasamatsu, Y. Yano, T. Ono "1.49-μm-band gain-shifted thulium-doped fiber amplifier for WDM transmission systems" *Journal of Lightwave Technology*, vol. 20, no. 10, pp.1826 – 1838, 2002.

[27] F. Roy, F. Leplingard, L. Lorcy, A. Le Sauze, P. Baniel, D. Bayart," 48% power conversion efficiency in single pump gain-shifted thulium-doped fibre amplifier, *Electronics Letters*, vol. 37, no. 15, pp.943 – 945, 2001.

[28] T. Komukai et al., "Upconversion pumped thulium-doped fluoride fiber amplifier and laser operating at 1.47 um", *IEEE Quantum Electronic*, vol. 3 no.11 pp.1880-1888, 1995

[29] S. Aozasa, T. Sakamoto, T. Kanamori, K. Hoshino, K. Kobayashi, M. Shimizu, "Tm-doped fiber amplifiers for 1470-nm-band WDM signals" *IEEE Photonics Technology Letters*, vol. 12, no. 10, pp.1331 – 1333, 2000.

[30] S. Aozasa, H. Masuda, H. Ono, T. Sakamoto, T. Kanamori, Y. Ohishi, M. Shimizu "1480-1510 nm band Tm-doped fibre amplifier with high power conversion efficiency of 42%" *IEEE Electronics Letters*, vol. 37, no. 19, pp. 1157 – 1158, 2001

[31] Gomes, M. Carvalho, M. Sundheimer, C. Bastos-Filho, J. Martins-Filho, J. Weid, R. Janeiro, W. Margulis "Low pump power, short-fiber dual-pumped (800 nm+1050 nm) TDFA" *Optical Fiber Communications Conference*, pp.632, 2003.

[32] P. R. Watekar, S. Ju, W. T. Han "A Small-Signal Power Model for Tm-Doped Silica-Glass Optical Fiber Amplifier" *IEEE Photonics Technology Letters*, vol. 18, no. 19, pp. 2035 – 2037, 2006.

[33] S. S. H. Yam, J. D. Kim, M. E. Marhic, Y. Akasaka, L. G. Kazovsky "14xx nm pumped thulium-doped fiber amplifier bursty traffic applications" *Optical Fiber Communication Conference*, vol. 2, pp.3, 2004

[34] S.D. Emami , S.W. Harun , F. Abd-Rahman , H.A. Abdul-Rashid , S.A. Daud , Z.A. Ghanic, H. Ahmad "A theoretical study of double-pass thulium-doped fiber amplifiers" *International Journal for Light an Electron Optics*, in press, 2009.

[35] S. D. Emami, S. W. Harun, F. Abd-Rahman, H. A. Abdul-Rashid, S. A. Daud, and H. Ahmad "Optimization of the 1050nm Pump Power and Fiber Length in Single-pass and Double-pass Thulium Doped Fiber Amplifier" *PIERB* 14 , pp. 431-448, 2009.

[36] E. Desurvire, "Erbium-doped fiber amplifiers: principles and applications", John Wiley & Sons, New York, 1994.T Press,*PIERB*14, pp. 431-448,2009.

[37] C.E. Chan, S.D. Emami, P. Hajireza, H.Y. Beh, S.A. Daud, S.S. Pathmanathan, S.W. Harun, H. Ahmad and H.A. Abdul Rashid 'Optimization of Fiber Length and Bending

Diameter in Depressed Cladding Erbium-doped Fiber Amplifier' Ninth IEEE Malaysia International Conference on Communications (MICC), 2009.

[38] P. Hajireza , S. D. Emami, S. Abbasizargaleh, S. W. Harun and H. A. Abdul-Rashid 'Optimization of Gain flattened C-band EDFA using macro-bending',2010, Vol. 20, No. 6, pp. 1–5.

[39] C. J. A. Bastos-Filho, J. F. Martins-Filho , A. S. L Gomes" 38dB gain from a double-pass single-pump thulium doped fiber amplifier" *Proceedings of the Microwave and Optoelectronics Conference*, vol. 1, 20-23 pp.125 - 128 vol.1, 2003.

[40] S. D. Emami, S. A. Daud ,F. A. Rahman , H. A. Abdul-Rashid, S. W. Harun "Modeling Dual-Wavelength (1050+1560) pumped Thulium Doped Fiber Amplifier" m2usic conference, Multimedia University,2007

[41] S. D. Emami, S.W.Harun, F.Abd-rahman and H.Ahmad "Effect of an auxiliary pump on performance of TDFA" *Laser Physics Journal*, PP. 977, 2008

[42] S. D. Emami, P. Hajireza, F. Abd-RahmanF. Abd-Rahman, H. Ahmad, "wide-band hybrid amplifier operating in s-band region" *Progress In Electromagnetics Research*, PIER pp. 301, 313, 2010.

[43] S. S. H. Yam, J. D. Kim, M. E. Marhic, Y. Akasaka, L. G. Kazovsky "14xx nm pumped thulium-doped fiber amplifier bursty traffic applications" Optical Fiber Communication Conference, vol. 2, pp:3, 2004

[44] S. D. Emami, P. Hajireza, H. A. Abdul-Rashid , S. W. Harun, H. Ahmad 'Gain Flatted Hybrid Optical Amplifier Using Thulium Doped Fiber and Raman Amplifier' The 5th Mathematics and Physical Sciences Graduate Congress (Thailand 2009).

[45] S. R. Luthi, G. F. Guimaraes, J. Freitas, A. Gomes, "TDFA-FOPA hybrid for S-band amplification and S-to-C, S-to-L band wavelength conversion", Quantum Electronics and Laser Science Conference, pp. 1 – 2, 2006.

[46] Uh-Chan Ryu, K. Oh, W. Shin, U. C. Paek, *IEEE J. of Quantum Electron*. 38,149-161 (2002).

In: Advances in Mechanical Engineering Research. Volume 2 ISBN: 978-1-61761-984-7
Editor: David E. Malach 

*Chapter 4*

# EFFECTS OF MICROELEMENTS ON LONG TIME CREEP RUPTURE PROPERTIES OF HEAT RESISTANT STEELS

***Norio Shinya****
Exploratory Materials Research Laboratory for Reliability and Safety
National Institute for Materials Science
1-2-1, Sengen, Tsukuba, Ibaraki 305-0047, Japan

## ABSTRACT

Some micro elements are very sensitive to long time creep rupture properties. It is well known that harmful impurities such as S, O, Bi, Sb and Pb diffuse to local areas such as grain boundaries, interface between inclusion and matrix and surface of grain boundary cavity during creep exposure, and accelerate nucleation and growth of grain boundary cavity and crack, which lead to premature and low ductility grain boundary fracture. On the contrary, beneficial trace and microalloying elements such as B, Zr, Ca, Ti, V, Nb and Ta counteract the injurious elements by the grain boundary, the interface and the surface refinements, which improve properties of local areas, and prevent premature and low ductility fracture. In this paper actual effects of these microalloying and trace elements on long time creep rupture properties of heat resistant steels are reported. In addition new microalloying methods preventing grain boundary fracture are introduced.

At National Institute for Materials Science Japan long time creep rupture data including longer than 100,000h have been obtained on several heats of principal heat resistant materials. The long time creep rupture life and ductility show a considerable amount of scattering among several heats of a same kind of steels, and it was thought that the scattering might include new effects of microelements on long time creep rupture properties, since the scattering is difficult to explain by using well-known effects. Experimental results showed that main cause of the scattering is difference in microelements. It was indicated that very small amount of Mo and N in solid solution causes the scattering for carbon steels, and also trace of Al content in austenitic stainless

* E-mail: SHINYA.Norio@nims.go.jp

steels causes long time creep rupture strength drop. Mo and soluble N atoms in the steels diffuse to dislocations, and the segregated pairs of the elements immobilizes dislocations. The Al in 12Cr and austenitic stainless steels precipitates as AlN at grain boundaries and accelerates nucleation and growth of creep cavities.

It is found that very small amount of B and N in austenitic stainless steels diffuse to creep cavity surface and cover creep cavity surface by segregation of B or precipitation of BN when S is removed almost completely. The segregated B and precipitated BN decrease surface diffusion rate of creep cavity and also creep cavity growth rateremarkably. The B segregates and also BN precipitates to creep cavity surface autonomously during creep exposure and provide the steels with self-healing function for the creep damage. The self-healing of creep cavity by B segregation and BN precipitation is a new and promising research area for improving creep rupture properties.

## INTRODUCTION

Microalloying is an essential technology for obtaining high performance and low cost steels by modifications of existing steels. Microalloyed steel products have been intended mainly for line pipe, strip and forging mainly for room or low temperatures use. Now microalloing steels are paid attentions as energy and resource saving materials. Microaloying cuts down product weight by increasing steel strength and improves energy efficiency by developing high performance heat resistant steels with addition of small amount elements, leading to the energy and resource saving.

It is well known that microalloying elements are added to structural steels for three principal reasons[1]; ① to impart precipitation hardening or solute hardening, ② to refine the austenite grain size during rolling and to aid in refining the ferrite grain size after transformation, and ③ to lower the transformation temperature; thereby also refining the ferrite grain size and increasing its dislocation density.

For heat resistant steels, precipitation and solute hardenings increase their creep rupture strength in the similar way as carbon and low alloy steels. Therefore microalloying methods for carbon and low alloy steels are usually applied to improvements for heat resistant steels, particularly for not long time creep rupture properties. Long time creep causes various microstructural changes, which cause unexpected results for heat resistant steels. At high temperatures atoms in solid solution are able to move freely, segregate to grain boundary, diffuse into precipitates, form pairs with other atoms in solid solution and precipitate carbides and nitrides in grain, at interface between matrix and precipitate, and at grain boundary. Also unpredicted reactions during creep sometimes cause improvements of performance or severe deteriorations.

In this chapter (1) typical effects of microalloying on creep rupture properties at high temperatures, (2) serious deterioration caused during long time creep by trace elements, leading to creep rupture strength drop and (3) self-healing for creep damages by microalloying, extending rupture life of heat resistant steels, are introduced. The serious deterioration mechanism by trace elements is vitally important information in order to prevent failures of high temperature structures and the self-healing by microalloying is a new technology for development of high performance heat resistant steels.

# TYPICAL EFFECTS OF TRACE AND MICROALLOYING ELEMENTS ON HEAT RESISTANT STEELS

Effects of trace and microalloying elements in heat resistant steels show some difference from microalloyed steels for room temperature use since the trace and microalloyed elements diffuse, segregate, precipitate and cause other high temperature reactions. It is well known that Type 321 stainless steel added with Ti, 347 steel with Nb, and 316 with Mo are typical microalloyed austenitic stainless steels, which show higher rupture strength, corrosion resistance and other improved performances. As such conventional microalloying as the cases for austenitic stainless steels is well known and popular, in this clause highly advanced microalloyed heat resistant steels and a peculiar effect at high temperatures observed in heat resistant steels are introduced as examples of typical microalloyed heat resistant alloys and unexpected effects of trace elements. They are 12% Cr TAF steels for ultra super critical power plant developed by microalloying of B and W and peculiar effects of trace elements of Mo on creep rupture strength.

## Microalloying in 12% Cr Steels for Ultra Super Critical Power Plant

High performance heat resistant steels play an important role in the process of developing new steam power plants with enhanced thermal efficiency and reduced environmental impact. Significant improvements of the creep resistance of the 12%Cr steels were achieved in the last decades through slight changes in chemical composition and microalloying. The main strategies for the improvements [2] are as follows:

- balancing the contents of C, V, Nb and/or Ta and N to generate stable MX precipitates (M: metal, X: C, N),
- increasing the contents of Mo and W for solution hardening and precipitation hardening by $M_{23}C_6$ and Laves phase,
  - adding Co, Cu, Mn and C to suppress delta-ferrite,
  - adding Cu to nucleate Laves phase at Cu precipitates,
  - alloying with B to stabilize $M_{23}C_6$ precipitates.

Wang et al. [2] developed a new 12%Cr steel of 59As in the German Research Foundation (DFG) project, and Uehara et al. [3] also developed higher rupture strength 12%Cr steels of TAF650R and TAF650B. Chemical compositions of the steels are shown in Table 1.

**Table 1. Chemical compositions of new 12%Cr heat resistant steels (mass %)**

| Steel | C | Si | Mn | Cr | Mo | W | Co | Cu | V | Nb | Ta | N | B | Al |
|---|---|---|---|---|---|---|---|---|---|---|---|---|---|---|
| 59As | .19 | .37 | .30 | 11.0 | .50 | 2.10 | 1.20 | .71 | .27 | | .09 | .030 | .020 | |
| TAF650R | .12 | .05 | .10 | 10.20 | .15 | 2.52 | 2.29 | | .21 | .08 | | .023 | .014 | .001 |
| TAF650B | .12 | .06 | .09 | 10.18 | .15 | 2.56 | 2.05 | | .21 | .08 | | .030 | .025 | .001 |

Microstructural feature to be emphasized in 59As [2] is that relatively fine MX particles found after creep consist of TaX particle in addition to the well known VX particles. It is probable that the volume fraction of MX has increased in consequence of the additional supply of MX forming atoms at temper temperature. Thus the Ta content is expected to enhance the strengthening of the subgrain interior by MX in 59As. Also it was suggested that growth of fine $M_{23}C_6$ particles is suppressed remarkably. The advantage of 59As is thought due to enhanced strengthening by fine precipitates, in particular Ta containing MX precipitates and sufficient resistance against coarsening of MX and $M_{23}C_6$ particles.

Uehara et al. [3] developed higher creep strength 12%Cr steels by the most suitable microalloying of W, Mo, V, Co, Nb, N and B. The higher creep strength is thought to be produced by fine and dense distribution of VC/NbC and stable $M_{23}C_6$ /$M_6C$. The 12%Cr steel named TAF650 improved creep rupture strength remarkably. For example, TAF650 shows higher creep rupture strength than 200MPa up to 1000h at 650℃. However the creep rupture strength decreases abruptly and sharply after 1000h at 650℃. It was thought that the serious drop in creep rupture strength is caused by decreasing amount of W in solid solution and softening during creep. The softening was thought to be caused by trace Al containing more than 0.02mass%. In order to prevent the creep rupture strength drop at longer time, new 12%Cr steels were developed. They are TAF650R with decreased amount of 0.001mass% Al and TAF650B with increased amount of 0.025mass% B and low amount of 0.001mass% Al. Increased amount of B prevented the decrease of W in solid solution and low amount of 0.001mass% Al maintained high temperature hardness and strength. The TAF650R and TAF650B showed high creep rupture strength after 1000h at 650℃. The 12Cr steels are expected to be used for ultra super critical power plant with highly enhanced thermal efficiency.

## Effect of Trace and Microalloyed Elements in Solid Solution on Creep Rupture Strength

In heat resistant steels some trace and microalloyed elements deteriorate seriously creep rupture properties and others improve dramatically, since the very small amount of elements are able to diffuse to grainboundaries, dislocations and interface at precipitates at high temperatures. The elements segregated to local area accelerate creep fracture initiation at the local area or immobilize dislocations leading to higher creep strength. Holt et al. [4] classified impurities and trace elements in nickel-base superalloys into detrimental elements and beneficial elements. Table 2 is a part of the classification.

**Table 2. Detrimental and beneficial elements for high temperature steels**

| Detrimental elements | Beneficial elements |
|---|---|
| Non-metallic impurities<br>S, P, N | Refining aids<br>Ca, Mg, Ce, La |
| Metallic or metalloid impurities Pb, Bi, Sb,<br>As, Se, Ag, Cu, Ti, Te | Minor and ppm alloying additions<br>B, Zr, Hf, Mg, C, |

Among the elements shown in Table 1 most detrimental element is S [4] and most beneficial and element is B , which are contained usually in heat resistant steels. Sulfur segregates to grain boundaries very easily and extensively, and cause brittle grain boundary fracture. Mobile S in solid solution decreases with addition of Ce and Zr, which form stable sulfides. In order to remove the S in solid solution thoroughly, adequate amount of the sulfide formers should be added. Although it is well known that B is beneficial element for creep properties, effect of B on creep properties has not been confirmed clearly, since behavior of B during creep exposure is complicated and difficult to detect in steels. Group of Abe [5] of NIMS proved that B content in $M_{23}C_6$ carbides in vicinity of prior-austenite grain boundaries in 9Cr heat resistant steels is relatively higher than that in inside grains, suggesting that B improves microstructural stability in the vicinity of grain boundaries through the stabilization of $M_{23}C_6$ carbides. Added 0.01mass% B diffuses into $M_{23}C_6$ in the vicinity of grain boundaries, suppresses growth of $M_{23}C6$ and improves long time creep rupture properties.

At National Institute for Materials Science Japan, Long time creep and rupture tests are being carried out on main high temperature materials. Creep rupture data on carbon steels show effects of trace and microalloyed elements clearly, since alloying elements are not added deliberately. Figure 1 shows relation between creep rupture times ofhigh strength carbon plates for pressure vessels under 118 and 235MPa at 500℃ [6]. The relation between creep rupture times and amount of Mo in the steels under 118MPa shows almost linear. However the relation under 235MPa shows scattering. The steels showing shorter rupture time down the relation were water quenched at lower temperature of 780-830℃, whereas other steels at higher temperatures than 900℃. The effect of difference in heat treatments is removed during longer creep, and the relation between rupture time and very small amount of Mo under 118MPa shows the linear relation. Effect of the very small amount of Mo is thought that the trace Mo forms pairs with C or N in solid solution, and the pairs interact with dislocations and provide friction stress impeding slips, as well as retarding recovery.

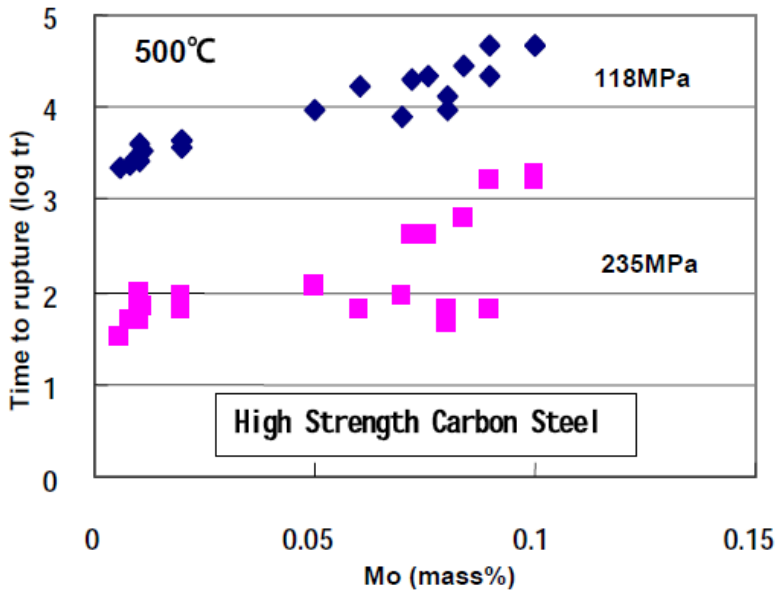


Figure 1. Relation between time to rupture and very small amount of Mo.

## SERIOUS DETERIORATION IN LONG TIME RUPTURE PROPERTIES CAUSED BY TRACE ELEMENT

Long time creep and rupture data up to 100 000h on 9 heats of 304 and 316 stainless steels have been published by National Institute for Materials Science, Japan [7, 8]. The time to creep rupture data of the steels shows considerable heat-to-heat difference particularly in long time rupture strength among 9 heats. Lower strength heats showed remarkable decrease in strength and ductility at longer rupture time and higher temperatures. The creep fracture mechanism maps constructed by metallographic examination of the ruptured specimens indicate that rupture strengths of the deterioration heats for times of 30 000 and 100 000h fall below the maximum allowable strength of The ASME International Boiler and Pressure Vessel Code. The unusual deterioration in long time rupture strength may cause failures in high temperature structures such as steam power plants and chemical plants. In order to prevent the failures, it is necessary to clarify causes for the deteriorations and provide measures for removing the deteriorations. In this paper effects of trace elements on the rupture strength deterioration are reported and cause of the deteriorations are clarified.

### Deterioration in Long Time Creep RuptureStrength

Long time rupture data up to 100 000h of austenitic stainless steels have been published as NRIM Creep Data Sheet No.4B (type 304 steel) [7], No.6B (type 316 steel) [8], No.5B (type 321 steel) [9], and No.28B (type 347 steel) [10]. Long time creep rupture properties for 9 heats of the four austenitic stainless steels show different behavior between 304/316 steels and 321/347 steels. Although there is considerable amount of scattering in creep rupture strength among 9 heats of 321 and 347 steels, all of stress-rupture time curves show similar trend, and unusual change in the curves is not observed with increasing rupture time. On the other hand, some heats of 304 and 316 steels show remarkable rupture strength drops with increasing time to rupture at higher temperatures than 650℃. Two groups of the heats showing normal trend and the long time rupture strength drop in stress-rupture time curve were selected, and their stress-rupture time curves are compared in Figures 2 and 3. The rupture strength falls remarkably with increasing rupture time longer than 1000h in stress-rupture time curves of Heat A of 304 steel and Heat F of 316 steel, which contain higher contents of Al, 0.047mass% and 0.095mass%, respectively, and difference in rupture strength between the normal and the lowest heats become larger and larger with increasing rupture time.

Creep rupture ductility of the Heats A and F of the steels also decreases remarkably simultaneously with the rupture strength drops [7, 8]. Heat B of 304 steel and Heat L of 316 steel, which contain lower contents of Al, 0.014mass% and 0.017mass%, respectively, show normal stress-rupture time curves. Metallurgical difference including other chemical elements for the heats is comparatively slight [7, 8]. Metallographic observation of ruptured specimens by scanning electron microscope (SEM) showed that creep fracture mechanism changes from trans-granular to grain boundary fracture with increasing rupture time. The grain boundary fracture contains three kinds of grain boundary fracture modes: wedge-type crack, grain boundary cavity andσ/matrix crack fracture.

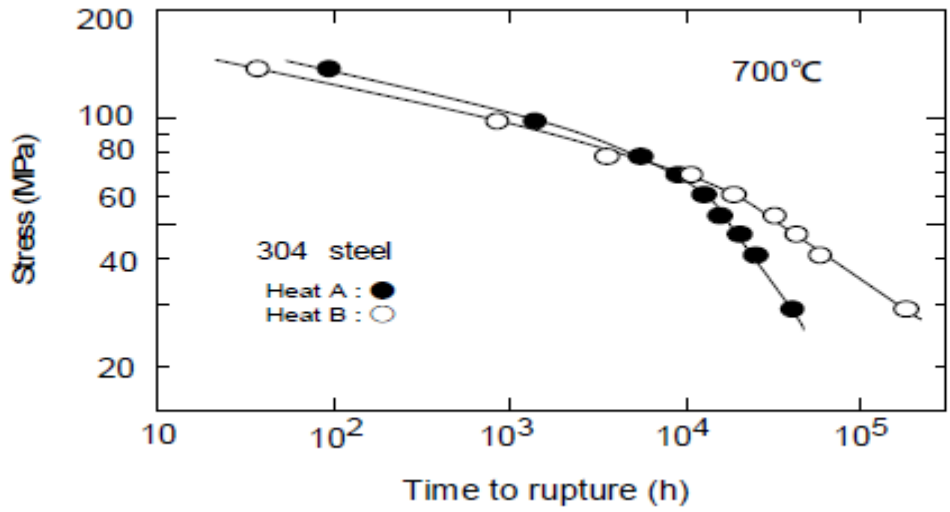


Figure 2. Stress-rupture time curves for Heats A and B of 304 steel.

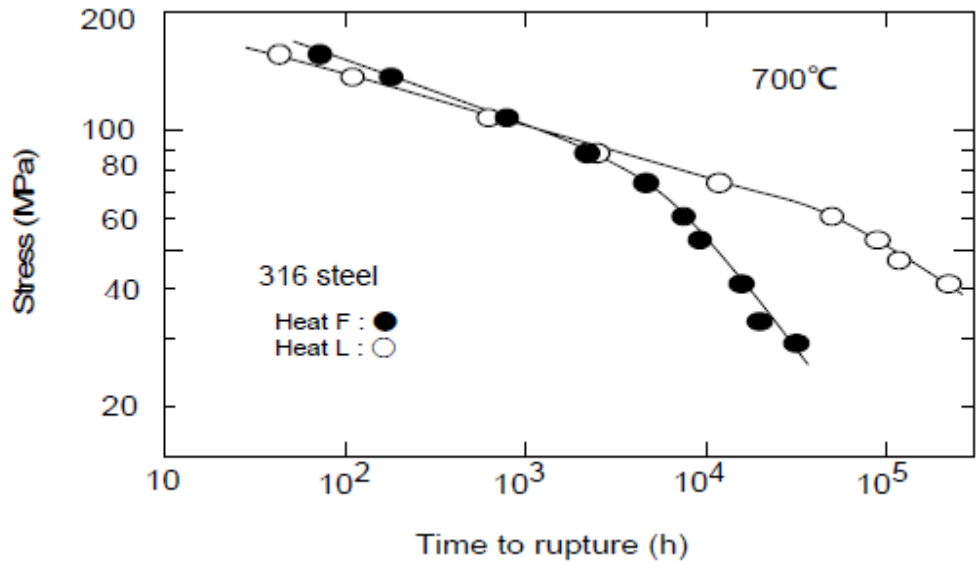


Figure 3. Stress-rupture time curves for Heats F and L of 316 steel.

The grain boundary fracture mode changes from wedge-type crack fracture to grain boundary cavity fracture, and further the grain boundary cavity fracture to σ/matrix crack fracture, with increasing time to rupture [11, 12]. The grain boundary cracks and cavities in Heat A of 304 steel observed by SEM are shown in Figure 4. The stress and temperature region of the rupture strength drop is included in the σ/matrix crack fracture region [11]. This suggests that the reason for rupture strength drop have relation with theσ/matrix crack fracture mechanism and grain boundary microstructure affecting the fracture.

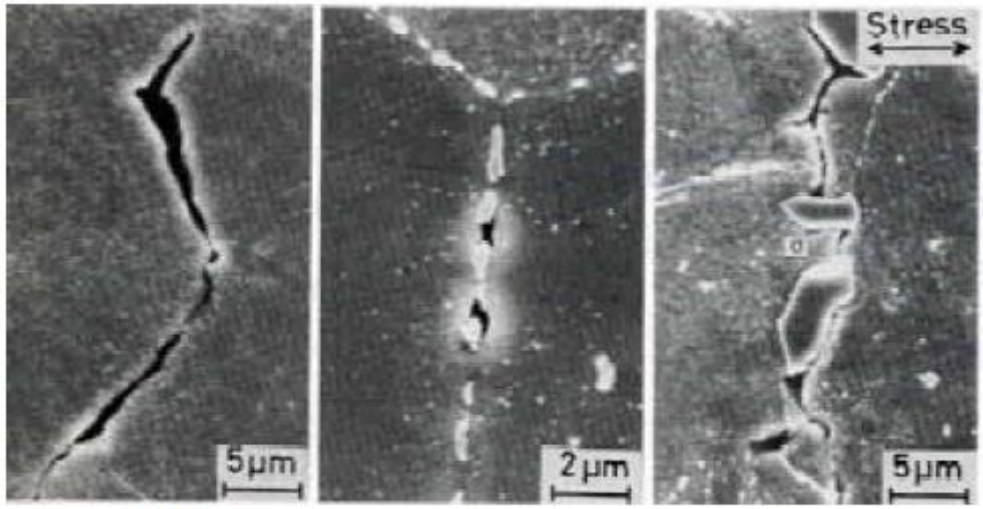


Figure 4. Grain boundary cracks and cavities observed in ruptured specimens of Heat A of 304 steel.

## Micro-Structural Change at Grain Boundary During Long Time Creep Exposure

It was thought that the differences between the normal and the rupture strength drop heats of 304 and 316 steels are related to grain boundary microstructures, and an unordinary grain boundary structure causes the long time rupture strength drops. Grain boundary microstructures, therefore, were investigated on ruptured specimens by SEM and transmission electron microscope (TEM).

Typical grain boundary microstructures observed by TEM are shown in Figure 5, which shows micro-structural changes in grain boundary precipitation due to creep exposure at 650℃ on Heat A of 304 steel. The carbide of $M_{23}C_6$ precipitates on grain boundary at first, grows along grain boundary and then becomes larger with cohering each other. In longer time ruptured specimens than 10 000h, massive σ phases are observed on grain boundary (Figure 5d). In the vicinity of σ phase, precipitate free zone is observed, which indicates that σphase grows with absorbing grain boundary $M_{23}C_6$ and also grain interior $M_{23}C_6$. All of the heats of 304 and 316 steel show similar grain boundary micro-structural change as shown in Figure 5.

In heats causing the longer rupture time strength drop, precipitation of rod-like AlN was observed on grain boundary in addition toσ phases and $M_{23}C_6$, whereas in normal heats no precipitation of AlN on grain boundary was found. Typical micrographs of the rod-like AlNby TEM are shown in Figures 6 and 7 for Heats of A and F of 304 and 316 steel, respectively. The AlN would precipitate at interface betweenσ phases on grain boundary and matrix at first, and then grows at the precipitated site without being absorbed in the σ phases, since the constituent of AlN is completely different from that of σ phase. Main constituent

element of both σ phase and $M_{23}C_6$ is Cr, which is the reason why $M_{23}C_6$ on grain boundary and matrix are absorbed into σ phases.

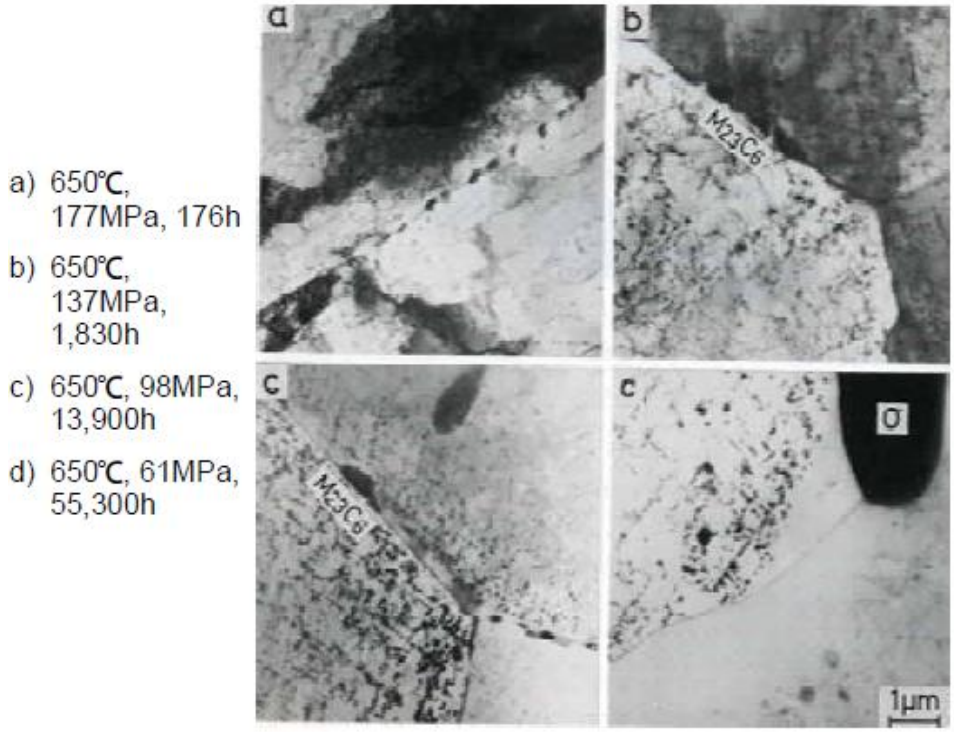


Figure 5. Micro-structural change at grain boundary in ruptured specimens of Heat A of 304 steel.

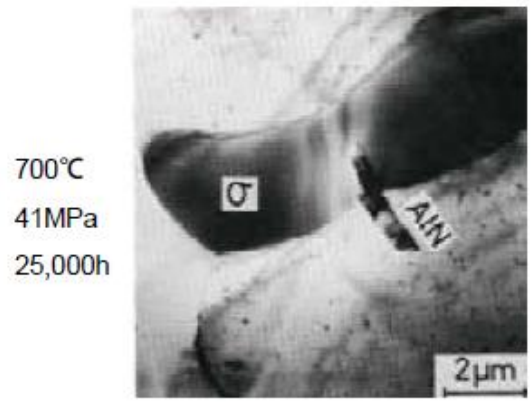


Figure 6. Rod-like AlN precipitated at σ phase In ruptured specimens of Heat A (Al:0.047mass%)of 304 steel.

All ruptured specimens of the heats were examined by using SEM and TEM, and time-temperature-grain boundary precipitation diagrams were constructedfrom the results. Figure 8 shows the time-temperature-grain boundary precipitation diagram for Heats A and B of 304 steel. In Heat A, AlN precipitates on grain boundary soon after precipitation of grain boundary at temperature range of 600-750℃. At higher temperature than 750℃ AlN

precipitatesearlier than σ phases. Time-temperature-grain boundary precipitation diagrams for Heats F and L of 316 steel are similar to those of the heats of 304 steel.

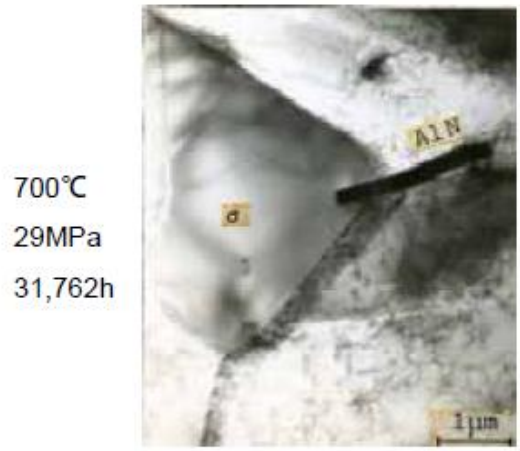


Figure 7. Rod-like AlN precipitated at σ phase In ruptured specimen of Heat F (Al:0.095mass%)of 316 steel.

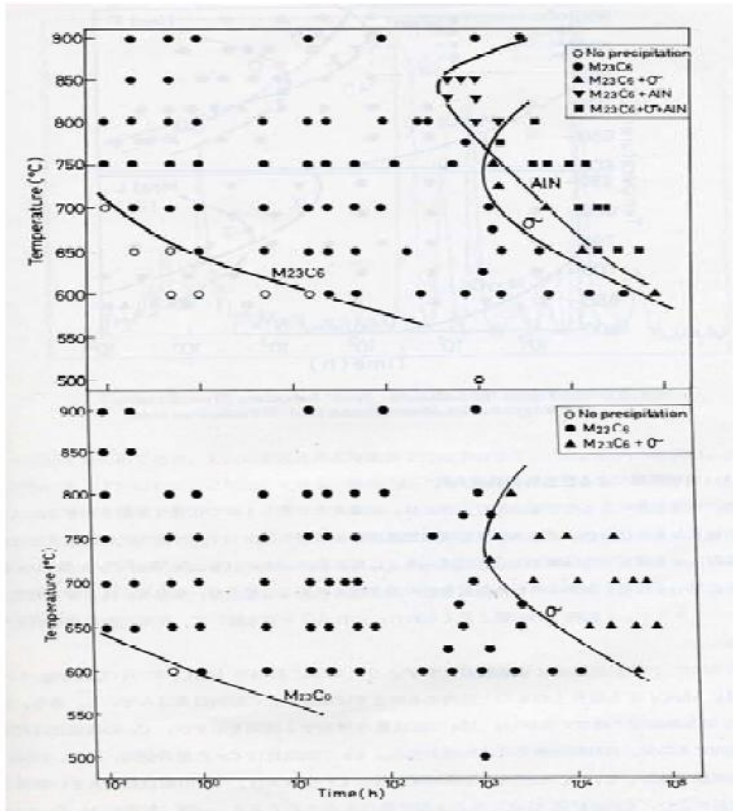


Figure 8. Timetemperature-grain boundary precipitation diagram for Heats A (Al:0.047mass%) and B (Al:o.014mass%) of 304 steel.

## Cavitation Accelerated by Trace Element

In Heat A of 304 steel and Heat F of 316 steel, it was found that rod-like AlN precipitated at σ phase on grain boundary and coexisted withσ phase during long time creep exposure, whereas no

AlN was found on grain boundary in Heata B and L of the steels. The difference in the grain boundary microstructure indicates that the precipitation of rod-like AlN atσ phase might cause the long time rupture strength drop due to early nucleation of creep cavity at interface between AlN andσ phase. Judging from the coexisting morphology of AlN and σ phase shown in Figs 6 and 7, the precipitation of AlN is thought to accelerate creep cavity nucleation remarkably.

In order to detect the creep cavity initiation, SEM observation was focused on the interface between rod-like AlN andσ phase at grain boundary.As shown in Figure 9, creep cavity initiation at the interface was found. It is indicated that the creep cavity is initiated at early creep stage by stress concentration at the interface. The stress concentration is thought to be formed by grain boundary sliding and to be very great, judging from the coexisting morphology (Figures 6, 7). The concentrated stress may be scarcely relaxed, since the AlN andσ phase are hardly deformed during creep because of their hardness.

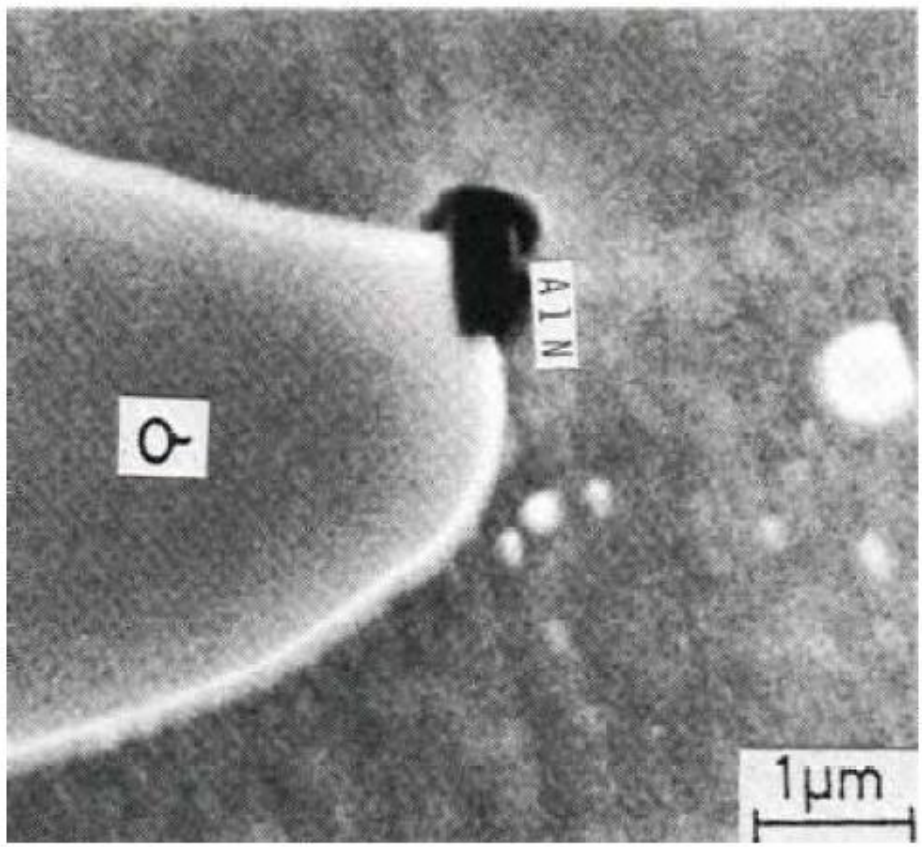


Figure 9. Creep cavity formation at interface between AlN and σ phase in crept specimen at 750℃and 37MPa for 5,000h of Heat A (Al:0.047mass%)of 304 steel.

In Heat B of 304 steel and Heat 316 steel, no AlN wasfound on grain boundary and at σ phase. This means that there is no accelerating site for creep cavity nucleation, leading to delay in the nucleation of creep cavity. Figure 10 shows dislocation structures in precipitate-free zone adjacent to σ phase on grain boundary in the ruptured specimen at 41MPa and 700℃ for 58200h of Heat B of 304 steel. It is found that a lot of dislocations pile up in precipitate-free zone around σ phase on grain boundary. The pile up of dislocations would be formed in tertiary creep stage with acceleration of creep deformation, and nucleate creep cavity at stress concentrated site aroundσ phase. The observation of grain boundary micro-structural change indicates that in Heats A and F, creep cavity nucleates in early creep stage by precipitation of AlN at σ phase, leading to cause premature creep rupture. On the other hand, in Heats B and L creep cavity nucleates in tertiary creep stage by dislocation pile up with accelerated creep deformation. The precipitation of AlN was observed in all heats of 304 and 316 steels with higher amount of Al than 0.03mass%, and not observed in heats with lower Al amount than 0.03mass%. The precipitation of Al was accompanied with creep rupture strength drop, whereas no precipitation of Al showed linear stress-rupture curves.

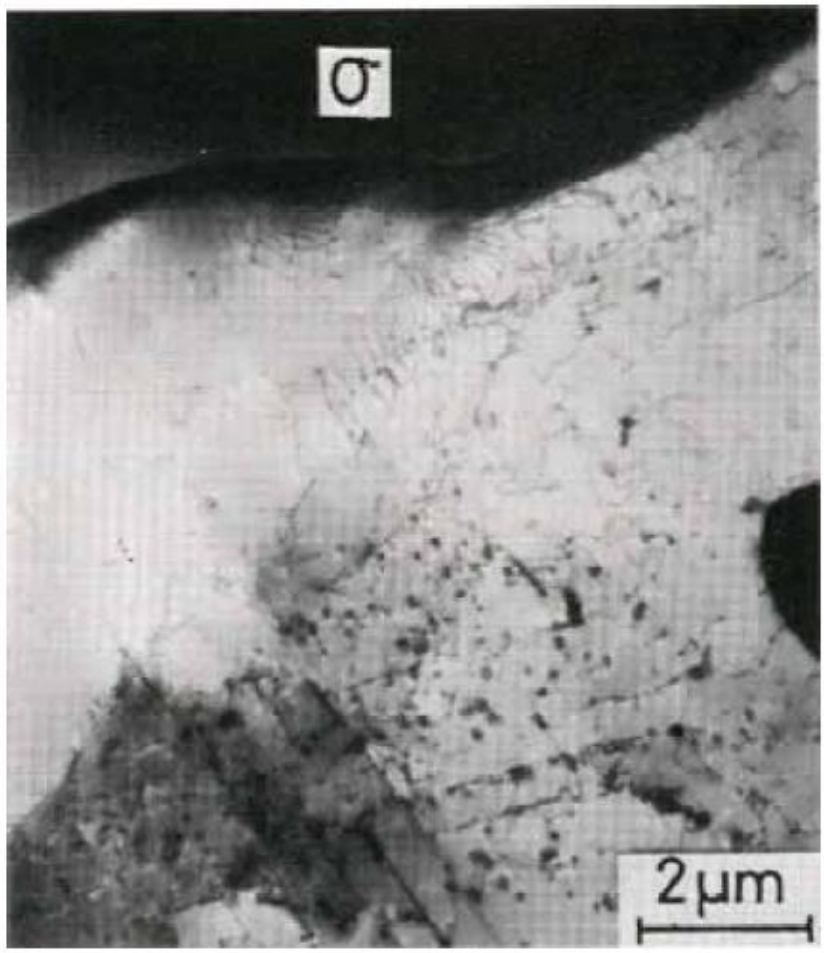


Figure 10. Dislocation pile-up at σ phase in ruptured specimen at 700℃, 41MPa and 58,200h of Heat B of 304(Al:0.014mass%) steel.

Miller et al. [13] constructed creep fracture maps on a 316 stainless steel by calculation based on creep fracture mechanism theories. According to the maps, the stress and temperature regions of the long time rupture strength drop of Heats A and F are included in the diffusion growth cavitation. The diffusion growth cavitation model [14-16] assumes that creep cavities nucleate simultaneously with creep exposure, and the creep cavity growth is controlled by grain boundary diffusion. According to the diffusion growth cavitation model, rupture time depends on stress and grain boundary diffusion as shown in following equation:

$$tr \propto A\, T/(D_{gb} \cdot \sigma) \quad (1)$$

where tr is time to rupture, A is constant, T is temperature, $D_{gb}$ is grain boundary diffusion coefficient, and σ is stress. Experimental activation energies for creep rupture in the long time rupture drop region were calculated by using rupture data at lower stresses, which were 160kJ/mol for Heat A and 220kL/mol for Heat F. Experimental stress exponents in the previous equation are −1.74 for Heat A and −1.3 for Heat F.

Activation energy of grain boundary self diffusion for 18-8 austenitic stainless steel is 195kJ/mol [17], which almost corresponds to the calculated creep rupture activation energies for Heats A and F. Also experimental stress exponents of creep rupture life are approaching to the theoretical value of −1 in the previous equation with lowering creep stress. These results indicate that rupture life in the region of the rupture strength drop is controlled by grain boundary diffusion growth of creep cavity.

In Heats B and L, creep cavities would be nucleated by dislocation pile up, which is formed in precipitate-free zone at σ phase with increasing creep deformation. Rupture time for Heats B and F are controlled not only by grain boundary diffusion rate but also creep deformation rate. The equation of the diffusion growth model, therefore, can't be applied to the heats. Effect of creep rate should be considered for the equation.

Trace element of Al higher than 0.03mass% precipitates AlN during longer creep exposure. From the very few and microscopic AlN creep cavities and cracks originate, leading to creep fracture.

Therefore the trace Al forms spots of the creep fracture origin.

## SELF-HEALING OF CREEP DAMAGE WITH MICROALLOYING

Creep fracture of higher strength heat resistant steels is caused by creep cavity nucleation and growth. Creep cavity nucleation and growth are very sensitive to trace and microalloying elements. New mechanism of the microalloying for suppression against nucleation and growth of creep cavity is reported.

### Creep Fracture Mechanism and Creep Cavity in Austenitic Stainless Steels

Long time high temperature services of heat resisting steels lead to premature and low ductility creep fracture due to cavitation . The creep fracture is caused by nucleation, growth and coalescence of creep cavities on grain boundaries. It might be possible to prevent most failures in high temperature structures when the creep cavities are self healed autonomously during high temperature service of the steels.

The self healing method has been proposed recently by Shinya et al. [18-24]. The method is as follows; creep cavity is thought to grow by diffusive transport of matter from creep cavity surface to grain boundary, which means that the physical property of creep cavity surface is closely connected to cavity growth. Boron segregation and boron nitride (BN) precipitation onto creep cavity surface are thought to improve the physical properties of the creep cavity surface, since B and BN are very stable at high temperatures. It was shown in the works that microalloyed B segregates and also microalloyed B and N precipitate at creep cavity surface, and reduced creep cavity growth rate remarkably, which improved long term creep rupture strength with long term ductility. The B segregation and BN precipitation onto creep cavity surface are developed autonomously during high temperature service, suppressing creep cavity growth. The autonomous self healing for creep damage due to the segregation and precipitation at creep cavity surface is innovative microalloying method.

Most high strength heat resisting steels, including austenitic stainless steels, show creep cavitation fracture, in which creep cavity causes transgranular creep fracture at their actual service conditions. Figure 11 shows SEM photographs of developing creep cavities with creep curve during creep test at 750℃ and 37MPa on a 304 austenitic stainless steel (SUS304H). Creep cavities are formed at interfaces between grain boundary carbides of $M_{23}C_6$ and matrix, and their sizes at the first stage of creep rupture life ($t/t_r \fallingdotseq 0.3$) are less than 0.5μm. These fine creep cavities grow along grain boundary perpendicular to tensile stress, leading to lens or rod like shapes at the second stage ($t/t_r \fallingdotseq 0.5$). Further growth and linking up each others lead to grain boundary cracks of about 5μm at the third stage ($t/t_r \fallingdotseq 0.9$). It is indicated that creep cavities at early stages of their developments are very fine size, suggesting that application of healing methods may be effective at the early stages.

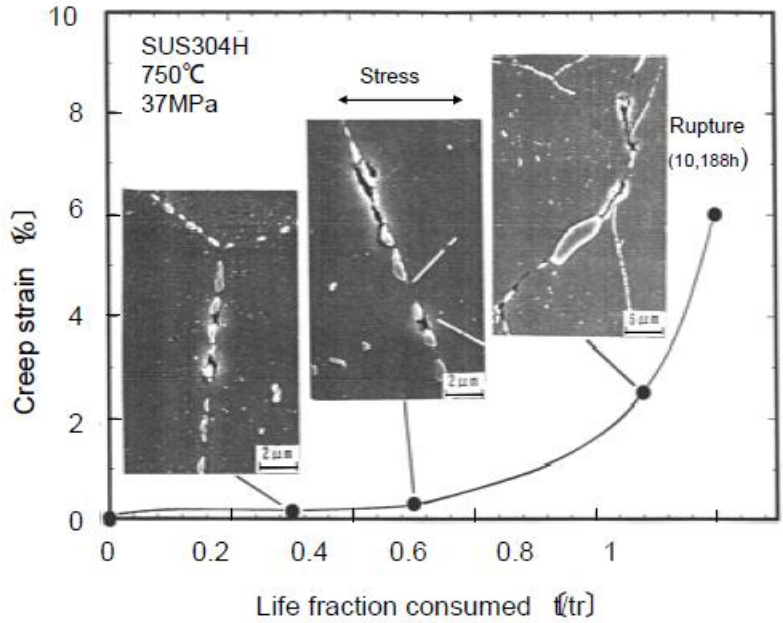


Figure 11. Typical appearances of creep cavities developed during creep. Creep cavities nucleate at M23C6, grow along grain boundary, and form grain boundary cracks.

## Self-Healing Mechanism of Creep Cavity

The creep rupture life and ductility in the region of cavitation field fracture depend on development of creep cavity [25]. While the development of creep cavity depends on nucleation and growth rates of creep cavity, the creep cavity growth is thought to be more influential, since most creep cavity nucleation is believed to occur at initial stages of creep rupture life.

Figure 12 shows an illustration of creep cavity growth mechanism, which is thought to act in the usual cavitation range, especially at lower applied stresses and higher temperatures. The creep cavity growth proceeds with diffusive transport of matter from creep cavity surface onto grain boundary, where they can be deposited. The deposition of matter on the grain boundary causes reduction of tensile stress at grain boundary, which is a driving force for the flow of matter.

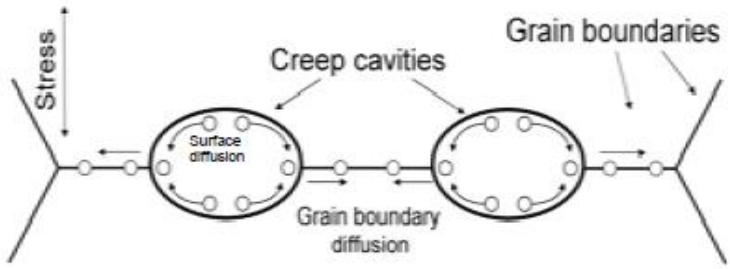


Figure 12. Illustration of creep cavity growth process controlled by grain boundary or surface diffusion wherein atomic transport occurs along the creep cavity surface and then down the grain boundary.

In usual cavitation rupture region, the stress acting on grain boundary associated with the deposition is compensated by tensile creep deformation and diffusion of the deposited matter through grain boundary, which makes it possible to continue unconstrained growth of creep cavity. Needham and Gladman [26] extensively studied the creep cavitation behaviors of a type 347 austenitic stainless steel. They concluded that the measured creep cavity growth rate could be well predicted by the unconstrained diffusive growth mechanism, considering the creep strain dependence of continuous creep cavity growth nucleation. Under unconstrained conditions, diffusivities along both grain boundary and creep cavity surface control creep cavity growth rate.

From Figure 12, the creep cavity growth rate is expected to be controlled by the slower process of either grain boundary diffusion or creep cavity surface diffusion [27]. The creep cavity growth under unconstrained condition is expected to be influenced substantially due to the change in self diffusion coefficient along both creep cavity surface and grain boundary, which are influenced by segregation of trace elements significantly. It may be possible to reduce the surface diffusion rate by modification of creep cavity surface, leading to reduction of creep cavity growth rate. Hence the modification of creep cavity surface was selected as a focusing target for a trial study of self healing of creep cavity.

The creep cavity surface diffusion is known to be influenced by segregation of trace elements on its surface [28]. Some trace elements diffuse to grain boundary and also creep cavity surface, and segregate there at high temperatures. It is known also that soluble S

segregates onto creep cavity surface very easily, which give rise to accelerate creep cavity growth through increase in surface diffusion rate [28]. Owing to the low melting point of S (112.8℃), the creep cavity surface contaminated with S becomes very active and surface diffusion rate increases by several orders of magnitude [28-30].

When the soluble S is removed almost completely by addition of Ce and Ti [31, 32], other elements such as B and N become possible to segregate onto creep cavity surface. Segregation of B is thought to suppress the surface diffusion at creep cavity surface, reducing the creep cavity growth rate, due to the high melting point of B （2080℃）. Co-segregation of B and N might form BN compound at creep cavity surface. The BN precipitation on creep cavity surface is expected to suppress the surface diffusion almost completely and then retard the creep cavity growth significantly owing to its higher melting point (3000℃).

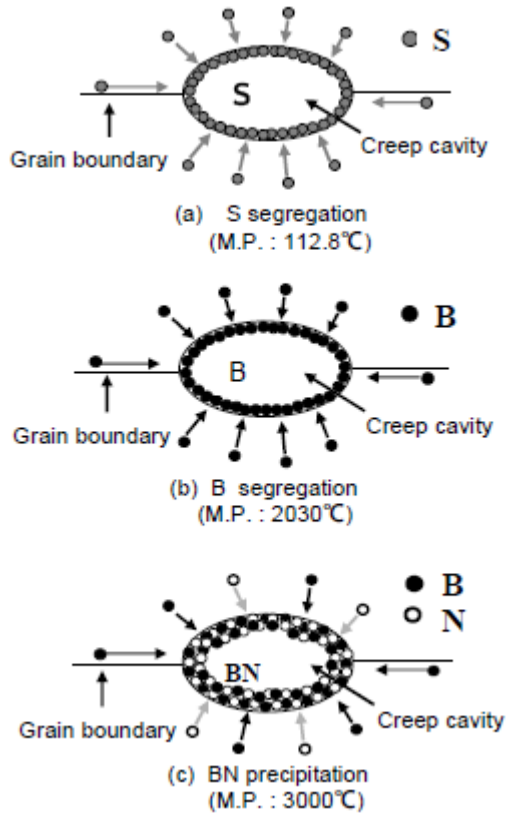


Figure 13. Illustration of self-healing layer formation of B segregation and BN precipitation on creep cavity surface. In usual steels, trace of S segregates onto creep cavity surface during high temperature service. In self-healing heat resisitant steels, the layers of segregated B and precipitated BN suppress creep cavity growth.

In usual heat resisting steels, a trace of S segregates onto creep cavity surface, and accelerates the surface diffusion rate of creep cavity significantly. Since the accelerated surface diffusion rate is by far the faster than the grain boundary diffusion rate, the creep cavity growth rate is controlled by the grain boundary diffusion rate in the usual steels. The surface layers of segregated B and precipitated BN is thought to reduce the surface diffusion of creep cavity significantly. The layer of BN precipitation, particularly, is thought to almost

freeze the diffusion rate. From the significant reduction in the diffusion rate, the surface layers should change the controlling diffusion process for the creep cavity growth from the grain boundary to the surface diffusion. The creep cavity growth rate controlled by the surface diffusion [33,34] is estimated as:

$$dr/dt = \Omega D_s \delta \gamma_s \{(\sigma_b / [(1-\omega)\gamma_s \sin(\psi/2)\}^3 / kT \quad (2)$$

Ds: surface diffusion coefficient, $\sigma_b$: normal stress acting on the grain boundary, ω: $\omega=(2r/\lambda)^2$ , ψ: angle at the chip of creep cavity.

Both the B segregation and the BN precipitation on creep cavity surface occur continuously and cover all of creep cavity surface autonomously during usual high temperature service of the heat resisting steels. These surface layers of B and BN are self healed by continuous segregation or precipitation during the service. In addition to the self healing of themselves, the surface layers provide the steels with self healing function for cavitation since they autonomously cover the creep cavity surface and suppress cavitation almost completely. Figure 13 is illustrations showing formations of the self healing layers for creep cavity by B segregation and BN precipitation.

## 4. Self Healing of Creep Cavity by B Segregation

Boron addition in high temperature alloys has been reported to increase creep rupture strength. It is widely believed that the addition of B increases creep rupture life and ductility through the increase in creep cavitation resistance of the steels by grain boundary strengthening. The reason for strengthening of the grain boundary is not precisely known. In most instances, it is thought B is concentrated on grain boundary, where it enters into the precipitates or matrix/precipitates on the grain boundary in such a way to suppress micro-cavity formation. While many beneficial effects of B have been reported, actual effects and behaviors of B are not certain on cavitation and creep fracture, due to their complexity.

Effects of trace elements have been studied on grain boundary behaviors extensively, whereas the knowledge concerned with cavitation is limited. For creep fracture mechanism and property, the physical state of creep cavity surface is thought to influence more directory and effectively than that of grain boundary. Modification of creep cavity surface, which might be very effective on suppression of creep cavity growth, has been tried by segregation of B and precipitation of BN.

In order to facilitate B to segregate onto creep cavity surface, a chemical composition of a 347 austenitic stainless steel was modified, which was melted in a vacuum arc furnace. Using the modified austenitic stainless steel microalloted with B and Ce, the presence of B segregated onto creep cavity surface and the self healing effect of B segregation on creep cavity growth were proved. Table 3 shows chemical compositions of a standard 347 and the modified 347 austenitic stainless steels. In the modified 347 steel(347BCe), the content of free S was removed almost completely by addition of 0.016mass% of Ce, which has a strong affinity to S and O, leading to formation of $Ce_2O_2S$[31] and $Ce_2S_3$. In addition to Ce, 0.07mass% of B was also added to the modified 347 steel. The steels were given a solution heat treatment at 1200℃ for 20min, followed by water quenching.

**Table 3. Chemical compositions of standard 347 (B-free steel) and modified 347 (B-added steel) austenitic stainless steels (mass %)**

| Alloy | C | Si | Mn | P | S | Cr | Ni | Nb | N | B | Ce |
|---|---|---|---|---|---|---|---|---|---|---|---|
| Standard 347 | 0.080 | 0.59 | 1.68 | 0.001 | 0.002 | 17.96 | 12.04 | 0.41 | 0.077 | - | - |
| Modified 347 | 0.078 | 0.68 | 1.67 | 0.001 | 0.002 | 18.15 | 11.90 | 0.38 | 0.072 | 0.069 | 0.016 |

Creep rupture tests were carried out at 750℃. The variation of creep rupture life and ductility of both steels with applied stress are shown in Figure 14. Addition of minute amount of B and Ce had remarkable effects on the creep rupture strength and ductility of the modified 347 steel. Creep rupture strength and ductility of the steel increased with addition of B and Ce, effects of which were pronounced on longer creep exposure.

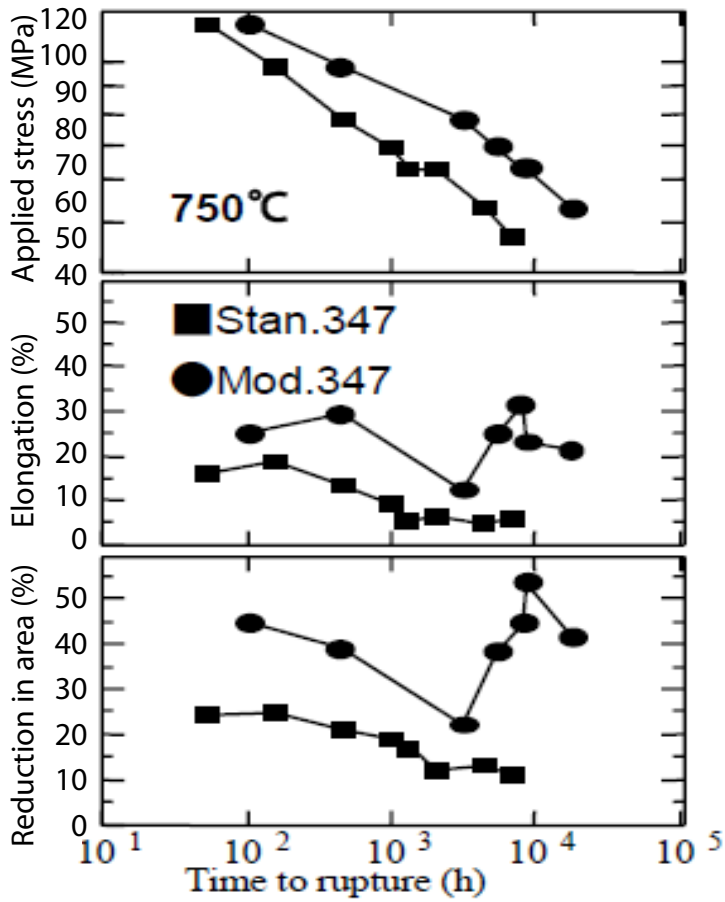


Figure 14. Creep rupture properties at 750℃for standard 347 and modified 347 (347BCe) austenitic stainless steels. Modified 347 steel shows higher strength and ductility.

Figure 15 shows creep cavities observed in the ruptured specimens of standard 347 and modified 347 (347BCe) steels. Creep cavities in the standard 347 steel grow quickly along grain boundary and form grain boundary cracks by linking up each others, whereas creep cavities in the modified 347 steel maintain fine size and isolated each others for longer time.

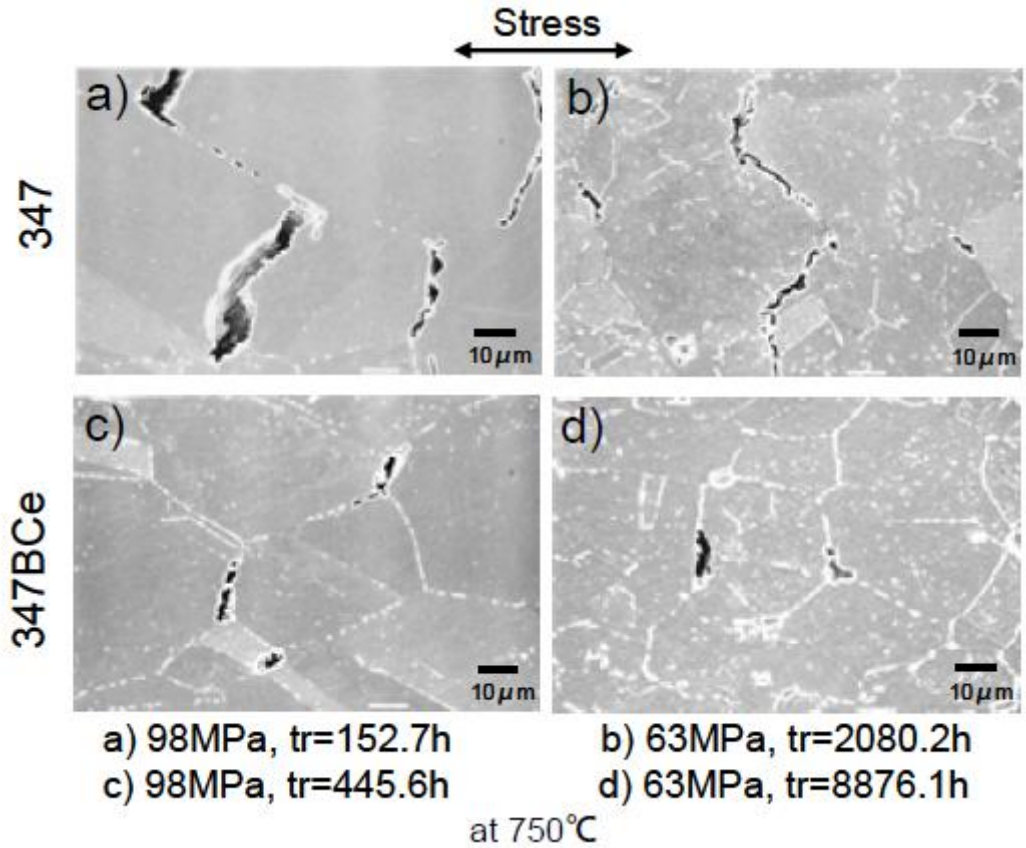


Figure 15. Creep cavities observed in ruptured specimens of standard 347 and modified 347 (347BCe) austenitic stainless steels.

X-ray diffraction analyses of the precipitates were carried out in both the steels after rupture at 750℃ and 69MPa. Precipitate residues were extracted from the steels by the electrochemical method. Figure 16 shows the presence of different precipitates in the B containing modified 347 steel. In both the steels, the presence of $Cr_{23}C_6$, $Nb_4C_3$, NbC and NbN precipitates were observed. The observed carbonitride precipitation in both the steels was reported by several investigators on the type 347 austenitic stainless steel [35, 36]. X-ray investigations also indicated the presence of $Ce_2S_3$ and $Ce_2O_2S$ precipitates in the modified 347 steel. The addition of Ce in steels may be an effective way of removing traces of S and O soluble in the steels. In addition to $Ce_2S_3$ and $Ce_2O_2S$, it was observed that a trace of Ti forms TiS, showing that Ti has also a strong affinity to S. Chromium boride ($Cr_2B$) particles were observed in the B containing steel. The solid solubility of B in a 18Cr-15Ni austenitic stainless steel has been reported to be about 90ppm at 1000℃ and the solubility boundary

recedes rapidly with decreasing temperature, which indicates high stability of the precipitates in the steel.

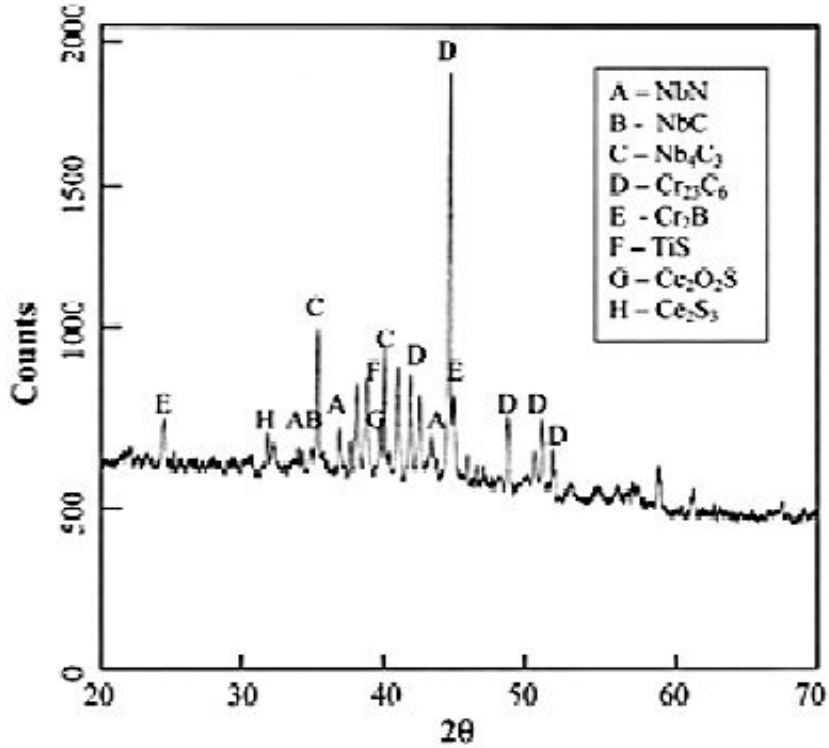


Figure 16. X-ray diffraction analysis of the precipitates extracted by electrochemical method from the B-containing modified 347 steel, creep tested at 750 and 69MPa.

Interrupted creep tests at 78MPa, 750℃ were carried out in argon atmosphere to measure the growth rate of creep cavities observed on the specimen surface. Individual creep cavity dimensions had been measured by SEM on interruption of the creep tests and average growth rates of the creep cavity for the intervals were calculated. Measurements were carried out on several creep cavities until they coalescence with each others. Figure 17 compares the modified steel with the standard steel in the growth rates of the creep cavities until they coalescence with each others. Addition of B in the modified steel decreased the creep cavity growth rate almost by an order of magnitude.

The chemistry of the creep cavity surface in both the steels was examined by an Auger electron spectroscope (AES). The AES is sensitive to only top few atom layers on fractured surfaces, making it a useful technique for studying any trace element segregation that might have occurred. The crept specimens of the steels were fractured by impact loading at liquid nitrogen temperature in the AES chamber to expose the creep cavity surface. Figure 18 shows fractured surfaces with creep cavities on grain boundaries and Auger spectra obtained from the creep cavity surfaces of the standard and the modified 347 steels. The fractured surface of both steels containing creep cavities on grain boundary indicates that this procedure is effective in exposing the creep cavity surface.

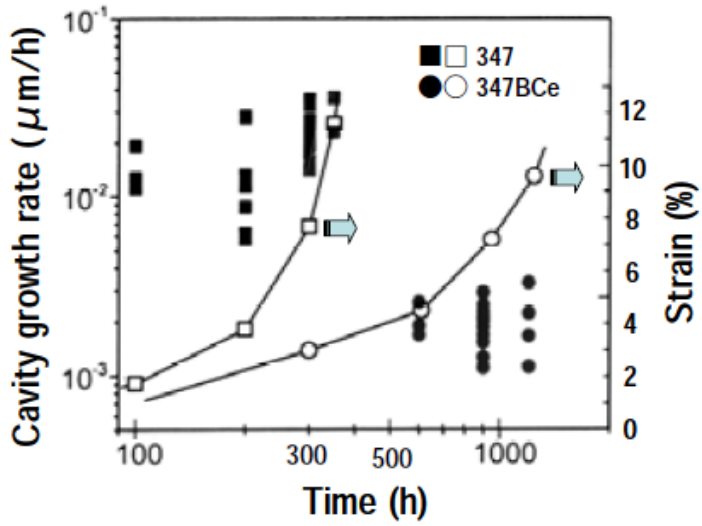


Figure 17. Creep cavity growth rate and creep strain with creep exposure time in Ar at 750℃and 78MPa. The growth rate in modified 347 steel is slower by an order of magitude than that of standard 347 steel.

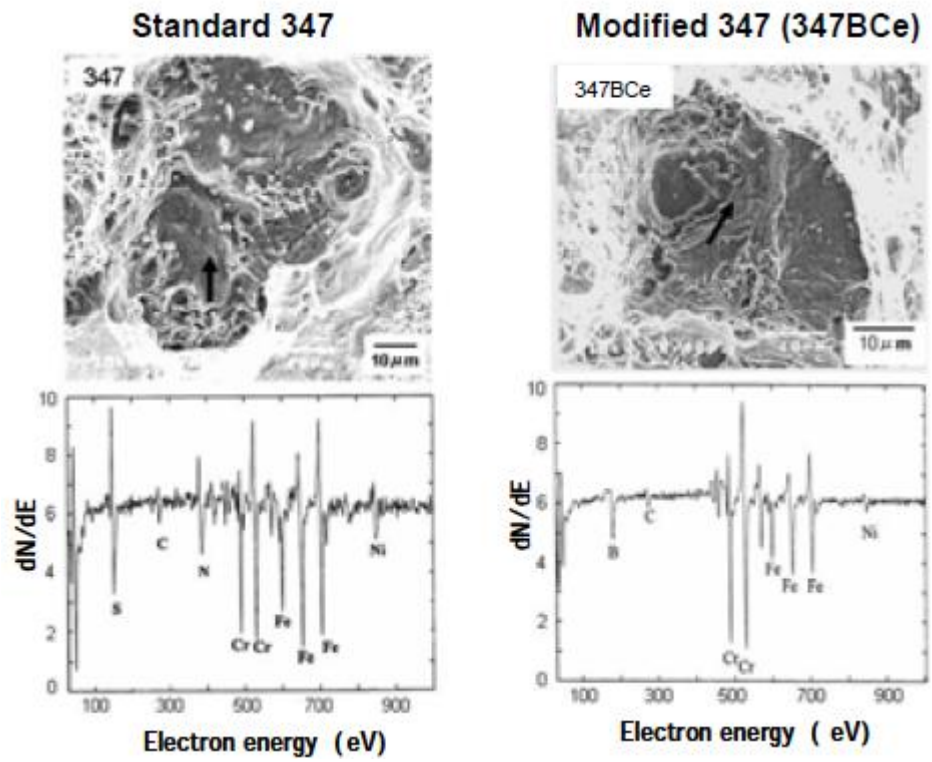


Figure 18. Creep cavities on fractured surfaces and Auger specat rfrom creep cavity surfaces of standard 347 and modified 347 steels creep exposedt a750℃and 69MPa. The crept specimens were fractured by impact loading at liquid nitrogen temperature In AES chamber.

Presence of S segregation was observed on the creep cavity surface of the standard 347 steel, whereas Auger peak of elemental B instead of S was observed in the modified 347 steel. The soluble S in the modified 347 steel might be removed almost completely with addition of Ce, by forming $Ce_2O_2S_2$ and $Ce_2S_3$. In the absence of S contamination, most nucleated creep cavity surfaces were covered with filmy layer of segregated elemental B. Figure 19 shows Auger S and B mapping of the fractured surfaces. It is indicated that S segregates onto creep cavity surfaces and covers up the surfaces in the standard 347 steel, whereas in the B containing modified 347 steel, B segregates onto the creep cavity surfaces. The S content in the standard 347 steel was ～0.002mass% (Table 3) and even such amount of bulk S could contaminate the creep cavity surface.White et al. [28], in their study on effects of S and P on creep cavitation in a 304 austenitic stainless steel, reported S concentration on the creep cavity surface approximately $10^3$ times that in the bulk. The strong tendency of B to segregate on interfaces is derived from an effect of large misfit of B atom in both substitutional and interstitional sites of the austenitic lattice.

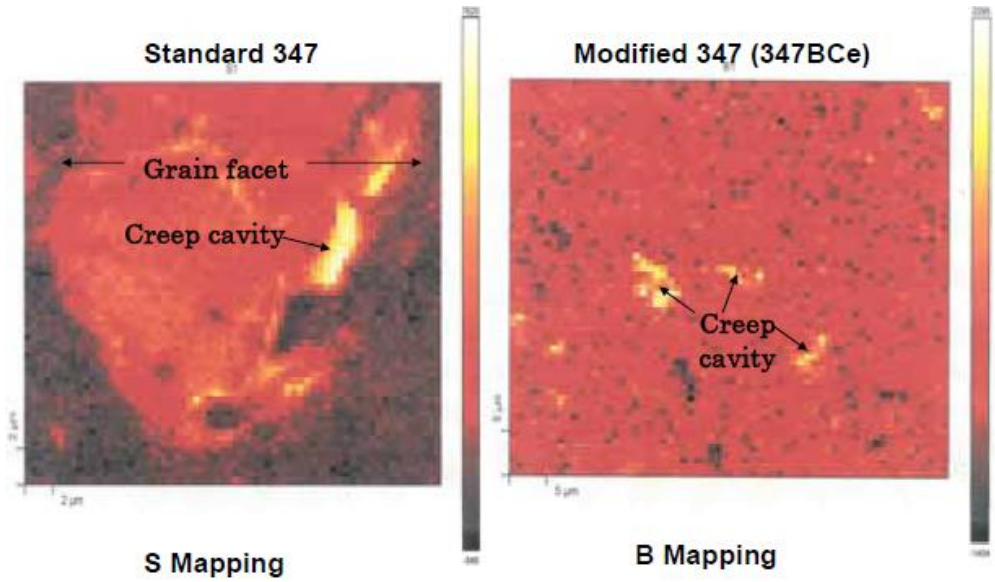


Figure 19. Auger S and B mapping of the fractured surfaces, creep exposed at 750℃and 69 MPa. In standard 347 steel, extensive segregation of S is shown on creep cavity surface and slight segregation on grain boundary, and in modified 347 steel segregation of B is noticed only on creep cavity surface.

The B segregation is expected to decrease the diffusivity along the creep cavity surface due to its relatively high melting point of around 2080℃. The suppression of creep cavitation observed in the modified 347 steel (Figures 15 and 17) is thought to be caused by the segregation of B on the creep cavity surface. The suppression of the creep cavitation should prevent from the steel causing early grain boundary fracture, which should increase significantly the creep rupture strength associated with increasing in ductility.

The segregation of B on creep cavity surface occurs autonomously and covers up the surface during high temperature service of the steel. The B segregated surface film prevents creep fracture due to suppression of creep cavity growth and provides the steels with superior creep rupture properties.

## Self Healing of Creep Cavity by BN Precipitation

The compound of BN is known to precipitate to outer free surface of B containing austenitic stainless steels with heating in vacuum. Stulen et al. [37] studied segregation of B onto outer free surface using an austenitic stainless steel of 21Cr-6Ni-9Mn, containing a bulk concentration of less than 10ppm of B. The segregation results with heating in vacuum show that B exhibits a strong surface activity at temperatures above 700℃. Above 700℃ B and N co-segregate to form a surface layer of BN which extends into the bulk of the steel. The results on 304L and 304LN further illustrate that the large concentration enhancement for B at the surface is due to the strong attractive B-N interaction. Thus, the surface N functions essentially as a chemical trap for the B, tying it to the surface. Nii et al. [38,39] also observed the precipitation of BN on outer free surface by heating in vacuum on a 304 austenitic stainless steel doped with N, B and Ce. They confirmed that the surface layer of BN uniformly covers almost all of the outer free surface by means of heating at 730℃ in vacuum, and also the layer itself is self healed by heating in vacuum again.

It may be possible to precipitate the BN thin layer on creep cavity surface during high temperature service of B containing austenitic stainless steels, since the inner surface of creep cavity is almost a vacuum. The precipitated BN thin film on creep cavity surface is expected to reduce creep cavity growth rate through suppressing surface diffusion rate at creep cavity surface since melting point of BN is considerably high (3000℃).

A 304 austenitic stainless steel was modified with additions of 0.07mass% of B, 0.064mass% of N, 0.33mass% of Ti and 0.008mass% of Ce, aiming at precipitation of BN onto creep cavity surface. Chemical compositions of the melted standard 304 and the modified 304 (corresponding to type 321) austenitic stainless steels are shown in Table 4. The additions of Ce and Ti are expected to remove soluble S through the formation of $Ce_2O_2S$ [31] and $Ti_4C_2S_2$ [32], respectively. In the absence of the S segregation, B and N become possible to segregate onto the creep cavity surface simultaneously and form BN compound there. The standard 304 steel was subjected to a solution heat treatment at 1130℃ for 29min, whereas the modified 304 steel was solution treated for 20min at 1180℃.

**Table 4. Chemical compositions of standard 304 and modified 304 austenitic stainless steels (mass %)**

| Steel | C | Si | Mn | P | S | Ni | Cr | B | N | Ti | Ce |
|---|---|---|---|---|---|---|---|---|---|---|---|
| Stan.304 | 0.082 | 0.49 | 1.62 | 0.021 | 0.009 | 10.05 | 19.07 | ----- | 0.0072 | ---- | ----- |
| Mod.304 | 0.096 | 0.50 | 1.52 | 0.020 | 0.002 | 10.07 | 19.16 | 0.070 | 0.0635 | 0.33 | 0.008 |

For preliminary experiments of BN precipitation, the B containing modified 304 steel was tensile tested, and a specimen including cavities in a necked zone was obtained by stopping the test just after forming a necking zone and before fracture. Samples taken from the specimens were heated for 120min at 750℃ and then fractured under impact loading at liquid nitrogen temperature in AES chamber. On the fractured surface, tensile cavities were observed. From the exposed tensile cavity surface, Auger spectra were obtained. The tensile cavities on the fractured surface and the obtained Auger spectrum are shown in Figures 20

and 21. The sharp and high peaks of B and N were observed, which indicate that B and N segregate simultaneously and cover extensively the tensile cavity surface. From the positions and shapes of B and N peaks, which are the same as those reported by Stulen et al. [37], it was concluded that the co-segregated B and N form the stable compound of BN [37,39]. The surface of tensile cavity should be covered extensively with the BN layer since peaks of other elements were not observed (Figure 21). The present preliminary experiment suggested that the stable compound of BN should precipitate onto creep cavity surface during creep exposure of the steel.


Figure 20. Tensile cavities observed by SEM on fractured surface of tensile tested specimen of B containing modified 304 steel.

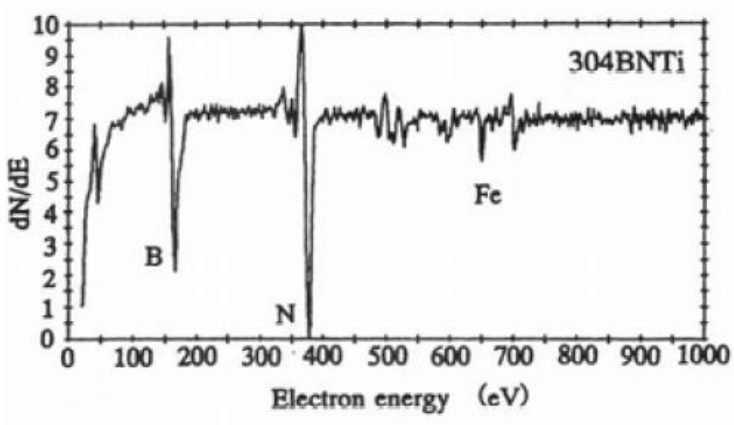


Figure 21. Auger spectrum obtained from surface of tensile cavity in tensile tested specimen heated for 120min at 750℃. The positions and shapes of B and N peaks indicate formation of BN compound at the surface.

The results of creep rupture tests carried out at 750℃ are shown in Figure 22. It is indicated that the addition of minute amount of B and Ce increases creep rupture strength coupled with ductility significantly, which is more pronounced on longer creep exposure. The creep cavities in the ruptured specimens of the modified 304 steel are few and fine as shown in Figure 23, when compared to those of the standard 304 steel. It is indicated that the creep cavity growth is suppressed remarkably in the modified 304 steel, which should give the improved creep rupture properties due to preventing the grain boundary fracture.

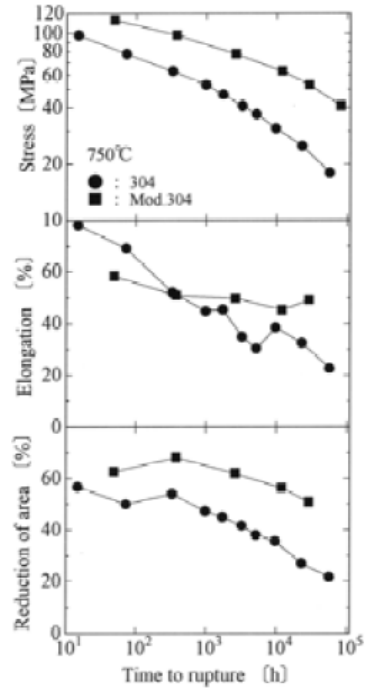


Figure 22. Creep rupture properties (strength, elongation and reduction of area) at 750℃of standard 304 and modified 304 steels. Modified 304 steel shows higher rupture strength and ductility, particularly for longer rupture life.

The crept specimens were fractured by impact loading at liquid nitrogen temperature in the AES chamber to expose the creep cavity surface. Figures 24 and 25 show facture surfaces with creep cavities and Auger spectra obtained from the creep cavity surfaces in the standard and the modified 304 steels, respectively. The sharp and high peak of S was observed in the standard 304 steel. In the modified 304 steel, the peaks of B and N on the creep cavity surface were observed, whereas the presence of S was not observed. The energy positions and the shapes of B and N peaks indicate that the segregated B and N form the stable compound of BN [37, 39]. In addition to the peaks of B and N, comparatively high peaks of C and O, resulting from the contamination, were observed. To find the suitable creep cavities for the AES observation on the fractured surface, it took longer time, since the creep cavities are few and fine in the steel. The delay might be the reason why the higher peaks of C and O, which are main contaminates in the residual gas in the AES chamber, were observed. The creep cavities in the notched specimen of the modified 304 steel were subjected to significant deformation by impact loading. The deformation may be also the reason why the peaks of B

and N are comparatively low when compared with those of tensile cavity (Figure 21). Figure 26 shows the shapes of elemental B peak in the modified 347 steel and B and N peaks of BN in the modified 304 steel. Auger peaks of elemental B and B as BN are clearly different.

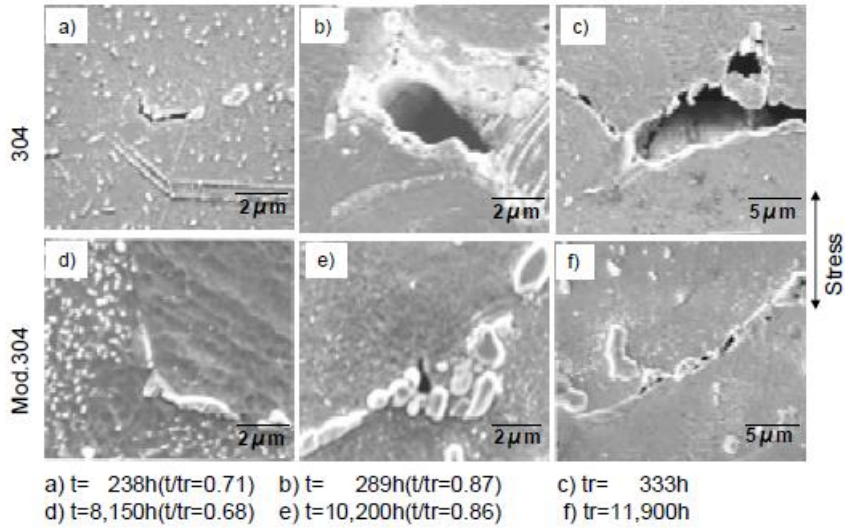


Figure 23. Scanning electron micrographs showing creep cavities in specimens crept at 750℃and 63MPa. Creep cavity growth in modified 304 steel is suppressed remarkably.

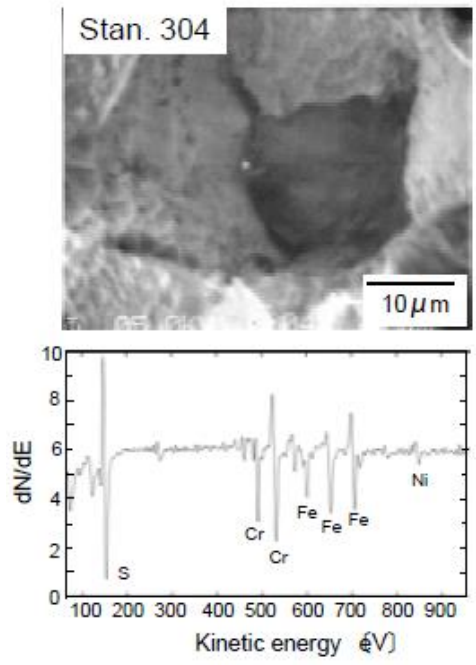


Figure 24. Scanning electron micrograph showing creep cavity surface, exposed by breaking at liquid nitrogen temperature under impact loading, of 304 steel crept for 290h ( t/tr=0.87) at 750℃and 63MPa, and Auger spectrum obtained from creep cavity surface.

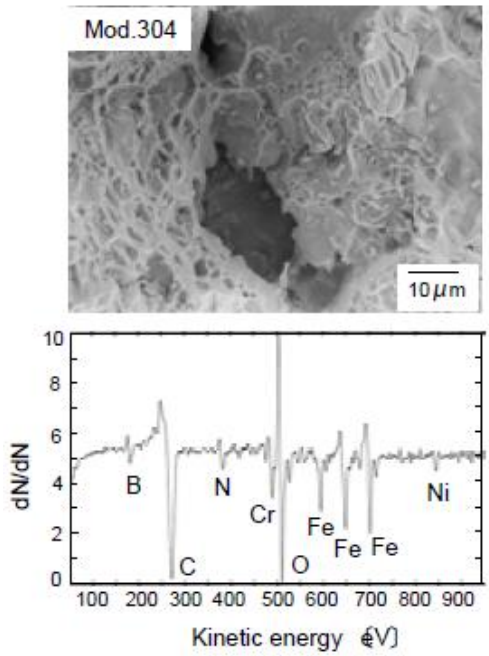


Figure 25. Scanning electron micrograph showing creep cavity surface, exposed by breaking at liquid nitrogen temperature under impact loading, of modified 304 steel crept for 10,200h (t/tr=0.86) at 750℃and 63MPa and Auger spectrum obtained from the creep cavity surface.

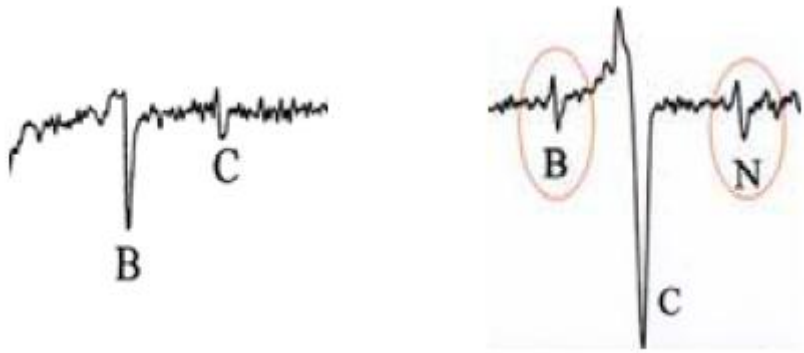


Figure 26. Comparison of Auger peak shapes between segregated B in modified 347 steel and segregated B and N in modified 304 steel. Different peak shapes of elemental B and B as BN compound are shown.

The X-ray diffraction patterns were obtained from the precipitate of the modified 304 steel after creep rupture tests. The pattern in shown in Figure 27 indicates the presence of $Ti_4C_2S_2$ and $Ce_2O_2S$. The co-addition of Ce and Ti should be highly effective to remove the soluble S in the steel and to prevent from its depositing on the creep cavity surface. In the absence of S contamination, B and N become possible to segregate onto creep cavity surface and form the filmy BN precipitates there, which reduce the creep cavity growth rate significantly (Figure 23). The suppression of the creep cavity growth rate provides the

modified 304 steel with higher rupture strength coupled with ductility, particularly for longer rupture time region (Figure 22).

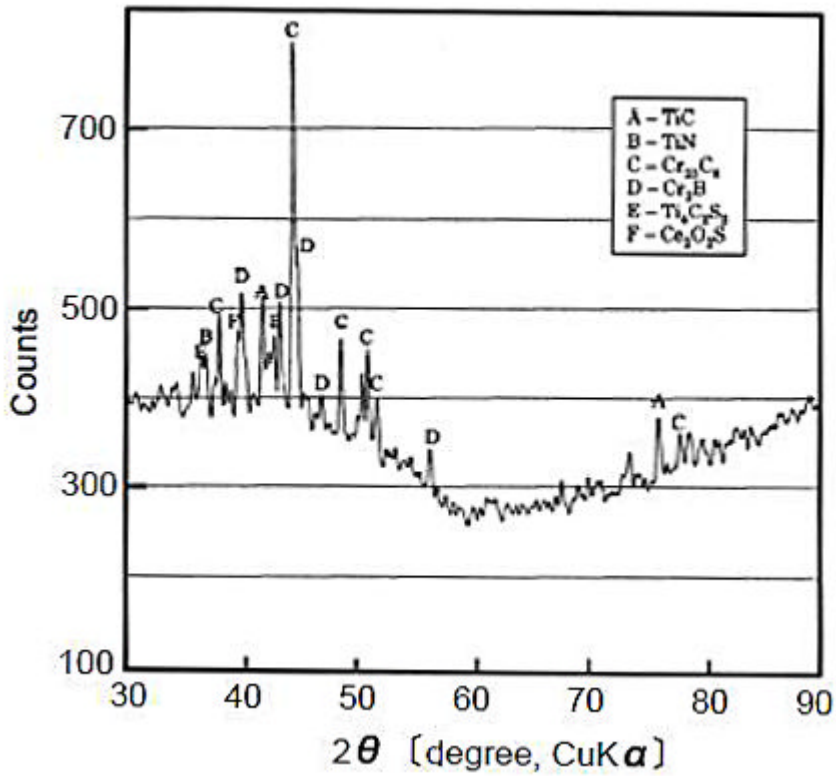


Figure 27. X-ray diffraction analysis of precipitate, extracted by electrochemical method from B containing modified 304 steel, creep tested at 63MPa, 750℃.

Creep rupture properties of the present modified 304 austenitic stainless steel and conventional 304 and 321 austenitic stainless steels for high temperature use, are shown to compare in Figure 28. The plots for the conventional 304 and 321 austenitic stainless steels include data on 9 heats for each of the two type steels, respectively, which were creep rupture tested at National Institute for Materials Science Japan. Absolute higher creep rupture strength and ductility of the modified 304 steel (304BNTi) than those of SUS 304 H (18Cr-8Ni) and SUS 321 H (18Cr-10Ni-Ti) steels was shown, particularly for prolonged creep rupture life region. This remarkable improvement in rupture properties is thought to be derived from the precipitation of BN onto creep cavity surface. It is indicated clearly that the BN precipitation is an excellent method not only to extend lives of high temperature structures by providing them with self healing ability but also develop superior heat resisting steels by preventing the notorious grain boundary creep fracture. The comparison of creep rupture properties between the modified 347 steel (Figure 14) and the modified 304 steel (Figure 22) indicates that the precipitation of BN gives rise to the higher rupture strength and ductility, particularly at longer rupture life than those of B segregation. The higher melting point and finer layer of BN than that of elemental B should be the reason for the superiority.

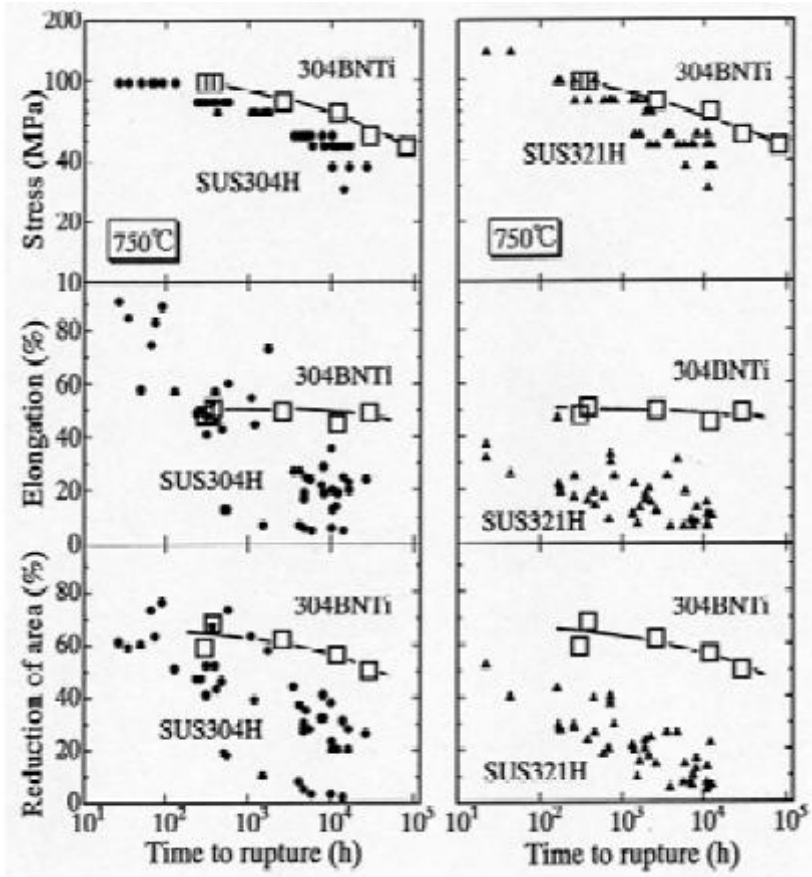


Figure 28. Comparison of creep rupture properties between modified 304 steel (304BNTi) and conventional 18-8 based austenitic stainless steels (304 and 321).

The B segregation and BN precipitation formed by minute addition of B, Ce and N suppress creep cavity growth remarkably through self-healing of creep cavity surface. The self-healing provides the steels with higher creep rupture strength and ductility. This new method of self-healing of material damage by microalloying should be applied to developing and improving new steels.

## CONCLUSION

Trace and microalloying elements sometimes cause unexpected deteriorations or improvements in creep rupture properties of heat resistant steels. The trace and microalloting elements are able to move freely at high temperatures, and segregate or precipitate at vital spots in heat resistant steels such as dislocation, grain boundary, interface between matrix and inclusion, creep damage and other parts. The segregated or precipitated elements sometimes cause premature fracture or heal material damage even if amount of the element is trace or minute. At National Institute for Materials Science Japan, long time creep rupture tests are being carried out on several heats of main high temperature materials. By analyzing the data

the mechanism of the deterioration was clarified, and also new methods of creep damagehealing were reported in this chapter. Followings are conclusions:

- The relation between long time creep rupture times and very small amount of Mo was analyzed on 21 heats of high strength carbon plate steels. The rupture lives at lower stress showed linear relation with Mo amount of 0.006 -0.10mass%. The microaloyed Mo atoms move freely to forms pairs with C and N atoms which interact with dislocation. It is thought that the interaction immobilizes dislocation and provides the steel higher rupture strength.
- Type 304 and 316 austenitic stainless steels with higher amount of Al than 0.03mass% showed creep rupture strength drop. The strength drop was accompanied with precipitation of AlN at σ phase on grain boundary. Creep cavities were nucleated very early at the interfaces between AlN andσ phase. The early formation of creep cavities lead to the premature creep rupture and the strength drop.
- Higher rupture strength heat resistant steels rupture due to creep cavity nucleation and growth process. The creep cavity growth rate is controlled by surface diffusion of creep cavity. Segregation and precipitation of stable elements at creep cavity surface suppress the creep cavity growth markedly. By microalloying of B, N and Ce, B segregates and BN precipitates at creep cavity surface. The B segregation and BN precipitation suppressed creep cavity growth remarkably. The segregation and precipitation are formed autonomously during creep and self-heal creep damage.

## ACKOWLEDGMENTS

The author would like to thank Mr. Kyono of National Institute for Materials Science Japan and Dr. Laha of IndiraGandhiCenter for Atomic Research India for their experimental practices, analyses and preparing figures.

## REFERENCES

[1] DeArdo, A.J., Microalloyed strip steels for the 21st century, Mater. Sci. Forum, 284-286, 1998, 15-26.

[2] Wang, Y., Mayer, K-h, Schlz, A., Berger, C., Chilukuru, H., Durst, K., Blum, W., Development of new 11%Cr heat resistant steels with enhanced creep resistance for steam power plants with operating steam temperatures up to 650℃, *Mater. Sci. Eng*., A510-511, 2009, 180-184.

[3] Uehara, T., Fujita, T., Improvement of creep rupture strength of 12% Cr ferrite heat-resistant steel (in Japanese), TAFR650, *Hitachi Gihou*, 19, 2003, 61-66.

[4] Holt, R.T., Wallace, W., Impurities and trace elements in nickel-base superalloys, *Int. Met. Rev*., 21, 1976, 1-24.

[5] Horiuchi, H., Igarashi, M., Abe, F., Improved utilization of added B in 9Cr heat-resistant steels containing W, *ISIJ Inter*., 42, 2002, S67-S71.

[6] NRIM Creep Data Sheet No.25B, Data Sheets on the Elevated-Temperature Properties of High Strength Steel (Class 590 MPa) Plates for Pressure Vessels, *National Institute for Materials Science*, (1994).

[7] NRIM Creep Data Sheet No.4B, Data Sheets on the Elevated –Temperature Properties of 18Cr-8Ni Stainless Steel for Boiler and Heat Exchanger Seamless Tubes (SUS 304 HTB), *National Research Institute for Metals*, (1986).

[8] NRIM Creep Data Sheet No.6B, Data Sheets on the Elevated-Temperature Properties of 18Cr-12Ni-Mo Stainless Steel Tubes for Boilers and Heat Exchangers (SUS 316 HTB), *National Institute for Materials Science*, (2000).

[9] NRIM Creep Data Sheet No.5B, Data Sheets on the Elevated –Temperature Properties of 18Cr-10Ni-Ti Stainless Steel for Boiler and Heat Exchanger Seamless Tubes (SUS 321 HTB), *National Research Institute for Metals*, (1987).

[10] NRIM Creep Data Sheet No.28B, Data Sheets on the Elevated-Temperature Properties of 18Cr-12Ni-Nb Stainless Steel Tubes for Boilers and Heat Exchangers (SUS 347 HTB), *National Institute for Materials Science*, (2001).

[11] N. Shinya, J. Kyono, H. Tanaka, M. Murata, S. Yokoi, Creep rupture properties and creep fracture mechanism maps for type 304 stainless steel(in Japanese), *Tetsu-to-Hagané*, 69 (14) (1983) 1668-1675.

[12] Shinya,N., Tanaka, H., Murata,M., Kaise,M., Yokoi,S., Creep fracture mechanism maps based on creep rupture tests up to about 100 000h for type 316 stainless steel(in Japanese), *Tetsu-to-Hagané*, 71 (1) (1985) 114-120.

[13] Miller,D.A., Langdon,T.G., Creep fracture maps for 316stainless steel, *Metall. Trans. A*, 10A (1979) 1635-1641.

[14] Hull, D., Rimmer,D.E., The growth of grain-boundary voids under stress, *Philos. Mag*., 4 (1959) 673-687

[15] Raj,R., Shih, H.M.,Johnson,H.H., Correction to"intergranular fracture at elevated temperature", *Scr. Mettall*., 11 (10) (1977) 839-842.

[16] Edward, G.H., Ashhby,M.F., Intergranular fracture during power-law creep, *Acta Metall*., 27 (1979) 1505-1518.

[17] Assassa, W., Guiraldeng, P., Bulk and grain diffusion on $^{59}$Fe, $^{51}$Cr, and $^{63}$Ni in austenitic stainless steel under influence of silicon, *Met. Sci*., 12 (1978) 123-128.

[18] Shinya, N., Kyono, J. and Laha, K., Self-healing efeect of boron nitride precipitation on creep cavitation in austenitic stainless steel, *JIMSS*, 17,2006, 1127-1133.

[19] Laha, K., Kyono, J. and Shinya, N., *Philos. Mag*., Some chemical and microstructural factors influencing creep cavitation resistance of austenitic stainless steels, 87,2007, 2483-2505.

[20] Laha, K., Kyono, J. and Shinya, N., *Scr. Mater*., An advanced creep cavitation resistance Cu0containing 28Cr-12Ni-Nb austenitic stainless steel,56,2007, 915-918.

[21] Shinya, N., and Kyono, J., *Mater. Trans*., Beneficial effect of boron nitride surface precipitation on cavitation and rupture properties, 47,2006, 2302-2307.

[22] 22. Laha, K., Kyono, J., Sasaki, T., Kishimoto, S. and Shinya, N., Improved creep strength and creep ductility of type 347 austenitic stainless steel through the self-healing effect of boron for creep cavitation,*Metall. Mater. Trans. A*,36A, 2005, 399-409.

[23] Laha, K., Kyono, J., Kishimoto, S. and Shinya, N., Beneficial effect of B segregation on creep cavitation in a type 347 austenitic stainless steel,*Scr. Metall. Mater*., 52, 2005, 675-678.
[24] Kyono, J. and Shinya, N., *JSMS*, Self-healing of creep cavities formed in austenitic stainless steel (in Japanese), 52,2003, 1211-1216.
[25] Shinya, N., Kyono, J. and Kushima, H., *ISIJ Int*., Creep fracture mechanism map and creep damage of Cr-Mo-V rotor steel, 46,2006, 1516-1522.
[26] Needham, N.G. and Gladman, T., *Met. Sci*., Nucleation and growth of creep cavities in a Type 347 steel, 14, 1980, 64-72.
[27] Nix, W.D., YU, K.S. and Wang, J.S., The effect of segregation on the kinetics of intergranular cavity growth under creep condition, *Metall. Trans. A*, 14A, 1983, 563-570.
[28] White, C.L., Padget, R.A. and Swindeman, R.W., Sulfur and phosphorus segregation to creep cavities and grain boundaries in 304 SS, *Scr. Metall*., 15, 1981, 777-782.
[29] Rhead, G.E., Diffusion on surfaces, Surf. Sci.,247,1975, 207-221.
[30] Delamare, F. and Rhead, G.E., *Surf. Sci*.,Increase in the surface self-diffusion of copper due to the chemisorption of halogens, 28, 1971, 267-284.
[31] Cosandey, F., Li, D., Sczerzenie, F. and Tien, J.K., The effect of cerium on high temperature tensile and creep behavior of a superalloy, *Metall. Trans. A*, 14A,1983, 611-621.
[32] Hua, M., Garcia, C.J. and DeArdo, A.J., Multi-phase precipitation in interstitial-free steels, *Scr. Metall*., 28, 1993, 973-978.
[33] Riedel, H., Fracture at High Temperatures (Springer, Berlin), 1987.
[34] Good, S.H. and Nix, W.D., *Acta Metll*., The kinetics of cavity growth and creep fracture in silver containing implanted grain boundary cavities, 26, 1979, 739-752.
[35] Minami, Y., Kimura, H. and Ihara, Y., *Mater. Sci. Technol*., Microstructural changes in austenitic stainless steels during long-term aging,2,1986, 795-806.
[36] Sourmail, T., Precipitation in creep resistant austenitic stainless steels, *Mater. Sci. Technol*., 17, 2001, 1-14.
[37] Stulen, R.H. and Bastasz, R., Surface segregation of boron in nitrogen-strengthened stainless steel, *J. Vac. Sci. Technol*.,16, 1979, 940-945.
[38] Yoshihara, K., Tosa, M. and Nii, K., *J. Vac. Sci. Technol. A*, Surface precipitation of boron nitride on the surface of type 304 stainless steels doped with nitrogen boron, and cerium, 3,1985, 1804-1808.
[39] Nii, K. and Yoshihara,K., Surface precipitation and its application to coatings,*J. Mater. Eng*., 9,1987, 41-50.

In: Advances in Mechanical Engineering Research. Volume 2 ISBN: 978-1-61761-984-7
Editor: David E. Malach 

*Chapter 5*

# SEISMIC ANALYSISOF ALOW-COST MASONRY HOUSE USING ELASTOMERIC BEARINGS AND SHAPE MEMORY ALLOYS

***Rachel L. Calafel[a], Paul N. Roschke[a,*] and Maria O. Moroni[b]***
[a]Zachry Department of Civil Engineering, Texas A&M University, 3136 TAMU, College Station, TX 77843, USA
[b]Department of Civil Engineering, University of Chile, Casilla 228/3, Santiago, Chile

## ABSTRACT

The mitigation of seismic damage to masonry housing structures is considered in this study. Traditional high-damping rubber bearings (HDRBs), two hybrid systems involving the use of HDRBs and shape memory alloy (SMA) wire, and fiber-reinforced bearings (FRBs) are numerically modeled as base isolators for a typical confined masonry, two-family house. The house is elastically modeled using multiple degrees-of-freedom (MDOF) that are based on experimental data collected through ambient vibration testing. Fuzzy logic is utilized to numerically model dynamic behavior of the HDRBs, SMA wire, and FRBs based on experimental and analytical data. The earthquake used for optimization of each isolation system is generated to match the design spectrum based on Chilean code through means of RSPMatch2005, an algorithm thatmodifies historic ground motions in the time domain through incorporation of wavelets. A suite of ground motions is used to evaluate seismic performance of the structure that is augmented with each of the isolation systems mentioned; results are compared to the performance of the traditionally-constructed structure. Simulations indicate that each of the isolation systems can be effective in reducing the structural shear, interstory drift, and floor acceleration of the structure compared to the fixed-base case, although the HDRB-only system exhibits superior performance overall.

*Keywords:* Ambient vibration testing, Fiber-reinforced bearings, Fuzzy logic, Elastomeric bearings, Confined masonry, Seismic analysis, Shape memory alloy, Wavelet analysis.

* Corresponding author. Tel.: +1 979 845 1985; E-mail address: p-roschke@tamu.edu (P.N. Roschke).

## 1. INTRODUCTION

The largest earthquake ever experimentally recorded occurred in southern Chile on May 22, 1960. The moment magnitude 9.5 earthquake was followed by a series of earthquakes, tsunamis, flooding, and landslides in Chile and in places as far away as Hawaii and Japan (National Geophysical Data Center). In fact, Chile has experienced over 75 earthquakes with Richter magnitude 7.0 or greater since 1900 (Servicio Sismologico). Because of the strong seismicity of Chile, the construction of structures to resist seismic loads is of great importance. Many structures in Chile, including low-cost housing structures, are constructed of confined masonry. Confined masonry is comprised of masonry walls that are confined by reinforced concrete columns and beams. The masonry walls are the main load-bearing elements, as they transmit both gravity loads and lateral loadsto the foundation (Murty *et al.* 2006). Performance of a confined masonry structure subjected to earthquake excitation depends significantly on design of the structure and the quality of its construction.

Based on previous experience, Moroni *et al.* (2004) identified the potential deficiencies of confined masonry walls as: (1) limited in-plane shear strength; (2) limited ductility; (3) lack of tie columns at all wall openings, thus reducing the shear strength and displacement capacity; (4) excessive distance between tie columns or lack of tie beams that may cause out-of-plane damage; and (5) shear cracks that propagate through the tie columns and reduce the wall stiffness and resistance capacity. However, they concluded that most confined masonry buildings have "appropriate seismic behavior." Moroni *et al.* (1996) explained that seismic codes are developed to ensure serviceability requirements for frequent moderate earthquakes and life safety for major earthquakes, thereby allowing extensive damage to occur in major earthquakes as long as collapse is prevented. As evidenced by the diagonal cracks at the first story level, shear damage to a confined masonry building resulting from the 1985 Chilean earthquake is shown in Figure 1. Because families residing in low-cost houses generally cannot afford to purchase a new house or perform extensive repairs to their home and its contents, it is important to prevent damage to the masonry homes, their contents, and the inhabitants.

Figure 1. Three-story confined masonry building; Melipilla, Chile, on March 3, 1985.

Seismic isolation theory shows that the reduction of seismic loading by an isolation system for a relatively stiff low-rise structure, such as a masonry house, is influenced primarily by the ratio of the isolated period to the fixed-base period. According to Kelly (2002), because the period of a masonry block or brick building that has a fixed-base is approximately 0.1 sec, an isolation period of 1 sec or longer would significantly reduce seismic loads on the structure and would not require design for a large displacement of the isolator.

One common method of seismic isolation is by means of elastomeric bearings, which include high-damping rubber bearings (HDRBs) and lead rubber bearings (LRBs). De la Llera *et al.*(2004) summarized the results of a testing program conducted on more than 260 full-scale elastomeric isolators. They concluded that the elastomeric compounds can be accurately represented by testing reduced-scale specimens. Although primarily referring to hospitals and other large structures, De la Llera *et al.* (2004) stated that seismic isolation is both a technically and economically feasible option for building design in Chile. Several numerical formulations have been proposed to model the hysteretic behavior of elastomeric bearings. Pan and Yang (1996) and Hwang *et al.* (2002) each proposed an analytical formulation for elastomeric bearings.

In addition to elastomeric isolators, the use of shape memory alloys (SMAs) has been suggested for application in the seismic protection of buildings in recent years (Bruno and Valente 2002). SMAs, including nickel-titanium (NiTi) and copper-aluminum-beryllium (CuAlBe), among others, are a certain class of metals that can undergo large strains and recover their initial shape at the end of the deformation process (Dolce *et al.* 2007). SMAs are characterized as exhibiting superelasticity at high temperatures and the shape memory effect at low temperatures (Andrawes and DesRoches 2007). SMAs can be introduced in a traditional base isolation system in order to, at least theoretically, eliminate plastic deformation of the structure, and to increase energy dissipation.In the current study, two hybrid base isolation systems, including the combined use of HDRBs and SMAs are analyzed.

Previous research related to base isolation devices that incorporate the use of SMAs has been performed. Wilde *et al.* (2000) carried out a numerical study on the use of a rubber bearing and SMA bar isolation system for application to highway bridges. The relative displacement of the bridge deck was decreased due to the isolation system, while the shear force transmitted to the pier and the acceleration response of the bridge were increased due to the isolation system. Dolce *et al.* (2007) performed shake table tests on reinforced concrete (RC) frames isolated using steel-teflon sliding bearings and SMA wire loops. They concluded that SMA-based isolation systems are able to protect non-structural elements even under strong earthquakes due to their significant softening behavior. However, Dolce *et al.* (2007) noted that although the isolation system involving steel-teflon sliding bearings and SMA-based devices produced favorable base displacement and base shear quantities, the resulting floor accelerations were often quite high.

Kelly (2002) performed experimental testing on elastomeric isolators that used fiber reinforcing plates instead of the typical steel reinforcing plates. The purpose of this study was to determine the feasibility of using fiber reinforcement to produce low-cost and lightweight elastomeric isolators for use in housing, schools, or other public structures in highly seismic regions of the world. The study concluded that it is possible to produce a fiber-reinforced strip isolator that matches the behavior of a steel-reinforced isolator. The fiber-reinforced bearing

(FRB) is significantly more lightweight and can be manufactured more easily than a traditional steel-reinforced isolator. Production of strips of FRBs would make the manufacturing process less expensive by avoiding the use of circular molds and allowing the strips to be cut to the appropriate size on-site. In addition, rectangular isolators would be more easily applied than circular bearings in structures that use walls as the lateral-resisting system. The use of fiber reinforcement instead of steel reinforcement would allow strips to be cut from a large specimen using a standard saw, and the lighter weight isolators would be easier to lift into place than conventional isolators.

The comparative study using HDRBs, HDRBs and SMA wires, and FRBs to base-isolate a confined masonry house that is reported here is an extension of previous comparative studies, such as the studies performed by Park *et al.* (2002) and Dolce *et al.* (2007). Although Park *et al.* (2002) considered the use of rubber bearings (RB) to isolate a bridge, the RBs were simulated using a bilinear model and no Chilean earthquakes were considered in the analysis. Also, while Dolce *et al.* (2007) used SMAs as part of a system to base-isolate an RC frame, they used two groups of SMA wires in combination with Teflon sliding bearings. In this study, the HDRBs are simulated using a nonlinear model, and the SMA wires are used with HDRBs in two different configurations. In addition, the structure studied here is a Chilean masonry house, not a bridge or an RC frame. The study of FRBs as one of the isolation systems is an extension of current research of FRBs, which has focused on laboratory studies (Kelly 2002) rather than their numerical and experimental application to structures. The inclusion of the HDRB-only case in this study provides a benchmark for which to compare the other isolation systems. The performance of the structure isolated using each of the systems is compared to the performance of the traditionally-constructed fixed-base structure to assess the impact of each base isolation system.

## 2. Model of Case Study Structure

### 2.1. Ambient Vibration Testing

The case study structure selected is representative of a housing layout that is commonly built in thousands of homes that are currently under construction in the vicinity of Santiago, Chile, and in other parts of the world. A 110 $m^2$ two-story dwelling which serves as the residence of two families is shown in Figure 2. To determine its fundamental natural frequencies and periods, ambient vibration testing was performed on the case study structure in Maipú, Chile. Four SS-1 Ranger seismometers manufactured by Kinemetrics were used to record the velocities of the structure. A 16-bit Daqbook 200 with DBK 18 by IO Tech was utilized with a laptop computer as the data acquisition system. A 20 min test was recorded with a sampling rate of 200 Hz. No external excitation was applied to the structure. The orientations and locations of the seismometers are shown in Figure 3, where seismometers 1, 2, and 3 were on the second floor concrete slab, and seismometer 4 was located outside of the house on the soil at ground level. The longitudinal and transverse directions of motion are also identified in Figure 3.

Figure 2. Front view of test structure.

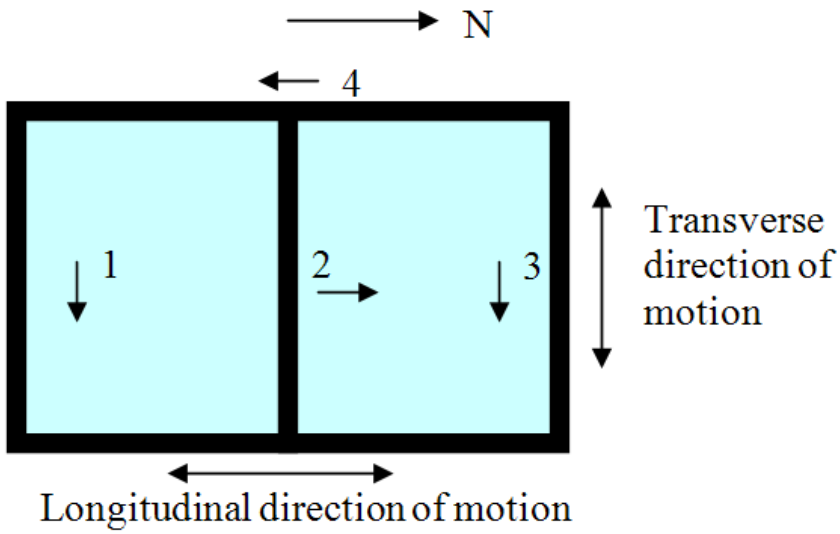


Figure 3. Second floor plan view and locations of seismometers.

The natural frequencies and periods are determined using a non-parametric system identification technique based on power spectra, transfer, and coherency functions (Boroschek *et al.* 2003). The structural periods are identified from the power spectral peaks and correlation analysis. The power spectral density (PSD) for each seismometer is included in Figure 4. The close correspondence between seismometers 1 and 3, which are both aligned in the transverse direction, is apparent. Figure 4(d) shows the response of the soil beneath the foundation of the case study structure. The soil is gravely in the top few meters. The influence of the soil on the seismic performance of the structure is not considered in the present study.

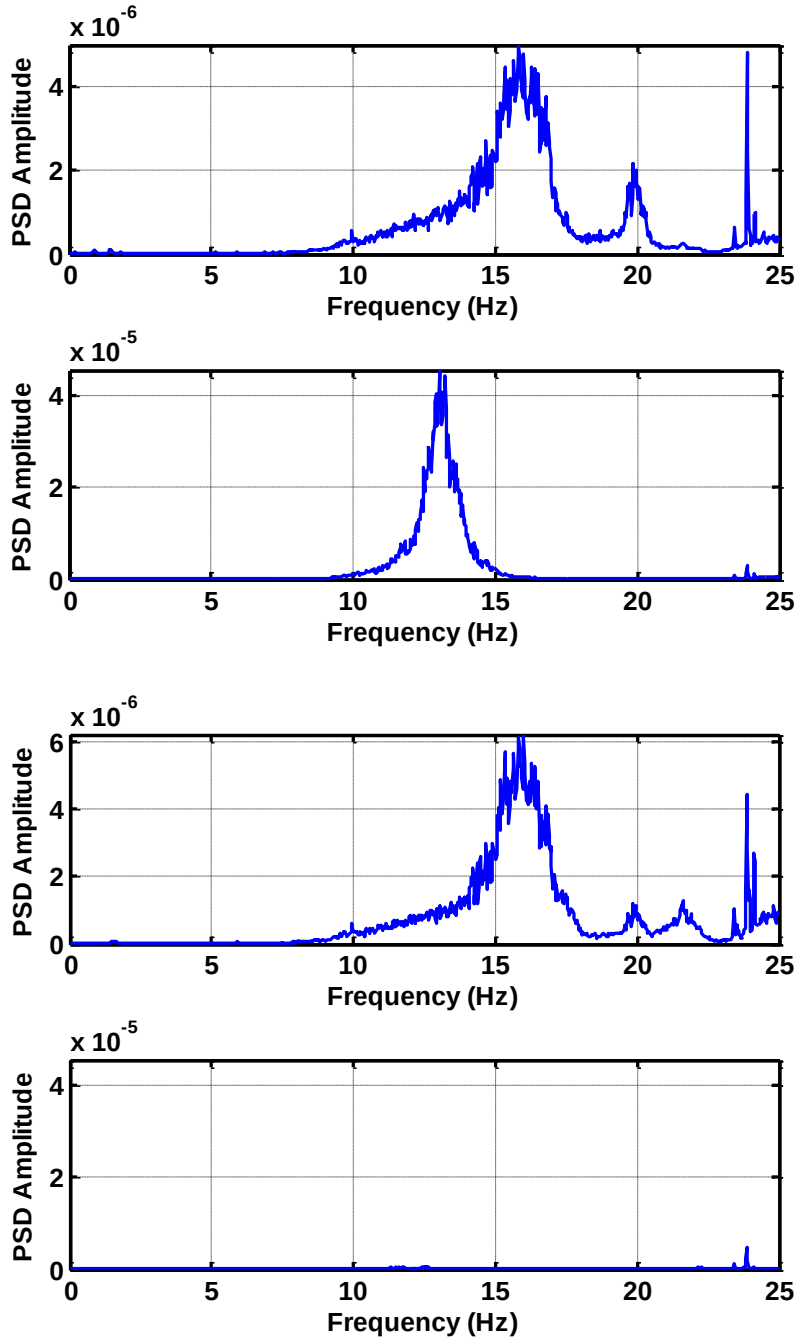


Figure 4.Power spectral density for seismometer (a) 1, (b) 2, (c) 3, and (d) 4.

Based on Figure4, it can be concluded that the natural frequencies corresponding to the first mode of the structure in the transverse and longitudinal directions are approximately 16 Hz and 13 Hz, respectively. The 16 Hz natural frequency corresponds to a period of 0.063 sec in the transverse direction, while the 13 Hz natural frequency corresponds to a period of 0.077 sec in the longitudinal direction. As expected, these periods are slightly less than those

measured by Astroza *et al.* (2005) for three- and four-story confined masonry buildings. The natural frequencies of the second mode of the structure can also be estimated. Based on the PSD, the natural frequencies of the second mode in the transverse and longitudinal directions are approximated as 20 Hz and 24 Hz, respectively. These values are confirmed by an initial finite element analysis of the structure.

## 2.2. Estimation of Equivalent Viscous Damping

An estimation of the equivalent viscous damping of the structure is made using the bandwidth method, in which $f_1$ and $f_2$ are the frequencies associated with one-half of the amplitude of the frequency peak (Boroschek *et al.* 2003). The formulation for the equivalent viscous damping is:

$$\psi = 0.5A\left(1-0.375A^2\right) \tag{1}$$

where:

$$A = \frac{f_2^2 - f_1^2}{f_2^2 + f_1^2},\ f_1 < f_2 \tag{2}$$

Using this method, the equivalent viscous damping of the structure in the transverse and longitudinal directions are approximately 5.77% and 3.82%, respectively. The difference in the equivalent viscous damping in the two directions is likely due to the strong sensitivity of the bandwidth method to the amplitude of the PSD. This sensitivity is also noted by Boroschek *et al.* (2003).

## 2.3. Mass Calculations

The two-family structure considered in this case study is analyzed using a multiple degree-of-freedom (DOF) model. The goal of numerical simulation with the model is to be able to analyze the effect of implementing the base isolation devices on the seismic behavior of the structure. The traditionally-constructed fixed-base house is modeled as a two DOF structure, while the base-isolated structure is modeled using three DOFs. The necessity of adding a third DOF for the modified structure is due to the fact that in order for a base isolation strategy to be implemented, the two-family house must have an RC slab-on-grade.It should be noted that only the seismic behavior of the house in the longitudinal direction is considered in this study (see Figure 3).

The mass of a 12 cm thick RC slab-on-grade is included in the total mass of the base-isolated structure. As required by *NCh433.Of96* (1996) 5.5.1, 25% of the live load on the structure is also included in mass calculations for the fixed-base and isolated structures. The only difference in the mass calculations for the two structures is that the fixed-base case does not include the mass of a RC slab-on-grade, while the base-isolated case does. The total mass

of the fixed-base and base-isolated structures are estimated as 67,400 and 83,900 kg, respectively. These calculations are made using the structural plans and unit weights included in the project specifications.

## 2.4. Stiffness Calculations

The classic equation of motion:

$$[M]\{\ddot{X}\} + [C]\{\dot{X}\} + [K]\{X\} = \{F\} \tag{3}$$

is applied to the two DOF model of the fixed-base structure to determine the stiffness values for each floor. In this equation $[M]$, $[C]$, and $[K]$ are the mass, damping, and stiffness matrices, respectively;$\{\ddot{X}\}$, $\{\dot{X}\}$, and $\{X\}$ are the acceleration, velocity, and displacement vectors, respectively; and $\{F\}$ is the external force vector. Writing these matrices out, the equation of motion is:

$$\begin{bmatrix} m_1 & 0 \\ 0 & m_2 \end{bmatrix} \begin{Bmatrix} \ddot{x}_1 \\ \ddot{x}_2 \end{Bmatrix} + \begin{bmatrix} c_1 + c_2 & -c_2 \\ -c_2 & c_2 \end{bmatrix} \begin{Bmatrix} \dot{x}_1 \\ \dot{x}_2 \end{Bmatrix} + \begin{bmatrix} k_1 + k_2 & -k_2 \\ -k_2 & k_2 \end{bmatrix} \begin{Bmatrix} x_1 \\ x_2 \end{Bmatrix} = \begin{Bmatrix} F_1 \\ F_2 \end{Bmatrix} \tag{4}$$

This equation can be solved for the general form when [*C*] = [0] and {*F*} = {0}. It should be noted that solving the equation of motion for the undamped, free vibration case yields the same stiffness values as that of the solution involving a small amount of damping. For the undamped, free vibration case, the solution of Eqn 4 is (Hart and Wong 2000):

$$\omega_1^2 = \frac{\left[\left(k_1 + k_2\right)m_2 + k_2 m_1\right] - \sqrt{\left[\left(k_1 + k_2\right)m_2 + k_2 m_1\right]^2 - 4m_1 m_2 k_1 k_2}}{2m_1 m_2} \tag{5}$$

In order to solve Eqn 5 for the values of $k_1$ and $k_2$, the ratio between the two values is calculated based on the amounts of masonry walls and RC columns per floor. These amounts are normalized with respect to the ratio of the concrete and masonry shear moduli. This assumption is consistent with findings by Moroni*et al.* (2000), who identify wall density as an appropriate indicator in determining the seismic vulnerability of a confined masonry structure. The result is that the first and second floors account for approximately 57% and 43% of the stiffness of the structure, respectively. This distribution is reasonable because the first floor has a larger area of masonry walls and concrete columns due to the vertical distribution of the masses. Using calculated values for $m_1$ and $m_2$,$\omega_1$ = 13 Hz (longitudinal direction), and the ratios between the stiffnesses, it follows from Eqn 5 that $k_1 = 4.33\times10^8$ N/m and $k_2 = 3.24\times10^8$ N/m.

## 2.5. Damping Calculations

Next components of the damping matrix of the structure are calculated using stiffness-proportional damping as follows (Chopra 2001):

$$[C] = a_1 [K] \tag{6}$$

where:

$$a_1 = \frac{2\zeta_1}{\omega_1} \tag{7}$$

and the natural frequency in the longitudinal direction of the first mode $\omega_1$ = 13 Hz, as measured by the ambient vibration testing. $[K]$ is the stiffness matrix as defined in Eqn 4, and the damping ratio $\zeta_1$ is taken to be 3.82% (see Section 2.2). Stiffness-proportional damping is applied to enable the fixed-base and base-isolated structures to have the same structural damping. The additional damping for the base-isolated structure is included in the models of each isolation device. Final calculated values for $[C]$ of the fixed-base structure in terms of *N* and *m* are as follows:

$$[C] = \begin{bmatrix} 7.08\times10^5 & -3.03\times10^5 \\ -3.03\times10^5 & 3.03\times10^5 \end{bmatrix} \tag{8}$$

# 3. EARTHQUAKE SELECTION

After the fixed-base structure has been selected and its fundamental dynamic properties have been determined by means of experimental tests and numerical analyses, time-histories of earthquake excitations that are used to evaluate the dynamic behavior of the structure need to be determined. The excitation used for optimization of the parameters of each base isolation technique is selected to conform to *NCh2745.Of2003* (2003), thestandard seismic code that governs the design of base-isolated structures constructed in Chile. This section describes the use of a wavelet method to modify the time-history record of a historical Chilean earthquake to create an acceleration time-history that matches the design spectrum based on *NCh2745.Of2003*, and the selection of other ground motions to analyze the performance of the fixed-base and base-isolated structures.

There are several methods to create an earthquake acceleration time-history to fit a design response spectrum. Most commonly-used methods create an artificial time-series from white noise and adjust the record to conform to the required response spectra (Hancock *et al.* 2006). However, the disadvantages of using these methods are that the artificial records are dissimilar to real earthquake ground motions in the number of cycles, phase content, and

duration. The result is that it can take a large number of analyses to obtain stable estimates of the inelastic response of the structure.

The method used in this study to generate a suitable earthquake was developed by Hancock *et al.* (2006). This technique adjusts an acceleration time-history in the time domain by adding wavelets to an acceleration signal recorded from an actual earthquake. Details have been coded into a program named RSPMatch2005b. Using this program, existing earthquake acceleration-time histories are modified to match the elastic design spectrum specified by *NCh2745.Of2003*. The Arias intensity (Arias 1970), which is proportional to the integral over time of the acceleration time-history squared, of the resulting motion is then checked with that of the original motion for fidelity.

RSPMatch2005b requires three input files to generate an output file of the ground acceleration time-history. The first file defines the target spectrum, which was created using *NCh2745.*Of2003 for the case study structure using a target isolated period of 1.0 sec and a damping ratio of 10%, upon determining that there is not a significant difference in the design spectra created using a target isolated period of 1.0 sec and damping ratios of 10, 15, and 20%. The case study structure located in Maipú, Chile, is characterized as being in seismic zone II.

The second file required contains a seed accelerogram. The accelerogram to be adjusted should be from a recorded significant seismic event that preferably occurred in a geographical region that is reasonably close and similar to the site of the structure that is being studied. Moreover, to minimize the amount of adjustment required by wavelets, the seed accelerogram should have a spectral shape and amplitude that is similar to that of the target accelerogram. In this study, the S80E component of the 1985 Chilean earthquake as measured in Llolleo, Chile, is utilized. The earthquake is scaled by a factor of 1.5 to speed convergence.

The third file required is an input file that specifies many parameters for the analysis by RSPMatch2005b, including the number of passes made by the program, the maximum number of iterations, the tolerance, the type of wavelet model to use, and the frequency range for spectral matching, among others. Three passes were specified to achieve an optimal match.

Output from RSPMatch2005b includes the modified acceleration time-history, the spectral response for the periods which were requested to be matched, and the average and maximum misfit for each iteration. The output is checked by plotting the target and resulting response spectra and the Arias intensity, which is a measure of the energy content introduced into the record, of the ground motion used for matching with the resulting ground motion (Hancock *et al.* 2006). Figure 5 shows a comparison between the 1985 Llolleo earthquake motion scaled by a factor of 1.5 and the earthquake record resulting from RSPMatch2005b.

To make a comparison of the performance for each isolation system and a recommendation of the most appropriate device for the case-study structure, a suite of earthquake time-histories is used to test the performance. Each earthquake is applied to the fixed-base and base-isolated structures and their dynamic responses are tabulated according to a set of metrics discussed in a subsequent section. The earthquake time-histories utilized in the analysis are listed in Table1, along with their PGA value. It should be noted that the 1985 Llolleo and the RSPMatch earthquake acceleration time-histories are scaled by a factor of one-half to prevent excessive displacement of the FRBs. Figure 6 shows the response spectrum for each earthquake considered in the analyses. The diversity of the earthquakes selected is evident.

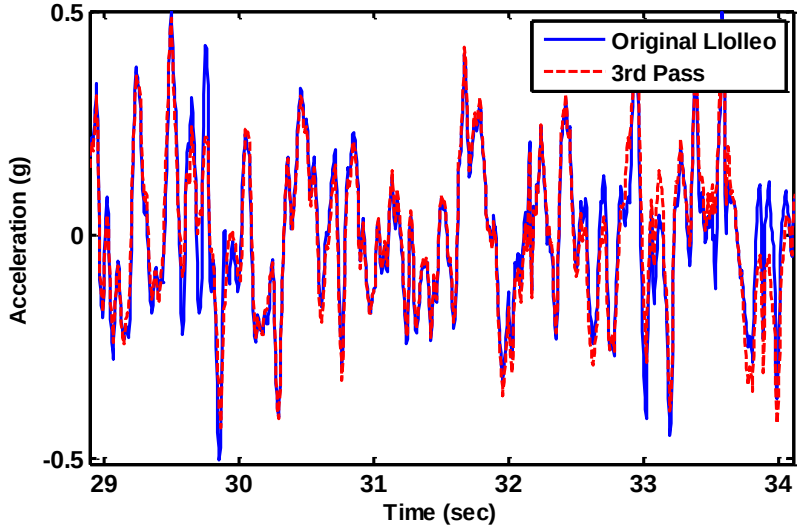


Figure 5. Time-history, Maipú base-isolated, 10% damping, $T_{iso}$ = 1.0 sec.

**Table 1. Earthquakes used in analyses**

| Earthquake | PGA (g) |
|---|---|
| 1981 Chile LPAN | 0.527 |
| 1985 Llolleo, Chile N10E | 0.653 |
| 2005 Tarapacá, Chile EW | 0.720 |
| 1940 El Centro S00E | 0.348 |
| RSPMatch based on *NCh2745*, $T_{iso}$ = 1 sec | 0.561 |

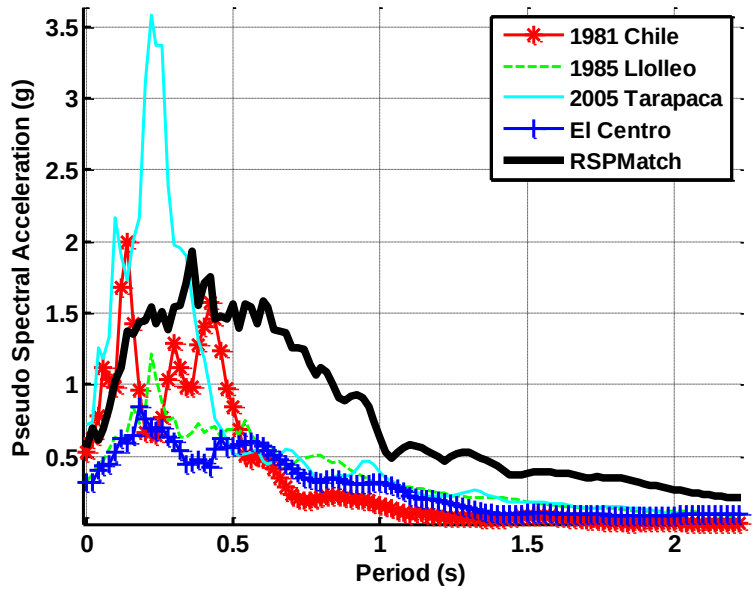


Figure 6. Response spectrum for each earthquake.

## 4. NUMERICAL MODELS AND OPTIMIZATION OF EACH DEVICE

Each of the isolation devices is modeled using a neuro-fuzzy approach that involves a training procedure incorporating experimental data. The output of each fuzzy inference system (FIS) is the force that the device exerts on the structure. The devices considered in this study are optimized by selecting the most appropriate bearings for the structure, and through a trial and error optimization of the number and length of SMA wires. The RSPMatch earthquake which was generated to match the design spectrum for the structure is the ground motion utilized in the optimization procedure. Eight bearings are used in each isolation system, due to the geometry and load of the structure. Kim and Roschke (2006) provide information on the application of fuzzy logic to model FPS bearings and a magnetorheological damper.

The effectiveness of each set of parameters for a given isolation system is quantified in terms of performance indices (PIs). The seven PIs considered in this study are peak base shear ($J_1$), peak base displacement ($J_2$), root-mean-squared (RMS) base displacement ($J_3$), RMS absolute floor acceleration ($J_4$), peak structural shear at the first story level ($J_5$), peak interstory drift for both floors ($J_6$), and peak absolute acceleration for both floors ($J_7$). $J_2$ and $J_3$ are not normalized with respect to the fixed-base case because this structure does not experience base displacement. However, for the normalized PIs, values less than unity indicate a reduction in response from that of the fixed-base case. The objectives are defined as follows (Narasimhan *et al.* 2006):

$$J_1 = \frac{\max_t \left| V_{0,isolated} \right|}{\max_t \left| V_{0,\,fixed} \right|} \tag{9}$$

$$J_2 = \max_t \left| d_i \right| \tag{10}$$

$$J_3 = \max \left| \sigma_d(t) \right| \tag{11}$$

$$J_4 = \frac{\max_f \left| \sigma_{a,isolated}(t) \right|}{\max_f \left| \sigma_{a,\,fixed}(t) \right|} \tag{12}$$

$$J_5 = \frac{\max_t \left| V_{1,isolated} \right|}{\max_t \left| V_{1,\,fixed} \right|} \tag{13}$$

$$J_6 = \frac{\max_f \left| d_{f,isolated}(t) \right|}{\max_f \left| d_{f,fixed}(t) \right|} \tag{14}$$

$$J_7 = \frac{\max_f \left| a_{f,isolated}(t) \right|}{\max_f \left| a_{f,fixed}(t) \right|} \tag{15}$$

where $V_0$ is base shear, $d_i$ is the peak displacement of any isolator, $\sigma_d(t)$ is the RMS base displacement, $\sigma_a(t)$ is the RMS acceleration, $V_1$ is structural shear at the first story level, $d_f$ is the peak interstory drift between two floors, and $a_f$ is the peak acceleration of any floor. The subscripts *t*, *i*, and *f* refer to all time, isolators, and floors, respectively.

## 4.1. HDRB Model and Optimization

There have been relatively few analytical models of HDRBs that can be used to perform time-history analyses of isolated structures. One analytical model, proposed by Pan and Yang (1996), uses two equations with a total of 11 parameters ($b_1$ to $b_{11}$) to represent the restoring force and the damping force of an HDRB. These parameters are determined from cyclic loading tests on the bearing. The restoring force calculation yields a skeleton curve of the shear force-displacement loop (Eqn 16), while the damping force calculation results in the proper hysteretic loop area (Eqn 17). Superposition of the two forces results in the total shear force in the bearing (Eqn 18). It should be noted that both Eqns 16 and 17 are independent of the loading history of the bearing, but are dependent on the displacement $x(t)$ and velocity $\dot{x}(t)$ at time *t*. One additional mathematical model that describes the behavior of an HDRB has been proposed by Hwang *et al.* (2002), but is not used in this study.

$$F_1\left(x(t),\dot{x}(t)\right) = \left[ b_1 + b_2 x^2(t) + b_3 x^4(t) + \frac{b_4}{\cosh^2\left(b_5 \dot{x}(t)\right)} + \frac{b_6}{\cosh\left(b_7 \dot{x}(t)\right)\cosh\left(b_8 x(t)\right)} \right] x(t) \tag{16}$$

$$F_2\left(x(t),\dot{x}(t)\right) = \left[ \frac{b_9 + b_{10} x^2(t)}{\sqrt{b_{11}^2 + \dot{x}^2(t)}} \right] \dot{x}(t) \tag{17}$$

$$F\left(x(t),\dot{x}(t)\right) = F_1\left(x(t),\dot{x}(t)\right) + F_2\left(x(t),\dot{x}(t)\right) \tag{18}$$

Due to limited accessibility to experimental data, the HDRB optimization involves determination of the most appropriate bearing from the HDRBs described by Jankowski

(2004). Jankowski reports numerical values for the Pan and Yang parameters for several bearings, each of which is larger than that required for this study. Therefore, for this study each bearing is scaled to the appropriate size by keeping the shearing stress-strain relationship and the normal stress on the bearing the same as that tested experimentally. The notion of being able to scale the properties of reduced-scale specimens to represent the behavior of full-scale bearings has been proven through experimental testing (De la Llera *et al.* 2004). This application uses the reverse approach, namely existing data from the testing of full-scale bearings are used to represent the behavior of reduced-scale bearings. For the installation of eight bearings, the axial load on each bearing is approximately 100 kN.

The HDRB selected is based on the testing of a 22.3 cm diameter circular bearing with a height of 18 cm that was tested by the Denryoku Company of Japan with an axial pressure of 3.14 MPa (Jankowski 2004). Here the bearing is scaled to a diameter of 20 cm. The FIS created to represent this bearing uses inputs of displacement and velocity to predict the force exerted by the HDRB on the structure.Displacement data are generated using a random white noise signal, and the corresponding force data are determined using the Pan and Yang (1996) model. The velocity data are determined using the fourth-order backward difference method(Chapra and Canale 1998). This HDRB is selected because it is horizontally stiff enough to prevent displacements larger than its capacity for each of the earthquakes considered. The FIS created to model the behavior of the 20 cm diameter HDRB is included as Figure 7.

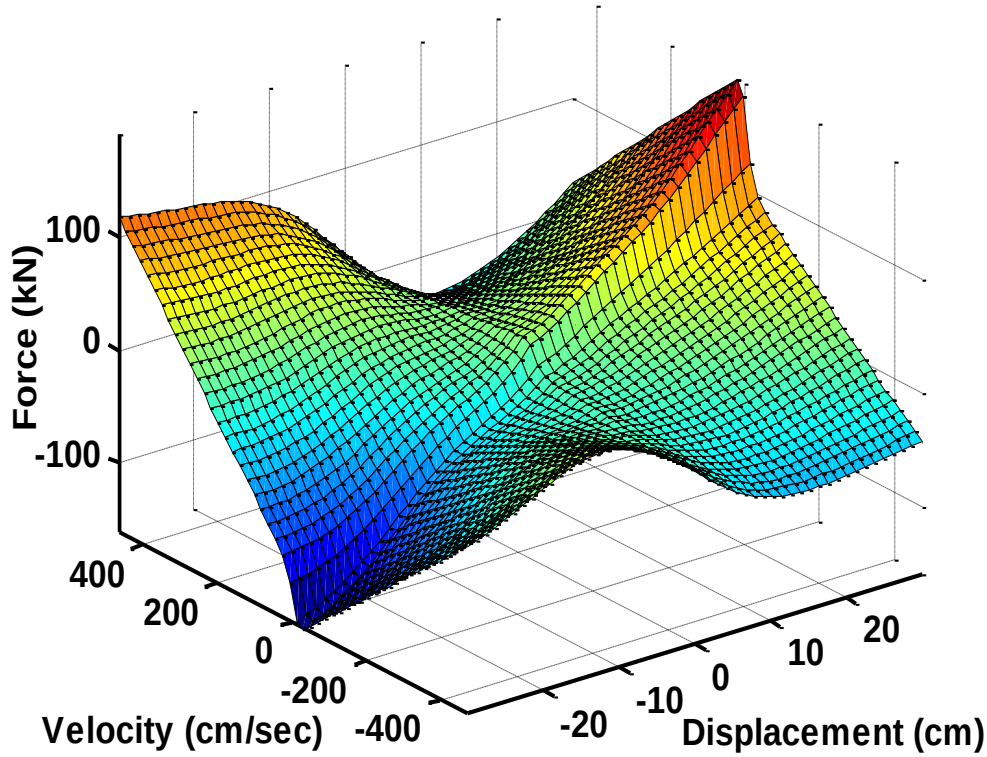


Figure 7. Fuzzy surface of 20 cm diameter HDRB with 100 kN axial load.

## 4.2. Hybrid HDRB+SMA Model and Optimization

The HDRB device modeled using the Pan and Yang (1996) formulation is utilized as a component of the hybrid HDRB+SMA systems. The other component of the hybrid systems is SMA wires. Although the use of SMA wires could increase the energy dissipation of the hybrid system over that of the HDRB system, the primary objective of the SMA wires in the hybrid system is to re-center the structure after the excitation from an earthquake ceases. NiTi is the SMA material that is considered in this study because of the alloy's ability to undergo large strains, and due to the availability of experimental data from testing.

For numerical simulation of the base-isolated structures that are equipped with the hybrid HDRB+SMA devices, the SMA wires are modeled using two different configurations. One configuration of the wires is that shown in Figure8, which involves the use of low-friction wheels connected to rods that are attached to the steel top or bottom plate of the HDRB. Using this configuration (HDRB+SMA1), each HDRB is not connected to adjacent HDRBs. Another configuration considered (HDRB+SMA2) is to connect the SMA wires diagonally from the bottom of one HDRB to the top of the adjacent HDRB (see Figure 9). The wires do not extend the entire length of the diagonal, and are assumed to be rigidly connected to a link element that connects them to each HDRB.

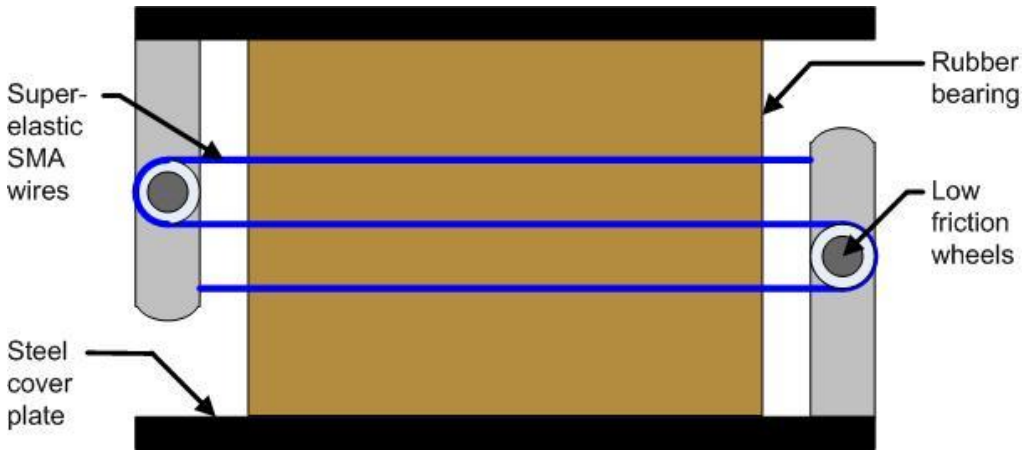


Figure 8.Hybrid HDRB+SMA1 configuration.

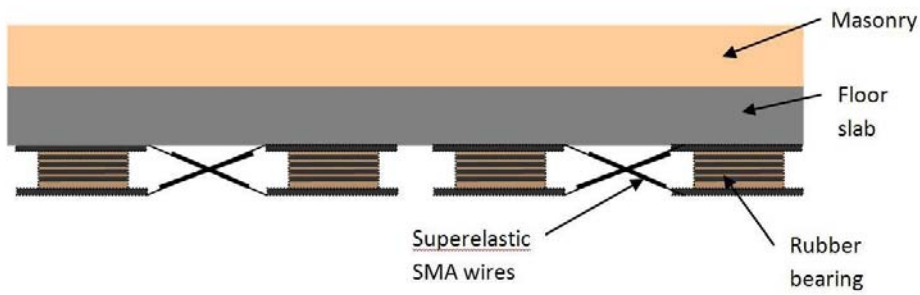


Figure 9. Hybrid HDRB+SMA2 elevation view.

The SMA wires are modeled by creating a FIS that is based on experimental testing of 1 mm diameter NiTi wire in tension at various frequencies with a sinusoidal displacement that imposed up to 7% strain and a strain rate of 0.6 m/m/sec. The data that were collected from tensile tests are modified to represent the behavior of an SMA wire in tension or compression by duplicating the set of data and reversing the sign of the duplicated data to represent the behavior of the wire in compression. More information related to the SMA testing and modeling is included by Ozbulut *et al.* (2010). The SMA FIS, shown in Figure 10, uses strain and strain rate as inputs to calculate the stress in the SMA. Using the FIS developed for a single NiTi wire, the force output from the FIS is multiplied by an integer number representing the total number of wires in the brace.

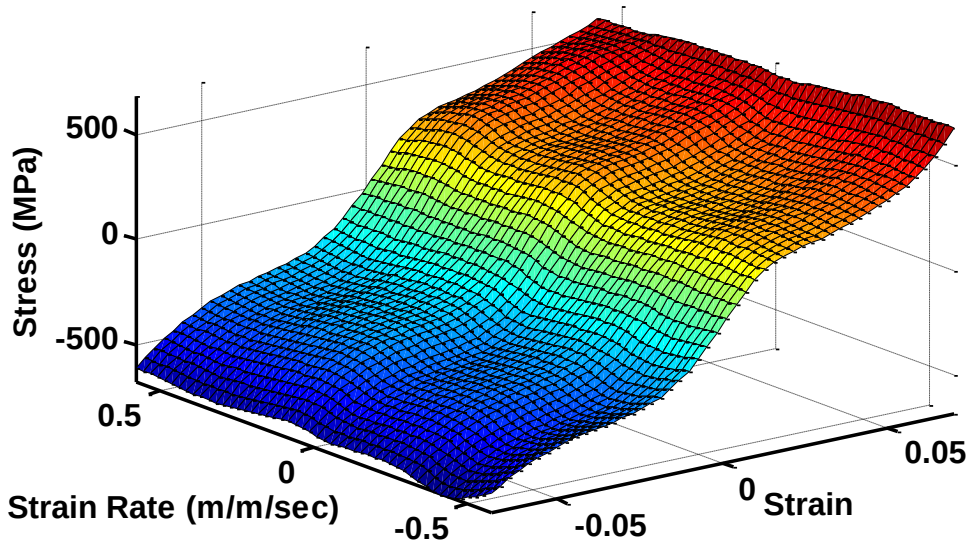


Figure 10. Fuzzy surface for 1 mm diameter NiTi SMA wire.

In determining the optimal number and length of SMA wires for the HDRB+SMA1 and HDRB+SMA2 configurations, the objective is to use the least amount of SMA wires possible to keep the hybrid isolator relatively flexible while using enough SMA to prevent the wires from being overstrained. Based on a trial and error optimization, the use of 20 – 1 mm diameter NiTi wires of 1 m length for the HDRB+SMA1 configuration and the use of 40 – 1 mm diameter NiTi wires of 4 m length for the HDRB+SMA2 configuration are selected.

## 4.3. FRB Model and Optimization

The FRB is modeled by creating a FIS that is based on experimental testing performed by Kelly and Takhirov (2002). The testing was performed on bearings constructed with carbon fiber reinforcement and natural rubber. Each bearing was subjected to a sinusoidal cyclic test in the horizontal direction. The bearings were not bonded to the test machine. Of the eight FRBs testing by Kelly and Takhirov (2002), the bearing they designate as “DRB6” is selected for use in this study because it is the bearing with the lowest horizontal stiffness, which

happens to be quite close to the horizontal stiffness of the HDRB utilized in this study. Using eight DRB6 FRBs with 37.7 cm length, 18.3 cm width, and 10.5 cm height, the actual normal stress on each FRB is approximately equal to the 1.73 MPa normal stress in one of Kelly and Takhirov's (2002) tests. The force-displacement and displacement-time results from the test of DRB6 with 1.73 MPa normal stress, loaded in the direction of the shorter side [referred to as the 90° direction (Kelly and Takhirov 2002)] are utilized in this study. The maximum displacement range of the test was +/- 10 cm. The FIS created using inputs of displacement and velocity to predict the force exerted on the structure by each FRB is included as Figure 11.

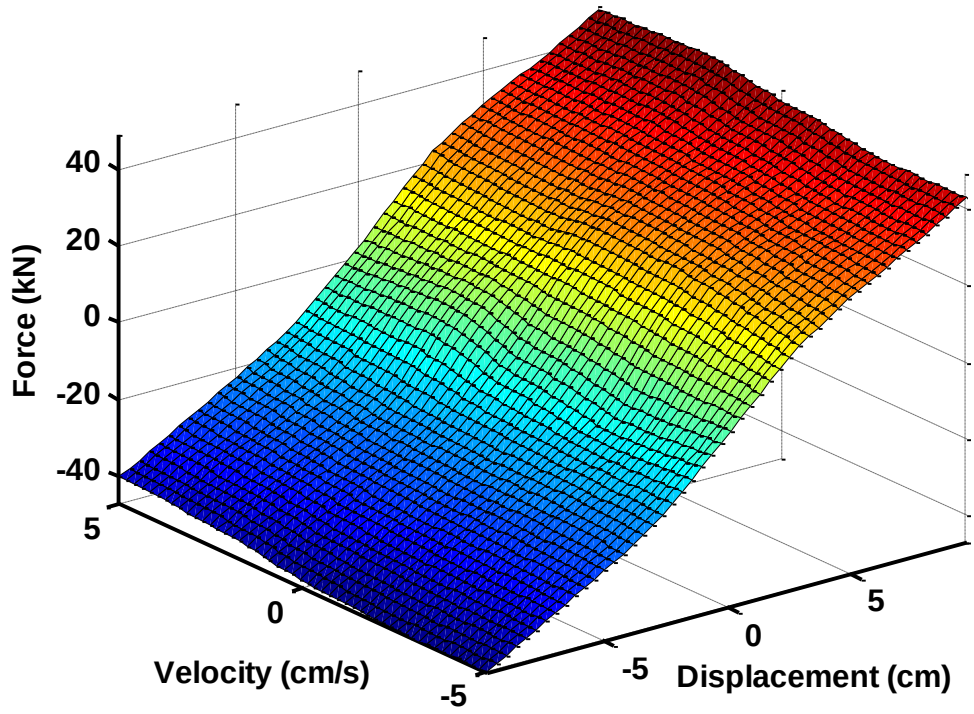


Figure 11. Fuzzy surface for FRB.

## 5. Numerical Analysis Results

To determine the fundamental period of the case study structure that is isolated using each of the isolation systems described, a Fast Fourier Transform (FFT) is performed on the displacement-time data that result from giving the structure a small initial horizontal displacement at each story, and subsequently allowing the structure to vibrate freely. The fundamental period of the isolated structure with eight HDRB, HDRB+SMA1, HDRB+SMA2, or FRB isolators is 0.96, 0.86, 0.91, or 0.96 sec, respectively. As expected intuitively, the isolated periods of the HDRB+SMA1 and HDRB+SMA2 structures are lower than those of the HDRB structure because the SMA wires increase the stiffness of the isolation system. The same displacement-time data are analyzed using the logarithmic decrement method (Chopra 2001) to determine the equivalent viscous damping ratio for each

base isolation case. The damping ratios for the structure isolated using HDRB, HDRB+SMA1, HDRB+SMA2, or FRB bearings are 0.225, 0.156, 0.197, or 0.048, respectively. The damping ratio of the FRB isolation system is relatively small compared to that of the isolation systems involving HDRBs because the rubber utilized in the FRB is not high-damping rubber, and because of the relative flexibility in the vertical direction of the FRB compared to the HDRB. Based on the experimental testing performed by Kelly and Takhirov (2002), it is apparent that as the normal stress on the FRB is increased, its' damping ratio decreases.

Using the optimized isolators, the performance of each isolated structure is assessed through numerical simulation by subjecting the structure to the suite of earthquake records listed in Table 1, which includes the RSPMatch earthquake that was used to optimize the parameters of each isolation system. The responses of the base-isolated structures, in terms of the PIs, are included in Table 2. Graphical results from the 2005 Tarapacá, Chile, earthquake, including plots of base displacement, interstory drift, and absolute floor acceleration with time, and the force-displacement behavior of the bearings are shown in Figures 12-15, respectively. Based on Table 2, it is evident that the HDRB isolation system yields the most favorable PIs for each earthquake. For small displacements such as those resulting from the 1981 Chile and 2005 Tarapacá, Chile, earthquakes, the HDRB and FRB isolation systems result in similar values for the PIs. However, for larger displacements such as those induced by the 1985 Llolleo, El Centro, and RSPMatch earthquakes, the effectiveness of the FRB isolation system becomes significantly less favorable than that of the HDRB isolation system.

The HDRB+SMA1 and HDRB+SMA2 isolation cases do not improve the performance of the HDRB isolation system. Due to the configuration of the HDRB+SMA isolation systems, the SMA wires typically result in lesser reductions of the base shear, structural shear, interstory drift, and absolute floor acceleration from the fixed-base case than that of the HDRB isolation system. The base and RMS base displacement values for the HDRB+SMA cases are quite similar to those for the HDRB case, and none of the isolation systems result in significant residual displacement. However, the HDRB+SMA isolation systems do still improve the performance of the structure from that of the fixed-base case.

From Figure 12, it can be seen that the FRB isolation system experiences larger peak base displacement than the other isolation systems, although the peak displacement of the FRB isolated structure is still acceptable for each of the earthquakes considered (see $J_2$ in Table 2). Figure 13 shows that the interstory drift of the structure is small in magnitude for the fixed-base and the base-isolated structures, although all of the base-isolated structures significantly reduce the interstory drift of the structure from that of the fixed-base case. The absolute acceleration of the base-isolated structures, as shown in Figure 14, is significantly less than that of the fixed-base structure for the 2005 Tarapacá, Chile, earthquake. The total force-displacement behavior for each of the isolation systems, as shown in Figure 15, indicates that the stiffness of each base isolation system is comparable, although the equivalent viscous damping of the FRB isolation system is noticeably less than that of the isolation systems involving the use of HDRBs.

**Table 2. Results from numerical simulation**

| | | **Base Shear** | **Base Displa-cement** | **RMS Base Displa-cement** | **RMS Floor Accel-eration** | **Structural Shear** | **Interstory Drift** | **Floor Accel-eration** |
|---|---|---|---|---|---|---|---|---|
| | | $J_1$ | $J_2$ (m) | $J_3$ (m) | $J_4$ | $J_5$ | $J_6$ | $J_7$ |
| 1981 Chile | HDRB | 0.581 | 0.020 | 0.003 | 0.226 | 0.156 | 0.156 | 0.189 |
| | HDRB+SMA1 | 0.736 | 0.022 | 0.003 | 0.295 | 0.202 | 0.202 | 0.240 |
| | HDRB+SMA2 | 0.643 | 0.021 | 0.003 | 0.246 | 0.173 | 0.173 | 0.210 |
| | FRB | 0.563 | 0.030 | 0.004 | 0.239 | 0.155 | 0.155 | 0.183 |
| 1985 Llolleo (scale = 0.5) | HDRB | 0.887 | 0.021 | 0.004 | 0.490 | 0.384 | 0.369 | 0.435 |
| | HDRB+SMA1 | 1.11 | 0.023 | 0.003 | 0.600 | 0.472 | 0.453 | 0.543 |
| | HDRB+SMA2 | 0.953 | 0.022 | 0.004 | 0.523 | 0.409 | 0.392 | 0.467 |
| | FRB | 1.79 | 0.082 | 0.009 | 0.806 | 0.709 | 0.749 | 0.875 |
| 2005 Tarapacá | HDRB | 0.448 | 0.029 | 0.005 | 0.195 | 0.154 | 0.154 | 0.173 |
| | HDRB+SMA1 | 0.555 | 0.026 | 0.004 | 0.233 | 0.190 | 0.190 | 0.215 |
| | HDRB+SMA2 | 0.498 | 0.026 | 0.004 | 0.207 | 0.168 | 0.168 | 0.193 |
| | FRB | 0.633 | 0.052 | 0.007 | 0.222 | 0.221 | 0.221 | 0.243 |
| El Centro | HDRB | 1.04 | 0.027 | 0.004 | 0.657 | 0.466 | 0.515 | 0.586 |
| | HDRB+SMA1 | 1.33 | 0.029 | 0.003 | 0.771 | 0.545 | 0.657 | 0.748 |
| | HDRB+SMA2 | 1.17 | 0.028 | 0.004 | 0.692 | 0.495 | 0.574 | 0.656 |
| | FRB | 1.60 | 0.066 | 0.013 | 1.52 | 0.788 | 0.810 | 0.900 |
| RSP-Match (scale = 0.5) | HDRB | 1.19 | 0.030 | 0.005 | 0.540 | 0.510 | 0.481 | 0.536 |
| | HDRB+SMA1 | 1.36 | 0.027 | 0.004 | 0.679 | 0.564 | 0.543 | 0.614 |
| | HDRB+SMA2 | 1.25 | 0.027 | 0.004 | 0.584 | 0.534 | 0.504 | 0.563 |
| | FRB | 2.70 | 0.105 | 0.013 | 0.995 | 1.13 | 1.06 | 1.21 |

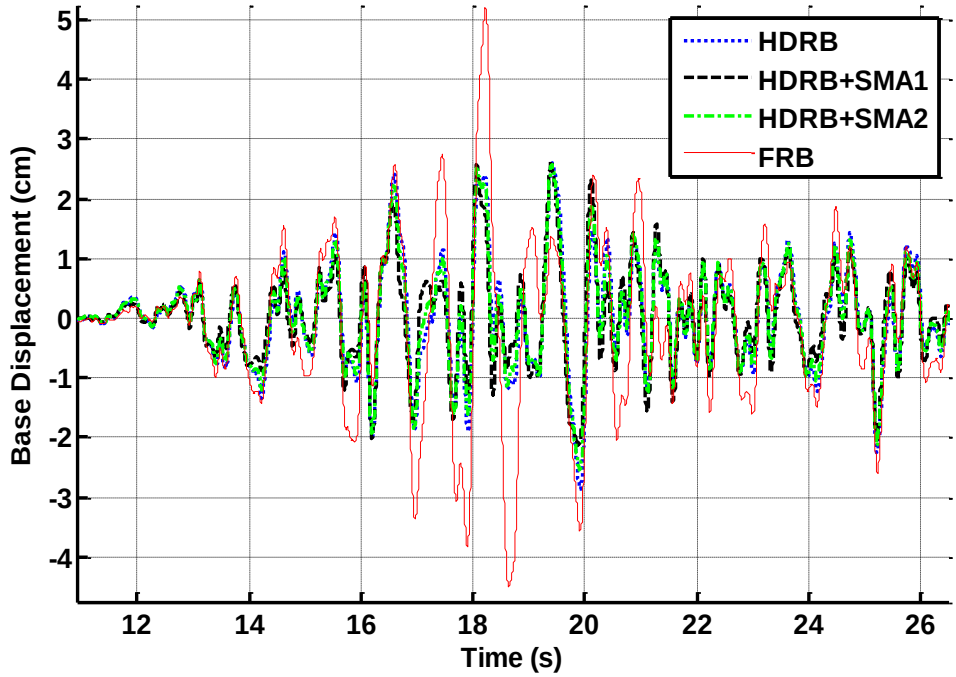


Figure 12. Base displacement from 2005 Tarapacá earthquake.

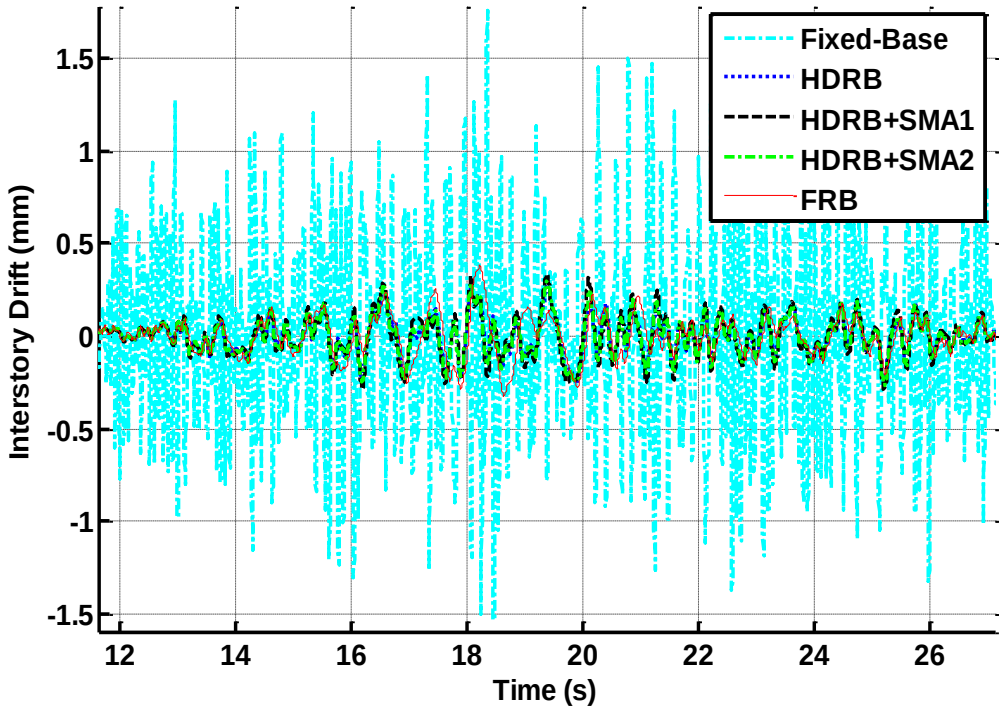


Figure 13. Interstory drift between base and 1st floor from 2005 Tarapacá earthquake.

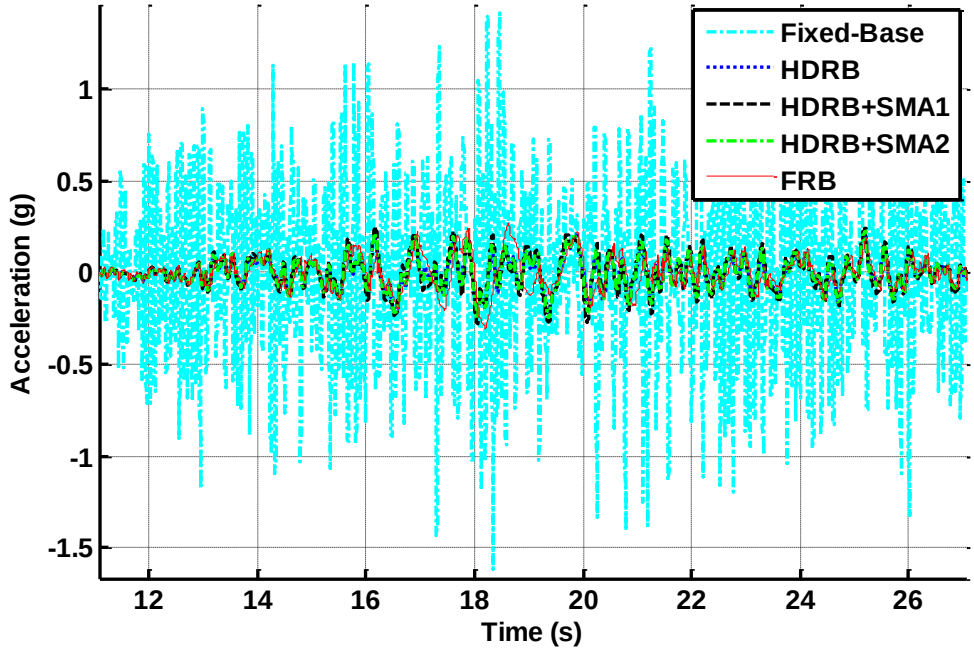


Figure 14. Absolute acceleration of 2nd floor from 2005 Tarapacá earthquake

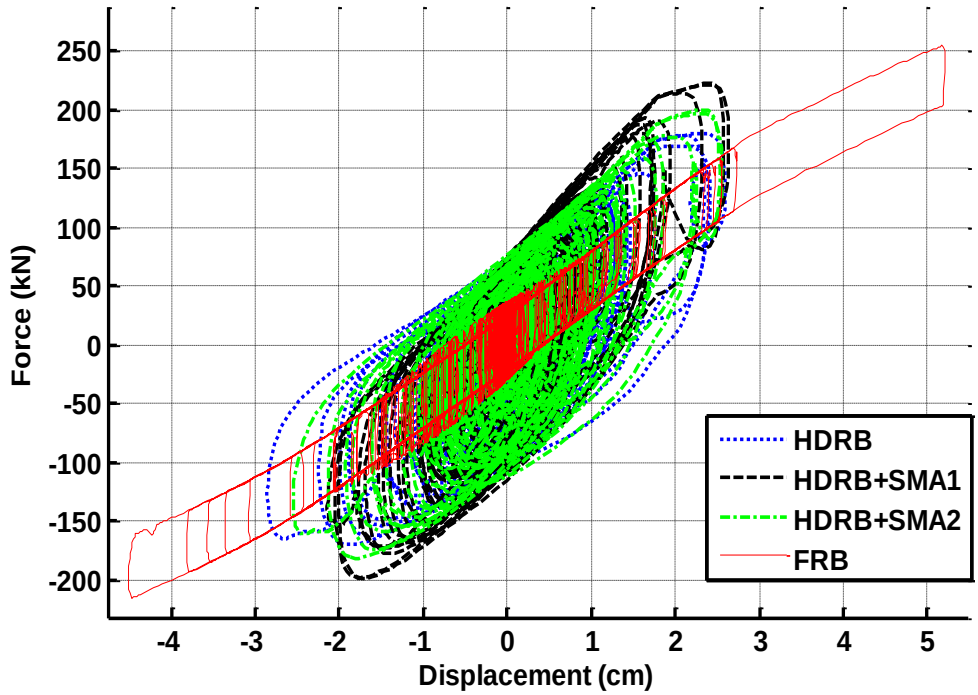


Figure 15. Total force from all isolation devices from 2005 Tarapacá earthquake.

## CONCLUSION

Several base isolation systems are employed to determine the most optimal system for a two-story confined masonry Chilean house. A numerical investigation, involving the use of fuzzy logic incorporating experimental data and analytical models for the force-displacement behavior of each isolator, is performed. The house is modeled using a MDOF approach with characteristics determined from ambient vibration testing performed on the case study structure. Results of numerical simulations show that the HDRB isolation system yields the best performance overall, as it significantly reduces each PI quantity from that of the fixed-base case for the earthquakes considered, except for a slight amplification of base shear for the El Centro and RSPMatch earthquakes.

The FRB isolation system performs similarly to the HDRB isolation system at small displacements, although behavior at larger displacements (larger than 6 cm, for this study) is inferior to that of the HDRB isolation system. The addition of SMA wires to the HDRB isolation system (HDRB+SMA1 and HDRB+SMA2) does not improve the performance of the HDRB isolation system, though the PIs are still generally reduced from those of the fixed-base structure. The magnitude of interstory drift of the fixed-base structure using the MDOF model implemented in this study is not significant for any of the earthquakes considered, although the base isolation systems reduce the interstory drift of the structure from that of the fixed-base case.

Future studies should include the use of FRBs with increased damping properties. This could be achieved by using FRBs with lesser normal stress or by incorporating the use of rubber with high-damping properties in the manufacture of the FRBs. The use of SMA wire is not recommended for application with the HDRBs in the configurations studied here, as it increases the stiffness of the device without improving the behavior of the HDRB-only case.

## ACKNOWLEDGMENTS

The authors gratefully acknowledge the assistance of Ernesto Herbach from the Chilean Ministry of Housing and Pedro Soto from the University of Chile. The United States National Science Foundation Graduate Research Program sponsored the graduate study of the first author.

## REFERENCES

Andrawes, B.; DesRoches, R. “Effect of ambient temperature on the hinge opening in bridges with shape memory alloy seismic restrainers” *Engineering Structures*, 2007, 29, 2294-2301.

Arias, A. “A measure of earthquake intensity” *Seismic Design for Nuclear Power Plants*, The MIT Press,Cambridge, MA,1970; 438-483.

Astroza, M.; Moroni, M.O.; Muñoz, M.; Perez, F. “Estudio de la vulnerabilidad sísmica de edificios de vivienda social”*Proceedings of IX Jornadas Sudamericanas de Ingeniería*

*Estructural*, Asociación Sudamericana de Ingeniería Estructural, V. 2005, paper no. A04-05, Conception, Chile.

Boroschek, R.L.; Moroni, M.O.; Sarrazin, M. "Dynamic characteristics of a long span seismic isolated bridge" *Engineering Structures*, 2003, 25, 1479-1490.

Bruno, S. and Valente, C. "Comparative response analysis of conventional and innovative seismic protection strategies" *Earthquake Engineering and Structural Dynamics*, 2002, 31, 1067-1092.

Chapra, S.; Canale, R. *Numerical Methods for Engineers: With Programming and Software Applications*,McGraw-Hill:Blacklick, OH, 1998.

Chopra, A.K. *Dynamics of Structures: Theory and Applications to Earthquake Engineering*, Prentice-Hall: Upper Saddle River, NJ, 2001.

De la Llera; J.C., Luders, C.; Leigh, P.; Sady, H. "Analysis, testing, and implementation of seismic isolation of buildings in Chile"*Earthquake Engineering and Structural Dynamics*, 2004, 33, 543-574.

Dolce, M.; Cardone, D.; Ponzo, F. "Shaking-table tests on reinforced concrete frames with different isolation systems" *Earthquake Engineering Structural Dynamics*, 2007, 36, 573-596.

Hancock, J.; Watson-Lamprey, J.; Abrahamson, N.A.; Bommer, J.J.; Markatis, A.; McCoy, E."An improved method of matching response spectra of recorded earthquake ground motion using wavelets"*Journal of Earthquake Engineering*, 2006, 10, 67-89.

Hart, G.C.; Wong,K. *Structural Dynamics for Structural Engineers*, John Wiley & Sons: New York, NY, 2000.

Hwang, J.S.; Wu, J.D.; Pan, T.-C.; Yang, G. "A mathematical hysteretic model for elastomeric isolation bearings" *Earthquake Engineering and Structural Dynamics*, 2002, 31, 771-789.

Jankowski, R. "Nonlinear rate dependent model of high damping rubber bearing" *Bulletin of Earthquake Engineering*, 2004, 1, 397-403.

Kelly, J.M. "EERI Distinguished Lecture 2001: Seismic isolation systems for developing countries" *Earthquake Spectra*, 2002, 18, 385-406.

Kelly, J.M.; Takhirov, S.M. "Analytical and experimental study of fiber-reinforced strip isolators" Report No PEER2002/11. PEER. Berkeley, CA, 2002.

Kim, H.-S.; Roschke, P.N. "Fuzzy control of base-isolation system using multiobjective genetic algorithm" *Computer-Aided Civil and Infrastructure Engineering*, 2006, 21, 436-449.

Moroni, M.O.; Astroza, M.; Acevedo, C."Performance and seismic vulnerability of masonry housing types used in Chile"*Journal of Performance of Constructed Facilities*, 2004, 18, 173-179.

Moroni, M.O.; Astroza, M.; Caballero, R. "Wall density and seismic performance of confined masonry buildings" *TMS Journal*, 2000, 18, 79-86.

Moroni, M.O.; Astroza, M.; Gomez, J.; Guzman, R. "Establishing $R_w$ and $C_d$ factors for confined masonry buildings"*Journal of Structural Engineering*, 1996, 122, 1208-1215.

Murty, C.; Brzev, S.; Faidon, H.; Comartin, C.D.; Irfanoglu, A. "At risk: The seismic performance of reinforced concrete frame buildings with masonry infill walls" Report No. WHE-2006-03,World Housing Encyclopedia, Oakland, CA, 2006.

Narasimhan, S.; Nagarajaiah, S.; Johnson, E.A.; Gavin, H.P. “Smart base-isolated benchmark building. Part I: problem definition” *Structural Control and Health Monitoring*, 2006, 13, 573-588.

National Geophysical Data Center. http://www.ngdc.noaa.gov.

NCh2745.Of2003 “Earthquake-resistant design of base-isolated buildings” Instituto Nacional de Normalización (INN), Chile, 2003.

NCh 433.Of96 “Earthquake resistant design of buildings” Instituto Nacional de Normalización (INN), Chile, 1996.

Ozbulut, O.; Roschke, P; Lin, P.-Y.; Loh, C.-H. “GA-Based optimum design of a shape memory alloy device for seismic response mitigation” *Smart Materials and Structures*, 2010, 16, 065004.

Pan, T.-C.; Yang, G. “Nonlinear analysis of base-isolated MDOF structures” *Proceeding of Eleventh World Conference on Earthquake Engineering*,International Association of Earthquake Engineering, Paper No. 1534, Acapulco, Mexico, 1996.

Park, K.-S.; Jung, H.-J.; Lee, I.-W. “A comparative study on aseismic performances of base isolation systems for multi-span continuous bridge” *Engineering Structures*, 2002, 24, 1001-1013.

Servicio Sismológico. http://ssn.dgf.uchile.cl/home/terrem.html.

Wilde, K.; Gardoni, P.; Fujino, Y. “Base isolation system with shape memory alloy device for elevated highway bridges” *Engineering Structures*, 2000, 22, 222-229.

In: Advances in Mechanical Engineering Research. Volume 2 ISBN: 978-1-61761-984-7
Editor: David E. Malach 

*Chapter 6*

# DIFFERENTIAL ASPECTS OF THE ROLE OF MICROALLOYING ELEMENTS ON MICROSTRUCTURE OF HOT ROLLED STEELS

***Manuel Gómez and Sebastián F. Medina***
National Centre for Metallurgical Research (CENIM-CSIC), Av. Gregorio del Amo 8; 28040-Madrid, Spain

## ABSTRACT

In this work, a comparative study of some of the most important effects of the diverse microalloying elements on austenite and ferrite microstructure of hot rolled microalloyed steels is carried out. Microalloying elements dissolved in austenite have a considerable effect on microstructure, but the main reason for the presence of these elements in microalloyed steels lies in their precipitation. Titanium is the most effective element to control grain growth at high reheating temperatures and a hypostoichiometric Ti/N ratio close to 2 is recommended. Aluminum can be useful to control grain growth at moderate temperatures, but it is found that its addition to Ti steels can be detrimental and promote abnormal grain growth below 1100 ºC. The fine initial austenite grain size of Ti steels ensures a fast recrystallization kinetics and a minor reduction of austenite grain size during hot rolling. Besides, the pinning forces exerted by TiN particles precipitated at high temperatures are about two orders of magnitude lower than the driving forces for recrystallization. This explains why the austenite in Ti-steels hardly experiences hardening during rolling. On this regard, niobium, even at very low contents, is the most effective microalloying element to inhibit static recrystallization of austenite during hot rolling, due to the adequate precipitation temperature range at deformation temperatures and the strong pinning effect of niobium carbonitrides. The incomplete recrystallization of austenite at temperatures below the no-recrystallization temperature ($T_{nr}$) causes the progressive strengthening of austenite, which can be characterized by the magnitude defined as "accumulated stress" ($\Delta\sigma$). It has been found that the accumulated stress measured at the end of hot rolling and prior to the austenite→ferrite transformation informs about the density of potential nucleation sites for ferrite and consequently the chances to refine the final ferritic grain microstructure. Finally, it has also been found that the preferential nucleation of intragranular ferrite on particles such as vanadium

carbonitrides (precipitated at lower temperatures than NbCN) makes an important contribution to enhance the ferrite grain refinement. In this paper the effect of the different types of microalloying elements and kinds of precipitates is discussed in terms of the values of different aspects such as pinning and driving forces, size of precipitates, activation energies or diffusion coefficients.

## INTRODUCTION

The type and amount of microalloying elements dissolved in austenite have a considerable effect on grain growth, progress of recrystallization, and phase transformation [1-5]. However, the main reason for the presence of elements such as Ti, Nb and V in microalloyed steels lies in their precipitation, and particularly in the interaction of particles of these elements and interstitials (C, N) with austenite grain boundaries in motion. Whereas solutes hinder the advance of grain boundaries by means of a friction effect originated by the difference in their atomic radius compared with iron, precipitates cause a decrease in the effective grain boundary area and thus in the associated surface energy. The latter leads to an obstruction of grain boundary motion or a pinning effect which is much stronger than the solute drag. The stronger effect of precipitates compared to the solutes can be seen, for example, when the values of the activation energy for static recrystallization of austenite in the presence of strain-induced precipitates are compared to the lower values found when the microalloying elements are in solution. The value of the activation energy in the presence of solutes can be expressed for Nb and V-microalloyed steels as [2]:

$$Q(J\cdot mol^{-1}) = 148636.8 - 71981.3\,[\%C] + 21180\,[\%Mn] + 56537.6\,[\%Si] + 121243.3\,[\%Mo] + 64469.6\,[\%V] + 109731.9\,[\%Nb]^{0.15} \quad (1)$$

where each amount in brackets indicates the mass percentage of the element indicated. On the other hand, the increase in activation energy due to the presence of precipitates in Nb and V-microalloyed steels will be respectively [6]:

$$\Delta Q(J\cdot mol^{-1}) = 1074\cdot 10^{3}\cdot (\%V\%N)^{0.223} \quad (2)$$

$$\Delta Q(J\cdot mol^{-1}) = 1577\cdot 10^{3}\cdot (\%Nb\%C^{0.7}\%N^{0.2})^{0.254} \quad (3)$$

Zener [7] proposed that the driving pressure for grain growth due to the curvature of the boundary would be counteracted in particle-containing materials by a pinning pressure exerted by the particles situated at the boundary. Normal grain growth would be completely inhibited when the grain size reached a maximum, given by the critical radius $R_c$:

$$R_c = \frac{4}{3}\cdot\frac{r}{f} \quad (4)$$

where $r$ is the radius of the pinning second-phase particles and $f$ their volume fraction.

This equation demonstrated for the first time that a decrease in the size of second phase particles and an increase in their volume fraction lead to grain refinement. This is crucial not only for microalloyed steels but also for aluminum alloys and many other materials of industrial interest. As proof of the value of Zener's equation, various authors have confirmed, completed or modified this equation for normal grain growth and have extended it to the case of abnormal growth [8]. All the interpretations of equation (4) can be adapted to a general expression:

$$R_c = K\frac{r}{f^m} \tag{5}$$

where the adimensional constant $K$ and the exponent $m$ depend on the model considered.

The different versions of equation (5) vary Zener's initial hypotheses, regarding the geometry of the zone of interaction between particle and grain boundary, the particle distribution, the relationship between boundary curvature and grain radius, and the original distribution of sizes [9-14].

To control the austenite grain size at high temperatures there must be a high proportion of fine particles and the solubility temperature $T_s$ must be high enough, and it is also essential that the particles do not coarsen or coalesce at temperatures below $T_s$ [15]. The amount of solute in the matrix will exert an important influence on precipitate coarsening and consequently on the ability to inhibit grain growth, both for simple additions and for steels with more than one type of microalloying element or precipitate.

One of the most interesting aspects of Zener's equation lies in its application to other annealing phenomena occurring in particle-containing materials besides grain growth, especially the static recrystallization of microalloyed steels. Many models on the inhibition of recrystallization by precipitates of microalloying elements have been presented [16, 17]. In summary, all of these hypotheses start from the same idea, similar to that of Zener: there is a driving pressure (usually taken as a "force") for recrystallization $F_R$ that comes from the stored energy of the deformation applied to the steel, and an opposite pinning force $F_P$ exerted by the precipitates that lessens the grain boundary surface energy. Depending on the net driving pressure ($F_R$-$F_P$), recrystallization progresses or stops.

The progress or blockage of the recrystallization and the control of grain growth have an effect on the grain size, grain elongation or dislocation density in the austenite during and at the end of thermomechanical processing, and this microstructure plays a crucial role on the microstructure after cooling. In this chapter some of the most important effects of the type and amount of microalloying elements are presented and discussed in terms of the values of different aspects such as pinning and driving forces, size of precipitates, activation energies or diffusion coefficients.

## EXPERIMENTAL PROCEDURE

Most of the steels studied in this chapter were manufactured by Electroslag Remelting (ESR) in a laboratory unit capable of producing 30 kg ingots. This technique avoids macrosegregation, both in alloying elements and impurities, and there is considerably less

microsegregation; these effects being present in conventional ingots and continuous casting billets. The hot rolling simulations and the tests to calculate the recrystallized fraction were carried out in a computer-controlled hot torsion machine on specimens with a gauge length of 50 mm and diameter of 6 mm, which were protected by an argon flow. The torsion magnitudes (torque and number of revolutions) were transformed into equivalent stress and strain according to Von Mises criterion [18]. The recrystallized fraction was determined using double deformation technique, in particular the method known as "back extrapolation" [19]. On the other hand, all the microstructural studies were done observing more than 20 fields on a longitudinal surface of the specimens at 2.65 mm from the axis. The austenite grain size ($D_\gamma$) was determined by means of quenching and subsequent metallographic analysis applying ASTM standard E-112. Finally, the characteristics of the precipitates were determined by transmission electron microscopy (TEM) using the carbon extraction replica technique.

## SOME EFFECTS OF MICROALLOYING ELEMENTS ON THE MICROSTRUCTURE OF STEELS

The behavior during reheating at high temperature and hot deformation of steels with **titanium** as the unique microalloying element forming nitrides or carbides is substantially different to that of other microalloyed steels. The reason for this is that, whereas niobium or vanadium precipitates are dissolved at the reheating temperatures, titanium nitrides (TiN) have low solubility in austenite and their complete dissolution is not possible unless the reheating temperature is very high, close to the melting point of steels, or in some cases, depending on the chemical composition, at temperatures corresponding to the liquid state [20-22]. This characteristic makes Ti and N ideal elements for controlling the austenite grain size in processes involving the application of heat, for instance in forging applications or in the heat affected zone in welding [23]. For this reason, the addition of Ti is indispensable in structural steels with weldability requirements.

The TiN particles precipitated in the austenite are typically square-shaped or “cuboidal”, as those shown in Figure 1. These particles exert a pinning effect on austenite grain boundaries in motion during reheating and help to control austenite grain growth. However, an increase in the titanium content in microalloyed steels does not necessarily mean that the grain will be always refined. Figure 2 shows the austenite grain size after reheating at 1300 ºC measured in several steels with similar C content (near 0.1%C) but different Ti and N contents represented versus their Ti/N ratio. It can be seen that $D_\gamma$ presents a minimum value for Ti/N ratios near but lower than the stoichiometric value, i.e. the ratio of the molecular weights of Ti and N (47.87/14 = 3.42) [24, 25].

Small precipitates grow by Oswald ripening according to Lifshitz, Slyozov and Wagner’s expression [26], which accurately predicts precipitate growth as a function of the temperature and holding time. Considering an initial precipitate radius ($r_0$), the average size ($r$) of a particle after time $t$ will be [27]:

$$r^3 = r_o^3 + \frac{8\gamma D V^2 C}{9RT} \cdot t \qquad (6)$$

where $\gamma = 0.8$ J·m$^{-2}$ is the interaction energy between the precipitates and the iron matrix (austenite); $D = 1.5 \cdot 10^{-5} \exp(-251000/RT)$m$^2$s$^{-1}$ is the volume diffusion coefficient of titanium in austenite; $V$=11.9·10$^{-6}$m$^3$mol$^{-1}$ is the mole volume of TiN; $C$ is the solute concentration in the matrix that is in equilibrium with a particle (mol·m$^{-3}$); $R$=8.3145 J·mol$^{-1}$·K$^{-1}$ is the universal gas constant; $T$ is the temperature (K) and $t$ is the time (s).

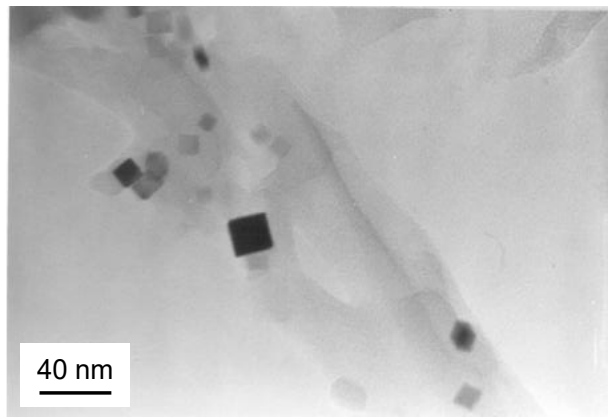


Figure 1. TEM image showing fine TiN precipitates in a Ti microalloyed steel reheated at 1300 ºC and quenched (0.11% C, 0.0083% N, 0.031% Ti). Carbon extraction replica.

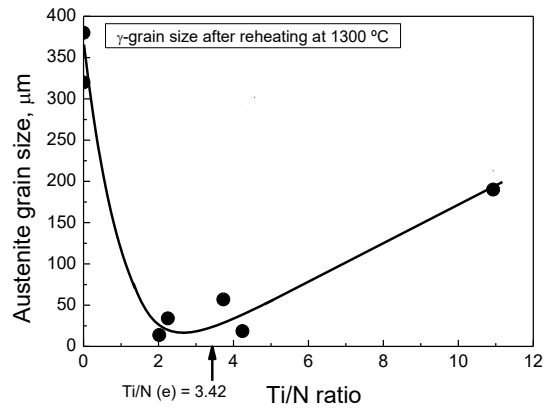


Figure 2. Austenite grain size measured after reheating at 1300 ºC in nine steels with 0.1% C represented versus their Ti/N ratio.

Ti/N ratio is closely related to the amount of Ti in solution, i.e. with the term $C$ of the equation. Therefore, according to the above expression, Ti/N ratio and precipitate size are linked [28]. This can be better observed in Figure 3, which shows the mean particle size for the steels studied as a function of Ti/N ratio [24, 25]. This plot focuses on the population of particles finer than 100 nm, which represents about 50% of the total amount, although a certain fraction of the coarser TiN particles can be bigger than 1 μm [24]. Particle size after reheating at 1300 ºC clearly shows a minimum for Ti/N ratios lower than the stoichiometric and close to 2. Consequently, pinning forces exerted by the TiN particles will be higher and

the austenite grain growth at high temperatures will be better controlled for hypo-stoichiometric ratios close to 2, as Figure 2 showed. It should be said that Ti/N ratio is basically a technical parameter upon which the grain size considerably depends, but other variables can strongly influence $D_\gamma$. A small value of precipitated volume fraction associated to small Ti and N additions can lower the value of pinning forces and consequently induce a coarser austenite grain size. In contrast, Ti in solution with hyper-stoichiometric Ti/N ratios can help to control grain growth to some extent.

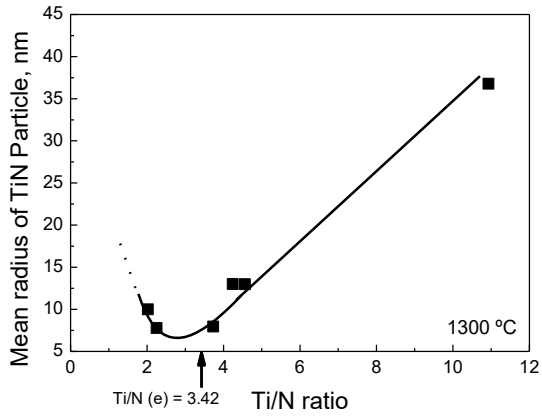


Figure 3. Mean particle size of fine TiN precipitates (smaller than 100 nm) after reheating at 1300 ºC as a function of Ti/N ratio.

The Ti/N ratio and the precipitation state associated to this parameter notably influence other phenomena occurring during thermomechanical processing of microalloyed steels. For example, a relationship between the precipitation state and the maximum strength of Ti microalloyed steels during hot deformation can be described and the precipitation state affects the value of the activation energy for deformation $Q_d$[29]. The increase of activation energy due to precipitation ($\Delta Q_d$) reaches a maximum when the Ti/N ratio is between 1 and 2, as Figure 4 shows. In other words, an increase in the titanium content in microalloyed steels does not necessarily mean that the deformation strength also increases. The curve of Figure 4 responds to the equation (7) [29] and the value of $Q_d$ can be introduced in the equation (8) of the Zener-Hollomon parameter [30]:

$$\Delta Q_d\,(J/mol) = -7678\left(\ln\frac{Ti\%}{N\%}\right)^2 + 3990\left(\ln\frac{Ti\%}{N\%}\right) + 20638 \tag{7}$$

$$Z = \dot{\varepsilon}\exp\left(\frac{Q_d}{RT}\right) = A(\sinh\,\alpha\sigma)^n \tag{8}$$

where, $\dot{\varepsilon}$ is the strain rate and σ is the equivalent stress.

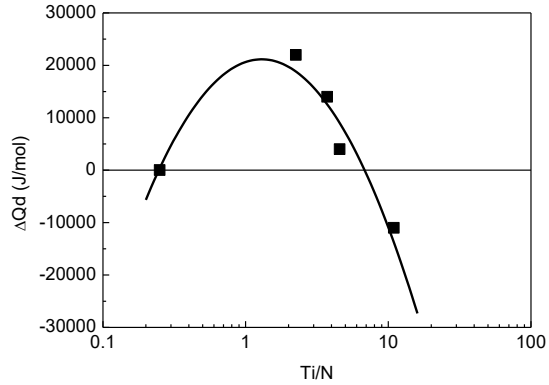


Figure 4. Increment of the activation energy ($\Delta Q_d$) for deformation of several Ti steels with regard to a Ti-free steel of the same composition.

The activation energy $Q_d$is a parameter that is connected with the deformation mechanism and its value is related with the greater or lesser difficulty that the nanometric precipitates pose to the climb of dislocations. Nonetheless, the increase obtained both for the peak stress and the activation energy in steels with the finest precipitate distribution is relatively small and barely represents an increase in the rolling forces. In Ti-containing steels, the driving forces of dynamic recrystallization are approximately two orders of magnitude greater than the pinning forces, and therefore the precipitation state (even for the finest sizes) is not able to impede the progress of dynamic recrystallization. The most notable influence of Ti is the grain refinement at the reheating temperatures seen above and the consequent reduction in the critical strain necessary for dynamic recrystallization to begin.

The parameter Ti/N has also an important influence on the static recrystallization of austenite after deformation. The recrystallization kinetics can be described by an Avrami equation in the following way [31]:

$$X_a = 1 - \exp\left(-\ln 2\left(\frac{t}{t_{0.5}}\right)^n\right) \tag{9}$$

where $X_a$ is the fraction of the recrystallized volume and $t_{0.5}$ is the time corresponding to half of the recrystallized volume, which depends practically on all the variables intervening in hot deformation and whose most general expression follows a law of the type:

$$t_{0.5} = A\varepsilon^p \dot{\varepsilon}^q D^s \exp\left(\frac{Q_x}{RT}\right) \tag{10}$$

where $\varepsilon$ is the strain, $\dot{\varepsilon}$ the strain rate, $D$ the grain size, $Q_x$ the activation energy for recrystallization, $T$ the absolute temperature, $R$ = 8.3145 J·mol$^{-1}$·K$^{-1}$ and $p$, $q$ and $s$ are parameters. While $p$ and $q$ are negative values, $s$ is positive [2]. The activation energy $Q_x$ is the parameter that basically reflects the influence of precipitation on the delay experienced by

static recrystallization kinetics. Similarly to what happened with dynamic recrystallization and hot deformation, the increase of activation energy due to precipitates ($\Delta Q_x$) and Ti/N follow a relationship that can be described with the curve shown in Figure 5 or the equation [29]:

$$\Delta Q_x(J/mol) = -50527\left(\ln\frac{Ti\%}{N\%}\right)^2 - 3262\left(\ln\frac{Ti\%}{N\%}\right) + 92485 \quad (11)$$

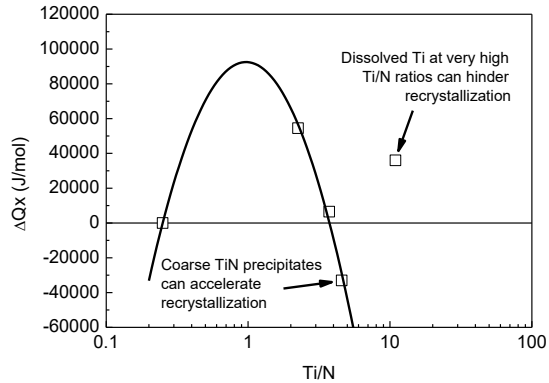


Figure 5. Increment of the activation energy for static recrystallization ($\Delta Q_x$) of several Ti steels with regard to a Ti-free steel of the same composition.

The highest value of the activation energy for static recrystallization $\Delta Q_x$ corresponds to hypo-stoichiometric ratios close to 1, i.e. with small precipitate sizes. Higher Ti/N ratios cause coarser sizes and it can even happen that the particles serve as a heterogeneous nucleation site for static recrystallization, i.e. $Q_x$ is lower than the value obtained for a Ti-free steel, as seen in Figure 5. However, a solute drag effect can be observed with very high Ti/N values, so Ti in solution can delay recrystallization and contribute to an increase in $Q_x$ value.

In sum, the addition of Ti usually delays static recrystallization kinetics, but the highest value of $\Delta Q_x$is around 90 000 J/mol (Figure 5), which is much lower than the values found for V or Nb steels, as will be seen later. As a result, Ti is often insufficient to inhibit recrystallization during hot rolling. Figure 6 shows the typical shape of the curves of static recrystallization kinetics of Ti-microalloyed steels, where the recrystallized fraction $X_a$ follows the sigmoidal shape of Avrami's law. In certain cases, as for high Ti additions and high Ti/N ratios, a short plateau of inhibition of recrystallization by strain-induced precipitates can be observed [24].

The driving forces for static recrystallization in Ti-microalloyed steels are normally much higher than the pinning forces exerted by the TiN particles irrespective of the Ti and N contents and the deformation conditions. Therefore, the austenite may recrystallize completely between steps during hot rolling even at low temperatures. In fact, in most cases, the curves of hot rolling simulation determined by the method of Jonas et al [32] do not show an increase in the slope of mean flow stress (MFS) versus the inverse of temperature or this change happens at temperatures near $A_{r3}$. In other words, the temperature of no-recrystallization ($T_{nr}$) cannot be determined, as shown in Figure 7 or it is very low [33].

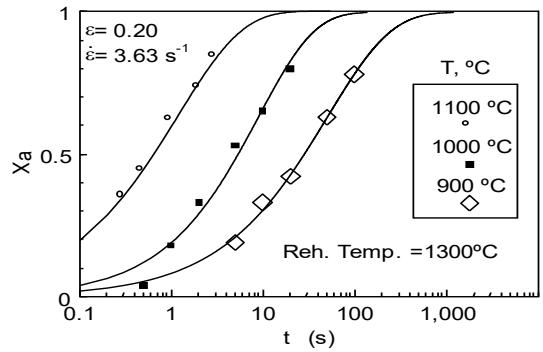


Figure 6. Recrystallized fraction ($X_a$) versus time ($t$) for a 0.12% C, 0.008% N, 0.018% Ti steel.

As will be seen later, the shape of MFS curves for V and especially Nb-microalloyed steels is usually different, as $T_{nr}$ can be determined for a broad range of rolling conditions, indicating a stronger recrystallization inhibition during hot rolling. However, the complete recrystallization of austenite between passes until low temperatures in Ti steels means that the austenite barely experiences hardening during and at the end of rolling, which involves that ferrite grain size refinement cannot be significantly enhanced by thermomechanical processing in this family of steels. On the other hand, austenite grain size hardly varies during hot rolling. TiN precipitates exert a strong control of grain growth from the reheating temperature, and according to equation (10) the small initial grain size obtained in Ti steels after reheating accelerates recrystallization kinetics. As Figure 8 shows, successive recrystallizations that occur during rolling do not serve to refine significantly austenite recrystallized grain size in a Ti-microalloyed steel, while Nb and V-microalloyed steels start from coarser grain sizes and suffer a strong grain refinement during the first deformation passes. As a result, it can be suggested that the hot rolling schedule of Ti-microalloyed steels could be simplified by suppressing several passes at intermediate temperatures [34]. To enhance ferrite grain size refinement, Ti steels should be processed by rolling to temperatures close to $A_{r3}$ and applying a fast cooling rate during $\gamma \rightarrow \alpha$ transformation.

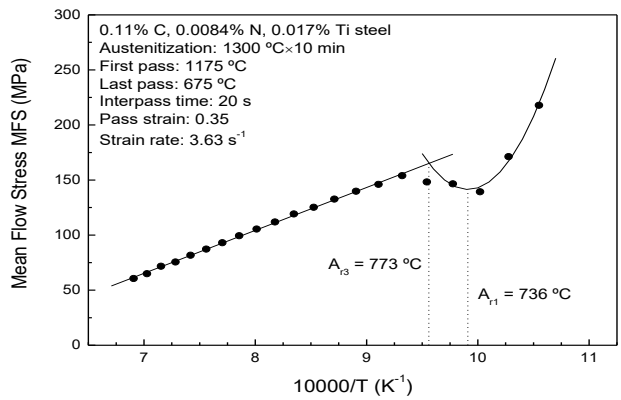


Figure 7. Dependence of Mean Flow Stress (MFS) on inverse of absolute temperature for a low carbon Ti-microalloyed steel. The no-recrystallization temperature ($T_{nr}$) does not exist, i.e. recrystallization between passes is practically complete until $A_{r3}$ temperature.

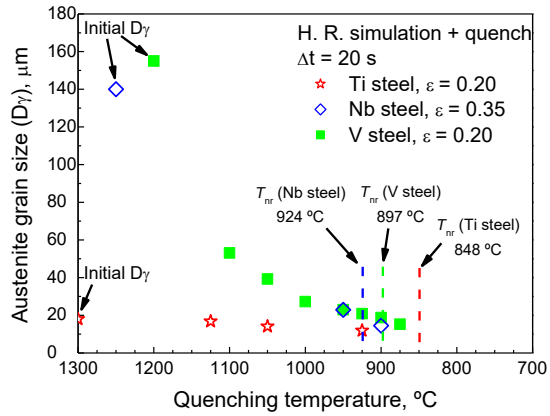


Figure 8. Evolution of austenite grain size from reheating to temperatures close to $T_{nr}$ during hot rolling simulations of three microalloyed steels with 0.017% Ti, 0.007% Nb and 0.13% V [34-36].

**Aluminum** is an element whose impact on austenite microstructure and precipitation state is usually underestimated. The presence of AlN in the austenite generates harmful effects on the hot-ductility of different kinds of steels [37, 38]. Crystallographic structure of AlN is hexagonal (h.c.p.). Nitrides and carbides of typical microalloying elements (Nb, V, Ti) have an f.c.c. crystallographic structure. These compounds, especially in the case of the smallest particles, frequently form precipitates which are semi-coherent with the (f.c.c) austenitic matrix. Their lattice parameter is slightly higher than that of the austenite [39].

Al can be detrimental for the control of austenite grain growth at high temperatures when this element is added to Ti-microalloyed steels [28, 40]. At equal level of microalloying, the precipitates are soluble in austenite as follows: TiN<AlN<NbN<VN, i.e. solubility temperature of AlN is generally lower than the temperature for TiN [21]. As a result, it has been found that AlN particles dissolve quickly at temperatures between 1000 and 1100 ºC, causing a drastic decline in the local pinning forces which gives rise to more pronounced abnormal growth (see Figure 9) of the affected grains in steels with relatively high Al contents [41].

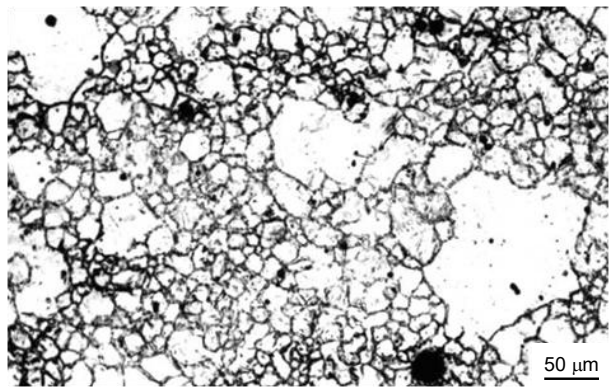


Figure 9. Example of abnormal austenite grain growth. High Al levels can facilitate local drop of pinning forces due to the dissolution of AlN.

AlN particles are usually finer than TiN that often precipitate during reheating. However, it has been found that the mean size of strain-induced AlN precipitates is almost one order of magnitude bigger than the size of other particles such as Nb and V carbonitrides [42, 43]. The diameter of a particle at any temperature can be expressed as [44, 45]:

$$\Delta d^2 = \alpha^2 D_0 \exp\left(-\frac{Q_d}{RT}\right)\Delta t \tag{12}$$

where, $D_0 \exp\left(-\frac{Q_d}{RT}\right)$ is the diffusion coefficient ($D$) of the different elements in austenite. This coefficient is represented as a function of temperature for different elements in Figure 10 [44, 46, 47]. The larger diffusion coefficient in austenite of Al compared to other elements (almost two orders of magnitude) together with the higher solubility temperatures of AlN (especially when compared to V precipitates) are the main reasons for the coarser size of AlN particles. As a result, the pinning forces exerted by coarse AlN precipitates are weak and accordingly (as occurred with TiN particles) the static recrystallization of austenite is not significantly inhibited by these particles. Figure 11 shows the curves of static recrystallization kinetics of an Al-microalloyed steel with a very short plateau that indicates that the distribution of AlN particles is not very effective to inhibit static recrystallization. In fact, the increase of activation energy for austenite recrystallization due to the presence of AlN is usually much lower when compared to V or Nb-microalloyed steels, which reveals the difficulty to achieve austenite strengthening during hot rolling by the effect of AlN pinning particles [43]. It is interesting to note that recrystallization kinetics obeys Avrami' s law before the start of the plateau and after its finish.

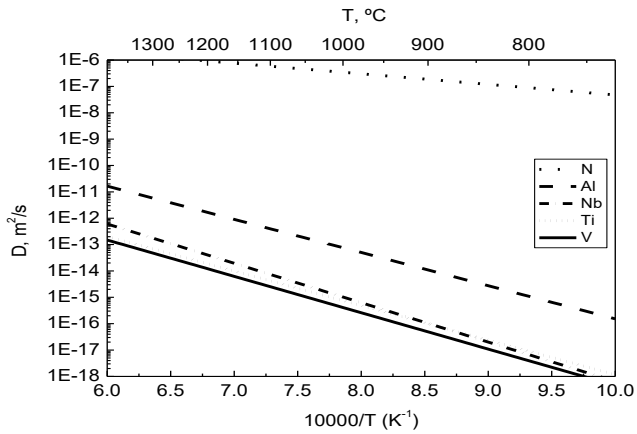


Figure 10. Diffusion coefficients in austenite for the main microalloying elements and N.

A reduction of the Al content in microalloyed steels can be beneficial because Al traps part of the N so reducing the precipitated volume of NbCN or VCN particles. A decrease in Al content can help to augment pinning forces and contribute to a more intense strengthening of the austenite during and at the end of hot rolling, thereby increasing the number of potential sites for the nucleation of ferrite [42].

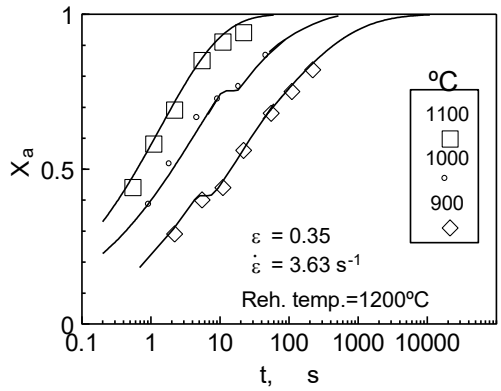


Figure 11. Recrystallized fraction ($X_a$) versus time ($t$) for a 0.1% C, 0.01% N, 0.037% Al steel.

Solubility temperatures of **niobium** carbonitrides are usually lower than the temperatures for TiN and AlN but higher than for VCN. On the other hand, Figure 10 shows that Nb presents a slightly higher diffusion coefficient than V. Therefore, as explained for Al, NbCN particles can then expected to be usually coarser than VN [48]. However, the typical range of precipitation temperatures of NbCN makes Nb an ideal element to inhibit static recrystallization during hot rolling. The isothermal curves of static recrystallization versus time for Nb steels show normally long plateaus of recrystallization inhibition. These curves sometimes display a double plateau (Figure 12) that results from the precipitation of two types of carbonitrides which start to form at very similar temperatures [6].

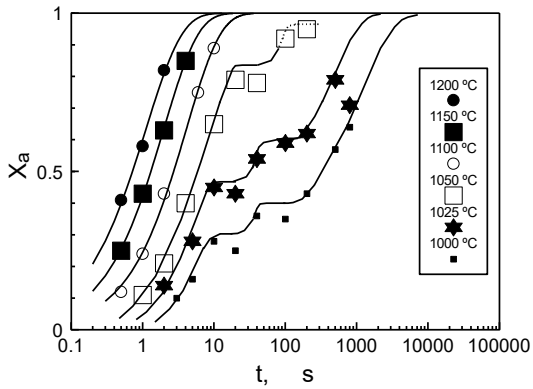


Figure 12. Recrystallized fraction ($X_a$) versus time ($t$) for a 0.21%C, 0.0061% N, 0.058% Nb steel. The curves show a double plateau associated to two types of precipitates with similar solubility temperatures.

Recrystallized fraction curves can be used to plot recrystallization-precipitation-time-temperature (RPTT) diagrams (Figure 13) as described elsewhere [6, 49]. RPTT diagrams provide useful information on aspects such as recrystallization-precipitation interaction or duration of precipitation. These diagrams also help to determine the activation energy for recrystallization $Q_x$ before and after precipitation. In Nb or V-microalloyed steels, $Q_x$ after strain-induced precipitation reaches values that are between two and three times those corresponding to the previous state, when all the elements are in solution [6]. Compared to Ti and Al steels, this increase of $Q_x$ is much more remarkable.

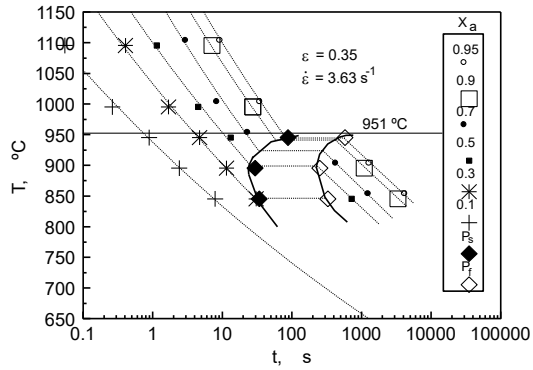


Figure 13. RPTT diagram of a 0.20%C, 0.0056% N, 0.007% Nb steel.

Under certain hot rolling conditions (short interpass times Δt and small values of pass strain ε), an addition of thousandths of Nb in the steel may be sufficient to inhibit the static recrystallization of austenite and to achieve fine final microstructures [50]. Compared to Figure 7, the curve of MFS versus the inverse of temperature in Nb steels usually presents a change in the slope that indicates a greater tendency to strengthening due to the incomplete recrystallization between passes. This change occurs at the temperature of no-recrystallization ($T_{nr}$), as shown in Figure 14. By means of thermomechanical tests and metallographic studies, it can be verified that $T_{nr}$ approximately corresponds to the temperature where recrystallization starts to be incomplete. However, incomplete recrystallization is visually evident at temperatures 50 ºC below $T_{nr}$, where grain elongation and increase in aspect ratio of the grains with temperature drop start to be significant [35, 36]. This can be seen in Figure 15, which presents the evolution of austenite microstructure during a hot rolling simulation of a medium carbon **vanadium** microalloyed steel. The strong grain refinement achieved in the first rolling passes shown in Figure 8 can be appreciated as well in this Figure. $T_{nr}$ does not always coincide with the start of strain-induced precipitation, as some fraction of precipitation can occur at temperatures above $T_{nr}$ [50]. Figure 16 shows an example of the aspect of NbCN precipitates in austenite during hot rolling.

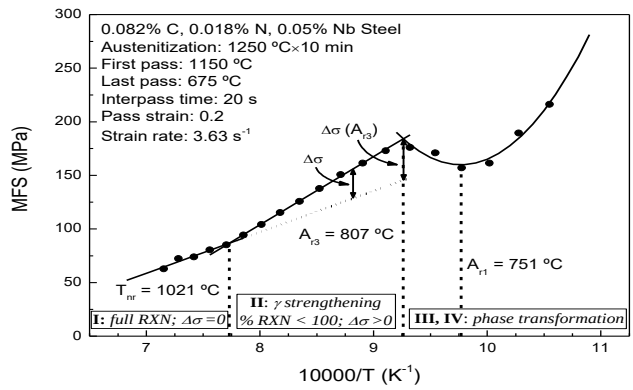


Figure 14. Dependence of Mean Flow Stress (MFS) on inverse of absolute temperature for a low carbon Nb-microalloyed steel. The no-recrystallization temperature ($T_{nr}$) is the temperature below which the recrystallization between passes starts to be incomplete.

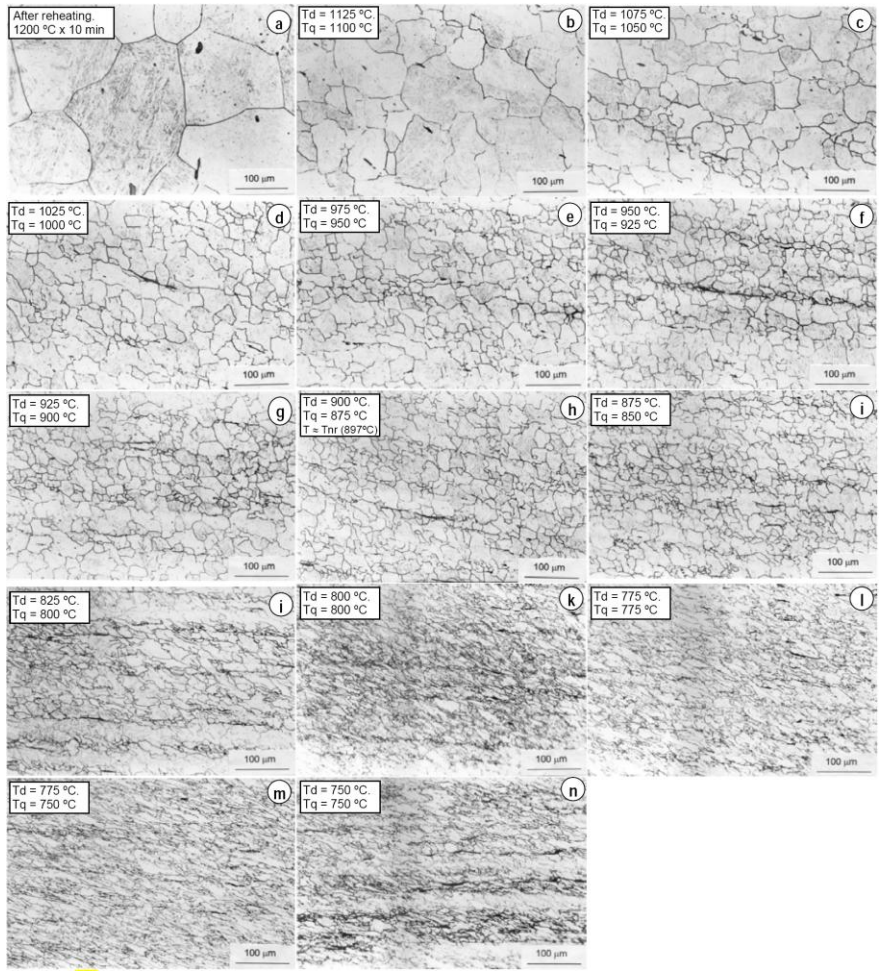


Figure 15. Microstructures obtained at different stages of a hot rolling simulation on a 0.48% C, 0.02% N, 0.13% V steel. Pass strain = 0.20; Strain rate = 3.63 $s^{-1}$; Interpass time = 20 s; "Td" means deformation temperature and "Tq" quenching temperature.

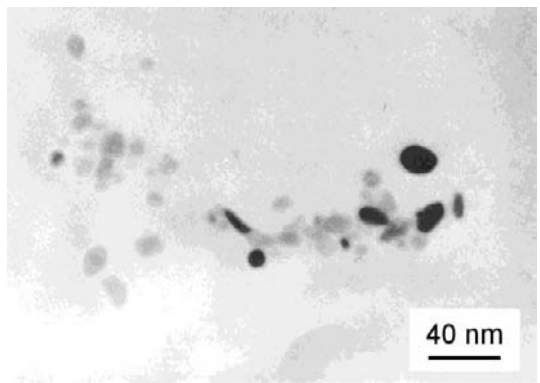


Figure 16. TEM image showing fine NbCN precipitates in a Nb-microalloyed steel (0.094% C, 0.0072% N, 0.040% Nb). Hot rolling simulation of 13 passes: reheating temperature = 1250 ºC, ε = 0.20, Δt = 100 s, last deformation pass at 850 ºC, quenching at 825 ºC. Carbon extraction replica.

Thermomechanical simulation also makes it possible to know the apparent $A_{r3}$ transformation temperature and even the $A_{r1}$ eutectoid temperature for low carbon contents [50]. On the other hand, the magnitude known as "accumulated stress" ($\Delta\sigma$) can be determined simultaneously and will be given by the length of the vertical segment drawn between the straight regression lines of phases I and II, as illustrated in Figure 14. $\Delta\sigma$, which reaches its highest value at $A_{r3}$, is a direct and precise assessment of the progressive strengthening of austenite at temperatures below $T_{nr}$ [35].

The value of $T_{nr}$ decreases significantly with increasing pass strain $\varepsilon$ [32, 50] and the same can be said for the value of $\Delta\sigma$ [51]. This results from the acceleration of recrystallization due to the higher stored energy and the successive recrystallizations of austenite at high temperatures (above $T_{nr}$). The influence of interpass time ($\Delta t$) is complex: for very short interpass times, the solute drag effect can be observed, so $T_{nr}$ strongly decreases for increasing times [32]. At longer values of $\Delta t$, the increasing volume fraction of fine precipitates makes $T_{nr}$ to increase. Finally, the coarsening of precipitates appears for long interpass times (approximately above 30-60 s) so $T_{nr}$ values drop [50, 51]. Strain induced coarsening of precipitates brings about that the decrease of $T_{nr}$ for higher strains is stronger at long interpass times. On the other hand, the value of $\Delta\sigma$ usually decreases for longer $\Delta t$ [50, 51]. As a result, in order to obtain strongly deformed austenite microstructures before the $\gamma\rightarrow\alpha$ transformation it is generally advisable to reduce the interpass time and the magnitude of the strain applied in the final passes.

The microstructure of deformed austenite, characterized by a higher value of $\Delta\sigma$, contains higher dislocation density within the grains, more elongated grains that increase the grain boundary area per unit volume and ledges in the grain boundaries. All these aspects contribute to increase the nucleation rate of ferrite during cooling and to refine the ferrite grain size [52, 53]. Figure 17 shows the microstructure obtained after different thermomechanical processing routes on a Nb-microalloyed steel. Shorter interpass times increase the value of $\Delta\sigma$ at the end of hot rolling, which ensures a finer size of ferrite after cooling from austenite. The influence of pass strain cannot be seen clearly in the figure: on the one hand, higher strains accelerate recrystallization and reduce the value of $\Delta\sigma$, but on the other hand the austenite recrystallization hardly occurs during cooling so the last deformation is accumulated in the austenite. As a result, a higher value of strain in the last pass can provide more potential sites for the nucleation of ferrite so enhancing grain refinement.

One of the most interesting technical advantages of vanadium microalloying is its contribution to enhance ferrite grain refinement thanks to the intragranular nucleation of ferrite on VN or VCN precipitates. If samples of a V-microalloyed steel are cooled after different post-deformation isothermal holding times corresponding to the beginning and the end of the plateau of inhibition of recrystallization, it is found that the existence of a distribution of strain-induced VCN precipitates at the end of the plateau leads to a significant decrease in the grain size, close to 50%, as Figure 18 shows. VCN precipitates can serve as nucleation sites for very fine (close to 1 micron size) ferritic grains (see Figure 19) [54]. The intragranular nucleation on precipitates is an important contribution to the ferrite grain refinement, although the nucleation of the ferrite on austenite grain boundaries and dislocations within the grains is usually more important. The positive influence of intragranular nucleation on precipitates is comparatively stronger for low strains applied. An increase in the strain favors nucleation of ferrite on austenite recrystallized grain boundaries,

as the austenite grain is finer, and on subgrains, in preference to intragranular nucleation on VN-precipitates [55, 56].

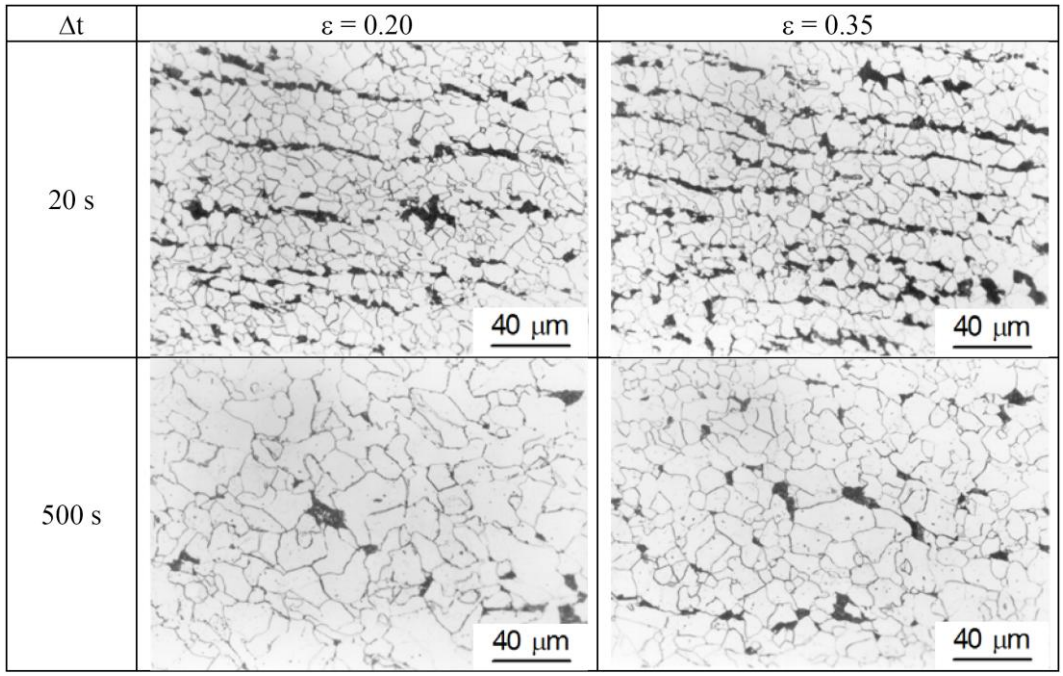


Figure 17. Ferrite-pearlite microstructures obtained after hot rolling simulations carried out under given conditions followed by argon cooling from 825 ºC. 0.09% C, 0.017% N, 0.017% Nb Steel.

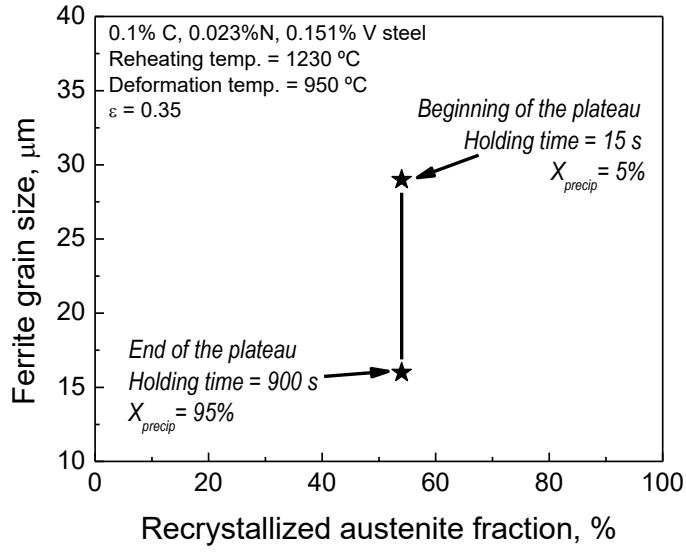


Figure 18. Ferrite grain size versus recrystallized austenite fraction. Grain size drops as post-deformation isothermal holding time increases and precipitated fraction grows.

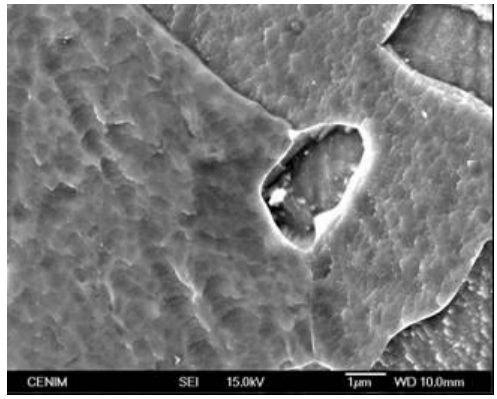


Figure 19. SEM-FEG image showing a small ferrite grain and a large VN precipitate. 0.1% C, 0.023% N, 0.151% V steel. Reheating temperature = 1230 ºCx10 min. Deformation temperature = 950 ºC; ε = 0.35; Post-deformation holding time = 900 s.

Figure 20 shows that the value of accumulated stress (Δσ) obtained at the end of hot rolling simulation of a certain family of steels provides an important information about the chances to achieve ferrite grain refinement after cooling. The data of this plot come from steels with different amounts of carbon and other alloying elements and slight variations in processing schedule and final rolling temperature, but this graph is a useful orientation. In general, Ti-microalloyed steels offer coarser ferrite grain sizes compared to Nb microalloyed steels, where the value of $T_{nr}$ is usually higher. On the other hand, the phenomenon of intragranular nucleation of ferrite on VCN particles can contribute to a stronger ferrite grain refinement in V-microalloyed steels. The aforementioned complex influence of pass strain can be observed: in general, a lower value of strain generates higher values of Δσ, but for a constant Δσ, the application of higher strains in the last pass enhances grain refinement due to the accumulation of the last deformation in the austenite. It is known that a simultaneous improvement of mechanical properties of strength and toughness with ferrite grain refinement can be expected according to the published equations that relate yield strength and impact transition temperature to ferrite grain size [39, 57].

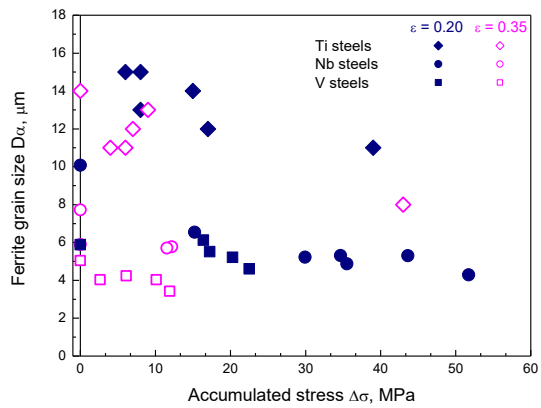


Figure 20. Ferrite grain size as a function of accumulated stress obtained at the end of hot rolling simulations carried out under different conditions of pass strain and interpass time on several low carbon microalloyed steels.

## CONCLUSION

Precipitates of the microalloying elements play a major role on several aspects of the thermomechanical processing of steels such as the austenite grain growth, static recrystallization kinetics and phase transformation. Titanium is the most effective element to control grain growth at high reheating temperatures and a hypostoichiometric Ti/N ratio close to 2 is recommended. Ti/N ratio also affects hot deformation behavior and static recrystallization. The static recrystallization kinetics in Ti-microalloyed steels is fast due to the fine initial austenite grain size and the higher value of the recrystallization driving forces compared to the pinning forces exerted by TiN particles precipitated at high temperatures. During rolling, the austenite in Ti-steels experiences a minor reduction of austenite grain size in the first passes and a limited hardening below $T_{nr}$. At medium reheating temperatures, aluminum can help to control grain growth, but its addition to Ti steels can be harmful because it promotes abnormal grain growth at temperatures near 1100 ºC. The inhibition of static recrystallization by AlN particles is not remarkable, whereas niobium carbonitrides are very effective to hinder static recrystallization of austenite during hot rolling, due to their adequate precipitation temperature range and strong pinning effect. This is seen in the high values of no-recrystallization temperature ($T_{nr}$) and accumulated stress ($\Delta\sigma$), which is a magnitude that helps to characterize the progressive strengthening of austenite due to the incomplete recrystallization below $T_{nr}$. A significant relationship between the value of $\Delta\sigma$ at the end of rolling (just before cooling) and the final ferritic grain size can be described. Finally, particles of vanadium carbonitrides (precipitated at lower temperatures than NbCN) serve as preferential sites for the intragranular nucleation ferrite and help to enhance the ferrite grain refinement.

## REFERENCES

[1] Jonas, J. J.; Akben, M. G. *Metals Forum*, 1981, 4, 92–101.
[2] Medina S. F.; Quispe A. *ISIJ Int*, 2001, 41, 774–781.
[3] Hillert, M. *Acta Mater*, 2004, 52, 5289–5293.
[4] Kim, S. G.; Park, Y. B. *Acta Mater*, 2008, 56, 3739–3753.
[5] Bäcke, L. *ISIJ Int*, 2010, 50, 239–247
[6] Medina, S. F.; Quispe, A.; Gomez, M. *Mater Sci Technol*, 2003, 19, 99–108.
[7] Smith C. S. *Trans Metall Soc AIME*, 1948, 175, 15–51.
[8] Manohar, P. A.; Ferry, M.; Chandra, T. *ISIJ Int*, 1998, 38, 913–924.
[9] Hillert, M. *Acta Metall*, 1965, 13, 227–238.
[10] Gladman, T. Proc R Soc London, 1966, 294, 298–309.
[11] Gladman, T.; Pickering F. B. *J Iron Steel Inst*, 1967, 205, 653–664.
[12] Ashby, M. F.; Harper, J.; Lewis, J. *Trans Metall Soc AIME*, 1969, 245, 413–420.
[13] Randle, V.; Ralph, B. *Acta Metall*, 1986, 35, 891–898.
[14] Gladman, T. *Mater Sci Forum*, 1992, 94-96, 113–128.
[15] Adrian, H.; Pickering, F. B. *Mater Sci Technol*, 1991, 7, 176–182.
[16] Hansen, S. S; Van der Sande, J. B.; Cohen, M. *Metall Trans A*, 1980, 11A, 387–402.

[17] Cuddy, L. J. In Proc. Int. Conf. Thermomechanical Processing of Microalloyed Austenite; ed. by A. J. DeArdo, G. A. Ratz and P. J. Wray; The Metallurgical Society of AIME: Pittsburgh, PA, 1982, 129–140.
[18] Faessel, A. *Rev Metall CIT*, 1976, 33, 875–892.
[19] Andrade, H. L.; Akben, M. G.; Jonas, J. J. *Metall Trans*, 1983, 14A, 1967–1977.
[20] Narita, K. *Trans ISIJ*, 1975, 15, 145–152.
[21] Turkdogan, E. T. *Trans ISS*, 1989, 3, 61–75.
[22] Inoue, K.; Ohnuma, I.; Ohtani, H.; Ishida, K.; Nishizawa, T. *ISIJ Int*, 1998, 38, 991–997.
[23] Pickering, F. B. In Titanium Technology in Microalloyed Steels; ed. by T. N. Baker; The Institute of Materials: London, 1997, 10–43.
[24] Vega, M. I.; Medina, S. F.; Quispe, A.; Gomez, M.; Gomez, P. P. *ISIJ Int*, 2005, 45, 1878–1886.
[25] Chaves, J. I.; Medina, S. F.; Gomez, M.; Rancel, L.; Valles; P. *Mater Sci Forum*, 2007, 550, 405–410.
[26] Lifshitz I. M.; Slyozov, V. V. *J Phys Chem Solids*, 1961, 19, 35–40.
[27] Kunze, J.; Mickel, C.; Backmann, G.; Beyer, B.; Reibold, M.; Klinkenberg, C. *Steel Res*,1997, 68, 441–449.
[28] Medina S. F.; Chapa, M.; Valles, P.; Quispe, A.; Vega, M. I. *ISIJ Int*. 1999, 39, 930–936.
[29] Medina, S. F.; Vega, M. I; Gomez, M.; Gomez P. P. *ISIJ Int*, 2005, 45, 1307–1315.
[30] Beynon, J. H.; Sellars, C. M. *ISIJ Int*, 1992, 32, 359–367.
[31] Sellars, C. M. In Proc. Int. Conf. on Hot Working and Forming Processes; ed. by C. M Sellars and G. J. Davies; Metal Society: London, 1980, 3–15.
[32] Bai, D. Q.; Yue, S.; Sun W. P.; Jonas J. J. *Metall Trans*, 1993, 24A, 2151–2159.
[33] Vega, M. I.; Medina, S. F.; Quispe, A.; Gomez, M.; Gomez, P. P. *Mater Sci Eng A*, 2006, 423, 253–261.
[34] Gomez, M.; Rancel, L.; Gomez, P. P.; Robla, J. I.; Medina S. F. *ISIJ Int*, 2010, 50, 868–874.
[35] Gómez, M.; Rancel, L.; Fernandez, B. J.; Medina, S. F. *Mater Sci Eng A*, 2009, 501, 188–196.
[36] Gómez, M.; Rancel, L.; Medina, S. F. *Met Mater Int*, 2009, 15, 689–699.
[37] Mintz, B.; Arrowsmith, J. M. In Proc. Int. Conf. on Hot Working and Forming Processes; ed. by C. M Sellars and G. J. Davies; Metal Society: London, 1980, 99–103.
[38] Funnell, G. D. In Proc. Int. Conf. on Hot Working and Forming Processes; ed. by C. M Sellars and G. J. Davies; Metal Society: London, 1980, 104–107.
[39] Gladman, T. In The Physical Metallurgy of Microalloyed Steels, The Institute of Materials, London, (1997).
[40] Cabrera, J. M.; Al Omar, A.; Prado, J. M. Z Metallkd, 1998, 89, 47–58.
[41] Medina, S. F.; Chapa, M.; Gómez, M.; Quispe, A.; López, V.; Fernández, B. *Rev Metal Madrid*, 2003, 39, 408–417.
[42] Gómez, M.; Rancel, L.; Medina, S. F. *Mater Sci Eng A*, 2009, 506, 165–173.
[43] Gómez, M.; Rancel, L.; Medina, S. F. *Mater Sci Forum*, 2010, 638-642, 3388–3393.
[44] Oikawa, H. Tetsu-to-Hagane, 1982, 68, 1489–1497.
[45] Okaguchi, S.; Hashimoto T. *ISIJ Int*, 1992, 32, 283–290.

[46] Vignes, A.; Philebert, J.; Badía, J.; Lavasseur, J. In Proc. 2nd Natl. Conf. Microprobe Analysis; Boston, 1967, Paper 20.
[47] Fast, J. D. In Interaction of Metals and Gases; Macmillan New York: London, 1976, 221.
[48] Medina, S. F.; Gomez, M.; Gomez, P. P. *J Mater Sci*, 2010, 45, 5553–5557.
[49] Medina, S. F.; Ouispe, A.; Valles, P.; Baños, J. L. *ISIJ Int*, 1999, 39, 913–922.
[50] Gomez, M.; Medina, S. F.; Ouispe, A.; Valles, P. *ISIJ Int*, 2002, 42, 423–431.
[51] Gomez, M.; Hernanz, O.; Medina, S. F.; Tarin, P. *Steel Res*, 2002, 73, 446–452.
[52] Umemoto, M; Hiramatsu, A; Moriya, A.; Watanabe, T.; Nanba, S.; Nakajima N.; Anan, G.; Higo, Y. *ISIJ Int*, 1992, 32, 306–315.
[53] Yu, Q.; Wang, Z.; Liu, X.; Wang, G. *ISIJ Int*, 2004, 44, 710–716.
[54] Medina, S. F.; Gómez, M.; Rancel, L. *Scripta Mater*, 2008, 58, 1110–1113.
[55] Medina, S. F.; Gómez, M.; Chaves, J. I.; Gómez, P. P.; Adeva, P. *Mater Sci Forum*, 2005, 500-501, 371–378.
[56] Medina, S. F.; Rancel, L.; Gómez, M.; Ishak, R.; De Sanctis, M. *ISIJ Int*, 2008, 48, 1603–1608.
[57] Pickering, F. B. In Physical Metallurgy and the Design of Steels; Ed. Science Publishers Ltd.: London; 1978, 66–88.

In: Advances in Mechanical Engineering Research. Volume 2 ISBN: 978-1-61761-984-7
Editor: David E. Malach 

*Chapter 7*

# EXPERIMENTAL AND NUMERICAL INVESTIGATION OF VACUUM INVESTMENT CASTINGON HEAT TRANSFER AND PART QUALITY OF BRASS

***A. N. Vassiliou[1], D. I. Pantelis[1] and G. -C. Vosniakos[2]***

[1]Shipbuilding Technology Laboratory, Department of Marine Structures, School of Naval Architecture and Marine Engineering, National Technical University of Athens, Heroon Polytechniou 9, 15780, Athens, Greece

[2]Department of Manufacturing Technology, School of Mechanical Engineering, National Technical University of Athens, Heroon Polytechniou 9, 15780, Athens, Greece

## ABSTRACT

Vacuum casting is widely used as an investment casting method for small parts of complex geometry. Selection of casting conditions for acquiring sound castings is not a trivial process. In modern casting machines, the application of pressure directly after completion of melt pouring is used to ensure proper filling of the very fine details of the casting tree.The present work concerns examination of casting conditions of brass on a modern vacuum-pressure casting machine, in order to reveal their influence on part quality. A parametric investigation was carried out with respect to pressure in the upper chamber and vacuum in the lower chamber of the machine. The obtained cast samples were examined with optical microscopy in order to identify possible defects, while image analysis was used in order to quantify porosity in each sample.In addition, casting simulation software was exploited to enhance process knowledge. The major issue in obtaining realistic results from simulation was the determination of the interfacial heat transfer coefficient (HTC). This was achieved using experimental cooling curves, obtained with K-type thermocouples during casting under pre-defined conditions. The heat transfer coefficient, once estimated in eachcase from the corresponding simulations, was, then, used in further typical casting scenarios. These scenarios were analyzed with commercially available casting simulation software. The purpose was to determine the influence of casting parameters on mould filling time, porosity and solidification time.

***Keywords:*** Vacuum–pressure casting, investment casting, heat transfer coefficient, porosity.

## 1. INTRODUCTION

Vacuum investment casting is used for producing small parts of complex shape [1], [2], [3]. The application of vacuum is intended to increase mould filling rate and to provide a protective atmosphere during melting of the alloy thusavoiding the creation of oxides. Moreover, the application of pressure directly after completion of the melt pouring process is used as an extra feature to improve filling of the very fine details of the casting tree [3], [4]. The effect of vacuum and pressure in solid investment casting has not been adequately examined in literature, so far.

Selection of casting conditions in general (e.g. initial melt temperature, mould temperature, casting atmosphere and pressure) for acquiring sound casts is not a trivial process. Appropriate casting parameters may be selected either by conducting a large number of experiments (experimental approach) or by using casting simulation software (computational approach). The experimental approach is directly dependent on expertise, involving both high cost and difficulty in defect investigation by microscopyand/or a destructive method. The computational approach, on the other hand, offers not only the possibility of trying any set of casting conditions but also easy monitoring of the process at every stage and convenient post-processing of the resulting casting (porosity, incomplete filling, solidification time etc).

Manufacturing sound parts without any defects is primarily necessary to avoid complete costly repair processes after casting such as grinding of surfaces, weld-filling of cavities and holes and or even recasting [5].Consequently, casting simulation is widely used in modern foundry industry, as a tool in product design and process development, keeping the costs of development low and competitive [6], [7]. Casting simulation software can enhance process knowledge; provided that initial conditions, boundary conditions, material properties and numerical analysis parameters are correctly defined [6]. [8], [9].A key-input is the Interface Heat Transfer Coefficient (IHTC or, simply, HTC) between the metal and the mold [10], [11].Determining the appropriate HTC value is a practical problembecause HTC is not a material property, but a parameter heavily dependent on the existing conditions notably: thermophysical properties of the contacting materials, casting and mould shape and size, processing techniques, roughness of the mould contacting surface, mould coatings, contact pressure, melt superheat [5], as well as initial temperature of the mould [6], [11], [12], [13], [14]. HTC governs in effect the heat flow and different heat flow rates across the cast metal and mold surface regions affect the evolution of solidification and the micro-structural properties of the casting.

Within this framework, casting of brass parts was investigated on a modern customised vacuum casting machine with embedded thermocouples. Experiments were conducted for five cases of pressure difference between the upper and the lower chamber of the machine. In this way, experimental cooling curves were obtained. A single HTC was, then,determined for each casting caseby comparingthese curves with those obtained by simulation with HTC values determined in a trial-and-error manner. Next, casting simulations were carried out in order to reveal the influence of the casting parameters including the influence of pressure difference between the two chambers on HTC values, solidification time, porosity and filling quality. The corresponding experimental samples were examined with optical microscopy to investigate microstructure and porosity defects.

# 2. EXPERIMENTAL PROCEDURE

## 2.1. The Casting Tree

Each part consisted of three concentric cylinders with decreasing diameter as shown in Figure 1. The wax pattern is shown in Figure 2. The part is fed by a central sprue of 6 mm diameter and 30mm height. The material used was brass composed of 66.7%Cu and 33.3%Zn. Melting was conducted in a graphite crucible, with a capacity of 1kgr.

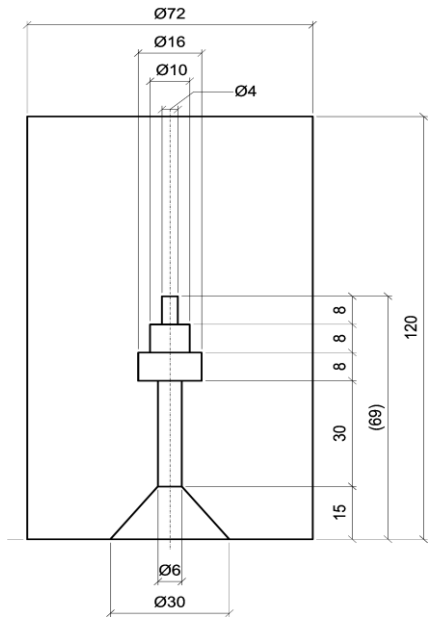


Figure 1. The casting tree, the dimensions of the pattern and the dimensions of the mould.

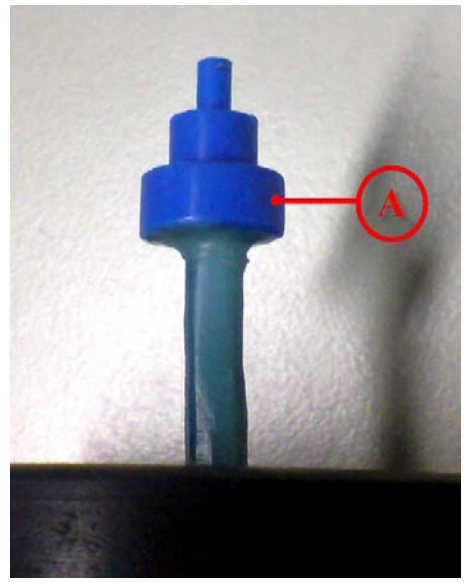


Figure 2. The wax pattern and the location where the thermocouple has been placed (point A).

## 2.2. Solid Investment Casting

The solid investment casting process uses plaster as the mould material and belongs to the lost-wax class of casting processes. The mould was produced by surrounding the wax tree with plaster slurry that sets at room temperature. The mould was then allowed to dry for two hours before the wax pattern was burned out (dewaxing) at 150$^{o}$C for two hours in a dewaxing oven, leaving the mould cavity ready to accommodate the melt. The mould was, afterwards, subjected to a burnout cycle to allow the plaster to dry out and obtain high toughness. Burnout consisted of heating in a furnace from 150$^{o}$C to 740$^{o}$C for 5 hours, holding at 730$^{o}$C for 2 hours, and then at casting temperature for temperature homogenization for another 2 hours.

The mould is setup in the casting chamber of the casting machine at a temperature high enough to help the alloy remain in the liquid phase long enough, so it can better fill the fine details of the cavity and to prevent the dissolution of the plaster due to thermal shock.

## 2.3. The Vacuum Casting Machine

A vacuum-pressure casting machine was used (Figure 3). The casting machine consists of two chambers: the melting chamber and the casting chamber with separate vacuum / pressure control.

The main objective of the experiments was to measure the variation of the temperature of the melt with time, as close to the mould – metal interface as possible using theromocouples.

The placement of thermocouples in the mould, should ensure impermeability. Typical vacuum casting machines do not allow thermocouple cables to enter the mould chamberwithout sacrificing vacuum sealing.

Sealing of the vacuum chamber around the thermocouple inlet/exit openings was ensured by special flanges with cable coupling extensions and with appropriate investment and ceramic connectors used to withstand the high temperatures developed within the chamber (see Figure 4).

Figure 3. The casting machine.

Figure 4.The casting chamber of the vacuum – pressure casting machine with appropriate modifications to accommodate the thermocouples.

## 2.4. Thermocouple Embedding

Calibrated K-type thermocouples were used. The thermocouples were inserted at location 'A', see Figure 2. The objective was to measure the temperature of the cast metal during cooling, as close to the casting-mould interface as possible. K-type thermocouples consist of two wires, welded at their end to form a tip.

The thermocouple was placed by taking advantage of the presence of the wax pattern. The thermocouple tip was heated up and then slightly pushed against the wax pattern at the desired location. This is easily achieved, since the diameter of the tip is about 1mm. A significant advantage in this case is that thermocouple wires are external to the mould cavity, ensuring non-interference with the melt.

Thermocouple characteristics were: K-type 24 AWG, operation range: -270 $^{o}$C to 1370 $^{o}$C and practically 0 $^{o}$C to 1100 $^{o}$C, positive lead material : Ni(90%)–Cr(10%), negative lead material Ni(95%)–Al (2%)–Mn (2%).The thermocouples were connected to a suitable D/A converter and this, in turn, to a recording computer and proprietary software.

## 2.5. Casting Conditions

The casting conditions that may be controlled are the mould temperature ($T_{mould}$), the initial melt temperature ($T_{inlet}$), the pressure in the upper and the vacuum in the lower chamber, independently. In this study the objective was the investigation of the effect of pressure conditions on final part, thus mould and melt temperatures were kept constant at 730°C and 960°C respectively, see Table 1. Vacuum casting experiments were conducted for five different cases of pressure conditions that concluded to five cooling curves. A fifth case, see Table 1, was added, i.e. gravity to serve as reference.

**Table 3. Casting Conditions**

| | Experiment #1 Vacuum | Experiment #2 Pressure | Experiment #3 Pressure-Vacuum | Experiment #4 50%Vacuum | Experiment #5 Gravity |
|---|---|---|---|---|---|
| Tmould (°C) | 730 ± 1.5 | | | | |
| Tmetal (°C) | 960 ± 1.5 | | | | |
| Pressure in the melting chamber(bar) | 1.00 | 1.50 | 1.50 | 1.00 | 1.00 |
| Pressure in the casting chamber(bar) | 0.03 | 1.00 | 0.03 | 0.50 | 1.00 |
| Flow rate (kg/sec) | 1.134 | 0.816 | 1.381 | 0.816 | 0.214 |

# 3. VACUUM CASTING SIMULATION

ProCAST 2004.0 by ESI Group was used as the simulation tool performing coupled thermal - flow analysis. The input parameters for the simulation were the same with the experimental conditions, seeTable 1.

The other initial and boundary conditions used were as follows:

**Table 4.Initial and Boundary Conditions for Casting Simulation**

| | | Experiment | | | | |
|---|---|---|---|---|---|---|
| | | #1 Vacuum | #2 Pressure | #3Pressure-Vacuum | #450% Vacuum | #5 Gravity |
| Boundary Conditions | Temperature (°C)<br>Pressure (bar)<br>Surface Load (bar)<br>Flow Rate (kg/sec) | 730<br>0.03<br>-<br>1.134 | 730<br>-<br>1.5<br>0.816 | 730<br>0.03<br>1.5<br>1. 381 | 730<br>0.5<br>-<br>0.816 | 730<br>-<br>-<br>0.214 |
| Initial Conditions | Tmould (°C)<br>Tmetal (°C) | 730<br>970 | 730<br>970 | 730<br>970 | 730<br>970 | 730<br>970 |

Plaster properties were taken from literature as follows: specific heat: 0.84 KJ/kg/K, thermal conductivity: 0.5 W/m/K, density: 1100kg/m$^3$.

Brass properties used were: liquidus temperature: 931$^o$C, solidus temperature: 886$^o$C, latent heat: 205KJ/kg. Variation of viscosity, density, thermal conductivity and enthalpy are shown in Figure 5.

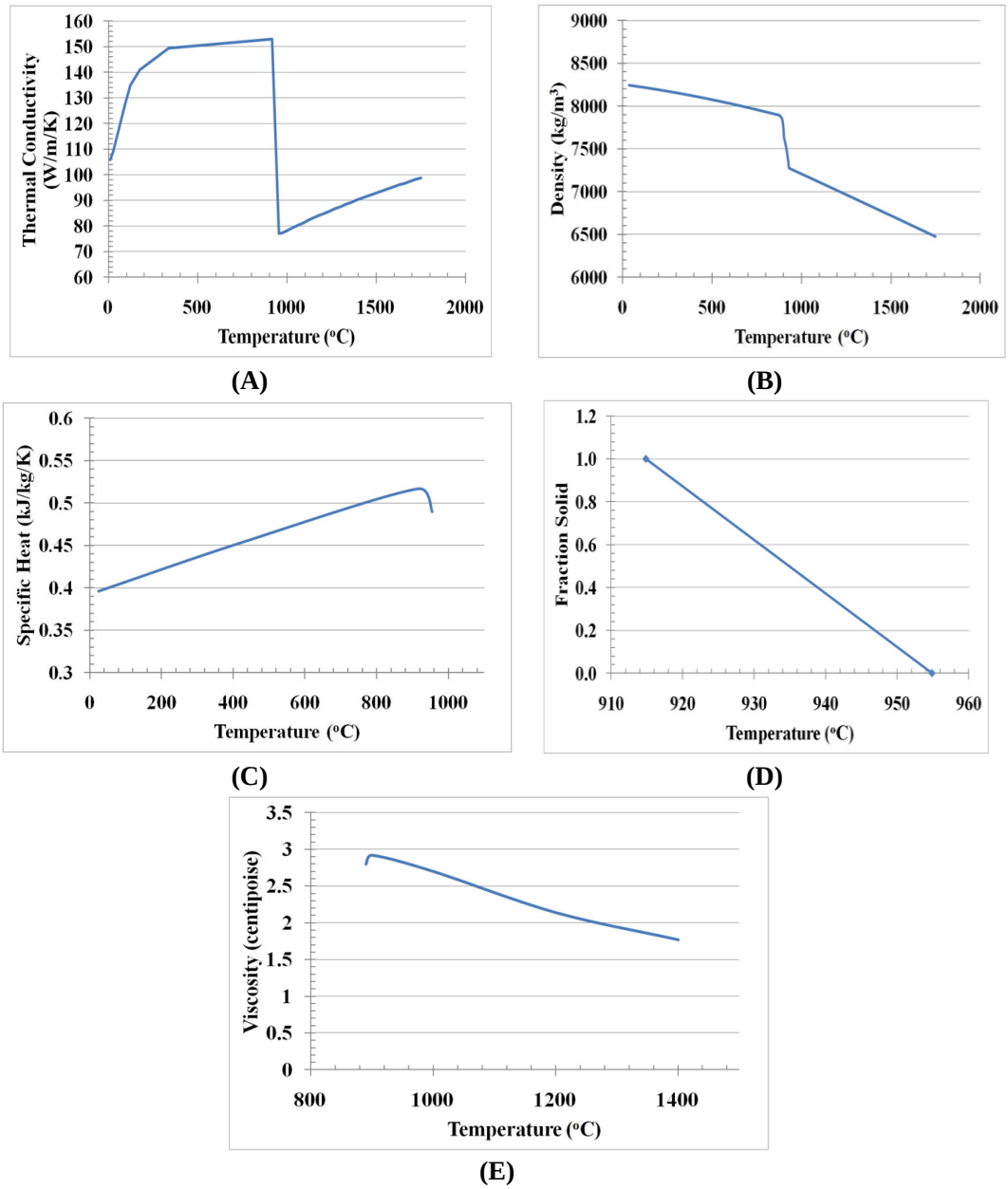


Figure 5. Brass properties with respect to temperature: (A) thermal conductivity, (B) density, (C) specific heat, (D) fraction solid and (E) viscosity.

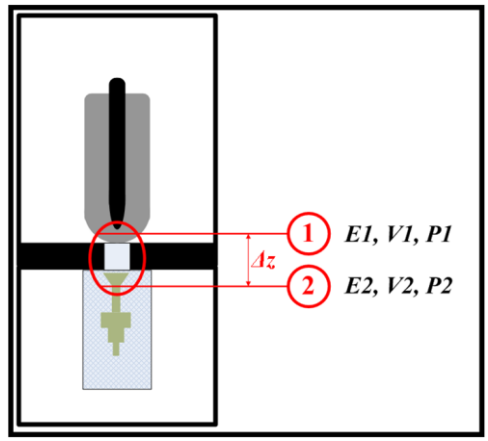


Figure 6. Schematic picture of the casting machine with the reference points for the Bernoulli equation.

The flow rate depends on the pressure difference between the upper and the lower chamber of the casting machine, the geometry of the crucible and the melt density (see Figure 6):

$$\dot{m} = Q\,\rho$$

where:

$\overset{o}{m}$ : mass flow rate (kg/sec)

$Q = v_2 A$ : volumetric flow rate($m^3$ /sec)

$v_2$ : inlet velocity

A : inlet cross section area ($m^2$)

$\rho$ : melt density (kg/ $m^3$)

Velocity at point 1 is $v_1$=0 and at point 2 it is approximated as:

$$v_2 = \sqrt{\frac{2(p_1 - p_2)}{\gamma} g + 2g\Delta z} \left(\frac{m}{s}\right)$$

where:

$p_1$: pressure in the melting chamber (inlet pressure)

$p_2$: pressure in the casting chamber

Δz: height difference between point 1 and point 2.

γ: specific weight of the melt ($\gamma = \rho\, g$ , g: acceleration due to gravity)

The behaviour of the mould - melt interface must be modelled by introducing a single appropriate value for the heat transfer coefficient, either constant or as a function of time. A detailed description of HTC determination follows.

## 4. CALCULATION OF THE HEAT TRANSFER COEFFICIENT

Heat Transfer Coefficient determination was attempted using a trial – and– error approach. At first, several random values were assigned to the HTC and simulations have been conducted. At the end of each simulation the resulting cooling curve at location 'A', see Figure 2, was plotted, and compared to the experimentally obtained curve.

The trial – and – error approach is not an automated process. It is dependent on the user's criterion of choosing the values to be tested, and assessing the convergence of the two curves. Nevertheless, it has an interesting advantage when compared to the inverse numerical methods often used in similar cases. These methods are fully dependent on the measurement accuracy during the first moments of the solidification process[5]. There is a critical difference in studies that have used K-type thermocouples compared to those that have used T-type ones, due to the slower response of the latter. This problem is circumvented by interpolation of the missing values due to the poor sampling. A trial – and – error method may also be used as the stable basis for other techniques of HTC estimation, e.g. for training appropriate neural networks.

A large number of HTC values were tested, until satisfactory agreement of experiment and simulation was achieved at point A, see Figure 2.

Figures 7-11 present experimental cooling curves (in bold) against numerically calculated cooling curves (thin lines). Convergence of the two curves is the sole criterion during the trial – and – error process for HTC determination. Figures 7-11(a) depict the cooling curves for the first 250 sec of the solidification process in the temperature range [800-980$^{o}$C]. Figures 7-11(b) depict the same curves, plotted for a much smaller duration (50 sec) and a correspondingly narrower temperature range [900-990$^{o}$C], in order to reveal the proximity of the two curves during the largest part of first stages of solidification.

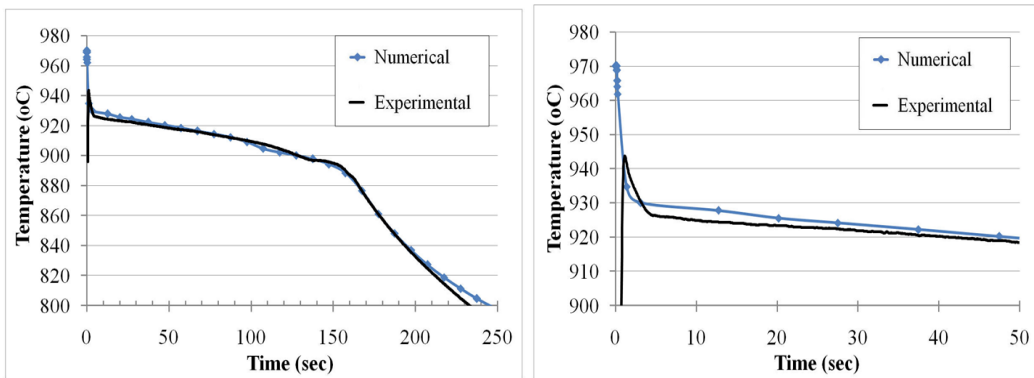


**(a)** **(b)**

Figure 7 Experimental and simulated 0cooling curves for gravity casting (ΔP=0bar) (a) 0-250 sec (b) 0-50 sec.

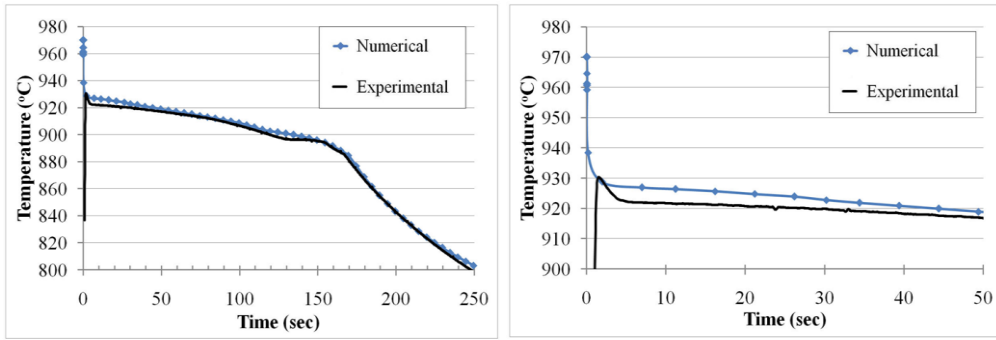


**(a)** **(b)**

Figure 8 Experimental and simulated cooling curves for pressure casting (ΔP = 0.5bar), (a) 0-250 sec (b) 0-50 sec.

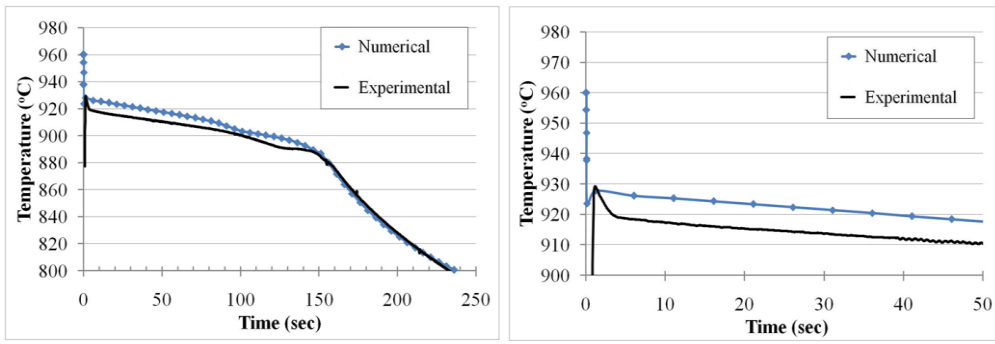


**(a)** **(b)**

Figure 9 Experimental and simulated cooling curves for 50% vacuum casting (ΔP = 0.5bar) (a) 0-250 sec (b) 0-50 sec.

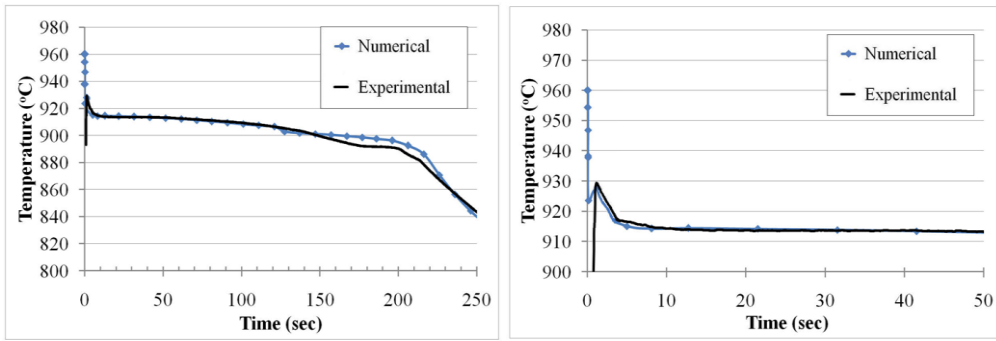


(a) (b)

Figure 10 Experimental and simulated cooling curves for vacuum casting (ΔP = 0.93bar) (a) 0-250 sec (b) 0-50 sec.

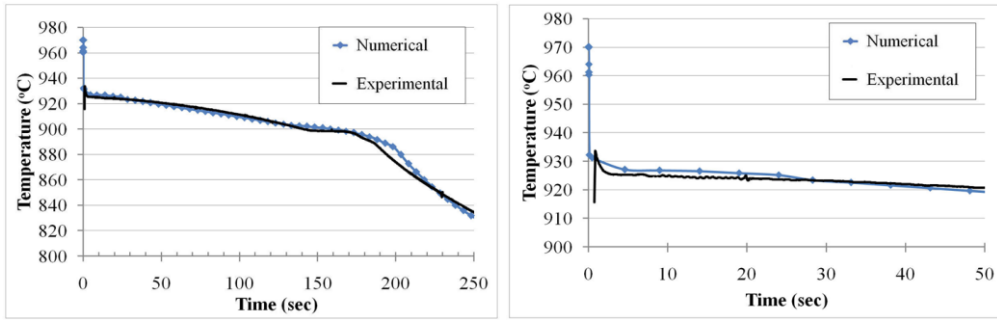


Figure 11. Experimental and simulated cooling curvesfor vacuum - pressure casting (ΔP = +1.47bar) (a) 0-250 sec (b) 0-50 sec.

Thus, five time–dependant heat transfer coefficients, one for each casting case, see Table 1, were determined, as depicted in Figures 12 (a) – (e).

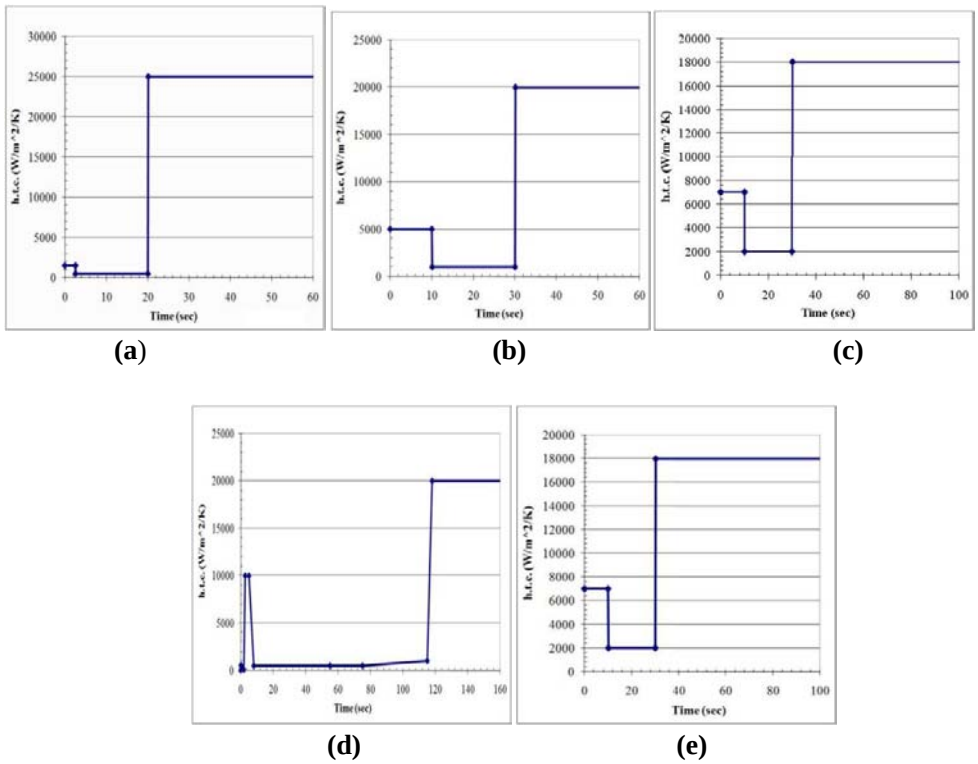


Figure 12. HTC as a function of time for (a) gravity casting (ΔP = 0 bar), (b) pressure casting (ΔP = 0.5bar), (c) 50% vacuum casting (ΔP = 0.5bar), (d) vacuum casting (ΔP = 0.97bar) and (e) vacuum – pressure casting (ΔP = 1.47bar).

It is relatively well-established in literature that variation of HTC with time can be distinguished into three stages, [16]**:** stage I, where the metal remains in liquid phase and HTC (h1) decreases rapidly from a high initial value, stage II, which starts when temperature drops below the liquidus line and HTC (h2) has a constant value, and stage III, where the

value of HTC (h3) either increases, due to an increase in contact pressure, or decreases due to the increase in the gap between the casting and the mould, or, even,remains constant, if the pressure is constant.

The pattern of HTC variation described above was observed in this work, too, see Figure 12.It is noted that the value of the third region of HTC ($h_3$) is higher than that of the first region. Since all cases have been handled in the same way, qualitative conclusions may be reached as far as the effect on HTC of the pressure difference in the melting and casting chambersis concerned.

In Table 2, the effect of pressure difference on the values for the first, the second and the third region of the HTC ($h_1$, $h_2$, $h_3$) and on the time at which the first and the second region respectively end ($t_1$, $t_2$) is depicted.The HTC value for the first region generally increases with pressure difference. In vacuum – pressure casting, the pressure difference of 1.5bar pushes the melt towards the mould wall, offering a rather good contact that concludes in a higher rate of heat flow. This is the reason why, in the first stage of HTC variation, the value in vacuum – pressure casting is higher compared to the case of gravity casting. In the cases of pressure casting and vacuum casting, where $\Delta P$=0.5 bar, the values of $h_1$are not the same, as one could expect. When a pressure difference of 0.5bar is applied using vacuum, the higher value of h1 indicates an improved contact between the melt and the mold, compared to the difference being created through pressure alone.

In Table 2, it can be seen that the value of $h_2$ in most cases is almost the same (around 500 W/m$^2$/K), with the exception of 0.5bar of vacuum, where a very high value is noted. It is also evident that in the case of vacuum – pressure casting ($\Delta P$=1.5bar), the value of $h_3$is rather high. Almost the same $h_3$ value applies in the cases of vacuum casting (50%Vacuum or Vacuum) and pressure casting (1.5bar). During gravity casting, the cooling rate is much slower. The mechanism depicted behind the $h_3$ values, is the contact between the solidified outer layer of the cast and the mould. The difference between cooling rate during the first two stages and the third stage is very pronounced indeed in the case of gravity casting.

Table 4depicts the duration of stages I and II for the cases examined.

**Table 5. Casting Conditions**

| HTC (W/m$^2$/K) | Exp. #1 Vacuum | Exp. #2 Pressure | Exp. #3 Pressure-Vacuum | Exp. #4 50%Vacuum” | Exp. #5 Gravity |
|---|---|---|---|---|---|
| h1 | 10000 | 5000 | 12000 | 7000 | 1500 |
| h2 | 500 | 1000 | 300 | 2000 | 500 |
| h3 | 20000 | 20000 | 8500 | 18000 | 25000 |

**Table 6.Duration of stages I and II of HTC variation**

| | Exp. #1 Vacuum | Exp. #2 Pressure | Exp. #3 Pressure-Vacuum | Exp. #4 50%Vacuum | Exp. #5 Gravity |
|---|---|---|---|---|---|
| t1(sec) | 8.0 | 10.0 | 5.4 | 10.0 | 2.5 |
| t2 (sec) | 118.0 | 30.0 | 28.0 | 30.0 | 20.0 |

Note that, in this case, HTC is a single value and describes an ideal case where all points of the melt/casting undergo the same changes. Casting simulation software often offers the possibility to define different HTC values at different interfaces. Such an assumption, especially in aresearch context and in the light of no available relevant literature data, would create a series of issues. First of all, the criteria according to which the original single cavity is to be split into sub-cavities for each of which one HTC will suffice are not clearly determined. These criteria might involve among others the casting modulus (cross-section variation), but a lot of experimentation would be required. Thus, any parametric study on casting conditions would be dependent on the way in which the part had been divided into smaller parts, as well as on the HTC individual values for each interface. In any case, the algorithmic complexity would be rather large for determining the HTC value for each interface. Therefore, this is an issue for future investigation. In our case, an "average" situation is considered to be adequate as an initial approach.

# 5. EFFECT OF PRESSURECONDITIONS

Quantification of the effect of pressure conditions on the final part would clarify the reasons why and under which circumstances a casting method might be preferable to another one.

Towards this direction, the effect of pressure conditions was examined comparing the five cases registered in Table 1, keeping mould and initial melt temperature constant at 730$^{o}$C and 960$^{o}$C, respectively. Comparison among these cases was two-fold. First experimentally obtained data were used concerning cooling curves and porosity and general microstructure examination. Secondly, numerical simulation data were used, namely minimum and maximum solidification time of the casting, shrinkage porosity and filling quality.

## 5.1. Experimental Investigation

### *5.1.1. Cooling Curves*

The experimental cooling curves for the five cases examined are shown in Figure 13. The three regions reflecting alloy cooling are easy to recognise, corresponding to temperatures higher than Liquidus, between Liquidus and Solidus and lower than Solidus.

In the first interval, see Figure 14, the peak temperature measured at the thermocouple in all cases is at least 13$^{o}$C lower than inlet temperature (960$^{o}$C), due to heat losses along the central sprue.

Furthermore, even though the nominal inlet temperature value was the same (960$^{o}$C), the peak temperatures of the cooling curves were not. In particular, the maximum temperature is observed for the case of gravity casting (T=947.69$^{o}$C at t=0.585sec after melt pouring). The next highest temperature peak is observed for the case of vacuum – pressure casting (T=945$^{o}$C, t=0.156sec). The cases of 50% vacuum casting and pressure casting are very similar, their peak values being T=932$^{o}$C. The smoothest temperature peak is present in the case of vacuum casting, at 919$^{o}$C.

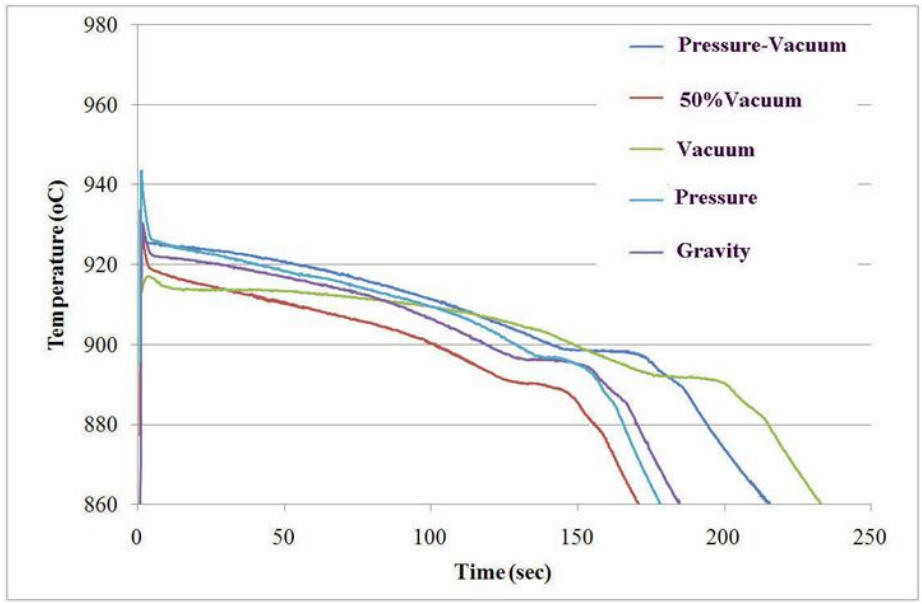


Figure 13. Experimental cooling curves obtained for the five casting cases examined, for the first 250sec of solidification.

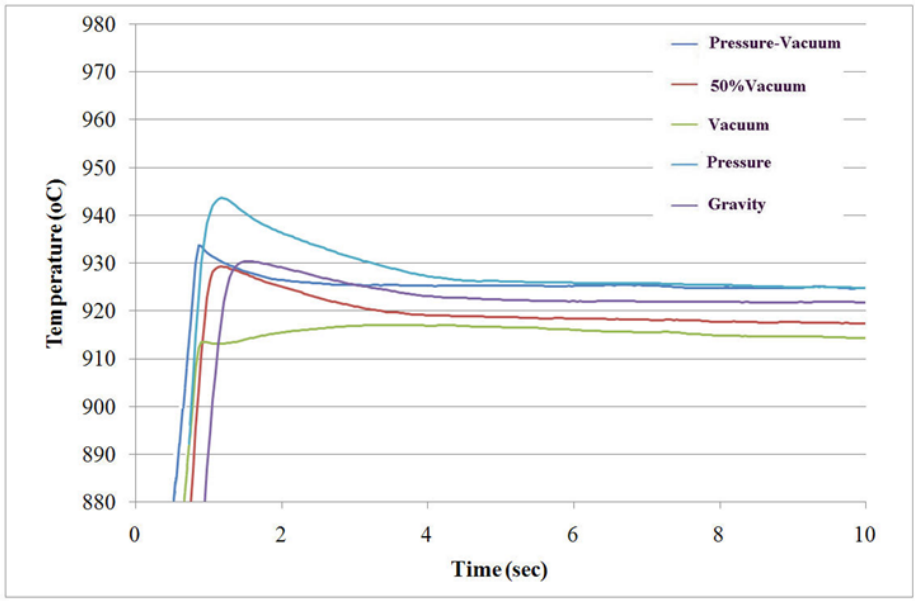


Figure 14. Experimental cooling curves obtained for the five casting cases examined, for the first 10sec of solidification.

The delayed appearance of mild peaks may be attributed to a slower filling of the space close to the measuring point, indicating a different filling mode of the cavity. Such cases occur when either but not both of the chambers are under positive or negative pressure (with respect to atmospheric pressure). Any attempt to explain these differences should take into account the generally poor repeatability of casting experiments, especially of initial

conditions, as well as possible variability of the thermocouple embedding location as well as variable thermocouple tip protrusion. Note that thermocouples measure correctly when their soldered tip head is fully dipped into the melt. Conduction phenomena enable rapid thermocouple response, whereas convection results in a slower response.

As far as cooling rate is concerned, in the case of gravity casting the time between appearance of the peak temperature and reaching the Liquidus temperature is 1.2sec, whereas in the case of vacuum-pressure casting, the corresponding time interval is 0.5sec, clearly indicating a higher cooling rate in the latter case.

With respect to the second interval, see Figure 13, duration of the mushy zone in the neighbourhood of the measured point for the case of vacuum casting was 202 sec which is longer than in all other cases, where the metal remains in the mushy zone for 153 sec on the average.

In Figure 13, comparison is interesting between the cooling curves that refer to pressure casting and 50% vacuum casting, both correspond to $\Delta P=0.5$ bar but materialized in alternative ways. It appears that the former has a positive temperature offset of $6^{o}C$ in the first two intervals and of $19^{o}C$ in the third interval compared to vacuum casting.

With respect to the third interval Figure 13 indicates that the slope of the curves is the same in all cases, i.e. the cooling rate is similar after full solidification. However, the starting point of the third interval differs significantly in these cases.

### *5.1.2. Porosity Measurement*

After standard metallography specimen preparation from the castings, observations were carried out on an MZ6 Leica stereoscope and a DMILM Leica microscope. Image analysis software (Image-Pro Plus) was used to quantify porosity in each sample. The porosity measurements referred to a cross-section on the symmetry plane of each of the five castings as in Table 1. On each cross-section the areas around points 1-5 have been examined, see Figure 15.

Porosity statistics are summarized in Table 3concerning the percentage of the area that the pores occupy on the region examined, the area of the maximum pore, the mean value of pore area and the standard deviation.Table 4 summarizes the corresponding micrographs.

Examining Table 3by row allows comparison of pore distribution at different locations on the same casting. Examining the table by column allows comparison of pores distribution at the same point of the casting for different casting conditions.

Gravity casting, is satisfactory as far as the maximum pore size is concerned. There is a large number of pores per image, uniformly distributed. The most “loaded” case is Point 3, which is located on the axis at the intermediate cross-section of the casting, see Figure 15.

In the case of pressure casting, pore presence is intensely reduced at points 2 and 4, see Figure 15, near the corners of the cast geometry, with some big pores still remaining. A huge defect appears in the middle of the casting (point 3) leading to the conclusion that pressure application has an intense effect on liquid metal flow.

In50% vacuum castingthough, where flow rate is the same with the previous case, porosity creation is clearly reduced. Points 3 and 5, in the middle of the two large cross – sections of the casting, see Figure 14, are the areas where some large pores appear, but the large number of small, homogenously distributed pores is eliminated. It appears that the presence of vacuum creates a smoother flow of the melt, eliminating the presence of huge defects. Moreover, vacuum reduces the formation of small pores. Compared to gravity

casting, the porosity at point 1 is clearly improved but the maximum pore size at points 3 and 5 remains larger in the case of 50% vacuum casting.

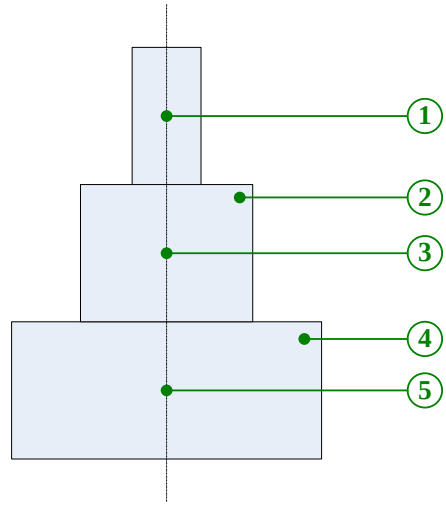


Figure 15. The positions on the symmetry plane of the cast specimens that were examined with optical microscopy to quantify porosity.

Observing the pure vacuum casting results, it can be figured out that it constitutes the most favorable casting condition, as it comes to porosity creation. It is remarkable that at the thinner parts of the cast (point 1) porosity is dramatically eliminated. Porosity distribution is similar in the middle of the cast and at the corners, i.e. there is high homogeneity of the part quality across the part. Moreover, the maximum pore size in the least favourable locations is the smallest of all cases compared.

Finally, in vacuum – pressure casting, defects are eliminated in the thicker parts of the casting, whereas porosity in the thinner cross – sections appears to have large values, an indication that the thinner parts of the cast may be filling too rapidly with increased turbulence. The presence of vacuum is manifested in the fact that apart from the large pores, there is no porosity across the whole region examined. Moreover, defects in the thicker cross – section of the part are eliminated. Based on the aforementioned observations, it seems that the best and the worst case scenarios are vacuum casting and vacuum-pressure casting respectively. Therefore, only these two representative cases will be further examined with respect to pore distribution, see Figures 16 and 17,where three ranges of pore area, namely [0-10], [10-100] and [100-more] $\mu m^2$, were taken into consideration, corresponding to pores characterized as ‘small’, ‘medium’ and ‘large’ respectively for points 1-5, see Figure 15. In vacuum casting, as shown in Figure 16, in the area around point 1 there are no large pores. At point 2, the number of small pores is rather large, whereas there are fewer medium pores and much less large pores. At points 3 and 5, the medium pores are much more than the small pores. At point 4, the number of small pores is approximately equal to the number of medium pores. The largest pores mainly appear at points 4 and 5.

**Table 7.Porositystatistics**

| | % Area | Standard Deviation ($\mu m^2$) | Mean ($\mu m^2$) | Max area ($\mu m^2$) |
|---|---|---|---|---|
| **Gravity Casting** | | | | |
| 1 | 1.74 | 31 | 14 | 709 |
| 2 | 1.99 | 25 | 19 | 460 |
| 3 | 3.34 | 30 | 17 | 756 |
| 4 | 1.64 | 23 | 23 | 217 |
| 5 | 1.78 | 23 | 19 | 178 |
| **Pressure Casting** | | | | |
| 1 | 0.56 | 16 | 11 | 187 |
| 2 | 0.09 | 15 | 12 | 70 |
| 3 | 25.51 | 15386 | 3754 | 103094 |
| 4 | 0.31 | 87 | 45 | 454 |
| 5 | 0.75 | 255 | 51 | 2773 |
| **50% Vacuum Casting** | | | | |
| 1 | 0.10 | 12 | 16 | 46 |
| 2 | 0.17 | 45 | 24 | 278 |
| 3 | 1.20 | 426 | 192 | 2306 |
| 4 | 1.12 | 34 | 12 | 532 |
| 5 | 1.74 | 355 | 185 | 2364 |
| **Vacuum Casting** | | | | |
| 1 | 0.09 | 12 | 13 | 54 |
| 2 | 0.49 | 45 | 19 | 438 |
| 3 | 0.27 | 40 | 31 | 249 |
| 4 | 0.45 | 27 | 19 | 167 |
| 5 | 0.56 | 44 | 30 | 354 |
| **Vacuum - Pressure Casting** | | | | |
| 1 | 0.87 | 38 | 28 | 241 |
| 2 | 1.45 | 24 | 11 | 692 |
| 3 | 1.95 | 61 | 37 | 626 |
| 4 | 1.20 | 26 | 26 | 234 |
| 5 | 0.69 | 38 | 38 | 298 |

As far as vacuum-pressure casting is concerned, as shown in Figure 17, point 1 is overwhelmed by pores of small size. At point 2, there are no large pores. Point 3 is the location where most of the largest pores appear. At point 4, there are a few small pores and medium pores. At point 5 there are significantly more medium pores than small ones. Comparing Figures 16 and 17, it is noticeable that in vacuum-pressure casting the majority of small pores are concentrated in one location (point 1), while in vacuum casting there is a more uniform distribution of the small pores.

**Table 8.**

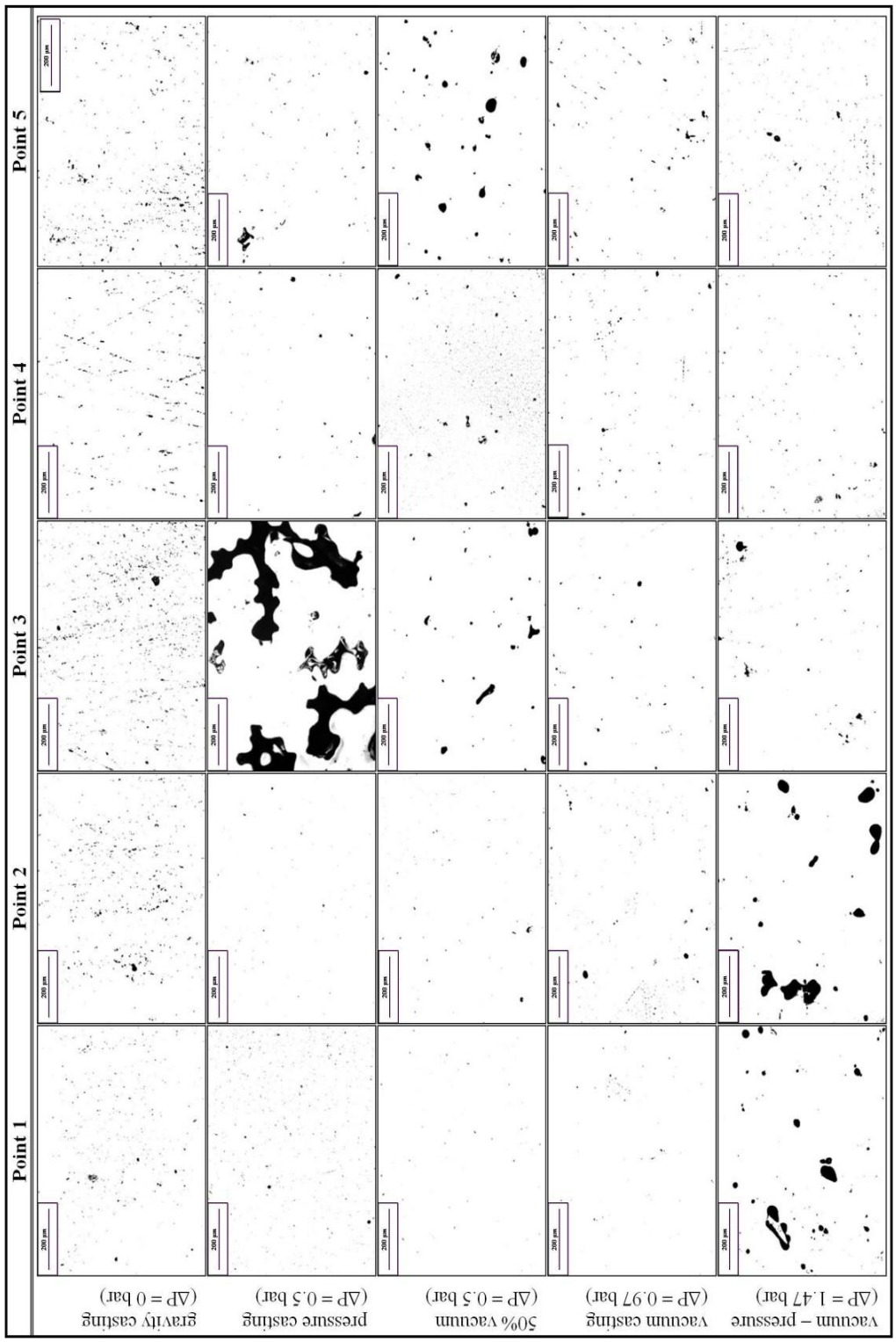

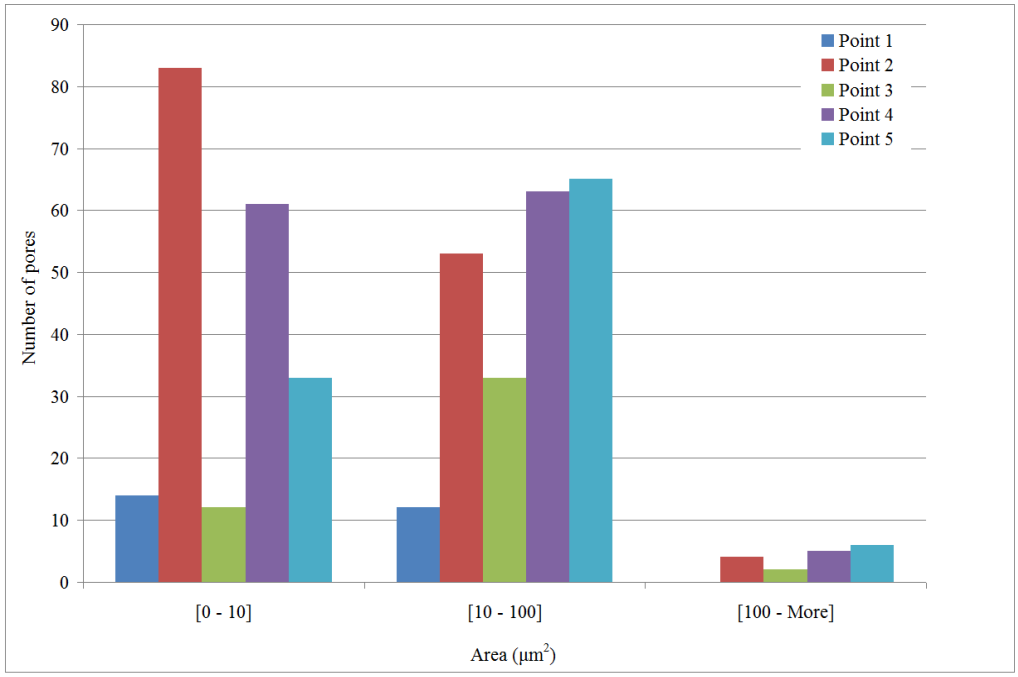


Figure 15. Histogram of pore size distribution in vacuum casting.

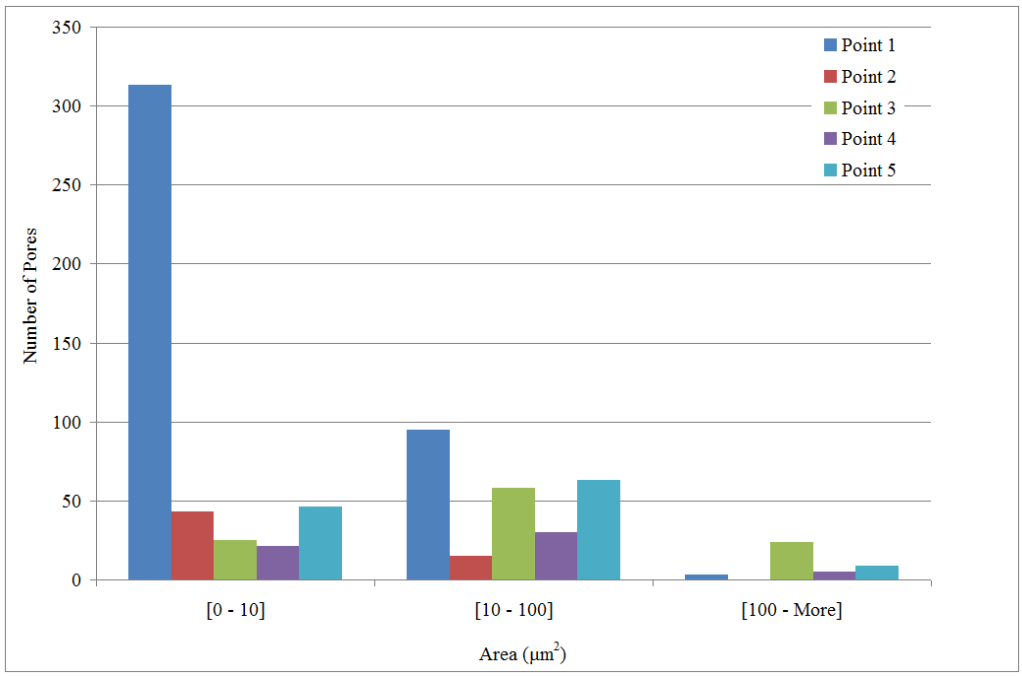


Figure 16. Histogram of pore size distribution in vacuum-pressure casting.

## 5.2. Numerical Investigation

Simulation results for the five casting cases described in Table 1 are presented. For the simulation, the HTC was estimated as described in section 4. The results include cooling curves at the point where the thermocouple had been introduced, the minimum and maximum solidification time of the casting, shrinkage porosity and filling quality.

### *5.2.1. Cooling Curves*

In Figure 18 the numerically estimated cooling curves, for the five casting methods examined, are plotted. Only the curve corresponding to the case of gravity casting seems to deviate from the others. It is illustrated that the cooling rate during the first few seconds of the solidification process, depends on the pressure conditions in the casting chambers, i.e. in an ascending order: vacuum-pressure, 50% vacuum, pressure, gravity and vacuum casting.

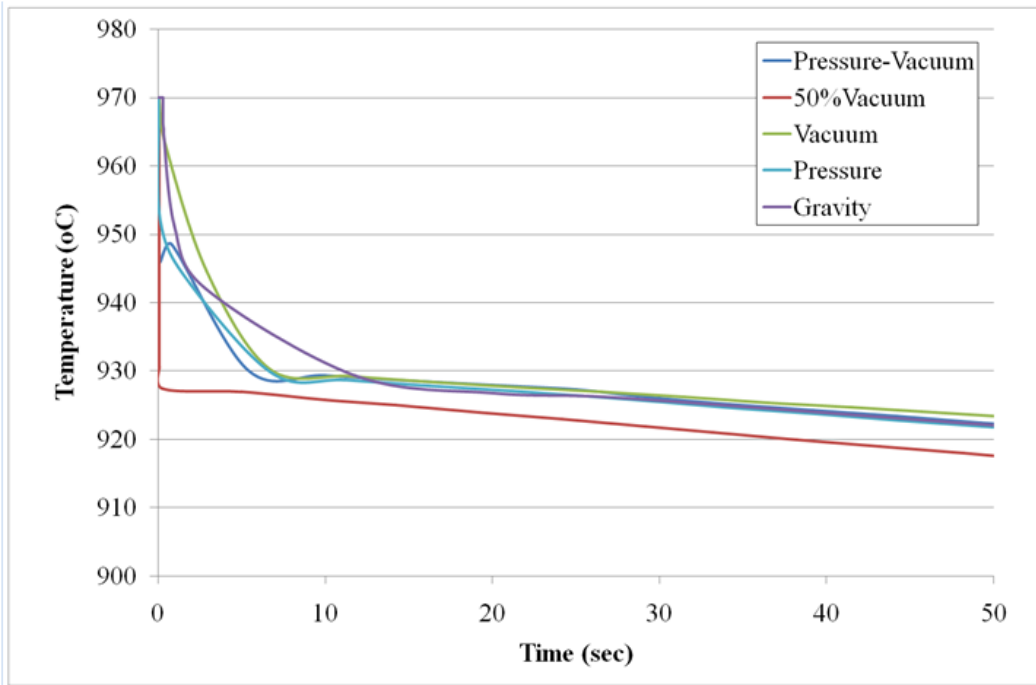


Figure 17. Numerical cooling curves obtained for the five casting cases examined, for the first 10sec of solidification.

### *5.2.2. Solidification Time, Porosity and Filling Quality*

Numerical results with respect to solidification time, porosity and filling quality are presented in Table 5. It is evident that filling quality in all cases is satisfactory, given the fact that no voids are present. The ascending order of the casting processes with respect to solidification time is: vacuum, vacuum-pressure, pressure and gravity. The corresponding order with respect to porosity is: vacuum, vacuum-pressure, pressure and gravity. It is noted that when solidification time is long, as in the case of vacuum casting, porosity remains at very low levels and is characterized as microporosity. Furthermore, in all other cases of Table 5, the resulting porosity is characterized as macroporosity.

Table 8 contains the contour plots for the solidification time and the porosity for the four cases presented in Table 7. Solidification evolution of the casting tree and the uniformity of solidification of the casting can be followed. In addition, the locations where porosity appears are clearly depicted. In gravity casting, porosity appears in the base of the casting tree and at points 3 and 5, see Figure 15. The application of pressure only is the next worst case, with porosity appearing at points 2, 3 and 5. Then, the vacuum-pressure casting case follows, with porosity appearing at points 3 and 5. Finally, in the case of vacuum casting the porosity is at very low levels.

**Table 9.Simulation results: solidification time, porosity and filling quality**

| ΔP | Casting Case | Solidification Time | | Porosity | | Filling Quality |
|---|---|---|---|---|---|---|
| | | min | max | max | Characterisation | |
| 0 | Gravity Casting | 120.4 | 129.0 | 0.825 | macro | Good |
| 0.97 | Vacuum Casting P=0.03bar | 234.2 | 250.8 | 0.00366 | micro | Good |
| 1.47 | Pressure (P=0.5bar) – Vacuum Casting (P=0.03bar) | 179.3 | 192.1 | 0.4801 | macro | Good |
| 0.5 | Pressure (P=0.5bar) | 158.9 | 169.9 | 0.519 | macro | Good |

Comparing porosity from experimental observations and simulation, some remarks can be made. Firstly, Tables 6 refers to experimental observation that yields from image processing and is related to the area of pores over the total area of the image. On the contrary, Table 8 refers to simulation results involving volumetric calculations, depending on the solid fraction and density values at unit volumes of the casting. Therefore, the results shown in Tables 6 and 8 may be compared only on a qualitative basis. In both cases, the vacuum casting process is the best case, since microporosity of very low values appears. In pressure casting, both simulation and experiment show that in points 3 and 5, the porosity values are comparable. Concerning point 3, the order of casting processes with respect to ascending value of maximum porosity is: vacuum casting, vacuum-pressure casting, gravity casting and pressure casting. Concerning point 4, experiment shows that porosity levels in all cases are rather low, which is confirmed by simulation. Concerning points 1 and 2, only vacuum-pressure casting results in large amounts of porosity based on the experimental observations. The distinguishing difference of the case of vacuum-pressure casting porosity levels that appears in the experimental observations is not clearly depicted in simulation. Though, simulation shows than in all casting cases, porosity levels at points 1 and 2 are below 0.032, thus characterized as microporosity.

**Table 10. Contour plots of the simulation results: solidification time and porosity**

| Casting Type | ΔP | Solidification Time | Porosity |
|---|---|---|---|
| Gravity Casting | 0 | 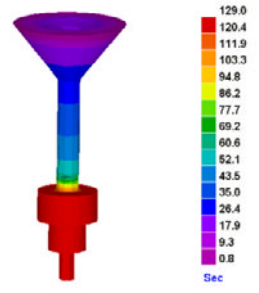  | 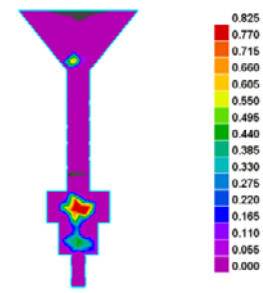  |
| Pressure | 0.5 | 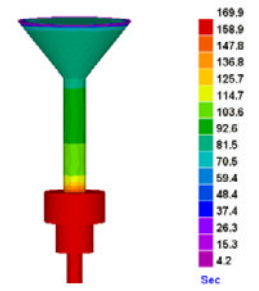  | 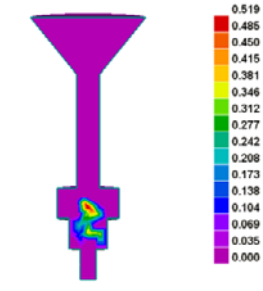  |
| Vacuum Casting | 1 | 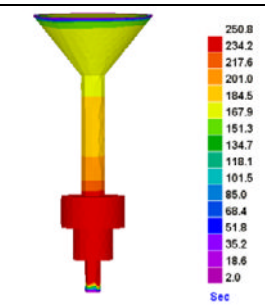  | 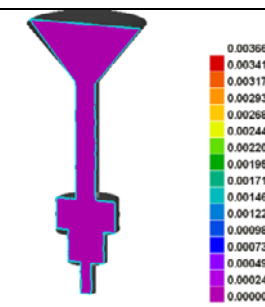  |
| Vacuum – Pressure Casting | 1.5 | 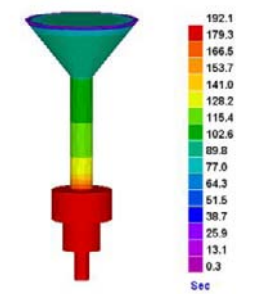  | 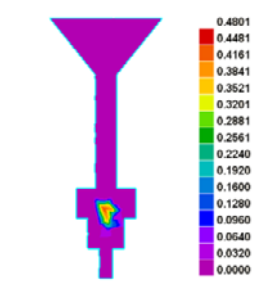  |

## CONCLUSION

The first goal of the present work was the determination of the heat transfer coefficient of brass during casting. Comparing experimental measurement of cooling curves with the corresponding results from casting simulation, single heat transfer coefficient as a function of

time has been determined, for five cases of pressure activation in the melting and the casting chambers of the vacuum casting machine.

The three stages describing time variation of HTC according to the literature have been confirmed in this work. The pressure difference seems to have an effect on solidification rate, especially during the first stage, when the melt temperature is higher than the liquidus. The value of HTC during the first seconds of solidification is significantly higher compared to gravity casting. A similar behavior is observed during the third stage of solidification when the metal temperature is below the solidus.

An issue arising from the present work is the necessity but also the complexity of determining and assigning different HTC values at significantly different cross-sections of the casting, which is considered as the next step in HTC-related research work.

Examining the effect of pressure conditions on cooling curves, it was noted that mainly the first and the second time intervals of the cooling curves are concerned.

As far as the porosity measurements are concerned, in vacuum – pressure casting, defects are eliminated in the thicker parts of the casting, whereas porosity in the thinner cross – sections appears to have large values. The vacuum casting results showedsuperiority of this method as it comes to porosity defects. It is remarkable that at the thinner parts of the cast porosity is dramatically eliminated. Overall, vacuum-pressure casting is worse than vacuum casting, because it results in more small, medium and large pores.

According to simulation results, when solidification time is long, as in the case of vacuum casting, porosity remains very low and is characterized as microporosity. With respect to porosity, the worst case according to simulation results is gravity casting. However, this is not in agreement with the experimental porosity measurements, where the worst case was vacuum-pressure casting. The positive contribution of vacuum is confirmed from both the analytical and numerical investigation.

## REFERENCES

[1] Campbell, J. *Castings*. Oxford, Boston:Butterworth–Heinemann;1993.
[2] Gainsbury, P. E. *GTech.* 1979, 12(1), 2-8.
[3] Lun Sin. S. *Mater. Sci. Eng., A*. 2004, 386, 34-42.
[4] Hero, H,; Waarli,M. *Eur J Oral Sci*. 1991, 99 (1), 55-59.
[5] Todoroki, H.; Phinichka, N. *ISIJ Int.* 2009, 49, 1347–1355.
[6] Pagratis, N.; Karagiannis, N.; Vosniakos, G.-C.; Pantelis, D.; Benardos, P. *J. Eng Manufact.*2007, 221, 967-979.
[7] Sabau, A. S. *AFS Trans.* 2005
[8] Ho,K.; Pehlke R.D.*Metall. Trans. B.* 1985, 16B, 585– 94.
[9] Hallam, C.P.; Griffiths W. D.*Metall. Mater. Trans. B.* 2004, 35B, 721–733.
[10] Lau F.; Lee, W.B.; Xiong, S.M.; Liu, B.C. *J. Mater. Process. Technol.* 1998, 79, 25-29.
[11] Nayak, R.K.; Sundarraj, S. *Metall. Mater. Trans. B.* 2010, 41B, 151-160.
[12] Krishna, P.; Bilkey, K.T.; Hao, S.W.; Pehlke, R.D.,*AFS. Transactions.* 2004, 71-78.
[13] Santos, C. A.; Siqueira, C. A.; Garcia, A.; Quaresma, J.M.V.; Spim, J.A. *Inverse Prob. Sci. Eng.* Vol.12, No 3, 2004, pp. 279-296.
[14] Santos,C.A.; Cuaresma, J.M.V.; Garcia, A.,*Alloys Compd.* 2001, 319, 174–86.

[15] Krimpenis, A.; Benards, P.; Vosniakos, G.; Koukouvitaki, A., *Int. J. Adv. Manuf. Technol*. 2006, 27, 509-517.
[16] Flemings, M.C. *Solidification Processing*, New York, McGraw-Hill, 1974.
[17] Hamasaiid, A.; Dour, G.; Loulou, T.; Dargusch, M.S. *Int. J. Therm. Sci*. 2010, 49, 365-372.
[18] Di Sabatino, M.; Arnberg, L. *Met. Sc. and Tech.* 2004, 22, 9-15.
[19] O' Mahoney, D.; Browne, D.J.,*Exp. Therm Fluid Sci.*. 2000, 22, 111-122.
[20] ASM, Liquids Metals and Solidification, Ohio 1958.
[21] ProCAST 2004.1 Release Notes and Installation Guide', ESI Group, May-2004.

In: Advances in Mechanical Engineering Research. Volume 2 ISBN: 978-1-61761-984-7
Editor: David E. Malach 

*Chapter 8*

# HIGH-STRENGTH TITANIUM BASE ALLOYS WITH MULTIPLE LENGTH-SCALE MICROSTRUCTURE

***Lai-Chang Zhang[1*], Mariana Calin[2] and Jürgen Eckert[2]***
[1]School of Mechanical Engineering, The University of Western Australia, MDBP M050
35 Stirling Highway, Crawley, Perth, WA 6009, Australia
[2]IFW Dresden,Institute for Complex Materials,P.O. Box 27 01 16,
D-01171Dresden, Germany

## ABSTRACT

The improvement of the strength and plasticity in titanium alloys has attracted considerable research interest. Strategies have been developed to improve their mechanical properties (strength, ductility or toughness) by introducing heterogeneities of multiple length scales into the microstructure, or called bimodal microstructure. In this chapter, it will show that the recently developed titanium alloys with multiple length-scale microstructure can be easily obtained in bulky form through simple and inexpensive casting techniques. These advanced titanium alloys exhibit superior mechanical properties, including high strength of 2000 − 2700 MPa and large plasticity up to 15%. The microstructure as well as the deformation and fracture behavior will be described in nanostructured/ultrafine-grained titanium alloys with different microstructure features. Of special interest is the interdependence between solidification conditions, alloy and microstructure design by composition variation *via* micro-alloying and the resulting mechanical properties and deformation mechanisms of the titanium alloys with multiple length-scale microstructure.

## INTRODUCTION

Recently, there have been considerable interests in the development of nanostructured (with grain size less than 100 nm) and ultrafine-grained (typically with grain size between 100 nm and 500 nm) metals and alloys for structural applications, because they exhibit

* E-mail address: lczhangimr@gmail.com; lczhang@mech.uwa.edu.au

remarkable improvement in strength. These nanostructured/ultrafine-grained metallic materials have a strength up to several times compared with their conventional coarse-grained counterparts. For example, nanostructured and ultrafine-grained pure copper has a yield strength over 400 − 900 MPa and 200 MPa, respectively [1], which are several times up to an order of magnitude higher than that of the conventional coarse-grained copper. The superior high strength creates the possibility of weight and energy savings, therefore, these fine-grained metallic materials are expected to have many potential applications. To date, a number of methods have been developed to produce nanocrystalline/ultrafine-grained metallic materials for both research and industrial purposes. However, most these super-strong advanced materials suffer from a severe drawback – lack of plasticity. They generally have a very limited plasticity, which makes them unusable in load-bearing applications. The major limitations of plasticity for these fine-grained metallic materials have been identified as [2,3]: (i) artefacts from processing, (ii) force instability, and (iii) crack nucleation and propagation instability. Therefore, considerable efforts are being made to improve the room-temperature plasticity of nanostructured/ultrafine-grained metallic materials as well as high strength in the development of advanced structural materials. For this purpose, several strategies to tailor nanostructured/ultrafine-grained microstructure have been developed to achieve good combination of enhanced plasticity and high strength [3,4]. As multiphase alloys rather than simple elemental metals are usually used in industrial applications, this chapter mainly describes the approach to improve plasticity by forming a composite microstructure with multiple length scales. This is then usually called bimodal or multimodal composites [4,5]. Recent investigations have proved that a bimodal grain structure containing micrometer-sized phases embedded in a nanostructure or ultrafine-grained matrix is effective to simultaneously achieve high strength and enhanced plasticity in these advanced structural materials [5-14]. The high strength is provided by the nanostructured/ultrafine-grained eutectic matrix, whereas the enhanced plasticity stems from the inhomogeneous microstructure (or multiscale hierarchical structure) that suppresses deformation instability. Thus, the bimodal composites exhibit unusual deformation mechanisms similar to the ductile-phase toughening brittle materials. Coarse-grained bands tend to deform locally at stress concentrations, arresting cracks by local blunting and resisting crack growth by bridging of crack wakes. The deformation mechanisms can be altered by tailoring morphology and dispersion of coarse-grained phase, as well as interface properties. With the promise of superior mechanical properties, it is likely that many structural applications should open up for nanostructured/ultrafine-grained metallic materials.

Titanium alloys are one of the best lightweight engineering materials for many industrial applications due to their excellent mechanical properties (high strength and high strength-to-density ratio) and good corrosion resistance [15]. Very recently, bulky titanium base bimodal nanostructured/ultrafine-grained alloys with heterogeneities of different length scale have received a lot of attention as an effective approach for novel microstructure design to enhance the plasticity of high-strength titanium alloys [6-13]. In particular, these titanium base nanostructured/ultrafine-grained bimodal composites have been highlighted for practical applications due to their easy and simple processing (*via* casting). The as-cast bulky titanium alloys exhibit high strength of 2000 − 2700 MPa and large plasticity up to 15%. It has been reported that $Ti_{60}Cu_{14}Ni_{22}Sn_4Nb_{10}$rods composed of micrometer-size β-Ti dendritesembedded in a nanostructured matrix exhibitsa high compressive strength of 2400 MPa and 14.5% plastic strain [6]. More recently, in a much cheaper Ti-Fe alloy,the hypereutectic $Ti_{65}Fe_{35}$

alloy consisting of β-Ti and FeTi phases exhibit better compressive mechanical properties (strength ~2200 MPa,plasticity ~6.7%) than the hypoeutectic and eutectic alloys [16]. In order to achieve good combination of high strength and large plasticity, studies have been being conducted on the alloy design to tailor the multiple length-scale microstructure of Ti-Fe alloys by micro-alloying (such as Co, Sn, Ta, Nb, Ga, etc.) [7-13,16-18]. It has been revealed that microstructural modification and optimization by additional micro-alloying elements in nanostructured/ultrafine-grained Ti-Fe alloys are key factors to control the mechanical properties. The addition of Cu and Nb improve plasticity and B, Cr, Mn and Ni significantly decreases the plasticity of the $Ti_{65}Fe_{35}$ alloy [11]. It is interesting to find that the common and cheap constituent Sn could simultaneously improve the strength and enhance the plasticity of Ti-Fe alloys. For example, a ultrafine-grained $Ti_{63.375}Fe_{34.125}Sn_{2.5}$ bimodal composite exhibits a ultimate strength of 2650 MPa and a large plasticity of 12.5% [7] and a nanostructured $Ti_{67.79}Fe_{28.36}Sn_{3.85}$ eutectics has high ultimate strength of 1900 MPa and enhanced plasticity of 9.6% [10].The strength and plasticity of the titanium base nanostructured/ultrafine-grained alloys are strongly related to the occurrence of the slip/shear bands in the micron-scale primary phase and the propagation of the primary and secondary shear bands in the nano-/ultrafine-scale eutectic matrix. It is apparent that controlling the length-scale and the intrinsic properties of the constituent phases can enhance the plasticity of high-strength nanostructured/ultrafine-grained titanium alloys.

## SYNTHESIS AND MICROSTRUCTURE DESIGN STRATEGY

A large number of bulky advanced nanostructured/ultrafine-grained metallic materials have been prepared either through multi-step processing, e.g., *via* powder consolidation [19] and crystallization from amorphous precursors [20], or by employing severe plastic deformation using equal channel angular extrusion [21]. The powder route often suffers from porosity and contamination problems in the consolidation step required to produce bulky samples [22], whereas the crystallization method has severe limitations on the sample size due to the limited dimensions of the amorphous precursors available (for example the critical sample sizes are very limited in aluminum and titanium base bulk metallic glasses [23,24]). In addition, the crystallization products are also often intermetallic phases that can be rather brittle. With the severe plastic deformation technique, due to the tremendous deformation needed to refine the microstructure, it is difficult to process very strong alloys. Therefore, it is of interest to employ a one-step process, e.g., through a casting processing, to directly prepare bulky nanostructured/ultrafine-grained alloys, which show a good combination of desirable mechanical properties, in particular both high strength and large ductility. This chapter introduces one-step formation of nanostructured/ultrafine-grained titanium alloys with multiple length-scale microstructures by employing arc melting and copper mold casting. All bulky nanostructured/ultrafine-grained titanium samples discussed in this chapter were formed as follows (arc melting and/or chill casting). Master alloys with desired chemical composition were prepared from elemental pieces with high purity by arc melting under a Ti-getteredargon atmosphere in a water-cooled coppercrucible. Rods of threemillimeter diameter (3 mm∅) werecast from the master alloy ingots into acopper mold under argon atmosphere.

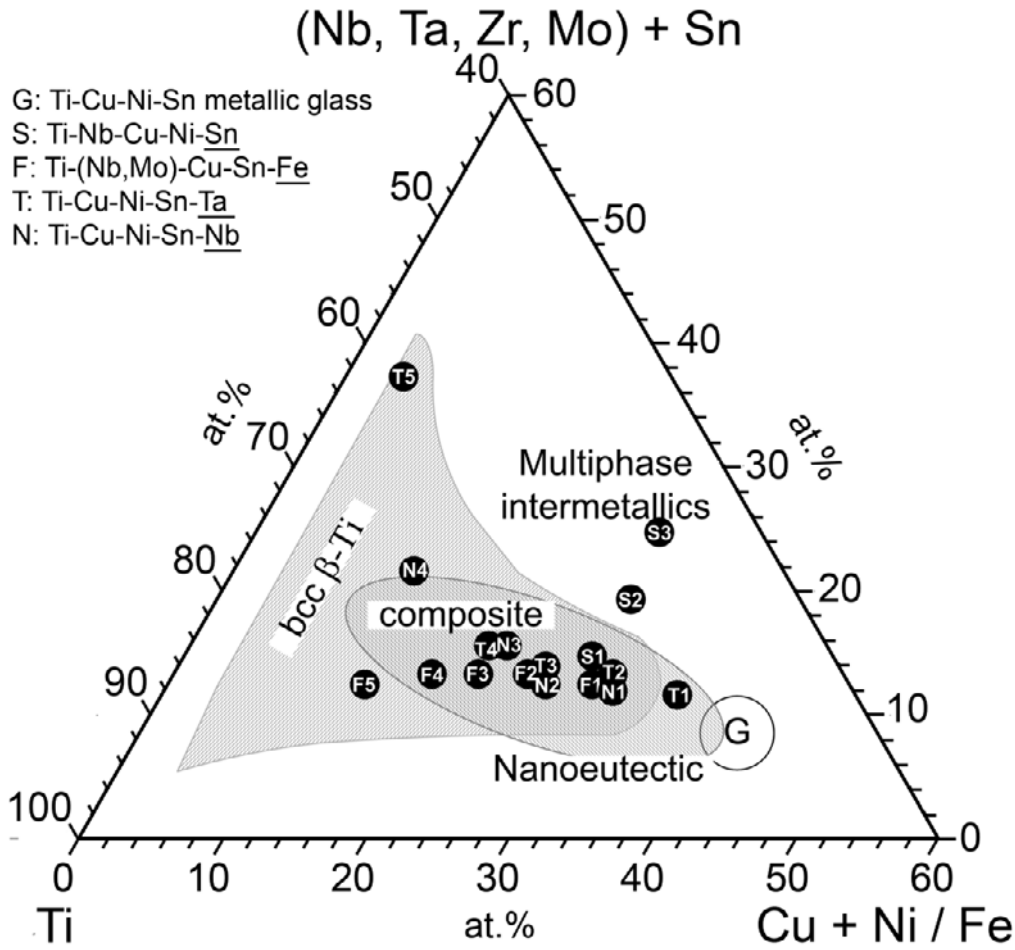


Figure 1Nanostructured/ultrafine-grained titanium alloys with multiple length-scale microstructure in pseudo-ternary phase diagram for Ti-(Nb,Ta,Zr,Mo,Sn)-(Cu,Ni/Fe) system.

Multiple length-scale microstructures could be obtained in multicomponent titanium base alloys by proper composition selection and microstructure manipulation via micro-alloying and control of the solidification process. The general microstructure design strategy is to form a microstructure that a ductile phase with a relatively larger grain size (e.g. in micron-scale) is designed to be among the solidification product together with a nanostructured/ultrafine-grained phase. An example is the micrometer-sized primary solid solution phase formed before eutectic reaction commences, forming a bimodal or composite microstructure. Figure 1 shows an example of development of nanostructured/ultrafine-grained composites in multicomponent titanium alloy system. The microstructure formation in titanium base alloys can be schematically illustrated with the help of a pseudo-ternary phase diagram considering three different groups of constituent elements: (i) Ti (base element), (ii) body centered cubic (bcc) β-phase isomorphous stabilizers (Nb, Ta, Zr, Mo) + Sn, and (iii) Cu + Ni / Fe (eutectic matrix formers). The phase fields are plotted on the basis of the microstructural evolution and metastable phase formation in different length-scale. There are three (partly) overlapping phase fields that can be distinguished: a glassy region, an eutectic region (nanometer length-

scale), and a region where a bcc β-Ti-type solid solution forms, which sometimes coexists with other crystalline phase rather than bcc or nano-eutectic phases (marked as multiphase intermetallics). The overlapping of these regions produces composite microstructures with different length-scale. Due to the limited glass-forming ability in titanium alloy (the glass-forming alloy compositions are marked by a circle (G), nanostructured/glassy composites with submicron-size hcp α-Ti particles are usually formed in the area with a high (Ti + Zr/Nb/Sn) content, which are located to the upper left to the glassy region in pseudo-ternary phase diagram. On the other hand, micrometer-size bcc β-Ti phase primary precipitates have been observed to form along with a nanostructured/ultrafine-grained eutectic microstructure. A number of titanium nanostructured/ultrafine-grained matrix – dendrites composites have been formed under casting in the glass-formation Ti-Cu-Ni-Sn alloy [25].

## TITANIUM NANOSTRUCTURED MATRIX − DENDRITES ALLOYS

The formation of nanostructured matrix – dendrite composites have been designed and their effect on mechanical properties have been investigated in a series of Ti-Cu-X-Sn-M alloy (X = Ni, Fe, Cr, Co; M = Nb, Ta, Mo, Zr) alloys, such as $(Ti_{40}Cu_{28}Ni_{24}Sn_8)_{1-x}(Ti_{80}Nb_{20})_x$, $(Ti_{40}Cu_{28}Ni_{24}Sn_8)_{1-x}(Ti_{80}Ta_{20})_x$ and $(Ti_{40}Cu_{28}Ni_{24}Sn_8)_{1-x}(Ti_{80}Mo_{20})_x$, where the compositions are in atomic percent and hereafter and $x$ is equal to 0.4 – 0.6. The details of the fabrication processes of the nanostructured matrix – dendrite composites have been described elsewhere [6,26-30]. These alloys provide high fracture strength, large plastic strain and strain hardening (e.g. dislocation storage) capability. The mechanical properties of some titanium alloys are summarized in Table 1. It is important to note that the mechanical properties of these titanium alloys are strongly dependent on the alloy compositions and the solidification processes. As seen from Table 1, the slight change of chemical compositions between $Ti_{56}Cu_{16.8}Ni_{14.42}Sn_{4.8}Ta_8$and $Ti_{60}Cu_{14}Ni_{12}Sn_4Ta_{10}$ leads to significant changes in mechanical properties (~270 MPa in $\sigma_{max}$). Furthermore, the $Ti_{60}Cu_{14}Ni_{12}Sn_4Ta_{10}$ alloys prepared by injection casting and by arc melting exhibit apparently different plasticity and yield strength, where the arc-melted sample has ~2.5 times plasticity but 2/3 yield strength of the inject-cast counterpart. The difference in mechanical properties comes from the final microstructure (grain size and volume fraction of phase constituents) in different compositions and/or under different solidification processes [26].

The representative microstructure of the titanium nanostructured matrix – dendrite composites is composed of a micrometer-size β-Ti phase with dendritic morphology dispersed in a nanostructured eutectic matrix, independent of the solidification processes. The finer microstructure is obtained for the cast alloy for which the solidification rate has been faster. Figure 2 shows two examples of the titanium base nanostructured matrix – dendrites composites formed in the $Ti_{60}Cu_{14}Ni_{12}Sn_4Nb_{10}$ and $Ti_{60}Cu_{14}Ni_{12}Sn_4Ta_{10}$ alloys by injection casting. The scanning electron microscope (SEM) backscattered electron images (Figures 2a and b) show a micrometer-size dendritic phase (bright) homogenously dispersed in a nanostructured matrix (dark phase) in both alloys. Energy dispersive X-ray (EDX) analysis reveals that the dendritic β-Ti solid solution phase is enriched in Nb or Ta and Sn compared with the matrix [6,26]. The details of the nanostructured matrix revealed by SEM are presented in Figures 2c and d, showing the eutectic morphology of the phases.

**Table 1 Summary of the room-temperature compressive mechanical properties of the as-prepared samples: Young's modulus $E$, 0.2% strain offset yield stress $\sigma_y$, strain at the yield point $\varepsilon_y$, ultimate compression stress $\sigma_{max}$, and plastic strain $\varepsilon_p$**

| Alloy composition (at.%) | Preparation | $E$ (Gpa) | $\sigma_y$ (MPa) | $\varepsilon_y$ (%) | $\sigma_{max}$ (MPa) | $\varepsilon_p$ (%) | Ref. |
|---|---|---|---|---|---|---|---|
| $Ti_{60}Cu_{14}Ni_{12}Sn_4Nb_{10}$ | Injection casting | 66.1 | 1312 | 2.2 | 2401 | 14.5 | [6] |
| $Ti_{60}Cu_{14}Ni_{12}Sn_4Ta_{10}$ | Injection casting | 70.8 | 1568 | 2.4 | 2322 | 6.0 | [6] |
| | Arc melting | 71.0 | 1037 | 1.7 | 2196 | 16.5 | [26] |
| $Ti_{56}Cu_{16.8}Ni_{14.42}Sn_{4.8}Ta_8$ | Arc melting | 49.0 | 941 | 2.1 | 2468 | 19.2 | [26] |
| $Ti_{60}Cu_{14}Fe_{12}Sn_4Nb_{10}$ | Arc-melting | 101 | 1442 | 1.6 | 1650 | 6.2 | [31] |
| $Ti_{47.5}Cu_{21.85}Ni_{19}Sn_{6.65}Mo_5$ | Injection casting | 106 | 2150 | 2.6 | 2246 | 0.5 | [27] |
| $Ti_{53}Zr_6Cu_{26.5}Ni_{4:5}Ta_{10}$ | Injection casting | 130 | 1852 | 2.8 | 1857 | 0.6 | [27] |

Transmission electron microscopy (TEM) observations prove that the nanostructured eutectic matrix in both alloys is composed of β-Ti and γ-CuTi phases [29,30]. The arc-melted alloys have a similar microstructure, but with different morphology and with a relatively larger grain size [26]. The finer microstructure is obtained for the cast alloy for which the solidification rate has been faster. When decreasing the solidification rate, more dendrites exhibiting a more equiaxed shape are formed. The dendrites cell sizes do not seem to be affected by the process contrary to the secondary arms spacing which becomes larger. Furthermore, the solidification process has a strong effect on the matrix grain size as a faster solidification leads to a finer grain size.

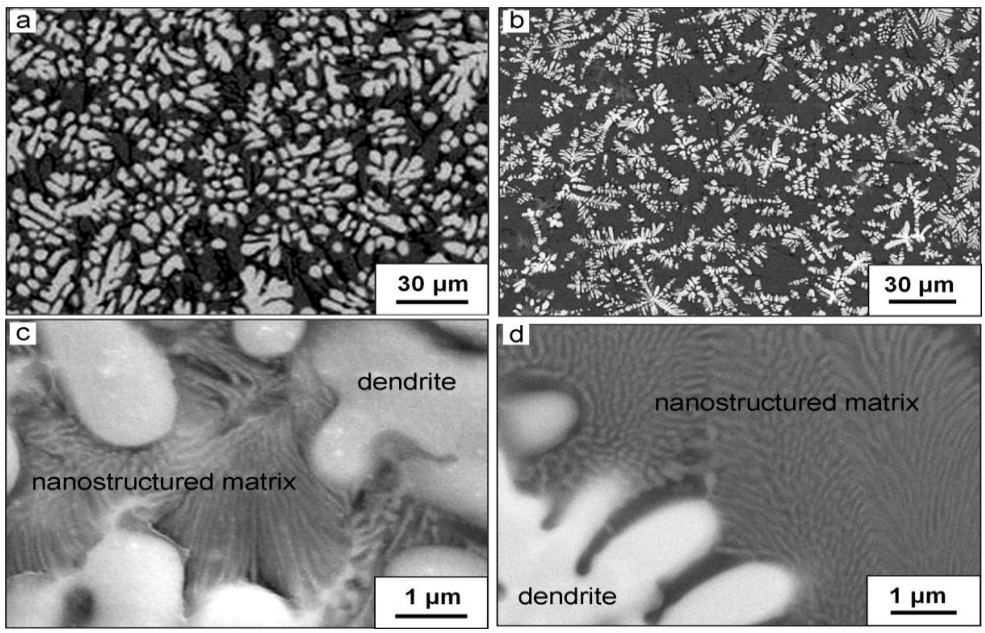


Figure2SEM backscattered electron images of as-cast (a) $Ti_{60}Cu_{14}Ni_{12}Sn_4Nb_{10}$ and (b) $Ti_{60}Cu_{14}Ni_{12}Sn_4Ta_{10}$ 3 mm∅ rods showing in situ formed dendrites (β-Ti phase) in a dark matrix, and magnified images of the dark matrix of (c) $Ti_{60}Cu_{14}Ni_{12}Sn_4Nb_{10}$ and (d) $Ti_{60}Cu_{14}Ni_{12}Sn_4Ta_{10}$ showing the nanostructured eutectic.

The co-existence of micrometer-size ductile bcc β-Ti solid solution dendritic phase and nanostructured eutectic matrix plays a crucial role in the good combination of high strength and large plasticity [6,29]. The high strength in these titanium alloys comes from several microstructural features including the nanostructured eutectic structure and high contents of multiple solutes that lead to solution hardening. SEM observations reveal that shear bands is visible on the deformed samples [6,29]. The rough direction of the shear bands makes an angle with the stress axis. Due to the existence of dendrites, almost all the shear bands are serpentine. This indicates that the spread of the shear bands is blocked and localized excessive shear banding can be avoided or retarded by the dendrites. The crack crossing (not along) the shear bands also reveals that excessive shear banding (which can induce cracks long the shear bands) is hindered by the dendrites. Therefore, the numerous slip bands due to dislocation activities in the much larger ductile dendrites contribute to the overall plasticity of these alloys. But, the contribution of nanostructured eutectics to plastic strain is limited although their contribution to the strength is expected [29].

## TI-FE BASE ULTRAFINE-GRAINED MATRIX − DENDRITES ALLOYS

The Ti-Fe-base ultrafine-grained alloys are more recently developed bimodal composites with high strength and large plasticity. As hypereutectic Ti-Fe alloys exhibit relatively better mechanical properties than eutectic and hypoeutectic alloys [16], considerable work has conducted to further improve the mechanical properties of the hypereutectic Ti-Fe alloy by manipulating the compositions via micro-alloying. Table 2 gives some examples of the influence of micro-alloying elements on the microstructure and mechanical properties of hypereutectic (e.g. $Ti_{65}Fe_{35}$), eutectic ($Ti_{70.5}Fe_{29.5}$) and hypoeutectic (e.g. $Ti_{72}Fe_{28}$) Ti-Fe alloys. Interestingly, compared to the titanium nanostructured matrix – dendrite alloys, the mechanical properties of the Ti-Fe-base ultrafine-grained alloys is not sensitive to the solidification process, but to the micro-alloying elements and their concentrations. For example, the arc-melted and the chill-cast $Ti_{65}Fe_{35}$ alloys have comparable mechanical properties (Table 2). As the majority of the Ti-Fe-base ultrafine-grained alloys tend to have a hypereutectic or hypoeutectic microstructure (Table 2), this session gives two examples of the ultrafine-grained titanium alloys having hypereutectic or hypoeutectic microstructure.

**Table 2 Examples of the microstructure and room-temperature compressive mechanical properties of the Ti-Fe-base ultrafine-grained alloysprepared by injectioncasting. Hypereutectic: primary phase with (FeTi + βTi) eutectic, hypoeutectic: primary βTi with (FeTi + βTi) eutectic, pseudo-binary eutectic: (FeTi + βTi) eutectic, $\sigma_y$: 0.2% strain offset yield stress, $\sigma_{max}$: ultimate stress; $\varepsilon_p$: plastic strain**

| Alloy (at.%) | Microstructure | $\sigma_y$ (MPa) | $\sigma_{max}$ (MPa) | $\varepsilon_p$ (%) |
|---|---|---|---|---|
| $Ti_{65}Fe_{35}$ [7] | Hypereutectic[1] | 1722 | 2365 | 7.4 |
| $Ti_{65}Fe_{35}$ [11]* | Hypereutectic[1] | 1800 | 2200 | 6.7 |
| $Ti_{60}Fe_{20}Co_{20}$ [11]* | Hypereutectic[1] | 1510 | 2100 | 15 |
| $(Ti_{0.655}Fe_{0.35})_{97.5}Sn_{2.5}$ [7] | Hypereutectic[1] | 1478 | 2652 | 12.5 |

**Table 2 (Continued)**

| | | | | |
|---|---|---|---|---|
| $(Ti_{0.655}Fe_{0.35})_{95}Sn_5$ [7] | Hypereutectic[1] | 1267 | 2345 | 10.0 |
| $Ti_{72}Fe_{28}$ [8] | Hypoeutectic | 2028 ± 20 | 2627 ± 50 | 7.5 ± 0.3 |
| $(Ti_{0.72}Fe_{0.28})_{98}Ta_2$ [8] | Hypoeutectic | 2300 ± 11 | 2560 ± 60 | 1.0 ± 0.1 |
| $(Ti_{0.72}Fe_{0.28})_{96}Ta_4$ [8] | Hypoeutectic | 2215 ± 6 | 2531 ± 22 | 5.0 ± 0.4 |
| $(Ti_{0.705}Fe_{0.295})_{95}Sn_5$ [18] | Hypereutectic[2] | 2205 | 2266 | 1.7 |
| $(Ti_{0.705}Fe_{0.295})_{93}Sn_7$ [18] | Hypereutectic[2] | 1651 | 1961 | 6.2 |
| $(Ti_{0.705}Fe_{0.295})_{91}Sn_9$ [18] | Hypereutectic[2] | 1304 | 2261 | 15.7 |
| $(Ti_{0.655}Fe_{0.35})_{97}Nb_3$ [13] | Hypereutectic[1] | 1910 ± 15 | 2160 ± 25 | 6 ± 2 |
| $(Ti_{0.655}Fe_{0.35})_{95}Nb_5$ [13] | Hypereutectic[1] | 1964 ± 15 | 2390 ± 25 | 13 ± 2 |
| $(Ti_{0.655}Fe_{0.35})_{93}Nb_7$ [13] | Pseudo-binary eutectic | 2182 ± 10 | 2574 ± 20 | 12 ± 1.5 |
| $(Ti_{0.655}Fe_{0.35})_{98}Ga_2$ [11] | Hypereutectic[1] | 2042 ± 15 | 2769 ± 25 | 6.5 |
| $(Ti_{0.655}Fe_{0.35})_{96}Ga_4$ [11] | Hypereutectic[1] | 1953 ± 15 | 2472 ± 25 | 4.9 |

*arc melted, [1]primary FeTi phase, [2]primary $Ti_3Sn$ phase.

## Ti-Fe-Sn Ultrafine-Grained Alloys

Compressive mechanical tests [7] show that all $(Ti_{0.65}Fe_{0.35})_{100-x}Sn_x$ (x = 0, 2.5 and 5%) alloysdisplay considerable work hardening, high strength and large plasticity. The obtained mechanical properties are summarized in Table 2. The addition of 2.5% Sn results in a significant increment in fracture strength by ~300 MPa and a noticeable enhancement of plasticity by ~5%. Further addition of Sn to 5% leads to a slight decrease in strength and plasticity compared to the $Ti_{63.375}Fe_{34.125}Sn_{2.5}$ alloy. However, 5% Sn addition still toughens $Ti_{65}Fe_{35}$ alloy by enhancing the plasticity as well as maintaining a high strength. Therefore, a suitable Sn concentration could both improve the strength and enhance the plasticity of $Ti_{65}Fe_{35}$ alloy.

X-ray diffraction (XRD) results [7] indicate that $Ti_{65}Fe_{35}$and $Ti_{63.375}Fe_{34.125}Sn_{2.5}$ mainly contain bcc β-Ti (A2 structure) and bcc FeTi (B2) phases and 5% Sn addition leads to the coexistence of hexagonal $Ti_3Sn(D0_{19})$ with the aforementioned two bcc phases. The lattice parameters of β-Ti ($a_{\beta\text{-Ti}}$) are 0.3162, 0.3242 and 0.3226 nm in $Ti_{65}Fe_{35}$, $Ti_{63.375}Fe_{34.125}Sn_{2.5}$ and $Ti_{61.75}Fe_{33.25}Sn_5$, respectively. Interestingly, Sn addition only changes $a_{\beta\text{-Ti}}$, while $a_{\text{FeTi}}$ remains unchanged (0.2991 nm). The back-scattered electron SEM overall and magnified microstructures of the as-cast alloys are shown in Figure 3. The $Ti_{65}Fe_{35}$ (Figure 3a) and $Ti_{63.375}Fe_{34.125}Sn_{2.5}$ (Figure 3b) display a typical hypereutectic microstructure, where micrometer-sized FeTi primary dendrites are homogenously dispersed in an ultrafine-grained matrix. A magnified image of the ultrafine-grained matrix (Figure 3d) reveals that the ultrafine eutectic matrix is composed of plate-shape FeTi (bright) and β-Ti (gray) phases. The 2.5% Sn addition in the $Ti_{65}Fe_{35}$alloy slightly decreases the sizes of the primary FeTi dendrites (i.e. length, trunk spacing and arm spacing) from ~50–100, 10–25 and 2–4 μmin $Ti_{65}Fe_{35}$ to ~20–70, 7–15 and 2–3 μmin $Ti_{63.375}Fe_{34.125}Sn_{2.5}$, respectively. Interestingly, the 2.5% Sn addition could considerably refine the grain size of the eutectic matrix in the in the $Ti_{65}Fe_{35}$ alloy, i.e. the width of the FeTi lamellae decreases from ~0.4 μm in $Ti_{65}Fe_{35}$ alloy to ~200 nm in the $Ti_{63.375}Fe_{34.125}Sn_{2.5}$) and that of β-Ti lamellae decreases from ~2.5 μm ($Ti_{65}Fe_{35}$) to ~160 nm ($Ti_{63.375}Fe_{34.125}Sn_{2.5}$). The volume fraction of the ultrafine (β-Ti + FeTi)

eutectic in the bimodal composites increases from ~65% in $Ti_{65}Fe_{35}$ to ~72% in $Ti_{63.375}Fe_{34.125}Sn_{2.5}$. EDX analysis indicates that the primary FeTi dendrites have a composition of approximately $Ti_{52}Fe_{48}$ in both alloys except for traces of Sn (0.4 ± 0.4 at.%) in the latter alloy. Most Sn dissolves in the eutectic matrix in case of $Ti_{63.375}Fe_{34.125}Sn_{2.5}$, which could further toughen the alloy due to solution hardening effect. As a result, the 2.5% Sn addition in $Ti_{65}Fe_{35}$alloy leads to the refinement of microstructure constituents (slightly smaller primary FeTi dendrites and significantly finer eutectic matrix, over 10 times finer β-Ti solid solution phase) and an increment of the volume fraction of the ductile ultrafine-grained eutectic matrix by ~7 vol.%), resulting in the improvement of the strength and plasticity in $Ti_{63.375}Fe_{34.125}Sn_{2.5}$. Detailed TEM observations (Figure 4) confirm that the $Ti_{63.375}Fe_{34.125}Sn_{2.5}$ is composed of FeTi dendrites embedded in ultrafine (β-Ti + FeTi) eutectic matrix and the $Ti_{65}Fe_{35}$ alloy shows a similar microstructure. The selected area electron diffraction (SAED) patterns from matrix reveal that there exists ω-Ti like short-range order (SRO) (denoted by arrows) in the matrix of both alloys. When further increasing the Sn concentration to 5% (Figure 3c), $Ti_{61.75}Fe_{33.25}Sn_5$ shows a complex microstructure composed of primary $Ti_3Sn$, FeTi dendrites and (β-Ti + FeTi) eutectic matrix, with volume fractions of ~20, 24 and 56 vol.%, respectively. The $Ti_{61.75}Fe_{33.25}Sn_5$ alloy has FeTi dendrites and eutectic with a close sizesto those in $Ti_{63.375}Fe_{34.125}Sn_{2.5}$, but contains a lower fraction of eutectic matrix, which is responsible for plasticity. Therefore, $Ti_{61.75}Fe_{33.25}Sn_5$ exhibits a lower plasticity than $Ti_{63.375}Fe_{34.125}Sn_{2.5}$.

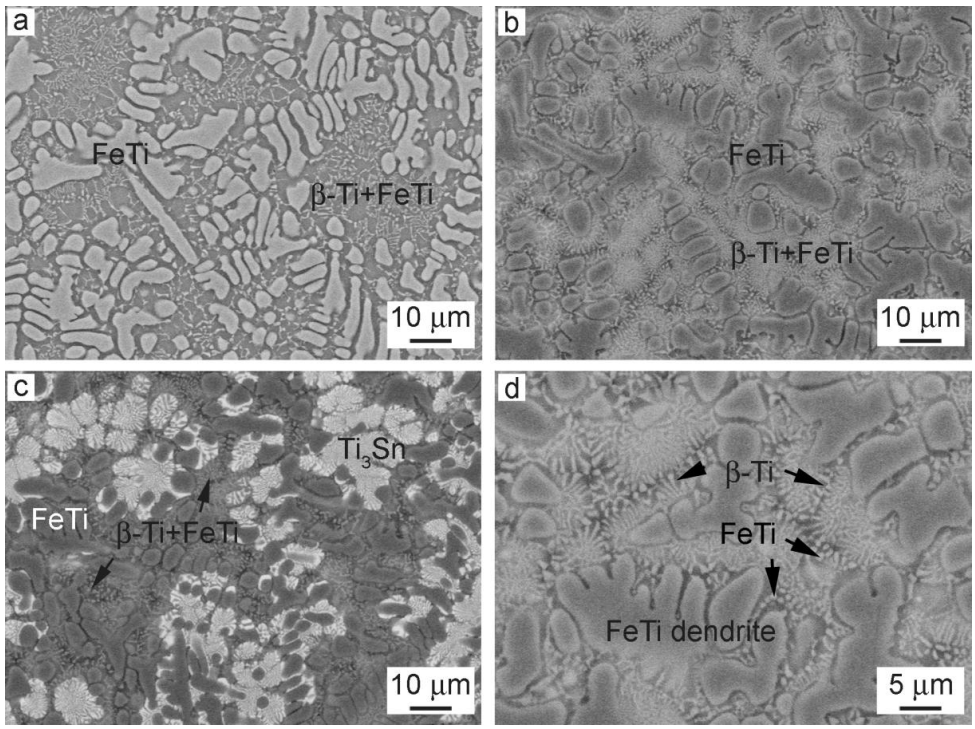


Figure3SEM backscattered electron images of the overall microstructurefor the as-cast $(Ti_{0.65}Fe_{0.35})_{100-x}Sn_x$3 mm∅ rods showing primary micrometer-size dendritic phase embedded in ultrafine-grained matrix (a) x = 0, (b) x = 2.5 and (c) x = 5, and (d) a magnified image of x = 2.5 rod showing a ultrafine-grained eutectic matrix.

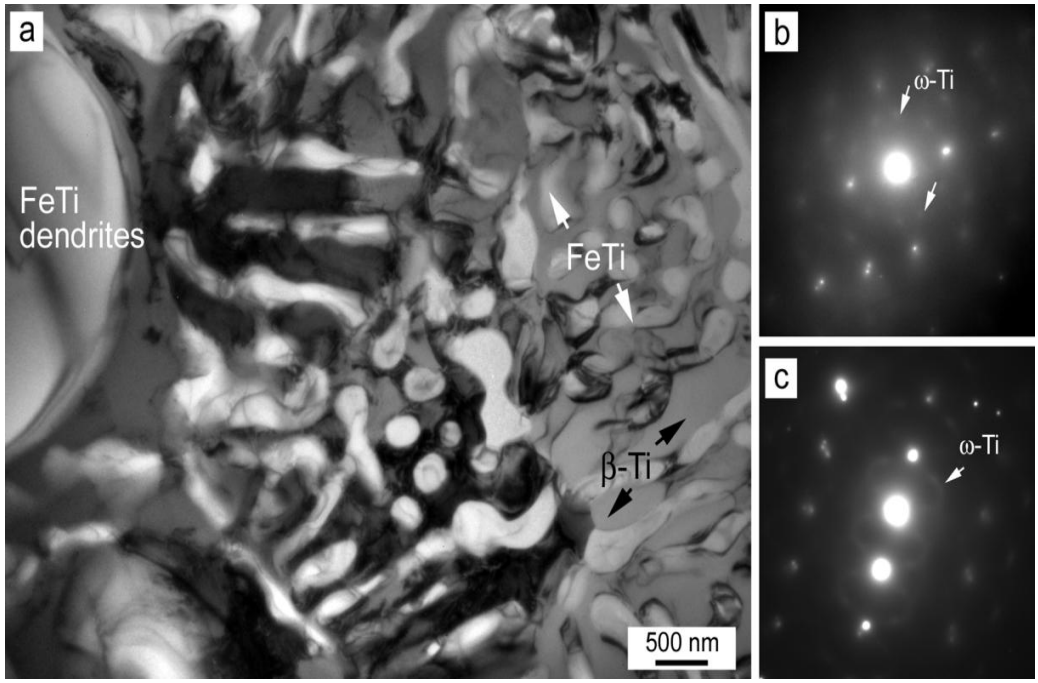


*Source*: from Ref. [9].

Figure 4 (a) Bright-field TEM image of the $Ti_{63.375}Fe_{34.125}Sn_{2.5}$ and selected area electron diffraction (SAED) patterns for the eutectic matrix in the (b) $Ti_{65}Fe_{35}$ and (c) $Ti_{63.375}Fe_{34.125}Sn_{2.5}$ alloys. The $Ti_{65}Fe_{35}$ alloy shows a similar microstructure as the $Ti_{63.375}Fe_{34.125}Sn_{2.5}$.

The $(Ti_{0.65}Fe_{0.35})_{100-x}Sn_x$ ultrafine-grained alloys display a fracture morphology (Figure 5) mainly consisting of cleavage fracture along with a few elongated dimples. The cleavage planes of the FeTi dendrites make multiple steps on the fracture surface displaying river-like patterns, as denoted by the arrows in Figures 5a–c. The morphology of the river-like patterns is somewhat different due to the size and volume fraction of the primary dendrites. An enlarged view of the fracture morphology of the primary FeTi dendrites (cleavage) and the eutectic matrix (dimple) is shown in Figure 5d. Interestingly, a blockage of many slip bands, which form in the (β-Ti + FeTi) eutectic matrix, by the primary FeTi dendrites at the dendrite/eutectic interface under compression can be observed on the fracture surface (Figure 5 inset). This is presumably due to the relatively higher hardness of the primary FeTi dendrites compared to the (β-Ti + FeTi) eutectic matrix. It is noted that cracks, as indicated by white arrows, are apparent around the $Ti_3Sn$ phase in the failed $Ti_{61.75}Fe_{33.25}Sn_5$ (Figure 5c). This is related to the structural incompatibility between hexagonal $Ti_3Sn$ ($D0_{19}$) and bcc FeTi (B2) and β-Ti (A2), which blocks the dislocation transfer across their interfaces, accelerates the failure around $Ti_3Sn$ phase [7]. Both A2 and B2 phases have the same main slip systems, while the $D0_{19}$ phase has different main slip systems. The compatibility between the A2 and B2 structures will enhance the plasticity by slip transfer to relieve dislocation pile-ups at the A2/B2 interface. In contrast, the mismatch of the structure between $D0_{19}$ and A2 and B2 will make the dislocation transfer across the $D0_{19}$/A2 and/or $D0_{19}$/B2 interfaces difficult, resulting in cracks around the $D0_{19}$ phase and inducing relatively early fracture.

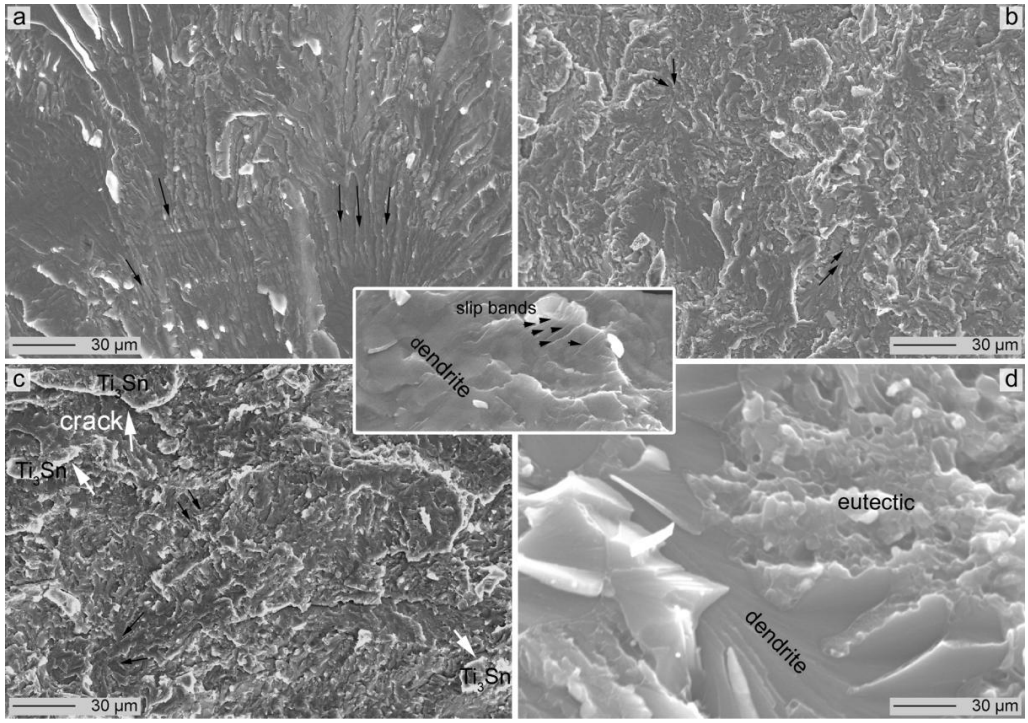


*Source*: from Ref. [7].

Figure5SEM secondary electron images of the fractured surfacesfor the $(Ti_{0.65}Fe_{0.35})_{100-x}Sn_x$rods: (a) x = 0, (b) x = 2.5, (c) x = 5 and (d) an enlarged view of the fracture morphology of the primary FeTi dendrites and the eutectic matrix. The inset shows the blockage of slip bands formed in the eutectic matrix at the dendrite/eutectic interface.

## Ti-Fe-Ta Ultrafine-Grained Alloys

The mechanical properties of the as-cast $(Ti_{0.72}Fe_{0.28})_{100-x}Ta_x$(x = 0, 2 and 4%) 3 mm∅ rods are given in Table 2. All three alloys show a high yield strength in excess of 2000 MPa, a high fracture strength exceeding 2500 MPa, and a large plasticity. XRD analyses reveal that all alloys mainly consist of β-Ti and FeTi solid solutions. The lattice parameters are $a_{\beta\text{-Ti}}$= 0.3154, 0.3152, and 0.3163 nm and $a_{FeTi}$= 0.2993, 0.2998, and 0.3001 nm for $x$=0, 2, and 4, respectively. Note that Ta addition has altered the lattice parameters of both β-Ti and FeTi, which is quite different from those in Ti-Fe-Sn ultrafine-grained alloys. The internal lattice strain of theβ-Ti phase is 0.57%, 0.81% and 0.93% for $x$=0, 2 and 4, respectively. As a result, the increase of Ta concentration leads to higher lattice strain in β-Ti phase. Both the $Ti_{72}Fe_{28}$ (Figure 6a) and $Ti_{70.56}Fe_{27.44}Ta_2$ (Figure 6b) alloys show a hypoeutectic microstructure; micrometer-sized β-Ti primary dendrites (indicated by black arrows) are embedded in an ultrafine-grained (β-Ti + FeTi) eutectic matrix (denoted by white arrows). In contrast, the $Ti_{69.12}Fe_{26.88}Ta_4$ alloy (Figure 6c) has a carcass microstructure (pseudo-hypoeutectic) composed of ultrafine FeTi (~250 nm) and micrometer-sized β-Ti (~1.2 μm) solid solutions. Although the $Ti_{72}Fe_{28}$ (Figure 6a) and $Ti_{70.56}Fe_{27.44}Ta_2$ have a close grain size of β-Ti dendrites, the $Ti_{70.56}Fe_{27.44}Ta_2$ has a significantly coarser eutectic matrix in comparison with $Ti_{72}Fe_{28}$. The average widths of the β-Ti and FeTi lamellae in the eutectic are about 1.0 μm

and 400 nm, respectively, which are ~3 times coarser than in case of $Ti_{72}Fe_{28}$. In addition, according to the areal fractions in the microstructure, $Ti_{70.56}Fe_{27.44}Ta_2$ contains a smaller volume fraction of the ultrafine eutectic than $Ti_{72}Fe_{28}$.

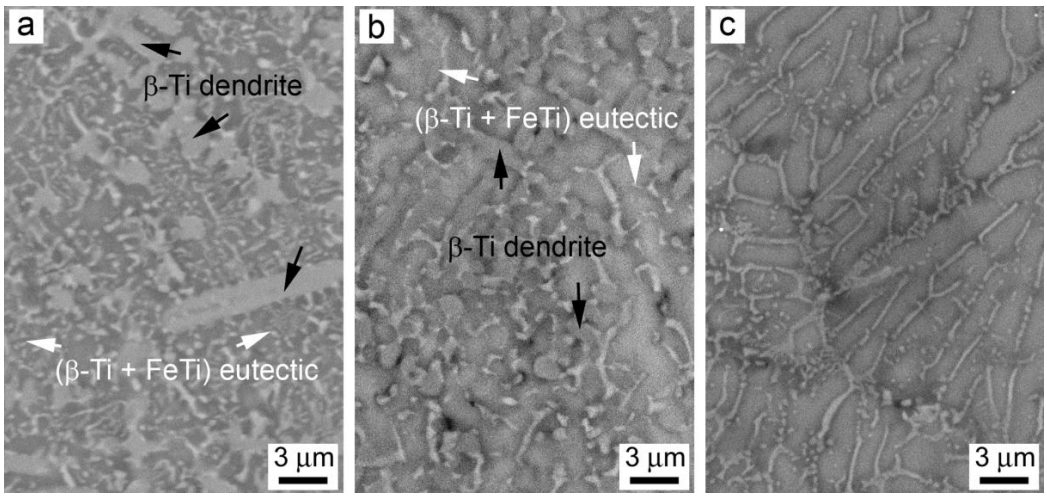


*Source*: from Ref. [8].

Figure6SEM backscattered electron images of the as-cast$(Ti_{0.72}Fe_{0.28})_{100-x}Ta_x$3 mm∅ rods: (a) x = 0 and (b) x = 2 showing a hypoeutectic microstructure with micrometer-sized primary β-Ti dendritic phase embedded in an ultrafine-grained (β-Ti + FeTi) matrix, and (c) x = 4 showing a carcass (pseudo-hypoeutectic) microstructure.

The TEM observations confirm that $Ti_{72}Fe_{28}$ is composed of micrometer-sized β-Ti primary dendrites embedded in an ultrafine-grained (β-Ti + FeTi) eutectic matrix (Figure 7a) and the $Ti_{70.56}Fe_{27.44}Ta_2$ alloy displays a similar microstructure. $Ti_{69.12}Fe_{26.88}Ta_4$ consists of nanoscale twins along with the β-Ti and FeTi phases (Figure 7b). However, the SAED patterns reveal that the $Ti_{72}Fe_{28}$ and $Ti_{70.56}Fe_{27.44}Ta_2$ alloys show different structural features in the matrix. The matrix of $Ti_{72}Fe_{28}$ displays only the diffraction spots of β-Ti and FeTi (Figure 7c). The two sets of spots are indexed as the diffraction patterns of the [011] zone axis of the β-Ti and FeTi phases. Their corresponding orientation relationships are $[011]_{β\text{-}Ti}$ // $[011]_{FeTi}$ and $(01\text{-}1)_{β\text{-}Ti}$ // $(200)_{FeTi}$. In contrast, the matrix in $Ti_{70.56}Fe_{27.44}Ta_2$ (Figure 7d) consists of a diffuse ω-Ti scattering (circular reflections around the FeTi diffraction spots) together with the diffraction spots of the β-Ti and FeTi phases. One set of the spots is indexed as the diffraction pattern of the (-112) zone axis of the β-Ti solid solution, and the other set corresponds to that of the [001] zone axis of FeTi.The corresponding orientation relationships between the β-Ti and FeTi phases are $[\text{-}112]_{β\text{-}Ti}$ // $[001]_{FeTi}$ and $(110)_{β\text{-}Ti}$ // $(110)_{FeTi}$. The appearance of ω-Ti-like phase and 0.24% higher lattice strain in β-Ti phase in the $Ti_{70.56}Fe_{27.44}Ta_2$ alloy will increases the dislocation pileup stress and decreases the intrinsic cleavage strength [32]. Therefore, the addition of 2 at.% Ta reduces the plasticity of 7.5% in the $Ti_{72}Fe_{28}$ alloy to 1.0% in $Ti_{70.56}Fe_{27.44}Ta_2$ alloy (Table 2). On the other hand, it has been reported that deformation twinning enhances the plastic deformation in Ti-base alloys [33]. Thus, the presence of nanoscale twins in the $Ti_{69.12}Fe_{26.88}Ta_4$ may facilitate the dislocation slip and enhance the plasticity. Therefore, the $Ti_{69.12}Fe_{26.88}Ta_4$ alloy regains a large plasticity.

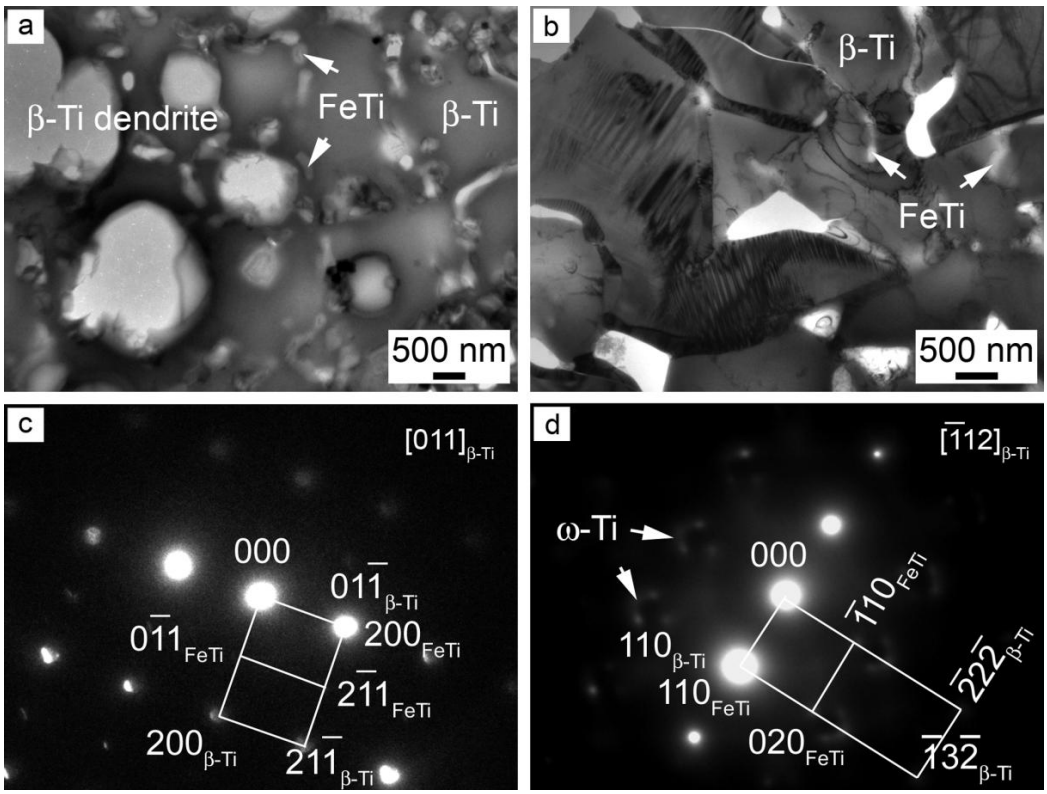


*Source*: from Ref. [8].

Figure 7.Bright-filed TEM images of the ultrafine-grained $(Ti_{0.72}Fe_{0.28})_{100-x}Ta_x$ alloys: (a) $x = 0$ and (b)$x = 4$, and the corresponding SAED patterns for the eutectic matrix in: (c) $x = 0$along the [011] zone axis and (d)$x = 2$ along the [-112] zone axis of β-Ti phase. The $x = 2$ alloy displays a similar microstructure as the x = 0 alloy.

## MECHANICAL PROPERTIES: MULTIPLE LENGTH-SCALE ALLOYS VS BULK METALLIC GLASS MATRIX COMPOSITE

Titanium base bulk metallic glasses (BMGs) and BMG matrix composites [34-45] have been developed with the aim to obtain high-strength titanium alloys. In general, the titanium base BMGs often exhibit a high fracture strength exceeding ~2000 MPa but very limited plasticity (<0.5%) [34-37]. Some titanium base BMGs also exhibit a larger plasticity of about 1–11%, however, their plasticity does not result from the glassy phase itself but is closely related to the amount of nanocrystals that are embedded in the glassy matrix [46]. Therefore, the plasticity originates from BMG matrix composites microstructure. Titanium base BMG matrix composites have shown large plasticity but sacrificing their strength by about 300–500 MPa. The titanium base nanostructured/ultrafine-grained alloys with multiple length-scale microstructure are designed in a similar manner to BMG matrix composites with the significant difference being that the continuous matrix material is comprised of a nanostructured eutectic instead of a metallic glass. Nevertheless, the multiple length-scale composites have shown a large plasticity without sacrificing their strength. Figure 8 compares

the mechanical properties of the as-cast titanium nanostructured/ultrafine-grained alloys with multiple length-scale microstructure with the commercial titanium alloy (e.g. Ti-6Al-4V grade 5 STA), Ti-base BMGs [34-37] and Ti-base BMG matrix composites [44]. Apparently, the nanostructured/ultrafine-grained titanium alloys with multiple length-scale microstructure have better mechanical properties (in terms of yield strength, ultimate strength and plasticity) than the titanium base BMGs and BMG matrix composites. Increasing the plasticity/strength of metals without sacrificing other properties (strength, plasticity, *etc*) is a critical issue in the alloy development, as they are competitiveness. Therefore, by introducing multiple length scales into microstructure may provide a possible route to optimize overall properties.

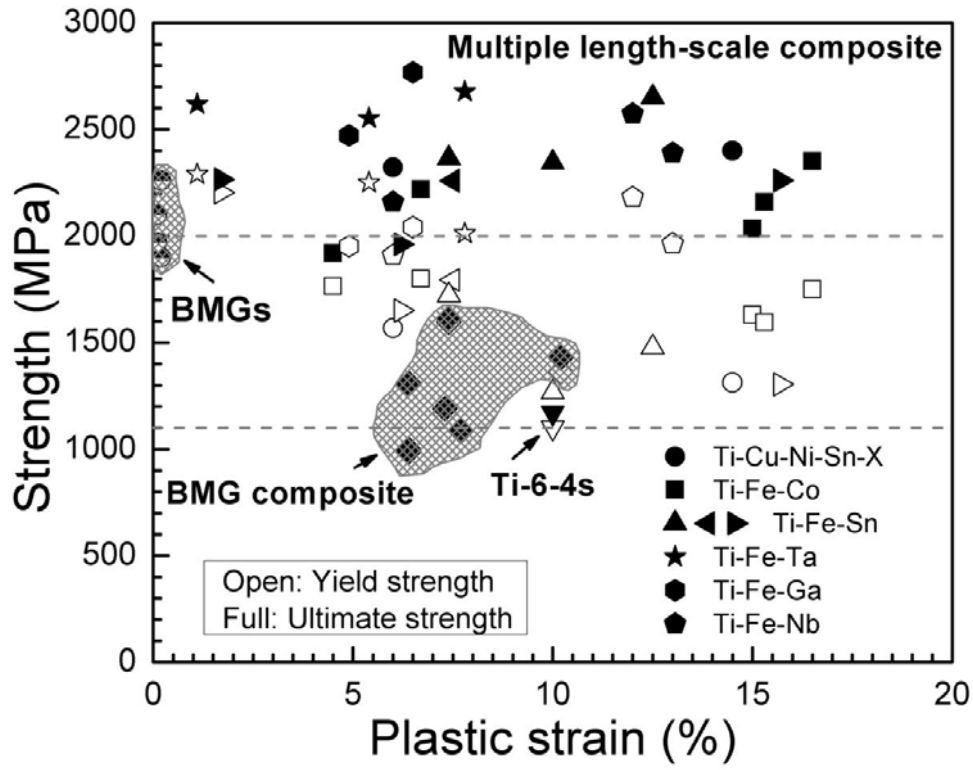


Figure 8.Comparison of the mechanical properties of the nanostructured/ultrafine-grained titanium alloys with **multiple length-scale microstructure** with some titanium base bulk metallic glasses [34-37] and their composites **[44]** as well as the commercial Ti-6Al-4V alloy.

Figure 9 compares the specific strength of nanostructured/ultrafine-grained titanium alloys multiple length-scale microstructure [12] with titanium base BMG matrix composites [44] and other commercial engineering structural materials. The specific strength of both titanium nanostructured/ultrafine-grained alloys and BMG matrix composites, as two advanced high-strength titanium alloys, is particularly attractive. But, titanium nanostructured/ultrafine-grained alloys have higher specific strength than the titanium base BMG matrix composites. Therefore, the combination of high strength and high specific strength of the titanium nanostructured/ultrafine-grained alloys with multiple length-scale microstructure may create opportunities in the application in the aerospace, chemical industries, architecture, medicine, power generation, marine and offshore, sports and leisure, and transportation, which are seeing increased application of titanium alloys.

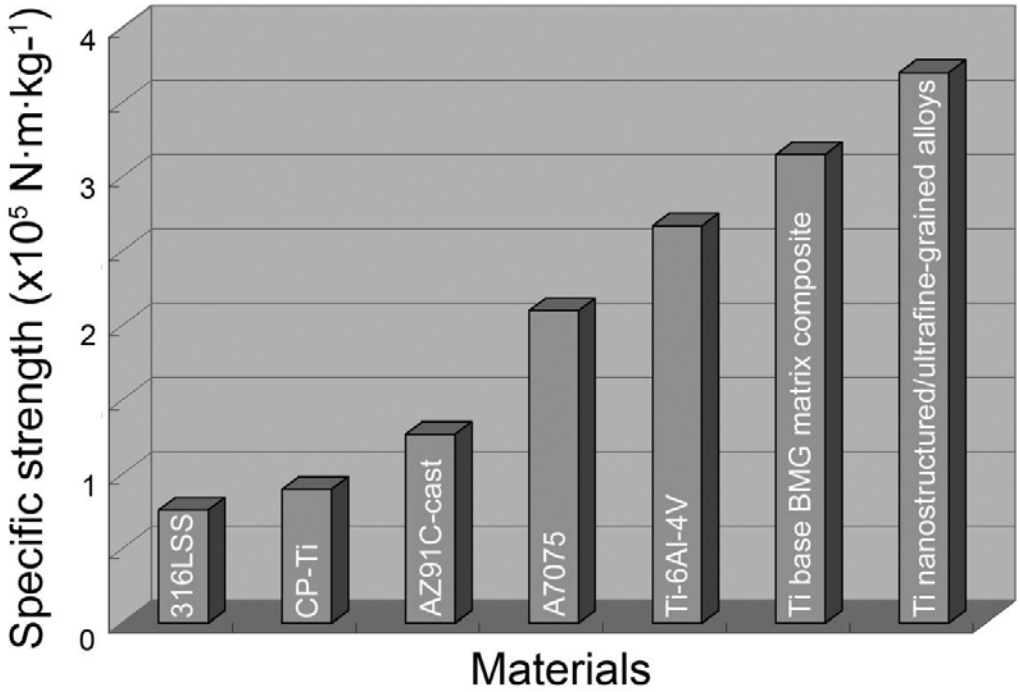


Figure 9.Specific strength of titanium nanostructured/ultrafine-grained alloys with **multiple length-scale microstructure**compared with different titanium alloys as well as selected commercial engineering structural materials.

## CONCLUSION

Titanium nanostructured/ultrafine-grained alloys with multiple length-scale microstructure have been developed by simple one-step processing and exhibited high strength and enhanced plasticity, as well as high specific strength. The mechanical properties of the nanostructured/ultrafine-grained alloys are determined by the combined effects of the refinement and the volume fraction of their phase constituents in the microstructure as well as the compatibility of the structures of the constituent phases. The deformation mechanism is strongly linked to the nanostructured/ultrafine-grained eutectic matrix by nucleation, pinning and multiplication of shear bands during deformation. Accordingly, it is very important to tailor the microstructural features of these **multiple length-scale composites by**proper selection of micro-alloying elements base on the structural point of view and controlling of the solidification process. The titanium nanostructured/ultrafine-grained alloys with multiple length-scale microstructure demonstrate competitive mechanical properties with conventional titanium alloys and other high-strength titanium alloys for some structural applications, particularly in the aerospace and aeronautics industry as replacements for some crystalline titanium alloy hardware where high strength and toughness are a necessity. **By introducing multiple length scales into microstructure** provide a promising route to enhance plasticity without sacrificing high strength. Therefore, the formation of multiple length-scale structures may become one of the subjects of significant research in the development of high-strength metallic materials [47].

## ACKNOWLEDGMENT

The authors thank H.B. Lu, C. Duhamel, J. Das and U. Kühn for stimulating discussions, and M. Frey, H.-J. Klauß, S. Donath and C. Mickel for technical assistance. L.C. Zhang is very grateful for the financial support of the Alexander von Humboldt Foundation.

## REFERENCES

[1] L. Lu, X. Chen, X. Huang and K. Lu,*Science*,323, 607 (2009).
[2] C. C. Koch, *J. Metastable Nanocryst. Mater*. 18, 9 (2003).
[3] E. Ma, *Scripta Mater*. 49, 663 (2003).
[4] E. Ma, JOM 58, 49 (2006).
[5] Y. M. Wang, M. W. Chen, F. H. Zhou and E. Ma, *Nature* 419, 912 (2002).
[6] G. He, J. Eckert, W. Löser and L. Schultz, *Nature Mater*. 2, 33 (2003).
[7] L. C. Zhang, J. Das, H. B. Lu, C. Duhamel, M. Calin and J. Eckert, *Scripta Mater*. 57, 101 (2007).
[8] L. C. Zhang, H. B. Lu, C. Mickel and J. Eckert, *Appl. Phys. Lett*. 91, 051906 (2007).
[9] L.C. Zhang, H.B. Lu, M. Calin, E.V. Pereloma and J. Eckert, *J. Phys. Conf. Ser*. 240, 012103 (2010).
[10] J. Das,K. B. Kim, F. Baier, W. Löser andJ. Eckert,*Appl.Phys. Lett*.87, 161907 (2005).
[11] D. K. Misra, S. W. Sohn, W. T. Kim and D. H. Kim, *Intermetallics* 18, 254 (2010).
[12] D. V. Louzguine, L. V. Louzguina, H. Kato and A. Inoue, *Acta Mater*. 53, 2009 (2005).
[13] J. M. Park, J. H. Han, K. B. Kim, N. Mattern, J. Eckert and D.H. Kim, *Phil. Mag. Lett*. 89, 623 (2009).
[14] L. L. Shi, H. Ma, T. Liu, J. Xu and E. Ma, *J. Mater. Res*. 21, 613 (2006).
[15] C. Leyens and M. Peters,*Titanium and Titanium Alloys: Fundamentals andApplications*, Wiley VCH, Weinheim, 2003.
[16] D. V. Louzguine, H. Kato, L.V. Louzguina andA. Inoue,*J. Mater.Res.*19, 3600 (2004).
[17] L. V. Louzguina-Luzgina, D. V. Louzguine-Luzgin andA. Inoue,*Intermetallic* 14, 255 (2006).
[18] J. H. Han, K. B. Kim, S. Yi, J.M. Park, S. W. Sohn, T. E. Kim, D. H. Kim, J. Das and J. Eckert, *Appl. Phys. Lett*. 93, 141901 (2008).
[19] L. He and E. Ma, *J. Mater. Res.* 11, 72 (1996).
[20] K. Lu, J. T. Wang and W. D. Wei, *J. Appl. Phys*. 69, 522 (1991).
[21] D. Jia, Y. M. Wang, K. T. Ramesh, E. Ma, Y. T. Zhu and R. Z. Valiev, *Appl. Phys. Lett*. 79, 611 (2001).
[22] C. C. Koch, *Scripta Mater*.49, 657 (2003).
[23] L. C. Zhang, M. Calin, M. Branzei, L. Schultz and J. Eckert, *J. Mater. Res*.22,1145 (2007).
[24] L. C. Zhang, J. Xu and E. Ma, *Mater. Sci. Eng. A*, 434, 280 (2006).
[25] J. Eckert, J. Das and K. B. Kim, "Nanostructured Composites: Ti-Base Alloys", in: *"The Dekker Encyclopedia of Nanoscience and Nanotechnology"*, (Eds. J. A. Schwarz, C. Contescu andPutyera). Marcel Dekker, Inc., New York, NY, USA, 2006.
[26] G. He, W. Löser and J. Eckert, *Acta Mater*. 51, 5223 (2003).

[27] J. Eckert, G. He, J. Das and W. Löser, *Mater. Trans. JIM* 44, 1999 (2003).
[28] G. He, J.Eckert, W. Löser and M. Hagiwara, *Acta Mater.* 52, 3035 (2004).
[29] B. B. Sun, M. L. Sui, Y. M. Wang, G. He, J. Eckert, E. Ma, *Acta Mater.* 54, 1349 (2006).
[30] Q. L. Dai, B. B. Sun, M. L. Sui, G. He, Y. Li, J. Eckert, W.K. Luo and E. Ma, *J. Mater. Res.* 19, 2557 (2004).
[31] G. He and M. Hagiwara, *Mater. Trans. JIM* 45, 1555 (2004).
[32] P. Lazar, R. Podloucky and D. Wolf, *Appl. Phys. Lett.* 87, 261910 (2005).
[33] X. P. Wu, S. R. Kalidindi, C. Necker and A. A. Salem, *Acta Mater.* 55, 423 (2007).
[34] T. Zhang and A. Inoue, *Mater. Sci. Eng. A* 304-306, 771 (2001).
[35] C. L. Ma, S. Ishihara, H. Soejima, N. Nishiyama and A. Inoue, *Mater. Trans.* 45, 1802 (2004).
[36] J. J. Oak, D. V. Louzguine-Luzgin and A. Inoue, *J. Mater. Res.* 22, 1346 (2007).
[37] Y. J. Huang, J. Shen, J. F. Sun and X. B. Yu, *J. Alloys Compd.* 427, 171 (2007).
[38] Y. L. Wang, E. Ma and J. Xu, *Phil. Mag. Lett.* 88, 319 (2008).
[39] J. M. Park, H. J. Chang, K. H. Han, W. T. Kim and D. H. Kim, *Scripta Mater.* 53, 1 (2005).
[40] F. Q. Guo, S. J. Wang, S. J. Poon and G. J. Shiflet, *Appl. Phys. Lett.* 86, 091907 (2005).
[41] L. C. Zhang, J. Xu and E. Ma, *J. Mater. Res.* 17, 1743 (2002).
[42] L. C. Zhang, J. Xu and J. Eckert, *J. Appl. Phys.* 100, 033514 (2006).
[43] M. Calin, L. C. Zhang and J. Eckert, *Scripta Mater.* 57, 1101 (2007).
[44] D. C. Hofmann, J.-Y. Suh, A. Wiest, M.-L. Lind, M. D. Demetriou and W. L. Johnson, *PNAS* 105, 20136 (2008).
[45] X. J. Gu, S. J. Poon, G. J. Shiflet and J. J. Lewandowski, *Acta Mater.* 58, 1708 (2010).
[46] T. Ohkubo, D. Nagahama, T. Mukai and K. Hono, *J. Mater. Res.* 22, 1406 (2007).
[47] K. Lu, *Science* 328, 319 (2010).

In: Advances in Mechanical Engineering Research. Volume 2 ISBN: 978-1-61761-984-7
Editor: David E. Malach 

*Chapter 9*

# MICROSTRUCTURES-MECHANICAL PROPERTIES CORRELATIONS OFMICROALLOYED STEELS

***S. N. Prasad and A. S. Mathur***
Research and Development Centre for Iron and Steel, Steel Authority of India Ltd., Doranda, Ranchi - 834002, Jharkhand, India

## ABSTRACT

Microalloying elements are generally Nb, V and Ti which are added to the steel either separately or in combination up to 0.1 wt. % primarily because of their tendency to form fine dispersions of alloy carbides and carbonitrides in either austenite or ferrite. It has also been found that the microalloying elements such as Nb and V increase the hardenability of austenite if they are in solid solution. In the recent work of Nb microalloyed weather resistant steel (C: 0.1%), Mn: 0.9%), increase in soaking temperature from 1000 to $1100^0$C has increased the YS, UTS and hardness of the rolled steel at a given rolling temperature and deformation due to dissolution of Nb (C, N) in the austenite which results in replacement of a part of pearlite into granular bainite. Increasing the rolling deformation from 25 to 50% has increased the YS but not UTS markedly. For $1100^0$C soaking, rolling 25% at 800, 900 or $1000^0$C results in much lower YS than that of simply air cooled samples. The YS is also lowered due to 50% reduction at $1000^0$ and $900^0$C. The inferior YS due to controlled rolling, though surprising, is attributed to lower amount of granular bainite. The optical microstructure after $1000^0$C soaking is ferrite-pearlite at 900 and 800C rolling temperatures whereas in addition to ferrite-pearlite, acicular ferrite/granular bainite are also observed after rolling at $740^0$C. After soaking at $1100^0$C, considerable amount of granular bainite has formed for all the rolling temperatures due to increase in hardenability. The TEM micrographs show ferrite and pearlite at 800 and $900^0$C rolling temperatures and acicular ferrite also at $740^0$C rolling after $1000^0$C soaking. On the other hand, presence of considerable amount of acicular ferrite and M/A (martensite – austenite) constituent is taken as an indication of granular bainite in addition to ferrite and pearlite after soaking at $1100^0$C and rolling at $1000\text{-}800^0$C.

The properties of Nb + V microalloyed weather resistant steel (C: 0.2%, Mn: 1.0%) have also been studied after the steel was deformed by rolling 50% at 900, 800 and $700^0$C. This study gave some very interesting results. The properties at $1100^0$C especially

the UTS and % EL, were vastly superior in comparison to the $1000^0$C soaking for a given rolling temperature and 50% deformation. The variation in all the properties, YS, UTS, Hv or %EL with respect to rolling temperature was insignificant in comparison to those observed after soaking at $1000^0$C. While the enhancement in properties is attributed to the presence of martensite (though termed M/A constituent) along with ferrite that contains fine precipitates of Nb, V (C, N),the virtual consistency of these properties is also due to lack of any difference in the microstructure of the as rolled products.

In view of the above, controlled rolling to be effective, higher soaking temperature (≥ 1100C) lower rolling temperature (≥ $800^0$C) and higher rolling reduction (≥ 50%) are recommended to take maximum advantage of the microalloying additions.

Key words: microalloyed steels, microstructure, mechanical properties, bainite, precipitation strengthening.

## 1. INTRODUCTION

Microalloying elements are generally Nb, V and Ti which are added to the steel either separately or in combination up to 0.1 % primarily because of their tendency to form fine dispersions of alloy carbides and carbonitrides in either austenite or ferrite. Thus the microalloying elements influence the mechanical properties of the finished steel by producing very fine grain size of ferrite and by dispersion of extremely fine alloy carbides of about 100 $A^0$ diameter.Grain refinement has a beneficial effect on properties such as hardness, yield strength, tensile strength, fatigue strength and impact resistance. The grain size influence is however, the largest on properties which are related to the early stage of the deformation. Since the grain boundary barriers are most effective at this stage, the yield strength is more dependent on grain size than tensile strength. The ultimate tensile strength is controlled mainly by complex dislocation interactions occurring within the grain and grain size is not a major controlling variable. The grain refinement is the only generalised method to simultaneously strengthen and toughen steels. In the controlled rolling of microalloyed steels, recrystallization during or immediately after hot rolling is restricted. This results in a pancake shaped unrecrystallised grains containing deformation bands, which act as sites for ferrite nucleation. This demands the usage of a low finish rolling temperature that retards the kinetics of dynamic recrystallisation. On cooling after controlled rolling the deformed austenite transforms to fine ferrite. Alloy carbide precipitation in the finished steel contributes additional strengthening.

It has also been found that the microalloying elements such as Nb and V increase the hardenability of austenite if they are in solid solution [1-4]. The segregation of microalloying elements at the austenite grain boundaries decreases the nucleation and growth of the austenite transformation products. The grain boundary segregation by V and Nb reduces the surface energy of the austenite grain boundary that results in decrease in its effectiveness as a nucleation site. This behaviour is very similar to the boron effect. The contribution of microalloying elements to the hardenability of austenite has not been extensively exploited. Steels containing multiple microalloying additions have revealed the possibility of asuper hardenability effect. V addition only can produce sufficient strength but not superior low temperature toughness. By the addition of 0.1% vanadium in a steel composition of 0.1%C,

1.3% Mn and 0.035% Nb the strength increment of about 70 MPa [5] has been obtained without any decrease in toughness.

The ideal strengthening which takes full advantage of grain refinement improves the transition temperature with the estimated gradient of 0.80 $^0$C/MPa [6]. When other strengthening mechanisms operate in combination with grain refinement, the gradient decreases. For example, the Mn addition which brings about the grain refinement combined with bainite transformation results in a gradient of 0.53 $^0$C/MPa [7]. On the other hand, the transition temperature rises with strengthening by the precipitation hardening and the transformation hardening and the relationship is approximately linear with the gradient of 0.46 $^0$ C/ MPa [6].

Precipitation hardening occurs in microalloyed steels due to the precipitation of M(C,N) [8] type carbonitrides in austenite or ferrite on cooling from the austenitisation temperature. The precipitation is sluggish in underformed austenite. However, during controlled rolling of Nb bearing steel in the low temperature $\gamma$ region, very fine niobium carbonitrides are precipitated profusely in the strained austenite lattice. The intensity of such precipitation is controlled by the amount of retained strain, which also determines the dislocation density.

The precipitates formed in austenite do not contribute to significant precipitation strengthening in the ferrite. However, only a portion of the available precipitate is formed in the austenite, the remaining in solution in the austenite precipitate either as interphase precipitates at the austenite ferrite interface during transformation or in the ferrite after transformation has occurred. In the later case, the precipitates form on dislocations or generally in the matrix if the dislocations density is low. The precise nature of the precipitate morphology and distribution depends on the supersaturation, the rate of cooling, the dislocation density and generally alloy content of the steel.

The refining effect of precipitation on the ferrite grain size is an important effect during the cooling of hot rolled strip in the coil and in preventing grain growth during tempering or the welding cycle. Obviously the precipitate size is important and is controlled by the transformation temperature or by the coiling temperature [9]; the lower the coiling temperature the smaller the particle size. The precipitates become smaller with increasing cooling rate as the transformation temperature decreases [10-12] but with very rapid cooling rates, precipitation can be inhibited [10, 11, 13]. Maximum precipitation strengthening was found to occur at a cooling rate of about $3^0$ C/s in V steel [11, 12, 14]. The DBTT is, however, increased by about $0.3^0$ C per MPa increase in yield strength [10].

Increasing the dislocation density, $\rho$, in a material increases the flow stress, $\sigma$, as given by the following equation:

$$\sigma = \sigma_\iota + \alpha\, Gb\, \rho^{0.5}$$

where G and b are shear modulus and the burgers vector of the dislocation [15].

In HSLA steels with ferrite - pearlite microstructures, which are not subjected to cold work, the dislocation density of ferrite increases gradually with the lowering of transformation temperature. Thus massive ferrite possesses a higher dislocation density than polygonal ferrite. In the light of the above, the present paper correlates the microstructures

and mechanical properties achieved after different thermal and thermomechnical treatments of multi alloyed microalloyed steels.

## 2. EXPERIMENTAL PROCEDURE

Microalloyed steels (Table 1) were made by melting in a 100 kg air induction furnace. The metal was poured into ingots of size 100 x 100 x 400 mm. The defective portion of the ingot comprising about 10% of the height of ingot from bottom and 25% from top were discarded. The remaining portion of the ingot was soaked at 1250 $^{o}$C for 2 hours and hot rolled to plates with a final thickness of 12 mm over an approximate temperature range of 1200-900 $^{o}$C. The chemical compositions of the steels are given in Table 1.

Samples of 150 x 25 x 12 mm were cut from the rolled plates for controlled rolling in a two high (Hille-50) rolling mill having 500 kN rolling load capacity. A 10 mm deep hole of 1.5 mm diameter was drilled in the centre of the length and thickness of the sample and a stainless steel sheathed mineral insulated chromel-alumel thermocouple was embedded into the hole so that the temperature of the steel could be recorded during the thermal and thermomechanical treatment of the samples. The samples were then heated to the required soaking temperature in a silicon carbide muffle furnace. After soaking for 40 minutes, the samples were quickly removed from the furnace (along with the embedded thermocouple) and were cooled in air to get to the rolling temperature before being hot rolled to the required deformation in single pass. The samples were cooled in air after the hot rolling. Some samples were also air cooled from different soaking temperatures to room temperature without any deformation.

Specimens cut from the rolled samples were mechanically polished and etched with 2% nital. The optical microstructures of the steel were recorded with a NEOPHOT light optical microscope. The ferrite grain size was measured using linear intercept method.

Transmission electron microscopes JEOL Model 400 EX and JEOL 200 CX were used for TEM examination. Specimens for TEM study were cut by slicing 0.1 mm thick discs in an isomet slow speed saw. The slices were mechanically thinned to 0.05 mm thickness and electrolytically polished at 30 V using a solution of 95% acetic acid and 5% perchloric acid maintained at –10 $^{o}$C.

The tensile properties were evaluated using an Instron machine (model 1273) at a constant cross head speed (2 mm/min). In each condition, two tensile specimens of 25 mm gauge length, 5 mm gauge width and 5 mm thickness were tested at room temperature.

**Table 1 Chemical composition of the experimental steels (Weight Percent)**

| Steel | C | Si | S | P | Mn | Ni | Cr | Cu | Al | Nb | V | N |
|---|---|---|---|---|---|---|---|---|---|---|---|---|
| 1 | 0.11 | 0.24 | 0.033 | 0.052 | 1.00 | 0.33 | 0.47 | 0.47 | 0.023 | 0.024 | - | 0.0077 |
| 2 | 0.10 | 0.19 | 0.025 | 0.116 | 0.88 | 0.34 | 0.48 | 0.47 | 0.006 | - | - | - |
| 3 | 0.20 | 0.27 | 0.035 | 0.023 | 1.03 | 0.32 | 0.51 | 0.46 | 0.078 | 0.054 | 0.046 | 0.0121 |

# 3. RESULTS

The results of the study carried out are presentes in the following sections:

## 3.1. Mechanical Properties

The influence of deformations at 800, 900 and 1000 $^{O}$C after soaking at 1100 $^{O}$C and that at 740, 800 and 900 $^{O}$C after 1000 $^{O}$C soaking on the YS, UTS and % EL of steel 1 is shown in Figure 1. While the range of YS values was wide (335 to 460 MPa), due to variation in rolling parameters, in which the lower values are for lower deformation and higher rolling temperatures, the UTS varied only over a narrow range of 530 to 585 MPa. The % EL values were in the range 27 to 36%. Soaking at 1100 $^{O}$C resulted in higher UTS and lower % EL as compared to 1000$^{O}$C soaking. This difference is much less for yield stength.

The range of tensile properties as a function of % deformation for various rolling temperatures after soaking at 1000 and 1100 $^{O}$C is shown in Figures 2 and 3 respectively. These figures show that the YS is more sensitive to deformation than UTS. The UTS was in a narrow range of 530 to 550 MPa and 560-585 MPa for the rolling after 1000 and 1100 $^{O}$C soaking respectively.

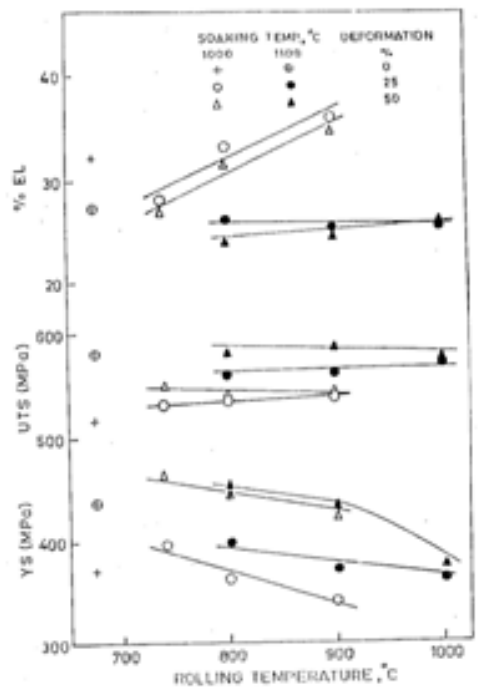


Figure 1. Influence of soaking temperature and rolling temperature on the tensile properties of steel 1.

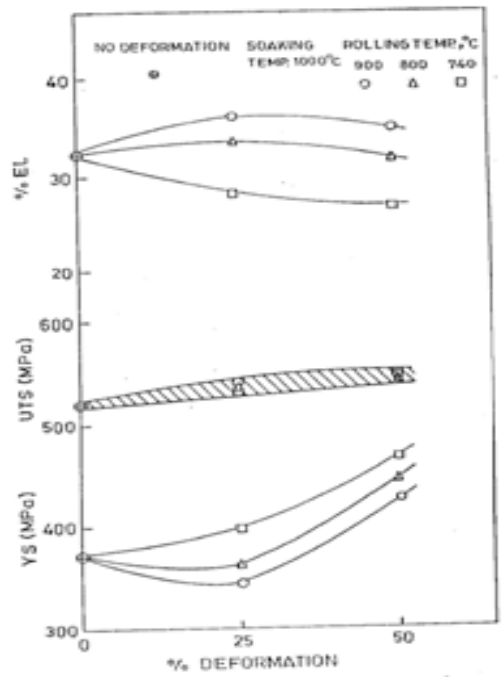


Figure 2. Influence of rolling reduction on the tensile properties of steel 1 at $1000^0$C soaking temperature.

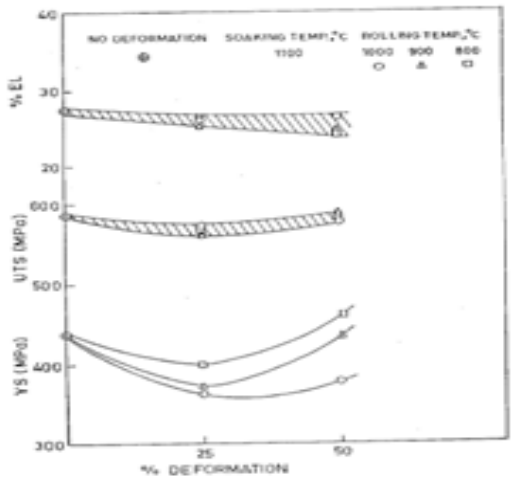


Figure 3. Influence of rolling reduction on the tensile properties of steel 1 at $1100^0$C soaking temperature.

Higher soaking temperature has resulted in higher hardness after rolling at all temperatures studied. The hardness was about 160 to 180 Hv when rolled at 900 to 740 $^O$C after 1000 $^O$C soaking. It was about 180 Hv when rolled at 800 to 1000 $^O$C after soaking at 1100 $^O$C.

## 3.2. Optical Microscopy

The composite micrographs showing ferrite-pearlite in the planer, longitudinal and transverse sections of the steel rolled at 900 $^{O}$C after soaking at 1000 $^{O}$C is given in Figure 4. The microstructures at 800 and 740 $^{O}$C are also ferrite and pearlite but finer. Figures 5, 6, and 7 show the microstructures at 1000, 900 and 800 $^{O}$C rolling temperatures respectively after soaking at 1100 $^{O}$C. These figures clearly indicate that the microstructures consist of a sizable amount of granular bainite in addition to ferrite and pearlite in steel samples rolled after soaking at 1100 $^{O}$C. The ferrite grains, found in the range of 5-9 μm, were finer at higher deformation and lower rolling temperature as shown in Figure 8.

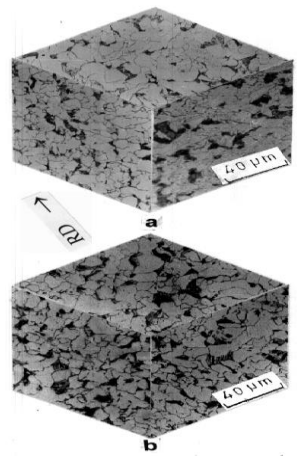


Figure 4. Composite micrographs of steel 1 soaked at 1000$^{0}$C, rolled at 900$^{0}$C and deforrmed (a) 25% (b) 50%.

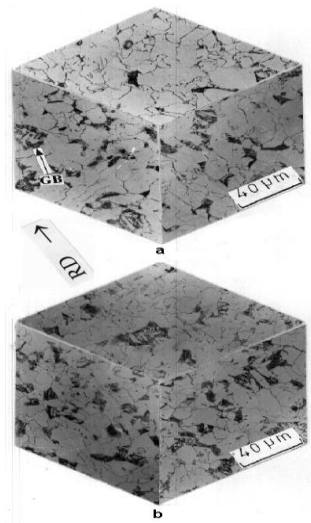


Figure 5. Composite micrographs of steel 1 soaked at 1100$^{0}$C, rolled at 1000$^{0}$C and deformed (a) 25% (b) 50%.

### 3.3. Transmission Electron Microscopy

The TEM micrographs after 1000 $^{O}$C soaking and 50% deformation show ferrite and pearlite at 740 – 900 $^{O}$C rolling temperatures. Figure 9 a shows ferrite-pearlite at 740 $^{O}$C. However the dislocation density in ferrite at lower rolling temperatures (800 – 740 $^{O}$C) is higher as shown at 740 $^{O}$C in Figure 9 b. The TEM micrographs of steel soaked at 1100 $^{O}$C and rolled 50% at 1000, 900 and 800 $^{O}$C are shown in Figures 10, 11 and 12 respectively. Figure 10 shows fine fibrous carbides as in bainite (Figure 10 a) coexisting with M/A constituent (dark area in Figure10 b) and ferrite of relatively low dislocation density (10 c). Figure 11 reveals long fibrous carbides (Figure 11 a), ferrite with high dislocation density (Figure 11 b) and dark M/A constituent (Figure 11 c). Figure 12 shows pearlite (Figure 12 a), ferrite with high dislocation density and martensite-austenite (M/A) constituent (Figure 12 b), ferrite containing extremely fine Nb (C,N) particles of about 100 Å size (Figure 12 c).

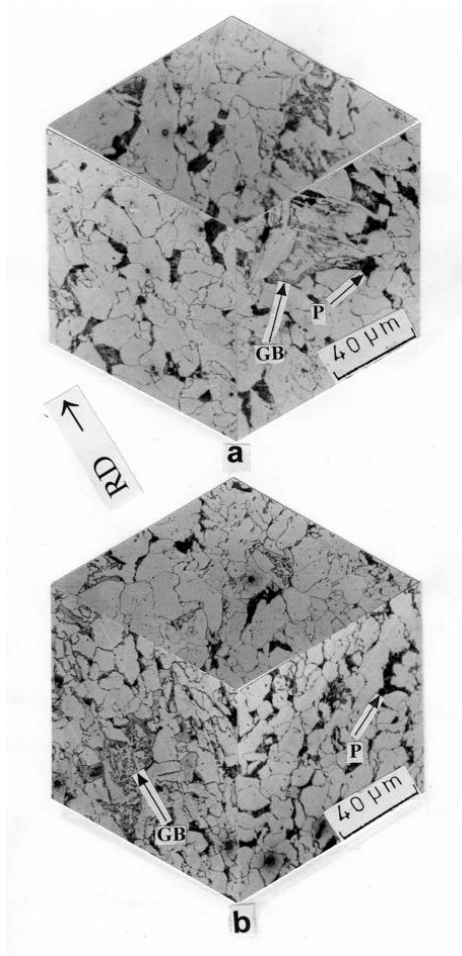


Figure 6. Composite micrographs of steel 1 soaked at 1100$^{0}$C, rolled at 900$^{0}$C and deformed (a) 25% (b) 50%.

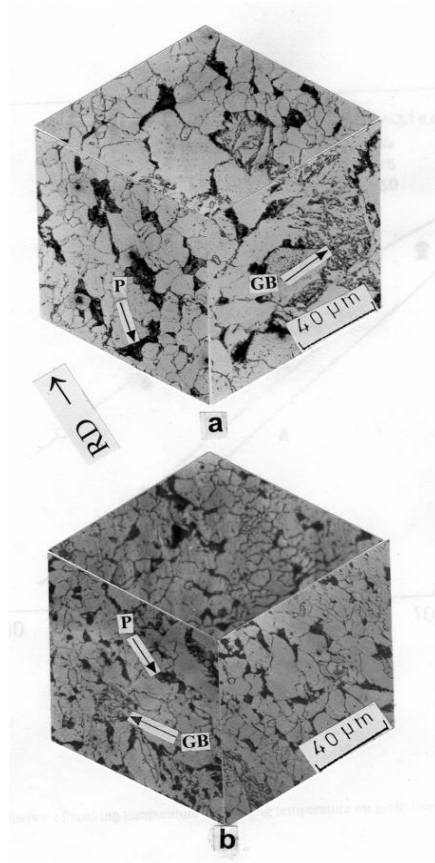


Figure 7. Composite micrographs of steel 1 soaked at $1100^0$C, rolled at $800^0$C and deformed (a) 25% (b) 50%.

## 4. DISCUSSION

The microstructure of conventional Cor- Ten A grade of steel is ferrite-pearlite with YS: 345 MPa and UTS: 480 MPa. The present weather resistant steel 1 which is very similar to Cor-Ten A with lower P (0.05% instead of 0.1%), has been additionally alloyed with 0.024% Nb. Controlled rolling of this steel has resulted in a fine grained microstructure consisting of ferrite with high dislocation density, pearlite and additionally martensite/austenite (M/A) constituent which has improved the yield strength and tensile strength as high as 460 and 580 MPa respectively even when P, which is one of the highest solid solution strengthening element, is reduced.

When YS and UTS of steel 1 are compared with that of steel 2 (Table 1) which is very similar to Cor-Ten A with higher Mn (0.88% instead of 0.45% max), they are far superior. The YS and UTS achieved in steel 2 [16] are 345-425 MPa and about 435 MPa respectively. The marked difference in the strength level may be attributed to the major change in microstructure. The microstructure of Nb bearing weather resistant steel 1 consists of ferrite, pearlite and granular bainite particularly at 1100 $^O$C soaking temperature as shown in optical micrographs (Figures 5, 6 and 7) and TEM micrographs (Figures 10, 11 and 12). On the other

hand, Mn rich weather resistant steel 2, has got ferrite-pearlite microstructure after soaking at 1000 $^{O}$C and subsequent rolling (Figures 13, 14 a). The ferrite is non-polygonal and has got higher dislocation density, which is the characteristic of acicular ferrite, at lower rolling temperature as shown in Figure 14 b.

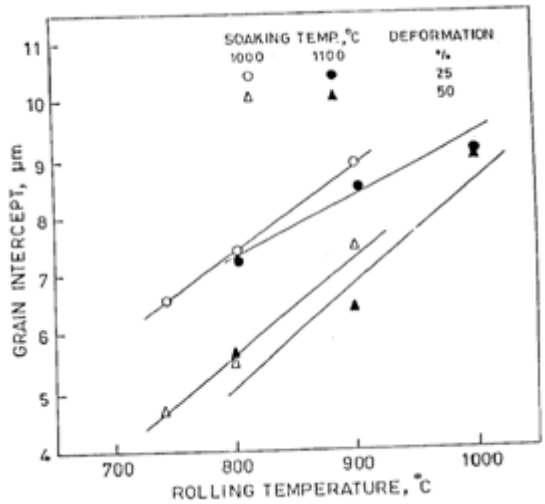


Figure 8. Influence of soaking temperature and rolling temperature on grain intercept of steel 1.

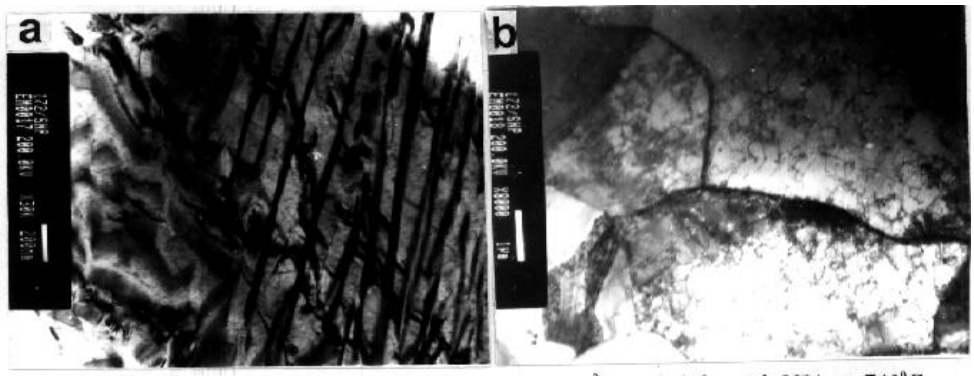


Figure 9. TEM micrographs of steel 1 soaked at 1000$^{0}$C and deformed 50% at 740$^{0}$C showing (a) ferrite-pearlite (b) non-polygonal ferrite with higher dislocation density.

The increase in YS of steel 1 (Nb bearing) on 25% deformation in the case of 1100 $^{O}$C soaking temperature over that of 1000 $^{O}$C soaking temperature may be attributed to the higher solubility of Nb at 1100 $^{O}$C. The following two equations [17] (1) and (2) are commonly used to determine the austenitisation temperature for complete dissolution of Nb.

$$\text{Log (Nb) (C)} = 2.96 - 7510/T \quad (1)$$

$$\text{Log (Nb) (C)}^{0.83}\text{ (N)}^{0.14} = 4.46 - 9800/T \quad (2)$$

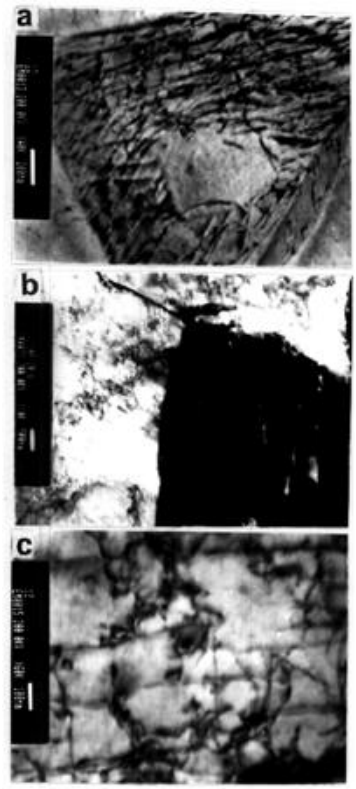


Figure 10. TEM micrographs of steel 1 soaked at $1100^0$C and deformed 50% at $1000^0$C showing (a) fine fibrous carbides (b) ferrite of relatively low dislocation density co-existing with M/A constituent (c) ferrite with low dislocation density.

Equation (2) also takes into account the % of nitrogen in steel. Using equations (1) and (2) the calculated austenitisation temperatures for complete solubility of Nb (0.024%) in the steel are 1083 and 1093 $^O$C respectively. Therefore, the Nb present (0.024%) is completely dissolved in austenite at 1100 $^O$C. Microalloying elements such as Nb and V increase the hardenability of austenite if they are in solid solution [18, 19]. The segregation of microalloying elements at the austenite grain boundaries decreases the nucleation and growth of austenite transformation products [20-23]. The grain boundary segregation by Nb and V reduces the surface energy of the austenite grain boundary that results in decrease in its effectiveness as a nucleation site. This behaviour is very similar to the boron effect [23, 24]. Thus, the increase in the soaking temperature causes formation of more bainite (Figures 5-7) which results in higher strength and lower tensile ductility in both deformed and undeformed samples. This is confirmed from the optical and TEM studies wherein granular bainite comprising highly dislocated ferrite with the dark M/A constituent is seen along with ferrite and pearlite in all samples soaked at 1100 $^O$C. The bainitic structure is only seen in the sample rolled (25%) at 740 $^O$C after soaking at 1000 $^O$C prior to rolling. The bainitic transformation at this lower temperature is attributed to the enrichment of alloy content in the remaining austenite due to rejection from the transformed ferrite leading to increase in bainitic hardenability.

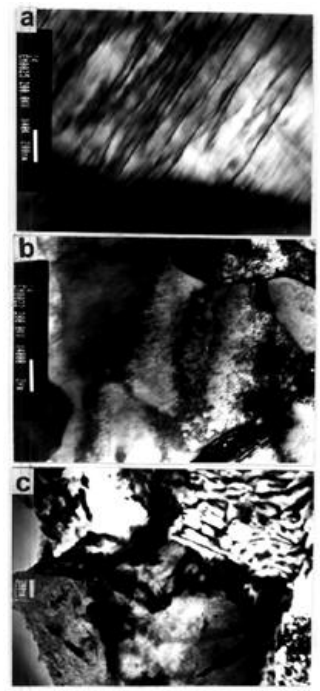


Figure 11. TEM micrographs of steel 1 soaked at $1100^0$C and deformed 50% at $900^0$C showing (a) long fibrous carbides (b) ferrite with high dislocation density (c) dark M/A constituent.

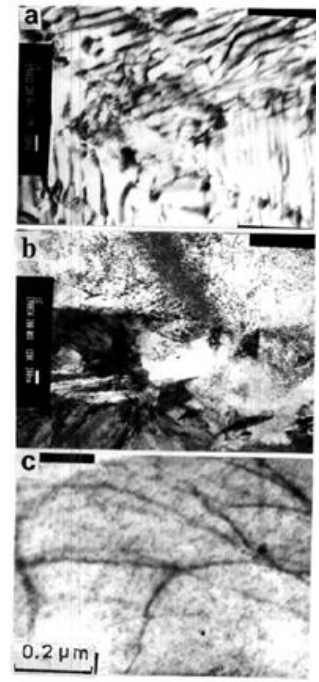


Figure 12. TEM micrographs of steel 1 soaked at $1100^0$C and deformed 50% at $800^0$C showing (a) pearlite (b) ferrite with high dislocation density and M/A constituent (c) ferrite containing extremely fine Nb (C,N) particles of about 100Å size.

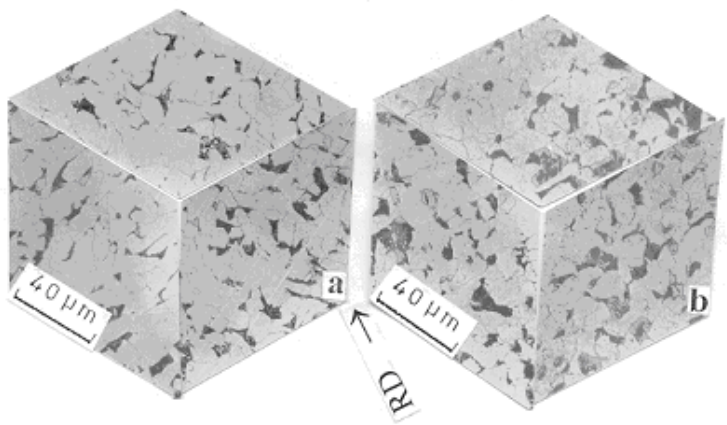


Figure 13. Composite micrographs of steel 2 austenitised at 900 $^{0}$C and deformed (a) 25% (b) 50%.

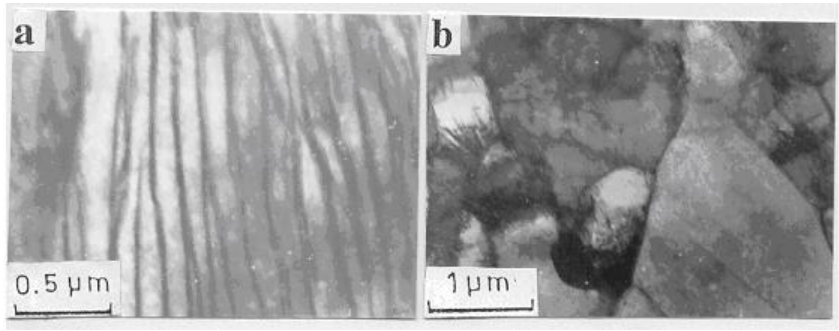


Figure 14. TEM micrographs of steel 2 deformed 50% at 800 $^{0}$C showing (a) pearlite (b) non-polygonal ferrite with high dislocation density.

The results of a similar study [25] on thermomechanical treatment of Nb and V bearing Cor-Ten B type weather resistant steel 3 (Table 1) are shown in Figure 15. After 50 % deformation, the YS varied markedly with soaking temperature as well as rolling temperature (increased from 440 to 575 MPa as temperature decreased from 900 to 700 $^{O}$C for 1000 $^{O}$C soaking temperature and from 520 to 565 MPa for 1100 $^{O}$C soaking temperature). The UTS after rolling at 800 $^{O}$C was nearly the same (~ 625 MPa) as that of 900 $^{O}$C and it was much lower than that for 700 $^{O}$C rolling (690 MPa) for steel soaked at 1000 $^{O}$C. It remained at about 875 MPa irrespective of rolling temperature for 1100 $^{O}$C soaking. The % elongation increased slightly on increasing the rolling temperature from 700 to 900 $^{O}$C.

Thus UTS of steel 1 (Nb bearing) is substantially lower than that of steel 3 (Nb+V bearing) after soaking at 1100 $^{O}$C and deformed 50%. The microstructure of steel 3 consists of ferrite- bainite with a small amount of pearlite at 900 $^{O}$C and 800 $^{O}$C rolling temperatures (Figures 16 a and b) and ferrite-bainite dual phase microstructure at 700 $^{O}$C rolling temperature (Figure 16 c). Higher bainitic hardenability due to higher carbon and more Nb in steel 3 (Table 1)) has resulted in bainite-ferrite dual phase microstructure. Figure 17 a shows a typical TEM micrograph consisting of ferrite and martensite/austenite constituent (granular

bainite) after 1100 $^{O}$C soaking and rolling 50% at 900 $^{O}$C. Such microstructure has contributed a lot for so high UTS (875 MPa) in steel 3. Additionally more precipitaes of fine Nb, V (C, N), which are shown in Figure17 (b, c, d, e and f), also significantly contribute to such a high level of UTS of steel 3. Figs 17 b and c are bright field and dark field micrographs showing very fine Nb, V (C, N) particles. These are identified by the rings in selected area diffraction pattern of Figure 17 d with its sketch in Figure 17 e and EDX in Fig 17 f showing Nb and V in fine precipitates.

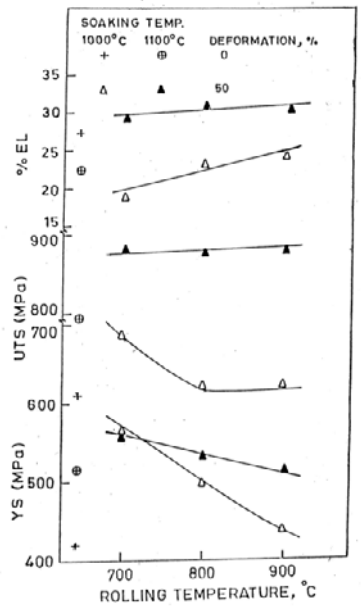


Figure 15. Influence of rolling temperatures on the tensile properties of steel 3.

The increase in yield strength with the decrease of rolling temperature for both the soaking temperatures of steels 1 and 3 is expected because of the finer ferrite grain size at lower temperature of rolling. The UTS is relatively insensitive to grain refinement. Therefore, rolling temperature has no significant effect on the UTS for both the soaking temperatures.

The substantial increase in yield strength of steel 1 due to higher deformation in the range of 800-900 $^{O}$C (Figures 1 and 3) may be attributed to the grain refinement during deformation in the non-recrystallised temperature region of austenite processing as the $Ar_3$ of this steel is calculated to be 763 $^{O}$C (using a relationship for $Ar_3$ with the chemical composition and thickness of the sample given by Ouchi et al [26]. Having soaked at 1000 $^{O}$C with 0.024% Nb, rolling at 800-900 $^{O}$C (in 0.1% C steel) is expected to be in the non-recrystallised temperature region [27] that causes elongation (pancaking) of $\gamma$ grains in the rolling direction [28, 29]. This results in grain refinement in Nb containing steels finish rolled with heavy reduction upto about 900 oC [30-32]. The increase in yield strength (about 100 MPa) because of 25% increase in reduction at 800-900 oC can only be partially attributed to the decrease in grain size (about 1.5 μm) as this enhances the YS by about 30 MPa only as per the Hall-Petch curve of Nb bearing C-Mn steel [33]. The additional strengthening (about 70 MPa) results

from high dislocation density observed in ferrite [34] and also from strain induced fine precipitates of Nb(C,N) as about 0.01 % Nb is in solution [30] at 1000 oC soaking temperature.

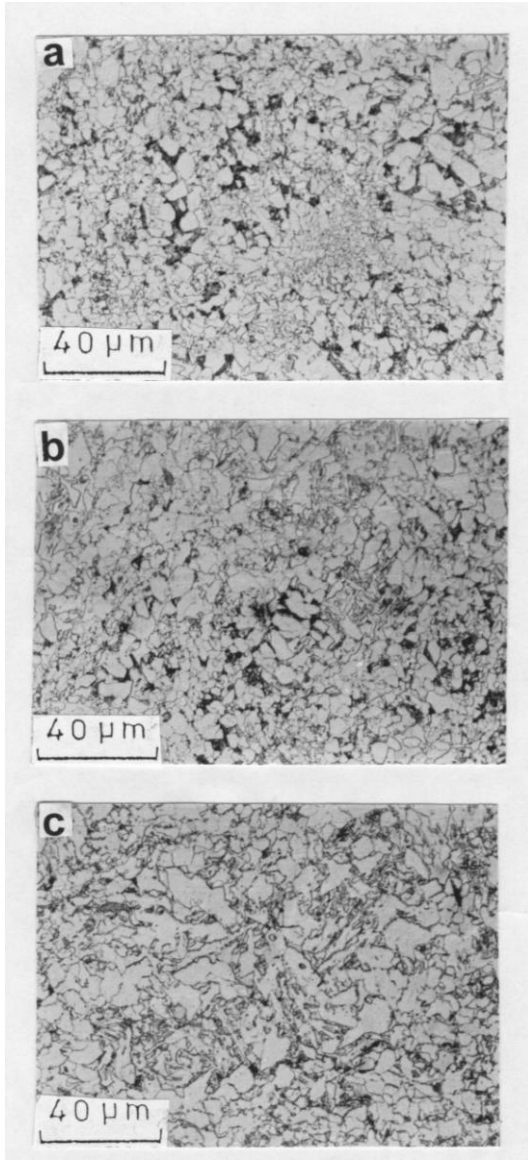


Figure 16. Optical micrographs of steel 3 soaked at 1100 $^0$C, rolled 50% at (a) 900 $^0$C (b) 800 $^0$C (c) 700 $^0$C showing granular bainite.

Rolling of steel 1 at 740 $^o$C is in the intercritical region as the $A_{C_1}$ temperature for this steel, using Andrews [35] relationship, is 722 $^o$C. Deformation in the intercritical region results in the formation of equiaxed $\alpha$ grains (formed from deformed austenite) as well as distorted grains of ferrite due to deformation. The strengthening in this case is not only because of ferrite grain refinement but also by the deformation of proeutectoid ferrite. This has resulted in about 70 MPa increase in YS due to higher deformation.

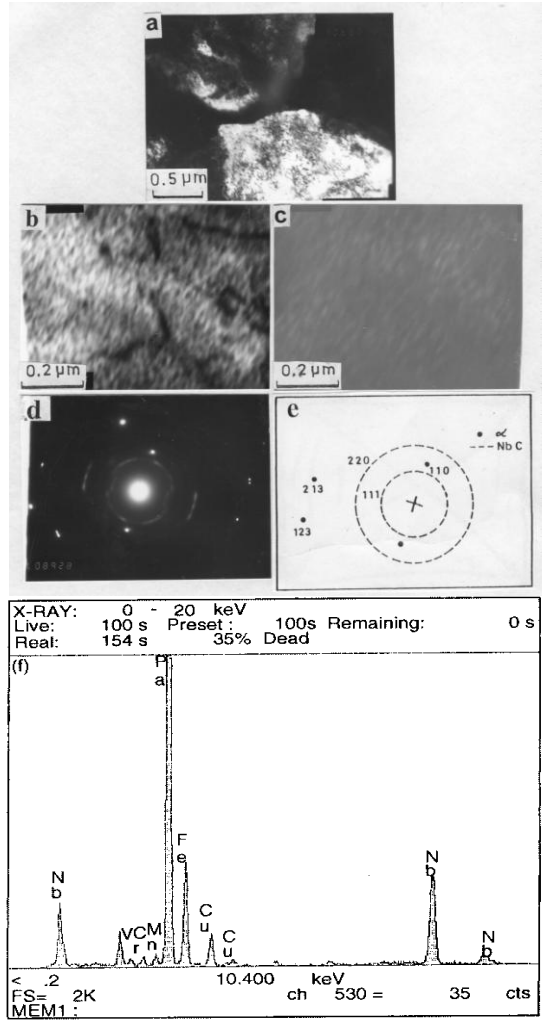


Figure 17. TEM micrographs of steel 3 soaked at 1100 $^0$C, rolled 50% at 900 $^0$C showing (a) ferrite and M/A constituent (b) Nb, V (C, N) precipitates, bright field (c) Nb, V (C, N) precipitates, dark field (d) NbC rings (e) schematic (f) EDX showing Nb and V in the fine precipitate.

Interestingly, the reported [36] yield strength of steel 1, air cooled (no deformation) from 1100 $^O$C austenitizing temperature, is more than that of all the deformed samples except the one deformed 50% at 800 $^0$C (Figure 3). This is attributed to the higher amount of granular bainite comprising acicular ferrite and M/A constituent and pearlite almost nil in the air cooled steel [36]. The formation of granular bainite is expected to be suppressed in the control rolled steel as it was air cooled from the much lower temperature of rolling that increases ferrite nucleation sites and decreases bainitic hardenability. These results thus show that TMT has no beneficial effect at higher temperatures and lower deformations of rolling of steel 1. However, since the magnitude of the YS and UTS are higher after 1100 $^0$C soaking, due to higher amount of granular bainite (Figures 5-7, 10-12) and strain induced fine Nb(C, N) precipitates (Figure 12 c), for a given rolling temperature and deformation, it (1100 $^O$C) is preferred to the lower soaking temperature. At higher soaking temperature, higher amount of

Nb is in solution which precipitates as fine Nb(C,N) leading to higher strengthening. In our earlier work [36] on this steel also, TEM micrographs (dark field, bright field and SAD) showed fine Nb(C,N) precipitates when the steel was air cooled from relatively higher soaking temperatures. It thus is clear that higher temperature of soaking, higher deformations (≥ 50%) and lower temperatures of rolling (~800 $^0$C) are to be recommended for superior mechanical properties of control rolled Nb bearing weather resistant steels.

In the case of steel 3, the YS and UTS of rolled samples are higher than that of air cooled (no deformatiom) sample. As more amount of microalloying additions at higher soaking temperature (1100 $^0$C) increase the non-recrystallisation temperature [38], rolling at 900 and 800 $^0$C is in the non-recrystallised region which produces finer microstructure as shown in Figures 16 a and 16 b respectively. Thus, the remarkable increase in the strength of steel 3 after 50% deformation is due to combined effect of harder M/A constituent, grain refinement and precipitation strengthening by Nb and V.

## CONCLUSION

The following conclusions may be drawn based on the results discussed in this chapter.

1) Increase in soaking temperature from 1000 to 1100 $^0$C has increased the YS, UTS and hardness of the rolled microalloyed weather resistant steels 1 and 3 at a given rolling temperature and deformation due to dissolution of Nb(C, N) in the austenite which results in replacement of a part of pearlite into granular bainite. Increasing deformation has increased the YS but not UTS markedly.
2) For 1100 $^0$C soaking of steel 1, rolling 25% results in much lower YS than that of undeformed aircooled sample. The YS is also lowered due to 50% reduction at 1000$^0$C. The inferior YS due to controlled rolling, though surprising, is attributed to a lower amount of granular bainite.
3) The optical microstructure after 1000 $^0$C soaking of all the steels is ferrite-pearlite at 900 and 800 $^o$C rolling temperatures where as in addition to ferrite-pearlite, acicular ferrite/granular bainite is also observed after rolling of steel 1 at 740 $^o$C and steel 3 at 700 $^0$C. After soaking at 1100 $^o$C, considerable amount of granular bainite has formed at all the rolling temperatures of steel 1 and 3. The TEM micrographs show ferrite and pearlite at 800 and 900 $^0$C rolling temperatures and non-polygonal ferrite with high dislocation density, which is the characteristic of acicular ferrite, also at 740 $^0$C rolling of steel 1 and at 700 $^0$C rolling of steel 3 after 1000 $^0$C soaking. Steel 2 also shows high dislocation density ferrite at 800 $^0$C rolling temperature. On the other hand, presence of considerable amount of ferrite/acicular ferrite and martensite – austenite (M/A) constituent is taken as an indication of granular bainite in addition to pearlite after soaking at 1100 $^0$C and rolling of steels 1 and 3 at 1000 – 800 $^0$C.
4) For controlled rolling to be effective, higher soaking temperature (≥1100 $^0$C), lower rolling temperatures (~800 $^0$C) and higher rolling reduction (≥50%) are recommended to take maximum advantage of the Nb and Nb+V microalloying additions.

## REFERENCES


[1] Katsumata, M et al. Katsumata et al, (1991), *Kobelco Technology Review*, 11, 29-32.

[2] George Eldis, T., and William C. (1997), Hagel, Hardenability Concepts with Application to Steel, Eds. Doane, D. V. and J.S.Kirkaldy, J. S.*Proceedings of a symposium held at Sheratonchicago Hotel*, 29-27 Oct., 397.

[3] Cizek, P., Wynne, B. P., C. H. J. Dvies, C. H. J. and Muddle, B. C.,(2002) P. D. Hodgson: *Metall. Mater. Trans. A*, 33A, 1331-1349.

[4] Sarma, D. S.and F. H., F. H. (1981) Solid-Solid phase Transformation, Eds Aaronson, E. Langhlin, H. I. D. E., Sekerka, R. F., Wayman, C. M. AIME, Pittsburgh, U.S.A, 1035.

[5] George, T. and Irani, J. J., (1968), *Australian Inst. Metals*, 13, 93.

[6] Takahashi, A. and Iino, M., (1996) *ISIJ Intern*., 36, 341.

[7] Takahashi A., and M.Iino, M. (1996), *ISIJ Intern*., 36, 235.

[8] Mangonon, P. L. Jr and Heitmann, W. E., (1977) Microalloying 75, Union carbide Corp., p 73.

[9] Kilworth, S. R. and Wannell, P. H., (1980) Hot Working and Forming Processes, Eds. Sellars C. M. and Davies, G. J., (1980), The Metals socirty, London, 113.

[10] Pickering, F. B., (1978) Hardenability Concepts with Application to Steels Eds. Doane D. V. and Kirkaldy, J. S. AIME, Warrendale.

[11] Bucher J. H. and Grozier, J. D., (1965), *Met. Eng. Quart*., ASM, 1.

[12] Lapointe, A. J., Ph.D. Thesis, (1975), University of Strathclyde.

[13] Pickering, F. B. Microalloying 75, (1977), Ed. M.Korchynsky, Union Carbide Corporation, New York, 9.

[14] Baker, T. N., (1978), Scientific Progress, Blackwell Scientific Publication, Oxford, 65, 493.

[15] Pickering, F. B., (1978), Physical Metallurgy and the Design of Steels, Applied Science Publishers Ltd., Essex, England, 65.

[16] Prasad, S. N. and Sarma, D. S., [2007), *Materials Science Research Journal*, Nova Science Publishers, NY, 7-19.

[17] Palmiere, E. J., (1995), Proceedings of the International conference "Microalloying 95" Iron and Steel Society, Inc. Pittsburg, PA, USA, June 11-14, 307-320.

[18] Isaac, C. Garcia, (1995), Procceedings of the International conference, "Microalloying 95", Iron and Steel Society, Inc. Pittsburgh, PA, USA, 365-375.

[19] Majta, J. et al, (2002), *Metrllurgical and Materials Transactions A*, 33 A, 1509.

[20] Fossaert, C., Rees, G., Maurickx, T., and Bhadeshia, H. K. D. H., (1995) *Metallurgical Transactions A*, 26 A, 21-30.

[21] Adrian, H., (1990), Microalloyed Vanadium Steels, Proceedings of the International Symposium, eds. Karchynski, M., Gorezyca S. and Blicharski, M., Cracon, Poland, 209-226.

[22] Garbarz, B.and Pickering, F. B., (1988), *Mat. Sci. and Tech*. 4, 967-970.

[23] DeArdo, A. J. Gray, J. M. and Meyer, I., (1984), The Metallurgical Society of AIME, 685-759.

[24] Pickering, F. B., (1967), Proceedings Transformation and Hardenability in steels, Climax Molybdenum Company, Ann Arbor, MI, 109-129.

[25] Prasad, S. N. and Sarma, D. S., (2005), *Materials Science and Engineering A*, 399, 161-172.
[26] Ouchi, C., Sampet, T. and Kazasu, L., (1982), *Trans. Iron Steel Inst. Japan*, 22, 1982,214.
[27] Tamura, I., Ouchi, C., Tanaka, T., and Sekine, H., (1988), Thermomechanical Processing of High Strength Low Alloy Steels, Butterworths, London, 80, 147.
[28] Sekine, H. and Maruyana. T., (1972), Tetsu-to-Hagne, Vol. 58, 1424, (1976), Trans. *Iron and Steel Inst. Japan*, 6, p 427.
[29] Kozasu, I., Shimizu, T., (1971), *Trans. Iron and Steel Inst. Japan*, 11, 359.
[30] Palmiere, E. J. (1991), Ph.D.Thesis, University of Pittsburgh.
[31] Noren, T. M., (1964), *Ship Structure Committee special Report* No.SSC-154, PB 181539.
[32] Duckworth, W. E. (1964), *Iron and Steel*, l 37, 385.
[33] Lebon, A. B. and de Saint-Martin, L. N., (1977), Microalloying 75, Ed. M.Korchynsky et al, Union Carbide Corporation, 90.
[34] Prasad, S. N. and Sarma, D. S., (2005), *Materials Science and Engineering A*, 408, 53-63.
[35] Andrews, L. W., (1965), *JISI*, 203, 721.
[36] Prasad, S. N., Mediratta, S. R. and Sarma, D. S., (2003), *Materials Science and Engineering A*, 358, 288-297.

## LIST OF ABBREVIATIONS

| | |
|---|---|
| M/A | Martensite/Austenite Constituent |
| YS | Yield Strength |
| UTS | Ultimate Tensile Strength |
| Hv | Vicker Hardness Number |
| μm | Micrometer |
| TEM | Transmission Electron Microscopy |
| Nb (C,N) | Niobium Carbonitride |
| α | Ferrite |
| SAD | Selected Area Diffraction |
| P | Pearlite |
| GB | Granular Bainite |
| RD | Rolling Direction |

In: Advances in Mechanical Engineering Research. Volume 2 ISBN: 978-1-61761-984-7
Editor: David E. Malach 

*Chapter 10*

# PERFORMANCE OF MASONRY STOVES IN MINOR EARTHQUAKES: EXPERIENCE FROM SCANDINAVIA

***Päivi Mäntyniemi****

Institute of Seismology, Department of Geosciences and Geography,
University of Helsinki,
P.O. Box 68, FI-00014 Helsinki, Finland

## ABSTRACT

Consequences of minor earthquakes on masonry stone stoves in Scandinavia (Northern Europe) are reviewed. Emphasis is laid on the earthquakes of June 23, 1882 and November 4, 1898 in the vicinity of the Bay of Bothnia. Cracked stoves posed an indirect earthquake hazard through increasing the proneness to fires. Fire prevention measures were therefore necessary also after minor earthquakes.

## 1. INTRODUCTION

Scandinavia (Northern Europe) appears almost aseismic on global seismicity maps, but earthquakes with felt effects occur there from time to time. The absence of severe destruction resulting from earthquakes over the centuries can be attributed to the low level of intraplate seismicity. The sparse and uneven distribution of population and building stock dominated by wooden structures also make the region less prone to earthquake effects. Unknown or lost documents may also be one reason for the paucity of information about earthquake-induced damage, or such incidents may have sunk into oblivion, because they were neither investigated nor documented in any way. Literacy remained rare in northern Scandinavia until the early 1900s. This contribution reviews what is known about earthquake effects on masonry parts of buildings in Scandinavia (Figure 1). Emphasis is laid on the late 1800s and

* Email: paivi.mantyniemi@helsinki.fi,
Phone: +358 9 191 51624, fax: +358 9 191 51598

the northern part of the region, especially the Bay of Bothnia bounded by Finland to the east and Sweden to the west.

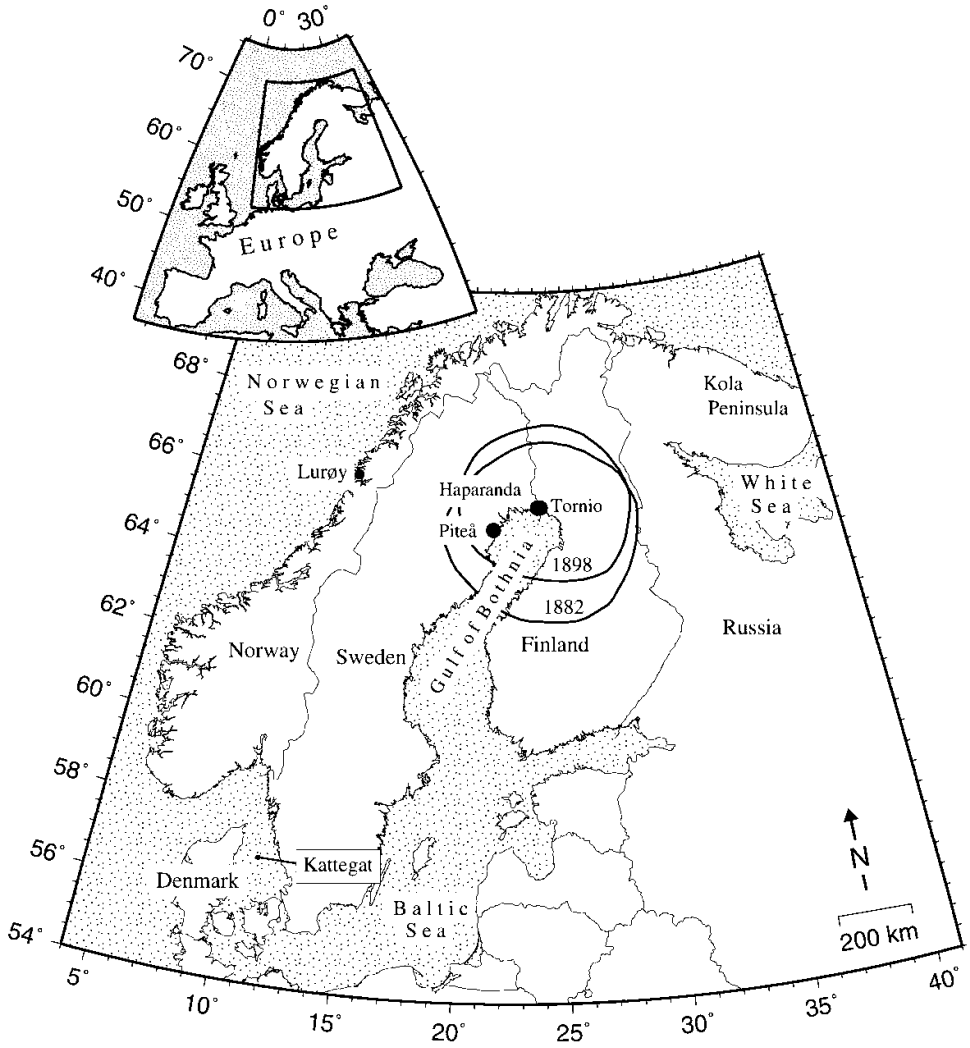


Figure 1. The region of interest withcurrent state borders. Filled circles denote places mentioned in the text. Kattegat is a strait between Denmark and Sweden. Solid lines outline the areas of perceptibility of the earthquakes of June 23, 1882 and November 4, 1898 (UTC).

## 2. BUILDING STOCK: WOOD AND STONE

Building materials were traditionally collected close to the building site. Scandinavia was rich in forests, and houses were built of one material over the centuries. All layers of a traditional wall were of wood: the outer boarding, bark, timber, boards, frame, sawdust, and paper. Similar materials were also used as roofing. For instance,the most common roof type was shingle (76.7%), and the rest were of straw or turf (10.5%), pulp or roofing felt (8.9%),

or planks, boards or laths (4.1%)in the countryside not far from Tornio (Figure 1) in 1900 (ASF, Governor's reports, Table no. 2).In northern Scandinavia, it was not uncommon that all buildings were wooden, or that houses built of stone constituted a tiny fraction of the building stock. Only 2 of 507 houses were made of stone in the vicinity of Tornio in 1900. The general impression of the building stock was rural and shallow, except for church steeples and belfries. The plans of the houses were predominantly rectangular with relatively few details(Figure 2).Uniform built-up environment and more prominent buildings with architecturally interesting details could be found mainly in towns.Churches, castles, public buildings, sometimes dwellings, warehouses, and walls were built of coarseor roughly hewn stones and tiles more often in southern Scandinavia. Industrial materials began to replace the traditional ones in the 1900s.

Figure 2. The street of Rantakatu in Tornio, Finland. The houses were built in the late 1700s and early 1800s. Construction of two-storey houses began around 1770. Photo: Päivi Mäntyniemi, March 2010.

Wooden houses had masonry stone parts such as chimney stacks, fireplaces, ovens, and stoves. They were either tile or natural stone structures with the outer and inner plastering and mortar of stone material. The oldest tiles were home-made and easily breakable. Dwellings were constructed directly on the ground in Tornio during the 17$^{th}$ century; only public buildings were built on stone foundations (Ylimaunu, 2007). Stone cellars could be found mainly in a few of the richer shopkeepers' houses. During the following century, dwellings began to be placed on low stone foundations, the height of which gradually grew.

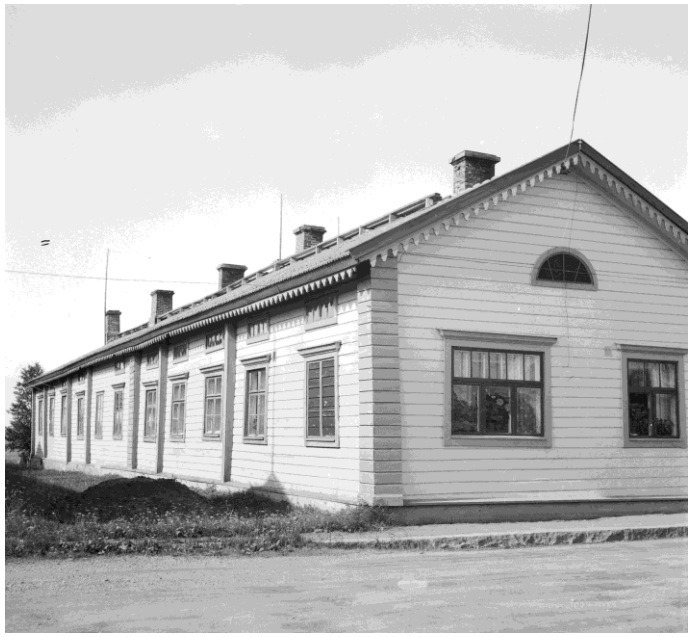

**(A)**

Source: National Board of Antiquities, Finland.

Figure 3a. Inhabited rooms needed heating in cold weather conditions. Examples from the town of Tornio, Finland. a) The Åström's house, a building at the southern end of the site. Photo: Carl Jacob Gardberg, summer 1952.

**(B)**

Source: National Board of Antiquities, Finland.

Figure 3b) The street of Keskikatu, house no. 27 from the back side. Photo: Carl Jacob Gardberg, summer 1952.

Heating was necessary in cold weather conditions, so basically the number of inhabited rooms could be approximated by the chimney stacks (Figure 3). Stoves also functioned as discharge flues. Kitchen stoves served for both cooking and heating. They were sometimes rather massive in proportion to the room size. Slender vertical stoves reaching the ceiling began to be built in other rooms, especially in larger houses, in the 1700s. Later technical improvements made them more economic with firewood and capable of storing heat (Tunander, 1973). Some had a whitewashed surface, but most vertical stoves came with an outer layer of glazed tiles and other decorative elements (Figure 4).

Wooden buildings and towns were fire-prone. The easily inflammable materials used as roofing added significantly to initiating and spreading of fires. Many towns in the region havebeen ravaged by fires, some of them frequentlythroughout their existence. Therefore the lifetime of wooden buildings tended to be relatively short. Statutes for fire prevention measures since the 1700s gave orders about the necessary equipment for fighting fires, as well as fire drills, guard patrol, and fire inspections. The town administrative court was responsible for carrying out the orders. It employed an officer of the fire brigade on an annual salary, and this person reported directly to the mayor and the court (Fire statute for Tornio, 1888). The high priority of the issue has helped some related documents to survive in archives. Useful sources of information are for instance the minutes of court meetings.

**(A)**

Source: National Board of Antiquities, Finland.

Figure 4a. Example of a vertical stove in Tornio, Finland at the end of the 1800s. A stove in the Vikgren's house. Photo: Carl Jacob Gardberg, summer 1952.

**(B)**

Figure 4b. Example of a vertical stove in Tornio, Finland at the end of the 1800s. A tiled stove in the Åström's house. Photo: Päivi Mäntyniemi, March 2010.

# 3. Earthquake Effects in the Region

## 3.1. The earthquake of June 23, 1882

An earthquake occurred in northern Finland and Sweden on the morning of June 23, 1882 (Figure 1). According to existing catalogs the magnitude was slightly below 5. It did not come as a complete surprise at the bottom of the Bay of Bothnia (the northern end of the Gulf of Bothnia), because a lesser earthquake had been felt there eight days earlier. However, the two earthquakes marked the end of a long quiescence of seismicity in the area. A search for previous occurrences in Finland had to go as far back as 1777.

The number of places from where some damage was reported after the larger earthquake is the highest known in the area (Figure 5). The main source of information is the contemporary press that published letters from different places in the area of perceptibility. The damage was minor, such as tiles falling off the chimneys, plaster falling off the stone foundation, planks falling off the roof, cracked or partly broken stoves, and broken windowpanes. Ground shaking was very strong in Swedish Sangis and Finnish Tornio, where a few chimneys stacks were knocked down. According to the statute for fire prevention for Tornio on the Finnish-Swedish border(Figure 1), issued in 1872, two fire inspections had to be conducted in the town every year, in spring and in fall (TTA, ABCD:2). Although the main officer of the fire brigade, masons, and chimney sweeps were paid a regular salary, their duties did not include the fire inspections, so receipts of the extra cost had to be written for

the town account books. They show that the obligatory fire inspections were conducted in Tornio in June and September 1882 (TTA, EII:38). An additional fire inspection was carried out on July 18 and 19; the earthquake may have been the reason for it. Numerous repairs of masonry parts of public buildings were billed in 1882, but the documents contain no further information. The repairs may have to be attributed to regular maintenance work. Repairs of damage sustained by private dwellings are even more difficult to trace. It was reported from the vicinity of Kalix, Sweden that the number of fires increased there after the larger earthquake. This was attributed to the failures in stoves and chimneys during the ground shaking that made them more prone to fires than usual (*Haparandabladet* July 15, 1882). It was reported that a brand-new house in Bondersbyn was fully destroyed in this way, the owner suffered burns in the face and hands, and had no fire insurance (*Norrbottenskuriren* July 4, 1882).

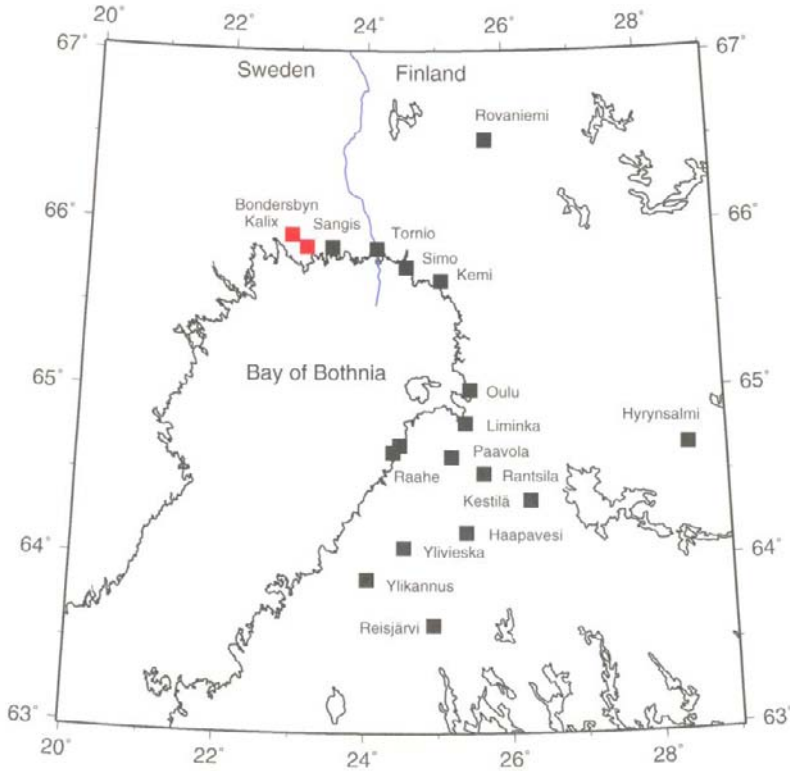


Figure 5. Squares denote places from where some damage was reported after the earthquake of June 23, 1882. Red squares show where the number of fires increased after the earthquake.

## 3.2.The Earthquake of November 4, 1898 (UTC)

Earth tremor was felt widely in northern Finland and Sweden soon after midnight on November 5, 1898 (Nov 4, 1898 UTC). The event together with the one 16 years earlier has the largest area of perceptibility in the northern part of the region (Figure 1). The magnitude was inferred to be in the range from 4,4 to 4,7 (Mäntyniemi, 2008). The number of places

from where some damage to masonry stoves was reported was smaller than in 1882, and the places were located mainly along the southern part of the state border between the two countries.

Extra fire inspections were conducted after the earthquake in at least three towns along the coast of the Gulf of Bothnia. According to press reports, earth shaking was strong in Piteå in Sweden (Figure 1), and the town administrative court ordered an extra fire inspection to be carried out there. The same was recommended for the surrounding countryside (*Norrbottenskuriren* Nov 5, 1898; *Norrbottensposten* Nov 14, 1898). The inspection in the town revealed that a number of chimneys and ovens had been cracked and fractured. Some of the failures were considered severe enough to pose a threat to heating. The house owners were urged to repair the damage as soon as possible (*Norrbottens Allehanda* Nov 16, 1898).

In Finnish Tornio, two fire inspections were obligatory annually also according to the Fire statute for Tornio (1888). In 1898, the obligatory fire inspections had been conducted on June 2-4 and from September 29 to October 1. The spring inspection gave cause for 27 admonitions to house owners (OPA, BI:53). They did not only concern stoves, but also the general tidiness of houses such as repairing a fence and the roof of a porch. Only a few admonitions were given after the fire inspection in fall.

After the earthquake the town administration ordered an extra fire inspection to be conducted. It was carried out on November 21-23, 1898. The surveyors were Erland Johansson, August Lehto and Karl Rönnbäck (TTA, EII:52). The findings were given as 34 damages in masonry stone components of houses (*Hufvudstadsbladet* Nov 28, 1898). The damage consisted mainly of severe cracks and fractures in the smoke flues. One tiled stove had totally become separated from the chimney. The damage had most often occurred close to the ceilings or in the ovens.

Chimneys had to be swept each month as part of the obligatory fire prevention measures, and the chimney sweeps had be given a book of fireplaces, ovens, and chimneys in the town (TTA, EII:d2). The total number of chimneys (293) can be counted with the help of this document and, consequently, the proportion of damaged stoves is known (about 11 %). The town administrative court forbade the use of the damaged stoves until repaired under penalty of a fine of 20 marks. For comparison, townspeople who did not show up at a fire drill had to pay a fine of 1,50 marks and officers of the fire brigade 6 marks. On the basis of this information and other felt effects, Mäntyniemi (2007) assessed the seismic intensity in Tornio at I = 6 on the European Macroseismic Scale.

In Swedish Haparanda (Figure 1) the need for a fire inspection seems to have been realized after the extra fire inspection had been conducted in contiguous Tornio. The two towns are divided only by a narrow bay, and both had populations of 1400−1600 at the time of the earthquake. The findings were also of the same order of magnitude: it was reported that 30 chimneys had been ‘more or less’ damaged in Haparanda during the earthquake (*Haparandabladet* Nov 23, 1898; *Haaparannanlehti* Dec 8, 1898).

## 3.3. Other Earthquakes

The coastal areas of Norway in particular exhibit enhanced seismic activity in the region, and several historical earthquakes with damaging intensities have occurred there. A list can be found in Ambraseys (1985). Among those is the Lurøy earthquake of August 31, 1819

(Figure 1). It ruined also some wooden frame structures, which is a rare incident in the region. Rather ample information about damages to houses is available also for the Kattegat earthquake of December 22, 1759 (Figure 1). Muir Wood (1988) estimated the magnitudes of the Kattegat and Lurøy earthquakes to be in the ranges of $M_S$ 5,4 – 5,6 and 5,8 – 6,2, respectively.

## 4. COMMENTS

The most common type of earthquake-induced damage in Scandinavia is failure of masonry stone elements of houses, usually stoves and ovens. In addition, broken windowpanes have been reported from time to time. There are fewer cases of harmed wooden structures. Cracks and fractures in masonry stone structures and broken windows are very minor non-structural damage. Knocked-down chimneys are typical examples of minor damage, but they have been reported more rarely in the region. However,in many instances the available information is so sparse that the interpretation of the degree of damage may depend on one or two words. Such texts are usually treated with caution in order not to overestimate the seismic intensity, but it may be more appropriate to point out the uncertainty. Spots of higher intensity and interesting details have probably occurred although they were not properly documented. Also, it is often not possible to assess the proportion of houses that sustained damage. Using conventional intensity scales in the region means using the masonry stone parts rather than whole buildings to assess damage (Ambraseys, 1985), but on average the rarity of damaging intensities in the region appears to be in agreement with intensity scales and seismicity there.

Cracked stoves pose an indirect earthquake hazard, because sparks escaping through the cracks could set the wooden components of houses on fire. This was realized at the bottom of the Bay of Bothnia in the late 1800s. Fire prevention measures continued to be a task for authorities in the 1900s, when widely felt earthquakes were followed by an admonition to inspect stoves and flues in the affected area. The importance of the issue benefits the study of earthquake effects, because some related documents have survived in archives. It is possible that not all of them have been discovered so far.

## REFERENCES

### Archives

ASF: Archives of Statistics Finland: Governor’s reports for the province of Oulu, 1900, Table no. 2

PAO: Provincial Archives of Oulu, Oulu, Finland: Documents on Tornio; BI:53 Judgment books of the town administrative court 1895-1898

TTA: Tornio Town Archives, Tornio, Finland: ABCD:2 Miscellaneous 1680-1920, Fire statute for the town of Tornio, September 1872, manuscript in Swedish; EII:38 Finance office, Town accounts for 1882, Receipts of the fire inspections; EII: 52 Town accounts for 1898, Receipts of the fire inspections; EII: d2 Miscellaneous, A list of fireplaces,

ovens and chimneys to be swept in the town of Tornio in 1898; A list of chimneys to be swept in the town of Tornio in 1899.

## Newspapers

*Haparandabladet*July 15, 1882, no. 2, p. 3.
*Haparandabladet* November 23,1898 no. 93, p. 2.
*Haaparannanlehti* December 8, 1898 no. 96, p. 2.
*Hufvudstadsbladet* November28, 1898 no. 323, p. 3.
*Norrbottens Allehanda* November 16, 1898 no. 91A, p. 2.
*Norrbottenskuriren* July 4, 1882, no. 53, p. 2.
*Norrbottenskuriren* November 5, 1898no. 173, p. 2.
*Norrbottensposten* November 14, 1898 no. 90, p. 2.

## Printed Literature

Ambraseys, N.N., 1985. The seismicity of western Scandinavia. *Earthquake Eng. Struct. Dyn.*, 13, 361-399.

Fire statute for Tornio, 1888. Brand-Ordning för Torneå stad, Tornion kaupungin Palo-Asetus (Fire statute for the town of Tornio). Haparanda Boktryckeri Aktiebolags boktryckeri, 15 pp. (in Swedish and Finnish).

Mäntyniemi, P., 2007. Town of Tornio in November 1898: a rare survey of earthquake damage inFinland.*J. Seismology*, *11*, 177-185.

Mäntyniemi, P., 2008. The earthquake of 4 November 1898 in northern Europe: New insights. Journal of Geophysical Research, 113, B11303,doi:10.1029/2007JB005461

Muir Wood, R., 1988. The Scandinavian earthquakes of 22 December 1759 and 31 August 1819. *Disasters*, 12, 223-236.

Tunander, B. and I., 1973. Kakelugnar (Tiled stoves). ICA-förlaget AB, Västerås, (in Swedish).

Ylimaunu, T., 2007. Aittakylästä kaupungiksi – arkeologinen tutkimus Tornion kaupungistumisesta 18. vuosisadan loppuun mennessä (A village of storehouses grown to a town − an archaeological study of the town development of Tornio until the end of the 18$^{th}$ century). Societas Historica Finlandiae Septentrionalis, Rovaniemi, Tornion kirjapaino, (in Finnish).

## Websites

Information about buildings and building techniques (in Finnish): *www.rakennusperinto.fi*.

In: Advances in Mechanical Engineering Research. Volume 2 ISBN: 978-1-61761-984-7
Editor: David E. Malach 

*Chapter 11*

# REVERSE ENGINEERING FOR QUALITY CONTROL IN INNOVATIVE MANUFACTURING OF ARTIFICIAL TEETH

***Paolo Minetola*[*], *Eleonora Atzeni, and Alessandro Salmi***
Politecnico di Torino –DISPEA
Department of Production Systems and Business Economics, Torino, Italy

## ABSTRACT

The recent development of non-contact digitizing systems dedicated to dental applications has introduced innovative procedures, based on Reverse Engineering techniques, for the production of artificial teeth. Starting from the reconstructed 3D model of each tooth, first the mold CAD model is created and then the milling path is computed for machining. At the moment there is no indication of the quality of such innovative procedure, so it is investigated in this chapter by evaluating the deviation introduced by each manufacturing step. For this purpose, a new methodology for quality control, based on the use of Reverse Engineering contactless devices in inspection activities, is proposedand applied to a machined mold for the production of molars and premolars. The error of mold machining is computed by comparing the original mold CAD model with the scan data. Then some teeth, produced by the same mold, are selected as manufactured samples. The samples are digitized by means of two different non-contact scanners before and after finishing. Each sample is compared with its original CAD model to compute molding error. Scan data of such samples allow us to evaluate the deviations introduced by each operation. A comparison of two optical digitizers is based on the results of this study and economic considerations related to costs and times are also included.

[*] e-mail: paolo.minetola@polito.it, Politecnico di Torino, Department of Production Systems and Business Economics (DISPEA), Corso Duca degli Abruzzi 24 – 10129 Torino (Italy), Phone: +39 (011) 090.7210 – Fax: +39 (011) 090.7299

## 1. INTRODUCTION

In recent years, traditional procedures in dentistry have been facing a challenge through the application of Reverse Engineering (RE) techniques together with Computer Aided Design and Manufacturing (CAD/CAM), as reported by Wu *et al.* (2001). The geometry of the single tooth as well as the whole oral cavity can be digitized and transformed into a three-dimensional virtual model by a digitizing device. These devices are based on the projection of a laser or a white light over the scan object. At the same time one or more digital cameras capture an image of the light stripe or pattern that is deformed by the object surface. This technology is limited by the optical characteristics of the surface that has to be dry and opaque to assure a correct readability by the scanner. Due to the complexity of dental geometries, multiple scans are usually required from different viewpoints to digitize optical occlusions areas. Computer software is then used to merge together different scans using a matching function. The availability of a virtual model opens up new opportunities: it can be used to design customized dental devices. Moreover, after converting the CAD model into STL format, physical replicas can be fabricated by machining (a CAM software computes the milling path) or directly by Rapid Prototyping (RP) techniques. So far, RE techniques have been applied in dentistry to create three-dimensional images of soft and hard tissues of a dental patient (Virtual Dental Patients) from stone replicas, for clinical purposes (that means to aid dentists in diagnosis and treatment planning) and for maxillofacial and oral surgery, as well as for the fabrication of crowns (DeLong *et al*. 2003, Wu *et al*. 2001, Kournetas *et al*. 2004) dentures, and removable prosthodontics (Williams *et al*. 2004). 3D data from each patient provide information on teeth shapes and sizes, relationships between a tooth and adjacent teeth or occlusive ones.

A new interesting application in the dental field is related to the production of molds for acrylic teeth. In the traditional way, a set of artificial teeth is produced by means of an electro-deposited mold. Electro-deposition is a time consuming process and mold fabrication involves several steps wherein the skills of a master craftsman are required. The possibility to create a 3D model of a tooth from scan data of a hand-modeled one opens up a new way to produce a teeth mold in a short time containing costs. In the innovative procedure RE and CAD/CAM are integrated.

## 2. FROM THE TRADITIONAL ACRYLIC TEETH PRODUCTION TO THE INNOVATIVE ONE

The term a*crylic tooth* is commonly used to describe a synthetic tooth that is generally made of three parts[1] which can differ in material and/or color, to best reproduce the three major tissues which make up the natural tooth: enamel, dentine and root.

[1]Depending on the quality of the artificial tooth, there could be a different number of parts: typically low-quality teeth are produced in two parts, medium-quality teeth in three parts and high-quality ones in four parts. The quality of an artificial tooth is mainly related to its surface hardness (and wear resistance) and on its look (the representation of labial striations or natural markings on a tooth and the necessary blend of color to give a natural appearance).

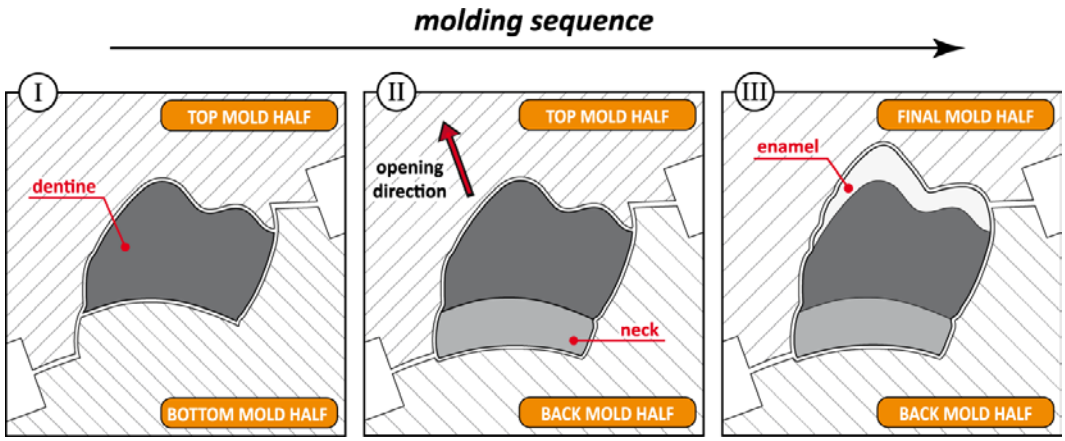


Figure 1. Steps in acrylic tooth manufacturing and corresponding molds.

With regard to manufacturing, to produce a tooth consisting of different layers,several molding stepsand molds are required. A single mold is composed by two monolithic halves, with no sliders because a proper orientation of the teeth figure allows us to easily solve undercut problems in the opening direction. Each intermediatemolding step involves the change of one mold half, since the other half is the same from the previous step. As shown in the schematic illustration of Figure 1, the first part produced is the dentine, that is the core of a tooth. The figures of *bottom mold half* and *top mold half* respectively shape the bottom and top surfaces of the core. Then the *bottom mold half* is replaced by *back mold half* to add the neck portion. Lastly the *top mold half* is swappedwith the *final mold half*, that forms the enamel layer. Usually molds for artificial teeth contain at least three sectors reproducing the same set of teeth (mandibular posterior teeth, mandibular anterior teeth, maxillary posterior teeth, and maxillary anterior teeth). Thus to realize a complete artificial denture, four series of molds are necessary. Moreover it can be observed that for common manufacturing rates,in order to meet the production demand, several sets of identical molds are used. Hence times related to the mold making

Figure 2. Final mold and molded sets of acrylic teeth with flash.

procedure are critical aspects beside the quality of the final part. A detailed description of the traditional and the innovative mold making procedures are presentedhereafter.

As shown in Figure 2, after the molding process, the teeth surface exhibits a flash that must be removed. This operation is fully automated if innovative molds are used, whereas a final hand-applied refining step is required after traditional molding, because of the bigger flash thickness. Finally the manual sorting step takes place: by visual examination the presence of defects (cracks, color …) is detected and teeth are divided by kind.

## 2.1. Traditional Mold Making Procedure

The traditional procedure of mold making requires skilled handcraftsmanship; it is very complex and time consuming. The molds are fabricated in the inverse order with respect to the teeth molding sequence: beginning from the final mold half backwards to the bottom one.

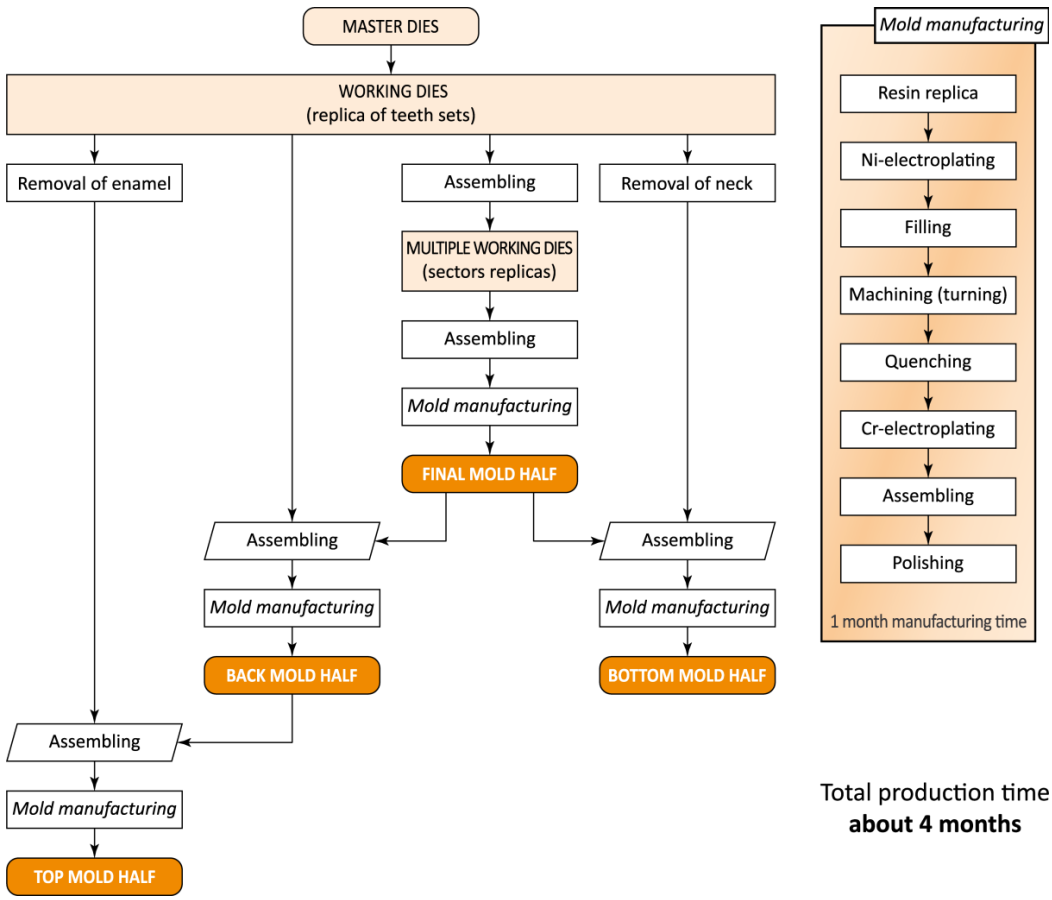


Figure 3. Flow chart of the traditional procedure for acrylic teeth manufacturing.

The starting point is the availability of individual *master dies* of a teeth set (Figure 3), which are used to produce several replicas made of resin (*working dies*). A first set of w*orking dies*isthen arranged on a template and replicated after impression to realize a

*multiple die*(that is one sector of the mold). Such *multiple die*is used to produce several replicas (*multiple working dies*) that are then assembled so thatmultipleidentical copies of the same teeth set can be fabricated by a single mold. From this assembly the final mold part is produced, by a procedure that involves the following steps:

- *Resin replica*: an impression of the assembled *multiple working dies* is taken of elastomeric material.Such impression is used to form a mandrel of resin;
- *Ni-electroplating*: the mandrel is sprayed with silver to acquire an electricalcharge and electroplated with Nickel to obtain a shell whose thickness is few millimeters;
- *Filling*: the electroplated shell is filled with a metal alloy to produce an insertwith improved strength;
- *Machining, Quenching, Cr-electroplating:* the insert is machined by turning, quenched and then Chromium-plated;
- *Assembling* and*Polishing*: the insert is mounted on an metallic frame, then the resultant mold is refined and hand polished. After inspection, it is referred as *final master mold*.

The next step is the production of the mold half used to produce the back of the artificial teeth. Sets of working dies are arranged on the *final mold half*. The *back mold half* is produced from this last assembly in the same way of the *final mold half*, that is by fabricating the epoxy mandrel, spraying, electroplating, assembling, quenching and hand- refining. At this point, the outer surface of the teeth is defined, but the boundary of the teeth cores should be still delineated. For this purpose, some *working dies* are filed to remove the enamel layer. Again, by the same procedure described above, the half mold that shapes the upper surface of the inner portion of the teeth (*top mold half*) is produced from the modified *working dies* arranged on the *back mold half*. The last mold that has to be produced is the one that forms the bottom surface of the teeth cores (dentine). At this aim, some *working dies* are filed to remove, in this last case, the tooth neck. These so modified *working dies* are then arranged on the *final master die* and from this assembly the *bottom moldhalf* is produced.

As already mentioned, several sets of molds are needed to meet the production rates and demands of the market. Thus exact copies of the four master molds are fabricated. Replicas are referred as *working molds* (Figure 4), since they are employed in manufacturing, while the masters are not. It takes approximately sixteen weeks to produce one set of master molds and six weeks to make working molds from them. As regards the quality of the working molds and consequently of the molded teeth, it must be remarked that:

- the conversion of the positive image from the master die into the negative image of the master mold involves at least six image reversals.Inevitably the sequential use of the replication process adversely affects the accuracy of the final mold and the one of the teeth;
- the limitations of the electroplating process have an impact on the copied geometry: it is very difficult to obtain an uniform thickness on free-form complex shapes, because the plating metal is well attracted by external corners and protrusions, while internal corners and recesses are arduously drawn. The use of specific tools or multiple anodes can minimize this effect, but the cost significantly increases;

- during molding process a minimum flash thickness of 0.5 mm is generated. This material has to be removed by an additional teeth finishing step.

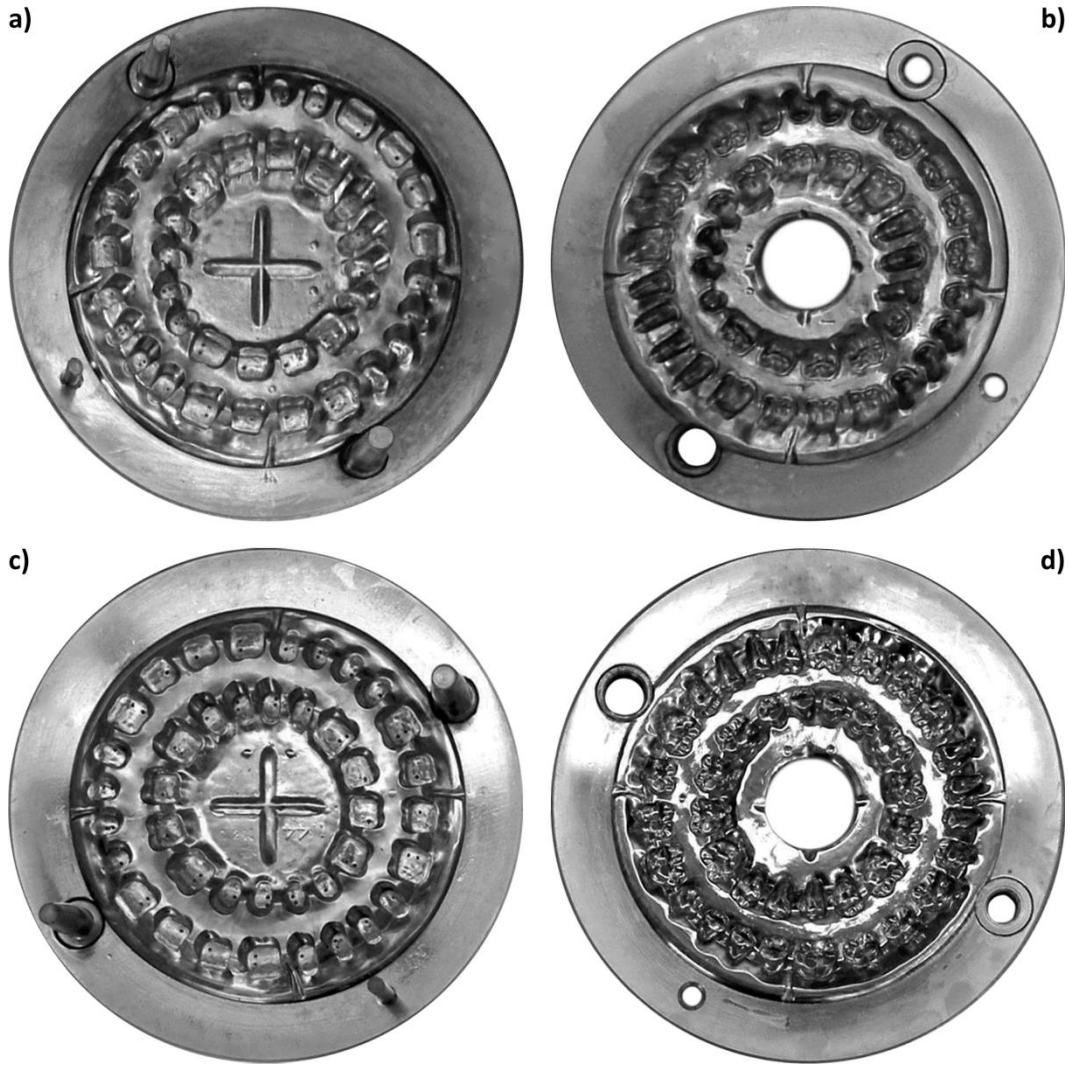


Figure 4. Sequence of working molds for the traditional production procedure
a) bottom mold half, b) top mold half, c) back mold half, and d) final mold half.

Moreover the electroplating waste management is extremely complex and expensive. A traditional mold normally has to be replaced within three years because of wear and consumption.

## 2.2. Innovative Mold Making Procedure

As can be appreciated from the previous description of the traditional method of teeth mold manufacturing, the process is lengthy, costly, and labor intensive. Recent developments

in computer aided technology offer new resources to overcome most of the limitations of the traditional production. The innovative procedure involves the integration of Reverse Engineering and CAD/CAM techniques.

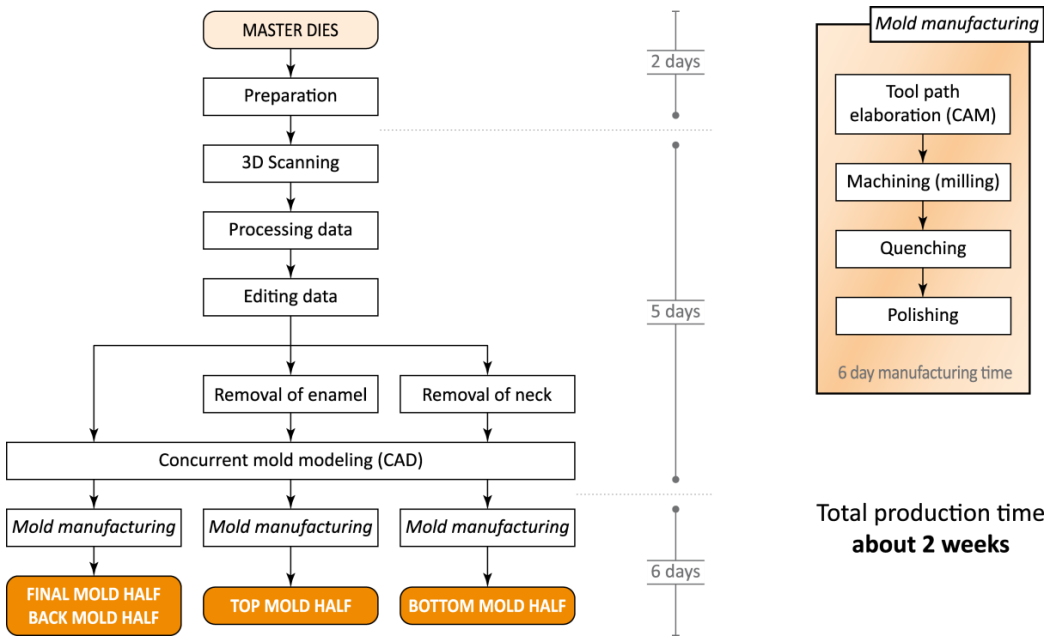


Figure 5. Flow chart of the innovative procedure for acrylic teeth manufacturing.

The starting point is the same as the conventional process: the availability of the master die of the teeth that have to be produced.This new mold making method includes the following steps (figure 5):

- *Preparation*: *master dies* are used to produce some replicas (*working dies*) made of opaque resin, able to be easily digitized;
- *3D scanning*: the three-dimensional surface of the *working dies* is scanned;
- *Processing data*: the point clouds are filtered, aligned and merged;
- *Editing data*: scan data are edited to create the mathematicalsurface of each tooth;
- *Concurrent molds design*: from the negative of several different teeth, the CAD models of the *back mold half* and the *final* one are designed by taking into account the volumetric contraction of the teeth during the molding cooling phase. The *top* and *bottom mold halves*are then obtained after *digital removal* from each tooth of enamel and neck respectively.
- *Mold manufacturing:* the machining tool paths are generated *(CAM),* the teeth molds are machined by five-axes NC milling (*Machining*) and then subjected to the required heat treatment (*Quenching*).The final refining phase includes thehand-applied finish/polish step (*Polishing*)

In this case no distinction is made between master and working molds, because each working mould is machined from the corresponding three-dimensional CAD model. This new

procedure involves less time and cost than the traditional one and does not require the skills of a master craftsman. An innovative mold (Figure 6) at a production rate of one million per year has an estimated life of more than fiveyears (due to the higher wearresistance of steel). So far, information about the quality of this new method of producing artificialteeth is lacking, thus more efforts are needed to quantify the error induced by each step of the manufacturing sequence.

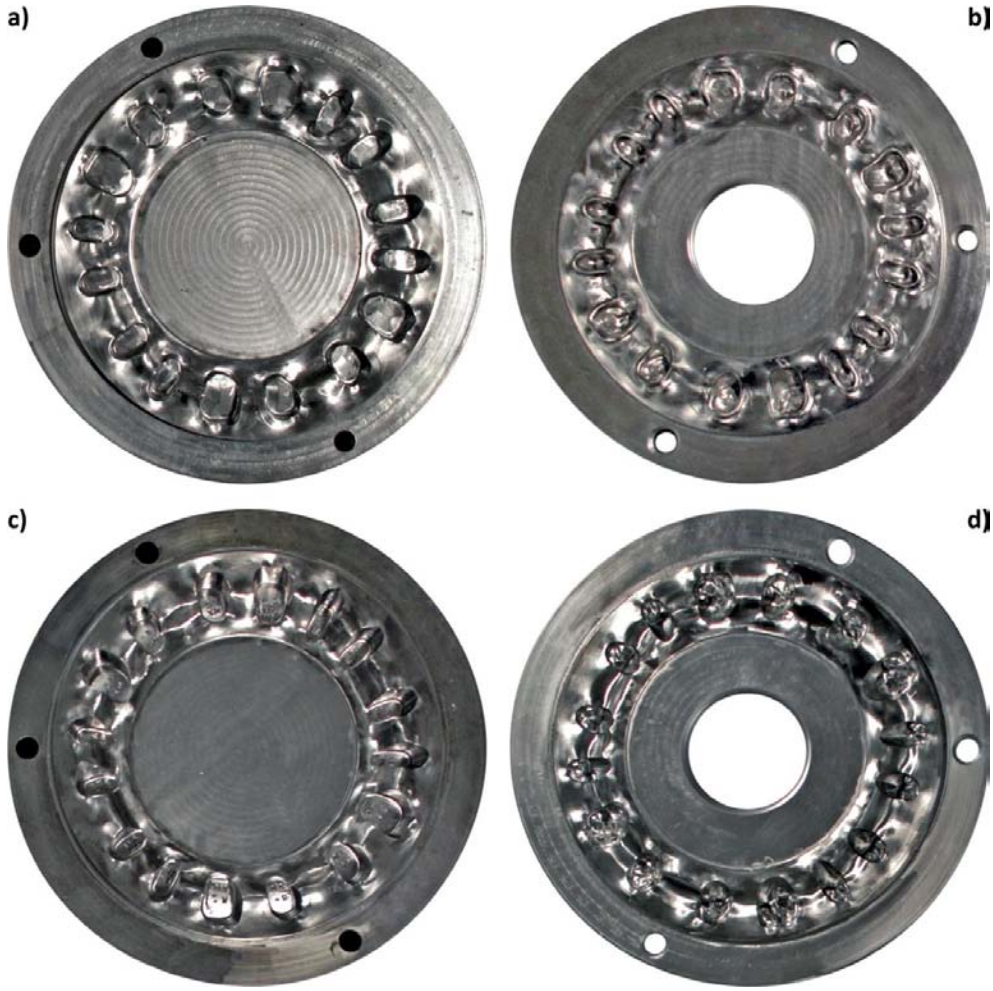


Figure 6. Sequence of molds for the innovative production procedure. a) bottom mold half, b) top mold half, c) back mold half, and d) final mold half.

## 3. Reverse Engineering for Quality Control

Until recently, the preferred way to perform inspections to evaluate dimensional and geometrical tolerances of products was by coordinate measuring machine (CMM), due to the high accuracy in measurements. The main limitation is the long time required to verify a large set of points on the surface, which is heightened for free-form surfaces. Some time has to be

spent for the set up of the inspection plan and the CMM measuring path as well. In contrast, three-dimensional scanners allowed to acquire complex surfaces in a very fast way, but with poor accuracy, limiting their interest on Reverse Engineering field. In the last years, a significant effort has been made to improve the performances of contactless scanning devices, both in terms of resolution and accuracy (Martinez *et al*. 2010). Today, improved repeatability and accuracy of three-dimensional scanners allow to use these devices for dimensional measurements. This means that RE tools can now be successfully applied to inspection activities, as an alternative to CMM in those application where complex shapes should be fast verified with an accuracy larger than few hundredths of millimeters (Iuliano *et al*. 2007, 2009 and Calignano *et al*. 2009). Moreover dense point clouds and the higher number of information obtained by digitizing devices in comparison to point-wise measurements allow to verify the whole surface of the inspected object. Scan data can be stored for new future evaluations, whereas new measurements by a CMM would require to reposition the part and set up a new probing program.

In dentistry, contactless scanners are preferred to contact digitizers because they require shorter scan times and they are adequate for even soft and brittle materials (Persson *et al*. 2006). Nowadays, three-dimensional optical scanners specifically developed for dental applications are available on the market. They can be classified as intra-oral or extra-oral scanning devices. The latter, which require an impression taking and model production procedure, are still more accurate and thus the stone replica is normally digitized (DeLong *et al*. 2003). These indirect systems are designed for scanning a single tooth as well as a completedental arch and scan data is used to create a virtual model of the oral cavity of the patient for the design of dental prosthesis or orthodontic devices(DeLong *et al*. 2003, Kournetas *et al*. 2004).

It could be concluded that the use of Reverse Engineering tools in dental applications is also best suitedfor quality control (Atzeni *et al*. 2009a, 2009b). However, nowadays contactless dental scanners, optimized for scanning positive teeth replicas, present some limitations when digitizing the negative shape of cavities having high depth/aperture ratio (typical of teeth geometries). Moreover the working volumes of dental scanners is large enough to digitize articulated models, but not adequate for scanning teeth molds. Therefore general purpose scanning devices have to be employed for molds digitizing.

From the perspective of the work illustrated in this chapter, that is the evaluation ofthe quality of the innovative procedure for artificial teeth production, two devices were selected among contactless scanners available on the market:DentalWings and GOM ATOS III. The former is specific for the indirect digitization of teeth and dental arches. The latter is a general purpose scanner, whose scanning volume can be adjusted for different object sizes, and so it is adequate for both teeth and molds digitizing. In such a way, a comparison of scanners performance was also possible with respect to teeth inspection.

## 3.1. Dentalwings and ATOS III

DentalWings (Figure 7) is a laser scanner specifically developed for dental applications and fabricated in Canada by the homonymous company. The contactless scanning device exploits laser triangulation in a fix scanning working volume of 140 × 140 × 95 mm. Up to 100,000 points are measured per single dies scan (up to 1,000,000 points per full dentalarch)

and the declared accuracy on the device data sheet is 20 µm. Thanks to thesynchronized 5-axes rotary table, in one scan multiple views are merged into one point cloud automatically. It takes a bit more than one minute to scan a tooth. The standard output format is STL. The diffusion of this system on the market was made easy thanks to the availability of proprietary applications that full integrate the scanning environment and the "Crown & Bridge" design modules.

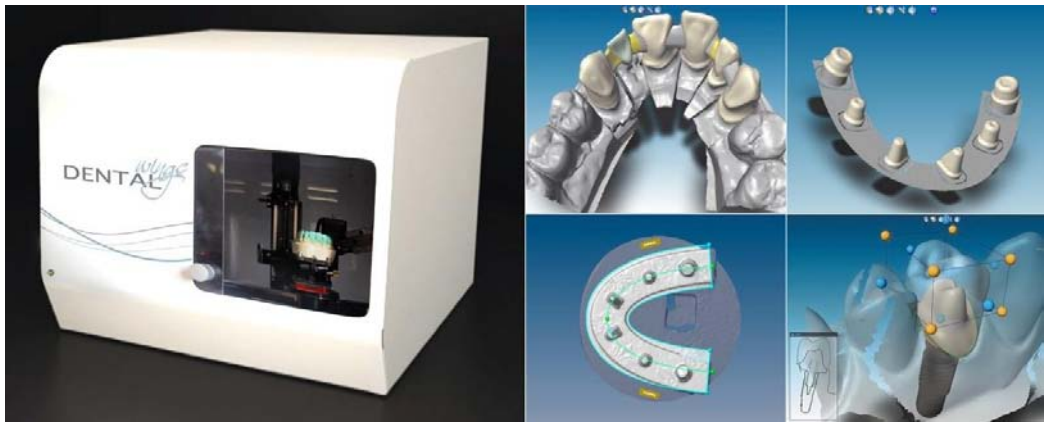


Figure 7. DentalWings laser scanner for dental applications.

Figure 8. ATOS III general purpose structured light scanner.

ATOS III (Figure 8) is a general purpose structured light scanner produced in Germany by GOM GmbH. It exploits binocular vision as it has two built-in 4Mpixel CCD cameras, which store images of the light fringes projected on the scanned object. The projector, placed in the centre of the sensor, projects a sequence of four interference patterns – phase-shift technique (Wang *et al*. 1996, Gühring 2001) – followed by six Gray coded binary images (Pagès *et al*. 2003). The scanner is VDI/VDE 2634 certified for inspection performances and the accuracy declared on the device data sheet is 20 µm, the same as DentalWings. Reference points are applied on the scanning object sticking adhesive targets (markers). Each scan takes about two seconds and multiple scans are automatically registered into one point cloud, as the scanning software recognizes the reference grid created by markers. Scan area can be adjusted

to the object size, from 150 × 150 mm to 1000 × 1000 mm, simply changing the projector and cameras lenses.

## 3.2. Evaluation Procedure

From the design of the mold (derived from the CAD model of each tooth) to the final teeth, the manufacturing sequence involves first the manufacturing of molds and then the molding and finishing of teeth. Each of these steps inevitably introduces a deviation. In order to control the whole process it is therefore necessary to evaluate each of the above-mentioned steps. However, only the molds used in the final phase of teeth fabrication affect the final shape and tolerance. Thus the investigation could be narrow down to the analysis of the last couple (*back* and *final*) of molds only.

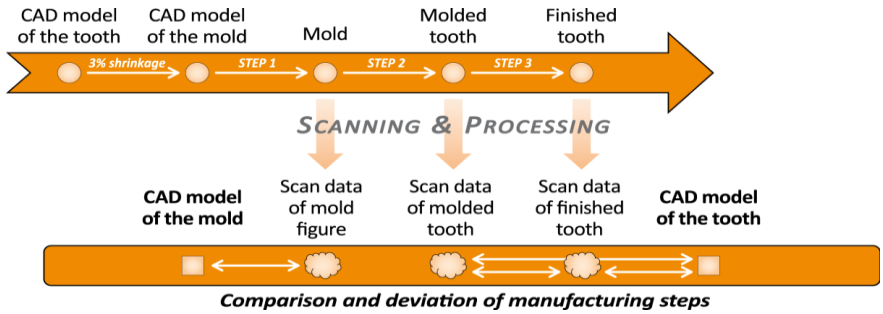


Figure 9. Procedure for evaluating the deviations introduced by each manufacturing step.

The procedureproposed for evaluating the dimensional deviations introduced by each manufacturing step, is detailed in Figure 9.Both the two contactless digitizing devices, described in the previous paragraph,areused for the inspection of teeth, whereas the geometry of the molds can be only acquired by means of ATOS III. For the first step, that is mold manufacturing, the ATOS III scan data of the back mold and the final one are compared with the corresponding original CAD models. The comparison could be limited to the mold active area that is to each tooth cavity plus the neighboring adjusted closing plane of the mold. Comparison is then made by means of a specific commercial RE inspection software(such as Rapidform, Geomagic, PolyWorks, etc.) after best fit registration of the compared freeform surfaces. Results are reported in terms of deviation average value, standard deviation and maximum value. Nevertheless maximum deviations are not significant as they refer to isolated single points or very small areas. The comparison allows evaluating the manufacturing error of mold surfaces for each sector. As a matter of fact, mold scan data are representative of the actual geometry of the mold after its fabrication.

To evaluate the teeth molding tolerances, the scan data of the molded molars are compared with the original CAD model of the teeth. Modifications introduced by the finishing operation are evaluated by comparing the scan data of the molars before and after that third production step. The overall deviations of the whole fabrication procedure of the acrylic teeth are computed by means of the comparison between the scan data of the finished molars and their original CAD model.

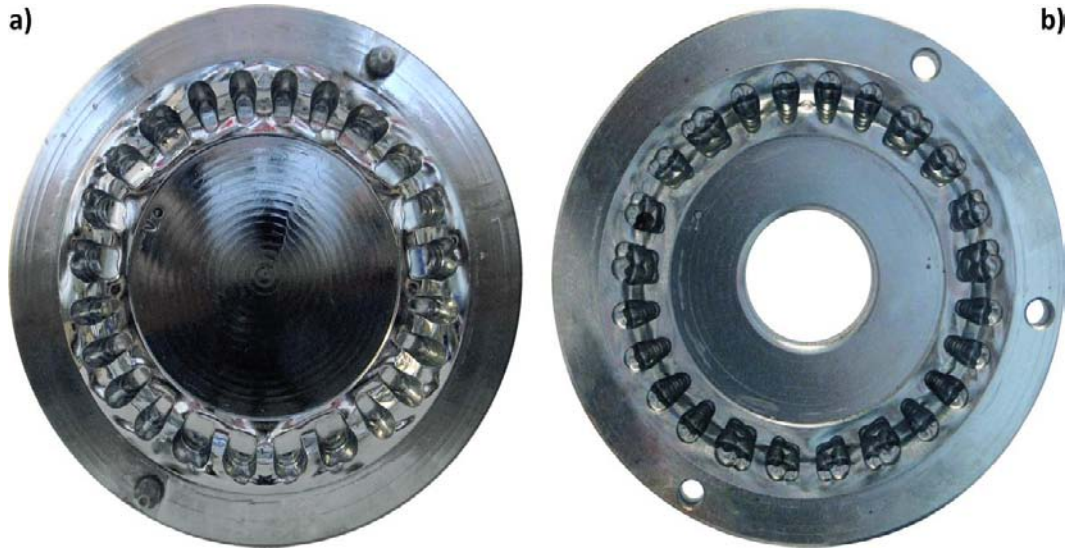


Figure 10. a) back and b) final mold halves selected as case study (diameter 130 mm).

## 4. CASE STUDY

Machined *back* and *final mold halves* for the final phase of acrylic posterior teeth fabrication were selected as case study (Figure 10), as well as two molded molars, taken as manufacturing samples. The right second molar tooth (Figure11) and the left one (teeth 17 and 27 according the FDI World Dental Federation notation), were selected and analyzed before and after the finishing operation.From the occlusal view, the second molar is almost squared in outline. There are four cusps and grooves that meet at a right angle to form the distinctive four sectors of this tooth.

The original CAD models of both the mold and the molars were used as reference geometry to evaluate the deviations.Each mold contains three sectors reproducing the same maxillary posterior teeth.For convenience back mold sectors are clockwise numbered and the first one is oriented along the vertical direction of Figure 12 (Y axis of the CAD reference system). The final mold is counter-clockwise numbered to have the same number for corresponding sectors.

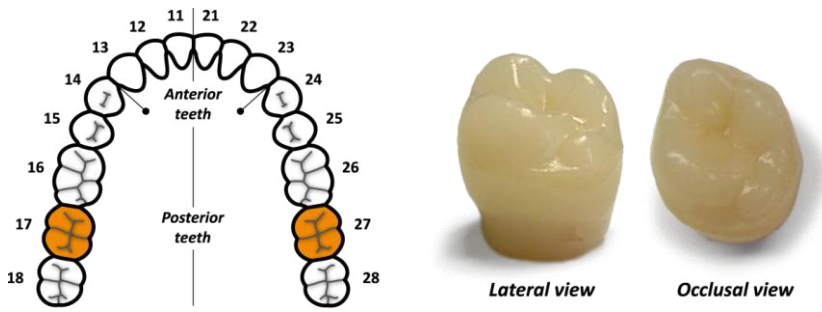


Figure 11. Right and left second molars selected as case study (8.5 × 8.8 × 9.8 mm).

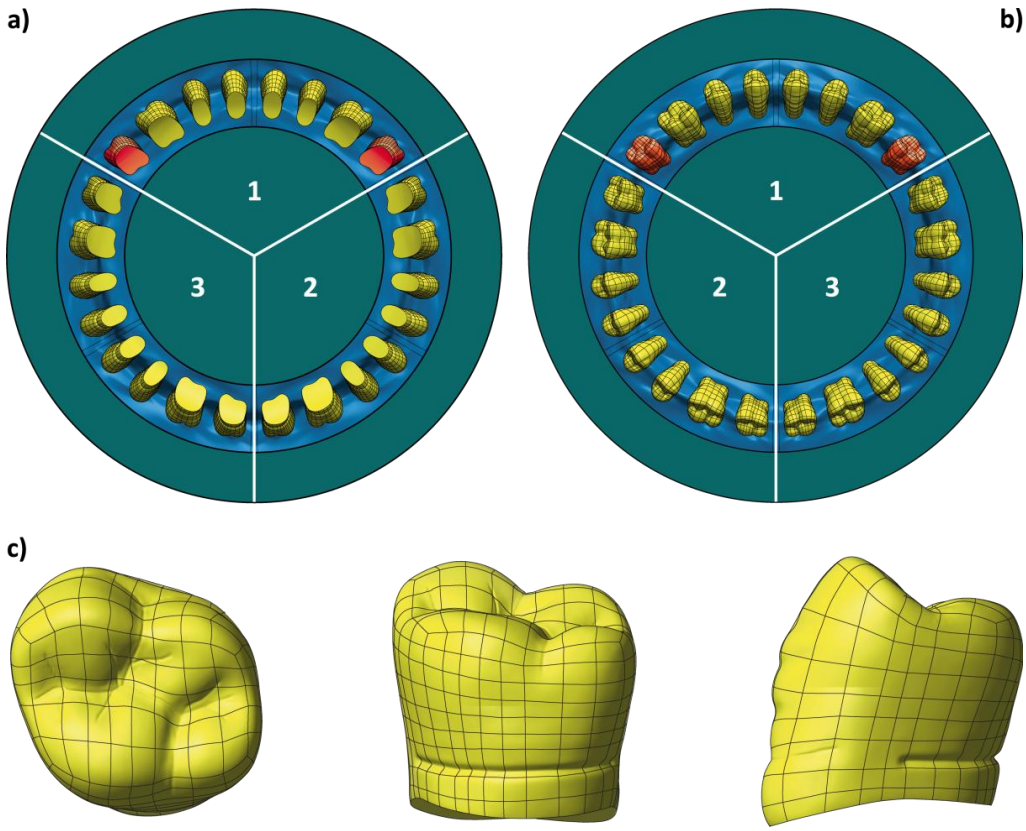


Figure 12. CAD models: a) back mold half, b) final mold half, and c) maxillary second molar.

The inspection procedure was applied on the following objects:

- selected teeth molds;
- molars 17 and 27 (extracted from the first mold sector) before polishing (in the following referred as molded molars);
- final molars 17 and 27 (the same as above) after finishing.

Prior to scanning, a thin layer of white opaque powder was sprayed on the surfaces of the mold and the two molars, in order to avoid light reflection and to improve the contrast. The number of scans needed to completely digitize the mold and the teeth by means of the two scanners are listed in Table 1. Digitizing time includes time spent for opaque powder spraying and data post-processing. The time for scanning teeth by ATOS III is twice the time required by DentalWings. The first device automatically aligns and merges multiple views, each one obtained by a single scan. Because the evaluation procedure proposed involves the comparison of the whole surface of teeth, a large number of scans is needed. Consequently, in spite of the short scanning time, the manual repositioning of the object or the scanner for a new view is time expensive and thus notably affects the total scanning time. Due to the small dimensions of a tooth, the minimum ATOS III scanning area was employed for digitizing the mold and the teeth.

**Table 1. Molds and teeth digitizing time.**

| Device | Scan object | Numbers of scans | Digitizing time*(min)* |
|---|---|---|---|
| ATOS III | Final mold half | 19 | 110 |
| | Back mold half | 13 | 90 |
| | Molded teeth 17/27 | 16 | 20 |
| | Finished teeth 17/27 | 16 | 20 |
| DentalWings | Molded teeth 17/27 | 16 | 20 |
| | Finished teeth 17/27 | 16 | 20 |

**Table 2. Scanning devices costs.**

| Device | Investment cost*(EUR)* | Hourly cost (scanning)*(EUR/hour)* |
|---|---|---|
| ATOS III | 150,000 | 150 |
| DentalWings | 20,000 | 50 |

**Table 3. Final mold half deviations:ATOS III scan data *vs*. mold CAD model.**

| Mold | Absolute deviation (*mm)* | | | Signed deviation *(mm)* | | | |
|---|---|---|---|---|---|---|---|
| sector | Av. | SD | Max | Av. | SD | Min | Max |
| 1 | 0.02 | 0.02 | 0.36 | 0.01 | 0.03 | -0.36 | 0.29 |
| 2 | 0.02 | 0.03 | 0.34 | -0.01 | 0.04 | -0.29 | 0.34 |
| 3 | 0.02 | 0.02 | 0.39 | 0.01 | 0.03 | -0.39 | 0.25 |

On the contrary, DentalWings captures the whole working area in one scan usingthe synchronized rotary table. Since the tooth surface placed on the device table cannot be digitized, a second scan is needed after reversing the object top-down to obtain the complete three-dimensional model of the tooth. Human intervention is only needed in this reversal of the tooth top-down for the second scan. Alignment and merging of the two point clouds are additional operations that in this study were carried out by means of Rapidform software and they took most of the time specified in Table 1 (10 minutes). Mold part digitization required 90 to 110 minutes by ATOS III from the dimming to the complete virtual model. The time difference between the two mold parts is mainly due to the higher complexity of occlusal surfaces of the face part that requires more scans. The costs for the two selected scanning systems are listed in Table 2.

**Table 4. Back mold half deviations:ATOS III scan data *vs*. mold CAD model.**

| Mold | Absolute deviation (*mm)* | | | Signed deviation *(mm)* | | | |
|---|---|---|---|---|---|---|---|
| sector | Av. | SD | Max | Av. | SD | Min | Max |
| 1 | 0.04 | 0.05 | 0.38 | 0.01 | 0.06 | -0.35 | 0.38 |
| 2 | 0.04 | 0.05 | 0.39 | 0.02 | 0.06 | -0.39 | 0.35 |
| 3 | 0.04 | 0.05 | 0.38 | -0.01 | 0.07 | -0.37 | 0.38 |

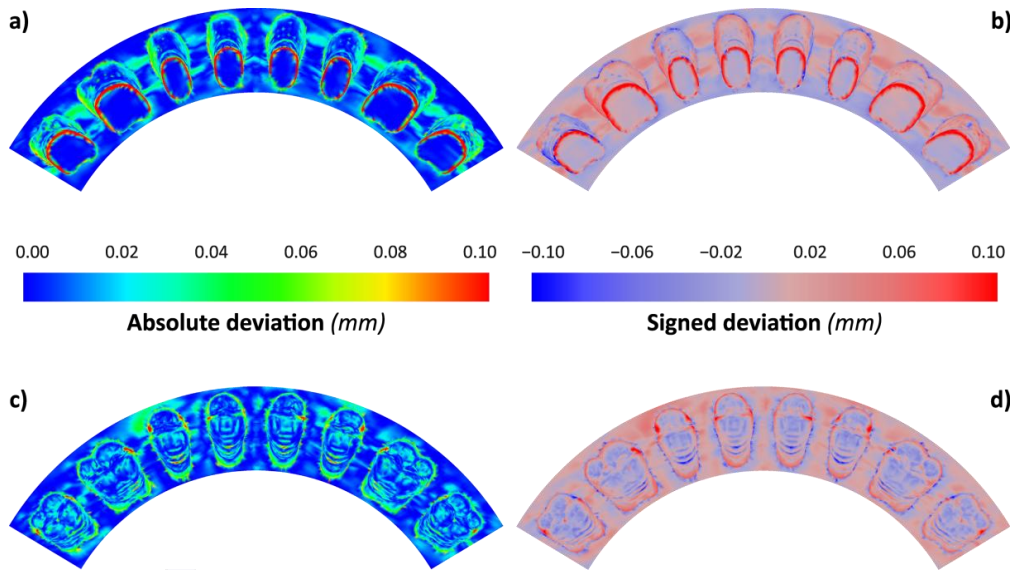


Figure 13. Maps of deviation: first sector of the final mold half (a, b) and back one (c, d).

As regards mold inspection, Rapidform software was used and the results of the comparisons between ATOS III scan data and the mold CAD model are reported for each of the three sectors in Tables 3-4 in terms of absolute deviation.

Deviations of this first manufacturing step can be also visualized as colored maps in Figure 13, both in absolute value and with sign. The average absolute deviation of the final mold half is comparable with the scanner accuracy, so the dimensional error induced by milling is lower or at worse equal to the value listed in Table 3. Such result allows to attest the high quality of the machined mold. Higher deviations are located on sharp edges, because sharp feature definition is an acknowledged limit of contactless scanners.Thus, sharp edges are acquired as chamfersand consequently in the colored maps of Figure 13b and 13d, representing the deviation with sign, external corners are blue (negative) whereas internal corners are red (positive). This fact also explains the difference between the final mold half and the back one in terms of average deviation. In fact the cavity of the back mold half contains the tooth planar base, whose boundary is a sharp edge.

In the second manufacturing step, the teeth are fabricated by molding. Deviations introduced by such process are computed by comparing the molars scan data with the tooth CAD model. Results are shown in Table 5.

**Table 5. Deviations between molded teeth surface and the teeth CAD model**

| Scan data | Tooth | Absolute deviation *(mm)* | | | Signed deviation *(mm)* | | | |
|---|---|---|---|---|---|---|---|---|
| | | Av. | SD | Max | Av. | SD | Min | Max |
| ATOS III | 17 | 0.09 | 0.09 | 0.50 | 0.05 | 0.12 | -0.50 | 0.47 |
| | 27 | 0.07 | 0.08 | 0.50 | 0.04 | 0.10 | -0.50 | 0.36 |
| DentalWings | 17 | 0.08 | 0.09 | 0.50 | 0.06 | 0.12 | -0.50 | 0.49 |
| | 27 | 0.07 | 0.08 | 0.50 | 0.04 | 0.12 | -0.50 | 0.36 |

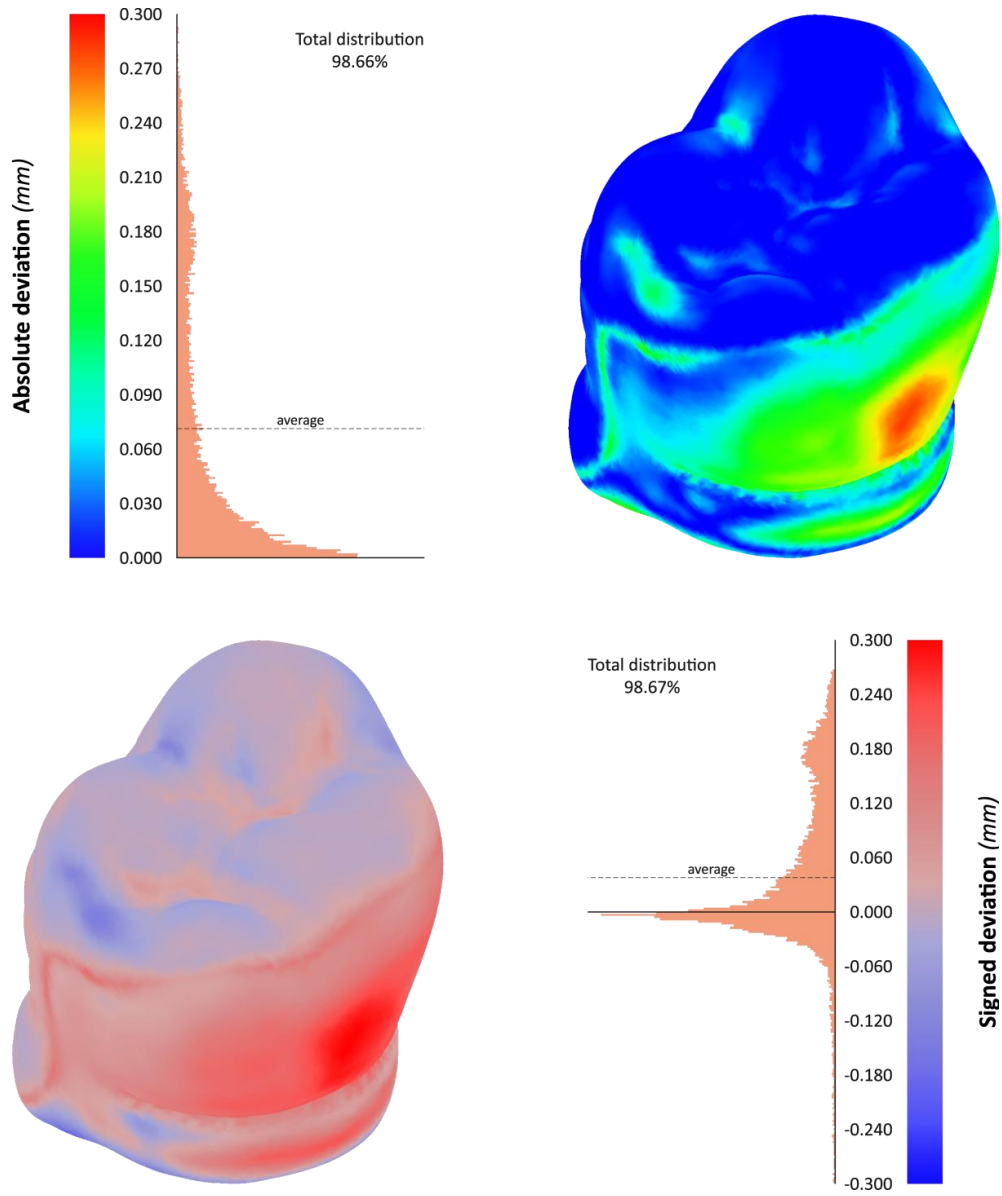


Figure 14. Maps of deviation between molded molar 27 and its CAD model.

The colored map of Figure 14 shows that on the occlusal surfaces deviations are lower than 0.07 mm with an average value of about 0.03 mm. These values satisfy the tolerance of the tooth molding process, that is on the order of few tenths of millimeter. Higher deviations are located on the lateral surfaces of the teeth, where flash is present. As shown in Figure 14 the scanned geometry is slightly bigger than the CAD model. The allowance is required for the following finishing operation.

**Table 6. Deviations between teeth surface before and after finishing operation**

| Scan data | Tooth | Absolute deviation (*mm*) | | |
|---|---|---|---|---|
| | | Av. | SD | Max |
| ATOS III | 17 | 0.03 | 0.04 | 0.33 |
| | 27 | 0.03 | 0.03 | 0.31 |
| DentalWings | 17 | 0.04 | 0.05 | 0.29 |
| | 27 | 0.05 | 0.04 | 0.27 |

**Table 7. Deviations between finished teeth surface and teeth CAD model**

| Scan data | Tooth | Absolute deviation (*mm*) | | | Signed deviation (*mm*) | | | |
|---|---|---|---|---|---|---|---|---|
| | | Av. | SD | Max | Av. | SD | Min | Max |
| ATOS III | 17 | 0.07 | 0.05 | 0.30 | 0.05 | 0.08 | -0.30 | 0.28 |
| | 27 | 0.07 | 0.07 | 0.45 | 0.05 | 0.09 | -0.15 | 0.45 |
| DentalWings | 17 | 0.08 | 0.08 | 0.50 | 0.03 | 0.11 | -0.50 | 0.28 |
| | 27 | 0.09 | 0.09 | 0.50 | 0.02 | 0.14 | -0.50 | 0.25 |

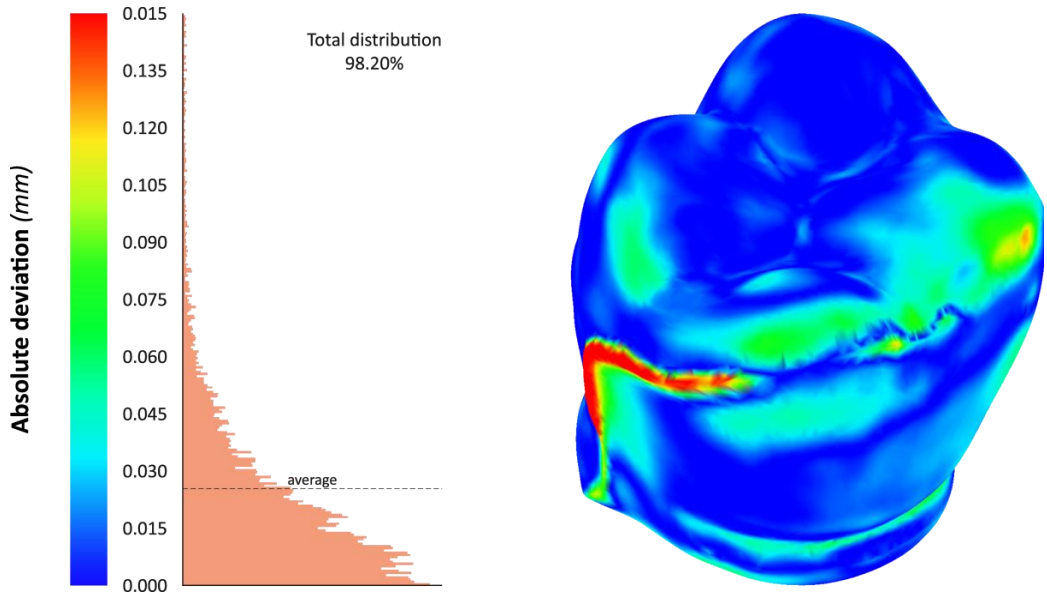


Figure 15. Map of absolute deviation between the finished and the molded molar 27.

The last manufacturing step involves the finishing of teeth surfaces. Such operation introduces the deviations listed in Table 6 on the molars geometry. Scan data of the molars before and after finishing are compared. The finishing operation is concentrated on the flash area, that is a small portion of the tooth surface. This is the reason of the low values of the average deviations in Table 6. The color map in Figure 15 shows that deviations on the flash surfaces are higher.

At the end, the total deviation of the molars is evaluated by comparing the scan data of the finished teeth with their original CAD model. Results are listed in Table 7.

The average deviations of the finished tooth with respect to the CAD model, shown in Figure 16, are comparable with those of Table 5. The flash is now removed, so the error associated with the corresponding area is reduced.

The comparison between ATOS III and DentalWings scan data was carried out for the finished teeth. Results shown in Table 8 and Figure 17, together with the preceding ones, allow to assess that the difference between the two scanners is negligible. The average value of the difference is again comparable with the systems accuracy.

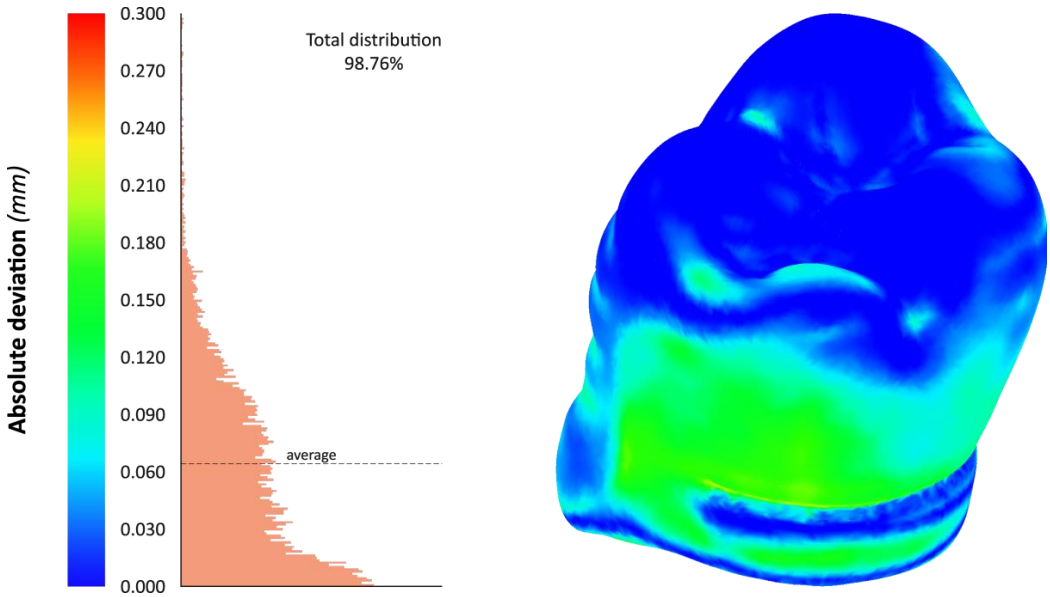


Figure 16. Absolute deviation map of the finished molar 27 *vs*. CAD model.

## CONCLUSION

The diffusion of RE techniques in dentistry has introduced innovative procedures, based on CAD/CAM, for producing acrylic teeth molds. A procedure to evaluate the quality ofteeth fabricated by NC milled molds was illustrated in this chapter. The proposed procedure was applied to a mold and a couple of molded molars, selected as case study. Two contactless scanners were employed for their inspection and the deviations of mold and teeth geometry were computed for each manufacturing step.

**Table 8. Deviations between ATOS III and DentalWings scan data for the finished teeth**

| Tooth | Absolute deviation *(mm)* | | |
|---|---|---|---|
| | Av. | SD | Max |
| 17 | 0.02 | 0.02 | 0.21 |
| 27 | 0.01 | 0.01 | 0.17 |

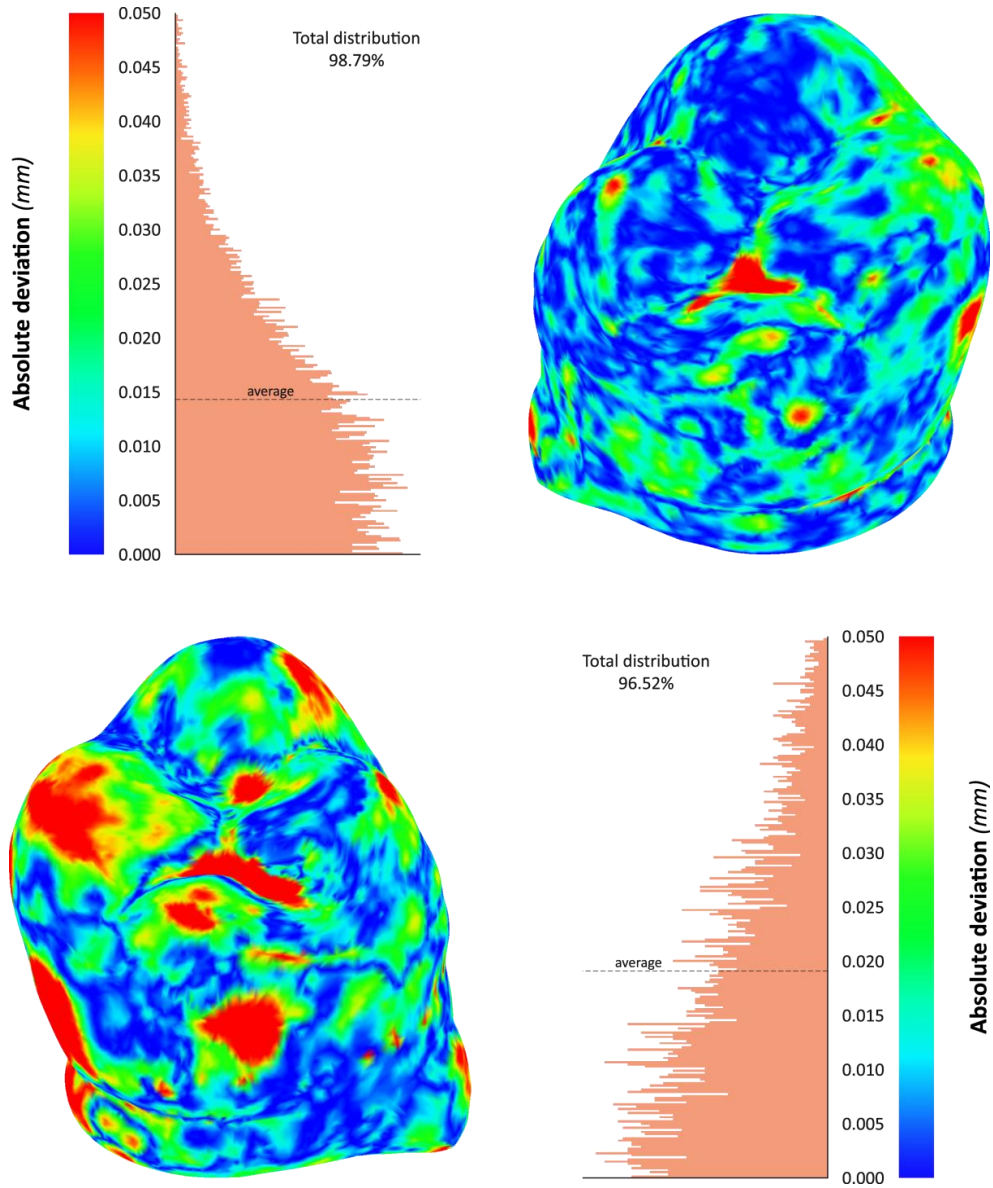


Figure 17. Maps of absolute deviation between ATOS III and DentalWings scan datafor finished molar 27 (above) and molar 17 (below).

Both employed scanning devices are adequate and suitable for teeth digitizing and inspection, as the declared accuracy is the same. The results of this study confirm it. Nevertheless DentalWings device, that was specifically designed for the dental sector, ispreferable to the general purpose ATOS III scanner for several reasons. First of all for the investment cost: 20,000 EUR for DentalWings versus 150,000 EUR for ATOS III. The ease of use of DentalWings is higher, since the single scanning phase is automated (even if scan data from the two positionings of the teeth on the device table have to be merged together). ATOS III requires a trained user for carrying out the scanning. Finally DentalWings is faster:

the whole working volume is acquired in a few seconds, that is several teeth can be digitized at the same time. The automated merging of different scans in ATOS III requires a new positioning of the tooth for each shot, so the scanning process is longer. As regards impressions or molds, at the moment, dental scanners are not suitable for scanning negative shapes. Thus, general purpose devices like ATOS III have to be employed, despite the higher times and costs. In the future, the development of dental scanners will probably make them suitable for this application as well.

The overall deviations evaluated for teeth manufacturing by the innovative machined mold are below the product specifications. As a matter of fact, current techniques for the fabrication and implant of dental prosthesis require manual adjusting operations with tolerances that are on the order of tenths of a millimeter. From the perspective of limiting potential sources of dimensional deviations, a new interesting improvement considers the use of hardened steels as raw material for the mold machining operation. In such a way, the quenching treatment is no longer required and molds are not subjected to dimensional variations induced by the thermal cycles.

## REFERENCES

Atzeni, E., Gatto, A., Iuliano, L., Minetola, P., & Salmi, A. (2009a). Artificial teeth manufacturing: inspection of mould and teeth by contactless scanning systems. In: Bartolo, P.J. *et al.* (Eds), *Innovative Developments in Design and Manufacturing* (pp. 131-136). Leiden: CRC Press.

Atzeni, E., Gatto, A., Iuliano, L., Minetola, P., & Salmi, A. (2009b). A benchmark for accuracy evaluation of dental crowns up-to-date manufacturing. In: Bartolo, P.J. *et al.* (Eds), *Innovative Developments in Design and Manufacturing* (pp. 425-430). Leiden: CRC Press.

Calignano F., & Minetola, P. (2009). Comparison of structured light scanners: a test beyond current guidelines. In: *Proceedings of 9th AITeM Conference*

DeLong, R., Heinzen, M., Hodges, J.S., Ko, C.C., & Douglas, W.H. (2003). Accuracy of a system for creating 3D computer models of dental arches. *Journal of Dental Research* 82(6), 438-442

Gühring, J. (2001). Dense 3-D surface acquisition by structured light using off-the-shelf components. Videometrics and Optical Methods for 3D Shape Measurement, San José, CA, *Proc. SPIE* 4309, 220-231.

Iuliano, L., & Minetola, P. (2007). Comparison of 3D scanner based on an innovative benchmark for computer aided inspection. In: *Proceedings of 8th AITeM Conference*

Iuliano, L., & Minetola, P. (2009). Enhancing moulds manufacturing by means of Reverse Engineering. *International Journal of Advanced Manufacturing* Technology 43, 551-562

Kournetas, N., Jaeger, B., Axmann, D., Groten, M., Lachmann, S., Weber, H., & Geis-Gerstorfer J. (2004). Assessing the Reliability of a Digital Preparation Assistant System Used in Dental Education. *Journal of Dental Education* 68(12), 1228-1234.

Martínez, S., Cuesta, E., Barreiro, J., & Álvarez, B. (2010) Analysis of laser scanning and strategies for dimensional and geometrical control. *International Journal of Advanced Manufacturing Technology* 46, 621–629.

Pagès, J., Salvi, J., García, R., & Matabosch, C. (2003). Overview of coded light projection techniques for automatic 3D profiling. *IEEE International Conference on Robotics and Automation ICRA*, Taipei, Taiwan, 133-138.

Persson, A., Andersson, M., Odén, A., & Sandborgh-Englund, G. (2006). A three dimensional evaluation of a laser scanner and a touch-probe scanner. *Journal of Prosthetic Dentistry* 95, 194-200.

VDI/VDE 2634-3 (2008). Optical 3D-measuring systems - Multiple view systems based on area scanning.

VDI/VDE 2634-2 (2002). Optical 3D-measuring systems - Optical systems based on area scanning.

VDI/VDE 2634-1 (2002). Optical 3D measuring systems - Imaging systems with point-by-point probing.

Wang, Z., Braynstone-Cross, P.J., & Whitehouse, D.J. (1996). Phase difference determination by fringe pattern matching. *Optics & Laser Technology* 28(6), 417-422.

Williams, R. J., Bibb, R., & Rafik, T. (2004). A technique for fabricating patterns for removable partial denture frameworks using digitized casts and electronic surveying. *The Journal of Prosthetic Dentistry* 91(1), 85-88.

Wu, M., Tinschert, J., Augthun, M., Wagner, I., Schädlich-Stubenrauch, J., Sahm, P.R., & Spiekermann, H. (2001). Application of laser measuring, numerical simulation and rapid prototyping to titanium dental castings, *Dental Materials* 17, 102-108.

# INDEX

## C

## D



## E

## F



## G

## H



## I



## J



## K

## L



## M

## N



## O



## P

## Q



## R



## S

## T



## U

## V



## W



## X



## Y